A Reproduced Copy

FOREWORD

This research was carried out by the Aeroelastic and Structures Research Laboratory, Department of Aeronautics and Astronautics, Massachusetts Institute of Technology, Cambridge, Massachusetts under NASA Grant No. NGR 22-009-339 from the Lewis Research Center, National Aeronautics and Space Administration, Cleveland, Ohio 44135, as part of the NASA Rotor Burst Protection Program. Dr. Arthur G. Holms and Mr. Solomon Weiss of NASA-LeRC served as technical monitors. The valuable advice and cooperation from these individuals is acknowledged gratefully.

For their effort, advice, and cooperation in carrying out tests and furnishing data on T58 turbine rotor tri-hub rotor-burst impact tests against containment rings at the Naval Air Propulsion Test Center (formerly NAPTC but now called NAPC), Trenton, New Jersey, and for their valuable comments and corrections offered in reviewing our discussion of some of that data in Sections 3 and 4 of this report, we wish to acknowledge appreciatively the help of Mr. G.J. Mangano, Mr. J.T. Salvino, and Mr. R.A. DeLucia of the NAPC.

The senior authors wish to point out that Appendix B and much of Section 6 was contributed by Mr. J.J.A. Rodal.

This manuscript was originally released for review to NASA-Lewis in August 1978.

The use of SI units (NASA Policy Directive NPD 2220.4, September 14, 1970) was waived for the present document in accordance with provisions of paragraph 5d of that Directive by the authority of the Director of the Lewis Research Center.

CONTENTS

LIST OF ILLUSTRATIONS

ILLUSTRATIONS--CONTINUED

ILLUSTRATIONS--CONTINUED

ILLUSTRATIONS--CONTINUED

ILLUSTRATIONS—CONTINUED

ILLUSTRATIONS--CONTINUED

ILLUSTRATIONS--CONTINUED

LIST OF TABLES

SUMMARY

Investigated in this study are finite-element modeling alternatives as well as the utility and limitations of the 2-D structural response computer code CIVM-JET 4B for predicting the transient large-deflection elastic-plastic structural responses of 2-D beam and/or ring structures which are subjected to rigid-fragment impact. These matters were assessed in a sequence of computer runs and by comparing predictions with experimental transient-response and permanent deformation data obtained for 6061-T651 aluminum beams with both ends clamped and subjected to perpendicular impact at midspan by a solid steel sphere. Investigated next was the applicability of the CIVM-JET 4B analysis and code for the prediction of steel-containment-ring response to impact by complex deformable fragments from a tri-hub burst of a T58 turbine rotor; corresponding experimental measurements were provided for comparison by the Naval Air Propulsion Test Center (NAPTC).

In another aspect of this study, dimensional analysis considerations were used in a parametric examination of (a) data from engine rotor burst containment experiments conducted by the NAPTC and (b) data from sphere-beam impact experiments carried out by the MIT-ASRL. The use of the CIVM-JET 4B computer code for making parametric structural response studies on both fragment-containment structure and fragment-deflector structure has been illustrated. A judicious combination of a few selected experiments plus the use of a computer code such as CIVM-JET 4B for parametric and tradeoff studies are believed to represent an effective procedure for the design of 2-D fragment-containment and/or fragment-deflector structure.

Since the CIVM-JET 4B computer code as actually implemented accommodates large-deflection, elastic-plastic, transient structural responses but only small strain, some modifications to the analysis/computation procedure have been developed to alleviate this restriction. Some preliminary exploratory results thereby obtained are presented.

SECTION 1

INTRODUCTION

Engine rotor burst fragments may impact against the engine casing and/or against special protective structures. These structures may be intended either to contain or to divert the fragment and to allow it to escape along a "harmless" path; the respective behavior is termed as being either fragment containment or fragment deflection. Of principal interest in this report is the theoretical prediction of the transient responses of container or deflector structures (C/D structures) which are subjected to fragment impact. Further, attention shall be restricted to single-layer metallic protective structures; consideration of multilayer multimaterial protective structures is beyond the intended scope of this report.

If the dimension of the protective structure in the direction of the axis of rotation of the turbojet engine is comparable to the corresponding dimension of the attacking-fragment, the deflections of the impacted structure will be essentially the same at all locations along that axial direction; in this case, the deformation is termed two-dimensional (2-D). However, if that protective-structure dimension is large in the above comparative sense, the structure will undergo general three-dimensional (3-D) structural deflections. In general, theoretical predictions of each of these two types of transient structural deflection should employ a theoretical model which can accommodate each of these types of behavior.

However, for preliminary design and parametric studies of prospective C/D structures, it is often useful to idealize the structural behavior as being, in fact, two-dimensional. An idealized model of this kind is indicated schematically in Fig. 1 where the actual structure which supports the C/D structure is represented by a "foundation" of normal and tangential springs; also, various end-support conditions can be accommodated in this type of idealized 2-D model. This type of model tends to include the main structural response features while minimizing the computational burden. Accordingly, a series of 2-D structural response codes for partial and/or complete rings of arbitrary initial shape, with uniform or nonuniform

thickness, and subjected to initial-velocity distributions, prescribed externally-applied loads, or fragment impact has been developed. The capabilities and features of these computer codes [1-5]* have been summarized in Ref. 6. Discussed later in this report is the application of two of these codes for the analysis of some example fragment-structure impact problems.

For structural response conditions wherein the use of a 2-D idealization is an excessive over-simplification and where one seeks to predict the response in greater detail, the structure needs to be modeled as a shell (with stiffeners, if present) [7-9] to permit accounting properly for the 3-D shell structural deflections which are present. On the other hand, an excessively fine modeling such as the use of 3-D solid elements to represent a single-layer shell, stiffeners, etc. leads to an excessive computational burden for many purposes. Hence, "shell-behavior modeling" serves as a logical next improvement over 2-D modeling of C/D structures. Accordingly, theoretical prediction methods to compute the responses of plates and shells to initial velocity distributions and prescribed externally-applied transient loads [7] are being adapted to predict 3-D structural response to fragment impact [10]. Such 3-D shell response predictions are discussed no further in this report.

Confining attention to 2-D structural response predictions, the availability of reliable transient response prediction methods for fragment-impacted 2-D C/D structures may be of use (as noted earlier) for preliminary design estimates and parametric calculations. Also, the use of such prediction methods may enable one to reduce the scope of actual impact/response experiments on candidate C/D structures; of course, it is essential to conduct certain types of experiments to establish concrete qualitative and quantitative behavior. This experimental information also can be used to test the accuracy and adequacy of proposed prediction methods for certain ranges of parameters and conditions. Properly conducted experiments of this type are very expensive; hence, the judicious complementary use of theoretical transient response prediction methods is of evident value.

---

*Numbers in square brackets [ ] denote references given in the reference list.

In order to evaluate the accuracy and adequacy of the cited transient structural response prediction methods, various experiments have been carried out to provide appropriate experimental data. Complex experiments involving impact of typical engine rotor fragments against containment rings have been conducted at the Naval Air Propulsion Test Center. Simpler impact experiments with an impacting fragment of simpler and fixed shape have been carried out at the MIT Aeroelastic and Structures Research Laboratory.

The Naval Air Propulsion Test Center has provided data on the responses of aluminum and steel containment rings to (1) impact by a single T58 turbine rotor blade and (2) tri-hub burst fragment attack from a T58 turbine rotor ([11-14]*, for example). In these cases the attacking fragment is complex and undergoes a considerable amount of deformation and geometry change during its impact interaction with the containment ring. For case (1), theoretical transient response predictions which take into account the changing geometry, mass moment of inertia, etc. of a single attacking-rotor-blade fragment have been carried out successfully [15]; even this simple case required a substantial book-keeping effort. If a similar procedure were applied to the T58 tri-hub rotor burst attack case (where each fragment consists of a segment of "rigid" rotor disk and 17 deformable blades), it is clear that an impractically huge amount of book-keeping and computation would be encountered. Accordingly, each actual bladed-disk fragment has been replaced in the computational model by an idealized model which may be visualized as a "hockey puck" of selected fixed diameter; frictional or frictionless impact between this idealized fragment and the containment ring is accommodated. The choice of an appropriate size for each idealized fragment involves some study and judgment, and is discussed later in this report.

To remove that judgmental question and to provide cleaner, better-defined, and more detailed transient structural response measurements for evaluating the proposed impact-induced-response prediction method, simpler impact experiments on a smaller scale were performed at the MIT-ASRL [16]. The fragment selected was a solid steel sphere of one-inch diameter; modeling of this fragment is simple and efficient since to determine its space occupancy at a given instant in time, it suffices to know its CG

*Also, see Ref. 37.

location and (assumed to be unchanging) diameter. Also, to provide a simply conducted clearly defined missile-structure impact problem whose subsequent analysis would involve a minimum of computation: (1) the impacted structure was chosen to be a simple initially-straight thin aluminum beam with both ends ideally clamped and (2) perpendicular steel-sphere impact at midspan was selected. Well-defined transient strains, permanent strains, and permanent deflection data were obtained. These data were envisioned to provide a definitive basis for evaluating the accuracy and adequacy of the basic 2-D transient structural response prediction scheme [3-15,17,18]. With verification thereby established, one could proceed with reasonable confidence to tackle the question of selecting an appropriate idealized model for typical complex fragments such as bladed-disk fragments.

Accordingly, discussed in Section 2 are calculations and comparisons with experiment for the sphere-beam impact problem. Section 3 is then devoted to analysis, modeling, and theoretical-experimental comparisons for the T58 tri-hub rotor fragment attack against a steel containment ring.

Discussed in Section 4 are parametric effects on structural response induced by fragment impact. Dimensional analysis considerations are discussed with respect to data from engine rotor burst containment experiments and to data from the simpler sphere-beam impact experiments. Illustrated in Section 4 is the application of the CIVM-JET 4B computer code to parametric type studies -- using for illustrative convenience the sphere-beam impact problem. Discussed are (a) the effects of the width-to-thickness ratio for "equal weight" containment structures, (b) the effects of idealized fragment size, and (c) geometric scaling effects. Illustrative applications of this code to a study of the responses of simple fragment deflectors are described in Section 5.

Since the CIVM-JET 4B code as actually implemented accommodates large-deflection elastic-plastic transient 2-D structures responses but only small strain, the results of a brief exploratory study to modify the code to include finite strain behavior are described in Section 6. Given in Section 7 are a summary, conclusions, and comments pertinent to this study.

Appendix A contains a concise review of the governing equations upon which the CIVM-JET 4B computer program is based. Information on analysis modifications employed to accommodate finite strain behavior for 2-D structural response behavior is given in Appendix B.

SECTION 2

STRUCTURAL RESPONSES OF ALUMINUM BEAMS WITH CLAMPED ENDS TO STEEL SPHERE IMPACT

2.1 Problem Definition

In order to obtain appropriate and detailed two-dimensional (2-D) transient structural response data under well-defined impact conditions so that a definitive evaluation could be made of the adequacy of the approximate collision-interaction analysis employed in the CIVM scheme, some simple experiments have been conducted at the MIT-ASRL and are reported in Ref. 16. Beams of 6061-T651 aluminum with nominal 8-in span, 1.5-in width, and 0.10-in thickness and with both ends ideally clamped have each been subjected to midspan perpendicular impact by a solid steel sphere of one-inch diameter as indicated schematically in Fig. 2. Impact velocities ranged from those sufficient to produce small permanent deflection to those needed for threshold rupture of the beam. Spanwise-oriented strain gages were applied to both the upper and the lower (impacted) surface of the beam at various midwidth and spanwise locations. In each test, transient strain measurements were attempted for 8 of the gages; after each test, permanent strain readings were obtained from all surviving gages. Also, permanent deflection measurements of the beams were made.

To provide ideally-clamped boundary conditions at the ends of the beams, these specimens were machined from a solid block of 6061-T651 aluminum (1.55 x 3.60 x 13.0-in) as indicated schematically in Fig. 3. The indicated "integral support collar" was in turn bolted securely to a heavy flat-ground steel channel support structure with close-clearance 1/2"-13 Holo-Krome shoulder screws; this design and arrangement is believed to have provided a very close simulation of "ideally-clamped" ends. To reduce the hazard of undesired or "premature cracking" at the boundary because of stress concentrations at a sharp re-entrant corner, all "inside corners" were machined to a radius of 1/8-in which is somewhat greater than the nominal beam thickness.

Target beams of 6061-T651 aluminum were employed because this material has well-known mechanical behavior, exhibits very little strain hardening, and is relatively insensitive to strain-rate effects. A 1-inch diameter steel sphere was chosen as the impacting fragment since its geometry is well defined (and preserved) throughout the impact attack, is devoid of sharp edges which might cause atypical local shearing penetration of a target, and was of convenient size, shape, and mass for use with the available experimental launching apparatus so as to achieve the desired levels of fragment kinetic energy at initial impact. The target beam dimensions: thickness $h = 0.100$-in, width $w = 1.50$-in, and span $L = 8.00$-in were chosen for various reasons, as follows. A small width w was desired so that the ensuing beam response would be of essentially 2-D character; however, the aiming accuracy of the available launching apparatus was limited and, hence, a 1.5-in width was selected to permit achieving impacts reasonably well centered at the beam's midwidth-midspan location. A length-to-thickness ratio of about 80 was chosen so that the beam model would possess a significant degree of bending as well as extensional rigidity. Further, the span was kept large compared with the diameter of the attacking fragment so that "local impact effects" would be confined in a region remote from the supported ends of the beam. Finally, the 8-in span was also selected such that the time to achieve peak deformation would be short enough to prevent the required computing time for the theoretical transient response prediction scheme from being excessive; this judgment was based upon much previous computational experience [17, for example] on similar structures. With these selected dimensions for the "missile" and the target beam, it was anticipated that the beam would exhibit essentially 2-D deformation everywhere except in the immediate vicinity of the "sphere-beam impact point". Thus, this experimental information could serve the dual purposes of providing data to check (a) beam 2-D response predictions and (b) narrow plate 3-D structural response calculations (in the future), to fragment impact. The reader is invited to consult Ref. 16 for further details of these experiments.

An inspection of each beam specimen indicates that except near the

point of impact itself (i.e., where $|x| \gtrsim 0.8$ in), the beam underwent essentially 2-D deflection behavior; pronounced 3-D behavior occurs nearer the point of initial impact. Hence, the 2-D structural response code CIVM-JET 4B [4] or CIVM-JET 5B [5] may be expected to provide valid comparisons in the regions $|x| \gtrsim 0.8$-in. Accordingly, calculations and comparisons with experiment have been carried out mainly for two typical conditions given in Ref. 16, and are discussed in subsequent subsections of this section; an additional case was also examined briefly. In particular, the test specimens and associated conditions identified as beam specimens and tests CB-13, CB-16, and CB-18 are employed, and the pertinent data are as follows.

Specimen and Test	Beam Dimensions (in)			Steel-Sphere Data	
	Thick., h	Width, b	Span, L	Weight (grams)	Initial Impact Velocity (in/sec)
CB-13	.100	1.501	8.002	66.738	2490
CB-18	.097	1.498	8.002	66.810	2795
CB-16	.098	1.495	8.002	66.809	2870

Specimen CB-13 exhibited moderate permanent deflection while specimen CB-18 displayed a state of large permanent deformation; model CB-16 experienced an even greater response: to just barely beyond threshold rupture for the entire cross section.

Before attempting to compare predictions with experimental measurements, it is useful first to examine the effects on the predicted response of the number of finite elements used to model the beam; this is discussed for both specimens CB-13 and CB-18 in Subsection 2.2 where the mechanical behavior of the beam material is assumed to be insensitive to strain-rate effects. Next, in Subsection 2.3 the effects of (small) strain-rate sensitivity of the beam material on the predicted transient responses of steel-sphere impacted beams CB-13 and CB-18 are illustrated. Then in Subsection 2.4 comparisons are made between structural response predictions and experimental measurements for specimens CB-13, CB-18, and CB-16.

Subsection 2.5 contains summary observations and some considerations of alternate selections for modeling the problem of structural response to fragment impact.

2.2 Effects of Finite-Element Modeling

To illustrate the effects of various finite-element modelings and of material strain-rate effects in Subsections 2.2 and 2.3, respectively, predictions are compared with each other. For this illustrative purpose a piecewise linear stress-strain material model which is represented by the mechanical sublayer model [see Ref. 17, for example] was used to approximate a stress-strain curve given in Ref. 19 for a similar aluminum alloy (6061-T6 and/or 6061-T6511); this piecewise linear approximation had been employed in similar predictions reported in Refs. 7 and 20 as well as in a number of computer runs made early in the present study before measurements of the static uniaxial stress-strain behavior of the 6061-T651 aluminum used in the present beam models was documented in Ref. 21 in 1977. Hence, rather than repeating many calculations employing the Ref. 21 stress-strain data, it was decided to present the predictions to be shown in Subsections 2.2 and 2.3 based on the earlier "illustrative" stress-strain approximation. That piecewise linear approximation to the σ_T, γ_{11} static stress-strain curve of Ref. 19 is given by the stress-strain pairs*: (σ_T, γ_{11}) = (0 psi, 0), (41,000 psi; 0.0041 in/in), (45,000 psi; 0.0120), and (53,000 psi; 0.1000). Since this applies to static conditions, this model is termed elastic, strain hardening (EL-SH). Finally, the use of both the "illustrative Fit A" stress-strain approximation and a similar approximation to the stress-strain behavior of 6061-T651 aluminum as documented in Ref. 21 will be discussed in Subsection 2.4 where predictions are compared with measured transient responses and permanent deflections of the present steel-sphere impacted beams.

Before discussing the prediction of beam structural response to steel-sphere impact, it is useful to consider briefly a simpler structural response problem in which impact is not involved and, hence, the modeling and analysis uncertainties are lesser. In particular, consider first an initially flat 6061-T651 aluminum beam of 0.102-in thickness,

* Hereinafter these values will be called stress-strain "illustrative Fit A".

1.493-in width, and 8.006-in span with both ends ideally clamped, and subjected to uniform impulse loading over its entire width and for a 1.8-in spanwise region centered at midspan; experimental data for such a case is given in Ref. 16 for a model identified as beam specimen CB-1. For this case, the impulsive loading produced essentially a uniform initial lateral velocity* of 6660 in/sec over the impulsively-loaded portion of the beam.

This case is employed here only to illustrate the effects on the predicted transient structural response of the number of uniform-length beam finite elements used to model this structure. In particular, the finite element computer code of Ref. 3 as modified in the studies of Ref. 20 was employed in three modeling calculations; namely, the half-span of the beam was modeled by 10, 20, and 30 equal-length 4DOF/node finite elements, and symmetry conditions were imposed at midspan. Over the central impulsively-loaded region, the model's elements were assigned "uniform" initial velocities such that the initial kinetic energy of the mathematical model matched that implied for the actual CB-1 test specimen whose density was taken as 0.098 lb/in^3.

For the CB-1 test conditions, the predicted midspan deflection w is shown in Fig. 4a as a function of time for the 10, 20, and 30 element/half-span calculations. It is seen that, the 20-element and 30-element predictions essentially duplicate each other; also, the 10-element prediction is very close to the other two predictions. Hence, it appears that the 10-element calculation represents nearly a "converged prediction", and the 20-element model provides a clearly converged result. Somewhat more sensitive indications of convergence are shown by the predictions of transient axial strains on the upper (non-loaded) surface of the beam at locations x = 0.4, 1.60, and 3.0 in measured from midspan; these predictions are shown, respectively, in Figs. 4b, 4c, and 4d. Except at x = 0.4 in, the 10-element prediction is in reasonable agreement with the 30-element prediction. At all locations, the 20-element and the 30-element

*The impulsively-imparted velocity was determined from calibration experiments (described in Ref. 19) using explosively-loaded flyer plates.

predictions agree reasonably with each other.

From the CB-1 calculations, one can conclude that the use of a 20-element per half-span FE model with 4 DOF/node elements will provide an adequate structural model for predicting large-deflection, elastic-plastic transient structural responses of this impulsively-loaded beam structure insofar as the number of finite elements used to model the structure is concerned. Hence, it is reasonable to expect that a similar modeling fineness should suffice for analyzing the responses of similar beams to steel-sphere impact -- provided that the impact-interaction and associated modeling requirements are not more stringent.

It should be noted at this point (as discussed also in Appendix A) that converged finite element predictions by the assumed displacement method depend not only upon using an adequately large number of elements but also upon employing a type of element-assumed-displacement field which includes continuity of w and its first spanwise derivative and continuity of the v displacement as well as constant strain terms and rigid body modes. These conditions are fulfilled by the present beam elements as noted in Appendix A. Sought here, however, is engineering convergence (accuracy to perhaps 5 to 10 per cent with the use of a modest number of finite elements) rather than strict mathematical convergence (accuracy to a fraction of a per cent by using a great number of elements); this is "achieved" in the present instance by using about 20 or more elements per beam half span.

Next, consider the analysis of beams CB-13 and CB-18 which were subjected to steel-sphere impact. To analyze these cases, various numbers of both uniform-length and nonuniform-length finite elements were considered for modeling the entire nominal 8-in span of the beam, as indicated in Fig. 5. Shown for only the half span are the finite-element arrangements examined; the length of each element is shown. For the several arrangements of elements of nonuniform lengths, the intent was to use fine meshing near the point of initial impact and near the clamped ends to provide detailed information where significant bending (as well as

stretching) was expected; in regions of small spatial variations of behavior and where very little bending was expected, coarser meshing (longer elements) were expected to provide adequate information. However, the presence of small-length finite elements causes the maximum natural frequency of the mathematical model of the entire structure to be much higher than would be the case if one were to use the same number of uniform-length finite elements. Thus, since the central-difference timewise finite-difference operator is used for the timewise solution of the equations of motion in CIVM-JET 4B, this means in turn that one must use a much smaller time increment Δt for a nonuniform mesh FE model than for a corresponding uniform-mesh FE model. Further, if one were to analyze a containment-ring structure that could be impacted by, perhaps, several fragments at any circumferential location of the ring, it would be infeasible and illogical to attempt to model the ring with nonuniform finite elements -- an array of uniform-length finite elements would be clearly the sensible choice. Therefore, in view of these considerations, subsequent finite element modelings and calculations of the steel-sphere-impacted beams utilized only uniform-length finite elements.

In particular as Fig 5 shows, the entire beam was modeled with either 23 or 43 uniform-length finite elements, with the midspan of the center finite element located for convenience at the midspan of the beam itself: the location of the point of initial steel-sphere impact. The effects of these two FE modelings upon the predicted responses of specimens CB-13 and CB-18 will be examined next. From the earlier "convergence discussion" with reference to impulsively-loaded model CB-1, it is expected that the present 43 element model ($\tilde{}$ 22 elements per half span) will exhibit "converged impact-induced response". It is also of interest to assess the sensitivity of the predicted impact-induced response to a similar but coarser FE modeling; namely, essentially one-half of the number of uniform-length elements used in the former case.

First, it should be noted that, as expected, the structural behavior of these steel-shpere impacted beams was two-dimensional at all spanwise stations except for those near (within about 0.8-in of) the center of initial irpact; nearer the point of initial impact, very

pronounced three-dimensional structural deformations are evident. Therefore, since the CIVM-JET 4B analysis and code pertains strictly to 2-D structural response, theoretical-experimental comparisons (see Subsection 2.4) can be made logically only at stations $|x| \gtrsim 1.0$ in. However, as a matter of curiosity, comparisons between experiment and 2-D predictions will be made in both of these regions: $|x| \gtrsim 1.0$ in and $|x| \lesssim 1.0$ in.

CIVM-JET 4B calculations were carried out to predict the impact-induced responses of specimens CB-13 and CB-18. In each case the impacting fragment was modeled as a rigid 2-D circular fragment of 0.5-in radius. In the impact-interaction portion of the computer code, locally perfectly-elastic impact was assumed;hence, a coefficient of restitution e of 1.0 was used. The aluminum beam material (ρ = 0.098 lb/in^3 weight density) was modeled as behaving in an EL-SH fashion by "illustrative Fit A". The time increment size Δt used was 1.0 and 0.5 μsec for the 23-element and the 43-element model, respectively.

Shown in Fig. 6 are the predicted time histories of the lateral displacement w for the 23- and the 43-element case at spanwise stations $x \doteq 1.2$, 1.9, and 3.6 in for specimen CB-13. A similar plot is given in Fig. 7 for the more severely impacted specimen CB-18. Both of these figures indicate very close agreement between the predicted time histories of displacements from these two modelings at each of these spanwise stations.

A more sensitive and meaningful comparison of these predictions involves axial strains γ_{11} on the upper (U) or the lower (L, or impact) surface of the beam at various spanwise stations. Such comparisons are shown in Figs. 8 and 9 for specimens CB-13 and CB-18, respectively. Summarized in the following tabulation are the comparisons of these two predictions (23 and 43 element, both EL-SH) with each other (and/or versus experimental data for rough comparison only) shown in these figures.

Specimen	Fig.	Station x(in)	Time Histories of Strain on Surface U(upper) and/or L(lower)	
			Predicted	Measured
CB-13	8a	0	U^a and L^a	-
"	8b	0.6	U	U
"	8c	1.2	U^b	-
"	8d	1.5	U and L	U and L
"	8e	2.1	U^a	-
"	8f	3.7	U and L	U
CB-18	9a	0	U^a and L^a	-
"	9b	0.6	U	U
"	9c	1.2	U^b	U
"	9d	2.1	U^a	-
"	9e	3.7	U and L	U

Superscript "a" denotes locations which coincide with the midspan station of a finite element.. Superscript "b" pertains to stations x which coincide with a nodal station of the FE model; the associated strain value plotted is the average value given by the two elements at that nodal junction station. Predicted strains at locations not marked by "a" or "b" occur at some station intermediate between the end and the midspan of a finite element.

The inclusion of measured strain data in these plots is intended to provide some intuitive guidance in assessing the 23-element vs. the 43-element predictions.

Figures 8a and 8b are included for academic interest; at these locations (x = 0 and x = 0.6 in), the computer values are legitimate for 2-D structural response and hence may be compared with each other. However, it is not proper to compare predictions with measurements at x = 0.6 since 3-D structural behavior is evident in the experiments and the measured strain history there must be affected accordingly; nevertheless, the "inappropriate" 2-D predictions are included vs. measurements in Fig. 8b. Strains predicted by nodal averaging at station x = 1.2 in are shown in Fig. 8c for both FE modelings. At x = 1.50 in, the predicted

strains are at element locations intermediate between midelement and a node; in Fig. 8d, 2-D predictions are compared with measured strains also under 2-D structural response conditions. Midelement strains for both calculations are shown in Fig. 8e for x = 2.1 in; again one observes similar qualitative and quantitative behavior between these two predictions. However, no measurements are available to aid one's assessment. Finally, Fig. 8f shows predicted and measured strains in a region where the importance of the bending behavior is changing rapidly with spanwise location; predictions at element locations intermediate between the midelement point and a node are "compared" with measured values on the upper surface at x = 3.70 in. Here the 23-element prediction differs markedly from the 43-element result; incidentally, the latter is in better but not really good agreement with experiment. Near x = 3.70 in the strains change rapidly with x in this region -- as shown in Fig. 8g where the predicted upper-surface strain vs. x at time after initial impact TAII ≈ 1020 μsec is plotted for the 23- and the 43-element calculation. Figure 8g demonstrates the severe strain gradients which occur near the "midspan impact region" and near the clamped end of the beam.

More extensive comparisons between EL-SH predictions of transient strains[+] are given in Fig. 9 for the more severe impact conditions prevailing for specimen CB-18. The midelement strains predicted at x = 0 again exhibit pronounced differences between the 23-element and the 43-element case. At x = 0.6 in, predicted upper-surface strains are shown and pertain to element locations between midelement and a node; also shown are measured strains on the upper surface at x = 0.6 in. Again, the 43-element predictions agree better with experiment than do the 23-element predictions, although these 2-D predictions are not strictly comparable with the 3-D measured data. However, at x = 1.20 in, 2-D predictions could be compared legitimately with measurements since the latter pertain to 2-D behavior also at that station, except for the use of illustrative stress-strain Fit A; here, better and rather reasonable (perhaps coincidental) agreement between the 43-element predictions of nodal-averaged strain and experiment is seen. Midelement predicted

[+]Comparisons of predictions with measured strains may be found in Fig. 17.

strain in the 2-D region is plotted in Fig. 9d at x = 2.1 in. Finally, near the clamped end at x = 3.70 in, predicted upper surface strains for CB-18 are compared with measurements; the severe strain gradients in this region can readily lead to pronounced theoretical-experimental discrepancies. The comparison here is similar to that noted earlier concerning specimen CB-13.

With respect to representing rapid variations of strain with spanwise distance at stations very close to the clamped ends, these variations can be represented adequately in principle by employing a finer finite element mesh in those regions. In addition, however, it should be noted that near the clamped ends of severely-impacted or loaded specimens there is visual (orange peel) evidence of the occurrence of transverse shear deformation -- whereas the present finite elements do not include this behavior. If transverse shear deformation effects become sufficiently important, finite elements which include this effect could be used but this use, in turn, will lead to a much larger highest frequency of the mathematically-modeled structure [17] thereby requiring one to use a much smaller time step size Δt if the central-difference operator were used for the timewise solution.

It was noted earlier that near the midspan impact point, the 43-element predictions differ from the 23-element predictions for each of the specimens CB-13 and CB-18. The principal reasons for this involve the details of the (approximate) impact-interaction claculation method employed, as described in the following. In essence, when the fragment impacts the beam, a calculation is made to determine the amount of momentum transferred from the fragment to a portion of the beam centered about that impact point -- called the "locally-affected region" which is defined as that which will experience an imparted velocity increment. The distance from the impact point to either end of this locally-affected region* is denoted by the "effective length" L_{eff}. One estimate** is that L_{eff} is the product of the simple elastic rod-wave velocity $(\frac{E}{\rho})^{1/2}$ times the time step size Δt being

*See, for example, Appendix A of Ref. 4 or Appendix B of Ref. 5.

**Another estimate of L_{eff} is discussed later in this subsection.

used, where E is the elastic modulus and ρ is the mass per unit volume of the beam material; for aluminum $(\frac{E}{\rho})^{1/2}$ = 198,486 in/sec. Since the CIVM-JET 4B computer code was employed and this program uses the central-difference time-wise solution operator, the time step size Δt must be less than $2/\omega_{max}$ to avoid calculation divergence, where ω_{max} is the maximum frequency of the mathematical model of the structure for small-displacement linear elastic behavior. For large-deflection elastic-plastic transient response calculations, experience has shown that one must use a smaller value for Δt such as $\Delta t \leq 0.8(2/\omega_{max})$. Shown in the following tabulation are ω_{max}, $2/\omega_{max}$, $0.8(2/\omega_{max})$, and the actual timestep size Δt used for the 23- and 43-element modelings of CB-13 and CB-18; included also are the finite element length and $L_{eff} = (\frac{E}{\rho})^{1/2} \Delta t$.

No. of Uniform Elements	ω_{max} (rad/sec)	Time Step Size Values: $(\Delta t)_{max} = \frac{2}{\omega_{max}}$ (μsec)	$0.8\frac{2}{\omega_{max}}$ (μsec)	$(\Delta t)_{used}$ (μsec)	$L_{eff} = (\frac{E}{\rho})^{1/2} (\Delta t)_{used}$ (in)	Elem. Length (in)
23	0.124349×10^7	1.608	1.287	1.00	0.1985	0.3478
43	0.232600×10^7	0.860	0.688	0.50	0.0993	0.1860

Note that since (1) impact occurs at the center of the finite element which is centered at midspan and (2) L_{eff} > one-half of an element length, the locally-affected impact region includes not only the center element but also a portion of one element on each side of the impacted element. These three elements, therefore, contribute to the mass portion of the beam which acquires a distributed increment of velocity associated with the momentum transfer. The mass involved and employed in the computational logic is that at the end nodes of the central element for the assembled finite element model and hence represents the mass of 2 complete elements: all of the center element and one half of the element on each side of the center element. Thus, it can be seen readily that for a given impact, the larger impact-affected region assumed to be associated with the 23-element model will experience a considerably smaller velocity increment than will the impact-affected region in the 43-element model; thus, near the impact

point, one expects and does see a much more severe response for the 43- than for the 23-element model (see, for example, Figs. 8a and 8b for specimen CB-13 and Figs. 9a and 9b for specimen CB-18). As in St. Venant's Principle, the predicted responses at locations remote from the "impact-affected" zone are in good agreement for the 23- vs. the 43-element calculation, except near the clamped end where pronounced bending occurs and produces significant differences.

The just-discussed estimate for the impact-affected half length $L_{eff} \doteq (\frac{E}{\rho})^{1/2} \Delta t$ for a single impact can be seen to yield unreasonable estimates if one were to employ a very large or a very small value for Δt. In the former case, the normal-direction momentum transfer produced by the impact-induced through-the-thickness (and spreading) stress waves will have ceased long before the large Δt (which may be permitted by another timewise finite difference operator) has elapsed; hence, the actual region receiving this normal-direction momentum transfer or velocity increment will be much smaller than the above estimate for L_{eff} assumes. On the other hand, for very small Δt, the impact-induced stress wave passing through the thickness may not yet have reached the opposite free surface -- thus, the momentum transfer envisioned in the calculation model could not have been completed physically. Thus, for a single impact, one can make a more rational estimate for L_{eff} from stress wave propagation considerations even though the basic structural response and impact/interaction model being used does not take explicit account of this type of "across-the-thickness" stress wave propagation behavior.

Figure 10 depicts in a simplified fashion two idealized types of impacting-fragment geometries: (1) a 2-D fragment of circular cross section, which contacts the target at a "line" and (2) a 2-D fragment of rectangular cross section. For impact of the 2-D beam target by the solid cylindrical fragment, a highly simplified picture is shown of the sequence of stress waves which propagate "across the thickness direction" of the beam. For present purposes let it be assumed that these stress waves are simple elastic waves. At the initial impact point, a "line source of compression" is produced; a compression wave propagates into the plate as a cylindrical

front from this "line source" and weakens as it expands because of "geometric divergence". The material particles being traversed by the compression wave are given a material velocity in the direction of the propagating wave front. When this compression front reaches the opposite free surface of the plate where the stress is required to remain at the zero-stress condition, a cancelling tension wave arises and can be viewed as emanating from source center SC-2 located at a distance h beyond this free surface. This reflected tension wave also weakens as it propagates (and diverges) through the plate and imparts an addition particle velocity to the material in a direction opposite to the direction of travel of the propagating tension wave front. When this tension wave front reaches a free surface, a corresponding reflected compression wave is generated at pseudo-source-center SC-3. When this new compression front reaches the opposite free surface, a new tension front is created with pseudo source center at SC-4. The wave front strength created initially by each new pseudo source becomes weaker and weaker for each successive source -- roughly inversely proportional to the square of the distance from the source center. Hence, by the time that wave front 4T from SC-4 reaches the originally impacted surface, one can argue reasonably that subsequent waves would be able to induce only slight additional increments to the particle velocity of the material traversed by the stress waves. Thus, a reasonable estimate of the beam length region L_{eff} which experiences a substantial velocity increment in the direction normal to the plate is selected as the intersection of wave front 4T with the half thickness station of the beam; from this geometric picture one can show that $L_{eff} \doteq 1.94\ h$ (see Fig. 10a). The actual stress wave propagation is much more complex than described here (see Refs. 22 and 23, for example); however, it is believed that the present description is adequate for the purposes of selecting a reasonable value for the beam impact-affected zone half-length L_{eff}. For this type of impact, therefore, it would not be unreasonable to choose $1.5h \leq L_{eff} \leq 2.0h$ -- independent of the calculation time step size Δt.

By similar arguments, the beam impact-affected zone half length

L_{eff} for the beam impacted by the rectangular section fragment depicted in Fig. 10b might be estimated as $\ell_r/2 + h \leq L_{eff} \leq \ell_r/ + 2h$.

With respect to the 43-element calculation discussed earlier, the present estimate for L_{eff} would be approximately $1.94h \doteq 0.194$ in; hence, the total impact-affected zone of $2L_{eff} \doteq 0.386$ in would amount to about two beam element lengths (i.e., 2(.186) = .372 in). This turns out to be consistent with the previously-discussed 43-element calculation wherein the L_{eff} employed resulted in estimating the impact-affected zone to include both nodes of the impacted center element of the assembled beam structure. Those two nodes are regarded as receiving the impact-imparted impulse and do represent the mass for 2 beam elements. Thus, the 43-element calculation can be regarded as valid from the collision-interaction standpoint, whereas the 23-element calculation assumes an unreasonably large region of the beam to receive the momentum transferred by the attacking fragment in a single impact. This means that near the point of impact, one should use shorter elements than in the 23 equal-length-element case in order to take into account properly the beam region which effectively receives the transferred momentum (and associated velocity increment) from a single impact.

Finally, it is of interest to note that 43-element EL-SH Fit A calculations were carried out for the steel-sphere-impacted CB-18 beam by using various Δt values in the CIVM-JET 4B program. For this modeling it was found that $2/\omega_{max} = 0.860$ μsec; hence, the rule-of-thumb choice for an acceptable Δt to avoid calculation instability from error growth for large-deflection elastic-plastic transient response predictions is $0.8(2/\omega_{max}) = 0.688$ μsec. Calculations were carried out for Δt values of (a) 0.5 μsec which corresponds to $.58(2/\omega_{max})$ and (b) 0.75 μsec which corresponds to $.87(2/\omega_{max})$. For $\Delta t = 0.5$ μsec, the transient response calculations were found to be well behaved and converged. However, at $\Delta t = 0.75$ μsec, the predicted impact-induced response became appreciably different (and larger) than for the converged calculations. This experience indicates that when carrying out impact-induced nonlinear response calculations which utilize the timewise central difference

operator (CIVM-JET 4B), one must be careful to choose a Δt well below the critical $\Delta t \equiv 2/\omega_{max}$ for this operator when applied to linear systems. It appears from this experience that the rough rule-of-thumb [17, for example] for selecting Δt (i.e., $\Delta t \leq 0.8(2/\omega_{max})$) is applicable and should not be "stretched" unduly.

2.3 Strain-Rate Effects

When the effect of strain rate on the mechanical behavior of the structural material is taken into account, the material is denoted as behaving in an elastic, strain-hardening, strain-rate sensitive fashion: EL-SH-SR. An approximation to account for the principal effects of strain rate on the uniaxial stress-strain behavior of ductile metals is given by the following Cowper-Symonds relation [24]:

$$\frac{\sigma_{yk}}{\sigma_{ok}} = \left(1 + \left|\frac{\dot{\varepsilon}}{D}\right|^{1/p}\right) \tag{2.1}$$

where σ_{ok} and σ_{yk} are, respectively, the static and the strain rate-dependent yield stresses of the kth elastic, perfectly-plastic mechanical sublayer*; $\dot{\varepsilon}$ is the strain rate, and D and p are material strain rate constants. For aluminum, Ref. 25 suggests the use of $D = 6500\ \text{sec}^{-1}$ and $p = 4$; these values are employed here also for illustration.

Although the stress-strain behavior of 6061-T651 aluminum is believed to be rather insensitive to strain rate, some illustrative 43-element calculations have been carried out for beam specimens CB-13 and CB-18, using the strain-rate constants $D = 6500\ \text{sec}^{-1}$ and $p = 4$. These EL-SH-SR predictions are compared with the previous EL-SH predictions and with experiment for specimens CB-13 and CB-18 in this subsection.

Shown in Figs. 11 and 12 for specimens CB-13 and CB-18, respectively, are 43-element EL-SH and EL-SH-SR predictions of midspan displacement w versus time as well as the measured and predicted permanent deflections of each specimen as a function of spanwise location x. As expected, the predicted deflections are less for the EL-SH-SR case than

* See Subsection A.4 for a description of the mechanical-sublayer material model.

for corresponding EL-SH calculation; although small strain-rate sensitivity is used, strain-rate effects in metals effectively "stiffen" the structure thereby leading to a lesser response.* Note that for both the CB-13 and the CB-18 example, the EL-SH prediction of the permanent deflection is in better agreement with experiment in the 2-D region than is the EL-SH-SR result; the experimental result is plotted along the midwidth station y = 0 of each beam and includes pronounced 3-D deformation evidence over the region $|x| \lesssim 0.8$ in.

For specimen CB-13, 43-element EL-SH and EL-SH-SR calculations were made wherein steel-sphere perpendicular impact was specified to occur initially at the midspan location of the beam. Theoretically, the ensuing beam response and fragment motion should remain symmetric. However, because of calculation roundoff error, one finds that after many time increments in the calculation have occurred some response asymmetry and consequent fragment motion asymmetry appear.* Hence, a second EL-SH-SR 43-element calculation was done wherein, at the end of each Δt time increment in the calculation, the fragment was required or "constrained" to move and remain in the x = 0 plane; for convenience, this calculation is termed herein 43C. This constraint resulted in only small changes in the predicted beam response -- affecting slightly the time at which peak strain was predicted to occur at a given station only near midspan, but not affecting the value of that peak significantly. These 43-element EL-SH, EL-SH-SR, and EL-SH-SR/43C strain predictions at x = 0 are shown in Fig. 13a for specimen CB-13.

EL-SH and EL-SH-SR predictions of transient strain on the upper and the lower surface of beam CB-13 at a representative 2-D location (x = 1.50 in) are compared with measurements in Fig. 13b; similar comparisons for the upper surface of the beam at station x = 3.70 in are shown in Fig. 13c. At both of these locations, the EL-SH-SR calculation provides the better agreement with experiment. Finally, Fig. 13d shows EL-SH and EL-SH-SR predictions versus measurements of the permanent strain as a function of spanwise location x. In the 2-D response region, the measured permanent strain is less than about 0.7 per cent for

*Figure 13c indicates an "exception" to this for the EL-SH-SR calculation but this occurred because of inadvertent asymmetric impact -- corrected subsequently by the EL-SH-SR/43C calculation.

specimen CB-13; it is seen that the predicted permanent upper-surface strains tend to be somewhat larger than the measured values, with the EL-SH-SR prediction being in closer agreement with experiment.

Similar comparison of EL-SH and EL-SH-SR strain predictions for beam CB-18 are shown in Figs. 14a, 14b, 14c, and 14d. Note in Fig. 14d that the measured permanent upper-surface strain vs. x in the 2-D region is less than about 1.5 per cent. Again predicted permanent strains are somewhat larger than measured.

Overall, the EL-SH-SR predictions are better in some regions while the EL-SH predictions are better in other regions, particularly near the point of impact. Because some predicted asymmetric behavior was observed for symmetric impact conditions when using the EL-SH-SR condition and also because of uncertainty of proper strain-rate parameter values, most of the following comparisons and studies are performed with only the EL-SH material modeling.

Finally, it should be noted that there is widespread agreement that the mechanical stress-strain behavior of tempered aluminum is relatively insensitive to strain rate at room temperature conditions (compared with mild steel [25] or titanium [26], for example), but the degree of the sensitivity is in doubt. Reference 27 indicates that at room temperature various of the common aluminum alloys in the soft annealed ("0") condition (such as 1060-0, 1100-0, 6061-0, 7075-0, for example) display distinct rate sensitivity; these same alloys when tempered to the T3 or T6 condition exhibit almost no strain-rate sensitivity. There is, however, scatter of strain-rate data amongst various reference sources [28-30].

2.4 Comparisons of Predictions with Experiment

Examined in Subsection 2.2 was the effect on the predicted deflections and strains of using various finite-element modelings of the steel-sphere-impacted beams when the beam material was treated as behaving as an elastic strain-harding (EL-SH) material. Next, in Subsection 2.3 the effects of including material strain-rate (SR) dependent behavior was explored (the material was treated as EL-SH-SR) by employing

illustrative strain-rate constant values D = 6500 sec^{-1} and p = 4 for aluminum [25]. In both of those subsections, the predictions were compared primarily with each other. Based upon those studies and the considerations discussed in those subsections, the combination of (1) a 43-element model to represent the entire beam and (2) material EL-SH behavior was chosen as being a reasonably satisfactory basis for predicting steel-sphere-impacted beam 2-D responses for the purpose of comparing predictions with experimental measurements for beam specimens CB-13, CB-16, and CB-18, except that now the stress-strain curve of Ref. 21 for the 6061-T651 beam material should be employed. These comparisons (experiment, predictions with illustrative stress-strain Fit A, and predictions with the new stress-strain fit for 6061-T651 aluminum) are discussed now in this subsection.

For convenient reference, the test conditions and observed effects on these beam specimens are summarized concisely in the following:

Specimen and Test	Steel Sphere Data			Post-Test Condition of Beam
	Weight (grams)	Initial Impact Velocity (in/sec)	Initial Kinetic Energy (in-lb)	
CB-13	66.738	2490	1187	Moderate permanent deformation
CB-18	66.810	2795	1489	Large permanent deformation
CB-16	66.809	2870	1569	Specimen ruptured; threshold rupture condition

Note that beam CB-13 exhibited a moderate degree of permanent deformation while the more severely impacted CB-18 beam displayed large permanent deformation. Within about 0.25 in of the center of impact and along a roughly circular band, some tiny cracks are observed on the upper surface of specimen CB-13 but these cracks do not extend through the

thickness of the specimen. Similar but somewhat more pronounced cracks are seen on the upper surface of specimen CB-18, but again, these cracks do not extend through the thickness of the specimen. The even-more-severely impacted beam CB-16 (2870 in/sec impact velocity) fractured across the entire thickness and width of the beam at essentially the midspan impact station; the crack line (see Fig. 15) suggests that crack initiation occurred along the "circular crack initiation zone" observed on CB-13 and CB-18 and then spread from the center toward both edges of the beam. The CB-16 impact condition is essentially that for "threshold complete fracture" since the steel sphere was stopped and rebounded; the sphere did not pass through the crack-produced opening. Also near the "fracture station" of specimen CB-16, a considerable degree of necking was observed in the beam-width direction -- indicating the presence of very large strains. All three specimens bore evidence of significant straining on the lower (tension) surface at each clamped end, with the degree of straining here varying from slight for specimen CB-13 to pronounced for specimens CB-18 and CB-16.

From an examination of these specimens, one can see readily that three-dimensional (3-D) deformation behavior occurred on all three specimens in a spanwise region totalling about 1.5 inches in length centered about the (midspan) station of initial impact ($x \doteq 0$). Also, very close to the clamped ends, a small amount of 3-D deformation occurred. Thus, since the present prediction method applies strictly to only 2-D deformation behavior and is restricted in its validity to strains which are only of small to moderate size (the basic formulation does not accommodate large strains*), predictions can be compared "legitimately" with measurements only in those beam spanwise station regions in which predominantly 2-D response behavior occurs; these regions are estimated to be roughly $0.8 \leq |x| \leq 3.70$ in. For comparisons made for curiosity at locations

*To account properly for large strains, a more comprehensive and rigorous formulation and implementation is needed; some further comments on this matter are given in Section 6.

beyond the "zone of validity", one must be aware of the tenuous nature of such comparisons. Also, the experimental structural response in the "region of 2-D behavior" can be argued to be tainted somewhat by the presence and indirect influence of 3-D response in the cited 2-D portions of the structure.

Because of the similarities among the three experiments (i.e., beam geometry, material properties, and fragment size), it is expected that the predicted 2-D responses for these beams will be similar qualitatively but of ascending magnitude from CB-13 to CB-18 to CB-16 — where the prediction model assumes throughout the predicted response that no material fracturing or cracking has occurred. Figures 16a through 16d show 2-D predictions (43 element, EL-SH illustrative Fit A) of the upper-surface axial strain γ_{11} at stations x = 0, 0.6, 1.5, and 3.7 in for specimens CB-13, CB-18, and CB-16 (listed here in the order of increasing severity). The expected ascendancy in response severity is evident; however, the CB-16 prediction exhibits only a slightly greater strain response at these locations than the CB-18 predicted response, which is expected since the pre-impact kinetic energy of the fragment is only about 5.4 per cent greater for specimen CB-16 than for specimen CB-18.

Comparisons of the γ_{11} beam-surface strain predictions versus measurements for specimens CB-13, CB-18, and CB-16 are shown in the figures listed concisely below for convenient reference:

Figures where Predicted Strain vs. Experiment are Shown						
Station |x| (in)→	0.6	1.2	1.5	3.0	3.7	Entire Span for Permanent Strain
Specimen						
CB-13	8b	-	13b	-	13c	13d
CB-18	9b	9c	14b	-	-	14d
CB-16	17b	17c	17d	17e	17f	-

It should be noted that all of these predictions utilize illustrative stress-strain Fit A and hence, should not properly be compared with experiment; later, predictions utilizing a corresponding stress-strain fit for the actual 6061-T651 beam material will be presented.

Since specimens CB-13 and CB-18 each retained its structural integrity throughout its transient response, one can compare strain predictions legitimately with experimental measurements for these specimens for the entire history, including the permanent deformation condition for the 2-D region $0.8 \leq |x| \leq 3.70$ in. In this regard for transient strains, see Figs. 13b and 13c for model CB-13, and Figs. 9c and 14b for model CB-18; for both specimens it is seen that the 43-element EL-SH prediction is in reasonably good agreement with experiment and that the strain levels involved do not exceed the bounds of validity of the present theoretical formulation and computer program. However, the bounds of validity appear to be exceeded near the midspan impact point and close to the clamped boundaries. Note also from Fig. 8b for CB-13 and Fig. 9b for CB-18 where "illegitimate" comparisons are made in the 3-D experimental response region at x = 0.6 in, that the 2-D predictions are in rough agreement with measurements during the early part of the time history but then tend to diverge vs. experiment as time progresses; also at station x = 0.6 in, the strain gages become detached from the specimen at an unknown time after initial impact and the strain trace on the oscilloscope record vanishes. Finally, the spanwise distribution of predicted vs. experiment permanent upper surface strain γ_{11} is shown in Fig. 13d for specimen CB-13 and in Fig. 14d for specimen CB-18; in both cases the experimental strain level is small in the 2-D region $0.8 \leq |x| \leq 3.70$ in, and the EL-SH-SR prediction is in better agreement with experiment than is the EL-SH prediction. Also, there is somewhat better theoretical-experimental permanent strain agreement for specimen CB-18 than for specimen CB-13.

For specimens CB-13 and CB-18, Figs. 11a and 12a, respectively, show 2-D predictions of the vertical deflection w as a function of time

after initial impact at spanwise stations x = 0, 1.2, 1.9, and 3.6 in; corresponding transient deflection measurements were not obtained. However, measurements were made of the spanwise distributions of permanent w-deflection; compared in Figs. 11b and 12b for specimens CB-13 and CB-18, respectively, are 2-D predictions of the permanent w-deflection versus measurements. These plots of measured w-deflection represent at each spanwise station x for $|x| \geq 1.0$ in, the average of measurements taken along lines y = -0.5, 0, and +0.5 inch since each specimen exhibited some permanent twist because impact did not occur exactly at the y = 0 width location (see Table 7 of Ref. 16). For $|x| < 1.0$ in, the measured w-deflection values plotted represent those along y = 0 and the average of those at y = -0.5 in and y = +0.5 in at each $|x|$ station; in this region, the 3-D nature of the deflection is evident from these plots. Note that in the 2-D region ($0.8 \leq |x| \leq 3.7$ in), the permanent deflection predictions (43 element, Fit A) compare much better with experiment for specimen CB-18 than for specimen CB-13; a similar but less dramatic result was noted earlier with respect to permanent strains. Further, the EL-SH-SR w-deflection prediction appears in each case to agree slightly better with experiment than does the EL-SH prediction. However, this might be accidental because only very approximate values for the strain rate parameters D and p in the Eq. 2.1 approximation were employed — the authors are unaware of better values for D and p which experimental data could confirm for 6061-T651 aluminum. Also, remember that all of the predictions discussed thus far have utilized "illustrative stress-strain Fit A". Shortly, CB-18 predictions which employ a corresponding stress-strain fit for the data of Ref. 21 for 6061-T651 aluminum (the beam material) will be discussed.

With respect to the predictions and comparisons given in Fig. 17 for specimen CB-16, note that the predictions assumed that CB-16 remained structurally intact throughout its transient response, whereas beam CB-16 fractured across its entire cross section at essentially the midspan impact attack station near its transient response peak at a time estimated to be between about 550 and 650 microseconds after initial impact. After through fracture occurs at midspan, there is rapid

unloading of the "membrane state" of the beam on both halves of the beam; this is seen most readily by comparing the measured strain trace on the upper surface at stations x = 1.50 in for CB-18 vs. that for CB-16. Similarly, the measured strain traces shown in Fig. 17 for specimen CB-16 depart progressively from predictions after about 600 microseconds from initial impact.

Recall that "illustrative stress-strain Fit A" was made from the uniaxial static tensile stress-strain data σ_T vs γ_{11} of Ref. 19 by a piecewise linear fitting of the Ref. 19 data. Now for 6061-T651 aluminum, a similar data fitting has been made of the data in Fig. 29a of Ref. 21; the resulting approximation is termed Fit B and is defined by the following stress-strain pairs: (σ_T, γ_{11}) = (0 psi, 0 in/in); (44,000 psi, 0.0044); (46,500 psi, 0.035); and (54,000 psi, 0.175), and serve to identify the quantities defining each of the three elastic, perfectly-plastic sublayers of the associated mechanical sublayer model. The cited Ref. 21 data and the Fit B (as well as the points of Fit A for the Ref. 19 data) are shown in Fig. 18. The piecewise linear Fit B was made to the Ref. 21 data shown on Fig. 18 whereas Fit A was made to similar data of Ref. 19 for a slightly different aluminum alloy condition. Note that although these fits were made to different sets of data, they are in reasonably close agreement with each other up to γ_{11} values of about 5 to 6 per cent; beyond this level, these fits differ somewhat but are still close with respect to the accumulated areas under these curves. Hence, one would expect the transient response predictions from using the "more realistic" Fit B to differ only a small amount from those obtained from using the previous "illustrative Fit A" for the conditions of either specimen CB-13 or specimen CB-18.

Predictions of steel-sphere-impact produced structural response for specimen CB-18 were made by using, as before, 43 equal-length 4 DOF/node elements for the entire beam and stress-strain EL-SH Fit B. The resulting predictions of w-deflections and strains are compared with the earlier EL-SH Fit A predictions and with experimental measurements for specimen CB-18 in Fig. 19. As expected, these two predictions are seen

to differ only slightly from each other; similar qualitative and quantitative comparisons were noted at other spanwise stations (not shown). Hence, corresponding Fit B calculations were not made for specimen CB-13.

To illustrate the effect of a simpler approximation to the stress-strain behavior of the aluminum material, an elastic, perfectly-plastic (EL-PP) approximation was employed wherein the yield stress was taken as 45,000 psi; this approximation, of course, involves no strain hardening. Shown also in Fig. 19 are transient response predictions for specimen CB-18 when the EL-PP approximation was used. It is seen that these predictions for w (Fig. 19a) and for upper surface strain at x = 1.2 in (Fig. 19c) are in very close agreement with the previous Fit A and Fit B EL-SH predictions. Only at the midspan impact station x = 0 (Fig. 19b) does the EL-PP prediction differ significantly from the earlier predictions; but here the predicted strains are larger than those for which the present analysis and computer code are valid.

From the CB-13 and CB-18 comparisons of 2-D predictions of impact induced transient and permanent strain as well as transient and permanent w-displacement, it is seen that predictions agree better with measurements for the more severely impacted CB-18 beam than for the less severely impacted CB-13 specimen. The former exhibits more pronounced 3-D deformation, necking, and shear deformation than does the latter; of course, none of these effects are included in the 2-D predictions. Since specimen CB-13 behaves in a manner more closely approximating that of the idealized 2-D prediction model than does CB-18, one would expect better agreement between CB-13 predictions and measurements than between CB-18 predictions and measurements in regions of 2-D response behavior, but this is opposite to the present findings.

If one assumes that the 2-D predictions will tend to overestimate the structural response for "gentle impact conditions" such as those of specimen CB-13, a similar overestimate might be expected also for severely-impacted specimen CB-18. However, in the latter case, the more pronounced roles of 3-D deformation, necking, and transverse shear

deformation would tend to produce larger structural deflections than otherwise would occur; this tendency, therefore, would bring predictions and experimental measurements of beam response into closer agreement. This is in accord with the comparisons observed. However, the question of why the predicted 2-D impact-induced structural response is too large for cases of dominantly 2-D structural behavior remains to be answered adequately.

An analogous situation was observed in the studies of Ref. 20 wherein 2-D predictions were carried out for aluminum beams with clamped ends and which were "geometrically identical" to the CB-13 and CB-18 beams. Those specimens, termed CB-1 and CB-4, were impulsively loaded [16] by the sheet explosive loading technique (SELT) over their entire width and for a total spanwise length of 1.8 in centered at midspan; a uniform initial velocity of 6660 and 10,590 in/sec for beams CB-1 and CB-4, respectively, was imparted to each beam in the explosive-covered region. The 2-D predictions for the more severely loaded CB-4 specimen are in better agreement with experiment than are those for the less severely impulsed CB-1 specimen.

An assessment of the uncertainties associated with (1) the explosively-imparted impulse for the CB-1 and CB-4 specimens [16] and (2) the pre-impact steel sphere velocity for the CB-13 and CB-18 tests [16] indicates that those uncertainties are far too small to contribute significantly to the removal of the discrepancies between 2-D predictions and experiment for the "gently loaded" specimens CB-1 and CB-13. For example, for specimen CB-13, it was estimated that at worst the sphere's pre-impact velocity might have been 2400 in/sec rather than the 2490 in/sec value cited in Ref. 16 from calibration firings tests. Shown in Figs. 20a and 20b are 43-element EL-SH Fit A predictions of transient and permanent deflection, respectively, for these two sphere-impact velocity values. It is seen for each calculation that the predicted permanent deflections exceed those measured.

While greater strain-rate sensitivity than assumed and a greater energy absorption in the 3-D region near the impact zone (leaving less to be absorbed by the remaining structure in 2-D deformation) would tend to

account for some of this overprediction, one cannot cite these as decisive factors. The inclusion of transverse shear deformation and/or the use of a larger number of the present finite elements would tend to increase the severity of the predicted response. Thus, as of now, a decisive quantitative explanation for the cited discrepancies remains elusive.

2.5 Comments

2.5.1 Utility and Limitations of the 2-D Analysis

The prediction method under discussion applies to the large-deflection elastic-plastic transient structural responses of simple structures which undergo strictly two-dimensional (2-D) displacements when subjected to fragment impact or to impulse loading, but only small to moderate strains ($\lesssim$ 10 per cent) are accommodated. The present analysis and associated computer programs do not take large strain conditions into account (properly); it would be timely and useful now to extend the analysis to include large strain behavior but the time and effort required to accomplish this task is a matter for future consideration.

The present 2-D analysis of structural response to fragment impact pertains to relatively low speeds of impact in the direction of the normal to the surface of the impacted 2-D structure. Accordingly, transient structural response rather than through-the-thickness severe stress-wave response dominates; hence, under sufficiently rigorous impact attack, the structure can undergo severe deformations which results typically in a tensile-type fracture near the fragment impact point for a ductile metal target structure [12, 16, for example]. At these impact velocities one does not observe (local stress-wave-induced) shear-plug failures -- which are commonly seen for much-higher-speed impacts [31].

The present analysis assumes both the target structure and the impacting fragment to act in a strictly 2-D manner. Conceptually, this implies that the structure is a narrow beam or ring and that the attacking fragment has the same geometry at all stations in a plane parallel to the "spanwise axis" of this impacted structure; in particular, the attacking

fragment is idealized as consisting of a non-deformable solid circular cylinder which extends across the entire width of the beam or ring. Clearly, this idealized model does not match the physical conditions present in the steel-sphere-impacted beam experiments used "to assess the accuracy" of the present prediction method: the fragment is not a 2-D fragment and the observed structural response behavior is not strictly 2-D in character; thus, a rigorous theoretical-experimental comparison cannot ensue. However, with recent improvements [32] in the experimental techniques and apparatus for conducting small-scale impact experiments having the same scope and objectives of those of Ref. 16, it is now feasible to conduct similar beam impact experiments with a solid cylindrical 2-D fragment rather than the one-inch diameter steel sphere employed in the Ref.16 experiments, and thus to obtain more nearly 2-D structural response data for impacted simple structures.

Clearly, the present 2-D analysis is inherently incapable of predicting the 3-D deformations expected and observed to have occurred in a region centered about the "impact point" in steel-sphere-impact specimens CB-13, CB-18, and CB-16. For the 2-D predictions, the idealized fragment was defined to be a solid 2-D cylindrical fragment of one-inch diameter and to have the same mass and impact velocity as the steel sphere in each case. Note that the present 2-D 43-element EL-SH predictions for the peak strain at the midspan impact station ($x = 0$) for cases CB-18 and CB-16 is about 16 per cent and 16.4 per cent, respectively; these 2-D predicted strains exceed the range of validity of the present analysis formulation and computer code implementation and may be very different from the actual peak extensional strains which are present in the clearly 3-D deformation region there. Experimentally, both beam CB-18 and beam CB-16 are close to the rupture threshold for these 3-D deformation conditions of strain and stress; a reliable quantitative characterization of the biaxial or triaxial strain state to define this rupture threshold for this 6061-T651 aluminum material is lacking. Severe necking of the material near the fracture station of specimen CB-16 is evident. It is uncertain also at which extensional strain level one would observe threshold rupture

of the 6061-T651 beam if a strictly 2-D fragment attack were actually performed; in this case also, the 2-D deformation state would be violated by the presence of necking which is of 3-D nature (and which precedes rupture).

Thus, the present strictly 2-D prediction method and code cannot be used, except as a (recognizably) rough indicator of threshold rupture. That is, one might select $\gamma_{11} = 0.164$ (or 16.4 per cent) corresponding to the CB-16 prediction as the "rupture threshold" for 2-D structures composed of the present 6061-T651 aluminum material, when the spanwise direction of the structure is aligned with the plate-roll direction of this aluminum stock (as was the case for beam specimens CB-13, CB-16 and CB-18). One might use this rough criterion to estimate for a 6061-T651 aluminum ring, the ring thickness necessary to contain a given energy level of attack by 2, 3, 4, or 6 etc. equal-size idealized fragments of given size. While experiments are necessary as final confirmation of the required containment ring thickness, the availability of this prediction scheme should reduce substantially the scope and number of the necessary confirmation experiments. In this sense, the present 2-D prediction method can, in spite of its inherent limitations, serve as a useful parametric analysis and preliminary design tool for 2-D type fragment containment and/or deflector structures.

2.5.2 Modeling and Analysis Considerations

Let it be assumed that:

(a) a specific 2-D type structure is to be subjected to impact by a 2-D fragment as accommodated in the CIVM-JET 4B computer program,

(b) the uniaxial static stress-strain curve of the structural material has been specified and fitted by piecewise linear segments for use in the mechanical sublayer model (also that values are specified for the strain rate parameters D and p), and

(c) the size, mass, and kinetic energy of each attacking fragment are given.

The next matter to be considered is the selection of the number and

size of the finite elements to be used to model the structure. The elements must be numerous enough and of small enough size: (a) to provide a converged solution at least in an engineering sense and (b) to accommodate with reasonable accuracy the "physically plausible" impact-affected effective length region = $2L_{eff}$ = 4h of the impacted structure to which momentum is transferred during a single fragment impact. The latter means that the length of each finite element near an impact station should not exceed about 2h (i.e., twice the thickness); otherwise, the collision-imparted velocity increment to impact-affected zone of the structure will become implausibly small and the resulting predicted response will be less severe than realistic in this region.

Further, if one has a structural configuration or arrangement wherein it is apparent that important levels of strain will be present and will be changing rapidly with spanwise location, relatively many short-length elements should be used in these regions to model the behavior there properly, whereas fewer larger-size elements could be used in regions of spatially slowly changing strains. However, as pointed out earlier (Subsection 2.2; also see Section 3), if one is considering a containment ring which may be impacted by fragments at many locations (which may also change as time progresses) around the periphery, the clearly-logical choice is to use only equal-length elements.

If one uses CIVM-JET 4B which employs the timewise central difference operator, the solution time step size Δt must be chosen to be $(\Delta t)_{max} \lesssim 0.8(2/\omega_{max})$ where ω_{max} is the maximum natural frequency of the mathematical model of the structure for linear behavior. One finds that for a given total number of 4DOF/node finite elements, the smallest ω_{max} occurs when equal-length elements are employed; this, in turn, permits the largest allowable Δt to be used for avoiding computational blow-up. The same number of nonuniform elements will require one to use a smaller Δt (and hence to incur more computing expense) in order to avoid computational disaster.* In most cases, therefore, the use of equal-length

*Alternatively, one can employ a larger Δt while avoiding blow-up of computational roundoff error by using a different type of timewise finite-difference operator (see Subsection 2.5.3).

elements to model the structure will be advisable.

As described in Refs. 4 and 17, the approximate impact-interaction model employed makes use of impulse-momentum and energy considerations to predict the momentum transferred to the impact-affected portion of the structure from each impact by a fragment. The structure, in turn, has been represented by finite elements whose mass matrix properties are evaluated from kinetic energy expressions using an assumed velocity distribution in each element consistent with this basic assumed displacement field of the element; accordingly, the resulting mass matrix is called the "variationally consistent mass matrix" -- this is a symmetric non-diagonal matrix. Reference 17 explored the use of this non-diagonal mass matrix for these "momentum transfer" calculations and encountered erratic behavior (see Ref. 17 for further details); hence, a diagonalized mass was constructed [17] and led to plausible behavior. Thus, the CIVM-JET 4B code [4] has utilized a diagonalized mass matrix model for the momentum transfer calculations. Finally, the momentum transfer prediction can be carried out by assuming the local impact to be perfectly elastic, perfectly inelastic, or intermediate between these conditions by assigning as input a value for the coefficient of restitution e of, respectively, $e = 1$, $e = 0$, or $0 < e < 1$; the Ref. 17 studies show results for various e values and conclude that the perfectly-elastic case $e = 1$ is the most reasonable engineering choice for most of the types of low-speed impact conditions under consideration here. The user of CIVM-JET 4B, however, can specify any value of e ($0 \leq e \leq 1$) as he wishes.

2.5.3 Use of CIVM-JET 4B versus CIVM-JET 5B

Both of these computer programs permit one to predict the large-deflection, elastic-plastic transient responses of 2-D structures which are subjected to low-speed impact attack by one or more idealized fragments. CIVM-JET 4B is restricted to the analysis of single layer (single material) structures and employs the timewise central difference operator for the transient solution calculation, whereas CIVM-JET 5B can deal with multilayer multimaterial 2-D structures and uses a different timewise finite-difference operator (the Houbolt operator) for the timewise solution. This latter

operator is unconditionally stable and thus permits one to use a very large time-step size, if desired, without encountering computational roundoff error blow-up; this "advantage" was the principal motivation for the adoption of the Houbolt operator in CIVM-JET 5B. However, the occurrence of impact and the attendant accounting for the impact-imparted velocities to the "locally affected" portion of the structures results in effectively changing the timewise operator at and for a short time following each impact from the Houbolt operator to an operator which is no longer unconditionally stable [10]. Therefore, the allowable Δt is also restricted although not as severely as in CIVM-JET 4B.

Some elaboration on this "correction for impact" matter follows. The CIVM-JET 4B program calculates the exact time of contact between the fragment and a local region of the impacted structure. This time will always occur at some sub-time increment which is smaller than the time-step size employed for the solution procedure. The use of the central difference operator allows an accurate correction to be applied to the structure during the remaining portion of the time-step increment. These corrections are done in a manner which allows a correct distribution of energy and momentum in the system even though a "nonuniform time step" has been employed. The Houbolt operator will not advance the solution properly if a nonuniform time step correction is imposed; hence, a different impact interaction procedure had to be introduced. The CIVM-JET 5B program performs an "approximate time of contact correction" to the structure displacement field; an impact is detected to have occurred within a time step by noting the presence of an overlapping of the fragment and the structure. The corrections are then applied in CIVM-JET 5B as though the initial contact occurred at the beginning of the time step. A response prediction iteration is then performed at this time to guarantee a complete correction, and then the structural response solution continues through time until another fragment-structure overlap is encountered. Since the applied impact-interaction model in CIVM-JET 5B is an approximation of the model used in CIVM-JET 4B, a comparison between the two solution techniques should prove useful for future impact-interaction models. It should be noted that the "exact time

of contact" solution gives a more "realistic" analysis of the impact-interaction, but it becomes very time-consuming as the number of elements used to model the impacted structure increases. Incidentally, the application of this "exact time of contact" impact-interaction solution technique when using plate elements [10, for example] for analyzing plate or panel response to fragment impact would be prohibitive.

Another factor that influences the largest allowable Δt in CIVM-JET 5B is the fact that the Houbolt operator is of implicit type; therefore, the internal forces associated with large deflections and plastic behavior depend upon the solution being sought. These terms, hence, have been approximated by extrapolating linearly from known solutions at the immediate two earlier time instants without iterating to convergence within each time step. Therefore, these pseudo-forces may become progressively less and less accurate particularly if large Δt time steps are used.

Since CIVM-JET 5B requires much more storage and computing for each time step of calculation than does CIVM-JET 4B, to be cost competitive with -4B, one must use for -5B a Δt at least 4 times larger than the allowable Δt for CIVM-JET 4B. Note that CIVM-JET 4B uses the unconventional form of the equations of motion while CIVM-JET 5B employs the equations of motion in their conventional form which involves more computing per time step; both of these formulations [4, 5, 17] are given concisely in Appendix A for the reader's convenience.

Figure 21 compares for the CB-18 experiment predictions of the CIVM-JET 4B and CIVM-JET 5B computer programs using the EL-SH Fit A material model and 43 equal-length finite elements. The predictions for the CIVM-JET 5B model are given for two time step sizes: $\Delta t = 0.5$ μsec and $\Delta t = 2.5$ μsec. The first time step size is identical to that used in the CIVM-JET 4B calculation which uses the central difference temporal operator. The second time step size represents the point at which the CIVM-JET 5B model becomes cost effective compared with the CIVM-JET 4B model.

Predictions are plotted for four spanwise locations (x = 0.0, 0.6, 1.5, and 3.7 in) which include the impact region, the mid-region which is dominated by 2-D deformation, and the region close to the clamped boundary. In each region the solutions are qualitatively similar to each other; for engineering purposes these are also quantitatively the same.

A CIVM-JET 5B calculation was carried out by using a Δt size which was about 10 times that permitted by the central difference method used in CIVM-JET 4B; this solution exhibited instability when impact and correction was encountered for the CB-18 example. It is not known for the CB-18 conditions the largest Δt permissible for well-behaved calculations when CIVM-JET 5B is used; 4 times and 10 times larger Δt than permissible for CIVM-JET 4B showed, respectively, well-behaved and unstable behavior for CIVM-JET 5B calculations.

The Houbolt operator as employed with the CIVM-JET 5B impact modeling is seen to be an alternative solution technique to CIVM-JET 4B, but care must be exercised that a cost effective time step be determined without encountering a region of instability.

The CIVM-JET 5B program was not used in further impact correlations and studies performed in this report. The 5B program compares favorably with the 4B program for predictive accuracy; however, the CIVM-JET 4B program had been exercised for a longer period of time and has provided plausible results for several impact-interaction modelings. These considerations led to the decision to study jet engine impact problems and the impact-interaction parameter variations (see Section 4) with the CIVM-JET 4B program.

The preceding discussion has dealt with the principal considerations for deciding whether to use CIVM-JET 4B or CIVM-JET 5B to predict impact-induced transient structural responses of 2-D beam and/or ring structures. Either code can be used to analyze single-layer structures but only CIVM-JET 5B can be employed to analyze multilayer, multimaterial structures. Earlier it was pointed out (see also Subsection A.2 of Ref.4) that a diagonalized mass matrix modeling of the structure is needed for

the prediction of momentum transfer from the fragment to only the translational degrees of freedom of the impact-affected region of the structure. Now, some discussion is given of various available choices for this diagonalized mass matrix modeling, and their consequences.

First, recall that the present beam and/or ring finite elements have 4 DOF/node; these are the in-plane and normal-direction translational displacements v and w, respectively, and the "extension" χ and "rotation" ψ (see Appendix A and Fig. A.1). In deriving the mass matrix for a single finite element from the kinetic energy expression or from the Principle of Virtual Work, one obtains a non-diagonal mass matrix termed the "variationally consistent mass matrix"; one obtains mass matrix entries on the diagonal associated with each of the 8 DOF's (4 at each end), as well as the off-diagonal "mass coupling" terms. The use of the consistent mass matrix as well as a mass matrix diagonalized in various ways has been studied [17, 33-36]; both types of matrices are used widely with reasonably similar transient response results. Where feasible or where considerations such as impact-induced momentum transfer calculations are needed, the computationally more efficient diagonalized mass matrix is preferred. Further, it was found that the predicted transient responses of 2-D structures to transiently applied loads when a diagonal mass matrix was used were affected only slightly by different choices for the diagonal entries associated with the non-translational degrees of freedom of the element as long as the diagonal entries associated with the translational degrees of freedom of the element were kept the same [17, 33-36].

For the case of single-layer structures of uniform thickness, one can readily define the diagonal mass matrix entries associated with the translational degrees of freedom v and w at each node: this is simply one-half of the mass of the element. The choice of the proper diagonal mass matrix entries corresponding to the non-translational ψ and χ degrees of freedom at each node is less apparent; these entries, however,

are generated automatically in the consistent mass matrix calculation. For a beam element which consists of several variable-thickness layers of different material, the "intuitive selection" of even the "translational entries" in a fully diagonalized mass matrix becomes a much more difficult and complex undertaking; however, the calculation of all of the mass matrix entries in the consistent mass matrix remains very simple and automatic. Therefore, it is convenient and natural to ask how one might select a diagonalized mass matrix by making use of the automatically-generated consistent mass matrix. This matter has been explored by Key and Beissinger [33], Clough [35], and Hinton [36]; there is general agreement on the selection of those entries associated with the translational degrees of freedom, but various selections have been suggested for the diagonal entries associated with the remaining degrees of freedom.

The approach suggested by Key and Beissinger [33] and by Hinton [36] may be summarized as: the procedure of lumping (mass matrix diagonalization) recommended in view of the infinite possibilities is to compute the diagonal terms of the consistent mass matrix and then to scale these terms so as to preserve the total mass of the element; that is, so that the sum of the mass entries at both ends of the element for each translational degrees of freedom shall equal the total mass [36]. A similar procedure has been proposed by Key and Beissinger [33]: the translational entries for the diagonalized mass matrix are determined from the consistent mass matrix by adding the corresponding off-diagonal translational term to the diagonal term -- this does result in identifying the total beam mass as the sum of entries at each end of the element for a given translational DOF. However, no clearly superior means for choosing the non-translational entries for the diagonalized mass matrix from the consistent mass matrix is apparent. One possibility suggested by Key and Beissinger is that these non-translational diagonal entries be scaled from the consistent mass matrix so that the highest natural frequency is matched with the highest natural frequency of the structure modeled with consistent mass (and stiffness) matrices. Since no clearly superior transient response results are demonstrated for such a choice and since

the preservation of the same largest natural frequency would impose the same Δt limit if one were to compute the transient structural response by using the timewise central-difference operator, this is regarded as an unattractive choice. Instead, a plausible choice for these non-translational entries of the diagonalized mass matrix is desired such that the highest natural frequency of the modeled structure becomes "as low as possible" -- this would have the effect of increasing the permissible time step size Δt for central-difference operator calculations, with no detrimental effects when one employs an implicit timewise operator such as the Houbolt operator.

Three candidate mass-matrix diagonalizing schemes are considered here. These are described concisely in the following. For clarity, consider a single initially-straight beam element with the following 4 degrees of freedom (q_i) at each end:

End 1 (or Node 1)	End 2 (or Node 2)
$q_1 = v$	$q_5 = v$
$q_2 = w$	$q_6 = w$
$q_3 = \psi \equiv \frac{\partial w}{\partial \eta}$	$q_7 = \psi$
$q_4 = \chi \equiv \frac{\partial v}{\partial \eta}$	$q_8 = \chi$

Mass Matrix Diagonalization Method 1

This is an "intuitive engineering method" which can be used readily only for single-layer elements of either constant or linearly-varying thickness. The same translational masses are assigned to DOF's q_1 and q_2 and another value to DOF's q_5 and q_6; the sum $m_{11} + m_{55} = m_{22} + m_{66} =$ total mass of the beam. Non-translational DOF's q_3 and q_4 are assigned m_{33} and m_{44} as being the same "estimated effective rotary inertia" for the beam; a similar assignment is made for m_{77} and m_{88}. See Appendix A of Ref. 4 for a fuller discussion. Concisely, these diagonal mass matrix entries are (non-diagonal entries are all zero):

$$m_{11} = m_{22} = \frac{1}{2}(h_1 + h_2)b\rho\ell\ (1 - C_1)$$

$$m_{55} = m_{66} = \frac{1}{2}(h_1 + h_2)b_1\rho\ell\ C_1$$

$$m_{33} = m_{44} = C_2\ \ell^3 b\rho(1 - C_1)$$

$$m_{77} = m_{88} = C_2\ \ell^3 b\rho\ C_1$$

where the thickness-dependent constants C_1 and C_2 are given by

$$C_1 = \frac{(2h_2 + h_1)}{3(h_1 + h_2)}$$

$$C_2 = \frac{h_1^2 + 4h_1h_2 + h_2^2}{36(h_1 + h_2)}$$

In these expressions ρ is the mass per unit volume of the beam element, b is the width of the beam, ℓ is the length of the beam element and h_1 and h_2 are the thickness values for the beam at ends 1 and 2, respectively. For present purposes, this description is considered to be adequate; see Ref. 4 for further details.

Mass Matrix Diagonalization Method 2

This method defines a diagonal mass matrix m^D_{ii} by using the entries already computed from the consistent mass matrix m^C_{ij}, as follows:

$$m^D_{11} = m^C_{11} + m^C_{15}$$

$$m^D_{22} = m^C_{22} + m^C_{26}$$

$$m^D_{33} = m^C_{33};\ m^D_{44} = m^C_{44}$$

$$m^D_{55} = m^C_{55} + m^C_{51}$$

$$m^D_{66} = m^C_{66} + m^C_{61}$$

$$m^D_{77} = m^C_{77}\ ;\ \ m^D_{88} = m^C_{88}$$

Hence, this method is readily applied to multilayer, multimaterial variable thickness structures.

Mass Matrix Diagonalization Method 3

This method is similar to Method 2, being different only with respect to how the non-translational degree-of-freedom entries m^D_{ii} are calculated. All diagonalized mass matrix entries are calculated by the rule

$$m^D_{ii} = m^C_{ii} + m^C_{i\ i+4}$$

Hence,

$$m^D_{11} = m^C_{11} + m^C_{14} \qquad m^D_{55} = m^C_{55} + m^C_{51}$$

$$m^D_{22} = m^C_{22} + m^C_{26} \qquad m^D_{66} = m^C_{66} + m^C_{62}$$

$$m^D_{33} = m^C_{33} + m^C_{37} \qquad m^D_{77} = m^C_{77} + m^C_{73}$$

$$m^D_{44} = m^C_{44} + m^C_{48} \qquad m^D_{88} = m^C_{88} + m^C_{83}$$

These three mass matrix diagonalizations as well as the consistent mass matrix were used to calculate the maximum natural frequency of clamped-ended beam CB-4 when modeled with twenty 4 DOF/node elements per half-span -- imposing symmetry conditions at midspan. The results are as follows:

Mass Matrix	ω_{max} (rad/sec)	$(\Delta t)_{cr} = \frac{2}{\omega_{max}}$ (μsec)
Consistent	$.7678 \times 10^7$	0.26
Diag. Method 1 (Intuitive)	$.2165 \times 10^7$	0.92
Diag. Method 2	$.4210 \times 10^7$	0.47
Diag. Method 3	$.9874 \times 10^7$	0.20

Since only diagonalized mass matrices are employed in the calculations of structural response to fragment impact, it is seen that Method 1 permits the largest allowable Δt to be used if one were to employ CIVM-JET 4B

which uses the central difference timewise operator; however, Method 1 has been developed only for single-layer elements. Hence, for multimaterial, multilayer variable-thickness elements, Methods 2 or 3 could be used; of these, Method 2 appears to be the preferred choice since it will permit the use of a larger Δt than will Method 3.

Some further comparisons are given in Table 1 for some predictions of large elastic-plastic transient response of impulsively-loaded beam CB-4. The half span was modeled with 20 equal-length 4DOF/node elements, the EL-SH Fit A stress-strain behavior was used, and a uniform lateral velocity of 10,707 in/sec was applied to the center node and to the next four nodes. Shown in Table 1 are predicted quantities (maximum Gaussian station strain, maximum nodal strain, elastic energy, kinetic energy, plastic work, and midspan w-displacement) at 100 μsec after the (sudden) initial velocity was applied -- for the use of: (a) the consistent, (b) the Method 2 diagonalized, and (c) the Method 3 diagonalized mass matrix. It is seen that the response quantities predicted at t = 100 μsec are close in all three cases; the two predictions which utilize the diagonalized mass matrix are very close to each other. Hence, it is recommended that until better mass diagonalization schemes are developed, Methods 1 and 2 should be adopted where applicable. These are the methods employed, respectively, in CIVM-JET 4B and CIVM-JET 5B.

SECTION 3

CONTAINMENT-RING RESPONSE TO T58 TURBINE ROTOR TRI-HUB BURST ATTACK

3.1 Problem Definition

In the spin-chamber facility of the Naval Air Propulsion Test Center (NAPTC) numerous experiments have been conducted wherein various types of actual and simulated engine rotors have been rotated at high rpm and caused to fail in various ways. High-speed Dynafax photographs nominally at 35,000 pictures per second have recorded the motions of the resulting fragments and their impact and interaction with a variety of containment-ring structures [12-14 and 37, for example]. Some of these containment rings were of single-layer construction; others were of multilayer multimaterial construction. In some cases, strain gages were applied to the containment ring, and the resulting transient strains and permanent strains were recorded.

Selected for discussion and analysis in this section of this study is NAPTC Test 201 [13,14] in which a 4130 cast steel* containment ring of 0.625-in thickness, 1.50-in axial length, and 15.00-in inside diameter and weighing 12.83 pounds rested horizontally on smooth support wires and encircled a T58 turbine rotor which was caused to fail in 3 equal 120-degree segments at about 19,859 rpm and to impact against this steel containment ring. Circumferentially oriented strain gages were attached to the ring at various circumferential locations at the ring's midwidth position. Transient strains were tape recorded for 10 such gages; transient strains from 4 of these 10 gages were also photographically recorded from swept oscilloscope displays. In addition after the test, permanent strains indicated by the four gages which survived intact were recorded.

Given in Table 2 are the weight and geometric data defining the containment ring, the rotor-burst fragment properties, and the test conditions for NAPTC Test 201. Note that the I.D. of the ring was 15.00 inches while

*From NAPTC's ACIPCO 2 billet [14].

the O.D. of the T58 turbine rotor was 14.00 inches; this 0.5-in clearance between the ring and the blade tip is untypically large but was selected to permit better photographic clarity and definition. Each fragment consisted of a "120-degree" sector of the rim with 17 attached blades; the distance from the axis of rotation of the rotor to the CG of the fragment was 2.797 inches. At the rotor burst rpm of 19,859, the translational velocity at the CG of each fragment was 5816.7 in/sec while the blade-tip speed was 14,557.2 in/sec. The resulting total kinetic energy of the 3 released fragments at burst was 908,820 in-lb, of which 476,766 in-lb was translational and 432,054 in-lb was rotational. Hence, each fragment at burst had nominally 158,922 in-lb of translational and 144,018 in-lb of rotational kinetic energy.

Shown in Fig. 22a is a schematic of the T58 power turbine rotor modified to undergo a tri-hub burst, and Fig. 22b shows a sketch of a typical fragment before impact. A photograph of one of the 3 fragments after the test is shown in Fig. 22c. The quality of the Dynafax photographs (taken at 35,000 pictures per second) of the impact of the 3 fragments and their interaction with the ring happened to turn out, unfortunately, to leave much to be desired; however, shown in Fig. 23 are a few sample photographs: (a) pre-test, (b) after rotor burst but before impact of the fragments with the ring, and at about 200, 514, and 1286 microseconds after initial impact in parts (c), (d), and (e), respectively. Figure 24 shows the permanently deformed containment ring; note that position marks have been provided at 5-degree intervals along the ring's midthickness location. Also shown in Fig. 24 is the post-test condition of the 3 attacking fragments. Note that only one of the fragments still possesses many of its original blades. The Dynafax pictures obtained show that this denuding occurred late, after the fragments fell by gravity below the plane of the containment ring and subsequently struck the heavy steel sides of the test chamber, resulting in greatly enhanced "fragment damage". Of course, very severe deformation and curling of many blades of each fragment can be seen to have occurred while the containment ring is still suffering the impact attack. This attack continues until well after the peak response of the containment ring has been

reached; only later do the fragments "escape the ring" by falling below "the containment plane".

Figure 25 indicates the circumferential locations of strain gages which were used to measure transient and permanent strains on the outer surface of the ring. These locations are defined by stations 1 through 72 marked at 5-degree intervals around the ring; station 1 is assigned $\theta = 0^{\circ}$, station 5 represents $\theta = 20^{\circ}$, etc. Note that permanent strains, as follows, were obtained from intact strain gages after the test at only four locations:

Station	θ(deg)	Permanent Strain(%)
9	40	- 0.95
13	60	- 3.23
33	160	- 1.07
37	180	- 3.31

Static uniaxial tensile stress-strain measurements for coupons of 4130 cast steel from NAPTC's National Forge billet were supplied [14]; these data were analyzed and used for the theoretical analysis of NAPTC Test 201 since according to Ref. 14 the Test 201 ring material is almost identical to that of the National Forge billet. Accordingly, these stress-strain data were approximated by piecewise linear segments defined by the following stress-strain (σ,ε) pairs: σ,ε = (0 psi, 0 in/in); (80,950 psi, .00279); (105,300 psi, .0225); and (121,000 psi, .200). This σ,ε fit is used in the mechanical sublayer material-behavior model and is referred to as elastic, strain-hardening (EL-SH). When strain-rate effects are taken into account, the perfectly-plastic yield stress of each (kth) mechanical sublayer for strain rate $\dot{\varepsilon}$ is taken to be that given by Eq. 2.1. Since measurements have not been made of the strain-rate dependence of the σ,ε behavior of the steel used in the NAPTC Test 201 ring, it has been assumed that its strain-rate dependence is approximately that of mild steel [25] for which $D = 40.4\ \text{sec}^{-1}$ and $p = 5$.

3.2 Ring Modeling and the Effects of Idealized-Fragment Size and Friction

In order to analyze the transient-structural response of the Test 201 steel containment ring to tri-hub rotor-burst attack with the CIVM-JET 4B computer program [4], it is necessary to represent the ring by finite elements of suitable number and size. Since as the impact attack proceeds, each fragment could conceivably perform a sequence of impacts with the "impact point" for each fragment moving circumferentially along the ring and also initial impact by each fragment might occur at any circumferential location, uniform-length ring finite elements form a logical modeling choice. Further, the present version of CIVM-JET 4B accommodates a maximum of 50 elements; hence, the largest number of elements which can be used and is also evenly divisible by 3 (since a 3-fragment "simultaneous" impact attack is involved) is 48 elements. Each element, therefore, subtends a 7.5-degree sector. In addition, considerable previous experience [3, 17] in the finite element analysis of rings subjected to intense loads over either a small or an extended circumferential region indicated that this size choice will permit one to obtain "converged transient response predictions" for large-deflection elastic-plastic structural behavior. Accordingly, 48 cubic-cubic Bernoulli-Euler ring finite elements were used to model the containment ring. This number of elements also provides a close approximation to the ring's actual geometry in the idealized impact portion of the CIVM-JET 4B analysis and code.

In the present effort, a supplementary convergence study was carried out. For this study a circular arch (or beam) covering a 60-degree arc, having both ends pinned-fixed, and having a width of 1.50 in, a thickness of 0.156 in, and an inner-surface radius of 7.50 in was used; this structure was subjected to a step-function radial outward concentrated load of 7,000 pounds at the midspan location and lasted for 150 microseconds. The stress-strain behavior of the aluminum material was assumed to be that identified previously as Fit A EL-SH-SR. The entire 60-degree structure was modeled by 6, 10, 14, 18, 22, and 30 equal-length 4DOF/node curved beam elements, and

the associated large-deflection elastic-plastic transient response predictions were carried out by using the JET 3A computer program of Ref. 3; this program employs the timewise central difference operator. Summarized in Table 3 for each of these modelings are: ω_{max}, $2/\omega_{max}$, $0.8(2/\omega_{max})$, the Δt actually used, and values calculated at t = 150 microseconds for (1) the midspan radial displacement w and (2) the total work input to the beam by the applied loading (at t = 150 μsec that applied loading has just terminated). Transient response predictions are compared for the 6, 10, and 30-element modelings in Fig. 26; Fig. 26a shows the midspan deflection w versus time, while Fig. 26b illustrates the predicted outer-surface strain time history at the quarter-span station (15° from midspan). Note that for this rather severe concentrated-load example, these illustrated predictions appear to have converged at least in an engineering sense* when 10 or more equal-length elements are used; that is, the results noted when 10, 14, 18, 22, or 30 elements were used were very close (peak deflections and strains are within about 3 to 5 per cent of a mean) to each other. Of these examples, only the 6-element case indicates convergence has not yet been achieved. Based on the study of Ref. 17 which demonstrates convergence of the transient solution for a forty-element complete ring, the above study which shows convergence for ten elements per sixth ring, and cost constraints (a function of the total number of degrees of freedom), the forty-eight equal-length element mesh for the complete ring was deemed acceptable for the tri-hub rotor burst analysis.

An examination of NAPTC Dynafax photographs of T58 turbine tri-hub rotor burst attack against single-layer steel containment rings reveals that shortly after initial blade-ring impact, the impacting blade begins to deform and curl; additional blades on the same fragment subsequently impact the ring and also curl. As this impact/interaction progresses, each of these bladed-disk fragments applies a load of continually changing distribution and magnitude to the ring including frictional forces; of course, the ring applies equal and opposite loads to the bladed-disk fragment. Thus, the geometry of each bladed-disk fragment changes rapidly and dramatically with time at least until the maximum response of the containment ring has been

*Also, the 22-element results were almost indistinguishable from the 30-element predictions.

reached. Similar changes continue thereafter but more slowly and less dramatically.

As noted earlier, a detailed accounting and following of the deformation of just one blade is a formidable task; hence, following the deformation behavior of the 17 blades on each of these 3-bladed-disk fragments represents a task which is impractical computationally at present. Thus, it is useful to employ idealized bladed-disk fragments each of which consists of a rigid circular disk of properly-selected diameter. Each idealized fragment shall have a mass and a mass moment of inertia equal to those of the initially-released bladed-disk fragment itself; requiring that the idealized fragment have a CG translational velocity and rotational velocity at "release" equal to those values for the actual fragment will insure duplicating the attack kinetic energy of the fragment for both translation and rotation. Further, one can account for a fixed coefficient of friction μ between the fragment and the ring by employing an appropriate value for μ in the CIVM-JET 4B program.

An examination of the basic dimensions of each undeformed bladed disk fragment (Fig. 22b) as well as plausible estimates of the probable state of severely-deformed bladed disk fragments of this type led to the following estimates of idealized fragment radius r_f: (a) minimum of 2.555 in, (b) maximum of 4.20 in, and (c) an "intermediate" value of 3.60 in. The minimum value represents the rigid-disk part of the bladed-disk fragment plus a small additional region encompassing severely curled blades. The maximum (or extreme) idealized radius selected lies between that necessary to circumscribe the greatest and the least lateral dimension of the undeformed fragment. Since the energy absorbed in blade curling is relatively small, the attacking fragment will still possess perhaps 95 per cent of its pre-impact kinetic energy when half of the 17 blades have curled over in a region outboard of about $r = 4.06$ in measured from the rotor shaft axis. Hence, although the actual impact attack begins at first-blade touching, the "serious impact attack" upon the containment ring comes much later when the blades have curled over against each other and against the

outer rim of the disk part of the fragment. At this stage the "effective radius" of the attacking fragment is approaching the cited "minimum plausible value" of r_f = 2.555 in. These choices are depicted schematically in Fig. 27.

The use of an implausibly-large idealized rigid circular fragment would clearly constrain the containment ring and unrealistically limit the amount of its deformation in the impact/contact region of each fragment. On the other hand, the physical dimensions of the rigid disk portion of the fragment and the region occupied by severely curled over and mutually contacting blades make the choice of an r_f smaller than choice (a) to be clearly illogical. Hence, for a severe threshold-containment type of fragment attack, one expects that the use of an idealized fragment of fixed $r_f \doteq 2.555$ in would result in a quite reasonable prediction of the maximum response of the ring; however, it is impossible physically for this type of idealized model to give a reasonable approximation of the actual transient response history of the containment ring -- actual impact will occur much earlier and, initially, much more gently than for the idealized fragment.

Figure 28 depicts the geometric test and modeling data for the 4130 steel containment ring subjected to tri-hub T58 turbine rotor burst in NAPTC Test 201. The ring is represented by 48 elements and EL-SH-SR material behavior is taken into account. Three equal-size idealized fragments are used; all three fragments are assumed to impact initially simultaneously at equidistant circumferential locations.

The effects of idealized-fragment size can be illustrated most conveniently perhaps by comparing the extreme deformed-ring configuration for each of these 3 cases, as shown in Fig. 29a; the time at which that extreme deformed state occurs is different for each of these 3 cases. For these 3 extreme defored states, Fig. 29b compares the circumferential distribution of the circumferential-extension strain (γ_{11}) on the outer surface of the ring. Clearly, the extreme response of the ring is greatest for the smallest and is least for the largest idealized fragment size. In these three calculations, it was assumed that there was zero friction between each fragment and the ring.

It may be of interest to examine the nature of the transient strains

which are predicted to occur at various circumferential locations of the containment ring. As a convenient means of identifying circumferential locations, Fig. 30 shows a predicted deformed ring configuration (and the 3 idealized fragments) at 1000 microseconds after initial impact; shown also are the element identification numbers. Predicted inner-surface and outer-surface circumferential transient strains are shown in Fig. 31 at elements 1, 4, 6, 9, 11, and 47 for the case r_f = 2.555 in and μ = 0. One may interpret the mean of the inner surface and outer-surface strains as representing roughly the "membrane strain" portion, and the deviation from this mean as the part arising from bending.

The effect of using a friction coefficient μ value of 0.3* is illustrated in Fig. 32a where the deformed ring configurations for μ = 0.3 and μ = 0 at 1200 microseconds after initial impact are shown for r_f = 2.555 in. Since these deformed ring profiles are shown with respect to the fixed y, z coordinates, it is seen that they are "slightly rotated" with respect to each other but the deformation severity is comparable. Shown in Fig. 32b at that same time instant is the outer-surface distribution of predicted circumferential strain; here also, it is seen that the effects of friction between the idealized fragment and the containment ring have little effect upon the magnitude of the peak strains predicted at this instant. Hence, most of the calculation cases carried out assumed frictionless impact.

Summarized in Table 4 are the pertinent data which characterize each of the various CIVM-JET 4B calculations made to predict the response of the present containment ring. The time increment size used in every case was 2.5 microseconds.

3.3 Comparisons of Predictions with Experiment

For reasons noted in Subsection 3.2, predicted time histories of impact-induced containment ring strains cannot be compared rationally with measured transient strains for this ring-fragment impact problem. Also,

*This choice as a plausible and reasonable value is indicated by the studies reported in Ref. 15.

because of poor photographic quality, reliable measurements of the extreme deformed ring configuration are not available. Hence, only the permanent deformed ring configuration and several measurements of ring outer-surface permanent strain are available for a meaningful comparison with predictions. As noted earlier, the prediction utilizing an idealized fragment radius r_f of 2.555 in and $\mu = 0$ is the most reasonable and plausible case for comparison with the NAPTC Test 201 experimental data.

Accordingly, Fig. 33 compares the measured permanent deformed-ring configuration with that estimated from the calculations. The latter configuration was chosen by examining a sequence of predicted deformed-ring configurations throughout the response to peak deformation, and subsequently to and beyond maximum springback. Peak response and maximum springback occurred, respectively, at about 1200 and 3180 microseconds after initial impact. The selected "predicted permanent-deformation configuration" was taken as that predicted at 2600 microseconds after initial impact; this corresponds to the time midway between the time at peak springback and the time at the next peak deflection of the ring. The circumferential distribution of predicted ring outer-surface strain at this same time instant is shown in Fig. 34. Measured permanent strains are shown at locations corresponding to "matching locations" between the predicted deformed ring profile shown in Fig. 33 and the configuration and location data depicted in Fig. 25. In terms of θ defined in Fig. 28, the strain gage locations (a different θ in Fig. 25) were "determined" by orienting the measured permanent deformed-ring configuration for a best match with the predicted deformed-ring configuration (as per Fig. 33). The resulting θ positions for the "permanent strain" gages were deduced to be:

Gage	θ of Fig. 25 (deg)	θ of Figs. 28 and 34 (deg)
9	40	10
13	60	30
33	160	130
37	180	150

From Fig. 33 it is seen that there is reasonable agreement between prediction and experiment for the permanently-deformed-ring configuration. The permanent strain agreement observed in Fig. 34 is less faithful but still reasonable. By varying r_f, μ, etc. over a plausible range of values, better theoretical-experimental agreement could be expected but such variations would lead only to predictions constituting results in an "uncertainty band" whose convincing narrowing would be difficult to achieve*. There will remain an inherent uncertainty band in predictions vs. experiment unless and until one employs a more faithful and complete model of the complex attacking fragment. Clearly, various steps in this direction are possible but at a price in complexity and computation.

Finally, an examination of the Dynafax photographs for NAPTC Test 201 indicates that the three fragments may not have been "released" simultaneously. It appears that one fragment initially contacted the ring; two pictures later a second fragment appear to have come in contact with the ring; and one picture later the third fragment appears to have made contact with the ring. Note that the time interval between pictures is about 28.6 microseconds. To examine the "sequential release and impact effect", a CIVM-JET 4B calculation for r_f = 2.555-in and μ = 0 was made wherein fragment 1 was released; fragments 2 and 3 both were released 60 microseconds later. An examination of the resulting predicted transient impact-interaction response revealed insignificant differences from the corresponding simultaneous impact case.

3.4 Comments

Although the present CIVM-JET 4B analysis and code employs a highly-idealized rigid-fragment model to represent a complex deformable fragment which impacts 2-D containment/deflection structures, it appears that the use of a plausibly-selected size of the idealized fragment and the faithful modeling of the translational (and, of lesser importance, the rotational) kinetic energy prior to impact will lead to reasonable engineering predictions of the peak response and the permanent deformation of the impacted containment ring. Calculations indicate that the use of plausible values for friction

*Also, the availability of $\sigma,\dot{\varepsilon},\varepsilon$ data for the particular lot of 4130 cast steel from which the NAPTC Test 201 ring was made could reduce further the uncertainty band of these predicted responses.

between the fragment and the impacted structure has very little effect upon the predicted transient response of a containment ring.

Of the various modeling parameters and values which the analyst must select, that having the greatest effect on the peak predicted structural response of the containment ring is the idealized fragment size itself.

Finally, two reminders concerning the limitations of the present CIVM-JET 4B analysis and code are pertinent. First, the analysis applies strictly only to the two-dimensional type of structural response; hence, cases involving an important degree of 3-D structural response cannot be represented by the present analysis and code. Second, the governing equations for this analysis apply to large-deflection and large-rotation elastic-plastic transient structural response but the strains themselves must be small. An upper limit on the strains for which this analyses is valid cannot be specified precisely; however, predicted strain values exceeding roughly 6 to 10 per cent should be regarded with caution. Clearly, rupture threshold predictions for ductile metal C/D structures will involve substantially larger strains; accordingly, an extension to accommodate large strain behavior properly will be necessary to achieve that end rationally and reliably.

SECTION 4

CONTAINMENT STRUCTURE PARAMETRIC EFFECTS ON STRUCTURAL RESPONSE INDUCED BY FRAGMENT IMPACT

Sections 2 and 3 of this report have been devoted to discussing numerical methods for predicting 2-d transient structural responses of, respectively, (1) clamped-ended beams subjected to rigid-fragment (steel sphere) impact and (2) containment rings subjected to impact attack by idealized engine rotor fragments. The capabilities and limitations of the associated computer codes CIVM-JET 4B and CIVM-JET 5B were reviewed together with guidelines for selecting an appropriate structural model so as to obtain reliable engineering predictions of fragment-impact-induced structural response (within the range of applicability of the prediction method as actually implemented in these computer codes). Also, predictions were compared with representative experimental data.

Since the scope and complexity of actual fragment attack against containment structure usually greatly exceeds that which is feasible to include in mathematical/numerical prediction models, it is often useful to employ a judicious combination of (1) mathematical/numerical predictions and (2) actual experiments -- in order to study in a cost-effective manner the effects of each of the numerous variables upon, for example, the (least) weight and/or cost of a containment structure which is to be selected to achieve threshold containment[+] of a given fragment attack; similar results for a series of different postulated fragment attacks may also be of interest. The use of mathematical/numerical predictions alone is hazardous because of the possible inadvertent omission of important ingredients present in the actual physical problem. On the other hand, the use of experiment alone is inadvisable because of the time and large cost per test as well as the great number of tests required to explore the effects of each of the potentially-important parameters and variables of the problem.

[+] That is, the dividing line between fragment containment and non-containment.

In this section the use of dimensional analysis in studying the effects of various pertinent parameters upon the containment threshold response of each of various 2-d containment structures to fragment impact attack is explored with reference to: (1) mathematical/numerical predictions and (2) actual experiments. The dimensional analysis is discussed first in terms of a rather general situation involving fragment attack against a broad class of containment structures. Then the analysis is specialized and applied to (a) NAPTC experimental studies [12,13,37] of 2-d containment ring responses to specific types of engine-rotor-fragment impact attack and (b) MIT-ASRL experimental [16] and numerical studies of steel-sphere impact attack against a simple ductile metal beam. Finally, the effects of scale are discussed; that is, the question of determining the physical parameter values for a "similar containment ring" required to achieve threshold containment when the "similar fragment attack" emanates from a rotor of N times the size of a given reference rotor of the same material is examined.

4.1 Dimensional Analysis Considerations

There are two basic mutually-complementary methods that can be used to quantify the containment threshold capability of a given containment structure which is subjected to a given fragment impact attack condition, and to identify the major parameters affecting a particular structure's containment potential:

(1) A mathematical model representing the governing equations of the large-deflection elastic-plastic responses of the containment structure and the impacting fragments, and of the impact-interaction behavior can be devised. These equations can then be rendered dimensionless. These dimensionless parameters can be varied in magnitude and the subsequent solutions of the mathematical model will determine the effects that these parameters have on the sought threshold-containment conditions.

(2) A physical approach can be used in which all of the "physical parameters" thought to be involved in the impact-interaction and response are identified and formulated into a set of dimensionless

parameters [38,39]. This set of dimensionless parameters can then be varied individually in a series of experiments to determine their effects on the sought containment threshold.

These two methods can be combined to form a systematic means of identifying the important impact-interaction variables and assessing the magnitudes of their effects in a cost-effective manner. The mathematical model readily identifies the "important parameters" from a theoretical approach; however, the accuracy of this process depends upon how closely and fully the equations model the physical problem. The impact-interaction and the associated transient structural response as addressed in this report is a highly nonlinear problem and the mathematical models of this interaction [4,5, and 17] contain a number of restrictive assumptions. Therefore, the mathematical model is itself subject to experimental verification/correlation to determine its applicability, accuracy, and reliability. The physical approach, by itself, is also limited by the complexity of the problem and cost considerations. In forming an "intuitive" set of governing parameters, one may neglect an important quantity and the subsequent series of experimental modelings will be extremely expensive if that incomplete and deficient characterization were used to study the effect of <u>each</u> parameter. (A "simple" experimental program could readily consist of over a hundred separate test runs in order to quantify the effects of five or six <u>major</u> parameters; an experimental program with five independent variables and a series of three test levels to analyze the effect of each variable would consist of 5^3 or 125 separate test runs.) It is evident that as the complexity of the problem to be analyzed increases, an analysis method combining both of the above basic procedures becomes both convenient and necessary.

A dimensional analysis is based solely on the relationships that must exist among the pertinent variables because of their dimensions rather than the laws of physics. However, once an assumed mathematical model of the physical problem has been formulated and correlated with the data obtained from a simple set of experimental models, the key parameters affecting containment can be visualized and cast into dimensionless form in a physically meaningful manner. As demonstrated by Langhaar [38], and utilized in

preliminary containment studies [39], a set of dimensionless parameters can be constructed from a set of pertinent variables by application of the Buckingham-Pi theorem. If n is the number of variables present and r is the number of least-order dimensions represented by these variables (i.e., mass, length, time, etc.), a complete set of m dimensionless parameters can be constructed where m = n - r. This set of dimensionless parameters will by no means be unique; but, by physically examining and justifying each dimensionless parameter, a meaningful set of m parameters can be constructed. The effect of each of these parameters can be studied individually by conducting a series of (1) experiments or (2) mathematical solutions, holding all other parameters constant. Of course, one could and should conduct partial factorial experiments to examine the possible presence of synergestic effects. This procedure is permissible if one knows that there are no synergestic effects between the parameters. In the absence of such knowledge, some type of factorial experiment would be appropriate.

4.1.1 General Description

It is necessary first to identify all of the principal variables influencing a general impact-interaction and response of a container or deflector structure which is subjected to fragment impact attack. Before these variables are assembled into a useful set of dimensionless parameters, the variable list should be reduced by eliminating those variables whose effect on the overall interaction is physically reasoned (or can be shown) to be insignificant. Once a "complete" set of primary variables is identified, they can be combined based on physical relationships into a convenient set of dimensionless parameters.

The variables describing an "impact-interaction" can be divided into two distinct groups: (1) those variables unique to the impacted structure, and (2) those variables unique to the impacting fragment(s). These variables can be further subdivided into geometric, kinematic/environmental, and material variables.

The containment structure is defined geometrically by its length, width, and thickness; if the structure is conceptualized as a complete (containment) ring, the radius of the ring becomes a primary variable rather than the length. If the container is a section of a doubly-curved 3-D body, two radii of curvature will become primary geometric quantities. For purposes of simplicity, the containment structures treated here are regarded as being three-dimensional thin-shell bodies of revolution (i.e., rings, cylinders,

or spheroidal sections, see Fig. 35), or as plates or beams. A thickness measure can be defined for any of these structures (here all are assumed to be of constant thickness); appropriate lengths, widths, or radii also can be defined.

For illustrative purposes the attacking fragments are considered to be portions of a jet engine turbine rotor, Fig. 36. The fragment could be either a single blade, a segment of the hub with attached blades, or a bladed-disk sector. All three of these potential fragments can be described geometrically by a width (i.e., axial projection which is assumed to be constant), the distance from the rotor axis of rotation to the fragment CG, and the length of the fragment from its CG to the blade tip, see Fig. 36. The movement of the fragment relative to the container must be defined geometrically. Since the container is initially motionless in the reference space used for the analysis, the fragment will possess all of the initial translational and angular velocity of the system. The angular velocity of the fragment is a primary variable while the translational velocity of the fragment is defined by the angular velocity and the location of the fragment center of gravity, r_{CG}.

These geometric and kinematic variables and their dimensions are summarized below for both the fragment and the containment structure (or container):

Geometric and Kinematic Variables			
	Quantity	Description	Units
Container	r_c (or ℓ_c)	Major Radius (or Span)	L
	r_{2c} (or w_c)	Minor Radius (or Width)	L
	h_c	Thickness	L
Fragment	ℓ_f	Length from Fragment CG to Blade Tip	L
	r_{CG}	Distance from Axis of Rotation to Fragment CG	L
			L
	w_f	Width (Axial Projection)	L
	ω_f	Angular Velocity	T^{-1}
	n	Number of Fragments	—
TOTAL: 8 Variables			

The material properties of both the fragment and the container are not as readily quantified as are the geometric and kinematic quantities. Both the fragment and the container have their own material mass densities ρ_o (assumed constant for each one) per unit initial undeformed volume. Each material can be quantified conveniently by an elastic modulus, a yield stress, an ultimate stress, a maximum strain, and strain rate parameters. These material values are obtained from standard tests conducted with a coupon of the structural material. The values σ_o and σ_u are defined in terms of engineering stress (also called the First Piola-Kirchhoff stress) σ_E, ($\sigma_E = P/A_o$, where P = applied force and A_o = initial cross sectional area) because the maximum engineering stress σ_u conveniently identifies the maximum load P_m that the structure can bear (and this occurs immediately prior to necking). The strain values are defined in terms of extensional linear strain, E_1 (where $E_1 = \frac{\ell - \ell_o}{\ell_o}$, ℓ = deformed length, and ℓ_o = initial length) because this is the conjugate to the engineering stress such that the total internal strain energy per unit initial volume $\bar{U}$ (proportional to the energy per unit mass $\bar{U}_m$) of the test coupon is:

$$\bar{U} = \int_0^{E_1} \sigma_E \, dE_1 = \int_{\ell_o}^{\ell} \frac{P}{A_o} \frac{d\ell}{\ell_o} = \frac{\int_{\ell_o}^{\ell} P \, d\ell}{A_o \ell_o} \equiv \frac{U}{V_o} \equiv \rho_o \left(\frac{U}{\rho_o V_o} \right) \equiv \rho_o \bar{U}_m \tag{4.1}$$

The ultimate stress, σ_u, is defined here as the maximum stress attained during the tensile test ($\sigma_u = P_m/A_o$) and the corresponding extensional strain is called "the maximum strain, ε_m". Strain rate dependency is approximated by a strain-rate-affected yield stress, $\sigma_y(\dot{\varepsilon})$, as defined from empirical data (Refs. 24 and 25) by:

$$\sigma_y(\dot{\epsilon}) = \sigma_o \left(1 + \left| \frac{\dot{\epsilon}}{D} \right|^{\frac{1}{p}} \right) \tag{4.2}$$

where D and p are empirical material constants and $\dot{\varepsilon}$ is the strain rate. To complete the set of material variables (assuming isotropic materials for both the fragment and the container) are Poisson's ratio and the coefficient of thermal expansion. Also, the impact-interaction is influenced by two material qunatities which "couple" both the fragment and the container

material together: the coefficient of friction and the coefficient of restitution, each of which is dimensionless.

These "material property variables" are summarized below.

Material Property Variables			
Quantity		Description	Units
Container	ρ_c	Material Density	FT^2/L^4
	E_c	Elastic Modulus	F/L^2
	σ_{c_o}	Yield Stress	F/L^2
	σ_{c_u}	Ultimate Stress	F/L^2
	ε_{c_m}	Ultimate Strain	L/L
	D_c	Strain Rate Constant	T^{-1}
	p_c	Strain Rate Constant	--
	ν_c	Poisson's Ratio	--
	α_c	Coefficient of Thermal Expansion	θ^{-1}
Fragment	ρ_f	Material Density	FT^2/L^4
	E_f	Elastic Modulus	F/L^2
	σ_{f_o}	Yield Stress	F/L^2
	σ_{f_u}	Ultimate Stress	F/L^2
	ε_{f_m}	Ultimate Strain	L/L
	D_f	Strain Rate Constant	T^{-1}
	p_f	Strain Rate Constant	--
	ν_f	Poisson's Ratio	--
	α_f	Coefficient of Thermal Expansion	θ^{-1}
	μ	Coefficient of Friction	--
	e	Coefficient of Restitution	--
TOTAL: 20 Variables			

To define completely the impact interaction, several variables associated with the surrounding "environment" are needed. The local gravitational acceleration, the local temperature, and the local time frame must be included in the analysis, and are listed below.

Environmental Quantities		
Quantity	Description	Units
g	Acceleration of Gravity	L/T^2
T	Temperature (above normal)	θ
t	Time	T
TOTAL: 3 Variables		

To this point, variables which characterize the containment structure and the attacking fragments have been discussed but no parameters have been chosen to describe the consequences or the results of the postulated fragment-impact attack. With respect to the containment structure itself, one must define the basic objective; two evident possibilities are:

(1) to prevent fragment penetration -- in this case one is interested in defining the dividing line between containment and non-containment of the fragments or

(2) to limit the maximum intrusion of the intact (non-ruptured) containment structure into the surrounding space (to avoid inflicting damage to critical components, controls, etc.) -- in this case one might select the maximum deflection z_c of the container to be a parameter of interest.

Also, it is conceivable (although unlikely) that one would be interested in describing the consequences to the deformable fragment of its deplorable impact attack against the containment structure. In this case one might choose one or more parameters to describe the maximum deflection z_f of the fragment. Accordingly, one might add the following two quantities to the variable list:

Effects Quantities		
Quantity	Description	Units
z_c	Maximum Deflection of the Containment Structure	L
z_f	Maximum Deflection of the Fragment	L

In summary, the posed problem of fragment impact attack against a containment structure and the consequent response may be described in terms of these 33 variables which are expressed in terms of four distinct units: length, force, time, and/or temperature. Hence, there are 29 (i.e., 33-4 = 29) independent dimensionless parameters that can be formed from the proposed set of variables.

The following is a list of these 29 dimensionless parameters, grouped in four descriptive categories: material, environmental, geometric, and kinematic:

SET OF PHYSICALLY PLAUSIBLE NON-DIMENSIONAL PARAMETERS			
Material	$\pi_1 = \varepsilon_{mc}$	Geometric	$\pi_{16} = n$
	$\pi_2 = \varepsilon_{mf}$		$\pi_{17} = (r_c n)/(r_{CG}+\ell_f)$
	$\pi_3 = \nu_c$		$\pi_{18} = h_c/(r_{CG}+\ell_f)$
	$\pi_4 = \nu_f$		$\pi_{19} = w_c/w_f$
	$\pi_5 = p_c$		$\pi_{20} = h_c/r_c$
	$\pi_6 = p_f$		$\pi_{21} = h_c/w_c$
	$\pi_7 = \mu$		$\pi_{22} = w_f/(r_{CG}+\ell_f)$
	$\pi_8 = e$	Kinematic	$\pi_{23} = (\omega_f r_{CG} t)/h_c$
	$\pi_9 = \rho_c/\rho_f$		$\pi_{24} = (\omega_f r_{CG})/(h_c D_c)$
	$\pi_{10} = \sigma_{co}/\sigma_{fo}$		$\pi_{25} = (\omega_f r_{CG})/(r_{CG}+\ell_f) D_f$
	$\pi_{11} = \sigma_{cu}/\sigma_{fu}$		$\pi_{26} = (\sigma_{cu}\ \varepsilon_{cm})/\rho_f[\omega_f^2(r_{CG}+\ell_f)^2]$
	$\pi_{12} = E_c/E_f$		$\pi_{27} = (\sigma_{fu}\ \varepsilon_{fm})/\rho_f[\omega_f^2(r_{CG}+\ell_f)^2]$
Environmental	$\pi_{13} = (g r_c)/(\Omega\ r_{CG})^2$		$\pi_{28} = z_c/h_c$
	$\pi_{14} = (T\alpha_c)/\varepsilon_{cm}$		$\pi_{29} = z_f/\ell_f$
	$\pi_{15} = (T\alpha_f)/\varepsilon_{fm}$		

In the "material" category, π_1 through π_8 are already dimensionless, while π_9 through π_{12} consist of ratios of container-to-fragment mass density, static yield stress, ultimate stress, and elastic modulus. The "environmental" category, π_{13} - π_{15}, includes gravitational to centrifugal acceleration effects, and thermally-induced strain ratioed to ultimate strain for the container and the fragment. Included in the geometric set, π_{16} through π_{22}, are the (dimensionless) number (n) of fragments (tacitly it is assumed that the bursting rotor fragments into n equal-size pie-shaped bladed-disk fragments) as well as pertinent geometric ratios of characterizing dimensions of the containment structure and the fragment(s). Next, the kinematic set, π_{23} through π_{29}, may be regarded as indicating the severity of the impact attack.

The π_{23} term may be interpreted as the ratio of the distance traveled by the fragment CG in time t to the wall thickness of the container. In π_{24} and π_{25} the CG velocity of the fragment is ratioed to "velocities" involving the strain rate constants D_c and D_f for the container and the fragment, respectively. Next, π_{26} and π_{27} may be regarded as representing the ratio of a rough measure of the maximum energy absorption capability per unit volume for the containment material and the fragment material, respectively, to the fragment tip kinetic energy per unit volume. Finally, π_{28} and π_{29} are the dimensionless "effects parameters", ratioing the maximum deflection to a characteristic length for the container and the fragment, respectively.

4.1.2 Reduction for Rigid-Fragment Attack

The 29 dimensionless parameters discussed in Subsection 4.1.1 pertain to a fairly general case of deformable-fragment impact attack against deformable containment structure, except that all materials involved are assumed to be isotropic and the container geometry is restricted to thin shells of revolution (or equivalent). This description is appropriate for certain experimental situations to be described in Subsection 4.2, for which the fragments are deformable. However, in certain experiments and in numerical predictions (both to be discussed in Subsection 4.3), the impacting fragment is rigid (non-deformable) for all intents and purposes. Hence, it is useful to examine the effects of considering a rigid fragment in reducing the number of characterizing dimensionless parameters for rigid-fragment impact attack.

If the fragment were assumed to be rigid, all of the fragment material variables (except density) and the fragment deflection z_f would be ignored, thereby reducing the variable list by 9. That is, E_f, σ_{fo}, σ_{fu}, ε_{fm}, D_f, p_f, ν_f, α_f, and z_f all would be eliminated as variables. This means the deletion of variables π_2, π_4, π_6, π_{10}, π_{11}, π_{12}, π_{15}, π_{27}, and π_{29}, thus leaving 20 dimensionless parameters for further consideration.

A further reduction in the number of basic dimensionless variables can be achieved by imposing further restrictions. For example, if all contemplated experiments and analysis were to be carried out for near-earth conditions, the local gravitational acceleration g could be removed as a variable.

Further if one assumes (1) that the containment structure is at essentially a uniform temperature even though that temperature be "elevated" so that there are no thermally-induced stresses and (2) that whatever calculations are carried out include the appropriate material property data (E_c, σ_{cu}, σ_{co}, ϵ_{cm}, D_c, p_c, ν_c) for that elevated temperature condition, one can eliminate both the temperature T and α_c from consideration as variables. With the elimination of the 9 rigid-fragment "variables" and these latest 3 variables (g, T, and α_c), there are now only 21 variables left and these are expressed in terms of the 3 fundamental units: length, force, and time. Accordingly, one is now left with a "reduced set" of (33-9-3)-3=18 independent dimensionless parameters (β), as renumbered and listed below:

REDUCED SET OF DIMENSIONLESS PARAMETERS
(Rigid Fragment, Near Earth, No Temperature Gradients)

Material	Geometric	Kinematic
$\beta_1 = \epsilon_{mc}$	$\beta_8 = n$	$\beta_{15} = (\omega_f r_{CG} t)/h_c$
$\beta_2 = \nu_c$	$\beta_9 = (r_c n)/(r_{CG}+\ell_f)$	$\beta_{16} = (\omega_f r_{CG})/h_c D_c$
$\beta_3 = p_c$	$\beta_{10} = h_c/(r_{CG}+\ell_f)$	$\beta_{17} = (\sigma_{cu}\ \epsilon_{cm})/\rho_f[\omega_f^2(r_{CG}+\ell_f)^2]$
$\beta_4 = \mu$	$\beta_{11} = w_c/w_f$	$\beta_{18} = z_c/h_c$
$\beta_5 = e$	$\beta_{12} = h_c/r_c$	
$\beta_6 = \rho_c/\rho_f$	$\beta_{13} = h_c/w_c$	
$\beta_7 = E_c/\sigma_{c_o}$	$\beta_{14} = w_f/(r_{CG}+\ell_f)$	

Finally, it should be noted that this is a possible but a non-unique set of characterizing dimensionless parameters. Other combinations of these (or equivalent related) variables could be constructed to give an equally-valid set of 18 dimensionless parameters.

Next in Subsections 4.2 and 4.3, related more-restricted categories of problems will be discussed involving certain experiments and/or numerical predictions. Also, an alternate set of dimensionless parameters will be considered.

4.2 Dimensional Considerations Applied to the NAPTC Rotor-Burst-Containment Experiments

As a part of the NASA study on Rotor Burst Protection, the Naval Air Propulsion Test Center (NAPTC) has conducted a series of experiments [15,37, for example] in which actual aircraft engine rotors have been rotated at high speed, caused to burst into various fragment patterns, and the subsequent fragment impact against containment rings has been studied. These experiments were conducted in order (1) to investigate the associated impact-interaction phenomena for containment structure impacted by typical complex deformable fragments, (2) to obtain an empirical data base to aid in containment-structure design, and (3) to obtain data which would be useful: (a) in guiding the development of and (b) in evaluating numerical methods for predicting the responses of bodies involved in fragment/structure impact, interaction, and response.

It is convenient for discussion purposes to consider two separate groups of the NAPTC experiments. In one group simple containment rings of a given material were used in an attempt to determine the containment threshold for rotor burst attack from a GE T58 turbine rotor spinning at 20,000 rpm, for cases in which the rotor was caused to rupture into 2, 3, or 6 equal-size pie-shaped bladed-disk fragments. The second group consisted of similar experiments but involved a different and larger turbine rotor (a P&W J65) with an 8500 rpm rotor-burst condition. Each group is considered separately in the following.

4.2.1 T58 Rotor Burst Containment

The T58 turbine rotor employed in these containment studies as depicted in Fig. 37 has a 14-in diameter, about a 1-in axial length, 51 blades -- each with a 3.5-in length, weighs 10.8 pounds, and was modified to rupture into 2, 3, or 6 equal-size fragments at a nominal 20,000 rpm.

In these containment experiments, there was a single source of fragments -- the T58 rotor -- hence, the fragment material parameters were not varied; also, the basic geometric parameters of the fragment source were not varied, only the number n of equal-size fragments used was varied, and the geometric parameters associated with each are implied when one specifies the value of n. With respect to the containment structure, it was intended that a single containment material (4130 cast steel) be employed. The only variables employed were the axial length (or width) w_c and the radial thickness h_c of the containment structure, the latter quantity being varied as a means of defining experimentally the containment threshold.

In view of these facts, it is convenient and useful to summarize the fixed quantities and the variables needed to characterize the containment ring and the fragments. Further, because of the restricted set of variables involved, it is useful to select a slightly different descriptive set of quantities for the fragment attack from the "general set" considered in Subsection 4.1. Since the fragment geometry is unchanging except as implied by the number n of fragments, it is useful to describe each fragment by

m_f = mass of the fragment

I_f = mass moment of inertia of the fragment about its CG

ω_f = angular velocity of the fragment (and rotor) at rupture

v_f = translational velocity at the CG of the fragment at release

r_{CG} = distance from the axis of rotation to the CG of the fragment

Automatically implied is the distance from the fragment CG to the blade tip. Accordingly, listed below are the characterizing quantities which remained fixed and those that were varied in this group of NAPTC experiments:

CONTAINMENT RING	FRAGMENT
Fixed Quantities	Fixed Quantities
Material	Material
Inner Surface Radius, r	ω_f, v_f
Variables	Variables (Only as Implied by n)
Radial Thickness, h_c	m_f, I_f, r_{CG}, r_f
Axial Width, w_c	

Note that for a given number, n, of equal-size bladed-disk fragments, the quantities m_f, I_f, r_{CG}, and r_f are fixed; in this case there are no fragment-attack variables -- and the value of n suffices to define the attack for given: fragment material and ω_f (v_f is defined automatically since r_{CG} and ω_f are given).

The above characterization of the fragment attack permits one to describe important scalar quantities present in this problem; namely, the pre-impact translational and the rotational kinetic energy of each fragment: $(KE)_{f_{ot}}$ and $(KE)_{f_{or}}$, respectively. The total kinetic energy $(KE)_o$ of the "fragment generator" may be expressed in terms of these individual fragment quantities by

$$(KE)_o \equiv \frac{1}{2} I \omega_f^2 = n\left[(KE)_{f_{ot}} + (KE)_{f_{or}}\right] \qquad (4.3)$$

where I is the pre-burst mass moment of inertia of the rotor about its axis. In these NAPTC experiments the "total attack kinetic energy $(KE)_o$" was held (essentially) constant. Hence, the geometry associated with a selected value of n dictates <u>for each fragment</u> both the actual value and the different proportion of translational and rotational pre-impact kinetic energy possessed by each fragment. This distribution is shown, for example, by Martino and Magano [40], Clarke [41], and McCarthy [42] as depicted in Fig. 38. Calculations show [18, and Subsection 3.2 of this report] and experiments confirm that metal containment ring response is affected strongly by the <u>translational</u> kinetic energy but almost negligibly by the rotational kinetic energy of each of the n attacking fragments.

Since the containment ring and fragment material remain unchanged during the present group of NAPTC tests, neither the coefficient of friction μ nor the coefficient of restitution e need be regarded as variables. Finally, all tests were conducted at room temperature conditions.

Hence, according to dimensional analysis principles, one may express the maximum-extensional-strain dimensionless parameter ε_c as a function of the following dimensionless variables [18,37,39]:

$$\underbrace{(\epsilon_c)_{max}}_{\text{RESULT}} = f\underbrace{\left(h_c/r\ ,\ w_c/r\ ,\ (KE)_o/(W_c r)\ ,\ n\right)}_{\text{VARIABLES}} \qquad (4.4)$$

where W_c denotes the weight of the containment ring. Alternatively, if the actual threshold rupture condition is being sought and described (thereby replacing $(\epsilon_c)_{max}$), one can represent the containment threshold by the following functional dimensionless description+:

$$\frac{(KE)_o}{W_c r} = g\left(h_c/r\ ,\ w_c/r\ ,\ n\right) \qquad (4.5)$$

Although this characterization is given entirely in terms of dimensionless quantities, it may be more useful and clear to describe the threshold containment condition in terms of only attack kinetic energy $(KE)_o$ and ring weight W_c instead of $(KE)_o/(W_c r)$ since both $(KE)_o$ and r are held fixed. Other "dimensionless-result displays" will be presented for similar reasons.

Summarized for convenience in Table 5 are the parameter values identifying the T58 turbine-rotor-burst fragment attack for n=2,3, and 6 fragments. Table 6 contains a summary of the NAPTC tests of the T58 turbine rotor bursts against 4130 cast steel containment rings. Note that while the ring thickness h_c was varied in tests using n=2,3, or 6 fragments, the effects of ring axial width w_c were studied to a meaningful extent only for the n=3 case. Finally, note that the 4130 cast steel material used for these containment rings came from two different suppliers and the associated mechanical properties turned out to be somewhat different (Table 6). This fact should be kept in mind in assessing the resulting experimental data; most tests involved the NF material but a portion of the tests (that is, some of the tests for n=3 only) involved the "different" ACIPCO material.

In the cited NAPTC tests there was no determination of the circumferential strain on the ring (either extreme peak transient or extreme permanent); however, the permanent deformed ring configuration was photographed for

---

+If desired, one could use $(W_c r)/(KE)_o$ rather than $(KE)_o/(W_c r)$ to obtain a small rather than a large dimensionless number.

documentation. The principal result from each of these tests was that the ring either contained (C) or did not contain (NC) the attacking fragments. Thus, unless conditions for C and NC are very close to each other, it is not possible to display results such as those indicated functionally by Eq. 4.4 or by Eq. 4.5. Instead, one could evaluate and display the ratio of the total translational pre-impact kinetic energy $(KE)_{ot}$ to the weight W_c of the containment ring (called herein the STFE -- specific translational fragment kinetic energy) as a function of the number of n of attacking fragments while holding constant the ring axial width w_c; in this category of tests, the ring thickness h_c would be varied, and would automatically imply a value for the ring weight W_c. A plot of this type is shown in Fig. 39 for the fixed value of ring width w_c = 1.0 in*; the symbol "O" indicates that the fragments were contained while the symbol "X" means that the fragments were not contained. Note that Fig. 39 is similar to Fig. 6 of Ref. 37 where the ratio of the total fragment kinetic energy $(KE)_o$ to the ring weight W_c -- called SCFE (specific contained fragment energy) -- is shown. In this report the STFE is chosen as a basis for discussion since rotor burst containment ring performance depends almost entirely upon the value of the translational portion of the fragment kinetic energy attack; the rotational portion is of comparatively insignificant importance. A "curve" has been faired through these data to identify (or estimate) roughly the dividing line between containment and non-containment; additional data would, of course, improve the reliability of this faired curve. One should expect this faired curve to approach an STFE asymptote as the number of equal-size fragments is increased indefinitely; this would correspond to a uniform membrane strain state in the ring and, hence, would enable the ring to absorb a maximum amount of strain energy before "simultaneous outer-surface rupturing" would occur at all circumferential stations of the ring. On the other hand, the least number (n=2) of equal-size fragments produces severe local bending in addition to the membrane straining; the result is that this locally-severe bending-membrane outer-surface extensional strain reaches rupture levels at the least total translational kinetic energy attack value. At all other values of n,

*There are insufficient data to permit making similar plots for other fixed values of containment ring width w_c.

this threshold containment curve lies between the n=2 value and the aforementioned asymptote. Also, only for n=2 is disk sharp-edge gouging of the ring evident.

Referring to Fig. 38, the amounts of translational and rotational kinetic energy possessed by fragments of varying sizes originating from the same rotor are shown. The three-fragment impact situation has more total translational kinetic energy than does the two-fragment attack. On an individual basis, the impact of one tri-hub fragment is more severe than the impact of one bi-hub fragment; however, the fragment-ring interaction of the three fragment attack lessens the severity of the impact-induced response. As the total number of rotor fragments approaches infinity, the deformation of the containment ring approaches that of pure membrane stretching. As the number of fragments present decreases, the severity of local bending deformation increases. This is readily visualized in Fig. 40 (from Ref. 37) where a comparison is made of the final deformed shapes of identical containment rings subjected to either two- or three-fragment impact. The two-fragment impact produces fewer regions where bending is present, but the level of bending will tend to be greater in these regions than in corresponding regions for rings impacted by more fragments. The hypothesis offered here is that a 1/3-rotor fragment contains more translational kinetic energy than a 1/2-rotor fragment, but the impact-induced ring response (taken as a collective action) appears to be more severe for the two-fragment attack.

A limited experimental study was made also of the effect of various ring widths w_c (or the ratio w_c/w_f) on T58 turbine rotor fragment containment -- only for the 3-fragment case. Figure 41 shows the STFE as a function of containment ring width w_c for the 3-fragment case of T58 turbine rotor burst. These data indicate an optimum "energy-coping capability" at a ring width w_c of 1.00 in, which is equal to the axial projected width of the attacking fragments. While w_c = 0.5 in and w_c = 1.0 in clearly involve 2-d structural responses of these rings, the former exhibits larger bending-induced strains compared with the latter, and hence reaches a rupture strain level at a smaller attack specific translational kinetic energy value than the latter. On the other hand, having w_c significantly larger than w_f will lead to 3-d structural response behavior in the immediate vicinity of the points of impact

attack; this locally more severe response results in producing rupture strain levels at these locations at a much smaller value of the attack STPE than for the 2-d structural response cases -- especially those near $w_c = w_f$.

It was noted earlier that the character of the ring response differs depending upon the number of equal-size fragments involved in the impact attack. Thus, for the present T58 turbine rotor burst containment tests, one may depict conveniently the threshold-containment data for the 2, 3, and 6-fragment cases on a single dimensionless plot (Fig. 42) of the ratio of ring mass to total fragment mass, $(m_r)/(nm_f)$, versus the ratio of total fragment translational kinetic energy $(KE)_{ot}$ to an "idealized maximum energy absorption index for the containment ring", U_c. The quantity U_c is a convenient but fictitious quantity which represents approximately the total strain energy which could be absorbed by the entire volume of ring material if all of the material were subjected to uniaxial tension and stretched to rupture. For the present 4130 cast steel material supplied by the National Forge Co., U_c was estimated by forming the product of $\bar{U}_c$ and the ring initial volume where $\bar{U}_c$ is this "energy capacity" per unit initial volume, as follows. Regarding this 4130 cast steel as a "mild steel", it is assumed that the strain rate constant values D=40.4 sec^{-1} and p=5 quoted in Ref. 25 apply. Next, for a fragment impact attack of sufficient severity to produce tensile rupture of the ring, the ring will experience time-varying and space-varying strain rates $\dot{\epsilon}$ which range up to perhaps 3000 sec^{-1} but over a substantial portion of the transient response (to local rupture) are considerably less; for present purposes an "effective rate" of ≈850 sec^{-1} is assumed* to apply throughout the volume of the ring material. Thus, according to Eq. 4.2 and Table 6 the rate-dependent effective yield stress of the NP 4130 cast steel material is estimated to be

$$\sigma_y = \sigma_o\left(1+\left|\frac{\dot{\epsilon}}{D}\right|^{\frac{1}{p}}\right) = 80{,}000\left(1+\left|\frac{850}{40.4}\right|^{\frac{1}{5}}\right) = 227{,}120 \text{ psi}$$

Since, the strain-rate dependent neck-initiation level of strain for this material is not known, the static value of 0.08 in/in from Table 6 will be

*As a rough estimate on the basis of the NAPTC Test 201 transient strain data, but it could be significantly less.

used. For the present rough determination of $\bar{U}_c$, the NF material is approximated as being "rigid, linearly strain hardening" to rupture; hence,

$$\left(\bar{U}_c\right)_{NF} = \epsilon_{m_o}\left[\sigma_y + \frac{(\sigma_{u_o} - \sigma_o')}{2}\right] = .08\left[227{,}120 + \frac{31{,}000}{2}\right] = 19{,}140 \ \frac{in\text{-}lb}{in^3}$$

Then U_c is found by multiplying this value for $\bar{U}_c$ by the initial volume of the material comprising the containment ring.

The solid curves shown on Fig. 42 for n=2, 3, and 6 were specified as follows. Since the total fragment mass is known and the nominal rupture rpm is given as 20,000, the total translational kinetic energy is known and is constant for each value of n; for a given containment ring, the ring mass and U_c (for the NF material) are both determined -- thus defining the solid curves associated with the NF material for each value of n. Similarly, the dashed curve was established for n=3 for the ACIPCO-supplied 4130 cast steel material; for this material, analogously the following very different value for $\bar{U}_c$ was used:

$$\left(\bar{U}_c\right)_{AC} = .15\left[235{,}637 + \frac{39{,}000}{2}\right] = 38{,}270 \ \frac{in\text{-}lb}{in^3}$$

which means that the ACIPCO material is much tougher than the NF material.

It should be noted that the curves shown on Fig. 42 indicate the nominal or intended rotor-burst condition of 20,000 rpm. In actuality rotor rupture occurred at a slightly different rpm in a given test. For a given ordinate value, rotor rupture actually occurred at a higher (lower) rpm than nominal for those points lying to the right (left) of a given curve. Thus, one can see readily how near the nominal condition that the actual rotor bursts occurred.

An examination of Fig. 42 reveals the following two trends:

(1) There is a ratio of ring mass to fragment mass below which there are few or no containments. This level is approximately 0.7.

(2) There is a ratio of total fragment translational energy to maximum energy absorbed by the containment ring above which there are few or no containments.

The first trend cited above occurs at nearly the same mass ratio for all three values of fragment number n. Evidently, as the mass of the containment ring decreases in comparison with the fragment mass, a point is reached where the deformations surrounding the "impact point" dominate the impact-interaction and lead to a local tensile failure without greatly deforming the surrounding containment structure. There is no fixed energy ratio for the second trend, but a different energy level prevails for each fragment configuration. This is because the magnitude of the total translational energy stored in the fragments is dependent upon the configuration (or value of n). From Fig. 38 it is noted that an individual tri-hub fragment possesses the greatest translational kinetic energy, but collectively the six-fragment configuration possesses the largest total translational kinetic energy (whereas an even larger total translational kinetic energy level is attained by a nine-fragment impact configuration). A hypothetical containment limit as $n \to \infty$ would be at an energy ratio of 1.0 if U_c were known accurately, because this is the point at which it is assumed that the maximum energy can be absorbed in just reaching tensile failure simultaneously at all circumferential stations in the containment structure.

This containment limit is based on the absorption of translational kinetic (impact) energy by the containment rings through membrane stretching. However, if bending deformations occur at a non-negligible level, the containment limit would shift to a value less than 1.0 because an equal volume of material would absorb twice as much energy by pure membrane stretching than it will by pure bending before reaching the "local rupture" condition. The extent of bending deformation for the 2, 3, and 6-fragment rotor burst was mentioned earlier in this section and is borne out in Fig. 42 as a shifting containment limit.

Two additional means of displaying the present NAPTC experimental data on T58 turbine tri-hub (n=3) rotor burst containment are useful and are shown as Figs. 43 and 44, only for the NF material for clarity. Figure 43 shows the ratio of ring thickness h_c to ring inner-surface radius r: (h_c/r) versus $(KE)_{ot}/U_c$ for fixed values of the width ratio w_c/w_f. Figure 44 shows the ratio of containment ring thickness h_c to ring width w_c versus the energy

ratio $(KE)_{ot}/U_c$ for fixed values of the width ratio w_c/w_f. Confining attention to tri-hub bursts (n=3), an examination of Figs. 42, 43, and 44 reveals the quantitative and the expected qualitative relationship between the thickness of the ring and the "containment potential" of that structure. To achieve containment by the NF 4130 cast steel material (for the present limited data only):

(1) Figure 42 indicates that a ring mass at least 0.7 times the total fragment mass should be used,

(2) Figure 43 shows that a ring thickness h_c at least 0.08 times the ring inner-surface radius should be chosen, and/or

(3) A ring width at least as great as but not much greater than the fragment width should be selected, according to Figs. 41 and 44; however, the data are too sparse to permit making a more precise choice.

These criteria for estimating the containment bounds do not guarantee containment (as is indicated in Figs. 42-44); however, all of the rings which contained fragments that were released from rotors at the design rpm meet all of the above-mentioned criteria; only test 177 fails to meet these bounds, but the rotor failed at an rpm significantly lower than the design speed. There appears to be a minimum width, thickness, and total mass for the containment ring of given material in order to insure a high probability of containment.

These observations are also discernible from similar NAPTC plots in Ref. 37 but are not as clearly apparent as in Figs. 41-44. In addition, the nondimensional plots in Fig. 42 readily separate differences based on material properties, show the relation of the data points to an "ideal curve" for that material impacted by a fragment released at the design rpm, and indicate the pertinent geometric variables.

The above exercise gives a brief illustration of the use of nondimensional analysis for displaying the major factors influencing the containment of a rotor fragment if all appropriate data had been obtained. This process can be applied to any set of experimental data in order to quantify more clearly the important interactions and parametric effects, particularly if the dimensionless combinations are chosen with some prior knowledge of the principal physical processes present.

4.2.2 J65 Rotor Burst Containment

The Curtiss-Wright J65 turbine rotor employed in this group of NAPTC experimental fragment-containment studies has a 30.64-in diameter, a 1.25-in axial length, 72 blades, a weight of 127.75 pounds, and was modified to rupture into 2, 3, or 6 equal-size bladed-disk fragments at a nominal 8500 rpm. The pre-impact fragment data characterizing these tests are given in Table 7. To date, the number of fragment-containment tests using this "large" rotor is small -- as summarized in Table 8 where the specific tests are identified by test number, the number of equal-size fragments, and the axial width w_c of the 4130 cast steel containment ring used in each test. Note that all of these tests (except two) utilized rings having $w_c = w_f = 1.25$ inch; also, each of these rings had an inner-surface radius r=15.82 inches. Listed also in Table 8 are the mechanical property data [37] for the ACIPCO-supplied 4130 cast steel batch from which these containment rings were made.

Since the geometry of the J65 rotor is different from that of the previously-discussed T58 rotor (that is, a simple scale factor multiplying the geometry of the T58 rotor does not result in giving the dimensions of the J65), one can not make direct comparisons between these two sets of test results in a simple straightforward dimensionless variable sense. In addition, the rotor-blade and disk materials for these two rotors are different. Also, the available data are too sparse to make any critical comparisons between these two sets of data (T58 and J65). Hence, the present J65 data are displayed in plots similar to some of those discussed earlier for the T58, as follows:

Figure No.	Quantities
45	STFE vs. n
46	$m_r/(nm_f)$ vs. $(KE)_{ot}/U_c$ for fixed n
47	h_c/r vs. $(KE)_{ot}/U_c$ for fixed n

For these J65 slower, more-massive fragments and more-massive containment rings (than for the T58 tests), the U_c value used was estimated by assuming

a (smaller) effective strain rate of 500 sec^{-1} for the "mild steel" ACIPCO 4130 cast steel indicated in Table 8. Analogously*,

$$\sigma_y = 60{,}000 \left(1 + \left|\frac{500}{40.4}\right|^{\frac{1}{5}}\right) = 159{,}000 \text{ psi}$$

$$\left(\bar{U}_c\right)_{AC-65} = .08\left[159{,}000 + \frac{40{,}000}{2}\right] = 14{,}320 \ \frac{in-lb}{in^3}$$

Then, U_c is found by multiplying this value for $\bar{U}_c$ by the initial volume of material in the containment ring.

Because of the relative paucity of the present containment ring test data for the J65, one can make only a few tentative observations, paralleling those made concerning the T58 test data:

(1) There is a minimum ratio of container thickness to ring inner radius (h_c/r) below which no containments are expected. This value appears to be 0.27 for the C-W J65 rotor fragments (Fig. 47).

(2) A ratio of container width to fragment width of one ($w_c/w_F = 1.0$) appears to be optimal for containment purposes.

(3) There is a maximum value of translational fragment energy to maximum energy absorption capability of the container $(KE)_{ot}/U_c$ above which no containments can be expected. This value varies with the number of fragments involved in the impact but in all cases must be less than 1.0 (Fig. 46) since this is the theoretical limit where pure membrane behavior (maximum energy absorption) occurs.

It is apparent from the brief study of the C-W J65 rotor impact data and the previously-reviewed GE T58 rotor impact data than an "optimal experimental process" can be carried out to find a containment threshold. First, a containment ring equal in width to the fragment axial length should be chosen. Then the ring thickness should be varied increasing from a value at which the mass ratio is one (since this is the theoretical lower limit of containment ring weight -- pure membrane behavior) until a containment is achieved. This process includes all three of the above-mentioned impact-interaction observations and should lead rapidly in experiments to the selection of a "light-weight" fragment container.

---

* Note that under these assumptions (admittedly rough), this ACIPCO material under the J65 test conditions appears to be less tough than for the T58 cases with either NF or ACIPCO material. It would act even less tough if the "effective strain rate" were smaller. See Tables 6 and 8.

4.2.3 Supplementary Comments

Typical engine rotor fragment velocities have been estimated (see Ref. 42, for example) as the maximum rim speed of a number of rotors to lie between about 400 and 1300 ft/sec. This location was picked [42] since the center of gravity of rim pieces with various numbers of attached blades would likely lie near this location -- and these velocity values would tend to be conservatively large. Of course, corrections can be made for fragments whose CG locations lie closer to or more distant from the axis of rotation. If the clearance between the containment ring and the blade tip were small, the velocity component of the fragment perpendicular to the impacted structure surface at initial impact would be reduced by the sine of the angle β between the trajectory and the tangent to the impacted surface; these sine values are typically well below 0.2. Alternatively, consider, for example, the idealization of the T58 tri-hub burst fragment as a nondeformable circular disk as discussed in Subsection 3.2; in this case $r_{CG} = 2.797$ in and the ring inner-surface radius $r = 7.50$ in leads to incidence angles β (given by $\cos\beta = r_{CG}/(r-r_f)$) whose sines for $r_f = 2.555$ in and $r_f = 4.20$ in are 0.825 and 0.531, respectively. These values, however, are rather large compared with the incidence angles for initial impact of bladed disk fragments in actual engines with "conventional tip clearance" between the blade and the casing. Thus, for many situations the component of the velocity of the impacting fragment normal to the containment structure may be expected to range from about 200 to 650 ft/sec or less. In this range of impact velocities, fragments such as (1) bladed-disk fragments [37, for example] or (2) 1-inch diameter solid spheres impacting ductile metal (a) containment rings [37], (b) beams [16], and/or (c) panels [21], respectively, produce a tensile-rupture type of local failure of the containment structure. No other types or containment-structure failures have been observed for fragments of this type with this range of normal-component impact velocity. It requires significantly higher impact velocities of "hard and compact" fragments or missiles such as rigid rods, for example, to produce shear plug failure [31, 43-45]. Cratering and stress-wave induced fracturing (spalling) require very much higher impact velocities still [31]. For all practical purposes, therefore, one is justified in restricting one's attention to the tensile mode of failure (rupture) insofar as aircraft engine rotor fragment penetration of ductile metal

containment structures is concerned. Almost without exception, these bladed-disk fragments act as "readily deformable" during their early stages of impact-interaction, and deceleration before the "effective fragment" reaches a more compact, hard, and stiff state; the containment ring becomes loaded over a "fairly large" circumferential region by each fragment and subsequent structural response ensues.

Some supplementary information to substantiate the expectation that shear plug failures are unlikely for the postulated types of fragments and range of normal-component impact velocities may be of interest from impact studies reported, for example, by Rinehart [31], Hagg and Sankey [43], Recht and Ipson [44], and Lethaby and Skidmore [45]. Both tensile rupture and shear-plug failure modes are encountered in the "sub-ballistic velocity range", and are discussed in those studies. It has been known [31] for a very long time that a "plugging failure" will occur very early in the impact-interaction-response process, whereas tensile rupture occurs very late in this process when the gross structural response of the slowly-responding structure "reaches a peak", roughly speaking. The following discussion, however, will be confined to shear plug failure and criteria for its occurrence, and follows the Hagg and Sankey [43] description. Of particular interest is the normal component impact velocity v_f below which no shear plug failure can occur and is given, according to simplified theory, by the following inequality:

$$K h^2 P \tau + \sigma_u \epsilon_m V_o > \frac{1}{2} m_f v_f^2 f(m_f, m_c) \qquad (4.6)$$

If v_f is large enough to violate this inequality, shear plug production is possible. Expression 4.6 means that plugging failure will occur if the energy absorbed by the target structure's "impact-affected" region is less than the energy lost during an inelastic impact (e=0), where

K is an experimentally-determined factor related to the shape of the impacting face of the missile ($\frac{1}{3} < K < \frac{1}{2}$)

h is the thickness of the target structure (in)

P	is the shearing perimeter of the contact region between the impacting fragment and the target structure (in)
τ	is the dynamic ultimate shear strength of the target (psi)
$\sigma_u \varepsilon_m$	represents approximately the energy absorption capacity of the structural material to failure, per unit initial volume
V_o	is the volume of the "impact-affected" portion of the structure
m_f	is the mass of the fragment
m_c	is the mass of the "impact-affected" portion of the structure
v_f	is the impact velocity component perpendicular to the impacted surface
$f(m_f, m_c)$	for an <u>inelastic</u> impact [23,43] is given by $m_c/(m_f+m_c)$

Restricting attention for present illustrative purposes to a 2-d containment ring or beam for which the width of the impacting fragment w_f is equal to the width w_c of the containment structure, one may write Eq. 4.6 (as an equality) as

$$K 2 w_c \tau h^2 + \sigma_u \varepsilon_m w_c h \ell = \frac{1}{2} m_f v_f^2 \left(\frac{\rho_c w_c h \ell}{m_f + \rho_c w_c h \ell} \right) \qquad (4.7)$$

where ρ_c is the mass per unit initial volume of the containment structure and ℓ is an as-yet-undetermined impact-affected spanwise length of the structure. Collecting terms and rewriting, Eq. 4.7 becomes

$$h \left[A h^2 + B h + C \right] = 0 \qquad (4.8)$$

where

$$A = 2 \rho_c w_c^2 \ell \tau K \qquad (4.8a)$$

$$B = 2 w_c m_f \tau \qquad (4.8b)$$

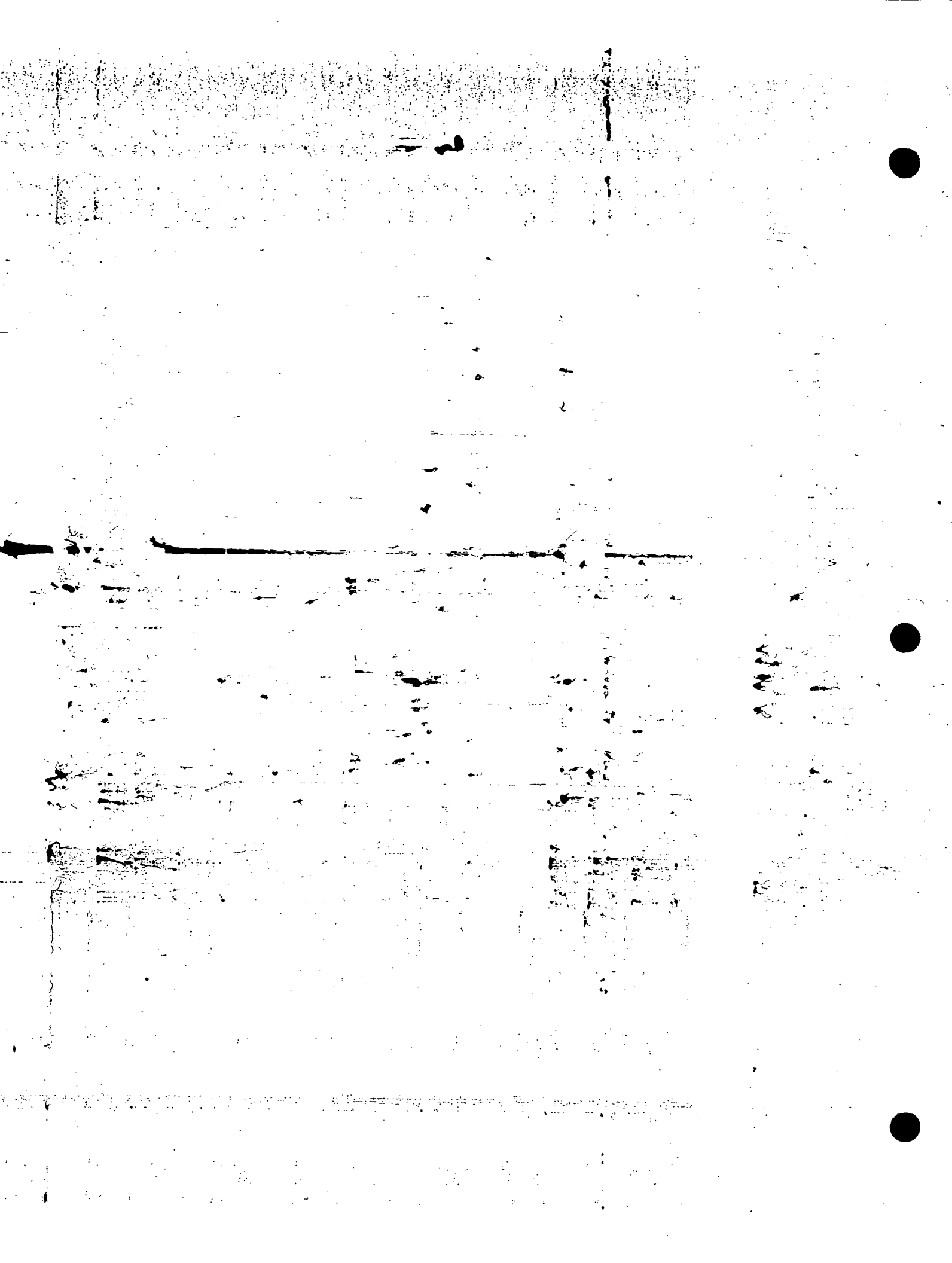

$$C = w_c \ell \left[\sigma_u \epsilon_m - \frac{\rho_c}{2} m_f v_f^2 \right] \qquad (4.8c)$$

The solution of Eq. 4.8 is given by:

(1) h=0: Trivial Solution

or (2) $Ah^2+Bh+C=0$ or

$$h = \frac{1}{2}\left[-\frac{B}{A} \pm \sqrt{\left(\frac{B}{A}\right)^2 - 4\frac{C}{A}} \right] \qquad (4.9)$$

Since $\frac{B}{A} > 0$, a physically-valid solution ($h \geq 0$) is possible only for C=0:

$$w_c \ell \left[\sigma_u \epsilon_m - \frac{\rho_c}{2} m_f v_f^2 \right] = 0 \qquad (4.9a)$$

Thus, the plugging threshold impact velocity is independent of both T and ℓ, and is given by

$$v_f = \left[\frac{2 \sigma_u \epsilon_m}{\rho_c} \right]^{\frac{1}{2}} \qquad (4.9b)$$

Applying the Table 6 values for the NF-supplied 4130 cast steel, the plugging-threshold perpendicular-impact velocity v_f is estimated by this simple theory to be:

$$v_f = \left[\frac{2(111{,}000)(.08)}{(.283)/(386.09)} \right]^{\frac{1}{2}} = 4922 \text{ in/sec.}$$

if the static properties are used or

$$v_f = \left[\frac{2(19{,}140)}{(.283)/(386.09)} \right]^{\frac{1}{2}} = 7277 \text{ in/sec.}$$

if the previously-discussed estimated dynamic properties are employed. The applicability of this analysis requires the missile to be essentially non-deformable; thus one can not apply this when considering the "readily deformable" blades of T58 bladed-disk fragments. However, if one considers

C-2

the previously-discussed idealized circular fragments for the T58 tri-hub (n=3) burst, the perpendicular component of the impact velocity would be 4833 and 3111 in/sec for r_f = 2.255 and 4.20-in respectively -- both of which are below this roughly-estimated threshold plugging condition.

4.3 Illustrative Parametric Studies of Beam Response to Fragment Impact

In Subsection 4.1 a set of dimensionless parameters which can be used to characterize the response of a containment structure to impact attack by deformable fragments such as bladed-disk fragments from a ruptured aircraft engine rotor was discussed; this set of parameters was then reduced to the case in which the attacking fragments are rigid rather than deformable. Next, in Subsection 4.2 an examination was made in terms of suitable dimensionless and dimensional quantities of NAPTC experimental data on a restricted set of conditions involving aircraft engine rotor deformable-fragment impact attack against steel containment rings. Now in the present subsection, a similar examination will be made of experimental data on impact-induced response of a simple beam structure subjected to rigid-fragment (steel sphere) impact attack; in addition, numerical predictions of beam response to rigid-fragment impact attack will be presented to illustrate the effects on the structural response of varying certain of the dimensionless parameters which can be used to characterize this problem.

4.3.1 Dimensional Analysis of MIT-ASRL Experiments on Beam Response to Steel-Sphere Impact

First, it should be recalled the subject MIT-ASRL experiments involved perpendicular impact of a 1.00-in diameter steel sphere at the midspan-midwidth location of 6061-T651 aluminum "containment" beams of thickness h=0.100-in, width w_c=1.50 in, and span ℓ=8.00 in with both ends ideally clamped. In these experiments only the initial impact velocity of the steel sphere was varied in order to produce various degrees of peak structural response including rupture; as reported in Ref. 16, experiments and test specimens CB-9, CB-13, CB-18, CB-16 and CB-14 with steel sphere initial impact velocities ranging from 1900 to 3075 in/sec permitted determining the initial impact velocity (or initial fragment kinetic energy) for threshold containment. The pertinent geometric, mass, and material property data are summarized in Table 9. Under

these fragment geometry and beam geometry impact conditions, the structural response of the beam was of 3-d character at and close to the point of midspan impact but appeared to be of 2-d character over the remaining (approximately 70 per cent volumewise) portion of the structure. Rupture at the midspan impact station appeared to be governed by the 3-d structural response behavior produced there; this rupture was of tensile character rather than a shear-plug failure.*

With respect to a dimensionless-parameter characterization of this sphere-beam impact-interaction and response problem, one might employ the set of dimensionless parameters discussed in Subsection 4.1.2 for containment-structure response to rigid-fragment attack -- since the steel sphere reasonably qualifies as a comparatively rigid fragment in the present instance. The 18 parameters $\beta_1 \ldots \beta_{18}$ cited in Subsection 4.1.2 need to be relabeled as appropriate for the present sphere-beam impact situation. First, since the same beam material was used throughout this test series, the dimensionless material parameters $\beta_1=\varepsilon_{mc}$, $\beta_2=\nu_c$, $\beta_3=\phi_c$, $\beta_4=\mu$, $\beta_5=e$, $\beta_6=\rho_c/\rho_f$, and $\beta_7=E_c/\sigma_{c_o}$ remain valid but are not variables. Next, the geometric parameters may be recast by using (a) the sphere diameter d to replace the previous $(r_{CG}+\ell_f)$ and/or w_f and (b) the beam span ℓ to replace r_c -- to obtain relabeled parameters $\beta_8 \ldots \beta_{14}$ as $\beta_8=n$, $\beta_9=(\ell)/d$, $\beta_{10}=h/d$, $\beta_{11}=w_c/d$, $\beta_{12}=h/\ell$, $\beta_{13}=h/w_c$, and $\beta_{14}=d/d$; here again all but the last parameter remain meaningful but none are variables. Finally, the "kinematic" set of variables can also be recast by using the normal-to-the-surface impact velocity v of the non-rotating sphere to replace $\omega_f r_{CG}$ and $\omega_f(r_{CG}+\ell_f)$ thereby rewriting $\beta_{15} \ldots \beta_{18}$ as $\beta_{15}=(vt)/h$, $\beta_{16}=v/(h\dot{\upsilon}_c)$, $\beta_{17}=(\sigma_{cu}/\varepsilon_{cm})/(\rho_f v^2)$, $\beta_{18}=z/h$ where β_{18} is an "effects parameter" -- the ratio of the maximum deflection to the beam thickness.

Note that the only independent variable is the initial impact velocity v. Hence, one may express β_{18}, for example, as a function of the dimensionless variables β_{15}, β_{16}, and β_{17}:

---

*Note that the previously-cited criterion for shear plug failure $v_f > \left[\frac{2\sigma_u \varepsilon_m}{\rho_c}\right]^{1/2}$ and the pertinent data cited in Table 9 indicates that for shear plug failure, the fragment velocity v_f should be > 8400 in/sec -- well beyond the range of test conditions needed to produce threshold rupture of the beam [16].

$$\frac{z}{h} = f(\beta_{15}, \beta_{16}, \beta_{17}) \equiv f\left(\frac{vt}{h}, \frac{v}{h D_c}, \frac{\sigma_{cu}\,\epsilon_{cm}}{\rho_f v^2}\right) \tag{4.10}$$

Next, if one is not interested in the time of occurrence of the maximum displacement z, β_{15} can be eliminated. Further, since only one beam material and one fragment material have been used, both β_{16} and β_{17} are defined when v is specified; hence, one can regard β_{17} as being the only significant variable, thereby obtaining

$$\frac{z}{h} = f(\beta_{17}) \tag{4.10a}$$

for a final cause-and-effect display.

Alternatively, rather than using z/h as a measure of the impact-induced effects, one might elect to employ the maximum longitudinal upper-surface strain ϵ_{max}. Hence, analogously one may write ϵ_{max} as a function of the only significant variable β_{17}:

$$\epsilon_{max} = g_1\left(\frac{\sigma_{cu}\,\epsilon_{cm}}{\rho_f v^2}\right) \tag{4.11}$$

Instead of displaying ϵ_{max} as a function of $\beta_{17} \equiv (\sigma_{cu}\,\epsilon_{cm})/(\rho_f v^2)$, it is convenient to replace β_{17} by the ratio of the initial kinetic energy $(KE)_f$ of the fragment[+] $(KE)_f \equiv V_f(\rho_f v^2)/2$ to the "idealized maximum energy absorption index for the containment structure" U_c as discussed in Subsection 4.2.1, where $U_c = \bar{U}_c$ times the initial volume of containment material and

$$\bar{U}_c = \epsilon_{m_o}\left[\sigma_y + \frac{\sigma_{u_o} - \sigma_o}{2}\right] = \text{"energy capacity" per unit initial volume} \tag{4.12}$$

Hence, one may write

[+] V_f is the volume of the fragment (steel sphere) material.

$$\epsilon_{max} = g_2\left(\frac{(KE)_f}{U_c}\right) \tag{4.13}$$

In the sphere-beam impact experiments under discussion [16], transient strain measurements were made at various spanwise stations for the upper and/or the lower surface of the beam. Steel-sphere impact occurred at midspan (x=0) on the lower surface. Although the spatially-maximum strain occurred at the upper surface at or near station x=0, transient strain measurements were not made successfully there; however, successful measurements of upper-surface transient strains were made, for example, at $|x| = 0.6$ in and $|x| = 1.50$ in on the beams cited in Table 9. Accordingly, the measured peak upper-surface longitudinal strains γ_{11} (denoted as ε for convenience) at stations $|x| = 0.6$ in and $|x| = 1.50$ in are shown in Figs. 48a and 48b, respectively as a function of $(KE)_f/U_c$. For convenient reference, the test/specimen, fragment velocity $(KE)_f$, and $(KE)_f/U_c$ are tabulated below:

Test and Specimen	Fragment Velocity v(in/sec)	$(KE)_f$ in-lb	$\frac{(KE)_f}{U_c}$	Remarks
CB-9	1896	686	.0657	Small permanent deflection
CB-13	2490	1183	.1133	Moderate permanent deflection
CB-18	2794	1489	.1426	Large permanent deflection
CB-16	2868	1569	.1503	Slightly beyond threshold containment; specimen ruptured
CB-14	3075	1804	.1728	Well beyond threshold containment; specimen ruptured very early

where $U_c = \bar{U}_c x$ (beam volume) $\equiv 8700\ (1.20\ in^3) = 10{,}440$ in-lb. Note in Figs. 48a and 48b that the measured peak strain at each of these stations increases with increasing $(KE)_f/U_c$ -- for specimens CB-9, CB-13, and CB-18. However, under more severe impact, specimen rupture occurs and thereby "releases the loading" which results in smaller peak strains at "remote"

stations $|x| = 0.6$ in and $|x| = 1.50$ in; this is particularly pronounced for specimen CB-14 which ruptured very early after initial impact.

By analogy with the manner of presenting the NAPTC data in Subsection 4.2 to identify threshold containment, Fig. 49 depicts the present MIT-ASRL sphere-beam impact test results in terms of the ratio of beam (containment structure) mass to fragment mass versus $(KE)_f/U_c$; fragment containment is represented by the symbol "O" and non-containment by "X".

Because fragment velocity was the only independent variable in the Ref. 16 sphere-beam impact experiments, this essentially completes the display of the pertinent dimensionless data. Next, numerical parametric 2-d studies which simultate in a restricted sense the sphere-beam impact problem will be discussed.

4.3.2 Parametric Numerical Predictions

It is convenient to use the sphere-beam impact problem to illustrate the use of the CIVM-JET 4B code for parametric numerical predictions because of (a) the small number of variables which can be employed usefully in studying this well-defined problem and (b) the relatively economical computations required to obtain pertinent results. Recall, however, that the CIVM-JET 4B code applies strictly to problems involving 2-d behavior and structural response. Therefore, in applying this code to simulate the sphere-beam impact problem, and particularly when one varies certain geometric and other problem parameters, changes in one parameter may imply changes in a number of other parameters. This matter must be kept in mind in defining the characterizing non-dimensional variables and fixed quantities for the following four illustrative cases considered here:

Case A: Only the diameter of the impacting fragment is changed in a sequence of calculations (i.e., d=1.00, 1.25, and 1.75 in) but the fragment mass and the initial impact velocity are unchanged from the CB-18 sphere-beam impact condition.

Case B: The fragment mass and initial impact velocity are fixed at the CB-18 values and d=1.00 in; the mass and the span of the aluminum beam are fixed at the CB-18 values. Varied in a sequence of calculations is the ratio w_c/h of beam width to beam thickness to assess this effect on the peak impact-induced strain.

Case C: The fragment mass and initial impact velocity are fixed at the CB-18 values, d=1.00 in, and the span and width of the aluminum beam are fixed at ℓ=8.00 in and w_c=1.50 in. Varied in a sequence of calculations is the thickness h of the beam to assess this effect on the peak impact-induced strain in the 2-d beam structure.

Case D: The fragment mass and initial impact velocity are fixed at the CB-18 value, d=1.00 in, and the span and the thickness of the aluminum beam are fixed at ℓ=8.00 in and h=0.100 in. Varied in a sequence of calculations is the width w_c of the beam to assess this effect on the peak impact-induced strain in the 2-d beam structure.

In all of these calculations, the beam with both ends ideally clamped was modeled, in accordance with the modeling guidelines established in Section 2, by 43 equal-length finite elements with 4 DOF/node, 3 spanwise and 4 depthwise Gaussian integration stations per element, and a fixed beam span of ℓ=8.00 in. Also, the uniaxial stress-strain behavior of the beam material was represented via the mechanical sublayer model by the following Fit A stress-strain pairs: (σ,ε) = 41,000 psi, 0.0041; 45,000 psi, 0.0120; and 53,000 psi, 0.1000. The material was regarded as behaving in an EL-SH fashion -- insensitive to strain rate; hence, the material strain-rate parameters D_c and p_c are deleted. The beam initial mass per unit volume was taken as 0.25384×10^{-3} $(lb\text{-}sec^2)/in^4$. The impacts are treated as frictionless and locally perfectly elastic (coefficient of restitution e=1).

Before discussing the numerical predictions obtained for Cases A, B, C, and D it may be useful to review in a summarized fashion the pertinent dimensionless parameters and variables. First, returning for a moment to the experimental sphere-beam impact results discussed in Subsection 4.3.1, the previously-discussed parameters for that 3-d structural response problem are listed for convenient reference and comparison in Table 10 where the set of 18 "usually significant parameters" has been reduced to 17 since the attacking fragment has only one significant dimension: its diameter for that experimental situation wherein only the peak strain (or threshold rupture) was of interest, only one significant variable was present while all other parameters remained at fixed values.

Shown also in Table 10 are the corresponding dimensionless parameters when one attempts to simulate the 3-d sphere-beam impact problem by the use of the 2-d CIVM-JET 4B computer code for each of the cases A, B, C, and D. For the 2-d simulation, the fragment may be regarded as a rigid circular disk of diameter d and width w_f rather than being a sphere. Hence, if one varies the fragment diameter while keeping the fragment mass constant (as in Cases A, B, C and D), one may envision this as being accomplished by (a) prescribing the fragment width w_f to match the beam width w_c and requiring the fragment mass per unit volume ρ_f to change accordingly or (b) keeping ρ_f fixed and envisioning w_f to change appropriately while stipulating at the same time that both $\beta_{11} \equiv w_c/w_f$ and $\beta_{14} \equiv w_f/d$ must have no effect upon the numerically predicted response; the latter is satisfied automatically by the basic ingredients of the 2-d CIVM-JET 4B code. Hence, this latter view is adopted in the Case A, B, C, and D studies. Indicated in Table 10 for each of these three cases are the dimensionless parameters which remain fixed and those which vary. In accordance with the preceding discussion, the following are the case-by-case variables and the result of primary interest:

	Variables		
Case	Primary	Secondary	Primary Result
A	$\beta_9 = \ell/d$	--	$\beta_{18} = \varepsilon_{max}$
B	$\beta_{13} = h/w_c$	$\beta_{10} = h/d$	$\beta_{18} = \varepsilon_{max}$
		$\beta_{12} = h/\ell$	
C	$\beta_{12} = h/\ell$	$\beta_{10} = h/d$	$\beta_{18} = \varepsilon_{max}$
		$\beta_{13} = h/w_c$	
D	$\beta_{13} = h/w_c$	$\beta_{11} = w_c/w_f$	$\beta_{18} = \varepsilon_{max}$

The results for each of these four cases are discussed separately in the following subsections.

4.3.2.1 Fragment Diameter Effects on Beam Structural Response

For Case A, the effects of various fragment diameters d=1.0, 1.25, and 1.75 in for the CB-18 conditions of impact velocity and kinetic energy (KE)

are shown in Fig. 50 for lower-surface impact occurring at the midspan station x=0; a calculation time step size Δt of 0.5 microsecond was used. Shown in Figs. 50a and 50b are the predicted upper-surface longitudinal strains γ_{11} at stations x=0 and x=0.6 in, respectively, as a function of time after initial impact. At each of these two illustrative locations there is very little difference between the predicted peak strains produced by impacting fragments of postulated diameters of 1.00, 1.25, and 1.75 in -- because of the fact that for the given level of initial KE attack, the peak response of the beam near midspan is such that the smallest radius of curvature of the beam exceeds that of each of these attacking fragments. However, under more severe impact attack, it is evident that at and near midspan the beam could deform enough so that the beam's least radius of curvature could approach or attempt to become less that that of the non-deformable attacking fragment; in the latter instance the fragment could interfere with or inhibit the beam from incurring such large bending (and membrane) strains as would occur under the same severe initial KE attack from a "sufficiently small diameter" fragment.

For the CB-18 level of initial KE attack, one would need to postulate an idealized fragment diameter equal perhaps to the beam span ℓ in order to influence the peak impact-induced strain or deflection response of the beam.

4.3.2.2 Effects of Width-to-Thickness Ratio on the Response of a Beam of Fixed Span and Mass

For this Case B study, the reference aluminum containment beam has dimensions h=0.10 in, w_c=1.50 in, and ℓ=8.00 in and is subjected to the CB-18 initial kinetic energy conditions of rigid-fragment impact attack. Examined here is the effect upon the beam's predicted transient and peak responses of varying the ratio w_c/h of the containment beam width w_c to the thickness h while preserving the cross-sectional area so as to maintain fixed the total mass of the beam. The following summarizes the geometric combinations studied, the reference calculation time step size $(\Delta t)_r$, and the Δt actually used:

Case	w_c (in)	h(in)	w_c/h	ℓ/w_c	$\omega_{max} \times 10^{-7}$ (rad/sec)	Time Step Size $(\Delta t) = \frac{(0.8).2}{\omega_{max}}$ (μsec)	Δt Used (μsec)
B1	.50	.30	1.67	16	.577	.27	.30
B2	1.00	.15	6.67	8	.289	.55	.50
B3	1.50	.10	15	5.33	.233	.68	.50
B4	2.00	.075	26.67	4	.233	.68	.50
B5	3.00	.050	60	2.67	.233	.68	.50

Here one might ask — for a given impact attack, containment beam span, and total beam mass, what ratio w_c/h would provide the best containment potential (or the smallest peak strain)?

For the postulated CB-18 level of impact attack and an idealized fragment diameter of 1.0 in, the predicted peak midsurface strain (also called membrane strain) and the predicted peak upper-surface longitudinal strain $(\gamma_{11})_{max}$ at midspan station x=0 are shown in Fig. 51a as a function of w_c/h. The difference between these two values represents the bending contribution to the upper-surface strain. It is seen that not only does the upper-surface peak strain increase as w_c/h decreases (toward narrower and thicker beams) but also the bending contribution to that peak upper-surface strain becomes a larger fraction of the total; further, the peak membrane strain appears to reach a maximum near $w_c/h = 10$ and then decreases for smaller values of w_c/h. Thus, it appears from Fig. 51a that the containment beam structure which leads to the smallest peak strain is that with the largest ratio w_c/h — which means a wide and thin beam. However, the present CIVM-JET 4B calculations are not valid for large w_c/h or small ℓ/w_c because the structure behaves in a platelike manner with significant <u>biaxial</u> stresses whereas the computer code ingredients assume a beamlike state of <u>uniaxial</u> stress. Also, as pointed out by Timoshenko [46] for elastic behavior and Jones [47] for elastic-plastic behavior of uniformly-loaded "beams", the deflection behavior deviates significantly from that for a "narrow beam" for aspect ratios ℓ/w_c less than about 2. Hence, the Fig. 51 predictions of upper-surface $(\gamma_{11})_{max}$ at x=0 should be paid little heed for $w_c/h \gtrsim 40$.

Another "limitation" on the wide-beam results may be described as follows. For the present 2-d simulation of the sphere-beam impact problem, the idealized fragment of given diameter may be visualized most properly as a circular cylinder of width w_f matching the beam width w_c, with a density changed appropriately to preserve the given total fragment mass. On the other hand, one may visualize the idealized fragment to consist of a circular disk of given material density, diameter, and fixed width w_f such that the total mass matches that of the reference fragment. However, there are no means by which the "small" width w_f of the latter fragment can be recognized by the 2-d CIVM-JET 4B code, although this latter fragment simulates more closely the physical sphere-beam impact situation which exhibits decisive 3-d features. Thus, one can not expect a 2-d structural response code such as CIVM-JET 4B to provide realistic predictions of threshold containment for fragments which produce significant 3-d structural behavior of the impacted structure.

Shown also in Fig. 51a is the maximum upper-surface strain at beam station x=1.50 in as a function of w_c/h; the peak deflection at station x=0 is shown in Fig. 51b as a function of w_c/h. Both of these quantities are seen to be rather insensitive to w_c/h for this fixed initial-kinetic-energy impact attack.

Note that in this Case B study the cross-sectional area is kept constant as w_c/h is varied. Thus, the extensional stiffness is the same for all cases but the bending stiffness increases rapidly as w_c/h decreases. Thus, it may be of some interest to examine the time histories of the predicted upper-surface strain at the midspan impact station x=0 and at a station a short distance from the impact station: x=1.50 in; these results are shown in Figs. 52a and 52b, respectively. It is seen that at station x=0, the maximum strain is predicted to occur earlier for the narrower and deeper beams. A similar but less distinct trend is observed for station x=1.50 in; however, the maximum strain predicted at "remote" station x=1.50 in is almost independent of w_c/h whereas the peak strain at x=0 (in the immediate impact-affected region where the beam acquires a velocity increment from each of a succession of fragment impacts) depends significantly upon w_c/h. This

response insensitivity to w_c/h is expected at stations $|x| \geq 2\, L_{eff}$ for the postulated fixed initial kinetic energy impact attack, in accordance with St. Venant's Principle; station x=1.50 in qualifies in this sense since from the equation $L_{eff} \doteq \Delta t(E/\rho)^{1/2}$, L_{eff} is estimated to be approximately .060, .099, .099, .099, and .099 in for Cases B1 through B5, respectively. In view of these L_{eff} values, only the nodes bounding the center impacted element receive impact-imparted velocity increments; there are 7 nodal stations between the nearest node receiving impact-induced velocity increments and station x=1.50 in.

It is perhaps useful at this point to remind the reader of the necessity of employing a sufficiently small time step size Δt for numerical predictions of nonlinear impact-induced transient structural response -- such as the use of the CIVM-JET 4B computer program. In carrying out the predictions for Case B4 (w_c/h=26.67, w_c=2.00 in, and h=0.075 in), a Δt value of 0.75 microseconds was tried; this is somewhat larger than the nominal guideline for selecting an appropriate Δt for this computer program: $(\Delta t) \leq 0.8\ (2/\omega_{max}) \equiv 0.68$ μsec. Hence, Δt=.75 μsec corresponds to $0.88\ (2/\omega_{max})$. For this case: (1) an unrealistically large value of $(\gamma_{11})_{max}$ was predicted at x=0 and (2) at and near the time of this $(\gamma_{11})_{max}$, there was a severe spatial variation of upper-surface γ_{11} along the center impacted element, whereas a slow spatial variation is expected physically and is observed in well-behaved computer runs. Thus, the use of a too large Δt was suspected. Accordingly, the Δt was reduced to a convenient value of 0.50 microsecond, and the calculation was repeated; this resulted in well-behaved predictions, and the peak γ_{11} at x=0 was plausible as seen on Fig. 51.

In view of the erratic results obtained for Case B4 when Δt=0.75 μsec = $.88\ (2/\omega_{max})$, the extensive printed-out results for Case B1 were studied carefully since Δt=0.30 μsec = $.89\ (2/\omega_{max})$ was used. For the latter case no evidence of erratic behavior was found. However, based upon the rather extensive set of calculations carried out in the present study, as well as in prior studies, it is concluded that restricting Δt such that $\Delta t \leq 0.8\ (2/\omega_{max})$ will lead to numerically reliable transient large-deflection elastic-plastic structural response predictions of simple beam/ring structures when

the timewise central-difference operator is used (as in CIVM-JET 4B, JET 3A, and JET 3C). To date, computational blow-up has never been encounted when one choses $\Delta t \leq 0.8\ (2/\omega_{max})$.

4.3.2.3 Effect of Beam Thickness on the Response of a Beam of Fixed Width and Span

To be discussed here are the results for Case C wherein the impacting fragment has a fixed mass and fragment diameter (d=1.00 in) and a given initial impact velocity which matches the CB-18 sphere-beam impact experiment. The span and the width of the aluminum containment beam are held fixed with ℓ=8.00 in and w_c=1.50 in. Varied in a sequence of calculations is the thickness h of the beam to assess this effect on the peak impact-induced strain in this 2-d beam structure; a time step size Δt of 0.5 microsecond was used for all calculations. When h is varied, the result is a change in (a) the beam mass per unit span, (b) the extensional stiffness, and (c) the bending stiffness of the beam, but these stiffnesses do not change in the same proportion. Table 10 indicates the dimensionless parameters which remain fixed and those which vary under these Case C conditions.

If one confines attention to only peak-response results (irrespective of when the peak occurs), the principal dimensionless variables reduce to three: $\beta_{10}=h/d$, $\beta_{12}=h/\ell$, and $\beta_{13}=h/w_c$. Since d, ℓ, and w_c are held constant, each of these variables varies proportionally to h. Hence, for convenience, the peak response results: (a) $(\gamma_{11})_{max}$ at the midsurface and at the upper surface and (b) peak deflection w/ℓ, both at the midspan impact station x=0 are shown in Fig. 53 as a function of beam thickness h. For this selected limited range of beam thickness, the peak values of total strain, membrane strain, and midspan deflection all vary linearly with h.

The result for h=0.10 in represents a 2-d simulation of the CB-18 sphere-beam impact result; the experimental CB-18 sphere-beam impact case involved an impact severity and accompanying significant 3-d beam response (near the impact station) verging on material rupture. For the 2-d simulation by the CIVM-JET 4B code (and the modeling employed), the predicted peak strains must be less than those produced in the actual CB-18 3-d response case. However, for discussion purposes it will be assumed that the peak upper-surface strain

predicted by this 2-d model represents the "containment threshold" value that can be used to judge whether or not a given 2-d beam under 2-d fragment attack can or can not contain the attacking fragment. Accordingly, that "critical" γ_{11} value is selected as 16 per cent. In turn this means, of course, that the thinner beam (h=.075 in) would have ruptured but the thicker beam (h=.15 in) would not since its $(\gamma_{11})_{max}$ at x=0 did not exceed 12 percent.

One can regard this set of Case C calculations as simulating numerically the procedure used in the NAPTC containment tests wherein containment rings of fixed inner-surface radius and fixed width were varied in thickness and then subjected to a given fragment attack (fixed number, mass, and initial kinetic energy) to determine experimentally the thickness for threshold containment. Hence, if desired, one may display the present results in a fashion analogous to Fig. 42 for the NAPTC results; namely, displayed in Fig. 54 are the "present predictions" in terms of the ratio of beam mass to fragment mass versus the ratio $(KE)_f/U_c$ of fragment initial kinetic energy (1489 in-lb) to the containment structure energy absorption index U_c. As noted earlier $U_c=\bar{U}_c$ times the volume of the beam material and $\bar{U}_c$ is 8700 (in-lb)/in^3. For convenient reference, the quantities characterizing the Case C calculations are:

Case	h	h/d	h/w_c	h/ℓ	$\bar{V}_c$ (in^3)	$\frac{m_c}{m_f}$	$\frac{(KE)_f}{U_c}$	Remarks
C1	.075	.075	.050	.0094	0.90	.6	.190	Did not contain
C2	.10	.10	.067	.0125	1.20	.8	.143	Containment Threshold
C3	.15	.15	.10	.019	1.80	1.2	.095	Contained

Included for convenient reference in Fig. 54 are the data points corresponding to the Ref. 16 sphere-beam impact experiments; the symbols O and X mean, respectively, that the fragment was contained or not contained. Similarly, the symbols □ and + mean that the predictions (Cases C1, C2, and C3) indicate, respectively, containment or non-containment for the CB-18 level of kinetic energy attack.

It is evident that one could carry out CIVM-JET 4B calculations to determine the beam thickness h required for threshold containment of other values of single-fragment kinetic energy midspan attack such as, for example, the CB-9 or the CB-14 values of 686 or 1804 in-lb on aluminum containment beams of 1.50-in width and 8.00-in span. For these cases it would be postulated that the selected critical γ_{11} of 16 per cent for threshold containment applies.

It should be noted that the Case C ranges of beam dimensions are such that the structure should exhibit beamlike behavior (rather than platelike behavior) as the computer code employed assumes.

4.3.2.4 Effect of Beam Width on the Response of a Beam of Fixed Thickness and Span

To be discussed here are the results for Case D wherein the impacting fragment has a fixed mass and diameter (d=1.00 in) and a given initial velocity which matches the CB-18 sphere-beam impact experiment. The span and the thickness of the aluminum containment beam are held fixed with ℓ=8.00 in and h=0.100 in. Varied in a sequence of calculations is the width, w_c, of the beam in order to assess this effect on the peak impact-induced strain in this 2-d beam structure. Note than when w_c is changed, the membrane stiffness and the bending stiffness are changed by the same percentage: $\Delta w_c/w_c$; also, a change in w_c results in a change in the beam mass per unit span. For these calculations a time step size Δt of 0.5 micro-second was employed. Table 10 indicates the dimensionless parameters which remain fixed and those which vary under the Case D conditions.

If one confines attention to only peak-response results (irrespective of when the peak occurs), the principal dimensionless variables reduce to two: $\beta_{11}=w_c/w_f$ and $\beta_{13}=h/w_c$; since only 2-d behavior is dealt with in the calculations, $\beta_{13}=h/w_c$ becomes the only meaningful dimensionless variable. For convenience, therefore, the peak response results: (a) the midsurface and the upper-surface values of $(\gamma_{11})_{max}$ and (b) the peak deflection w/ℓ, both at the midspan impact station x=0 are shown in Fig. 55 as a function of containment beam width w_c. For this limited range of w_c values (from 1.125 in to 2.25 in), the peak value of midspan deflection varies linearly with w_c,

but the membrane and outer surface peak strains show a concave upwards relationship as the width decreases. This effect occurs because of the increase in curvature at peak deflection as w_c decreases, and with a constant thickness, h_c, the bending strain will increase.

As w_c varies, the mass per unit span of the aluminum beam varies. Thus, for a given fragment impact velocity, the velocity imparted to the impact-affected spanwise region of the beam will vary with w_c accordingly, with the result that the "rate of absorption of the fragment's kinetic energy" as a function of time will also vary significantly with w_c as shown in Fig. 56.

Both this subsection and Subsection 4.3.2.3 have dealt with the effects of varying the beam mass by varying either the beam width w_c or the beam thickness, h_c, respectively, while holding the fragment properties constant. Figure 57 is a composite of Figs. 53 and 55 showing the effects on peak mid-span deflections and peak outer-surface and membrane strains as the mass per unit span is varied (by varying either the width or the thickness). At equivalent values of beam mass per unit span, the two results show the effects of varying the beam cross-sectional area. Referring to Fig. 51 in which five values of w_c/h are plotted for a constant beam mass, the effects of varying the beam cross sectional aspect ratio are illustrated and apply directly to the results of Fig. 57. In Fig. 57 there are two mass-variation plots, one for a variable thickness and the other for a variable width as tabulated in the following:

Thickness Variation			Width Variation		
w_c = constant = 1.5 in			h = constant = 0.1 in		
h	w_c/h	$w_c \cdot h = A_c$	w_c	w_c/h	$w_c \cdot h = A_c$
0.075	20	.113	1.125	11.25	.113
0.100	15	.150	1.500	15.0	.150
0.150	10	.225	2.250	25.5	.225

From this tabulation it is noted that there are three values of beam cross sectional area, A_c; at each value of A_c there are two values of w_c/h corresponding to a variation in thickness or a variation in width. For A_c = .113 in^2

the smaller value of w_c/h produced by varying only the width produces higher peak strains, which is expected from examining Fig. 57. For an increase in A_c to .225 in^2 (or an increased mass), the smallest value of w_c/h is attained by a thickness variation. The peak strain is slightly larger than that attained by varying the width but the increase in strain is not as large as would be expected from an examination of Fig. 51. An explantion of this is readily attainable by noting that the relative change in slope of $(\gamma_{11})_{max}$ vs. w_c/h as seen in Fig. 51 is dependent upon the magnitude of $A_c (A_c = w_c h)$. It is likely that as A_c decreases, the change in slope will increase, while for an increasing A_c the effects of varying the aspect ratio will not be as great as that shown in Fig. 51.

All of the parametric variations examined above were performed numerically on containment beams which were expected to demonstrate largely 2-d deformations. The principal result of the studies conducted in this subsection and in Subsection 4.3.2.3 is the demonstration of the effects of variations both (a) mass per unit span and (b) aspect ratio, and their interdependency.

4.3.2.5 Comments on Scaling Effects on Beam 2-D Structural Response

Let attention be restricted to a "containment beam" of appropriate structural proportions and/or proportions in relation to the impacting fragment(s) such that 2-d structural response will ensue. Further, let the component of the velocity of the impacting fragment normal to the impacted surface be large enough to produce large-deflection elastic-plastic transient structural response (up to, perhaps, tensile rupture) but small enough to avoid the "shear plug" type of failure. Within this 2-d structure and 2-d impacting-fragment framework, the CIVM-ET 4B computer code can provide reasonable estimates of the transient structural responses (within its specified domain of validity) of single-layer 2-d containment beams.

Impact attack against a given target structure may be characterized by (1) the time-zero location or the spanwise station and time of initial impact of each of the n attacking fragments as well as (2) the following data on each impacting fragment: (a) mass, (b) mass moment of inertia, (c) components of translational velocity, (d) rotational velocity, and (e) size of each

idealized nondeformable fragment; these fragments are required in the present code not to interfere with each other. The resulting structural response for a given (postulated) attack can be computed readily, but the effect of changing one of the many variables in this n-fragment attack is not readily determined in this highly nonlinear problem except from direct calculations. However, if one confines attention to a single-fragment perpendicular-impact attack at a given spanwise station of the structure, one may assess more readily the effect upon the maximum predicted strain in the containment structure of moderate changes of (a) the cross-sectional dimensions of the 2-d structure and/or (b) the kinetic energy (via mass and/or pre-impact velocity) and/or size of the idealized attacking fragment. Hence, it is to this restricted set of conditions that the following observations are directed.

For the postulated single-fragment impact attack (that is, a fragment of given diameter, mass, and perpendicular-impact velocity) against, for example, a containment beam of given material, of given span, width, and thickness, and having both ends ideally clamped, the location and value of the maximum extensional strain predicted will depend upon the spanwise location of the initial fragment-beam contact. If $d \ll \ell$, midspan impact will result in having $(\gamma_{11})_{max}$ occur at midspan -- and "rupture" at that station can be expected if the pre-impact $(KE)_f$ is sufficiently large. However, if initial fragment-beam contact occurs between midspan and a clamped end, the maximum strain γ_{11} will, in general, no longer occur at the spanwise station of initial impact; as the initial-impact spanwise station approaches one end from midspan, the location of $(\gamma_{11})_{max}$ is expected to shift "rapidly" toward and to remain very close to the clamped end.* Accordingly, it is necessary to consider single-fragment impact at only a fixed spanwise station in order to assess readily the effects of beam and fragment parameter changes upon the peak strain produced in the structure. For this purpose, therefore, let attention be confined to midspan perpendicular impact against a given beam by a single non-rotating idealized fragment.

---

* It should be noted that the 43 equal-length finite element modeling of the beam by elements with 4 DOF/node is inadequate to represent accurately the strain behavior near the clamped end. A much finer finite-element mesh is needed near a clamped end to provide reasonable strain predictions in that region; this, however, will result in a much larger ω_{max} and an attendant required smaller Δt for the timewise solution by CIVM-JET 4B.

With respect to the fragment itself, its modeled behavior may be described in terms of 3 quantities: diameter, mass, and velocity. First, assuming that the containment beam has been modeled by a sufficient number of (uniform-length) finite elements so that "converged structural response" can be realized both from (a) basic structural modeling requirements and (b) an adequate description of the local impact-interaction "momentum transfer" behavior, it has been shown earlier that fragment diameter has a "negligible effect" upon $(\gamma_{11})_{max}$ for small $(KE)_{fo}$; however, for a $(KE)_{fo}$ large enough to produce large deflections and substantial changes of curvature of the beam, a large-diameter fragment can constrain the structure and thereby change significantly both the spanwise distribution of (γ_{11}) and the value-and-location of $(\gamma_{11})_{max}$. On the other hand, if the idealized fragment diameter is very small, neither the spanwise distribution of peak γ_{11} nor $(\gamma_{11})_{max}$ will change since no fragment-beam constraint occurs and the basic finite-element modeling of the structure will leave unchanged the value and the spanwise distribution of locally-imparted velocity changes experienced by the beam from a fragment-beam impact -- for sufficiently small diameter values of the idealized fragment.

Hence, let the structure be modeled adequately and the idealized fragment diameter be properly small in the above sense. In that event, the remaining "fragment variables" (mass and velocity) can be represented by only <u>one</u> significant (and scalar) quantity: $(KE)_{fo}$, the pre-impact kinetic energy of the fragment. Thus, one can evaluate $(\gamma_{11})_{max}$ as a function of $(KE)_{fo}/U_c$ for the postulated containment beam of fixed h, w_c, and ℓ.

It would be interesting and instructive to see if the energy <u>ratio</u> $(KE)_{fo}/U_c$ for threshold containment (based upon producing a $(\gamma_{11})_{max}$ of 16 per cent) by a beam of fixed span ℓ=8.00 in and width w_c=1.50 in but changed thickness would be the same for various values of initial fragment kinetic energy $(KE)_{fo}$ or would change somewhat, since the only changes would be in (a) the beam thickness h and (b) the initial 2-d fragment kinetic energy or velocity (since a fragment of fixed mass is employed). Accordingly, the following calculations were carried out by modeling the beam with 43 equal-length 4 DOF/node elements and using an idealized fragment diameter of 1.00 in with a fixed mass of 0.315×10^{-3} $(lb\text{-}sec^2)/in$:

Case	h(in)*	$(KE)_{fo}$ (in-lb)	$(KE)_{fo}/U_c$	Spanwise Length (in) of Impact-Affected Zone, L_{eff}	
				Used in 43-Element Model	Plausible Value ≐ 2h
C4	.046	686	.143	.186	.092
C5 ≡ C2	.100	1489	.143	.186	.200
C6	.121	1804	.143	.186	.242
C7	.200	2978	.143	.186	.400
C8	.200	2978	.143	.400	.400

Note that Case C5 (the same as C2) represents the nominal CB-18 beam geometry and impact conditions and also serves as the "2-d threshold containment reference" corresponding to $(\gamma_{11})_{max}$ at x=0 of 16 per cent and $(KE)_{fo}/U_c$=0.143. For this given energy ratio and the indicated values of $(KE)_{fo}$ ranging from 686 (CB-9) to 2978 in-lb (which is double the CB-18 reference value), the associated beam thicknesses were determined -- ranging from 0.046 to .200 in. For Cases C4 through C7, the beam was assumed to experience velocity increments imparted by fragment impact only at the end nodes of the center element which the fragment impacts at midspan; this means that the region being used in these calculations as the impact-affected length is the distance from the impact point to the midspan of the next element -- which is a distance of 0.186 in. On the other hand, as argued in Subsection 2.2, a physically plausible estimate for this impact-affected length is about 2h. Hence, Cases C5 and C6 are reasonable in this regard but Cases C4 and C7 involve "unreasonable L_{eff} values". The consequences of this particular "choice" for L_{eff} in Cases C4-C7 are shown in Figs. 58a and 58b for the time history, respectively, of (a) upper surface strain at the midspan station x=0 and (b) fragment kinetic energy loss ratio $[(KE)_{fo} - (KE)_f]/(KE)_{fo}$ -- or energy ratio transferred to the beam -- where $(KE)_{fo}$ and $(KE)_f$ represent, respectively, the initial and the current kinetic energy of the fragment. Both of these time histories are very similar for Cases C5 and C6, but those for Cases C4 and C7 are very different; the value of $(\gamma_{11})_{max}$ and its time of occurrence are quite similar between Cases C5 and C6 but are distinctly different for Cases C4 and C7.

* Nominal values for h are used here for the sake of convenience.

The "improper effective-length modeling" for Cases C4 and C7 could be remedied by using finite elements of different and appropriate length for a spanwise region centered about the midspan impact point. For Case C4 this would mean using elements of about 0.092-in length in the central region and, for efficiency, longer elements for the remainder of the beam. On the other hand, Case C7 could be "remedied" without changing from the present 43 equal-length element model by distributing the imparted velocity increments to the 4 rather than the 2 nodes nearest to the midspan impact point; this rather convenient and simple change has been used in carrying out Case C8 where the L_{eff} used is 0.40 in compared with the physically plausible estimate* of 0.40 in (≡2h). The results from Cases C7 and C8 are compared in Fig. 59 (which corresponds to Fig. 58a).

In Fig. 59 the peak strain of Case C8 is greater than for Case C7 (which are identical numerical examples except for a variation of the "impact-affected length"). It would be expected that as the impact-affected length is increased, the effects of the impact interaction would be spread over a greater region and reduce the peak strain noted at the point of impact. However, as the impact-affected length L_{eff} increases, the mass of the beam in the impact-affected region increases; for the CIVM (collision imparted velocity method) scheme of subimpact momentum transfer (Appendix A), the amount of kinetic energy transferred to the beam increases during each subimpact. This may be seen more readily from the following tabulation and sketch which depicts for the present 43 equal-element example:

(a) impact occurring at the center of the element centered at beam midspan,

(b) the adjacent equal-length elements,

(c) various values of assumed impact-affected length L_{eff} expressed in terms of element length,

(d) the number of associated impact-affected nodes on one side of midspan according to L_{eff} itself and according to CIVM-JET 4B logic,

(e) the total kinetic energy transferred to the beam in a single (first) impact ratioed to the pre-impact fragment kinetic energy $(KE)_{fo}$ for

(1) the entire impact-affected beam region and

(2) only the center 2-element region associated with the two nodes on either side of the midspan impact point, and

*See pages 17-19 and Fig. 10.

(f) the ratio of item (2) to item (1) expressed as per cent:

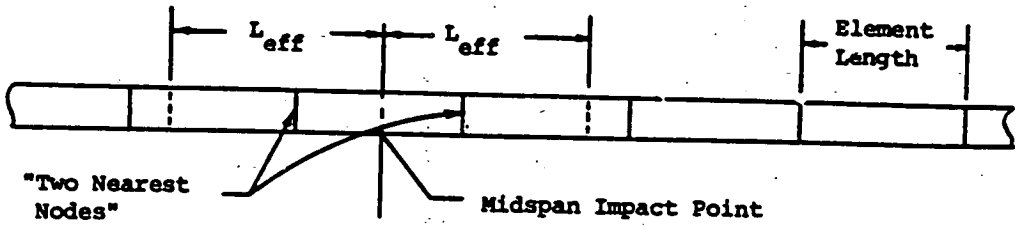

$\left(\frac{L_{eff}}{\text{Elem. Length}}\right)^*$	No. of Affected Nodes on One Side of Midspan		Ratio of KE transferred-to-Beam to $(KE)_{fo}$ for First Impact		Per Cent to Region of Two Nearest Nodes
	By L_{eff}	By Code	To Entire Beam	To Two Nearest Nodes	
0 to 1	1	1	.250	.250	100
1 to 1.5	2	1	.250	.250	100
1.6	2	2	.289	.265	91.6
1.8	2	2	.340	.276	81.2
2.0	2	2	.370	.278	75.0
2.2	3	2	.390	.276	70.8
2.4	3	2	.401	.272	67.8
2.5	3	3	.406	.270	66.6
2.6	3	3	.430	.273	63.6
2.8	3	3	.463	.273	59.0
3.0	3	3	.490	.271	55.4
3.2	4	3	.508	.268	52.8

It is readily seen that the central portion of the beam surrounding the point of impact receives more kinetic energy for Case C8 during the first subimpact when the effective length is chosen as two times the beam thickness than for Case 7. This tends to increase the peak strain predicted at the impact location.

A similar kinetic energy transfer calculation was carried out for Case C4 with the present element length and for a reduced element length. The initial

* Note that this value for Cases C1 through C7 is .532 and for Case C8 is 2.09.

energy absorption ratio for the central two element region with the present element length (0.186 in) is 0.066 while for the reduced element length (0.092 in) the ratio would be 0.034. This would result in a large decrease in the rate of absorbed kinetic energy, which will lower the peak strain.

The ratio of container width to thickness, w_c/h, was not preserved during this study. It is conceivable for scaling purposes to vary the mass per unit span by varying the beam width and holding the thickness constant. For a given mass or cross sectional area, A_c, the containment beam will have two different aspect ratios, w_c/h, for a single mass value by the variation of either the thickness or the width and holding the other two dimensions constant. Referring to Figs. 51 and 57, it would be expected that Case C4 would attain higher peak strains if the width had been reduced rather than the thickness. However, from Fig. 57, a small decrease in peak strains is expected for Case C7 with an increased width.

To this point in Subsection 4.3.2.5, a change in $(KE)_{fo}$ has been assumed to occur by a change in the fragment velocity v; the fragment mass m_f has been assumed to be fixed. Alternatively, one could change $(KE)_{fo}$ by holding v fixed and changing m_f. Suppose, for example, that $(KE)_{fo}$ is increased by 75 per cent over the CB-18 value by maintaining v=2794 in/sec but increasing m_f by 75 per cent. On the basis of calculations already done for a containment beam of fixed span (ℓ=8.00 in) how can one choose beam dimensions w_c and h such that $(\gamma_{11})_{max}$ at midspan will be a pre-selected value such as the 16 per cent found for the basic CB-18 beam-fragment impact condition (Case C2 or C5)? For this endeavor, let it be assumed that a matching of $(KE)_{fo}/U_c$ shall be required -- thus defining the cross-sectional area $w_c h$ as being 75 per cent greater than the CB-18 value of 0.15. This means, in turn, that the ratio of beam mass per unit length to fragment mass is exactly the same as in Cases C2 and C5 for the CB-18 example itself. Further, if one requires that the ratio w_c/h to be the same as in the CB-18 beam (i.e., 15), one obtains h=0.132 in and w_c=1.98 in. Hence, <u>all</u> of the dimensionless parameter values of the postulated example match exactly those of the CB-18 problem except for h/ℓ and w_c/ℓ; these two parameter values are sufficiently close to those for CB-18 that little effect is expected. Accordingly, one expects $(\gamma_{11})_{max}$ for the proposed beam-fragment impact problem to match rather closely that of the CB-18 example (see Fig. 51a). The predictions of upper-surface γ_{11} as a

function of time at the midspan impact station x=0 for these two cases are shown in Fig. 60, and confirms this expectation.

It appears, therefore, that the scaling of one containment configuration to another* in order to contain a geometrically similar fragment can not be accomplished by merely scaling the volume of the beam to preserve the ratio of fragment kinetic energy to beam energy absorption capability ($\beta_{17}=(KE)_f/U_c$). Instead the proper scaling or preservation of the ratios of beam mass to fragment mass and beam width to beam thickness must also be taken into account.

4.4 Comments on Container Design

The effects that various material, geometric, and kinematic parameters have on a fragment-container impact-interaction have been discussed briefly in the preceding subsections of Section 4. Two sets of experimental data (NAPTC multi-fragment impact on steel rings and MIT-ASRL single-steel-sphere impact on aluminum beams) were analyzed in order to identify some of the primary parametric effects. In addition, a plausible 2-d numerical analysis was applied for both of these experimental situations for a more extensive parameter-variation analysis.

There is a basic difference between the numerical analysis carried out on the NAPTC fragment-ring impact data (Section 3 and Subsection 4.2) and the MIT-ASRL fragment-beam impact data (Subsection 4.3). The NAPTC fragment's initial impact angle is very different; all of the fragment-ring impacts occurred at oblique angles while all of the fragment-beam impacts occurred at normal (90°) incidence angles. In order to make certain comparisons between these two parametric studies, it is necessary to examine the effects that impact incidence angle has on the impact interaction.

Figures 61a and 61b show the results of a fragment-beam impact interaction for a 60° initial impact incidence angle. The fragment and beam are geometrically identical to the CB-18 fragment-beam impact experiment described in Section 2 and in Subsection 4.3. The fragment is a rigid disk with a 1.0-in diameter. The double clamped 6061-T651 aluminum beam has a length of 8.0 in, a width of 1.5 in, and a thickness of 0.1 in. The CIVM-JET 4B computer code is used for the analysis with 43 equal-length finite elements to represent the beam and an EL-SH material approximation for the aluminum

*Based on a structure of fixed span as stated on page 105.

via the mechanical sublayer model and stress-strain Fit A (see page 8). The fragment was allowed to impact the beam at the midspan location with a vertical velocity of 2794 in/sec and a tangential velocity of 1613.12 in/sec (total velocity of 3226.23 in/sec, a total kinetic energy of 1985 in-lbs, and an initial incidence angle of 60° measured from the tangent to the beam lower surface). The coefficient of friction, μ, was set equal to zero (as was the case with all calculations reported in Subsection 4.3). Therefore, this fragment's translational kinetic energy component normal to the beam (1486 in-lb) is identical to the total translational kinetic energy used in the earlier normal impact calculations.

Figure 61a is a time history of fragment trajectory angle θ. One set of data points corresponds to the present example of a 60° initial incidence angle. The second set of data points corresponds to the CB-18 normal impact incidence case. Note that both examples have identical preimpact normal velocities of 2794 in/sec and that fragment rebound occurs almost at the same time after initial impact (approx. TAII=650 microseconds). For the 60° initial incidence angle the fragment is 0.97 in from the beam midspan location at the time of rebound.

Figure 61b is an upper surface strain profile at TAII=655 microseconds for both the 60° and 90° initial incidence angle cases. This time corresponds to the time of peak transient response for the 60° case, is about 25 microseconds before peak response for the 90° case, and is the approximate time of fragment rebound for both cases. Note that the 60° case has a much wider region of significant beam deformation, but the peak strain is greater for the 90° case.

The absolute peak strain predicted for the 90° case is 0.16 which is the assumed threshold failure strain. In the 60° case the beam permanently absorbed a total of 1660 in-lb of energy while the beam in the 90° case absorbed permanently only 1411 in-lb of energy. It is apparent from this study that the normal pre-impact velocity component is the most critical (for an interaction in which a negligibly small value of friction coefficient, μ, is used), and that an analysis assuming a normal impact for the same initial total kinetic energy will be conservative. Therefore, parametric

effects on predicted peak strains that were identified from the analytical study of fragment-beam normal impacts should also be applicable to fragment-ring oblique impacts.

It should be noted that there are some basic deficiencies in the parametric studies of Subsections 4.2 and 4.3 for fragment-ring and fragment-beam impact interactions. All of the parametric studies assumed a constant container geometry. In none of the parametric evaluations was the container thickness or width allowed to be a function of the circumferential location or span. Additionally, none of the studies considered the possibility of fragment deflection (see Section 5) rather than total containment. However, these two additional parameters (variable spanwise container geometry or fragment deflection) both assume that a specific zone on the container will be impacted or that only a specific exterior region is to be protected. The purpose of Section 4 is to identify the primary parameters affecting containment and in doing so it must be assumed that every region of the container's circumference or span has an equal probability of being impacted and that the entire exterior region needs to be protected. Consideration concerning what might be a high-probability impact-region or the protection of only specific exterior regions will vary widely based on fragment type, container location, container geometry, and many other problem dependent parameters. The analysis of Subsections 4.2 and 4.3 is meant to be "general" and applicable to a wide variery of beam or ring type containers. Not considered, however, was variable spanwise geometry, fragment deflection, or selective fragment penetration.

Having identified the most prominent parameters affecting the peak response of a general ring-like or beam-like container, (assuming 2-d deformations, and restricting oneself to small strain theory), how can these analysis techniques (empirical and analytical/numerical) be applied to container design? First, two basic criteria upon which the design of an engine rotor container might be based should be identified:

(1) A specified region needs to be protected. A fixed container surface area is defined and for this geometry a minimum weight container needs to be designed.

(2) A "costing function" is applied to the air vehicle system and a fixed mass is allocated for containment purposes. A container material and geometry must then be decided upon to maximize the containment potential of this fixed-mass structure.

A design program will most likely utilize both of these criteria during different stages of the design process. First, a fragment generation problem is identified and a specified region to be protected is then defined. An analysis will then proceed to determine a first estimate of cost (weight, labor) to contain various sizes and configurations of fragments for that particular aircraft engine. Then, a "costing function" based on the cost of protection versus the level of uncontainment that can be tolerated (or regulated) is defined and an upper limit is placed on the mass of the container and on the costs of manufacture, installation, and maintenance.

In each phase of this design work, a set of empirical and/or analytical impact data is needed. A design procedure which depends totally on empirical data of adequate scope will arrive at a design which might be viewed as having been "proof tested", but likely will be costly and time consuming. If there is an attempt to decrease the experimental costs by arbitrarily or "intuitively" limiting the scope of the experimental program or by using "scaled" experimental models, there is a probability of alternate containment designs being undiscovered or of the erroneous assessment of key parametric effects (because of insufficient data or inadequately scaled experiments). Conversely, a design program relying solely upon 2-d analytical/numerical prediction data should be less expensive but may not address the actual containment problem adequately because of the basic restrictive assumptions of the analytical method, and will not provide a "proof tested" design.

A more rational and cost-effective design process might consist of a small preliminary set of "full-scale" experiments to assess the effects of a few basic parameters and to obtain sufficient data to calibrate a numerical analysis to "compensate" for the "restrictive assumptions" in the analysis. The analytical technique (once correlated with preliminary data from the pilot tests) could then be used for more extensive parametric studies. Also, it could be used to aid in the design of an "adequately-scaled" model of the

fragment-structure impact-interaction to be used in further experimental studies. The adequacy of the containment structure thus designed could be verified by a small selective set of full-scale proof tests.

The parametric effects that are identified in Subsections 4.2 and 4.3 could be utilized as a guide for determining the original pilot experiments and the series of analytical studies to be used in the design process.

SECTION 5

ON THE USE OF A DEFLECTOR FOR FRAGMENT CONTROL

5.1 Problem Outline

The preceding sections have dealt with the containment of a fragment, in which the impacted structure is required to absorb essentially all of the fragment's translational kinetic energy. For many practical applications, only a particular region is required to be free from fragment intrusion, and a structure could be utilized to deflect the fragment from a path that would otherwise enter this region. A deflector can be described by the same set of dimensionless parameters that has been used already to characterize a container, plus three additional interactive parameters: α, the angle change of the path of the fragment; θ, the angle of initial impact; and ξ, the point along the structure at which initial impact occurs. Table 10 lists the 18 dimensionless parameters used to describe a beam containment of a rigid spheroidal fragment. To this list will be added $\beta_{19} = \alpha$ (measured positive clockwise), $\beta_{20} = \theta$ (measured positive counter clockwise), and $\beta_{21} = \xi$ (fractional distance along beam). An illustrative cantilever-type deflector is depicted in Fig. 62 with the appropriate approach and deflection angles (θ and α) indicated.

For the deflector system, there are three equally-important dimensionless parameters which describe the effectiveness of the deflector: ε_{max}, the maximum strain attained by the deflector; z/h, ratio of maximum deflection (z or w) to the beam thickness h which indicates the extent to which the deflector impinges upon the space that is being protected; and α the change in flight path of the fragment. There are, therefore, three means by which a deflector can "fail": (1) the deflector remains structurally intact but the fragment is still allowed to enter the protected region (insufficient path-angle-change α); (2) the deflector structurally fails and it either proceeds into or allows the fragment to enter the "protected region (ε_{max} is too large); and/or (3) the deflector remains structurally intact and the magnitude of α is sufficiently large to deflect the fragment but the transient deflection of the deflector carries it into the region to be protected (z/h is

too large). In each of these cases the protected region suffers an intrusion by either the fragment or the deflector.

The primary purpose of this brief section is to study the response of an illustrative deflector type structure to the variation of two of the dimensionless parameters discussed above: θ, and ξ; the results will be assessed on the basis of the transient values of α and z/h, and of ϵ_{max}. There is an insufficient amount of experimental data on fragment-deflector impact and response to construct "effects plots", but based on the evaluation set forth in Sections 2 and 4 of this report, a brief numerical parametric study was performed and will be described. The remaining dimensionless parameters, β_1 - β_{18}, will not be addressed in this section. These parameters have been discussed in Section 4 and it is believed that their roles will be similar for a deflector as they are for a container structure.

5.2 Numerical Model of a Cantilevered-Beam Deflector

In order to keep the parametric evaluation of a deflector as simple as possible, a numerical model nearly identical to that used to model the "beam-containers of Section 4 is utilized. The deflector is modeled simply as a cantilever beam of length 8.0 in, width 1.5 in, and thickness 0.1 in composed of 6061-T651 aluminum. The CIVM-JET 4B computer code is used to analyze the beam as 43 equal-length finite elements (44 lumped mass nodal points). The material properties of the 6061-T651 aluminum are assumed to be elastic-strain hardening (EL-SH) approximated by the mechanical sublayer model using Fit A (see page 8). A single attacking fragment is modeled as a 1.0-in diameter rigid circular disk with a translational velocity of 2794 in/sec and a mass of $.3815 \times 10^{-3}$ (lb-sec^2)/in. This model is identical to the model CB-18 conditions used in Section 4.

The boundary conditions of the beam deflector represent a critical factor influencing the effectiveness of the deflector. In Subsection 4.4 a numerical study of an identical beam that was doubly clamped was performed for a fragment incidence angle of θ=60°. A fragment deflection occurred during that analysis; however, for the purposes of this study, a deflector will be defined to have one end free. Therefore, the analyzed deflector has one end clamped and the other end free.

5.3 Parametric Evaluation of a Cantilever-Beam Deflector

In this analysis, parameters β_1-β_{17} (Table 10) are held constant and only parameters β_{20} and β_{21} (θ and ξ) are varied. Thus, the evaluation of a fragment-deflector impact is based on an examination of the following:

(a) $\beta_{18} = z/h = f_1(\theta,\xi)$ } Deflector Response

(b) $\beta_{18} = \varepsilon_{max} = f_2(\theta,\xi)$ }

(c) $\beta_{19} = \alpha = f_3(\theta,\xi)$ Fragment Response

There are an infinite number of values that could be chosen for either ξ or θ, however, for this analysis, only a few selected values will be examined. If the beam were freely supported (resting on wires, for instance), the best possible impact location for maximum energy absorption would be at the beam center. Because the beam is clamped at one end and since the beam dimensions have been chosen to be equal to the "threshold containment size" for a doubly-clamped beam when impacted at midspan by the same fragment size and KE as utilized here), the probability of a successful deflection/containment should increase as the value of ξ decreases.[+] Note that the CIVM-JET 4B analysis can not properly evaluate the 3-d stress state that will be found at the clamped end so that impacts which occur close to the clamp will provide meaningless predictions near the clamped end. Therefore, ξ will be selected as $0.5 \leq \xi < 1.0$. For ξ=0.5 the impact-interaction will initially be identical to the containment studies of Section 4, and this value (ξ=0.5) is chosen to be the first point of evaluation; the subsequent structural response will be different since now one end of the beam is free while the other is clamped.

For each of the ξ values examined, there are three values of θ that are analyzed: θ=30°, 60°, and 90°; (where θ=90° is an initially normal impact). The values θ=90° was chosen to determine the amount of "tangential velocity" that the deflector can impart to the fragment as the beam deforms; also, "cross-correlations" can be drawn to the normal-impact containment studies of Section 4 for beams with both ends clamped. Corresponding studies of θ=120° and 150° were not performed because the deflected fragment would travel towards the clamped end in these two situations, rather than towards the free end and, hence, would not "escape".

[+] Assuming that transverse shear-induced failure can be ignored.

Figures 63a through 63c show the results of a fragment impact upon a cantilever beam for ξ=0.5 and θ=30°, 60°, and 90°. Figure 63a is a plot of α resulting from these three impact configurations. Note that for all three situations, including the relatively "shallow" impact angle θ=30°, the fragment has become "embedded" within the confines of the deflector. Figure 63b depicts this situation more clearly as a plot of beam profile and fragment location at 905 microseconds after initial impact. Note from Fig. 63a that this corresponds to the time at which the fragments are all being deflected towards the clamped end since α is decreasing (the θ=30° case does not show a negative value of α during the time span presented). The beam has deformed greatly and for each θ case there is a portion of the beam which is below any portion of the disk-like fragment. The impact-interaction with a doubly-clamped containment beam (Section 4) is generally finished by 900 microseconds after initial contact. It is interesting to examine the energy remaining in the fragment at this time after impact with a deflector:

INITIAL IMPACT LOCATION: ξ=0.5				
Impact Incidence Angle θ (deg)	Fragment Kinetic Energy Before Impact		Fragment Kinetic Energy At 905 Microseconds TAII	
	Total $(KE)_f$ (in-lb)	Normal $(KE)_f$ (in-lb)	Total $(KE)_f$ (in-lb)	$(KE)_f$ Parallel to z axis (in-lb)
30°	1489.1	372.3	912.8[61]*	47.4[13]*
60°	1489.1	1116.8	459.9[31]	296.6[27]
90°	1489.1	1489.1	544.6[37]	534.8[36]

The fragments for each value of θ possess the same pre-impact total kinetic energy; after 905 microseconds, the fragments still possess a significant level of kinetic energy, and will continue to impact the deflector. The peak transient strains, however, have already occurred by this time and Fig. 63c shows a plot of upper-surface strain versus deflector location at

*The bracketed numbers are the percent ratios of the energies at 905 microseconds to the corresponding pre-impact energy values.

905 microseconds after impact, plus the value of the peak strain which occurred earlier during the impact interaction. Note that the peak strains for θ=60° and 90° occur at or very near the point of initial impact. For the θ=90° case the fragment remains at the same $\bar{x}$ location (Fig. 63b) and there is only one significant peak for the upper surface strains. The θ=60° case shows the fragment traversing the span of the deflector, creating two locations of significant peak upper-surface strains. The first (and largest peak) occurs at the point of initial impact while the second peak occurs at the spanwise location where the fragment has become "embedded" (Figs. 63a and 63b). However, the θ=30° case shows a very small peak at the point of initial impact and a significantly larger peak upper-surface strain at the spanwise location of fragment "embedding". The θ=30° fragment still possesses 60 percent of its initial kinetic energy at 905 microseconds after initial impact; as can be seen from Fig. 63b, the fragment will continue to impact the deflector at this new spanwise location creating a large peak upper-surface strain. The fragments for θ=60° and 90° have expended most of their original kinetic energy during the early impacts while for θ=30° the fragment still possesses most of its original kinetic energy and will expend it during a later succession of impacts.

Further examination of Fig. 63c shows a predicted large concentrated strain at the clamped end for all three θ cases. However, as was pointed out earlier in this subsection and also in Section 2, the 2-d CIVM-JET 4B analysis can not accurately evaluate the large 3-d strains which occur near a clamped boundary; also, even within the 2-d framework, a finer finite element mesh would be needed near the clamped end to permit a reasonable approximation to the spatially rapidly-varying strains near the clamped end. Therefore, care must be exercised when examining the strain distribution along the deflector, and strain predictions at and near the clamped end should be viewed skeptically.

Overall, the peak strains for these three impact conditions (θ=30°, 60°, and 90° -- all at ξ=0.5) are significantly lower than the peak strain predicted for θ=60° and θ=90° for an identical doubly-clamped containment beam. However, the beam deflections are very large and could result in either (1) the excursion of the deflector into the protected region or (2) the eventual

failure of the deflector at the clamped end because of the large induced strain and/or bending moment. It appears that the fragments will continue to remain in contact with the deflector and will probably not enter the protected region without a tensile failure of the deflector.

To complete this brief examination of fragment-deflector impact-interaction, it is desired to consider a value of initial-impact-station location ξ that will allow the fragments from all three θ cases to escape from contact with the deflector. In order to "guarantee" this occurrence, a value ξ=.875 was chosen for θ=30°, 60°, and 90° with all other parameters identical to the ξ=.50 situation. Figures 64a through 64c show the results of this impact scenario.

Figure 64a shows that little fragment deflection (α) has occurred for any of the impact θ's. The θ=30° and 60° cases show identical final values for α; in all three θ's, the fragment has ceased impacting the deflector by 300 microseconds after initial contact. Figure 64b shows the large (continuing) excursions of the deflector's free end; for θ=30° and 60°, the fragment has completely left the vicinity of the deflector by 905 microseconds after initial impact. Examining the fragment kinetic energies, the following is noted:

INITIAL IMPACT LOCATION: ξ=0.875				
Impact Incidence Angle θ (deg)	Before Impact		At 905 Microseconds TAII	
	Total $(KE)_f$ (in-lb)	Normal $(KE)_f$ (in-lb)	Total $(KE)_f$ (in-lb)	$(KE)_f$ Parallel to z axis (in-lb)
30°	1489.1	372.3	1337.2[90]*	234.6[63]*
60°	1489.1	1116.8	1048.0[70]	718.2[64]
90°	1489.1	1489.1	964.1[65]	963.3[65]

For each θ case, a significant portion of the fragment's kinetic energy still remains at 905 microseconds after initial impact and it is evident from

*See footnote on page 114.

Fig. 64b for all three cases that the fragments either have escaped or will escape. Figure 64c depicts the upper-surface profile at this time with only one peak registered for each value of θ and each peak upper-surface strain occurring at or near the point of initial impact. Note that very low strain levels have been recorded at the clamped boundary because the rotations at the clamp at this time (Fig. 64b) are also very small. It appears for all three values of θ that the deflector has sustained a "permanent hinge" near the midspan location (Fig. 64b) and indeed this is a point of peak upper-surface compressive strain (Fig. 64c).

Overall, an impact in the vicinity of ξ=0.875 appears to result in the "failure" of the deflector. The deflector has failed by allowing the fragments to escape with most of their original kinetic energies along paths very close to their original path. The deflector also sustains extremely large deflections of its free tip, the excursions of which may easily enter the "protected region". It appears that tensile failures of the deflector are not imminent or likely for large values of ξ. The deflector has formed a secondary plastic hinge at a location remote from the clamped end, resulting in relatively low bending strains. The peak strain at the point of impact for the θ=90° case is relatively large (0.14 compared with a "failure strain" of 0.16 deduced from an identical beam that was doubly clamped and subjected to the CB-18 impact conditions); however, since the fragment has escaped, a tensile failure at this location would be inconsequential to the flight path of the fragment. It is interesting to note that the peak upper-surface strains for θ=60° and 90° at ξ=0.875 are larger than those recorded for ξ=0.50. This is because of the larger levels of local bending that occurs for ξ=0.875, which can be seen from a comparison of Figs. 63c and 64c. For the θ=30° case the relatively low level of total energy transferred from the fragment to the deflector for ξ=0.875 prevents upper-surface strains from becoming larger than those predicted for ξ=0.50. For ξ=0.50 the θ=30° case had its peak upper-surface strain located at a spanwise location removed from the point of initial impact. For ξ=0.875 the fragment has escaped, which precludes the transfer of kinetic energy to the deflector by "later" subimpacts.

5.4 Comments on Deflector Design

A brief overview of deflector structures that are assumed to be geometrically identical (except for the boundary conditions) to the previously-analyzed container beams was presented in Subsections 5.1 - 5.3. A simple parametric evaluation was performed on the effects of (1) the spanwise location of initial impact and (2) the initial fragment incidence angle. The deflectors analyzed were assumed to have all geometric and material parameters independent of spanwise location.

The user of a deflector type structure assumes that only a specific region is to be protected, thus the criticalness of a given fragment attack against a given deflector structure of this type is dependent upon the spanwise location of the initial impact. It is conceivable that a systematic variation of the spanwise mass distribution of the deflector (in the region near the clamp, between the clamp and the initial impact region, in the impact region, and between the impact region and the deflector's free end) will lead to a container of minimum total mass and an optimal mass distribution for fragment-deflection purposes. The question of mass-distribution effects was not studied in this report, but could be carried out readily with the CIVM-JET 4B code.

The boundary conditions for the deflector are themselves extremely critical in determining the effectiveness of a fragment deflector. An actual deflector may be attached at one end to a "rigid" structure but may also be attached at a number of spanwise stations to a relatively flexible surrounding structure (e.g., the thin engine casing, stiffeners, etc.) which will tend to limit the deflector's deformation and also absorb some of the fragment's kinetic energy. Considerations of this type are highly problem dependent and would require an extensive set of numerical or empirical studies in order to assess the parametric effects adequately.

The purpose of Section 5 was not to identify all of the parameters affecting a fragment-deflector impact-interaction nor to arrive at a deflector design by optimizing the mass distribution or the applied boundary attachments. Instead, only a brief illustrative examination of a structure that is identically geometrically configured for either a containment or a deflection role is intended. Recognizing the limitations of the previously-discussed deflector analysis, it is still possible to make some overall

comments concerning the use of a deflector structure for fragment control.

In Subsection 4.4 a possible process was reviewed for the design of a fragment containment structure using a combination of empirical and analytical/numerical data. A similar process is recommended for the design of a deflector. A design is guided by cost (weight, manufacture, installation, and maintenance) considerations. A careful decision must be made concerning the extent of the fragment control (the maximum size and energy of the considered fragment, the size of the region to be protected, and the implications of selective fragment penetration or deflection) based on these cost constraints. The final design is bounded by these considerations, and the allowable mass must be optimized to control the widest variety of possible fragment-structure impact interactions. A deflector may be the "first choice" as a fragment control structure. However, if a container[+] is designed, there is the possibility that a portion of the container support structure might fail (either early in the impact-interaction or due to a direct impact by a second fragment). This situation would necessitate the treatment of the combined container and its failed support as a single "deflector type" structure. Therefore, a deflection analysis may be needed in a wide variety of fragment control designs.

Given an adequate set of pilot deflection experiments for correlation purposes, the 2-d impact-interaction analysis described in this report should give a reasonable evaluation for a deflector design. The last stage of a design process for a container, deflector, or dual container/deflector would require full-scale proof-tests because of the inherent limitations of the present numerically-generated code predictions or of empirical "scale-model" generated experimental data.

[+] That is, a partial ring or a panel which is intended to contain rather than to divert or deflect the fragment.

SECTION 6

EXPLORATORY MODIFICATIONS AND EXTENSIONS OF THE ANALYSIS

6.1 General Considerations

In the present calculations discussed thus far, the finite-element analysis procedure described in Refs. 4 and 17 for the large-deflection elastic-plastic transient responses of Bernoulli-Euler beams and rings has been utilized. The retention of the classical Bernoulli-Euler assumption that normals to the reference axis of the beam undergo no change in length during deformation implies a restriction that strains are not large, since large straining will produce thinning (in tension) or thickening (in compression) of the body's depthwise dimension. Also, the change-of-curvature part of the strain-displacement relations used in Refs. 4, 17, and 20 (and named strain-displacement relations A, B, C, D, and E in Ref. 20; also, see Eq. B.5 of Appendix B) are restricted to small membrane strains, since the membrane strains have to be included in the Lagrangian bending strain expression when they are finite. The term "finite strain" (as compared with "small" or "infinitesimal" strain) refers to strains that are not negligible when compared with unity. Considering a curved beam, for example, as depicted in Fig. A.1 with curvilinear coordinates ξ, η, ζ in directions 1, 2, and 3, respectively, if the strain measure is the Green ("Lagrangian") strain tensor in mixed component form* γ_2^2, expressions of the type $(1+2\gamma_2^2)$, for example, occur in the constitutive equations (see Eq. B.21 of Appendix B); if $\overset{o}{\gamma}{}_2^2$ is the Green-strain-tensor mixed component <u>at the reference axis</u> of the beam (or "membrane strain"), expressions of the type $(1+2\overset{o}{\gamma}{}_2^2)$ occur in the ζ^o-dependent part of the strain-displacement relations (see Eq. B.2 of Appendix B). If $\gamma_2^2 \ll 1$ so that $1+2\gamma_2^2 \approx 1$, one usually refers to the strain as being "infinitesimal" or "small"; otherwise, the strain is referred to as being "finite" or "large". Since it is always true that $\gamma_2^2 \geq \overset{o}{\gamma}{}_2^2$, the small-strain approximation breaks down first in the constitutive equations and later in the strain-displacement equations.

---

* Tensor mixed components (identified by both subscripts and superscripts) are used here for general applicability since in curvilinear coordinates the formulation takes a much simpler form when formulated in terms of the tensor <u>mixed components</u> (for example, γ_j^i instead of γ_{ij}, and S_j^i instead of S^{ij}); in rectangular Cartesian coordinates, $\gamma_{ij}=\gamma_j^i=\gamma^{ij}$ is satisfied identically.

In addition to the Bernoulli-Euler assumptions, the mechanical-sublayer model of the material was used in Refs. 4 and 17; this model, in turn, requires that the stress-strain curve being modeled must be monotonically increasing -- the stress associated with this stress-strain curve must not decrease with increasing strain -- and unloading must proceed elastically at the same modulus as the original elastic modulus. Thus, since the stress $\tau_k = \frac{\rho_o}{\rho} \sigma_T$ (see Ref. 21 page 23, where it was assumed that the original mass density ρ_o was equal to the final mass density ρ so that τ_k was equal to the "true stress" σ_T) versus axial Lagrangian strain tensor component[+] γ_{11} approximately exhibits this type of monotonic behavior (whereas S_{11} vs. γ_{11} does not), a mechanical-sublayer fit to this uniaxial tension stress-strain curve was made and the resulting values as reported in Subsection 2.2 (termed Fit A) and in Subsection 2.4 (termed Fit B) were employed. The resulting stresses τ_k were used in the JET 3 and in the CIVM-JET 4B program as playing the role of the second Piola-Kirchhoff stress which appears in the basic governing equations [4, 17 and Appendix A of the present report] upon which the above programs are based. In view of the above considerations as well as the data scatter in the experimental measurements of uniaxial stress-strain behavior of a number of 6061-T651 aluminum test specimens, the adopted compromise procedure was believed likely to provide reasonable predictions of structural response involving small levels of strain. At what strain levels these approximations lead to unreliable predictions remains quite uncertain. Therefore, some additional exploratory studies of limited scope designed to remedy, in large part, these noted deficiencies were carried out and are discussed in this section.

The modifications made consist essentially of five aspects as described concisely in the following, and discussed further in Appendix B:

1. The proper second Piola-Kirchhoff stress tensor components S^{ij} appearing in the basic governing equations are employed in the computer program by making proper transformations in the constitutive equations of certain stress and strain measures employed in a

[+]In Ref. 21 rectangular Cartesian coordinates are used; for these coordinates, $\gamma_{11} \equiv \gamma_1^1 \equiv \gamma^{11}$. However, in this section and Appendix B the "axial direction for a beam or the circumferential direction" for a ring is regarded as the η or "2" direction.

new mechanical sublayer fitting of uniaxial stress-strain data for 6061-T651 aluminum [21] as cited under item 2.

2. The uniaxial stress-strain data [21] of the 6061-T651 aluminum material expressed in terms of the Kirchhoff stress τ_k (or simply τ_u for uniaxial) versus ε^* has been fitted in a piecewise-linear fashion by means of the mechanical-sublayer model, where

$$\tau_u \equiv \frac{\rho_o}{\rho}\sigma_T = \frac{P}{A_o}\frac{\ell}{\ell_o} = \frac{P}{A_o}\left(1+\tilde{E}_u\right) \qquad (6.1a)$$

$$\varepsilon^* \equiv \ln\frac{\ell}{\ell_o} = \ln\left(1+\tilde{E}_u\right) \qquad (6.1b)$$

and where

P = uniaxial load applied to the test specimen

$A_o(A)$ = cross-sectional area of the original undeformed (current deformed) specimen

$\ell_o(\ell)$ = the original undeformed (current deformed) gage length

$\rho_o(\rho)$ = mass per original undeformed (current deformed) unit volume of the material

$\tilde{E}_u = \frac{\ell-\ell_o}{\ell_o}$ = longitudinal component of the elongation strain tensor

$\sigma_T \equiv \frac{P}{A}$ = Cauchy ("true") stress = $\frac{P}{A_o}\frac{\rho}{\rho_o}(1+\tilde{E}_u)$

$\varepsilon^* \equiv \ln\frac{\ell}{\ell_o}$ = logarithmic ("natural" or "true") strain = $\ln(1+\tilde{E}_u)$

$\tau_k \equiv \frac{\rho_o}{\rho}\sigma_T$ = Kirchhoff stress = $\sigma_E(1+\tilde{E}_u)$; $\sigma_E = \frac{P}{A_o}$

$\rho_o A_o \ell_o = \rho A \ell$ = mass conservation

It is perhaps useful to recall that the second Piola-Kirchhoff stress tensor component S_{22} or S_2^2 = (pseudo force)/(undeformed area) = $[P/(1+\tilde{E}_u)]/A_o \equiv \sigma_E/(1+\tilde{E}_u)$.

It turns out [46, p. 29] that the uniaxial stress-strain curve for ductile metals such as aluminum is essentially perfectly antisymmetric (i.e., for tension and compression) and monotonically increasing when expressed in terms of τ_u and ε^*. Hence, the mechanical-sublayer model is well suited to describe this type of behavior. In particular, the uniaxial stress-strain behavior for the 6061-T651 material of Ref. 16 (as given in Fig. 29a of Ref. 21 for longitudinal tensile specimens of circular cross-section and converted to τ_u vs. ε^*) is given by the following τ_u, ε^* pairs for mechanical-sublayer piecewise-linear fitting: $(\tau_u, \varepsilon^*) = (0,0)$; (44,200 psi, 0.00442); (49,200 psi, 0.075); and (76,400 psi, 0.615).

3. It is assumed that strain-rate effects can be approximated by an equation of the form of Eq. 2.1, as follows[+]:

$$(\tau_u)_k = (\overset{s}{\tau}_u)_k \left(1 + \left|\frac{\dot{\varepsilon}^*}{d}\right|^{\frac{1}{p}}\right) \qquad (6.2)$$

where

$(\overset{s}{\tau}_u)_k$ = static yield stress of the kth elastic, perfectly-plastic mechanical sublayer (superscript s and subscript k)

$(\tau_u)_k$ = rate-dependent yield stress of the kth elastic, perfectly-plastic mechanical sublayer (subscript k)

$\dot{\varepsilon}^* = \frac{d\varepsilon^*}{dt} = \frac{\dot{\ell}}{\ell}$ = longitudinal component of the rate-of-deformation tensor (also called D_u in Eq. B.10 of App. B)

For illustrative purposes, the material strain-rate constants d and p for aluminum cited in Ref. 25 are used: d=6500 sec^{-1} and p=4.

4. Thickness changes are accommodated approximately.

5. The change in length of the reference axis because of finite membrane strains is included in the expression for the changes-of-curvature in the Lagrangian strain-displacement equation.

[+] Equation 6.2 is similar to Eq. 47 of Ref. 47 which dealt with multiaxial conditions.

To illustrate the effects of these modifications upon the predicted transient 2-d responses of simple structures, calculations were carried out for two severely-loaded beams [16]: (a) explosively-impulsed beam CB-4 and (b) steel-sphere-impacted beam specimen CB-18.

6.2 Explosively-Impulsed Beam CB-4

Specimen CB-4 was an initially-flat 6061-T651 aluminum beam of 0.102-in thickness, 1.497-in width, and 8.005-in span with both ends ideally clamped, and subjected to uniform impulse loading over its entire width and for a 1.8-in spanwise region centered at midspan; experimental data for this test specimen are given in Ref. 16. For this case, the impulse loading produced essentially a uniform initial lateral velocity of 10,590 in/sec over the impulsively-loaded portion of the beam. For analysis, the half span of specimen CB-4 was modeled by using 20 equal-length 4 DOF/node finite elements, and symmetry conditions were imposed at midspan. Four spanwise Gaussian stations and four depthwise Gaussian stations were used for the volume numerical integration of the finite-element equations. A consistent mass (CM) matrix was employed for each finite element. A time increment size Δt of 0.25 microseconds was used (equal to $1.6/\omega_{max}$, where ω_{max} is the maximum frequency of the discrete numerical model). The aluminum material was treated as behaving in an EL-SH-SR fashion, with material rate constants d=6,500 sec^{-1} and p=4. The mass per unit initial volume ρ_o was taken as 0.25384×10^{-3} $(lb\text{-}sec^2)/in^4$. Response predictions for specimen CB-4 were carried out for the above modeling and conditions for: (a) the new mechanical sublayer fitting procedure of τ_u vs. ε^* (Subsection 6.1, item 2) and strain-displacement relation Type F of Appendix B and (b) the former scheme (employing stress (τ_k) vs. strain (γ_{11}) Fit A of Subsection 2.2 and strain-displacement relation Type C of Appendix B and Ref. 20).

Indicated in the following tabulation are the comparisons of these two predictions with each other (and/or versus experimental data) as shown in the indicated figures for the time histories of the longitudinal Green strain tensor component* γ_{11} on the upper (non-loaded) and/or the lower (impulsively-loaded) surface at various spanwise stations of beam specimen CB-4:

---

*On these figures γ_{11} is used to denote the longitudinal component of this strain since this is the notation used in corresponding earlier figures in this report. However, this would be γ_2^2 in the more systematic notation of Appendix B.

Figure	Station |x| (in)	Time Histories of* γ_{11} on Surface Upper (U) and/or Lower (L) Predicted	Measured
65a	0.0 (Midspan)	U and L	--
65b	1.4	U and L	U
65c	2.2	U	U
65d	3.0	U	U

With the exception of the midspan station (x=0), all other stations coincide with finite-element nodes, and the associated strain value plotted is the average value given by the two elements at the nodal-junction location.

It is seen that, of the spanwise stations shown, the major differences between the two procedures occur at the midspan station x=0 in, where the finite-strain formulation shows that between 150 μsec and 500 μsec the lower (loaded) surface experiences larger strains than the upper surface while the former "small-strain" formulation indicates the opposite behavior. Also, at this midspan station, the strains predicted by the finite-strain procedure are considerably larger than the strains predicted by the small-strain procedure. At the other stations, where smaller strains occur, the differences between the two predictions are correspondingly smaller.

Shown in Fig. 65e is the spanwise strain distribution at t=300 μsec from x=0 in (midspan) to x=4.00 in (clamped end), of the upper (non-loaded) surface. This time instant is taken as typical, since the strains have already achieved their peak and about 97% of the initial kinetic energy has been transformed into strain energy by that time. The strains predicted by the finite-strain formulation are larger than those predicted by the small-strain formulation with the exception of a region at the end of the impulsively-loaded zone (x=0.9 in) and a region at the middle of the half-span (x=2.0 in to x=2.4 in). The nodal strain discontinuities typical of the 4 DOF/node finite element (employed in the JET 3 and CIVM-JET 4B programs) are evident from the graph. This assumed-displacement finite-element model involves cubic polynomials in the assumed-displacement field for v (the axial displacement) and w (the lateral displacement). The degrees-of-freedom (DOF) involved

*See the footnote on the preceding page.

at each end of the finite-element are the displacements v and w and the "displacement gradients" $\chi = \frac{\partial v}{\partial \eta} + \frac{w}{R}$ and $\psi = \frac{\partial w}{\partial \eta} - \frac{v}{R}$. These degrees-of-freedom provide continuity of displacement (v and w) and continuity of membrane strain ($\gamma_2^{o2} = \chi + 1/2\ \chi^2 + 1/2\ \psi^2$) but the bending strain ($\zeta\kappa = \zeta[(-\frac{\partial \psi}{\partial \eta})(1+\chi) + \psi \frac{\partial \chi}{\partial \eta}]$) is not continuous at the nodes since $\frac{\partial \psi}{\partial \eta}$ and $\frac{\partial \chi}{\partial \eta}$ are not degrees-of-freedom. Hence, strain jumps appear at each finite-element node since inside each element the displacement function is continuous to derivatives of all orders but at the nodes only continuity of displacement and its first derivative is preserved.* The strain-displacement equations (Appendices A and B) involve the displacement gradients $\chi = \frac{\partial v}{\partial \eta} + \frac{w}{R}$ and $\psi = \frac{\partial w}{\partial \eta} - \frac{v}{R}$ and their derivatives $\frac{\partial \psi}{\partial \eta}$ and $\frac{\partial \chi}{\partial \eta}$. The degree of the polynomial involved in the displacement gradients χ and ψ is of the second order (or quadratic) for an initially-straight beam. The degree of the polynomial involved in the representation of the first derivatives of the displacement gradients $\frac{\partial \psi}{\partial \eta} = \frac{\partial^2 w}{\partial \eta^2} - \frac{\partial}{\partial \eta}(\frac{v}{R})$ and $\frac{\partial \chi}{\partial \eta} = \frac{\partial^2 v}{\partial \eta^2} + \frac{\partial}{\partial \eta}(\frac{w}{R})$ is of the first order or linear, for an initially-straight beam (using the 4 DOF/node cubic-cubic element). From Fig. 65e it is observed that the degree of the polynomials involved in the spanwise strain distribution is (mainly) either quadratic or linear.

It is also observed that the largest discontinuities occur at locations where bending strains are largest: at the end of the impulsively-loaded zone (x=0.9 in) and at the immediate zone adjacent to the clamped end (x=3.8 in to x=4.0 in). At the clamped zone, a very large strain discontinuity is evident. The reason for this is that this region involves high levels of nonlinearity. The strain discontinuity at the clamped zone is significantly larger with the finite-strain formulation, which involves a more nonlinear representation of the behavior than the "small-strain" formulation. It is evident that a finer mesh of finite elements is needed in this clamped-zone region to represent accurately this nonlinear behavior. However, time and fund restrictions have prevented a more thorough study of this matter at this time.

*See Ref. 20 for an evaluation of a formulation which includes element-junction continuity of bending strain for the small-strain approximation.

Finally, the predicted transient midspan transverse displacement w is shown in Fig. 66. It is seen that the finite-strain formulation and small-strain formulation predictions are in fairly good agreement with each other.

The computing time required for the two formulations for explosively-impulsed beam CB-4 is displayed conveniently in the following tabulation (for 4000 time steps with a time step size of 0.25 microseconds; all runs were conducted on an IBM 370/168 computer):

Formulation	No. of FE	No. of Gaussian Sta. per Elem.		Total No. of Unknown DOF
		Spanwise	Depth	
Small Strain	20	4	4	79
Finite Strain	20	4	4	79

Formulation	Strain-Displ. Relation Type	Mass Matrix	No. of Cycles	CPU Time (min)	CPU(min) / (DOF)(Cycles)
Small Strain	C	CM	4000	8.63	27.3×10^{-6}
Finite Strain	F	CM	4000	11.07	35.0×10^{-6}

The effects on CPU time of the more lengthy expressions used and manipulations required for the finite-strain calculations are evident from an inspection of the last column.

6.3 Steel-Sphere-Impacted Beam CB-18

Steel-sphere-impacted 6061-T651 aluminum beam specimen CB-18, the geometry and impact conditions for which have been described in Subsection 2.1, has been analyzed only for EL-SH material behavior by (a) the (new) finite strain procedure (employing the stress (τ_k) vs. strain (ε^*) mechanical-sublayer fit of Subsection 6.1, item 2; and strain displacement relation Type F of Appendix B) and (b) the former scheme (employing stress (τ_k) vs. strain (γ_{11}) Fit B of Subsection 2.4 and strain-displacement relation Type B of Appendix B). The beam was modeled with 43 equal-length 4 DOF/node elements; locally perfectly-elastic impact (e=1) was assumed. Three spanwise Gaussian stations and four depthwise Gaussian stations were used for the volume numerical integration of the finite-element equations. A diagonalized (lumped) mass (DM) matrix for each element was employed. A time increment size Δt of

0.5 microseconds was used (equal to $1.16/\omega_{max}$, where ω_{max} is the maximum frequency of the discrete numerical model). Summarized in the following tabulation are the comparisons of the two predictions with each other (and/or versus experimental data) shown in the indicated figures for the time histories of the longitudinal component of the Green ("Lagrangian") strain tensor γ_{11} on the upper (non-impacted) and/or the lower (impacted) surface at various spanwise stations of beam specimen CB-18:

Figure	Station $\|x\|$ (in)	Time Histories of γ_{11} on Surface U (Upper and/or L (Lower) Predicted	Measured
67a,b	0.0	U and L	--
67c,d	0.3	U and L	--
67e	0.6	U	U
67f	1.2	U	U
67g,h	1.5	U and L	U and L
67i,j	3.0	U and L	--
67k,ℓ	3.7	U and L	--
67m,n	4.0	U and L	--

Location x=0 in (at the midspan of the beam) coincides with the midspan Gaussian integration station of a finite element. Location $x = \pm 4.0$ in is at the clamped end of the beam and coincides with a finite element node, at which clamped-end conditions have been imposed (namely that the displacements v and w and the lateral-displacement gradient ψ are zero). All other stations occur at locations intermediate between the end and the midspan of a finite element, and do not coincide with spanwise Gaussian integration points. Also, measured permanent strains are indicated on these figures where available.

These figures show that the strains γ_{11} predicted (a) by the current "finite-strain procedure" and (b) by the former "small-strain procedure" agree reasonably well with each other and/or with experiment at all of these stations except x=0, 3.7, and 4.0 in. Large strains do occur at both x=0 and x=4.0 in; also, the occurrence of large strains at x=4.0-in exerts a distinct and pronounced effect at "nearby station" x=3.7 in (located in the element adjacent to the finite element at which the clamped end condition

has been imposed). Although the calculations have been carried out for only 900 microseconds, it appears that the current "finite strain procedure" would provide better permanent strain comparisons with measurements at all spanwise stations (if carried out long enough in time) than by the former "small-strain procedure".

Figure 68 shows that the time histories of the midspan lateral deflection w from these two predictions for beam CB-18 are very close to each other. Finally, the time histories of the support reactions M_y, S_z, and F_x at station x=4.0 in are shown in Figs. 69a, 69b, and 69c, respectively, for these two predictions. The agreement between these two predictions is very good for the longitudinal support reaction force F_x (associated with the membrane strains), but one observes some differences in the transverse support reaction (shear) force S_z and large differences for the support reaction bending moment M_y. These differences are believed to be caused by the fact that the expressions of CIVM-JET 4B for the bending part of the strain are valid only for small rotations and small strains, while the finite strain version of the program does not have this restriction. Of course, the support reaction bending moment M_y is most influenced by the bending part of the strain-displacement relations.

The computing time required to analyze steel-sphere-impacted beam CB-18 by the two procedures, under otherwise-identical conditions, is conveniently displayed in the following tabulation (for a time step of 0.50 microseconds; all runs were conducted on an IBM 270/168 computer):

Formulation	No. of FE	No. of Gaussian Sta. per Elem.		Total No. of Unknown DOF
		Spanwise	Depth	
Small Strain	43	3	4	170
Finite Strain	43	3	4	170

Formulation	Strain-Displ. Relation Type	Mass Matrix	No. of Cycles	CPU Time (min)	CPU(min) / (DOF)(Cycles)
Small Strain	B	DM	2250	5.11	13.4×10^{-6}
Finite Strain	F	DM	1850	6.81	21.7×10^{-6}

Here again, the finite-strain-formulation calculations require more CPU time per (DOF)(cycle) than for the small-strain formulation. The smaller CPU time per (DOF) (cycle) noted here for steel-sphere impacted beam CB-18 compared with explosively-impulsed beam CB-4 arises from the use in the latter of the more-heavily populated consistent mass matrices vs. diagonalized mass matrices for the CB-18 calculations, and the use of 3 rather than 4 spanwise Gaussian stations for the CB-18 calculations.

It appears that (a) the use of the proper (second Piola-Kirchhoff) stress tensor in the constitutive equations by making proper transformations of certain stress and strain measures, (b) the use of τ_k vs. ε^* for representing the monotonic strain-hardening antisymmetric (in tension and compression) mechanical behavior of the material by the mechanical sublayer model, and (c) the use of a finite-strain strain-displacement equation, and (d) the inclusion of thickness changes can provide significantly improved predictions of transient strains (the most important and sensitive quantities).

SECTION 7

SUMMARY, CONCLUSIONS, AND COMMENTS

7.1 Summary

The type of response exhibited by a given protective structure to engine rotor fragment impact attack depends, among other things, upon the lateral (axial) dimension of that structure compared with the corresponding dimension(s) of the attacking fragment(s). If these dimensions are comparable, the structural response of the protective structure is essentially the same at all of its axial stations at a given circumferential location; accordingly, this structural response is termed "two-dimensional" (2-D). However, if the axial length of the protective structure is substantially greater than the corresponding dimension of the attacking fragment, the structure exhibits a three-dimensional (3-D) type of structural response. The present report is devoted to considering only the former (2-D) category of structural response problems. In particular, the present report describes studies performed to assess the applicability, feasibility, and utility of employing a 2-D structural response computer code (a) for predicting the transient large-deflection elastic-plastic structural responses of 2-D ductile metal protective structures to fragment impact and (b) for carrying out variation-of-parameters studies to assess the consequent impact-induced structural responses of such fragment-impacted structures. These studies involved the use mainly of the CIVM-JET 4B computer program which permits analyzing the 2-D structural responses of single-layer curved Bernoulli-Euler beams and/or rings which are subjected to impact attack by one or more idealized non-deformable fragments. Some calculations were also carried out with the CIVM-JET 5B program which has features and capabilities similar to the former code except that it can represent Bernoulli-Euler 2-D beam/ring structures that consist of (a) a single layer or (b) several layers of different materials which are hard bonded at each interface. CIVM-JET 4B employs the central-difference timewise operator while CIVM-JET 5B uses the Houbolt timewise finite-difference operator. The spatial description of the structures in both codes is accomplished by the use of finite elements. In general, one seeks to employ the smallest number of finite elements, which will result in converged or accurate transient response predictions.

A study to select appropriate finite element (spatial) modeling was carried out for an aluminum beam which had both ends clamped and was subjected to explosive-impulse loading over its entire width and over a short-spanwise region centered at midspan; this represents a well-posed initial value problem and does not involve the added complexities present when fragment impact against the structure occurs. Transient response and permanent deformation measurements were available for comparison with predictions.

Following this study, an assessment was made of the adequacy of the CIVM-JET 4B analysis and code for predicting the response of a beam with both ends clamped and subjected to perpendicular impact at midspan by a (non-deformable) solid steel sphere. Experimental transient response and permanent deformation data were available for comparison with predictions. This problem was modeled as involving a 2-D structure subjected to 2-D fragment impact attack; the assumed 2-D type of structural response behavior appeared to have been present at nearly all spanwise stations of the beam except near the midspan impact regions (and very close to the clamped ends) where significant 3-d behavior was present. Included in this modeling investigation was a study of the effects of (a) various number of equal-length finite elements to represent the beam, (b) including or ignoring strain rate effects on the stress-strain behavior of the beam material, (c) the use of alternate choices for the impact-affected length of the beam measured from the impact station, (d) various diameters for the idealized fragment, and (e) various selections to represent the diagonalized mass matrices for the beam finite elements.

Next, the CIVM-JET 4B program was used to predict the response of a 4130 cast steel containment ring which was subjected to T58 turbine rotor tri-hub burst impact attack in NAPTC Test 201. For analysis, each bladed-disk fragment was modeled as a non-deformable circular body of selected radius r_f; the effects of using various plausible and extreme values for r_f were investigated. The non-deformable idealized fragment model can not represent properly the behavior of each bladed-disk fragment since the blades deform severely during the impact/interaction and response of the containment ring and the disk. Hence, the predicted and observed transient response details must be different. However, if one selects a reasonable and plausible

value for the idealized fragment radius r_f, one can reasonably expect that the predicted peak response should compare favorably with that measured; this was the principal aim of this particular study. Examined also was the effect upon the predicted responses of the containment ring and the fragments of friction between each fragment and the containment ring.

Dimensional analysis considerations to identify pertinent dimensionless parameters were employed in examining experimental data obtained (a) by the NAPTC on engine rotor-burst impact tests on steel containment rings and (b) by the MIT-ASRL on aluminum beams subjected to steel-sphere impact attack. The use of the CIVM-JET 4B computer code for carrying out parametric structural response studies has been illustrated for both fragment-containment structure and fragment-deflector structure.

Finally, since the CIVM-JET 4B computer code as actually implemented accommodates large-deflection elastic-plastic transient structural responses but only small strain, some modifications to the analysis/computation procedure have been developed to alleviate this restriction. Some preliminary results from this study were obtained and are included.

7.2 Conclusions

Within the context of employing the present type of computer code(s) to represent: (a) 2-D Bernoulli-Euler large-deflection, elastic-plastic transient structural responses such that the maximum strains are not large (i.e., less than roughly 8-10 per cent) and (b) the fragment (assumed to produce the impact-induced structural response) idealized as a non-deformable circular 2-D fragment, the following observations are made from the present study and from related similar MIT-ASRL studies [4,5,15,17,18,20]:*

1. For the analysis of single-layer** structures subjected to fragment impact, the CIVM-JET 4B code is more efficient that CIVM-JET 5B. Since CIVM-JET 4B uses the explicit conditionally-stable timewise central-difference operator together with the very compact and efficient unconventional form of the equations of motion whereas

---

* The listed conclusions are based upon the present study unless indicated otherwise.

** However, for the analysis of hard-bonded multi-layer Bernoulli-Euler structures, only one of these two codes (CIVM-JET 5B) is applicable.

CIVM-JET 5B uses the unconditionally-stable (for linear systems) timewise Houbolt finite-difference operator together with the less-compact conventional form of the equations of motion, it was speculated that the latter combination might be more efficient mainly because (hopefully) of a larger allowable time step size Δt than for the former. This has turned out not to be true because the Δt is found to be limited by the "momentum-transfer and correction procedure" employed to account for momentum transfer from the fragment to the target structure at each of a succession of impacts.

All further comments pertain to the application of only the CIVM-JET 4B computer code.

2. To insure numerical stability, the time increment size Δt for solution of typical nonlinear transient response problems should be selected such that $\Delta t \lesssim 0.8(2/\omega_{max})$ where ω_{max} is the highest natural frequency of the mathematical model of the system for small-displacement linear-elastic behavior [17]. No numerical instabilities have been encountered when this guide has been followed; however, either local or global numerical instabilities have been observed for $\Delta t \gtrsim 0.88(2/\omega_{max})$.

3. At each of a succession of impacts of the non-deformable fragment against the 2-D target structure, impulse-momentum relations are employed to predict the velocity decrement suffered by the attacking fragment and the associated velocity increment acquired by an impact-affected region of the target structure. Alternate schemes have been used to estimate the size of this impact-affected region. Since physically the size (or spanwise length) of that impact-affected region must be independent of both the time increment size Δt used in the calculation and the size (length) of the finite elements used to model the structure, elementary stress-wave-propagation arguments have been used to estimate the distance L_{eff} from the impact station to each end of the impact-affected region to be approximately twice the thickness h of the structure. Accordingly,

in regions of expected impact, the finite element lengths should not exceed 2h; smaller finite-element length values should be used, if needed, for other non-impact considerations such as solution convergence.

4. To be consistent with certain assumptions employed in the approximate procedure for predicting the velocity increment received by the impact-affected region of the structure from a given impact, a diagonalized mass matrix of the finite-element model of the structure is employed. Various means of achieving the diagonalized mass matrix were explored. The main effect of these alternate choices was to affect ω_{max} which, in turn, influences the selection of the size of Δt required for numerically stable calculations (see Subsection 2.5.2).

5. The inclusion of plausible values for the coefficient for friction μ between the target structure and the idealized fragment reveals very little effect upon the transient response of the impacted structure but can affect significantly the rotational motion of the idealized fragment [15, 18, and the present report].

6. Conclusion 5 implies in part that the response of a fragment-impacted structure is only slightly affected by friction and/or by the rotational motion (or rotational kinetic energy of the attacking fragment) but that the structural response is dominantly affected by the translational velocity (or translational kinetic energy) of the attacking fragment. This observation is consistent with the findings in this study.

7. From the present series of calculations of the transient responses of fragment-impacted 2-D structures, it is noted that the peak structural response is affected: (a) only slightly if one ignores strain-rate sensitivity effects for relatively rate-insensitive materials such as 6061-T651 (or T6) aluminum* but (b) very significantly for rate-sensitive materials such as mild steel. Hence, it

*However, for aluminum beams and/or rings subjected to severe impulsive loading, strain rate effects are found to have a very significant effect upon the predicted responses of these structures. In these cases a larger volumetric proportion of the structure experienced higher strain rates and for a longer period of time than in the present fragment-impacted structures.

is important to determine whether or not the mechanical behavior of the material under consideration exhibits significant rate sensitivity and, if so, to include that description quantitatively. Further, uniaxial material stress-strain measurements (or data) are required from material coupons whose lengthwise axis is aligned with the main direction of tensile or compression stress expected in the 2-D fragment container or deflector structure -- since mechanical anisotropy present could lead to the inadvertent use of improper mechanical data in the analysis with attendant misleading results.

8. The presently-available experimental data on the responses of both beam and ring structures subjected to fragment impact are inadequate to represent both (a) 2-D structural response and (b) 2-D fragment impact attack -- up to the threshold rupture condition of the impacted structure; conditions short of this rupture state are widely-agreed to be inadequate for containment assessment purposes. Since suitable techniques are now available for conducting such tests and making the essential measurements, experiments to remedy this data deficiency are recommended.

9. The fact that the present computer codes [4,5] as actually implemented can accommodate large-deflection, elastic-plastic transient 2-D structural responses but only small strain means that although large numerical values of transient strain can be and are predicted from these programs, those predicted large strain values (i.e., greater than about 8-10 per cent or even less) can not be correct. Steps are described in Section 6 to remedy this deficiency and preliminary results show that significant differences in transient strain predictions in certain portions of the structure are revealed by this more comprehensive treatment. However, the predicted transient deflections (displacements) are almost unaffected by those improvements.

10. The present calculations and comparisons with NAPTC experimental measurements of a steel containment ring subjected to T58 turbine rotor tri-hub burst attack in NAPTC Test 201 indicates that the use

of an idealized non-deformable fragment of plausibly-selected size (as an approximation for each of the deformable bladed-disk fragments) for use in the CIVM-JET 4B program can provide predicted peak and permanent ring deflection configurations in reasonably close agreement with experimental observations. The current CIVM-JET 4B predictions of large (or finite) transient and permanent strain for this case can not be correct but the breadboard CIVM-JET 4C program now available should remedy this deficiency. However, the available measurements of transient and permanent strain for this case are inadequate to permit a definitive assessment of the accuracy of either of these predictions.

Finally, the following two additional observations are offered:

11. In the present model of fragment/structure impact and interaction, impulse-momentum relations are used to estimate the momentum transfer. Hence, the velocity increment imparted to the "impact-affected portion" of the structure for each of a succession of impacts depends upon the ratio of the mass of the fragment to that of the impact-affected region of the structure. Hence, in seeking to define scaled conditions to preserve the peak structural-response strain which is induced by fragment impact, one must preserve certain energy absorption and "incremental momentum-transfer" parameters as noted in Subsection 4.3.2.5.

12. An examination of NAPTC experimental data in which spinning rotors were caused to rupture into n equal-size bladed-disk fragments (n=2,3,4, or 6) and subsequently to impact against containment rings, shows clearly why the bi-hub (2 fragment) attack at a given burst rpm produces more severe ring response than observed for 3-, 4-, and 6-fragment attacks -- even though a 3-fragment burst results in fragments with the greatest amount of translational kinetic energy and hence were often viewed as posing the most severe threat to a containment ring. For n=3 and greater, the deforming blades "cushion" the impact, and peak ring response is reached while only

the "smooth contour" of the fragment is in contact with the ring; all of these transiently and permanently deformed unfailed rings exhibit a smooth contour. However, for the 2-fragment case, a sharp corner of each of these 2 fragments attacks the ring and causes extremely severe and localized bending (and perhaps some shearing) of the ring -- resulting in local failure at significantly smaller attack kinetic energy levels than for the n>2 cases.

7.3 Comments

Included here are indications of some analysis development needs, recommendations for experiments to remedy important deficiencies in experimental data on severe fragment-impact-induced structural response, and some related observations.

Analysis Needs

Within the framework of 2-D structural response of containment or deflector structure subjected to 2-D non-deformable fragment impact attack, the type of nonlinear transient response analysis and computer code discussed herein which includes large-deflection, elastic-plastic behavior but only small strains (as actually implemented in the computer code) should be extended to include finite strain effects; the preliminary work to this end as discussed in Section 6 and Appendix B should be carried forward to completion, including comparisons with appropriate well-defined experimental structural response data for a range of maximum responses extended to and including material rupture.

Although under the conditions representative of engine rotor fragment impact, the type of ductile metal containment structure rupture observed has been, in almost all cases, noted as being "tensile rupture" without clear evidence of significant transverse shearing effects, it may be useful to extend the theoretical prediction method to include transverse shear deformation effects so as not to preclude the proper treatment of this behavior where and when it occurs. This inclusion, however, will tend to make the predictions more complex and expensive.

The necessity of taking into account the fact that fragments such as rotor blades, bladed-disk segments, or bladed-rim segments often deform severely during impact attack against containment or deflector structure is a matter which has been weighed and debated considerably. One school of though holds that taking into account transient fragment deformation would involve a great amount of extra computation and book-keeping because, it is argued, one can predict the peak containment-structure response with adequate accuracy (in view of the various uncertainties present in many other aspects of the impact/response problem) by representing each attacking deformable fragment as a simple non-deformable fragment of plausibly-selected size, mass, as well as pre-impact translational and rotational velocity -- although there is clear recognition that the time history details between the actual response and that predicted by the idealized model are certain to be different. Another school, while conceding the plausibility and the analysis feasibility and efficiency of the above-described viewpoint, argues that fragment deformation and possible subsequent multiple fragmentation will alleviate and distribute the impact-induced loads on the structure such that the actual response of the containment structure will be less severe than one would predict by the above-indicated idealized rigid-fragment analysis. However, no proposals for deformable-fragment models to represent specific categories or conditions of importance for containment-structure design are offered, but sometimes there are implied wishes and suggestions that engine rotor failure presents no real safety problem and should be ignored. Although aircraft losses and fatalities caused by or stemming from engine rotor fragments have been small to date, the annual rate of uncontained engine rotor fragments in commercial avaiation has persisted at about one per million engine hours since about 1962 as reported by Mangano et al. [37], McCarthy [42], and Gunstone [55].

It should be noted that both deformable-fragment and rigid-fragment analyses have been carried out successfully for impact-attack by a single blade of a T58 turbine rotor against an aluminum containment structure [15,17]; the amount of computing required and the type of impact/interaction analysis used for these two cases are very different. Thus, either approach can be employed if required. Thus, if a persuasive case can be made for including deforming-fragment behavior in the analysis of aircraft engine rotor fragment impact attack against containment or deflector structure, this can be done -- but with an attendant addition in computational complexity and cost.

It should be noted that methods and computer programs for predicting the large-deflection elastic-plastic structural responses of ductile metal panels which undergo 3-D structural response when subjected to appropriate transient loading or fragment impact attack are being developed [10]. However, as actually implemented these computer codes accommodate properly only small strain. Hence, it is recommended that this work be extended to finite strains in a fashion analogous to that indicated in Section 6 and Appendix B.

Although there are significant unfinished aspects of the transient large deformation response analysis of single-layer ductile metal protective structures subjected to fragment impact (and these should be pursued vigorously and resolved), it would be both timely and useful to initiate the development of methods to predict the severe transient responses of multilayer, multimaterial 2-D structures under fragment impact attack, including conditions which produce sequential failure of the various structural layers. These materials, in general, will be anisotropic, and each layer can have substantially different mechanical properties and failure behavior from its neighbors. Both despite and because of the complexity of this type of structure, the development of appropriate analysis methods should be pursued without delay; in parallel with and closely coordinated with that effort should be an experimental impact-induced response program for well-defined experimental conditions and careful detailed measurements.

Experimental Needs

To provide appropriate and definitive data for the efficient evaluation of the adequacy and accuracy of proposed methods for predicting the impact-induced responses (including threshold rupture) of ductile-metal protective structures, the following experiments are recommended:

(a) To generate well-defined 2-D structural response data, 6061-T651 aluminum beams like those of Ref. 16 should be subjected to midspan perpendicular 2-D impact by a solid steel cylindrical body. Transient strains should be measured on each surface at various spanwise stations. For a suitable region centered at midspan and for regions close to each clamped end of the beam, a pattern of

mechanically-lightly-scirbed closely-spaced grids should be provided to permit the determination of the values and distribution of the permanent strain since these are regions where significant strains are expected.

(b) To generate well-defined 3-D structural response data for efficient theoretical-experimental correlation evaluation of the adequacy of the proposed finite-strain extension of the analysis of Ref. 10, 6061-T651 aluminum beams like those of Ref. 16 should be subjected to midspan perpendicular 3-D impact by a solid steel sphere. Measurements similar to those described under (a) should be made; of special importance are the proposed permanent strain determinations from the mechanically-scribed grids.

This currently unavailable experimental information is essential for a meaningful evaluation of the adequacy and accuracy of the cited predictions methods to predict structural responses up to and including material rupture.

More comprehensive experimental data than are now available on containment ring response to engine rotor fragment impact would be valuable both in its own right and for checking the adequacy of prediction methods such as CIVM-JET 4B or alternate approaches. In particular, it is recommended that 4130 cast steel containment rings much like that in NAPTC Test 201 be subjected to T58 turbine rotor tri-hub burst impact attack such that the peak impact-induced response will be (a) much closer to ring rupture than in NAPTC Test 201 and (b) slightly exceed the threshold ring rupture condition. This could be achieved at the nominal rotor-burst kinetic energy level of NAPTC Test 201 by using somewhat thinner containment rings. The recommended measurements include:

(a) Transient strain at a number of circumferential locations on the ring's outer-surface midlength location, and at the midsurface on both end faces at several circumferential locations.

(b) Finely-spaced lightly-scribed closely-spaced lines on the entire outer circumference of the ring should be provided, and both their pre-test and post-test spacings measured to permit determining the permanent outer-surface strain.

(c) High-speed photographs should be made to observe the transient motions of the fragments and of the ring; photographic quality similar to that achieved in NAPTC Test 67 should be sought.

This would provide representative and detailed data on containment-ring response to complex deformable bladed-disk fragment impact attack.

For each of these types of experiments, uniaxial static tensile stress-strain tests to rupture should be carried out on containment-structure coupons whose axial orientation of each is (1) parallel to the spanwise or circumferential direction, (2) perpendicular to orientation (1), and (3) at an intermediate orientation angle; these measurements should reveal whether or not the material is isotropic. Such tests* should be carried out at (a) the slowest and (b) the fastest feasible constant cross-head speed; these speeds should be recorded. Lightly-scribed mechanical grids should be provided on each specimen to permit determining the distribution and value of the permanent outer-surface strain on each specimen. Measurements should also be made to permit determining the pre-test and post-test cross-sectional areas of each specimen along its axial test-region length.

General

Although improvements in the capabilities of the CIVM-JET 4B computer code are needed and are planned, it is believed that the CIVM-JET 4B computer code can be of significant assistance to industry for many parametric and preliminary design purposes in rotor burst protection studies and in the design of fragment-containment and/or fragment-deflector structures.

It is suggested that an effective procedure for the designing of fragment containment or fragment deflector structure to a given type of engine rotor fragment attack would be to conduct a few well-instrumented full-scale tests. With these preliminary data as guidance, computer codes such as CIVM-JET 4B, for example, could be used to carry out parametric and tradeoff studies. Of course, all other relevant empirical and semi-empirical information should also be applied in developing a proposed protective-structure

*This recommended set of mechanical property tests represents the absolute minimum of such tests. In addition, tests should be carried out to determine the strain-rate-dependent behavior of the materials under both uniaxial and multiaxial stress conditions, including the entire strain range to rupture and strain rates up to at least 3,000 sec^{-1} -- to permit constructing an adequate stress, strain, strain-rate description for each material.

design. Then several carefully-selected full-scale proof tests should be conducted to demonstrate the adequacy of the final design and to confirm that important effects had not been overlooked. Such a procedure should be much more time and cost effective than a largely experimental approach.

REFERENCES

1. McCallum, R.B., Leech, J.W. and Witmer, E.A., "Progress in the Analysis of Jet Engine Burst-Rotor Containment Devices", ASRL TR 154-1, Aeroelastic and Structures Research Laboratory, Massachusetts Institute of Technology, August 1969. (Available as NASA CR-107900.)

2. McCallum, R.B., "Simplified Analysis of Trifragment Rotor Disk Interaction with a Containment Ring", AIAA Journal of Aircraft, Vol. 7, No. 3, May-June 1970, pp. 283-285.

3. Wu, R.W.-H. and Witmer, E.A., "Computer Program - JET 3 - Calculate the Large Elastic-Plastic Dynamically-Induced Deformations of Free and Restrained, Partial and/or Complete Structural Rings", ASRL TR 154-7, Aeroelastic and Structures Research Laboratory, Massachusetts Institute of Technology, August 1972. (Available as NASA CR-120993.)

4. Stagliano, T.R., Spilker, R.L. and Witmer, E.A., "User's Guide to Computer Program CIVM-JET 4B to Calculate Large Nonlinear Transient Deformations of Single-Layer Partial and/or Complete Structural Rings to Engine Rotor Fragment Impact", MIT ASRL TR 154-9, March 1976. (Available as NASA CR-134907.)

5. Wu, R.W.-H., Stagliano, T.R., Witmer, E.A. and Spilker, R.L., "User's Guide to Computer Programs JET 5A and CIVM-JET 5B to Calculate the Large Elastic-Plastic Dynamically-Induced Deformations of Multilayer Partial and/or Complete Structural Rings", MIT ASRL TR 154-10, February 1977.

6. Witmer, E.A., Stagliano, T.R., Spilker, R.L., and Rodal, J.J.A., "Analysis of Simple 2-D and 3-D Metal Structures Subjected to Fragment Impact", Workshop Proceedings on An Assessment of Technology for Turbojet Engine Rotor Bursts, NASA CP-2017, August 1977, pp. 151-216.

7. Wu, R.W.-H. and Witmer, E.A., "Finite Element Predictions of Transient Elastic-Plastic Large Deflections of Stiffened and/or Unstiffened Rings and Cylindrical Shells", AMMRC CTR 74-31 (also MIT ASRL TR 171-4), April 1974.

8. Pirotin, S.D., Berg, B.A. and Witmer, E.A., "PETROS 3.5: New Developments and Program Manual for the Finite-Difference Calculation of Large Elastic-Plastic Transient Deformations of Multilayer Variable-Thickness Shells", BRL CR 211 (MIT ASRL TR 152-4), February 1975.

9. Santiago, J.M., Wisniewski, H.L. and Huffington, N.J., Jr., "A User's Manual for the REPSIL Code", BRL Report No. 1744, October 1974 (AD A003176).

10. Spilker, R.L., Witmer, E.A. and French, S.E., "Finite Element Nonlinear Transient Response Analysis of Panels Subjected to Impulse or Impact Loads", MIT ASRL TR 154-14 (in preparation).

11. Private Communication from A. Martino, U.S. Naval Air Propulsion Test Center, Phila, Pa., 1970.

12. Mangano, G.J., "Rotor Burst Protection Program -- Phases VI and VII: Exploratory Experimentation to Provide Data for the Design of Rotor Burst Fragment Containment Rings", NAPTC-AED-1968, March 1972. (Available as NASA CR-120962).

13. --- "Rotor Burst Protection Program". (Study for NASA Lewis Research Center on NASA DPR-105 and NASA Interagency Agreement C-41581-B), U.S. Naval Air Propulsion Test Center, Aeronautical Engine Dept., Progress Reports Sept. 1969 - Jan. 1977.

14. Private communications from G.J. Mangano, R. DeLucia, and J. Salvino, U.S. Naval Air Propulsion Test Center, Trenton, New Jersey 1975-1976.

15. Zirin, R.M. and Witmer, E.A., "Examination of the Collision Force Method for Analyzing the Responses of Simple Containment/Deflection Structures to Impact by One Engine Rotor Blade Fragment", ASRL TR 154-6, Aeroelastic and Structures Research Laboratory, Massachusetts Institute of Technology, May 1972. (Available as NASA CR-120952.)

16. Witmer, E.A., Merlis, P. and Spilker, R.L., "Experimental Transient and Permanent Deformation Studies of Steel-Sphere-Impacted or Impulsively-Loaded Aluminum Beams with Clamped Ends", MIT ASRL TR 154-11, October 1975. (Available as NASA CR-134922.)

17. Wu, R.W.-H. and Witmer, E.A., "Finite-Element Analysis of Large Transient Elastic-Plastic Deformations of Simple Structures, with Application to the Engine Rotor Fragment Containment/Deflection Problem", ASRL TR 154-4, Aeroelastic and Structures Research Laboratory, Massachusetts Institute of Technology, January 1972. (Available as NASA CR-120886.)

18. Collins, T.P. and Witmer, E.A., "Application of the Collision-Imparted Velocity Method for Analyzing the Responses of Containment and Deflector Structures to Engine Rotor Fragment Impact", MIT ASRL TR 154-8, August 1973. (Available as NASA CR-134494.)

19. Witmer, E.A., Wu, Richard W-H. and Merlis, F., "Experimental Transient and Permanent Deformation Studies of Impulsively-Loaded Rings and Cylindrical Panels, both Stiffened and Unstiffened", ASRL TR 171-3, Aeroelastic and Structures Research Laboratory, Massachusetts Institute of Technology, April 1974. (Available as AMMRC CTR 74-29.)

20. Rodal, J.J.A. and Witmer, E.A., "Finite Element Nonlinear Transient Response Analysis of Simple 2-D Structures Subjected to Impulse or Impact Loads", MIT-ASRL TR 182-1 (also MIT-EL-76-004), June 1976.

21. Witmer, E.A., Merlis, F., Rodal, J.J.A. and Stagliano, T.R., "Experimental Transient and Permanent Deformation Studies of Steel-Sphere-Impacted or Explosively-Impulsed Aluminum Panels", MIT ASRL TR 154-12, March 1977 (Available as NASA CR-135315).

22. Kolsky, H., Stress Waves in Solids. Dover Publications, Inc., New York, 1963.

23. Goldsmith, W. Impact: The Theory and Physical Behavior of Colliding Solids. Edward Arnold (Publishers) Ltd., London 1960.

24. Cowper, G.R. and Symonds, P.S., "Strain-Hardening and Strain-Rate Effects in the Impact Loading of Cantilever Beams", Tech. Report No. 28, ONR Contract Nonr-562(10), NR-064-406, Div. of Appl. Math., Brown University, Sept. 1957.

25. Ting, T.C.T. "The Plastic Deformation of a Cantilever Beam with Strain Rate Sensitivity under Impulsive Loading". Brown University TR 70, Contract Nonr-562(10), July 1961.

26. Isbell, W.M., Christman, D.R., Babcock, S.G., Michaels, T.E., and Green, S.G., "Measurements of Dynamic Properties of Materials, Vol. I: Summary of Results", General Motors Materials and Structures Laboratory, DASA-2501-1 (MSL-70-23, Vol. 1), July 1970.

27. Holt, D.L., Babcock, S.G., Green, S.J., and Maiden, C.J., "The Strain Rate Dependence of the Flow Stress in Some Aluminum Alloys", Transactions of the ASM, Vol. 60, No. 2, June 1967, pp. 152-159.

28. Eleiche, A-S.M., "A Literature Survey of the Combined Effects of Strain Rate and Elevated Temperature on the Mechanical Properties of Metals", AFML-TR-72-125, Sept. 1972.

29. Hoggatt, C.R. and Recht, R.F., "Stress-Strain Data Obtained at High Strain Rates Using an Expanding Ring", Experimental Mechanics, Vol. 9, No. 10, Oct. 1969, pp. 441-448.

30. McClellan, D.L., "Constitutive Equations for Mechanical Properties of Structural Materials", AIAA Journal, Vol. 5, No. 3, March 1967, pp. 446-450.

31. Rinehart, J.S. and Pearson, J. Behavior of Metals Under Impulsive Loads. American Society for Metals, Cleveland, Ohio, 1954.

32. Lush, A.M. and Witmer, E.A. "Studies of Impact-Induced Responses of a Generic Crushable-Rigid Rodlike Missile Against Rigid and Deformable Targets", MIT ASRL TR 190-1, September 1977.

33. Key, S.W. and Beissinger, Z.E., "The Transient Dynamic Analysis of Thin Shells by the Finite Element Method", Proceedings of the Third Conference on Matrix Methods in Structural Mechanics, AFFDL-TR-71-160, Dec. 1973, pp. 479-518.

34. Krieg, R.D. and Key, S.W., "Transient Shell Response by Numerical Time Integration", Advances in Computational Methods in Structural Mechanics and Design, UAH Press, University of Alabama in Huntsville, 1972, pp. 237-258.

35. Clough, R.W., and Wilson, E.L., "Dynamic Finite Element Analysis of Arbitrary Thin Shells", Conference on Computer Oriented Analysis of Shell Structures, Lockheed Missile Division and A.F.F.D.L. at Palo Alto, California, August 1971.

36. Hinton, E., Rock, T., and Zienkiewicz, O.C., "A Note on Mass Lumping and Related Processes in the Finite Element Method", Earthquake Engineering and Structural Dynamics, Vol. 4, 1976, pp. 245-249.

37. Mangano, G.J., Salvino, J.T., and DeLucia, R.A., "Rotor Burst Protection Program — Experimentation to Provide Guidelines for the Design of Turbine Rotor Burst Fragment Containment Rings", Proceeding of the Workshop on an Assessment of Technology for Turbojet Engine Rotor Failures, NASA CP-2017, 1977, pp. 107-149.

38. Langhaar, H., Dimensional Analysis and Theory of Models, John Wiley and Sons, New York, 1951.

39. Leech, J.W., Witmer, E.A. and Yeghiayan, R.P., "Dimensional Analysis Considerations in the Engine Rotor Fragment Containment/Deflection Problem", MIT ASRL TR 154-3, Dec. 1971. (Available as NASA CR-120841.)

40. Martino, A. and Mangano, G.J., "Rotor Burst Protection Program Initial Test Results", Phase IV Final Report on Problem Assignment NASA DPR R-105, Naval Air Propulsion Test Center, NAPTC-AED 1869, 1968.

41. Clarke, R.B., "Rotor Disk Burst Characteristics Data Analysis", Boeing Commercial Airplane Co., Report No. S&A 73-1, February 28, 1973.

42. McCarthy, D., "Types of Rotor Failure and Characteristics of Fragments", NASA CP-2017, 1977, pp. 65-92.

43. Hagg, A.C. and Sankey, G.O., "The Containment of Disk Burst Fragments by Cylindrical Shells", Journal of Engineering for Power, Trans. of ASME, April 1974, pp. 114-123.

44. Recht, R.F. and Ipson, T.W., "Ballistic Perforation Dynamics", Journal of Applied Mechanics, Trans. of ASME, Sept. 1963, Vol. 30, pp. 384-389.

45. Lethaby, J.W. and Skidmore, I.C., Mechanical Properties at High Rates of Strain, Inst. of Physics London and Bristol, Inst. of Physics Conference Ser. N21, 1974, p. 429.

46. Hill, R., "The Mathematical Theory of Plasticity", Oxford, 1950.

47. Key, S.W., Biffle, J.H. and Krieg, R.D., "A Study of the Computational and Theoretical Differences of Two Finite Strain Elastic-Plastic Constitutive Models", U.S.-Germany Symposium on Finite Element Analysis at the Massachusetts Institute of Technology, Cambridge, Mass., August 9-13, 1976.

48. Malvern, L.E., Introduction to the Mechanics of a Continuous Medium, Prentice-Hall, Inc., Englewood Cliffs, N.J., 1969.

49. Dahlquist, G. and Björck, A., (translated by Ned Anderson), Numerical Methods, Prentice-Hall, Inc., Englewood Cliffs, N.J., 1974.

50. Leech, J.W., "Stability of Finite-Difference Equations for the Transient Response of a Flat Plate", AIAA Journal, Vol. 3, No. 9, Sept. 1965, pp. 1772-1773.

51. Leech, J.W., Hsu, P.T. and Mack, E.W., "Stability of a Finite-Difference Method for Solving Matrix Equations", AIAA Journal, Vol. 3, No. 11, Nov. 1965, pp. 2172-2173.

52. Houbolt, J.C., "A Recurrence Matrix Solution for the Dynamic Response of Elastic Aircraft", Journal of the Aeronautical Sciences, Vol. 17, 1950, pp. 540-550.

53. Park, K.C., "An Improved Stiffly Stable Method for the Direct Integration of Nonlinear Structural Dynamic Equations", Journal of Applied Mechanics, ASME, June 1975, pp. 464-470.

54. Rodal, J.J.A. and Witmer, E.A., "Finite-Strain Large-Deflection Elastic-Plastic Finite-Element Transient Response Analysis of Structures", MIT ASRL TR 154-15, July 1979.

55. Gunstone, G.L., "Engine Non-Containment: the UK-CAA View", NASA CP-2017, 1977, pp. 11-32.

TABLE 1

COMPARISONS OF RESPONSE PREDICTIONS FOR VARIOUS MASS MATRIX MODELINGS OF IMPULSIVELY-LOADED CLAMPED-ENDED BEAM CB-4 AT 100 MICROSECONDS AFTER APPLICATION OF THE INITIAL VELOCITY

Mass Matrix Modeling	Consistent Mass	Diagonal Method 2	Diagonal Method 3
Midspan Displacement w (in)	0.7099	0.7141	0.7114
Max. Gaussian Sta. Upper-Surface Strain (per cent)	10.04	10.12	10.07
Max. Upper-Surface Nodal Sta. Avg. Strain (per cent)	10.39	10.49	10.39
Kinetic Energy (in-lb)	809.1	813.2	812.5
Elastic Energy (in-lb)	30.5	29.3	31.0
Plastic Work (in-lb)	1118.9	1161.4	1162.0
Initial Kinetic Energy (in-lb)	1958.5	2003.9	2005.5

TABLE 2

DATA CHARACTERIZING NAPTC TEST 201 FOR T58 TURBINE ROTOR TRI-HUB BURST AGAINST A STEEL CONTAINMENT RING

Containment Ring Data

Inside Diameter (in)	15.00
Radial Thickness (in)	0.625
Axial Length (in)	1.50
Material	4130 cast steel
Elastic Modulus (psi) 4130 Cast Steel	29×10^6

Fragment Data*

Type T58 Tri-Hub Bladed Disk Fragments
Material Disk: A-286 Blades: SEL-15

Outer Radius (in)	7.00
Fragment Centroid from Rotor Axis (in)	2.797
Fragment Pre-Test Tip Clearance from Ring (in)	0.50
Fragment CG to Blade Tip Distance (in)	4.203
Fragment Weight Each (lbs)	3.627
Fragment Mass Moment of Inertia about its CG (in lb sec^2)	0.0666
Rotor Burst Speed (rpm)	19,859
Fragment Tip Velocity (ips)	14,557.2
Fragment CG Velocity (ips)	5816.7
Fragment Initial Angular Velocity (rad/sec)	2079.6
Fragment Translational KE (in-lb)	
Each Fragment	158,922
Total for Three Fragments	476,766
Fragment Rotational KE (in lb)	
Each Fragment	144,018
Total for Three Fragments	432,054

*Applies to each fragment unless specified otherwise.

TABLE 3

MODELING AND SELECTED PREDICTIONS FOR A 60-DEGREE CIRCULAR ARCH WITH BOTH ENDS PINNED-FIXED AND SUBJECTED TO A SHORT-DURATION CONSTANT CONCENTRATED OUTWARD LOAD APPLIED AT MIDSPAN

Number of Equal Length Elements	Max. Nat. Frequency of Model ω_{max} (rad/sec)	$\frac{2}{\omega_{max}}$ (μsec)	$0.8(\frac{2}{\omega_{max}})$ (μsec)	$(\Delta t)_{used}$ (μsec)	Predictions at t = 150 μsec	
					Midspan Displ. w (in)	Total Work Input to Arch (in-lb)
6	0.977×10^6	2.05	1.64	1.0	0.389	2720
10	1.63×10^6	1.23	0.983	0.9	0.412	2883
14	2.28×10^6	0.877	0.702	0.7	0.415	2906
18	2.93×10^6	0.683	0.546	0.5	0.418	2924
22	3.58×10^6	0.559	0.447	0.4	0.420	2938
30	4.88×10^6	0.410	0.328	0.3	0.418	2926

TABLE 4

SUMMARY OF CIVM-JET 4B CALCULATIONS MADE TO ANALYZE 4130 STEEL CONTAINMENT RING RESPONSE TO T58 TURBINE ROTOR TRI-HUB BURST ATTACK IN NAPTC TEST 201

Calculation[a] Identif. No.	r_f(in)	μ	Simultaneous Impact
THR-1	2.555	0	Yes
THR-2	3.360	0	Yes
THR-3	4.203	0	Yes
THR-4	2.555	0.3	Yes
THR-5	2.555	0	No[b]

a: In all cases: (a) 48 equal-length cubic cubic elements with 4 DOF/Node were used and (b) the steel ring material behavior was modeled as EL-SH-SR.

b: Fragment 1 was released first and 60 microseconds later, fragments 2 and 3 were released; unsymmetric response subsequently occurred.

TABLE 5

DATA CHARACTERIZING THE PRE-IMPACT FRAGMENTS IN THE NAPTC T58 TURBINE ROTOR BURST TESTS AGAINST 4130 STEEL CONTAINMENT RINGS

Quantity	Number of Equal-Size Fragments, n		
	2	3	6
Mass of Fragment m_f, $(lb\text{-}sec^2)/in$	1.43×10^{-2}	9.22×10^{-3}	4.66×10^{-3}
Mass Moment of Inertia about Fragment CG, I_f $(in\text{-}lb\text{-}sec^2)$	.120	.0666	.0164
Distance from Axis of Rotation of Rotor to Fragment CG, r_{CG} (in)	2.266	2.797	3.05
Distance from Fragment CG to Blade Tip, ℓ_f (in)	4.734	4.203	3.95
Nominal Pre-Impact Translational Kinetic Energy per Fragment+ $(KE)_{f_{ot}}$, (in-lb)	161,050	158,200	95,079
Nominal Pre-Impact Rotational Kinetic Energy per Fragment+ $(KE)_{f_{or}}$, (in-lb)	262,216	115,125	35,921
Nominal Translational Velocity+			
Fragment CG, V_f (in/sec)	4,746	5,858	6,388
Blade Tip (in/sec)	14,661	14,661	14,661

+Nominal Failure Speed

ω_f = 20,000 rpm = 2094 rad/sec

TABLE 6

SUMMARY OF CONTAINMENT RING TESTS, CONDITIONS, AND MATERIAL PROPERTIES FOR THE NAPTC T58 TURBINE ROTOR BURST CONTAINMENT TESTS[+]

Ring Width Conditions Studied		
Axial Width w_c (in)	Test Identification	
	Number of Fragments	NAPTC Test Number
0.5	2	135,137
1.0	2	129,131,133,142
0.5	3	168,169,172,177,178,189,207
1.0	3	126,127,128,130,132,138,139,141,188
1.5	3	192,193,195,196,197,199,201,202
2.0	3	170,173,174,176
1.0	6	134,136,140

Identification of Containment Ring Material Supplier		
Supplier	Test Identification	
	Number of Fragments	NAPTC Test Number
National Forge (NF)	2	129,131,133,135,137,142
	3	126,127,128,129,130,132,138,139,141,168 169,170,172,173,174,176,177,178
NF	6	134,136,140
ACIPCO	3	188,189,192,193,195,196,197,199 201,202,207

Nominal Mechanical Properties of 4130 Cast Steel Containment Ring Material[+]						
Supplier	σ_o (ksi)	σ_{u_o} (ksi)	ε_{m_o} (in/in)	E (psi)	ρ lb/in^3	ν
NF	80	111	0.08	30×10^6	.283	0.3
ACIPCO	83	121	0.15	30×10^6	.282	0.3

[+]Ref. 37 -- subscript "o" refers to static properties.

TABLE 7

DATA CHARACTERIZING THE PRE-IMPACT FRAGMENTS IN THE NAPTC_J65_ TURBINE ROTOR BURST TESTS AGAINST 4130 STEEL CONTAINMENT RINGS

Quantity	Number of Equal-Size Fragments, n		
	2	3	6
Mass of Fragment m_f $(lb\text{-}sec^2)/in^4$	.146	.0960	.0471
Mass Moment of Inertia about Fragment CG, I_f $(in\text{-}lb\text{-}sec^2)$	7.92	3.63	0.891
Distance from Axis of Rotation of Rotor to Fragment CG, r_{CG} (in)	5.405	6.843	8.155
Distance from Fragment CG to Blade Tip, ℓ_f (in)	9.915	8.478	7.165
Nominal Pre-Impact Translational Kinetic Energy per Fragment $(KE)_{f_{ot}}$, (in-lb)	1,689,640	1,780,810	1,240,920
Nominal Pre-Impact Rotational Kinetic Energy per Fragment $(KE)_{f_{or}}$, (in-lb)	3,139,150	1,438,390	352,910
Nominal Translational Velocity+			
Fragment CG, V_f (in/sec)	4811	6091	7259
Blade Tip (in/sec)	13,637	13,637	13,637

+Nominal Failure Speed

ω_f = 8500 rpm = 890 rad/sec

TABLE 8

SUMMARY OF CONTAINMENT RING TESTS, CONDITIONS, AND MATERIAL PROPERTIES FOR THE NAPTC J65 TURBINE ROTOR BURST CONTAINMENT TESTS

Ring Width Conditions Studied		
	Test Identification	
Axial Width w_c (in)	Number of Fragments	NAPTC Test Number
1.25	2	167,175,180,181,182,203
2.50	2	204,209
1.25	3	211
1.25	6	205,210,214

Nominal Mechanical Properties of 4130 Cast Steel Containment Ring Material[+]						
Supplier	σ_o (ksi)	σ_{u_o} (ksi)	ε_{m_o} (in/in)	E (psi)	ρ lb/in^3	ν
ACIPCO	60	100	0.08	30×10^6	.283	0.3

[+]Ref. 37 -- subscript "o" refers to static properties.

TABLE 9

SUMMARY OF TESTS, CONDITIONS, AND MATERIAL PROPERTIES FOR THE MIT-ASRL SPHERE-BEAM IMPACT-TESTS[+]

Test Identification and Impact Conditions			
Beam[a] and Test No.	Fragment Data[b]		Remarks
	Impact Vel. (in/sec)	Initial Kinetic Energy $(KE)_{fo}$, (in-lb)	
CB-9	1896	686	Small Perm. Deflection
CB-13	2490	1183	Moderate Perm. Deflection
CB-18	2794	1489	Large Perm. Deflection
CB-16	2868	1569	Just Beyond Threshold Rupture
CB-14	3075	1804	Well Beyond Threshold Rupture

a: Nominal Beam Dimensions are h=0.10 in, w_c=1.50 in and ℓ=8.00 in; both ends are ideally clamped.

b: Fragment is a 1-inch diameter steel sphere of nominal mass 0.3815×10^{-3} $(lb\text{-}sec^2)/in$; midspan impact.

Nominal Mechanical Properties of 6061-T651 Aluminum Beam Material					
σ_o (ksi)	σ_{u_o} (ksi)	ε_{m_o} (in/in)	E (psi)	ρ lb/in^3	ν
42	45	0.20	10×10^6	0.098	0.3

[+]Ref. 16 -- subscript "o" refers to static properties.

TABLE 10

SUMMARY OF DIMENSIONLESS PARAMETERS TO CHARACTERIZE EXPERIMENTS OR 2-D NUMERICAL SIMULATIONS OF A BEAM TARGET STRUCTURE SUBJECTED TO RIGID-FRAGMENT (STEEL-SPHERE) IMPACT

Non.-Dim. Parameter	Sphere-Beam Impact Experiments		2-D Simulation of Sphere-Beam Impact				
	Quantity	Use	Quantity	Case A[a1]	Case B[b1]	Case C[c1]	Case D[d1]
β_1	ε_{mc}	Fixed	ε_{mc}	Fixed	Fixed	Fixed	Fixed
β_2	ν_c	"	ν_c	"	"	"	"
β_3	p_c	"	p_c	Deleted	Deleted	Deleted	Deleted
β_4	μ	"	μ	Fixed	Fixed	Fixed	Fixed
β_5	e	"	e	"	"	"	"
β_6	ρ_c/ρ_f	"	ρ_c/ρ_f	Vary(a2)	"	"	"
β_7	E_c/σ_{c_o}	"	E_c/σ_{c_o}	Fixed	"	"	"
β_8	n=1	"	n=1	"	"	"	"
β_9	$(n\ell)/d$	"	$(1\ell)/d$	Vary	"	"	"
β_{10}	h/d	"	h/d	"	Vary(b2)	Vary(c2)	"
β_{11}	w_c/d	"	w_c/w_f	Fixed(a2)	Fixed	Fixed	Vary(d2)
β_{12}	h/ℓ	"	h/ℓ	Fixed	Vary(b2)	Vary(c2)	Fixed
β_{13}	h/w_c	"	h/w_c	"	Vary(b2)	Vary(c2)	Vary(d2)
β_{14}	d/d	N.A.	w_f/d	Vary(a2)	Fixed	Fixed	Fixed

TABLE 10 (Concluded)

Non.-Dim Parameter	Sphere-Beam Impact Experiments		2-D Simulation of Sphere-Beam Impact				
	Quantity	Use	Quantity	Case A[a1]	Case B[b1]	Case C[c1]	Case D[d1]
β_{15}	$(vt)/h$	Vary	$(vt)/h$	Fixed(a3)	Vary(b2)	Vary(c2)	Fixed(d3)
β_{16}	$v/(hD_c)$	Vary } Net of One	$v/(hD_c)$	Deleted	Deleted	Deleted	Deleted
β_{17}	$(\sigma_{cu}\ \varepsilon_{cm})/(\rho_f\ v^2)$	Vary } Net of One	$(\sigma_{cu}\ \varepsilon_{cm})/(\rho_f\ v^2)$	Fixed	Fixed	Fixed	Fixed
β_{18}	z/h or ε_{max}	Result	ε_{max}	Result	Result	Result	Result

a1, b1, c1, d1: See pages 88 and 89 for descriptions of these cases.

a2: Varying the diameter d of the fragment while keeping the mass and pre-impact velocity fixed implies changing ρ_c/ρ_f and w_f/d.

a3: This parameter may be viewed as "fixed" if time history information is of no concern but only peak response is of interest irrespective of when it occurs.

b2: These quantities may vary since $w_c h$ is preserved while w_c and h vary.

c2: These quantities vary because of changes in h; width w_c and span ℓ remain fixed.

d2: These quantities vary because of changes in w_c; thickness h and span ℓ remain fixed.

d3: Comment a3 applies.

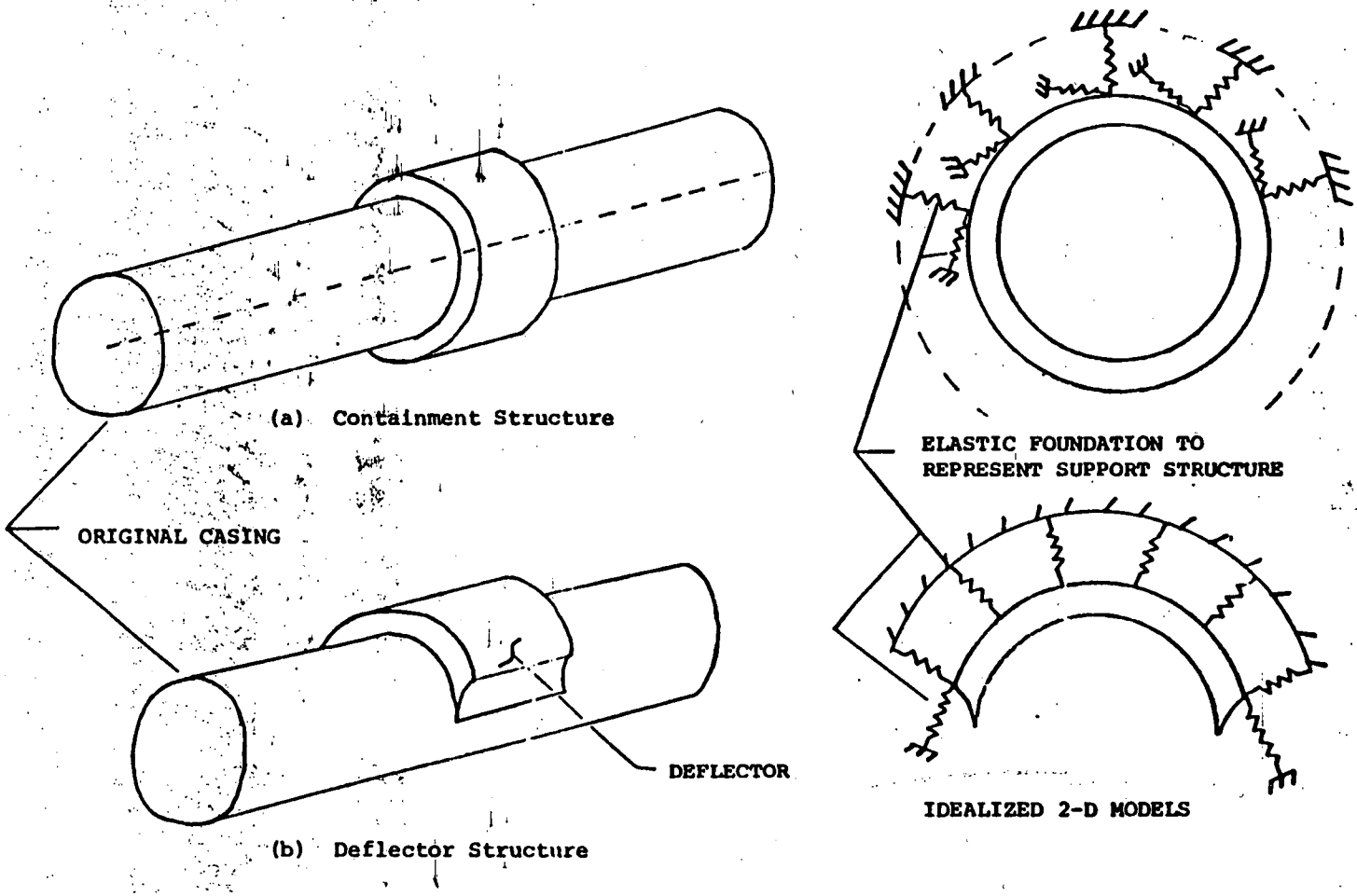

FIG. 1 SCHEMATICS OF CONTAINMENT AND DEFLECTOR STRUCTURES, AND ASSOCIATED IDEALIZED 2-D STRUCTURAL MODELS

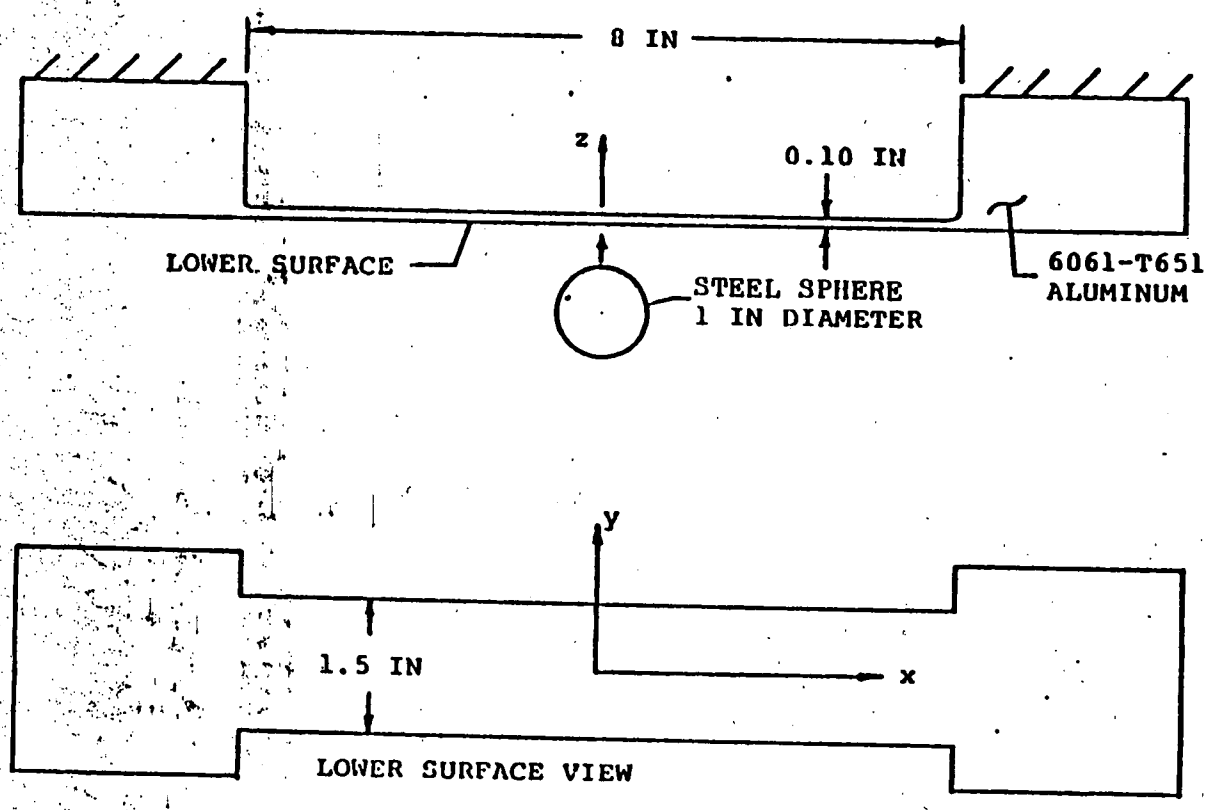

FIG. 2 SCHEMATIC OF A 6061-T651 BEAM MODEL SUBJECTED TO IMPACT BY A ONE-INCH DIAMETER SOLID STEEL SPHERE

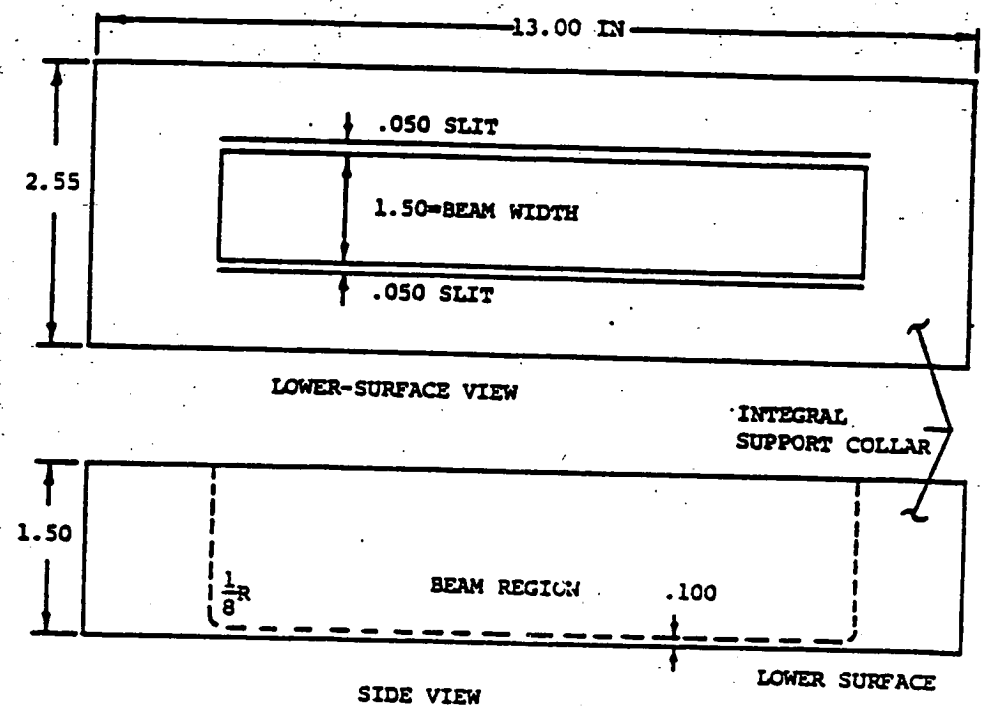

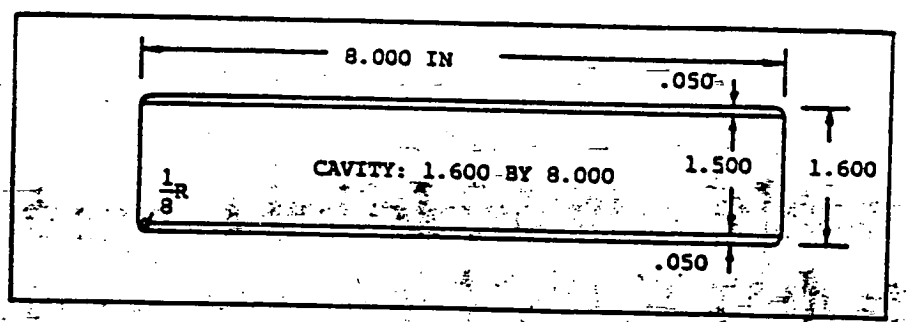

FIG. 3 NOMINAL DIMENSIONS FOR THE 6061-T651 ALUMINUM CLAMPED-BEAM MODELS

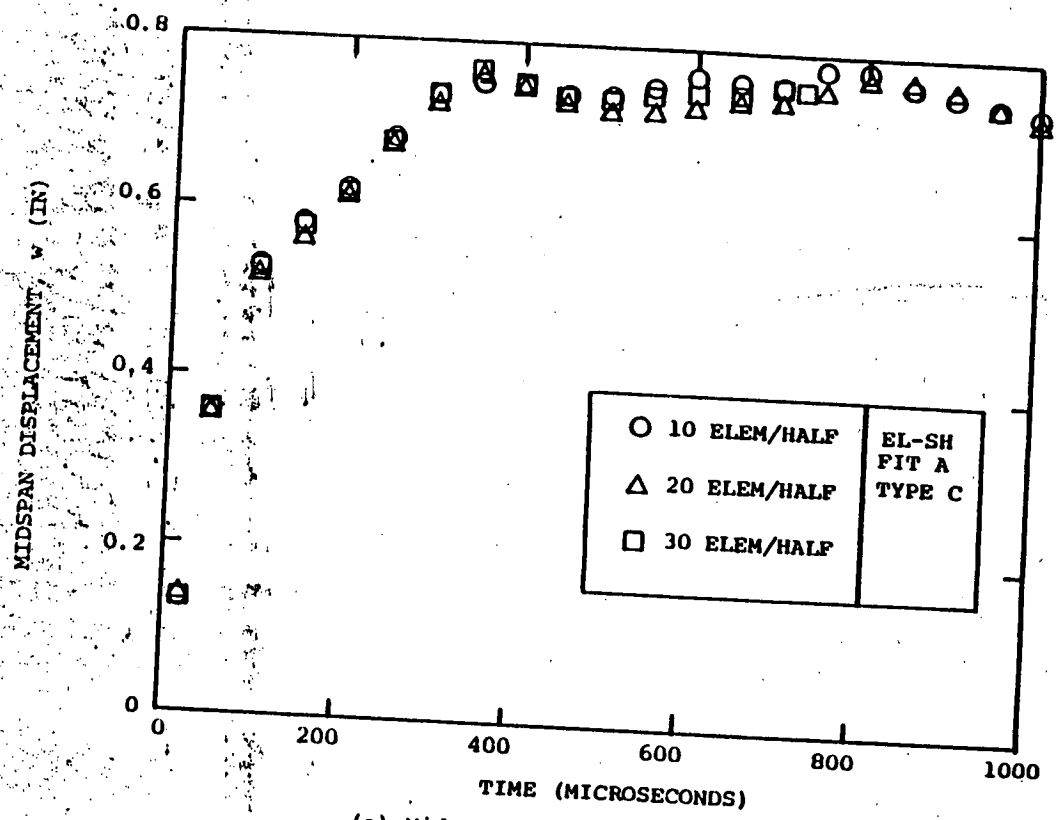

(a) Midspan Displacement w

FIG. 4 INFLUENCE ON THE PREDICTED BEAM RESPONSE OF THE NUMBER OF FINITE ELEMENTS USED TO MODEL THE HALF-SPAN OF IMPULSIVELY-LOADED 6061-T651 ALUMINUM BEAM CB-1 (4 DOF/N, EL-SH)

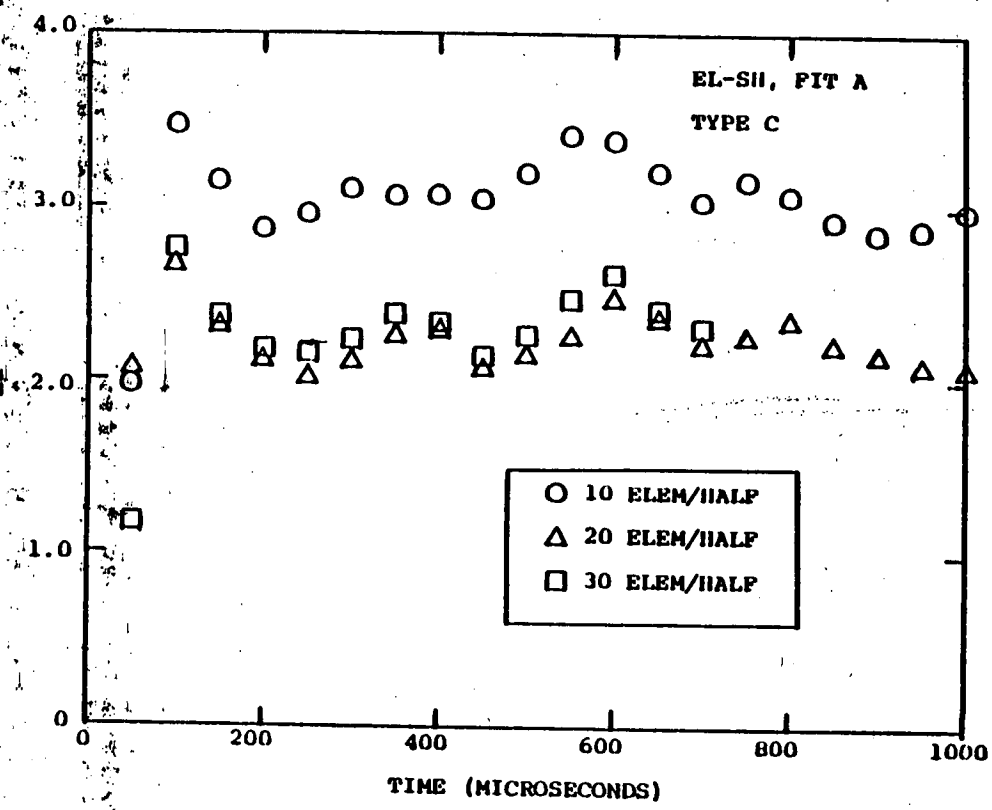

(b) Upper-Surface Strain at x=0.4 in

FIG. 4 CONTINUED (4 DOF/N, EL-SH)

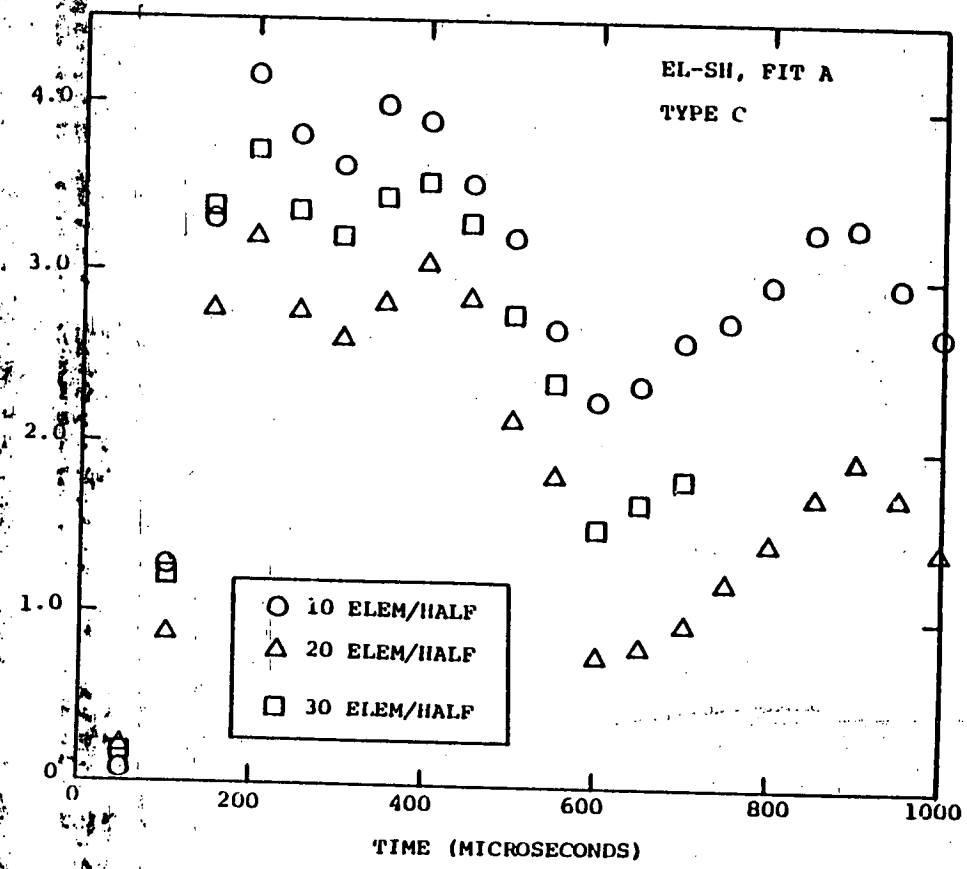

(c) Upper-Surface Strain at x=1.60 in

FIG. 4 CONTINUED (4 DOF/N, EL-SII)

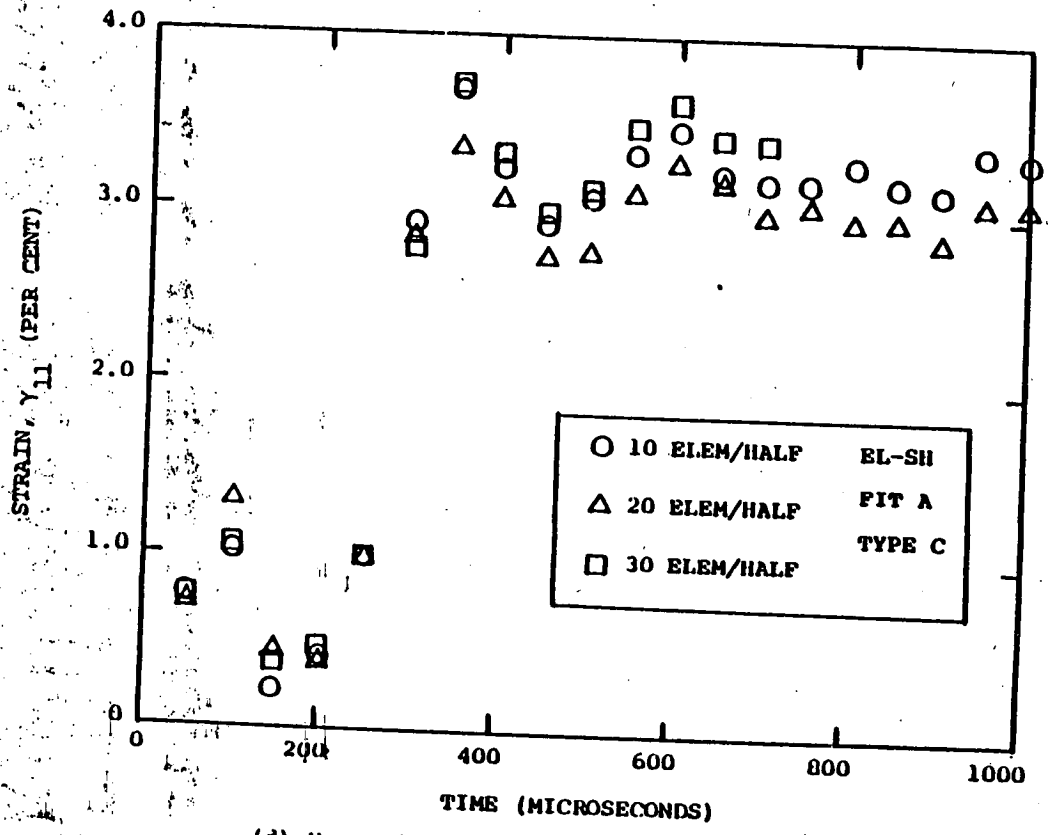

(d) Upper-Surface Strain at x=3.00 in

FIG. 4 CONCLUDED (4 DOF/N, EL-SH)

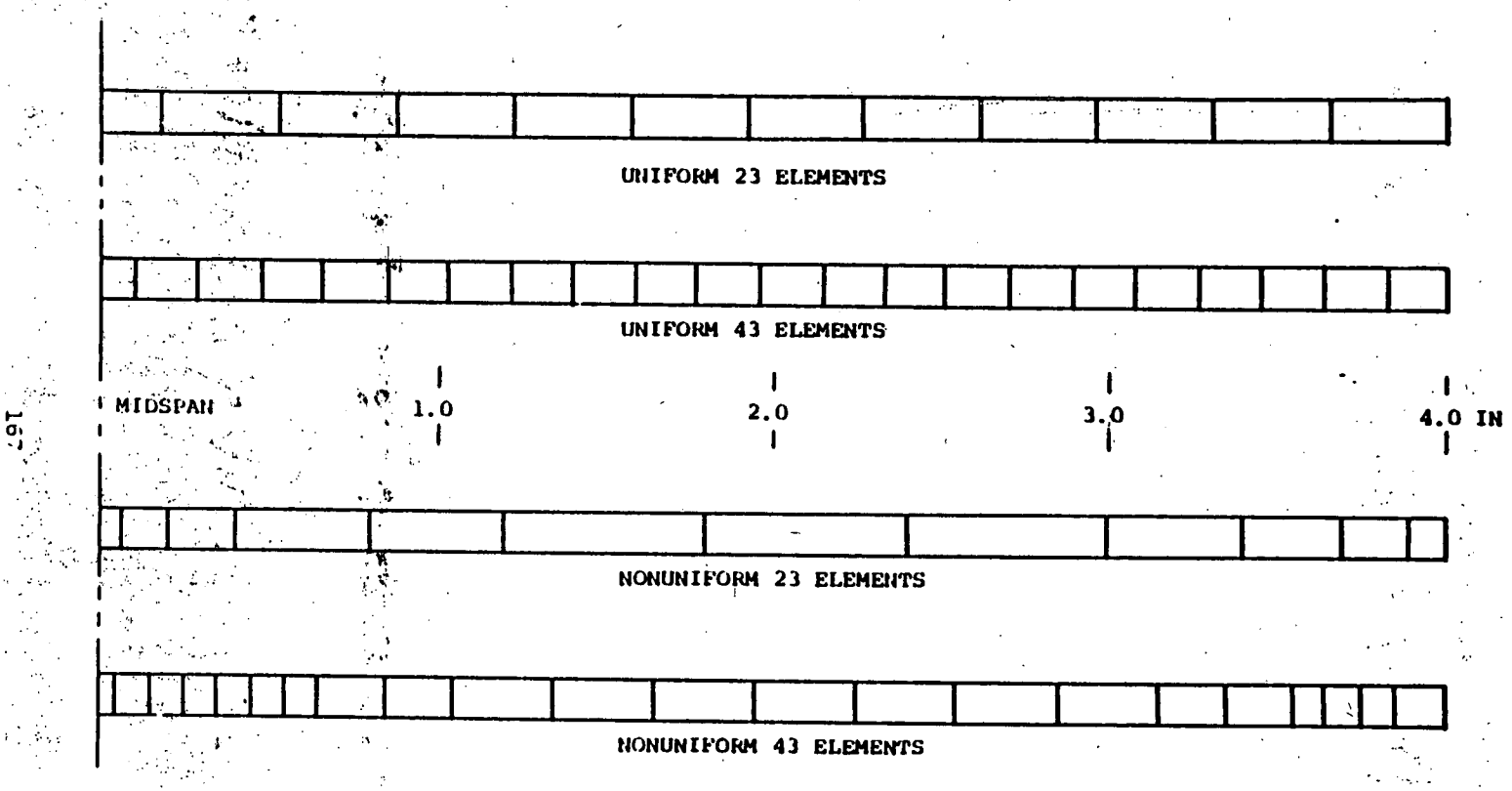

FIG. 5 UNIFORM AND NONUNIFORM FINITE ELEMENT MESHES EXPLORED FOR THE ANALYSIS OF BEAM RESPONSE TO STEEL-SPHERE IMPACT

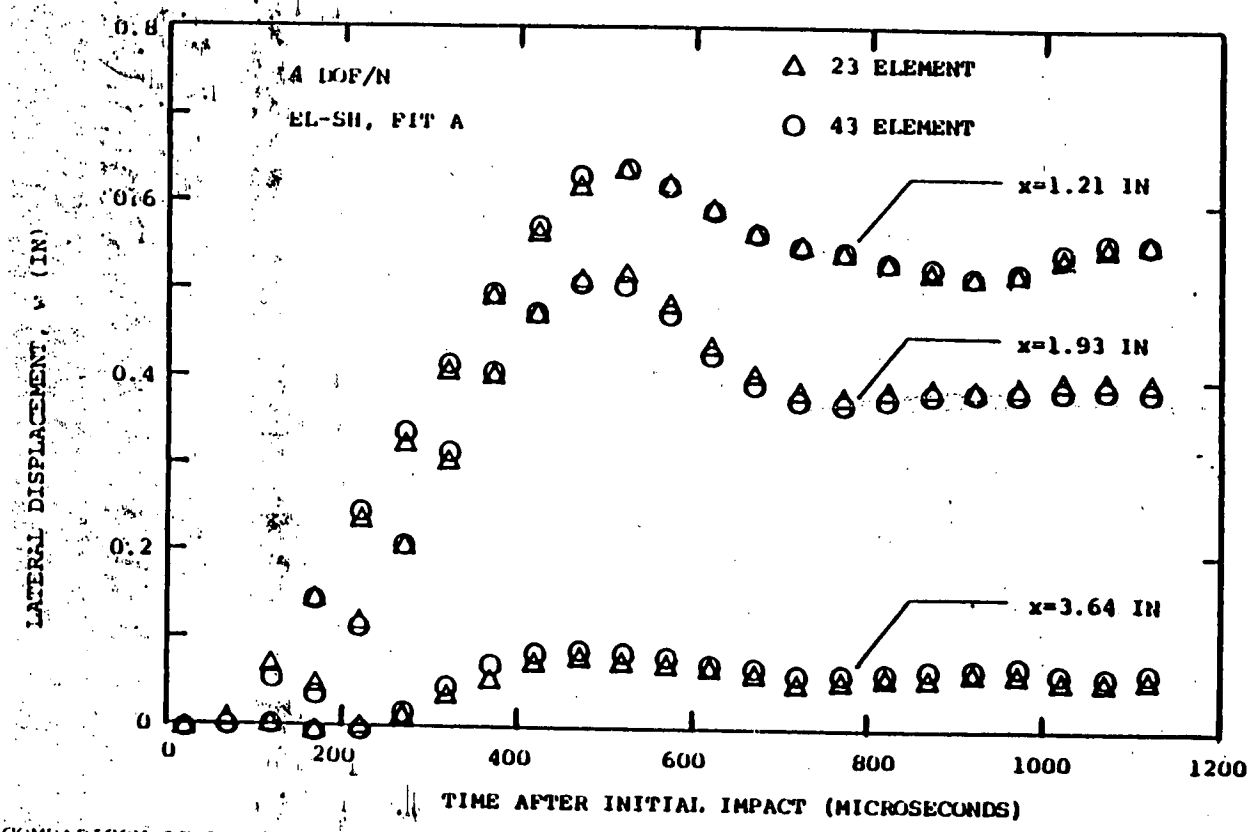

FIG. 6 COMPARISON OF PREDICTED LATERAL DISPLACEMENTS BY USING 23 OR 43 FINITE ELEMENTS TO MODEL THE ENTIRE SPAN OF STEEL-SPHERE-IMPACTED 6061-T6 ALUMINUM BEAM CB-13; IMPACT VELOCITY = 2490 IN/SEC

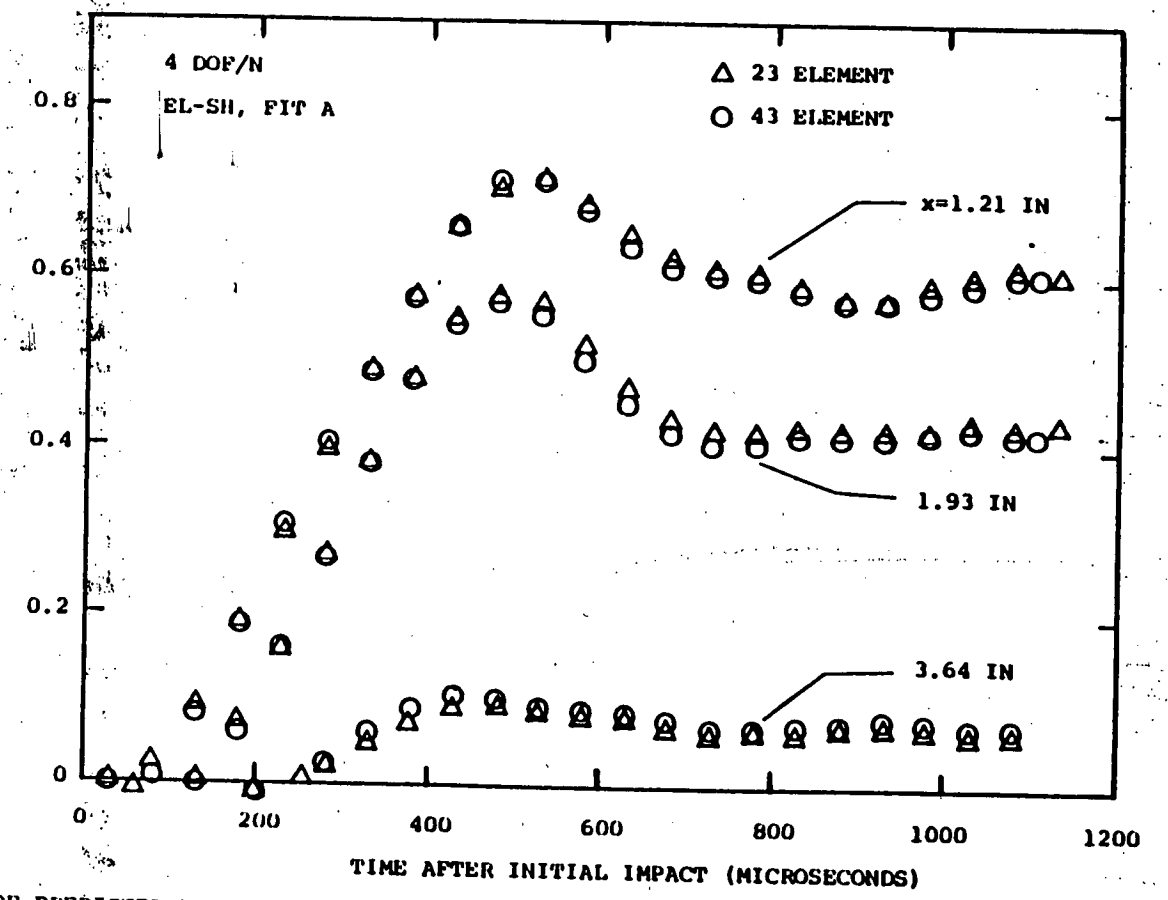

FIG. 7 COMPARISON OF PREDICTED LATERAL DISPLACEMENTS BY USING 23 OR 43 FINITE ELEMENTS TO MODEL THE ENTIRE SPAN OF STEEL-SPHERE-IMPACTED 6061-T651 ALUMINUM BEAM CB-18; IMPACT VELOCITY = 2794 IN/SEC

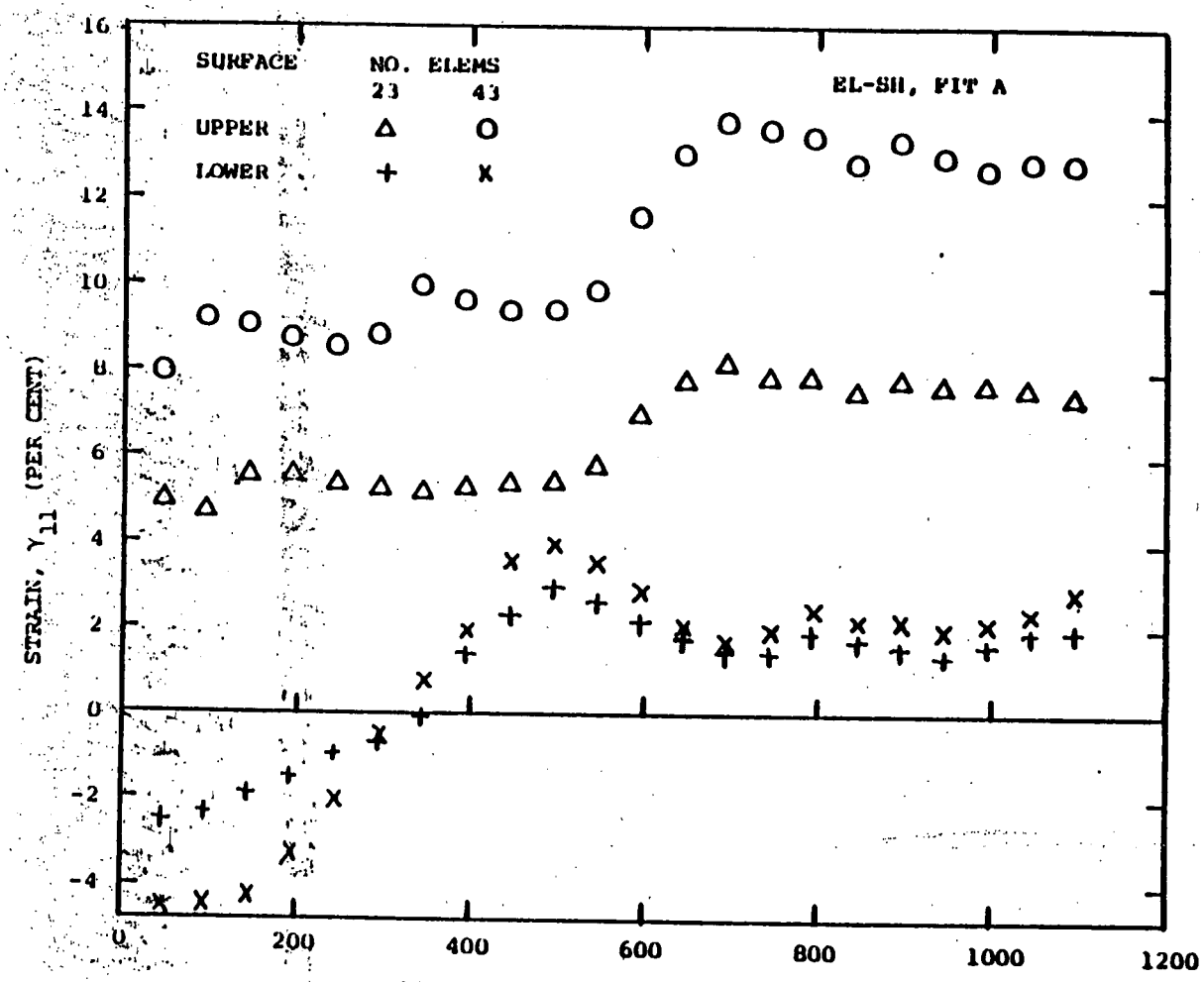

(a) Station x=0

FIG. 8 COMPARISON OF 23-ELEMENT AND 43-ELEMENT PREDICTIONS OF TRANSIENT STRAINS AT VARIOUS SPANWISE STATIONS OF STEEL-SPHERE-IMPACTED 6061-T651 ALUMINUM BEAM CB-13

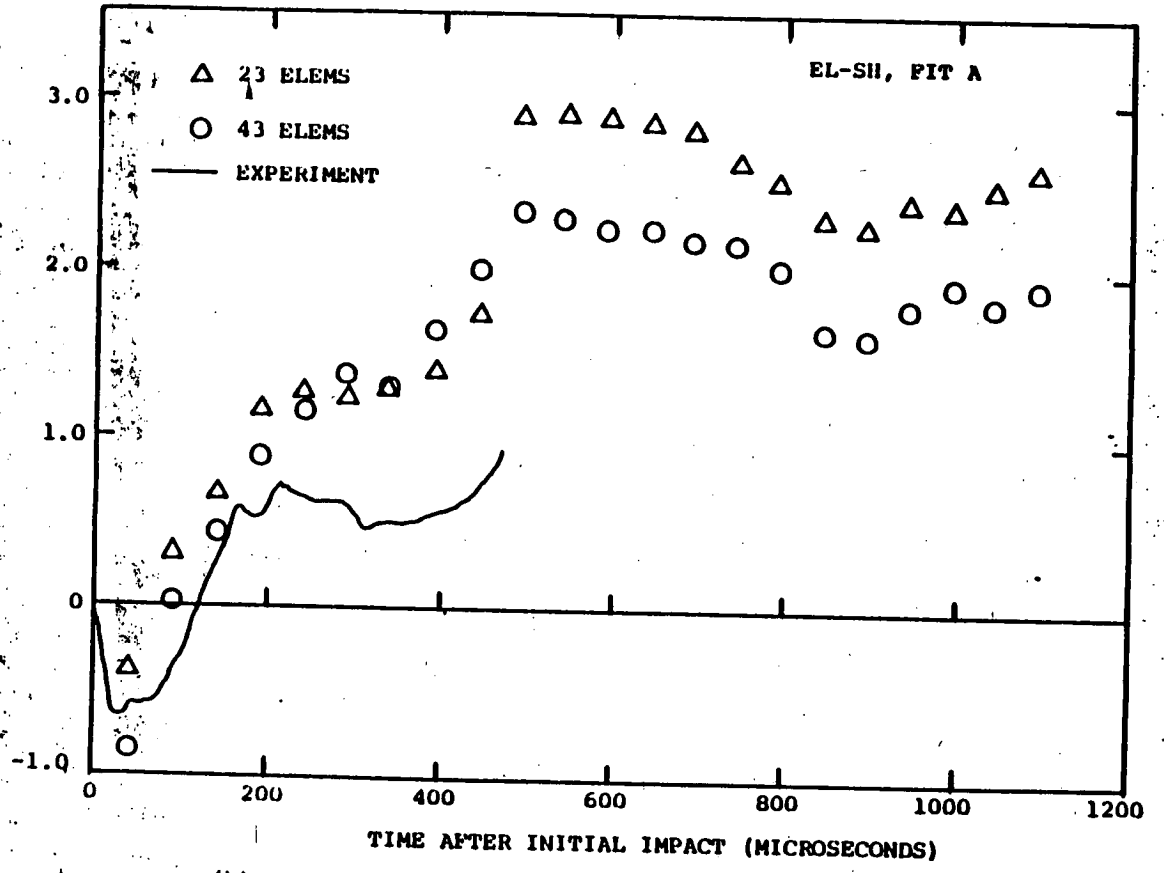

(b) Upper Surface Strain at Station x=0.6 in

FIG. 8 CONTINUED (CB-13, 23 ELEM VS. 43 ELEM, EL-SII)

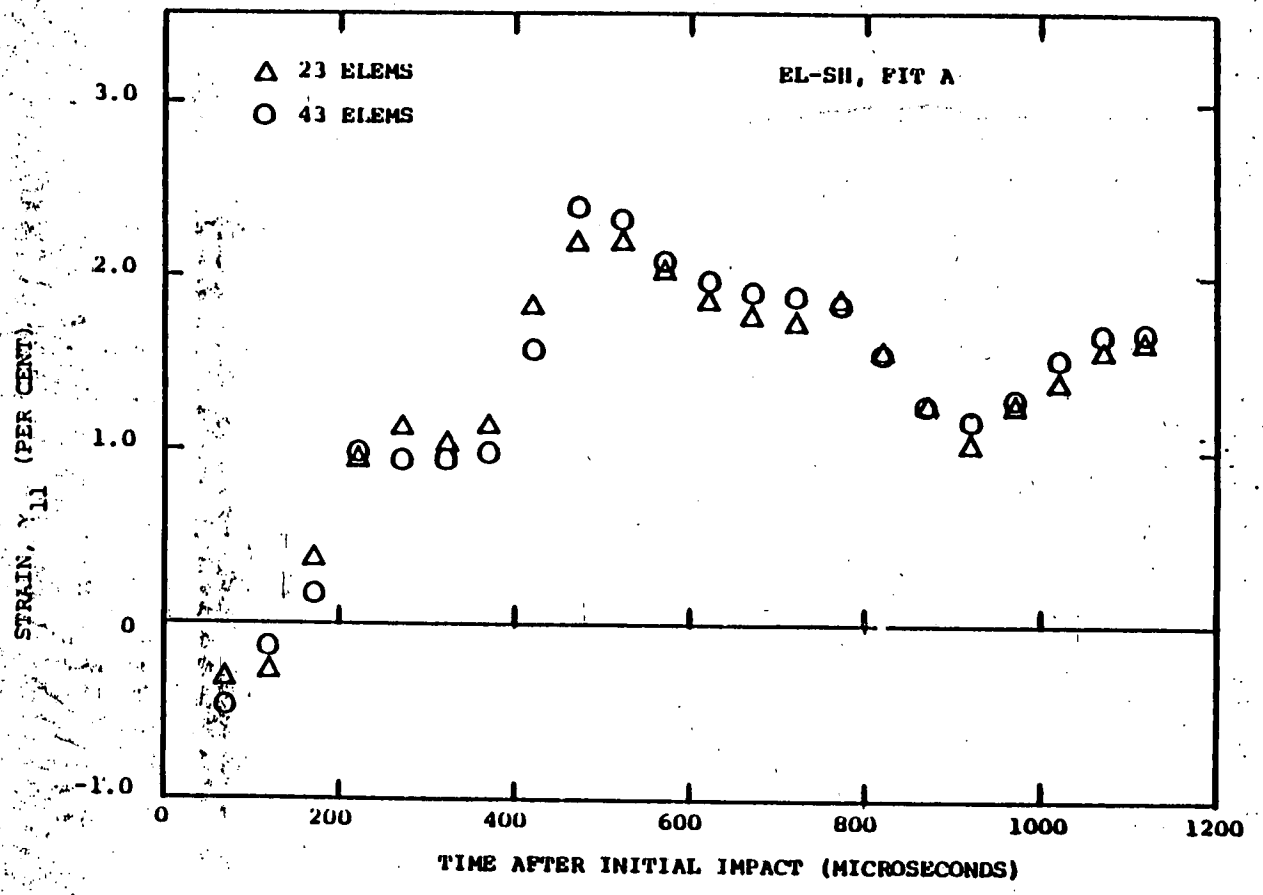

(c) Upper Surface Strain at Station x=1.20 in

FIG. 8 CONTINUED (CB-13, 23 ELEM VS. 43 ELEM, EL-SII)

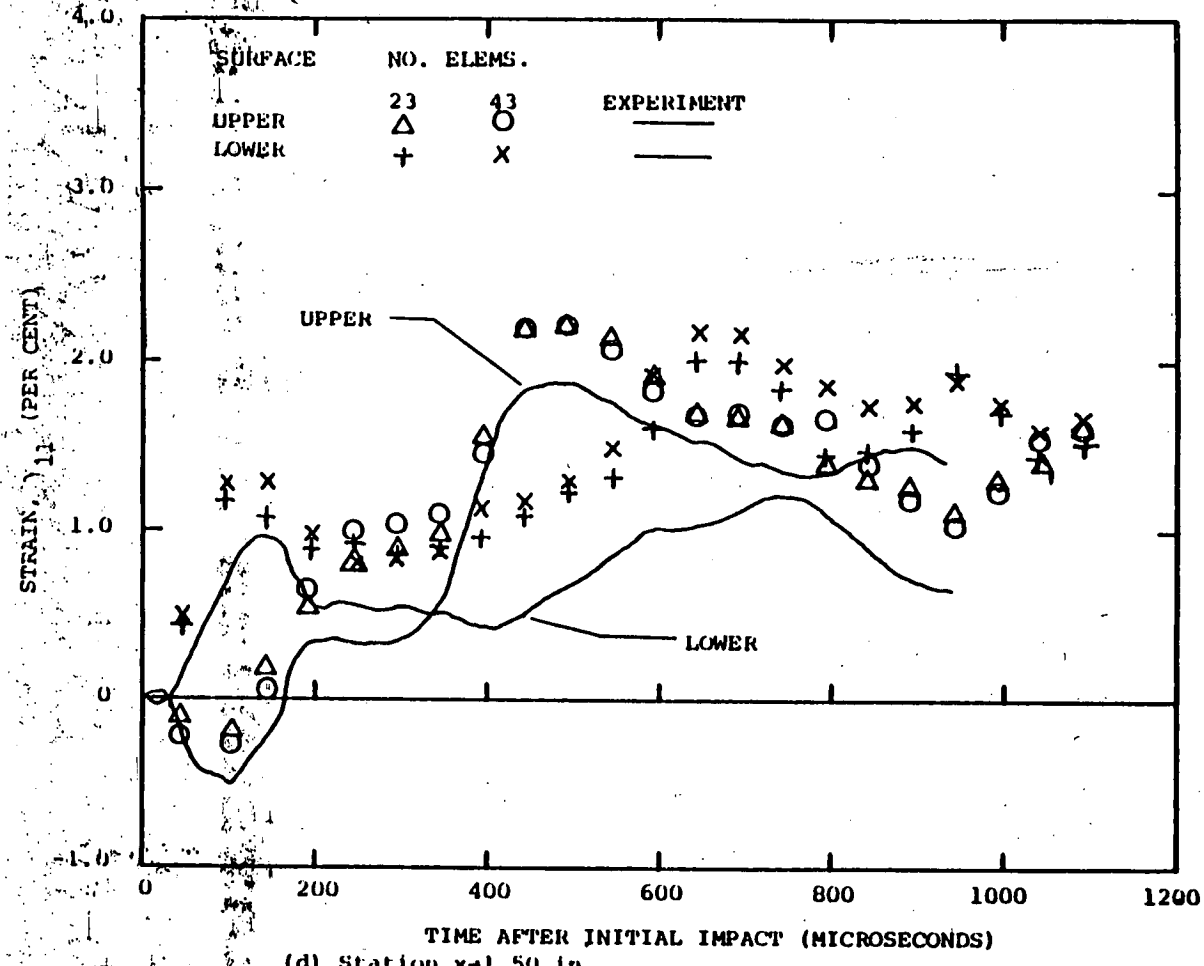

(d) Station x=1.50 in

FIG. 8 CONTINUED (CB-13, 23 ELEM VS. 43 ELEM, EL-SH)

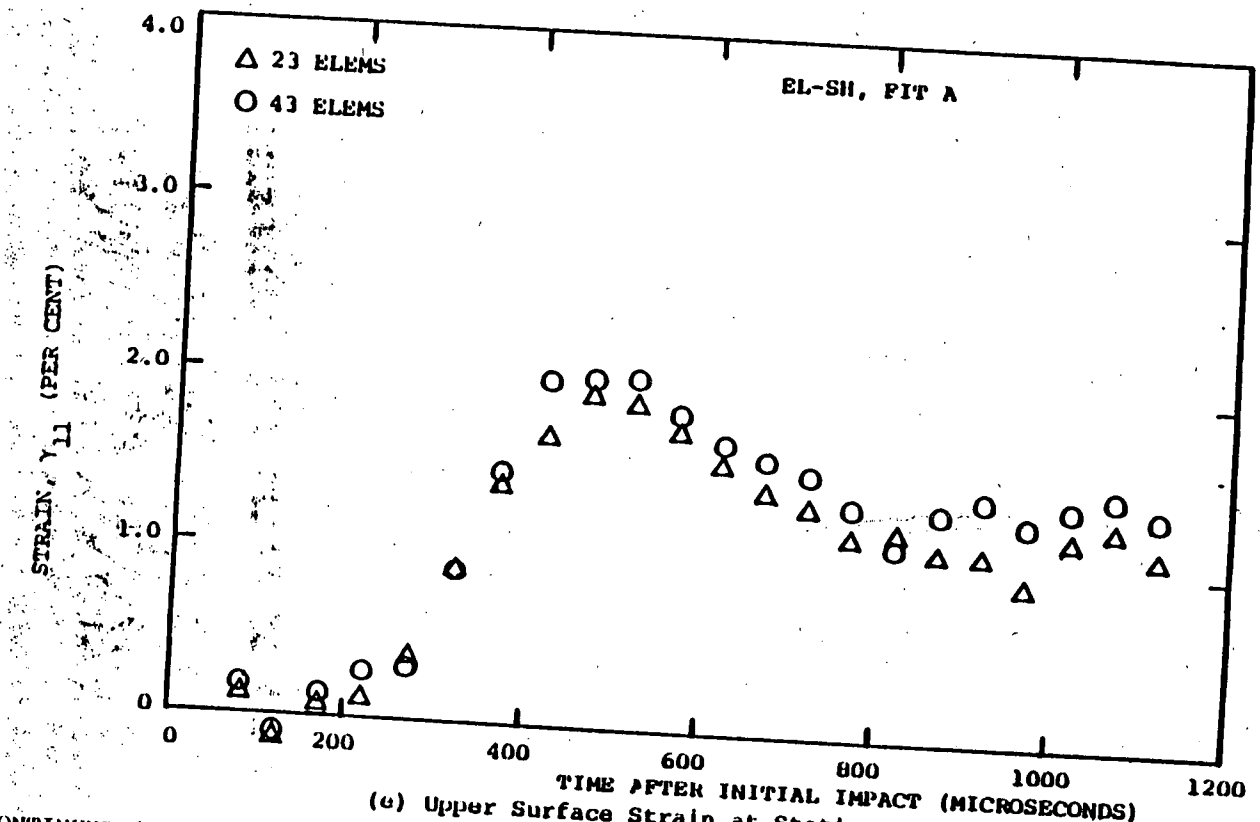

(e) Upper Surface Strain at Station x=2.10 in

FIG. 8 CONTINUED (CB-13, 23 ELEM VS. 43 ELEM, EL-SII)

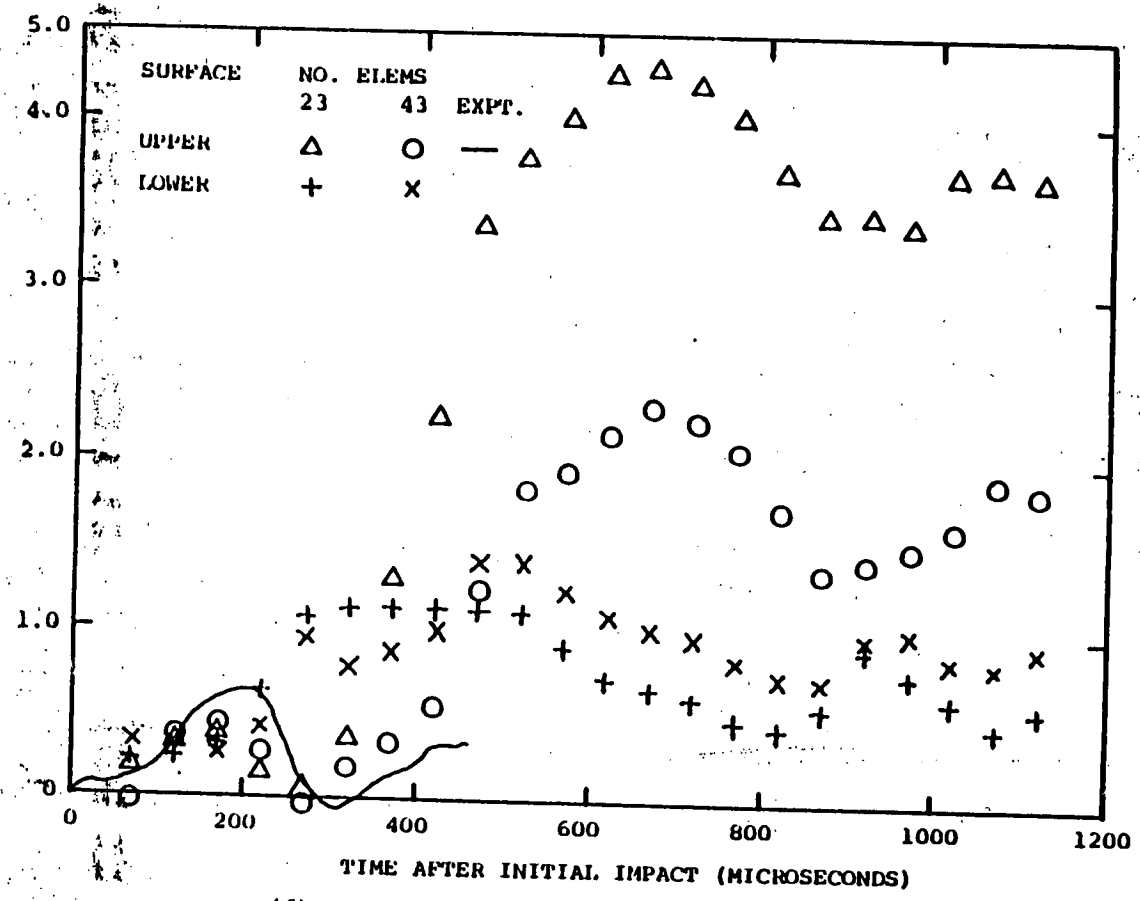

(f) Station x=3.70 in

FIG. 8 CONTINUED (CB-13, 23 ELEM VS. 43 ELEM, EL-SII)

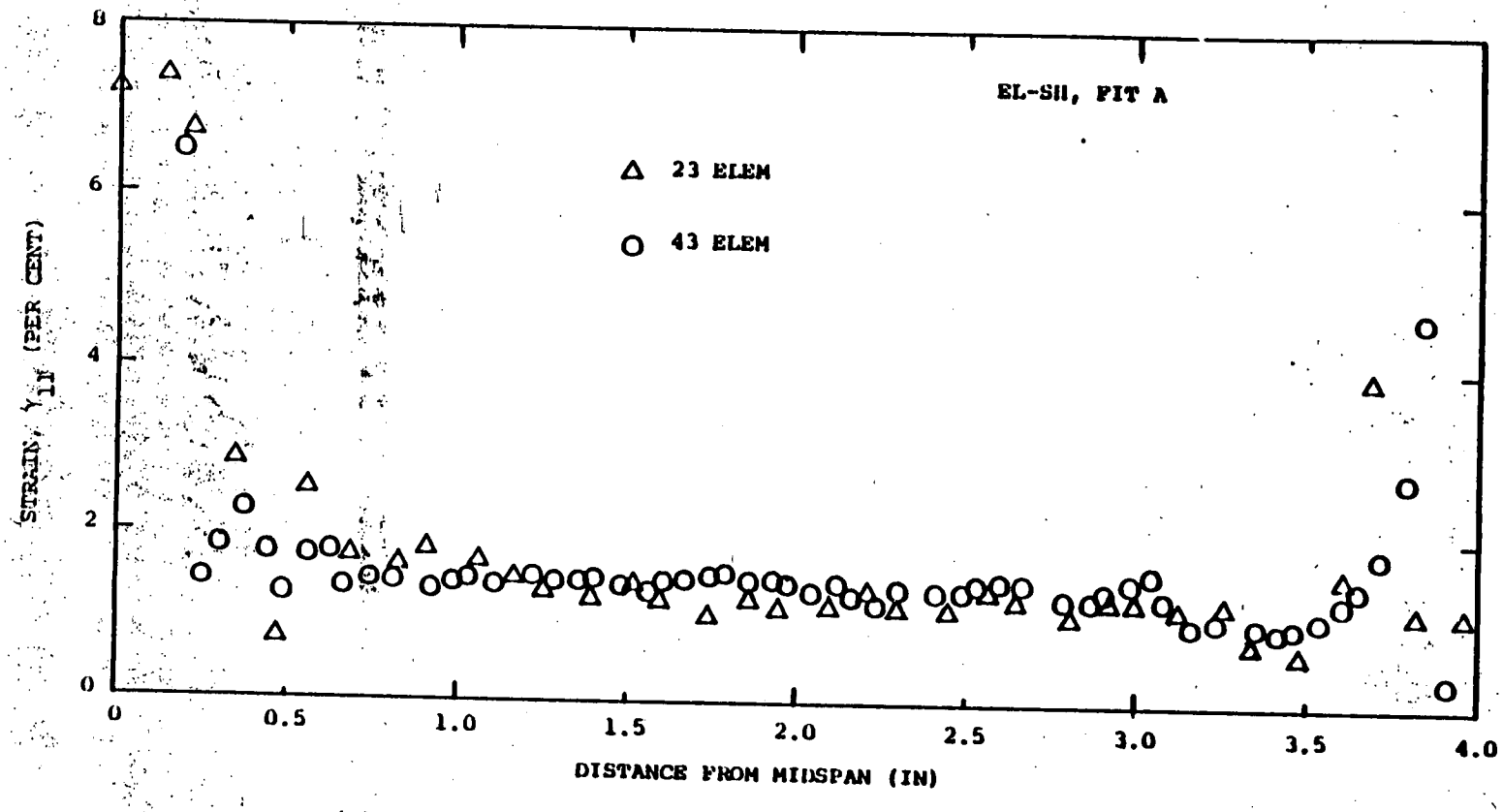

(g) Upper-Surface Strain Along Beam at 1020 μsec

FIG. 8 CONCLUDED (CB-13, 23 ELEM VS. 43 ELEM, EL-SII)

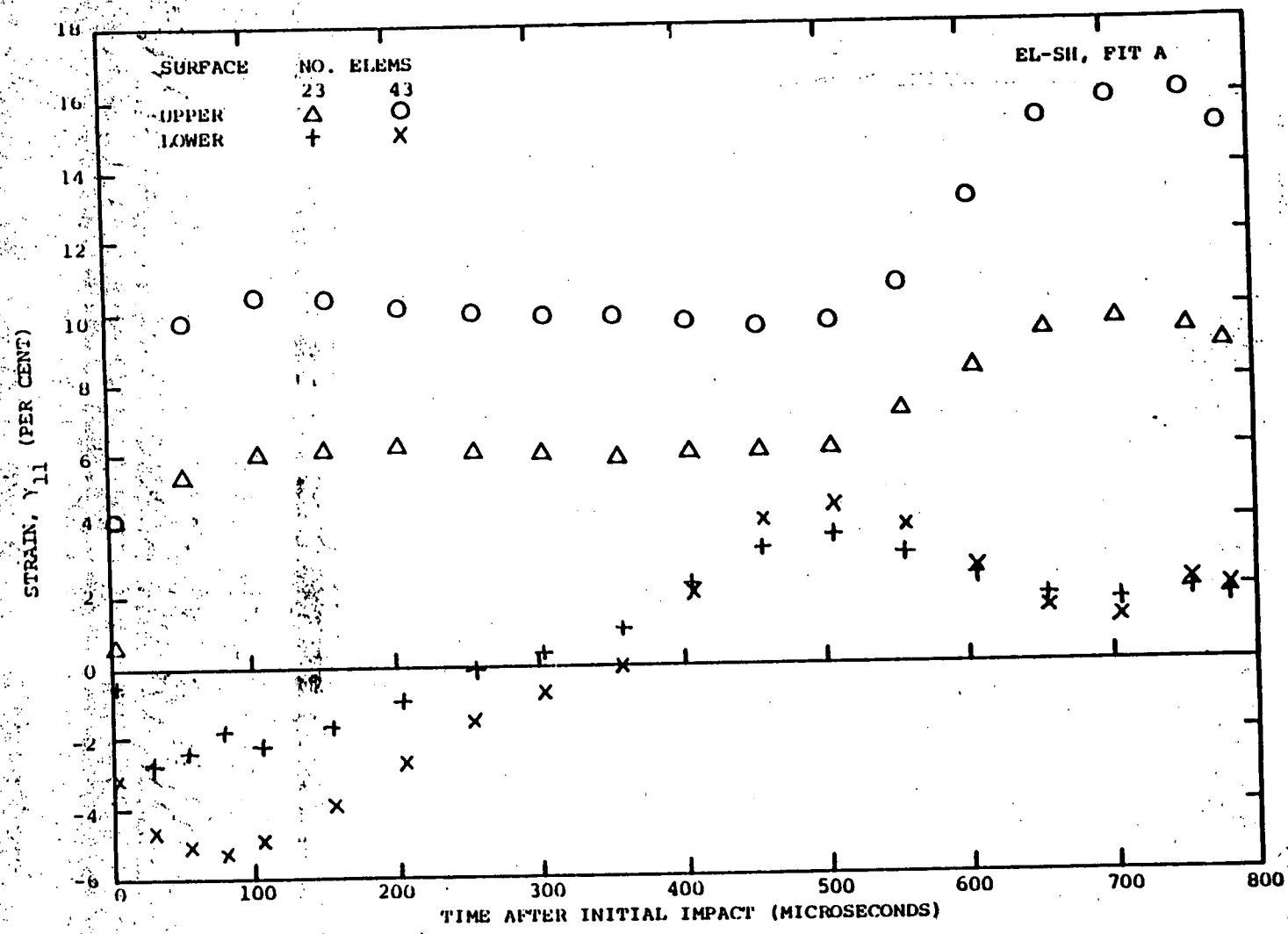

(a) Station x-0

FIG. 9 COMPARISON OF 23-ELEMENT AND 43-ELEMENT PREDICTIONS OF TRANSIENT STRAINS AT VARIOUS SPANWISE STATIONS OF STEEL-SPHERE-IMPACTED 6061-T651 ALUMINUM BEAM CB-18

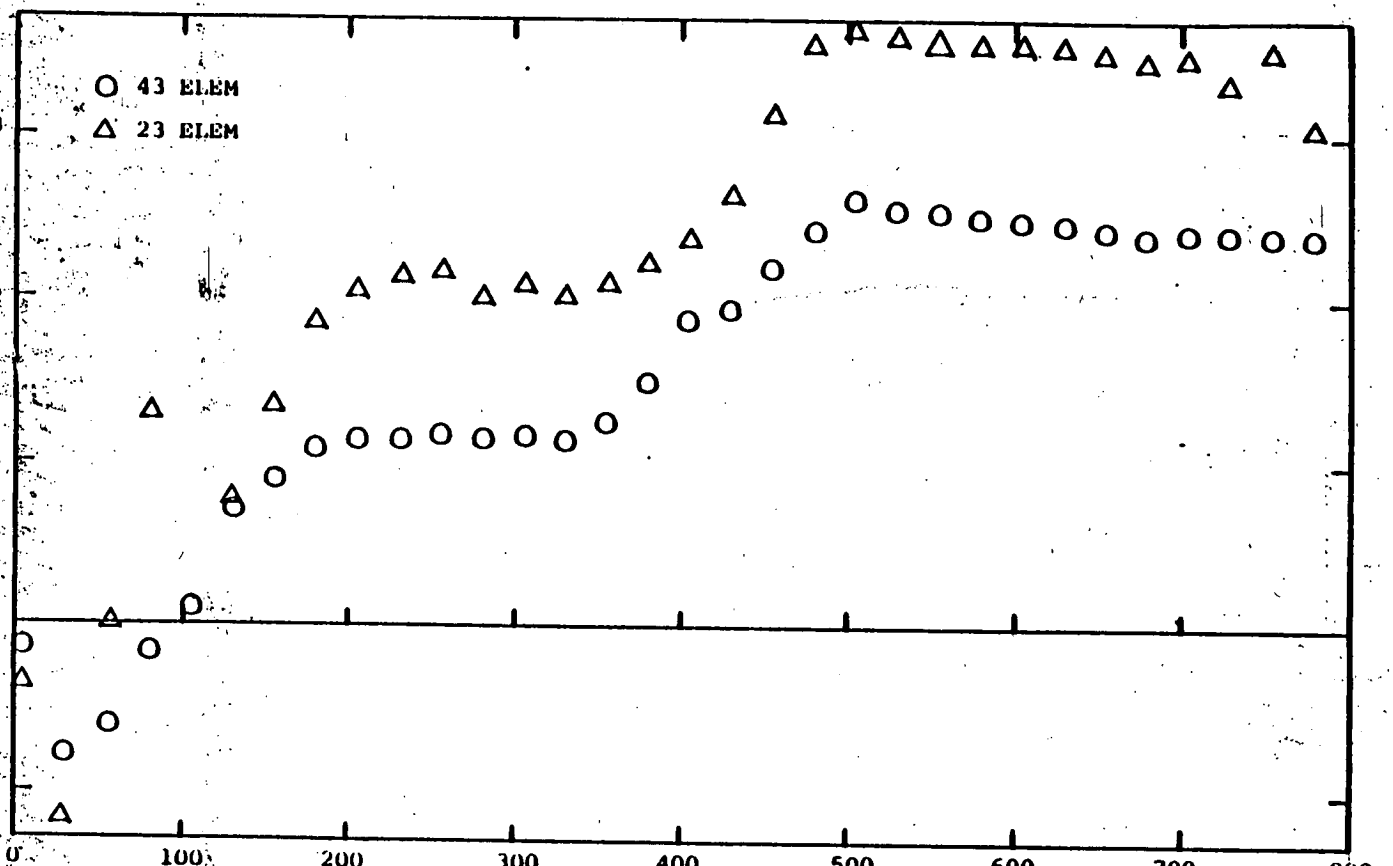

(b) Upper-Surface Strain at Station x=0.6 in

FIG. 9 CONTINUED (CB-1B, 23 ELEM VS. 43 ELEM, EL-SII)

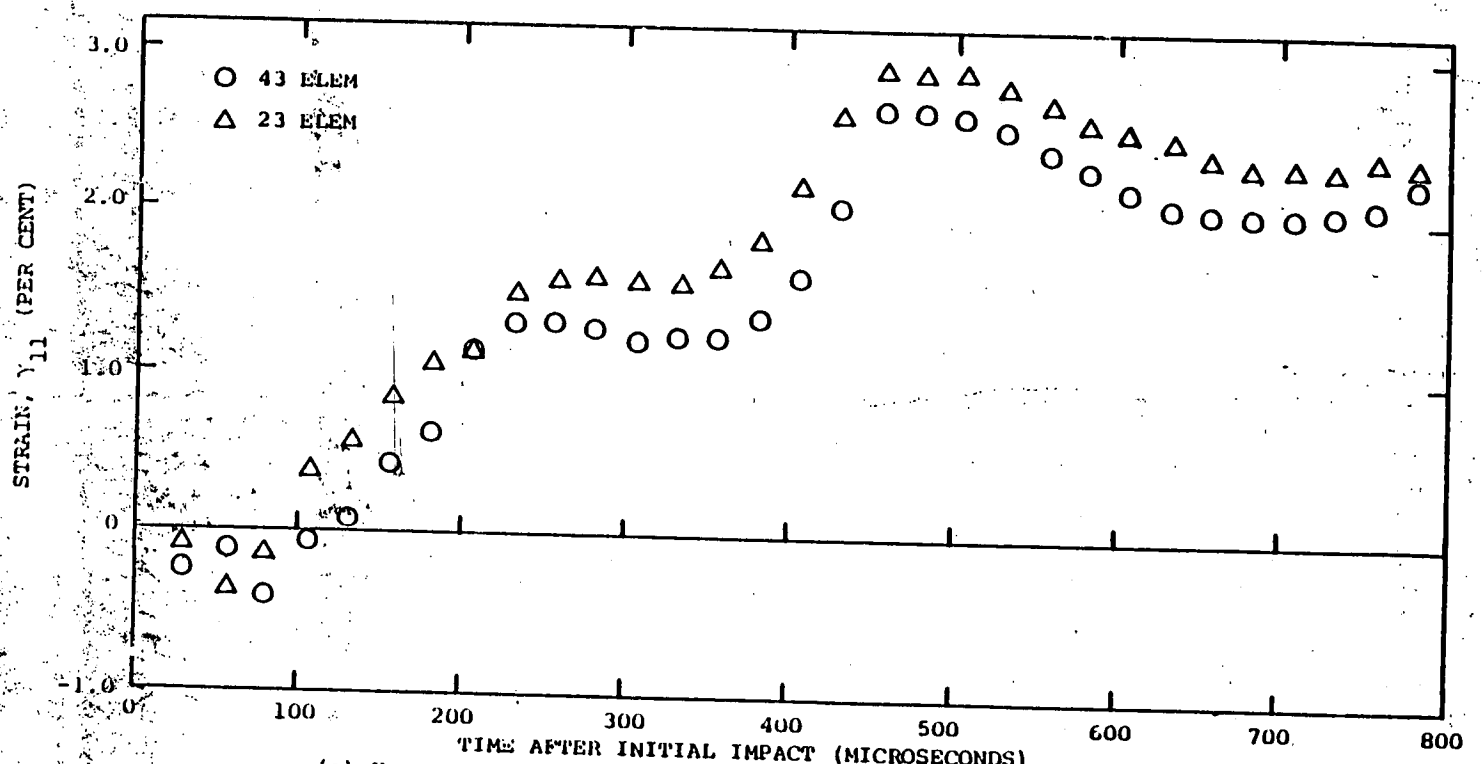

(c) Upper-Surface Strain at Station x=1.20 in

FIG. 9 CONTINUED (CB-18, 23 ELEM VS. 43 ELEM, EL-SH)

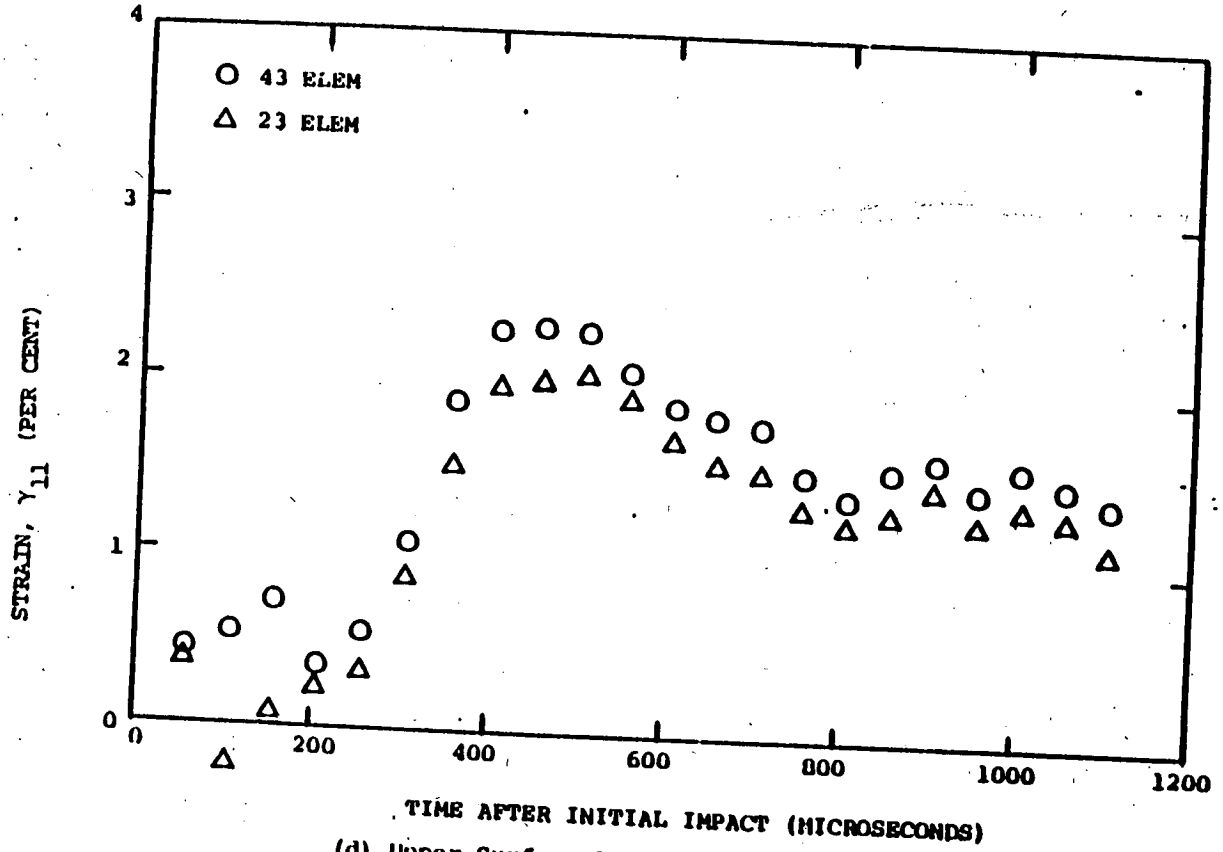

(d) Upper-Surface Strain at Station x=2.10 in

FIG. 9 CONTINUED (CB-18, 23 ELEM VS. 43 ELEM, EL-SH)

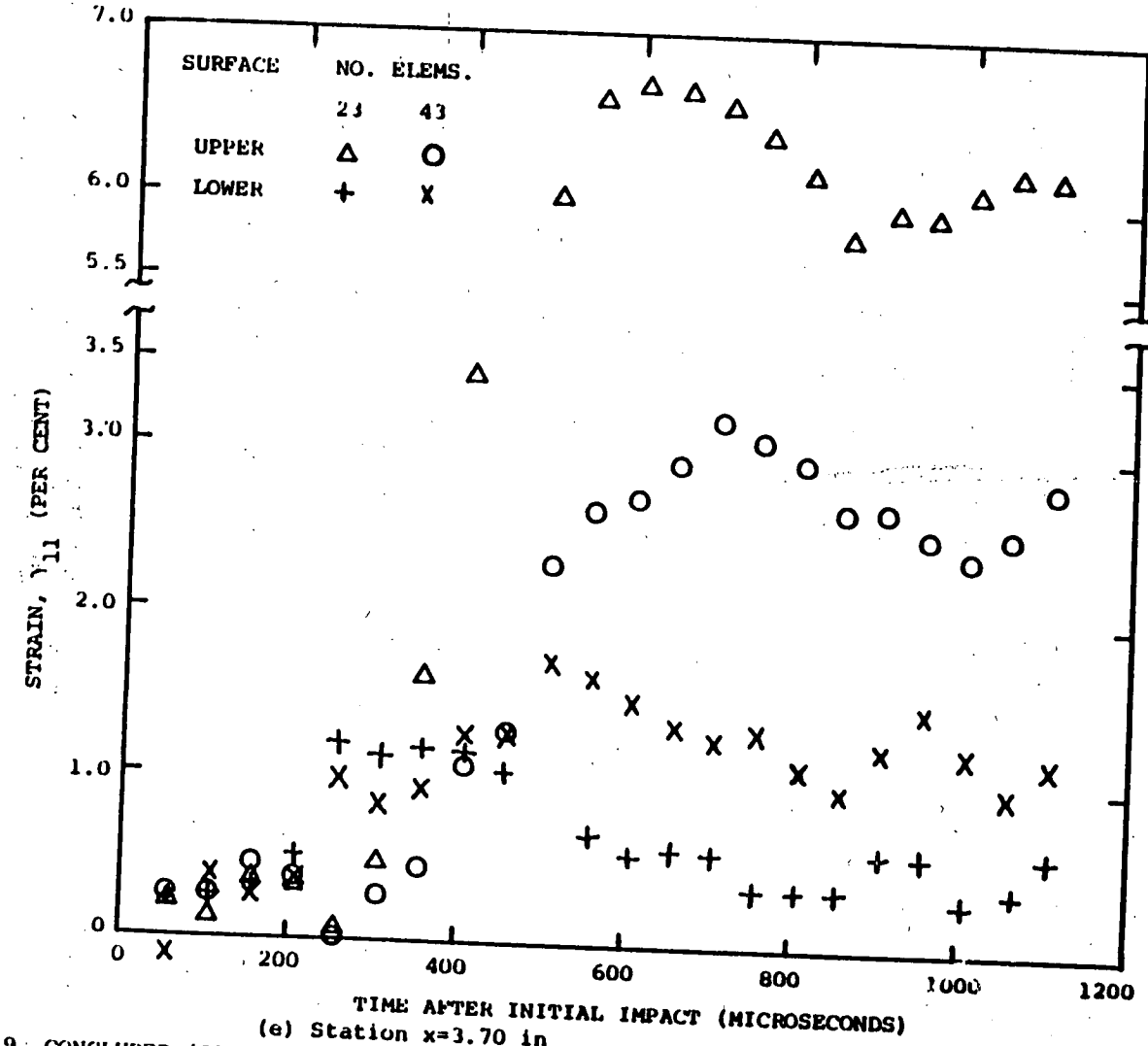

(e) Station x=3.70 in

FIG. 9 CONCLUDED (CB-18, 23 ELEM VS. 43 ELEM, EL-SH)

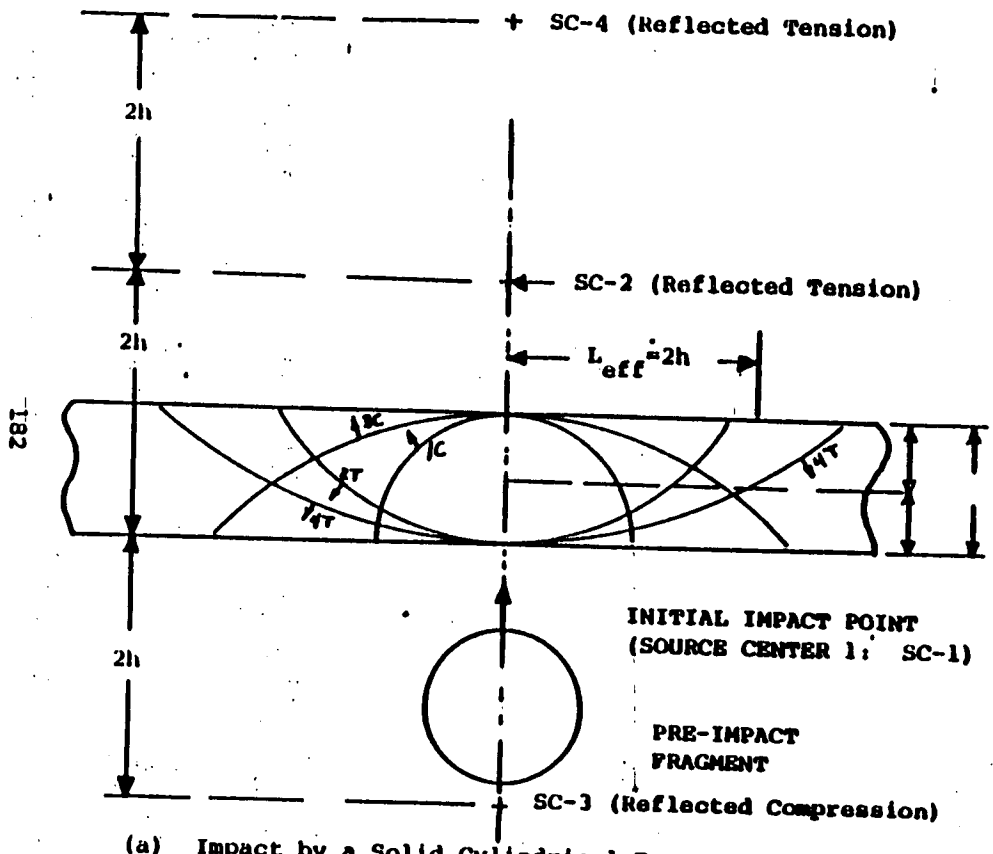

(a) Impact by a Solid Cylindrical Fragment

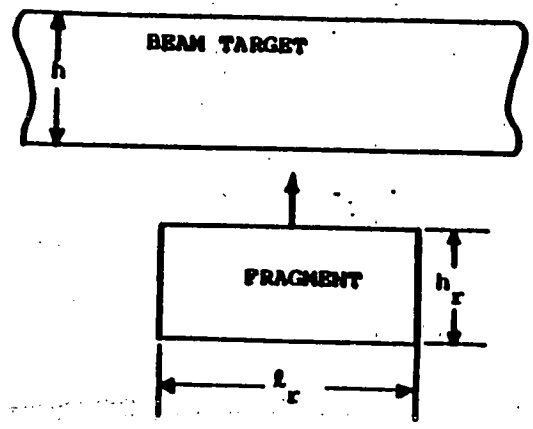

(b) Impact by a Rectangular Section Fragment

FIG. 10 SCHEMATIC OF 2-D FRAGMENT IMPACT AGAINST A 2-D BEAM-TYPE STRUCTURE

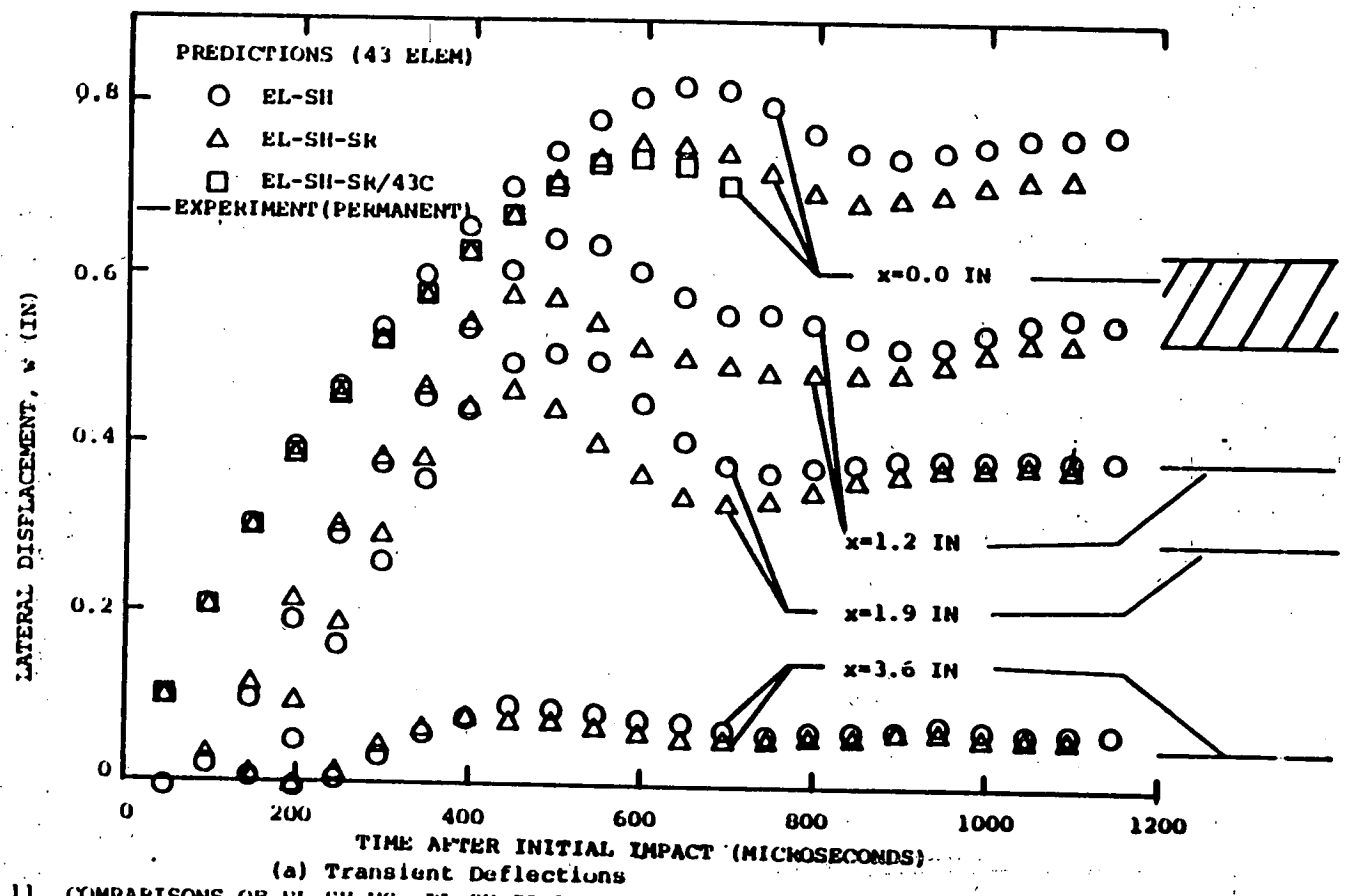

(a) Transient Deflections

FIG. 11 COMPARISONS OF EL-SH VS. EL-SH-SR PREDICTIONS OF TRANSIENT AND PERMANENT DEFLECTIONS OF STEEL-SPHERE-IMPACTED BEAM CB-13 MODELED BY 43 EQUAL-LENGTH ELEMENTS FOR THE ENTIRE SPAN

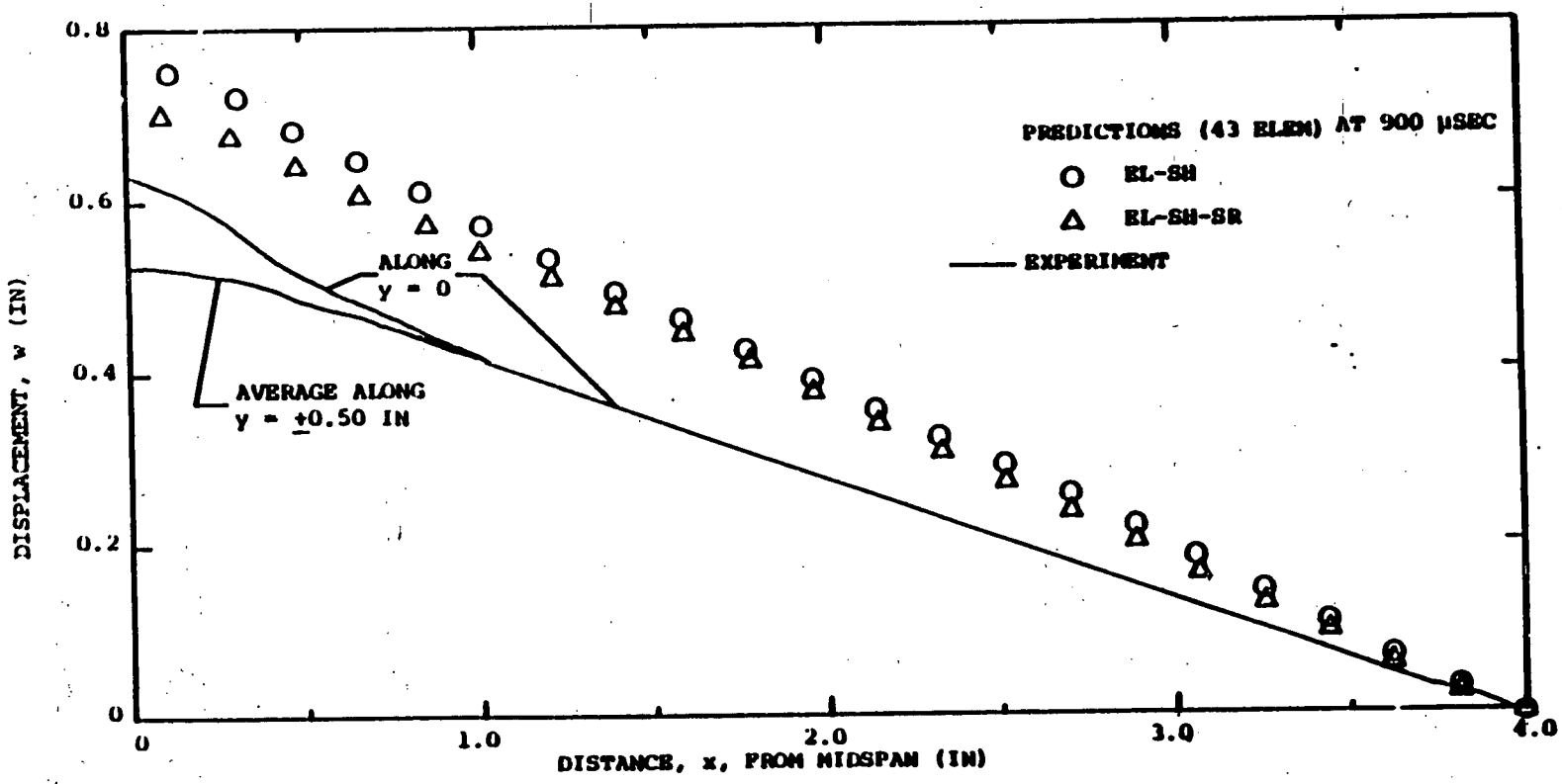

(b) Permanent Deflection

FIG. 11 CONCLUDED (CB-13, EL-SH VS. EL-SH-SR, 43 ELEM)

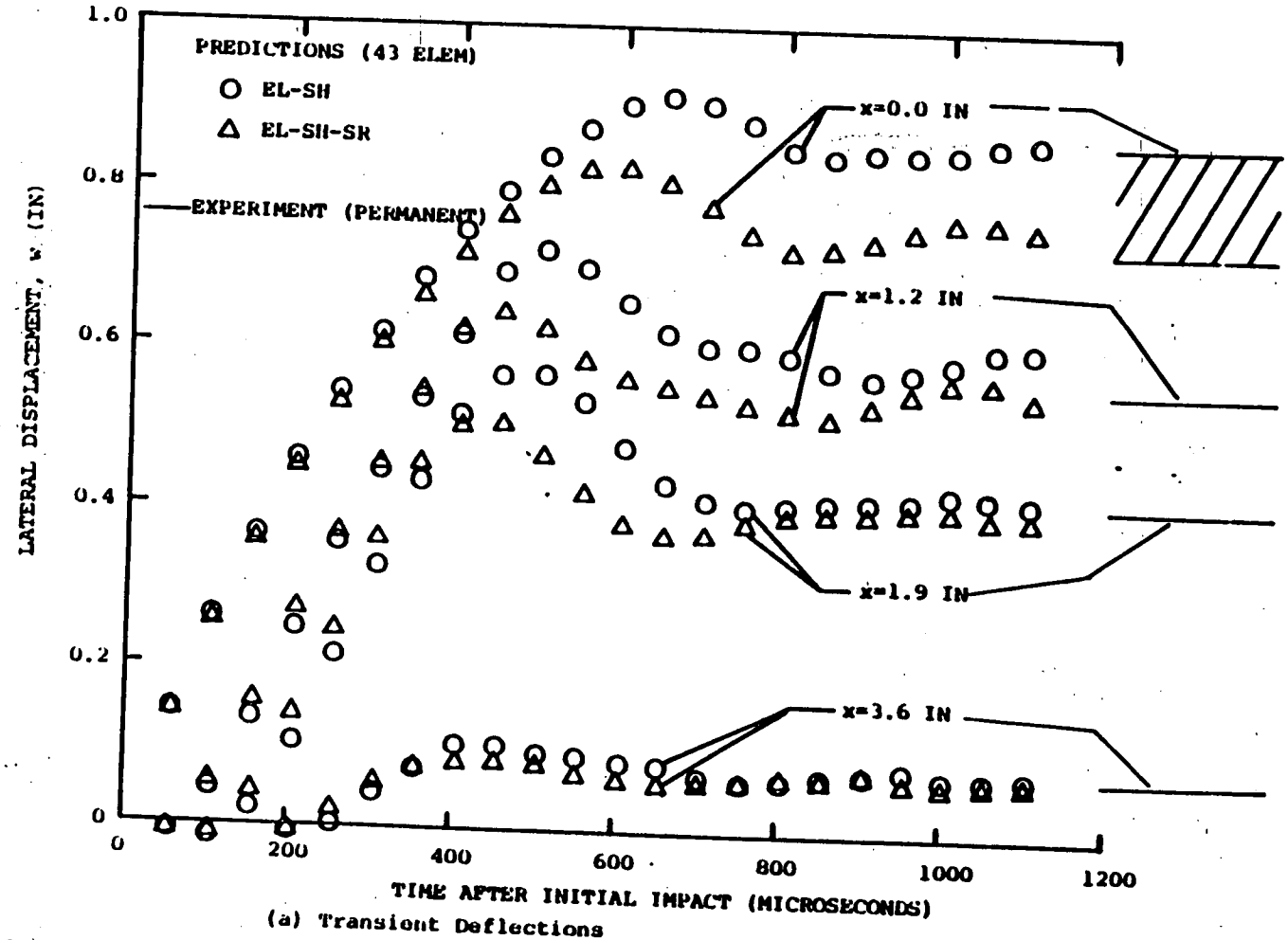

(a) Transient Deflections

FIG. 12 COMPARISONS OF EL-SH VS. EL-SH-SR PREDICTIONS OF TRANSIENT AND PERMANENT DEFLECTIONS OF STEEL-SPHERE-IMPACTED BEAM CB-18 MODELED BY 43 EQUAL-LENGTH ELEMENTS FOR THE ENTIRE SPAN

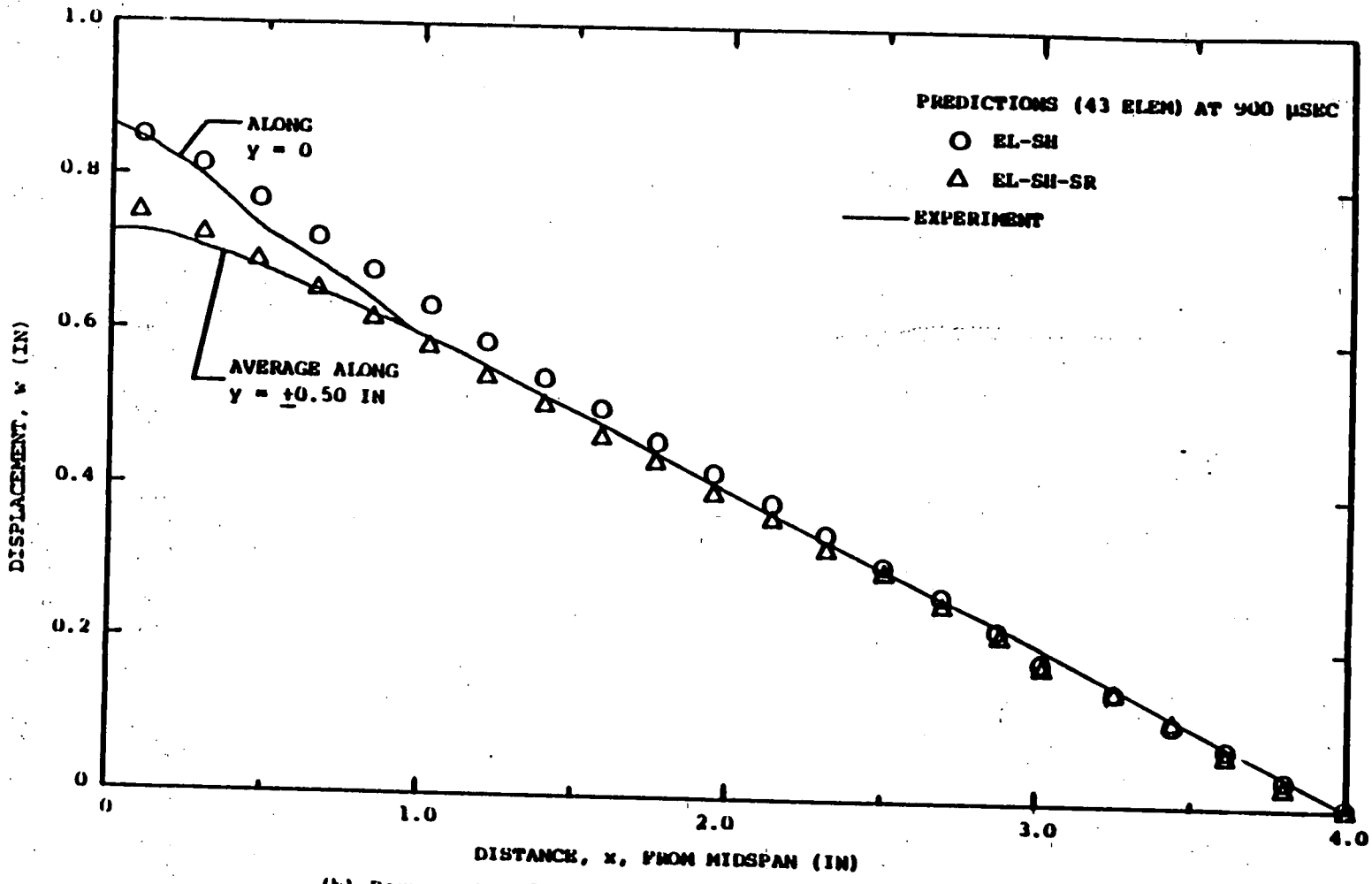

(b) Permanent Deflection

FIG. 12 CONCLUDED (CB-18, EL-SH VS. EL-SH-SR, 43 ELEM)

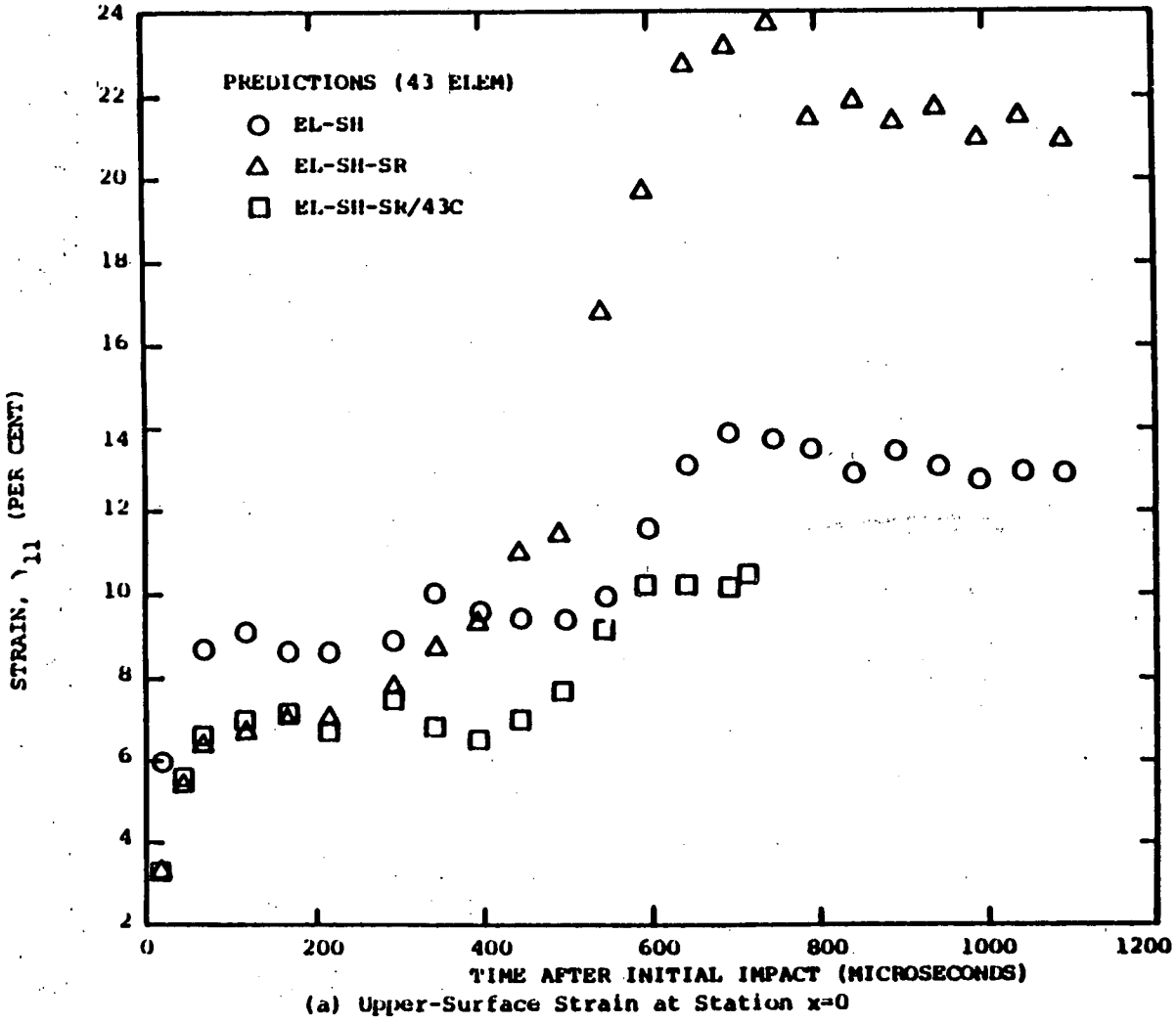

(a) Upper-Surface Strain at Station x=0

FIG. 13 COMPARISONS OF EL-SH VS. EL-SH-SR PREDICTIONS OF TRANSIENT AND PERMANENT STRAINS FOR STEEL-SPHERE-IMPACTED BEAM CB-13 MODELED BY 43 EQUAL-LENGTH ELEMENTS FOR THE ENTIRE SPAN

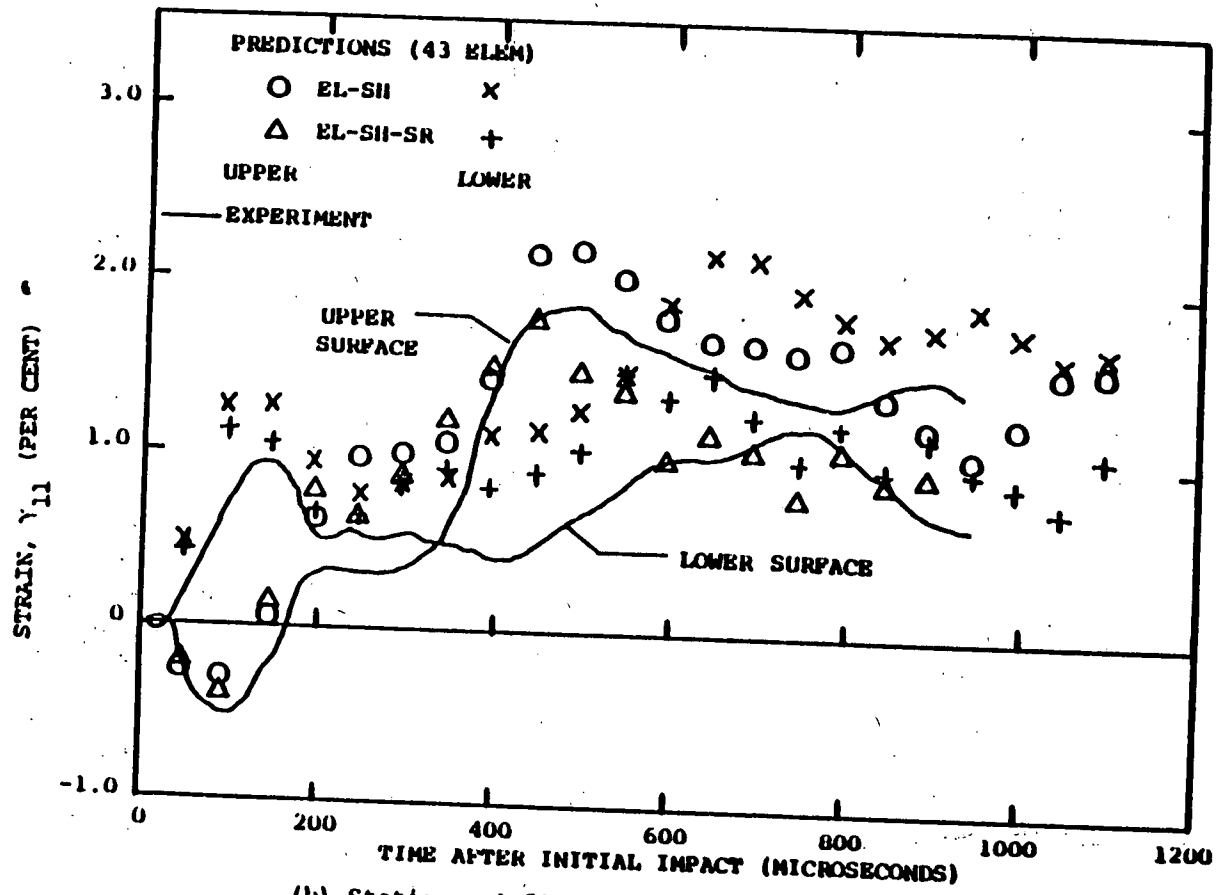

(b) Station x=1.50 in

FIG. 13 CONTINUED (CB-13, EL-SH VS. EL-SH-SR, 43 ELEM)

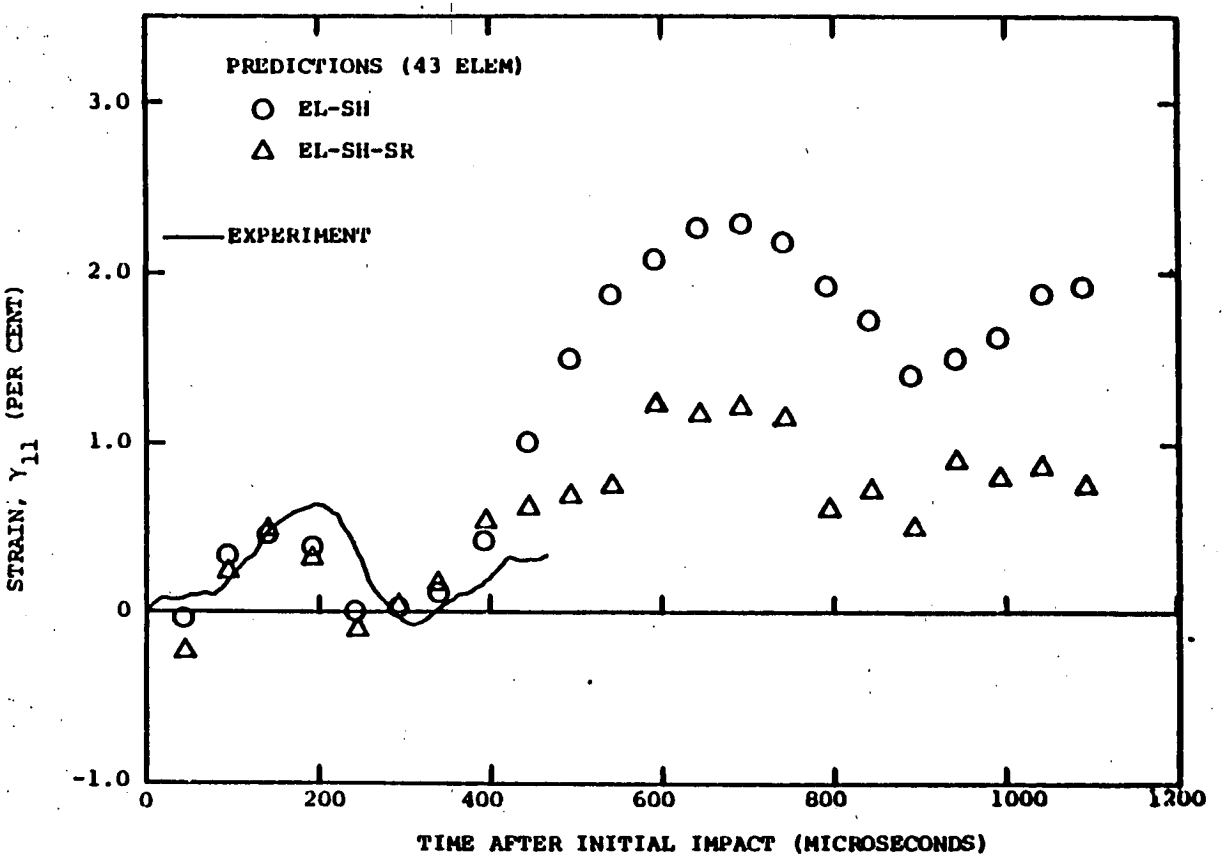

(c) Upper Surface Strain at Station x=3.70 in

FIG. 13 CONTINUED (CB-13, EL-SH VS. EL-SH-SR, 43 ELEM)

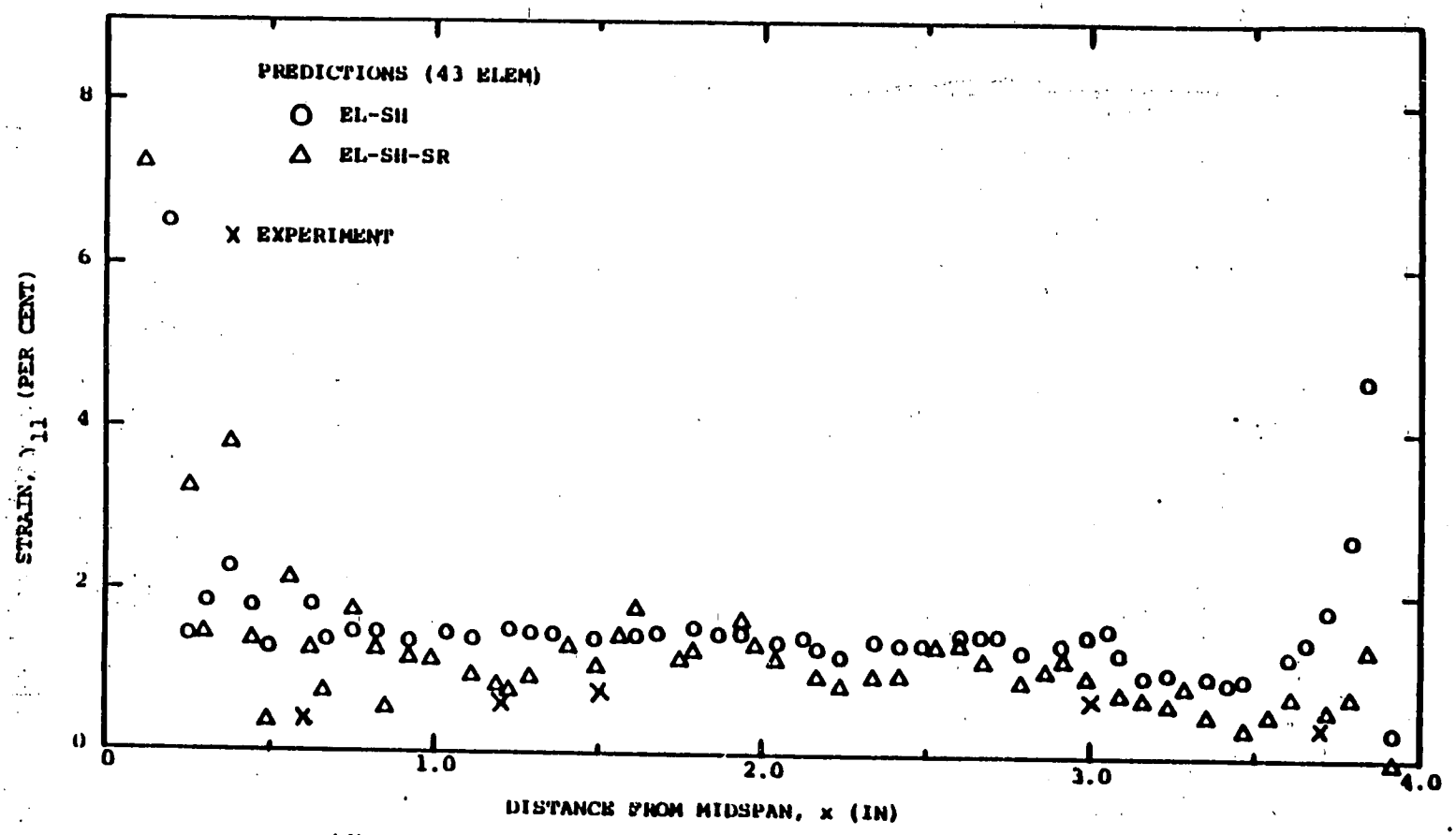

(d) Permanent Strain on the Upper Surface

FIG. 13 CONCLUDED (CB-13, EL-SH VS. EL-SH-SR, 43 ELEM)

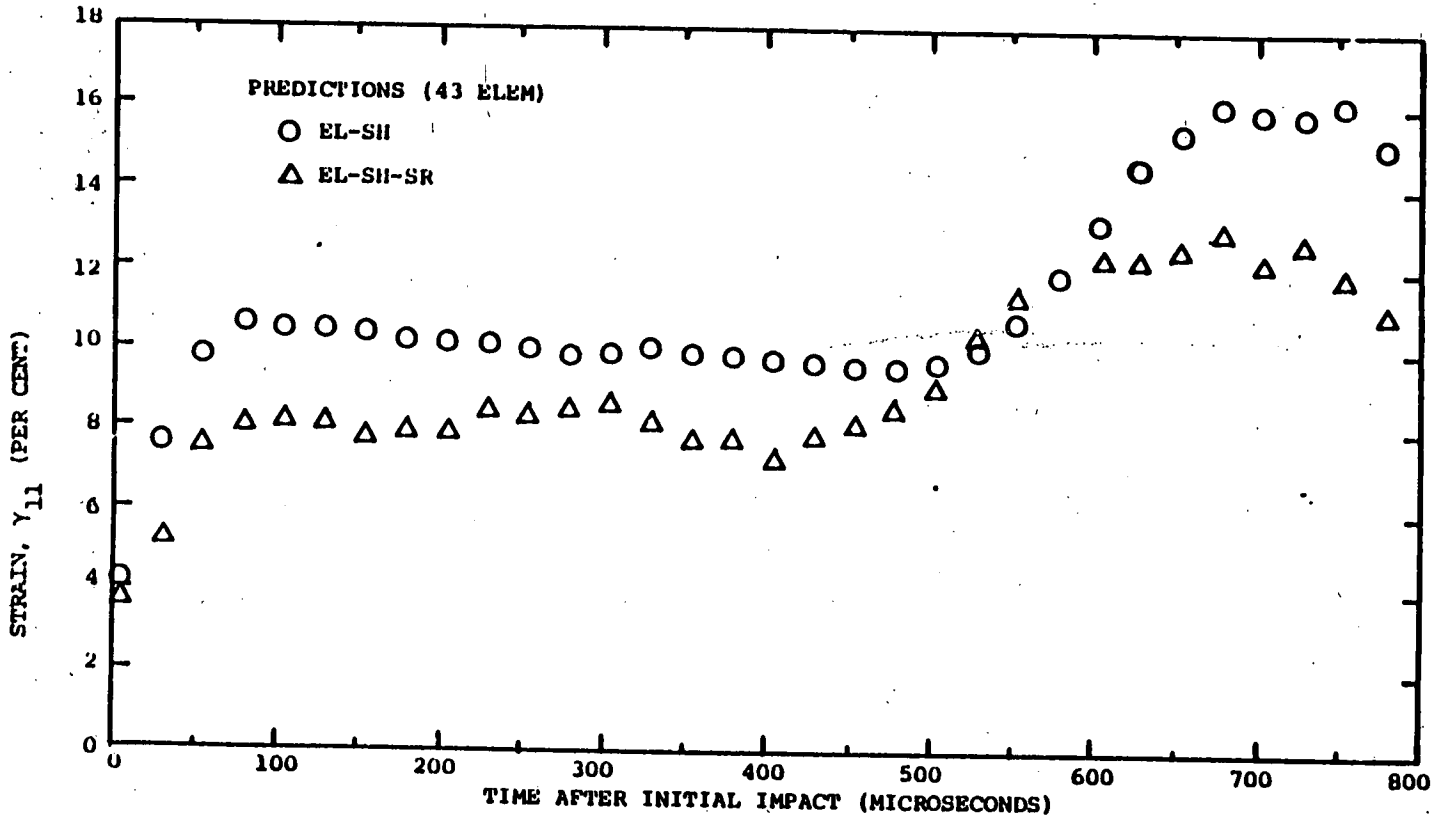

(a) Upper-Surface Strain at Station x=0

FIG. 14 COMPARISONS OF EL-SH VS. EL-SH-SR PREDICTIONS OF TRANSIENT AND PERMANENT STRAINS FOR STEEL-SPHERE-IMPACTED BEAM CB-18 MODELED BY 43 EQUAL-LENGTH ELEMENTS FOR THE ENTIRE SPAN

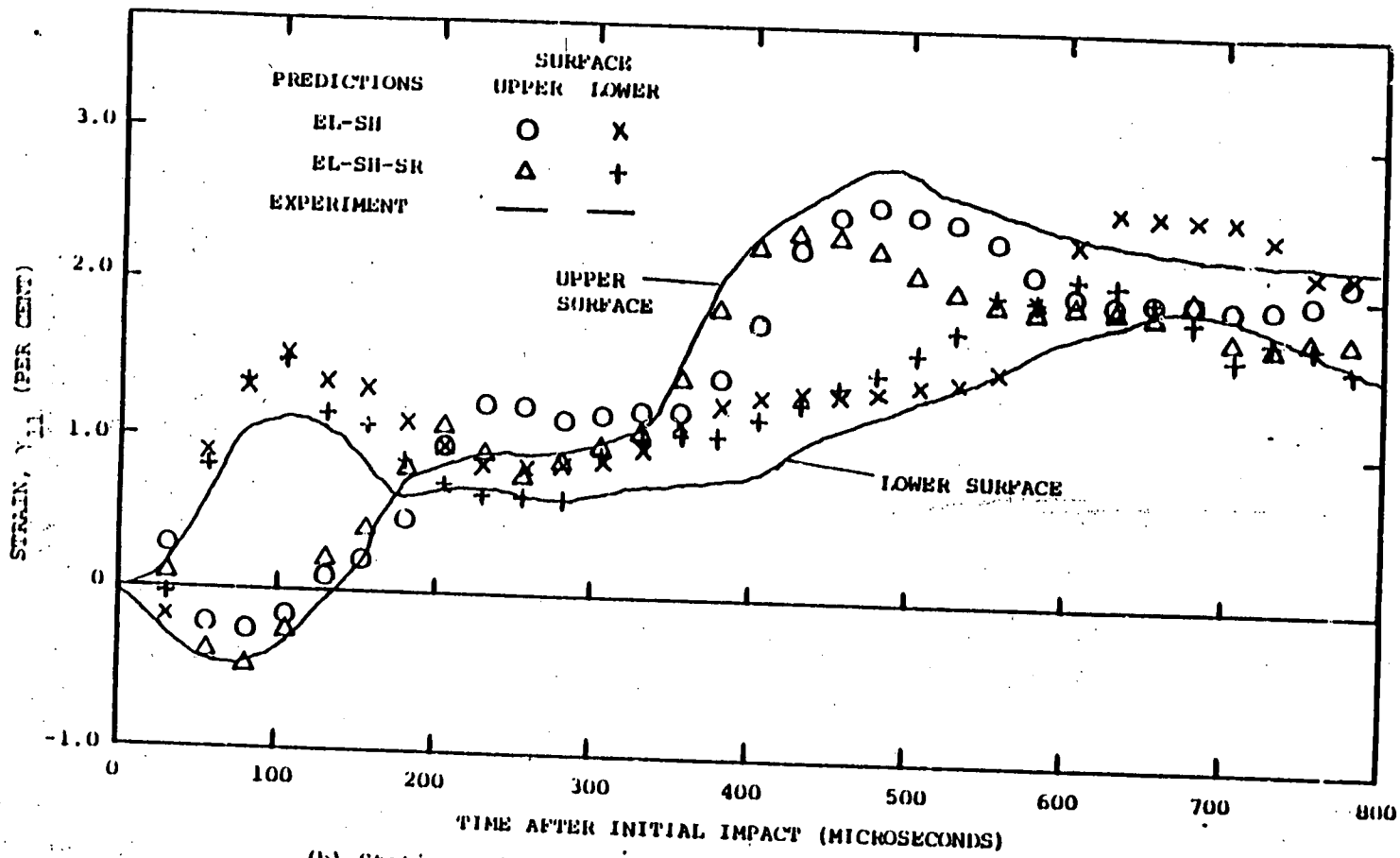

(b) Station x=1.50 in

FIG. 14 CONTINUED (CB-18, EL-SH VS. EL-SH-SR, 43 ELEM)

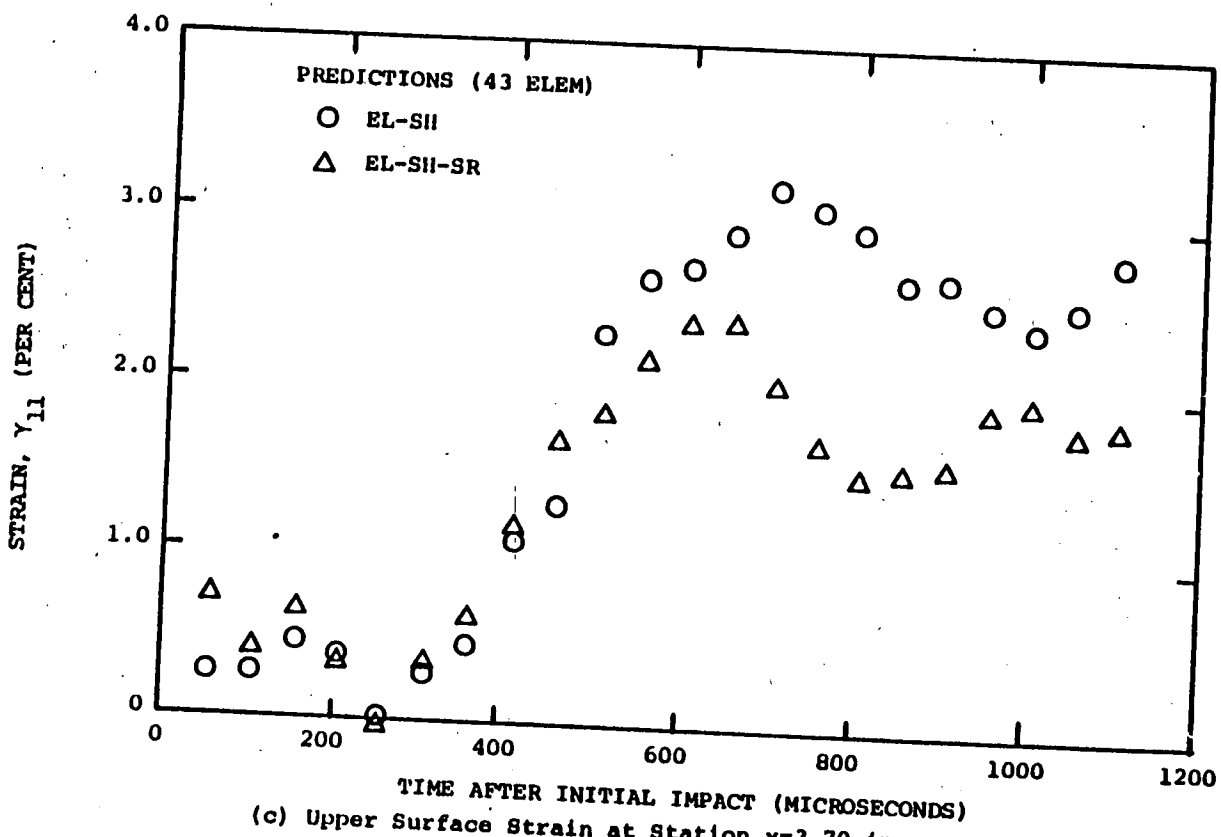

(c) Upper Surface Strain at Station x=3.70 in

FIG. 14 CONTINUED (CB-18, EL-SH VS. EL-SH-SR, 43 ELEM)

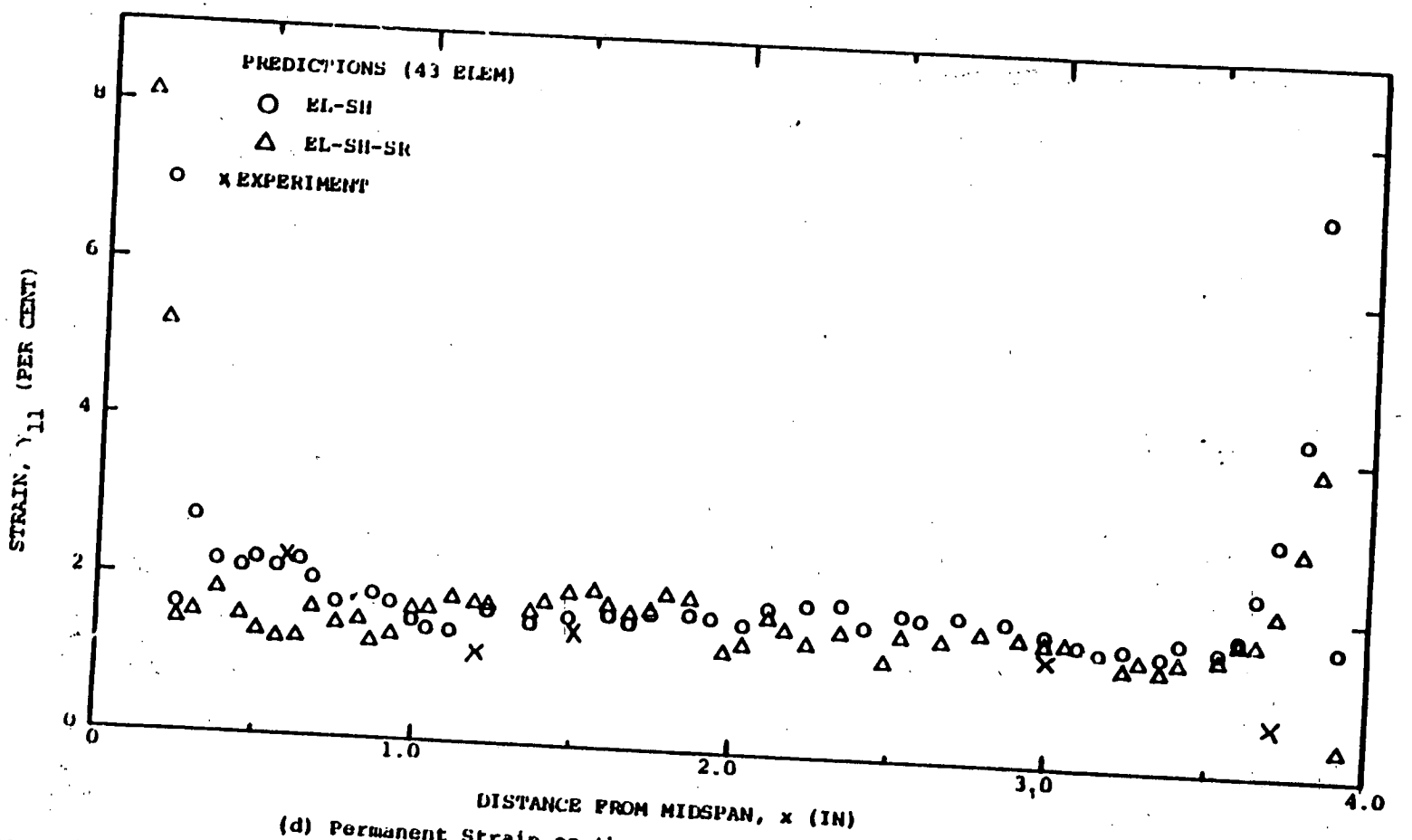

(d) Permanent Strain on the Upper Surface

FIG. 14 CONCLUDED (CB-18, EL-SII VS. EL-SII-SR, 43 ELEM)

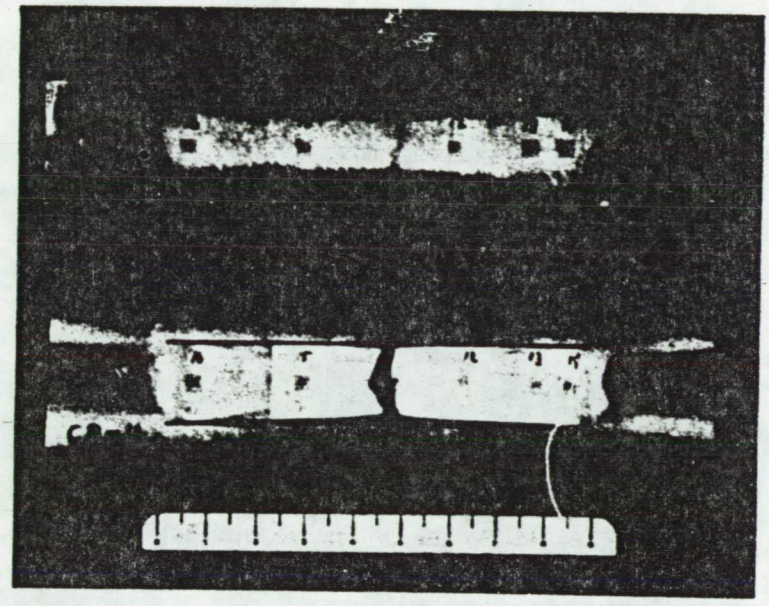

LOWER
SURFACE
VIEW

FIG. 15 POST-TEST PHOTOGRAPH OF STEEL-SPHERE-IMPACTED 6061-T651 ALUMINUM BEAM CB-16; IMPACT VELOCITY = 2870 IN/SEC

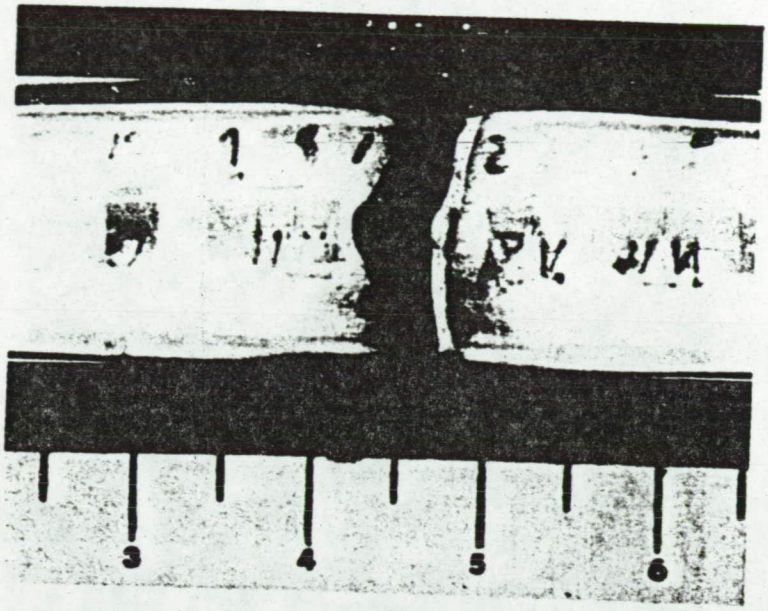

CLOSEUP
UPPER
SURFACE
VIEW
(INTO
CAVITY)

CB-16

CLOSEUP
LOWER
SURFACE
VIEW

CB-16

FIG. 15 CONCLUDED (CB-16)

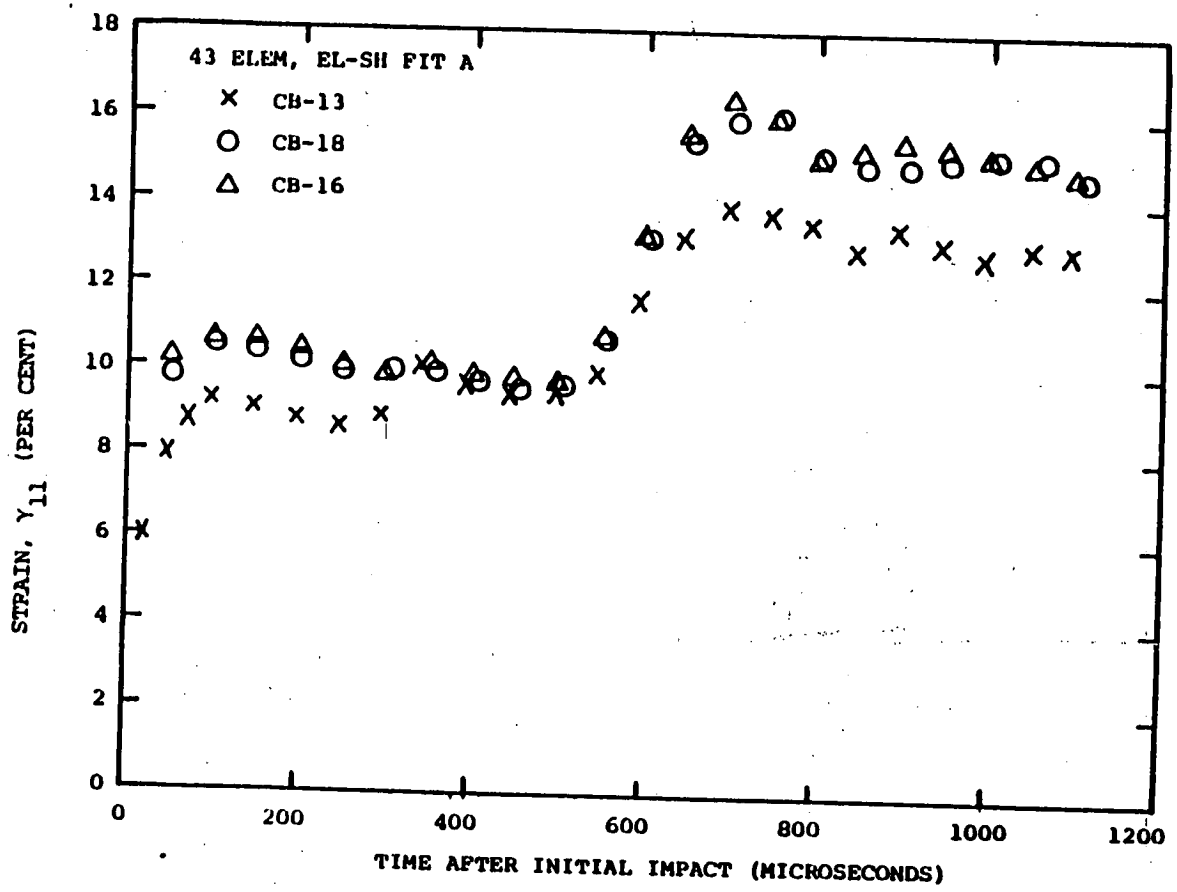

(a) Upper-Surface Strains at Station x=0

FIG. 16 COMPARISON OF 43-ELEMENT EL-SH TRANSIENT STRAIN PREDICTIONS FOR STEEL-SPHERE-IMPACTED BEAM SPECIMENS CB-13, CB-18, AND CB-16, WITH RESPECTIVE INITIAL IMPACT VELOCITIES OF 2490, 2795, AND 2870 IN/SEC

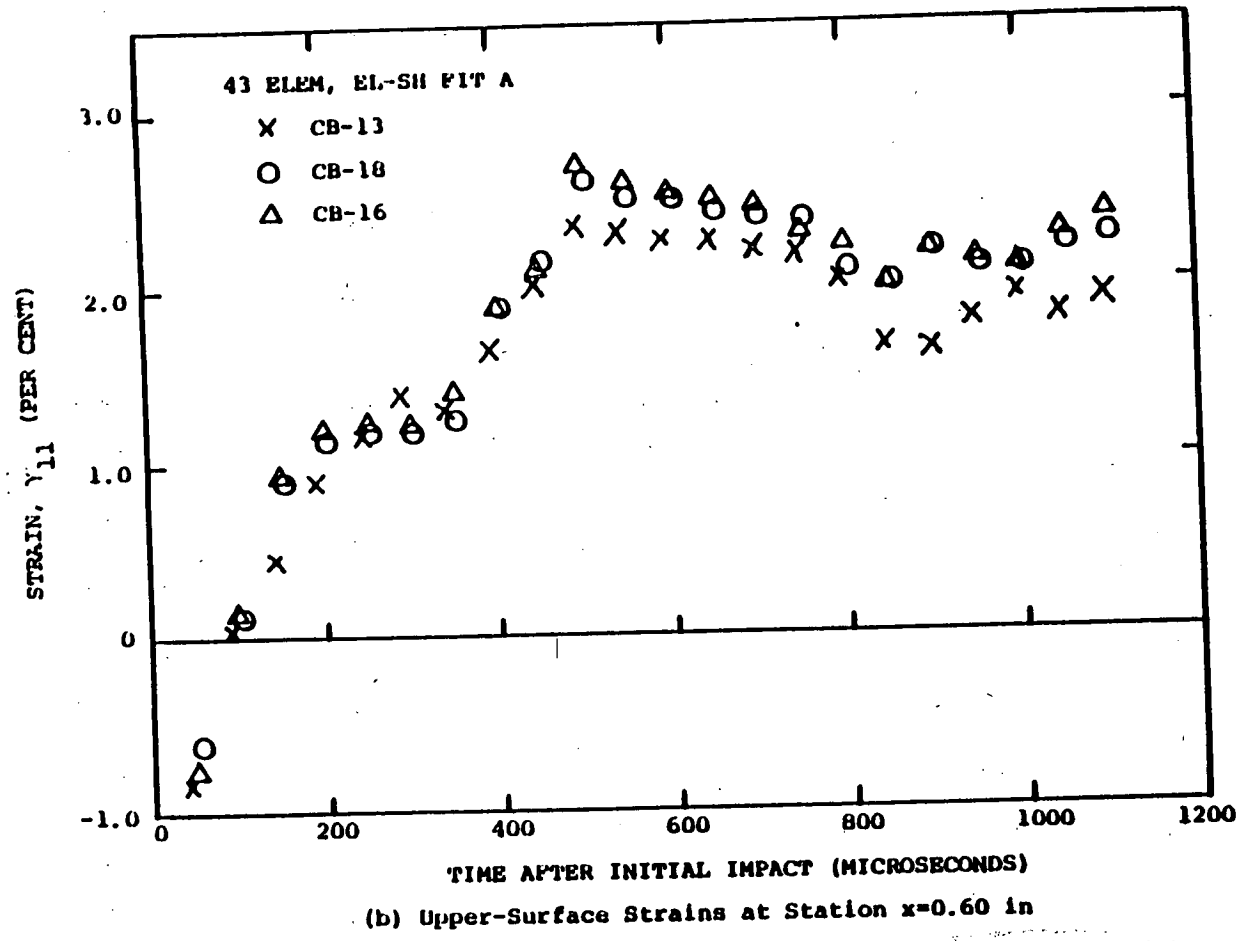

(b) Upper-Surface Strains at Station x=0.60 in

FIG. 16 CONTINUED (CB-13 VS. CB-18 VS. CB-16, 43 ELEM, EL-SH)

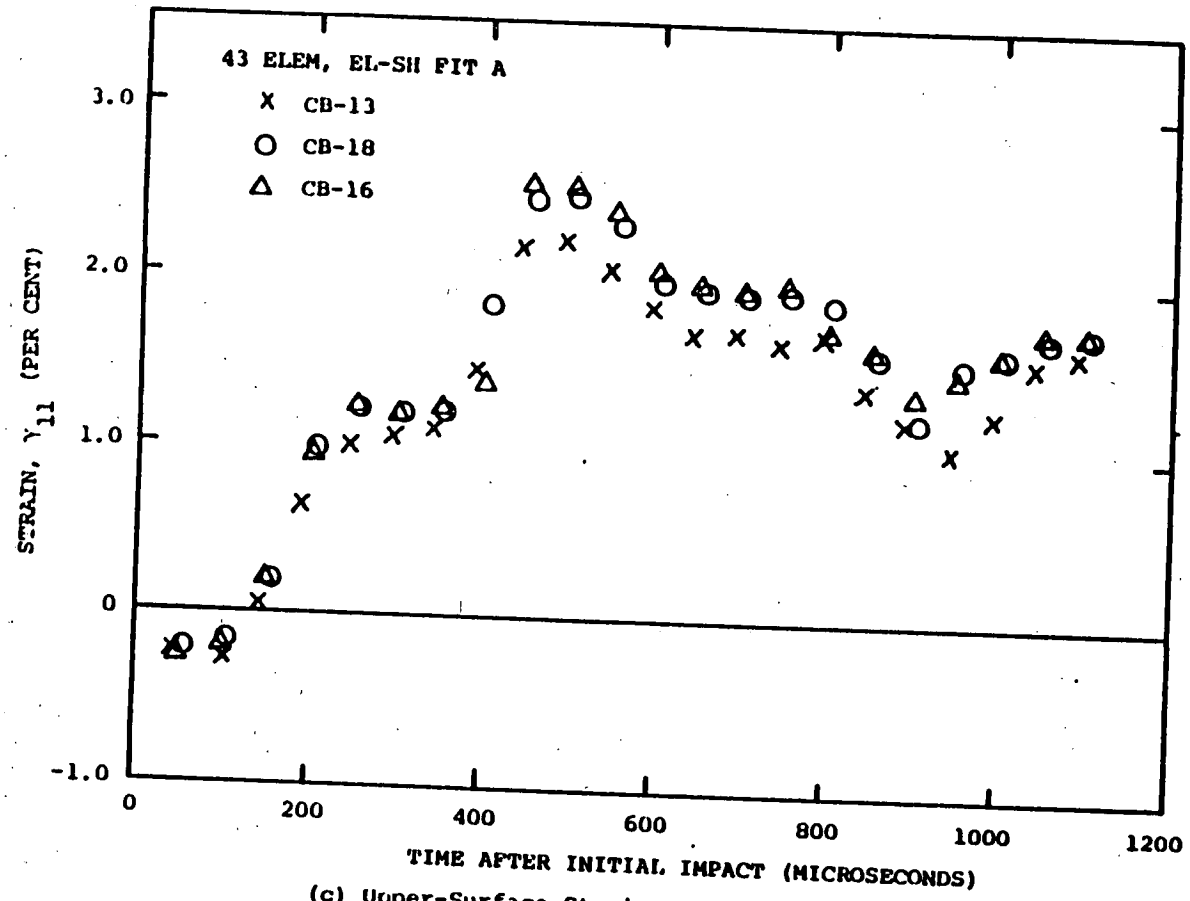

(c) Upper-Surface Strains at Station x=1.50 in

FIG. 16 CONTINUED (CB-13 VS. CB-18 VS. CB-16, ELEM, EL-SH)

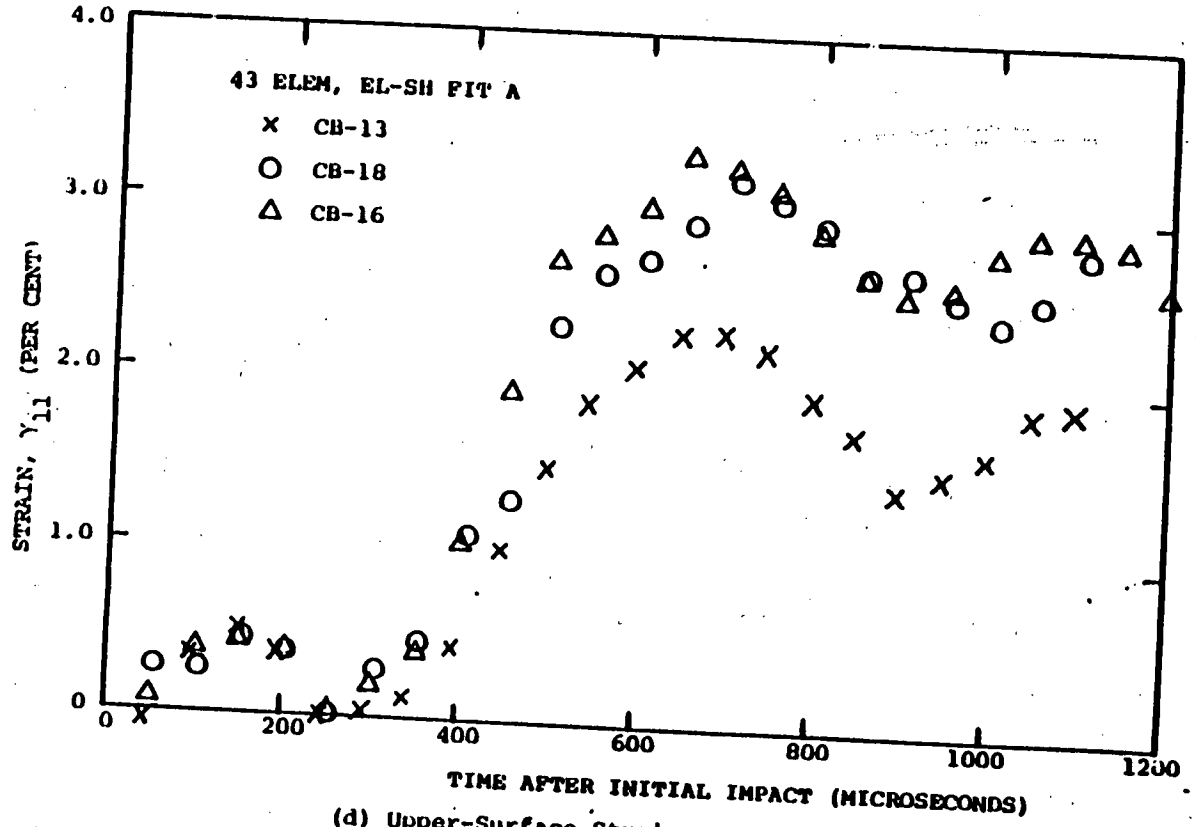

(d) Upper-Surface Strains at x=3.70 in

FIG. 16 CONCLUDED (CB-13 VS. CB-18 VS. CB-16, 43 ELEM, EL-SH)

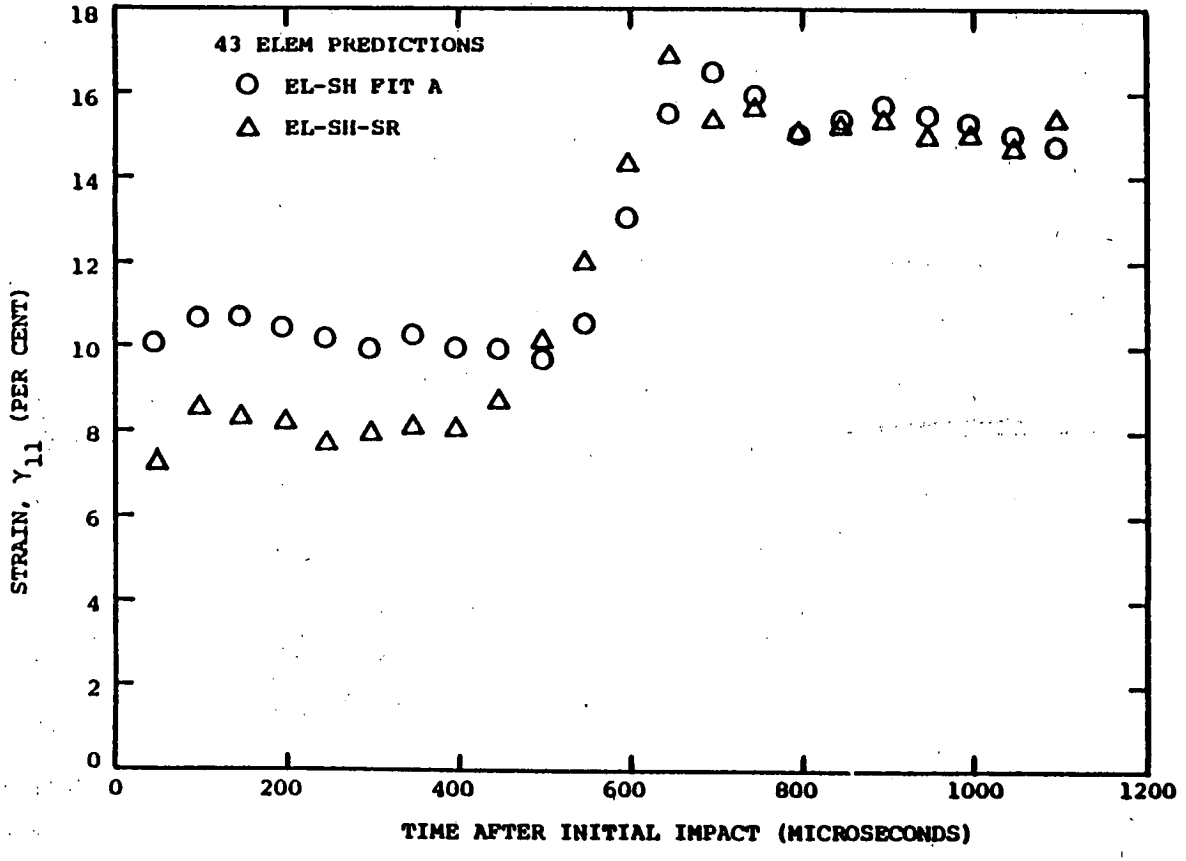

(a) Upper-Surface Strains at Station x=0

FIG. 17 COMPARISONS OF EL-SH VS. EL-SH-SR PREDICTIONS OF TRANSIENT STRAINS FOR STEEL-SPHERE-IMPACTED BEAM CB-16; INITIAL IMPACT VELOCITY=2870 IN/SEC

(b) Upper-surface station at station x=0.60 in. CONTINUED (CBT-6, FIG. 11 VS. EL-SII-SR, 43 ELEM)

FIG. 17

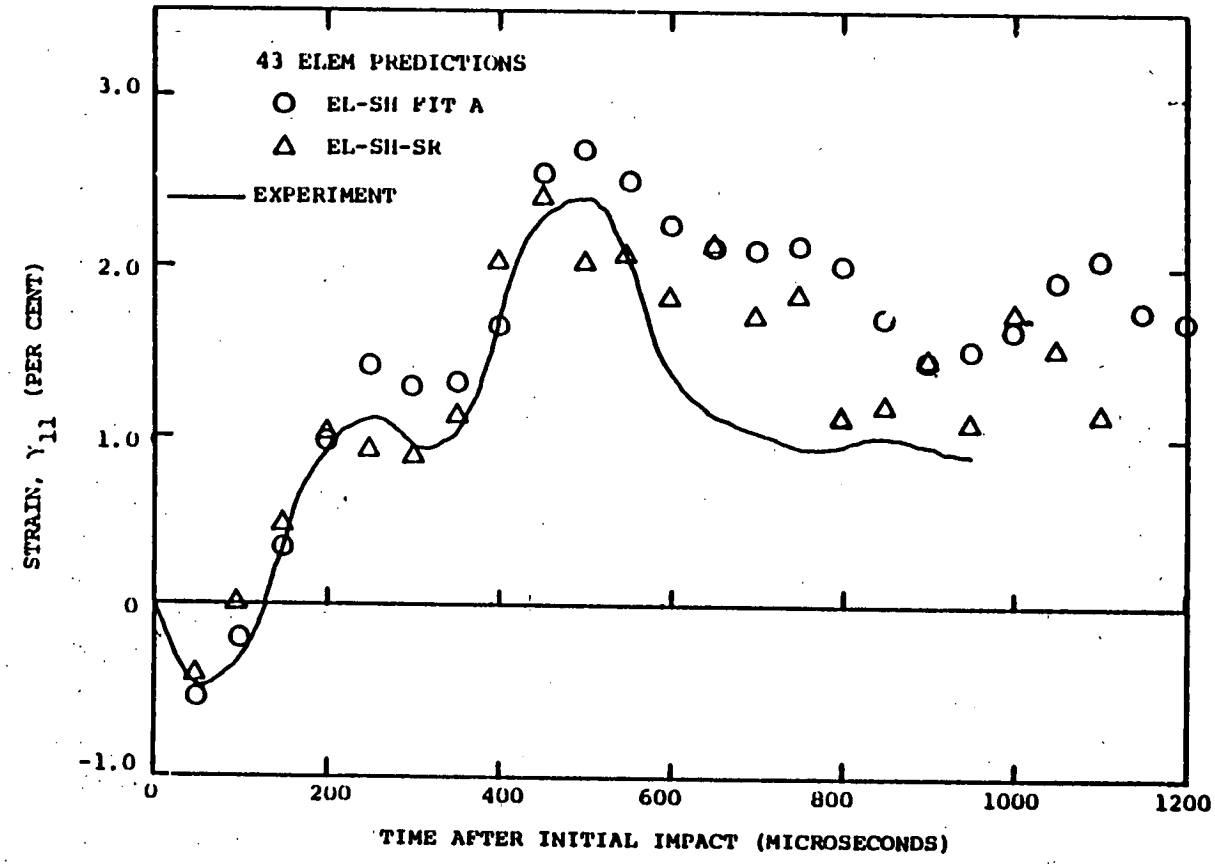

(c) Upper-Surface Strain at Station x=1.20 in

FIG. 17 CONTINUED (CB-16, EL-SH VS. EL-SH-SR, 43 ELEM)

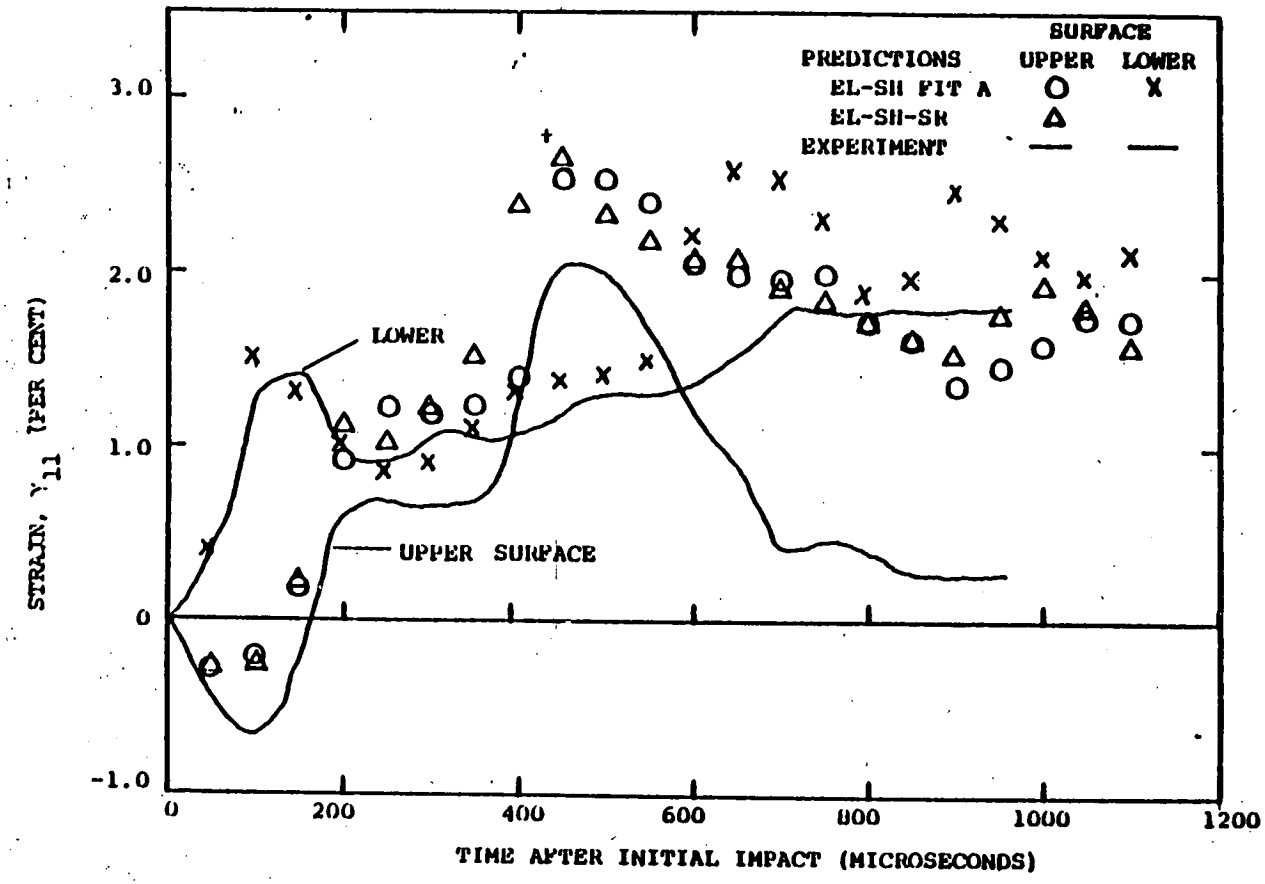

(d) Upper-Surface and Lower-Surface Strains at Station x=1.50 in

FIG. 17 CONTINUED (CB-16, EL-SH VS. EL-SH-SR, 43 ELEM)

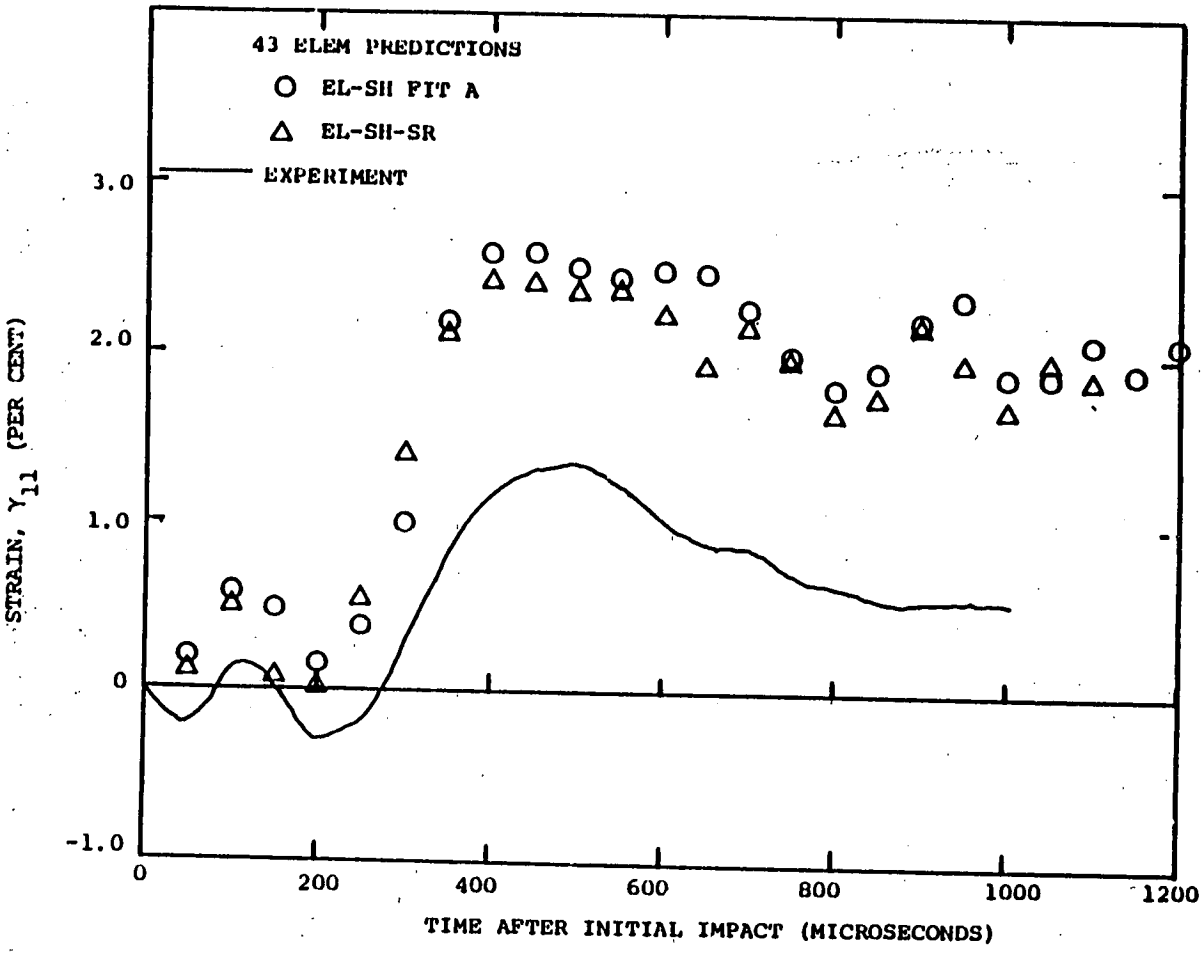

(g) Upper-Surface Strains at Station x=3.00 in

FIG. 17 CONTINUED (CB-16, EL-SH VS. EL-SH-SR, 43 ELEM)

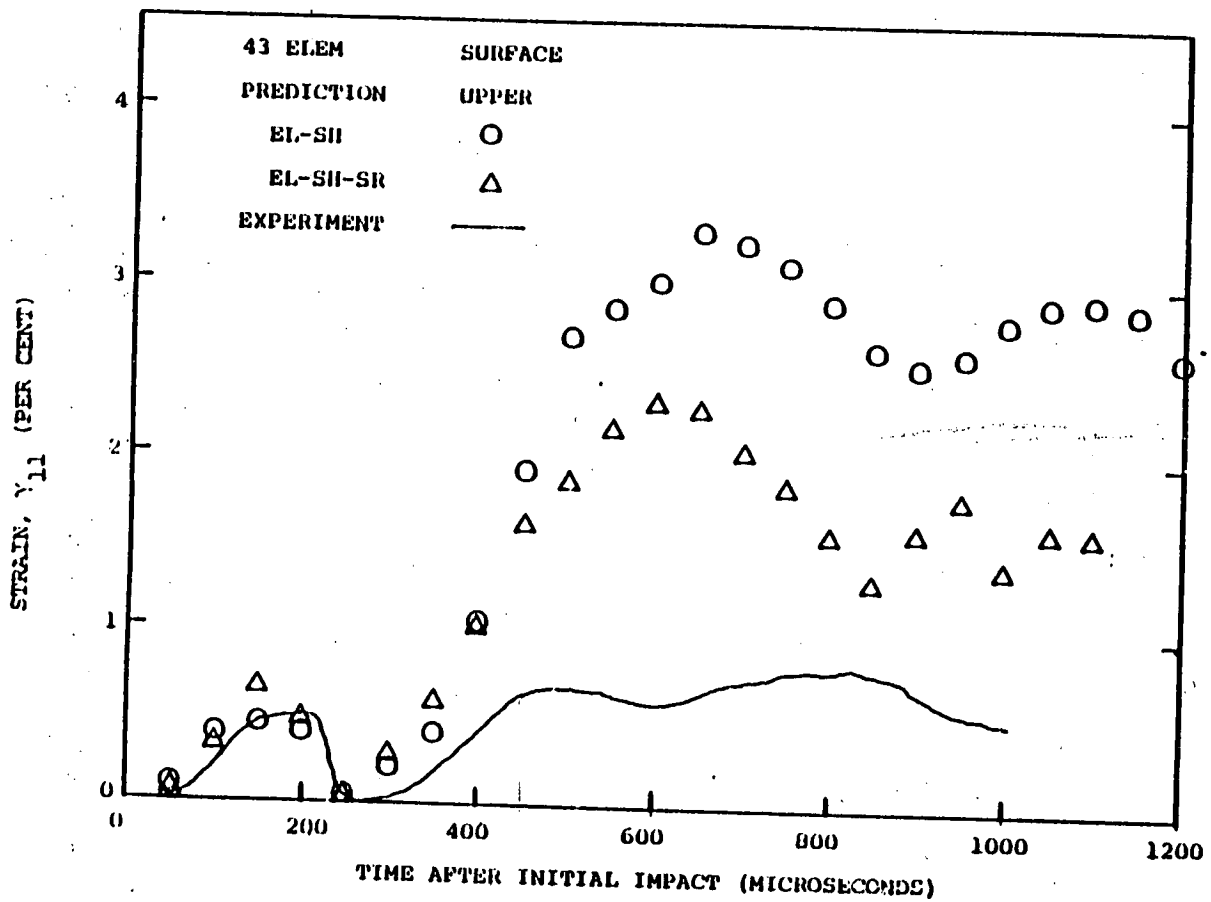

(f) Upper-Surface Strains at Station x=3.70 in

FIG. 17 CONCLUDED (CB-16, EL-SH VS. EL-SH-SR, 43 ELEM)

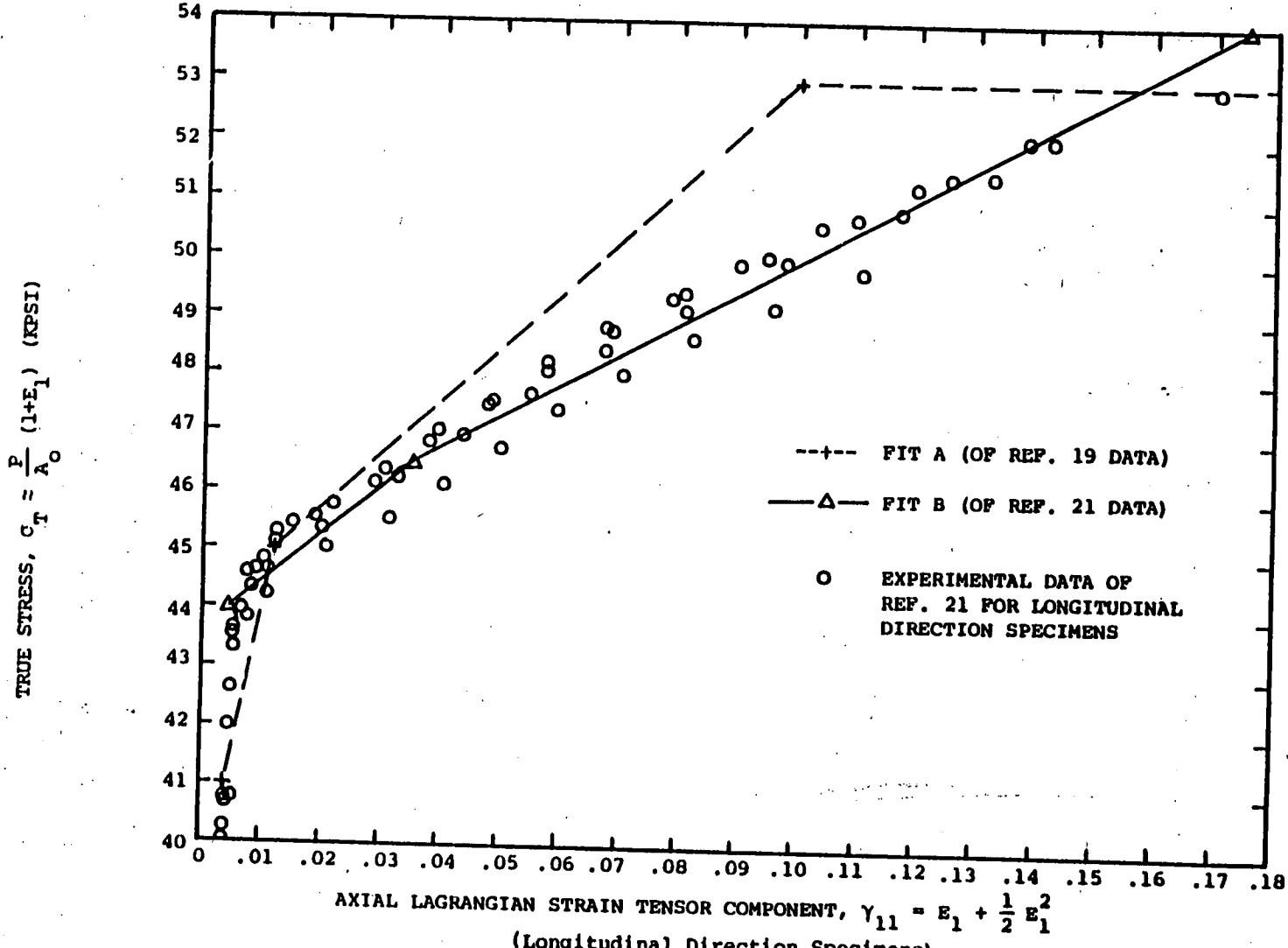

FIG. 18 TENSILE UNIAXIAL STATIC STRESS-STRAIN DATA FOR CIRCULAR CROSS-SECTION SPECIMENS OF 6061-T651 ALUMINUM PLATE STOCK: σ_T VS. γ_{11} OF REF. 21, AND DATA FITS A AND B

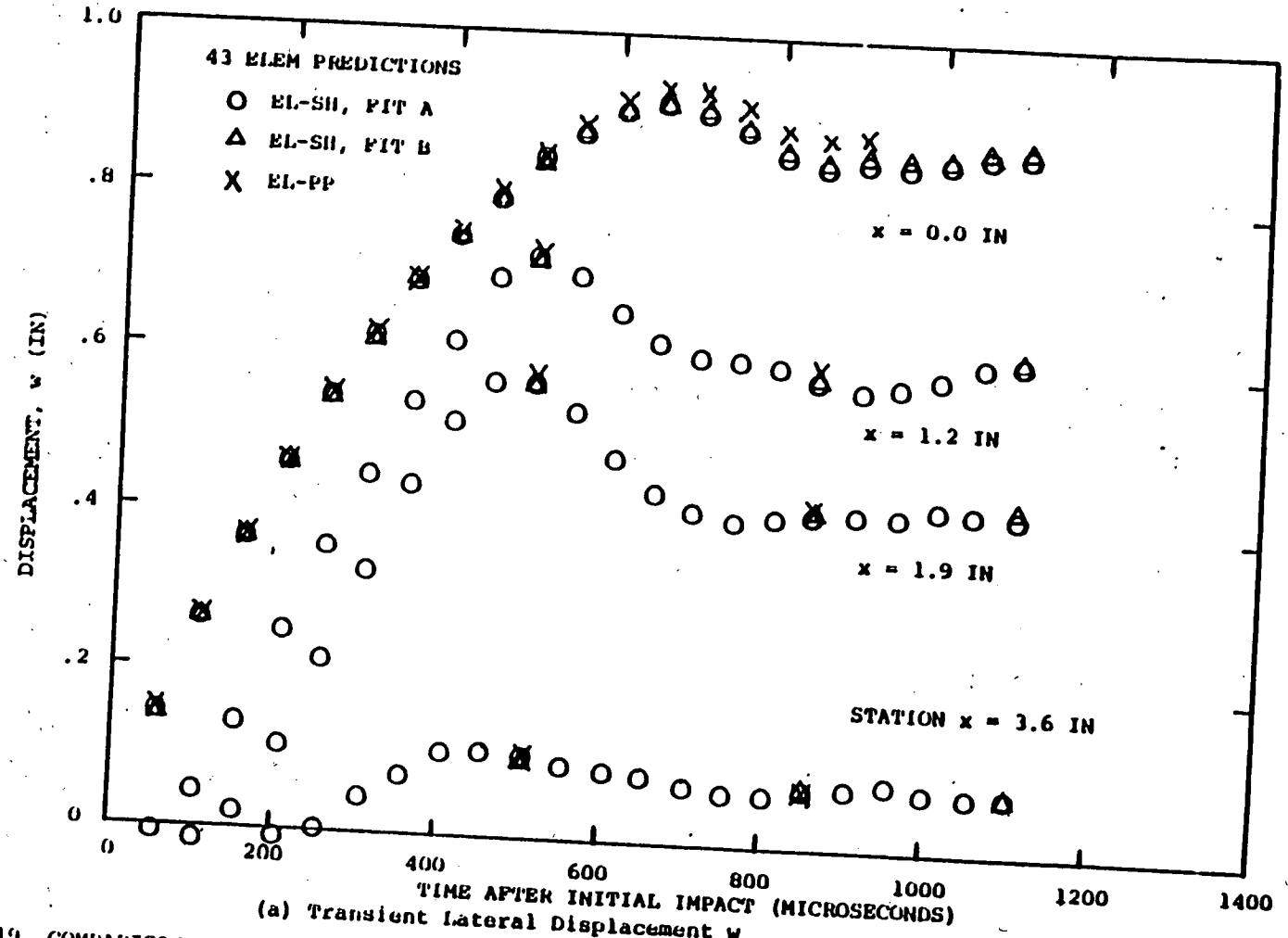

(a) Transient Lateral Displacement w

FIG. 19 COMPARISON OF 43-ELEMENT PREDICTIONS OF TRANSIENT RESPONSE OF STEEL-SPHERE-IMPACTED BEAM CB-18, USING STRESS-STRAIN APPROXIMATIONS EL-SH-FIT A VS. EL-SH-FIT B VS. EL-PP

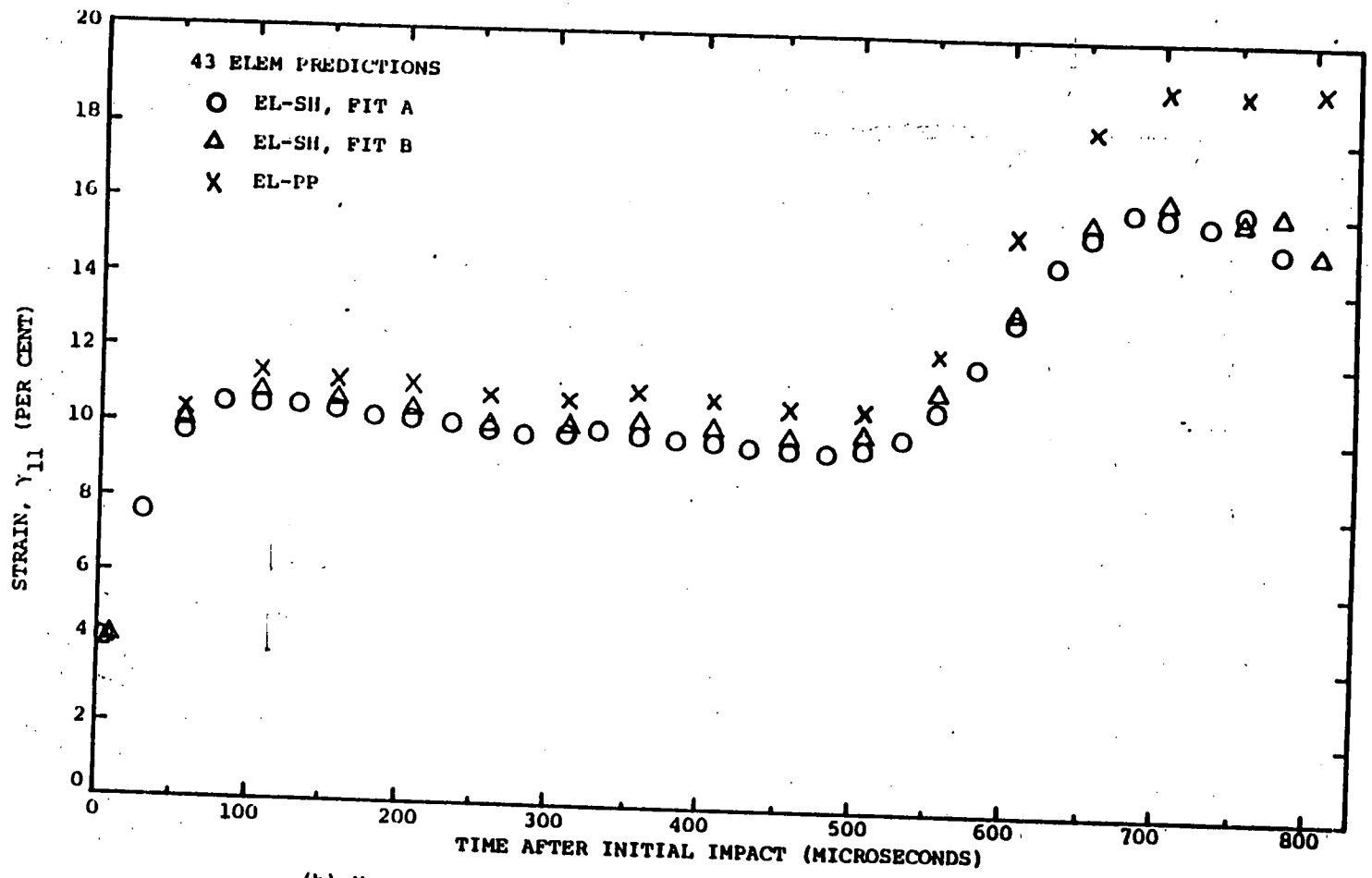

(b) Upper-Surface Strain at Station x=0

FIG. 19 CONTINUED (CB-18, EL-SH-FIT A VS. EL-SH-FIT B VS. EL-PP, 43 ELEM)

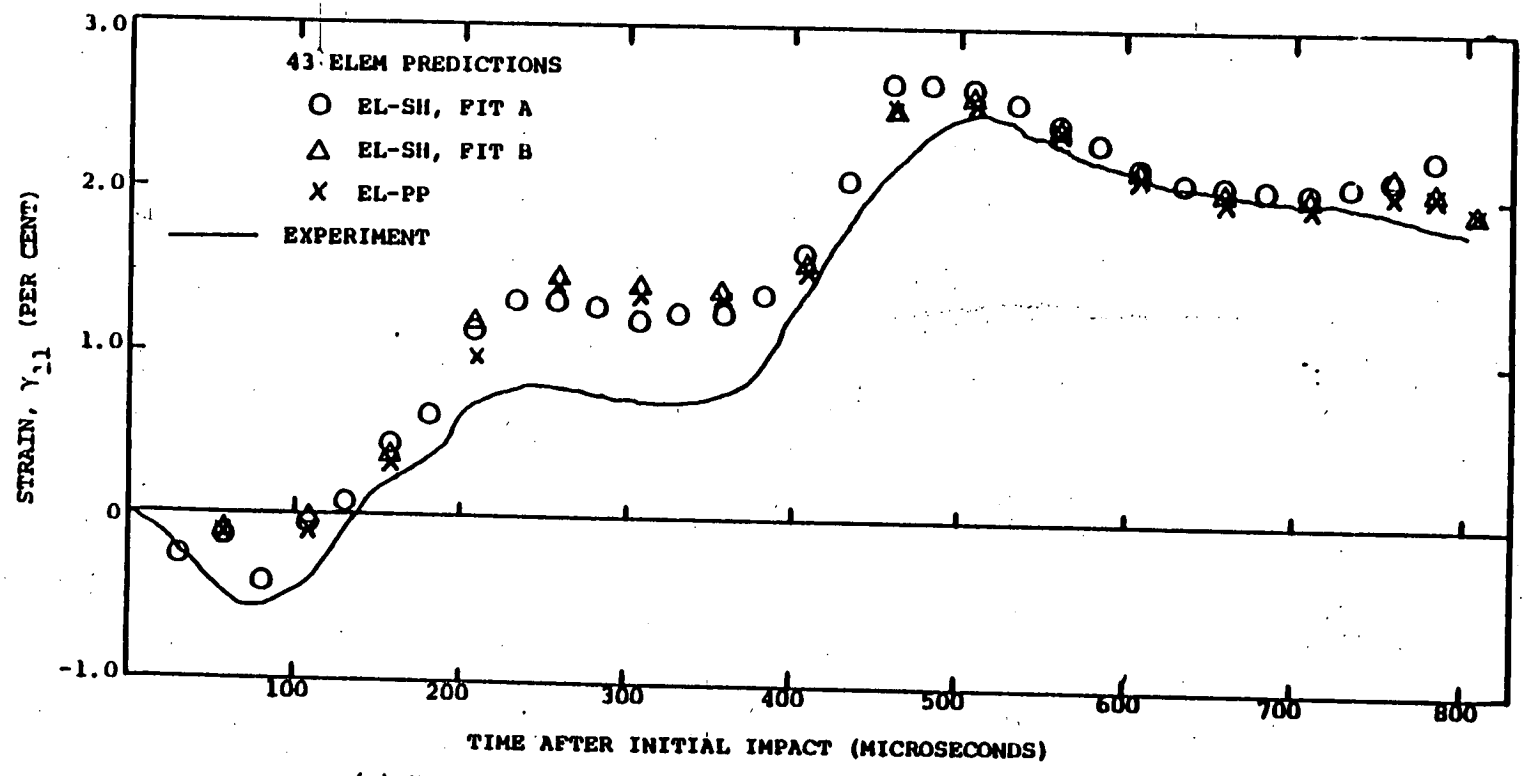

(c) Upper-Surface Strain at Station x=1.20 in

FIG. 19 CONCLUDED (CB-18, EL-SH-FIT A VS. EL-SH-FIT B VS. EL-PP, 43 ELEM)

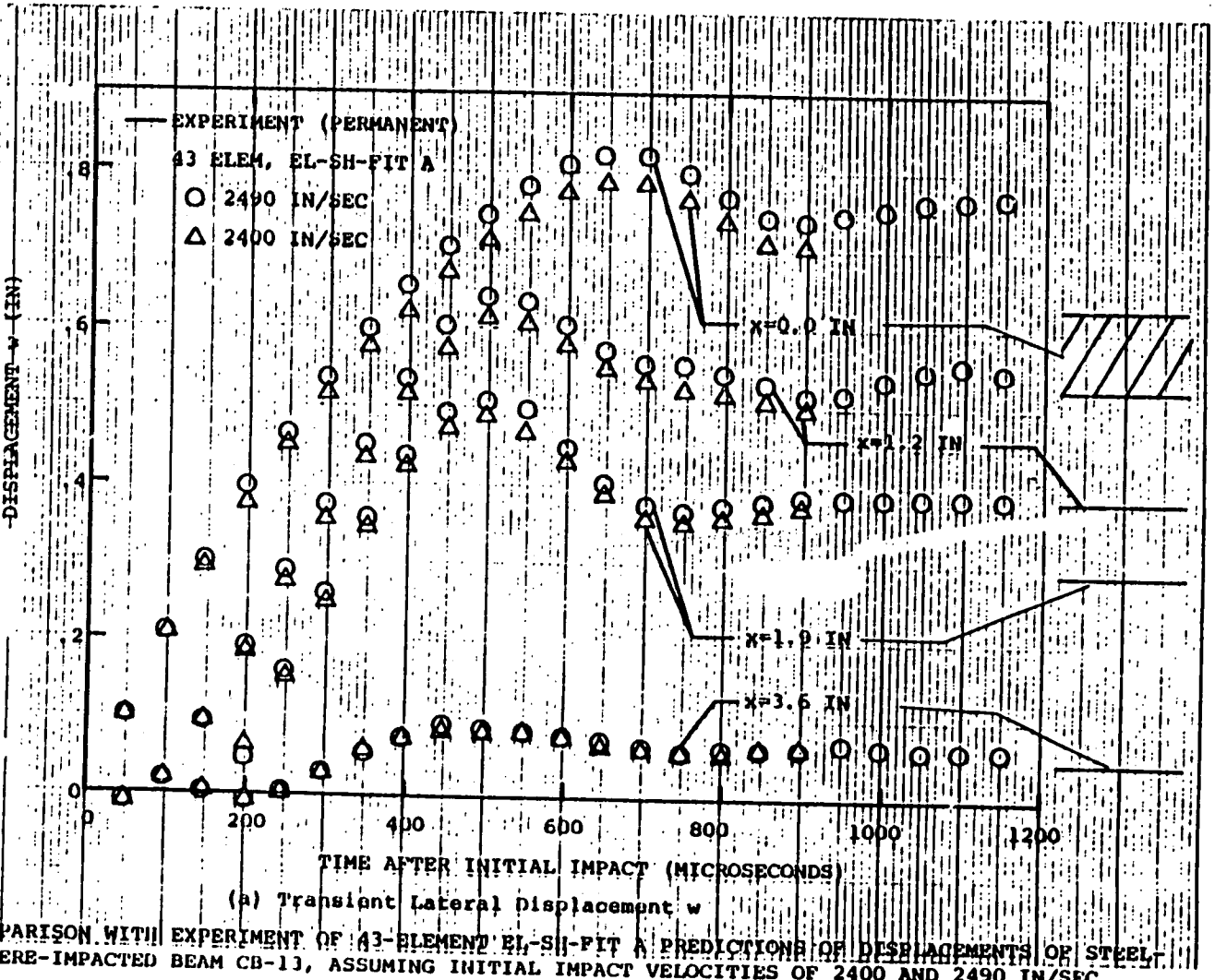

(a) Transient Lateral Displacement w

FIG. 20 COMPARISON WITH EXPERIMENT OF 43-ELEMENT EL-SH-FIT A PREDICTIONS OF DISPLACEMENTS OF STEEL-SPHERE-IMPACTED BEAM CB-13, ASSUMING INITIAL IMPACT VELOCITIES OF 2400 AND 2490 IN/SEC

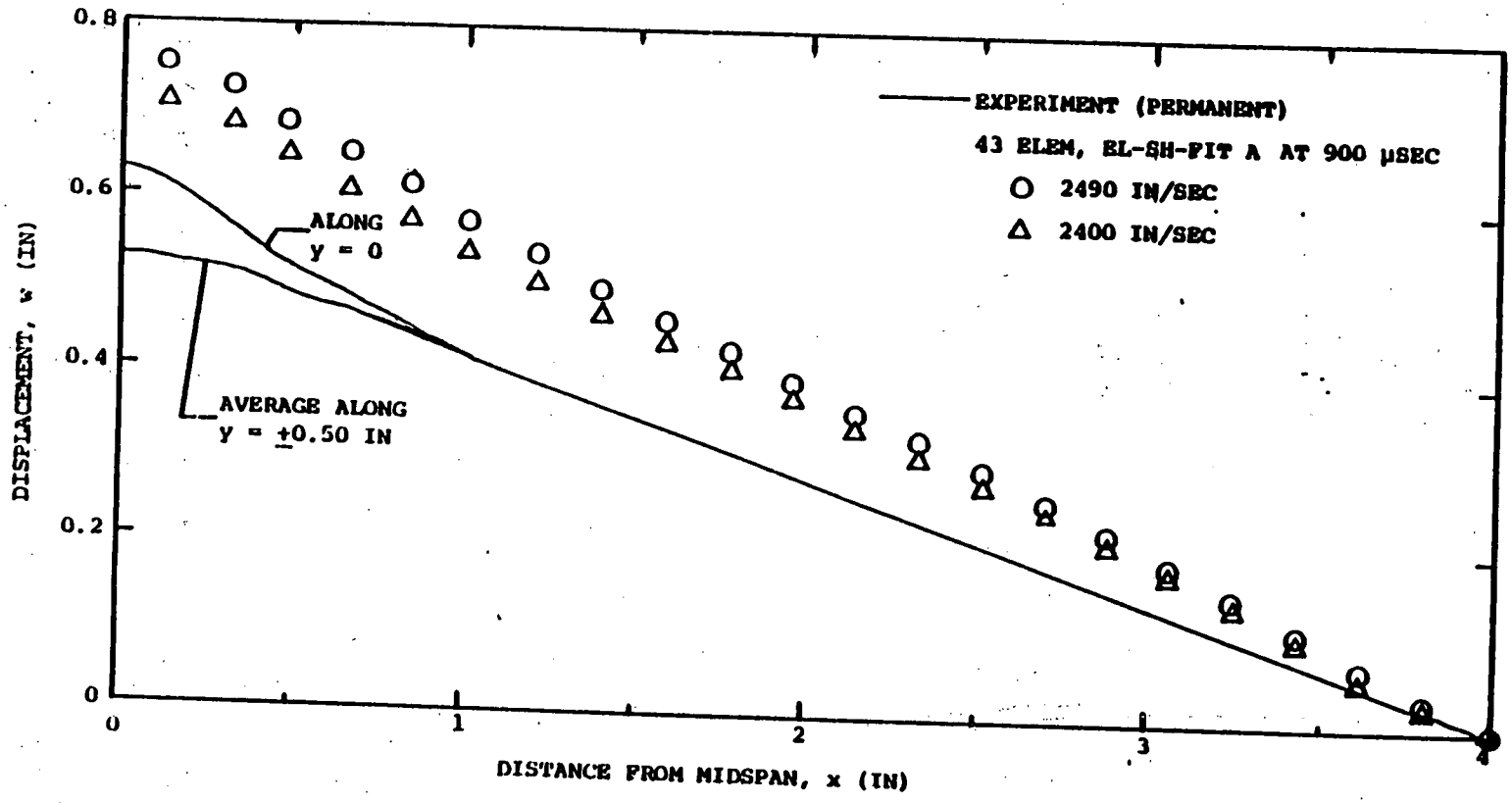

(b) Permanent Deflection

FIG. 20 CONCLUDED (CB-13, 43 ELEM, EL-SH-FIT A, IMPACT VELOCITY 2400 VS. 2490 IN/SEC)

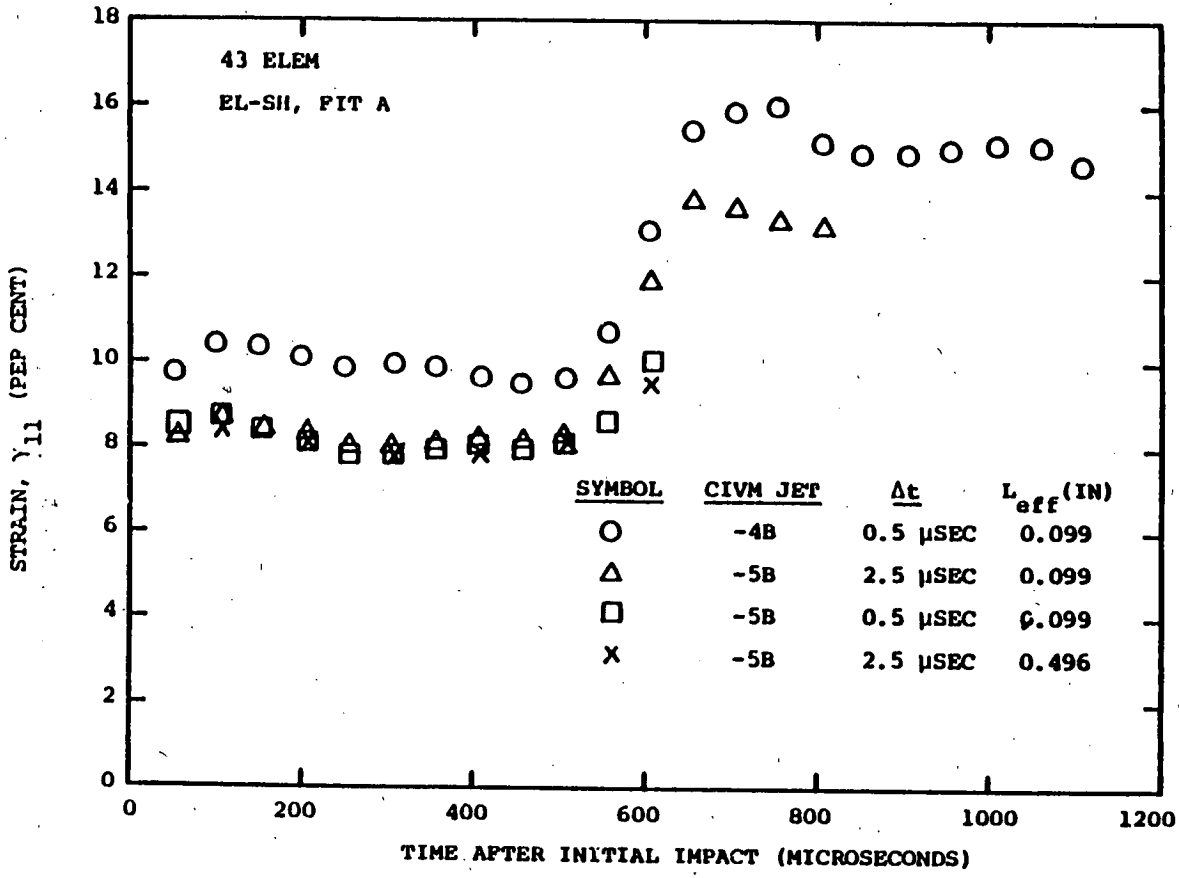

(a) Upper-Surface Strain at Station x=0

FIG. 21 COMPARISON OF CIVM-JET 4B WITH CIVM-JET 5B PREDICTIONS OF THE TRANSIENT STRAINS FOR STEEL-SPHERE-IMPACTED BEAM CB-18

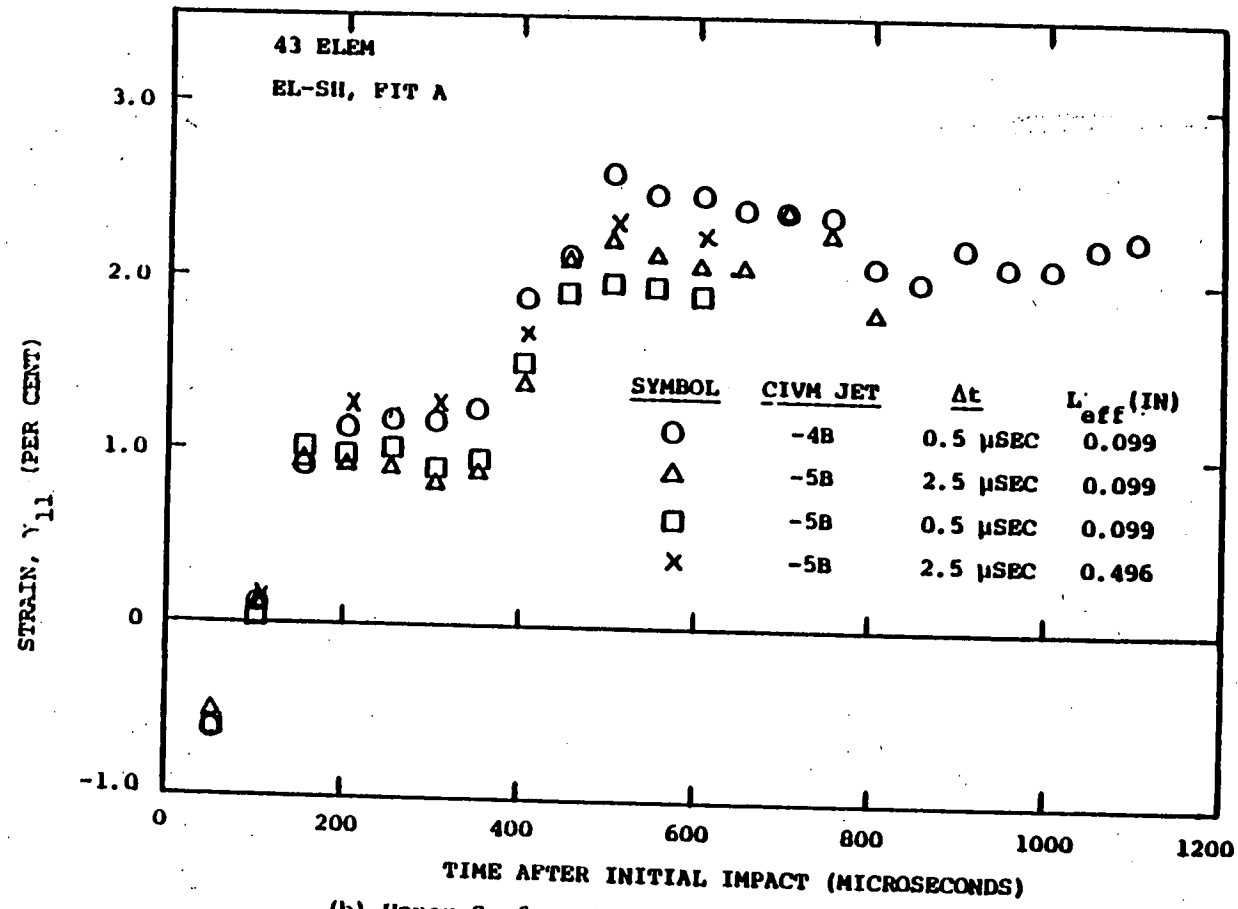

(b) Upper-Surface Strain at Station x=0.60 in

FIG. 21 CONTINUED (CB-18; CIVM-JET 4B VS. CIVM-JET 5B; 43 ELEM, EL-SH-FIT A)

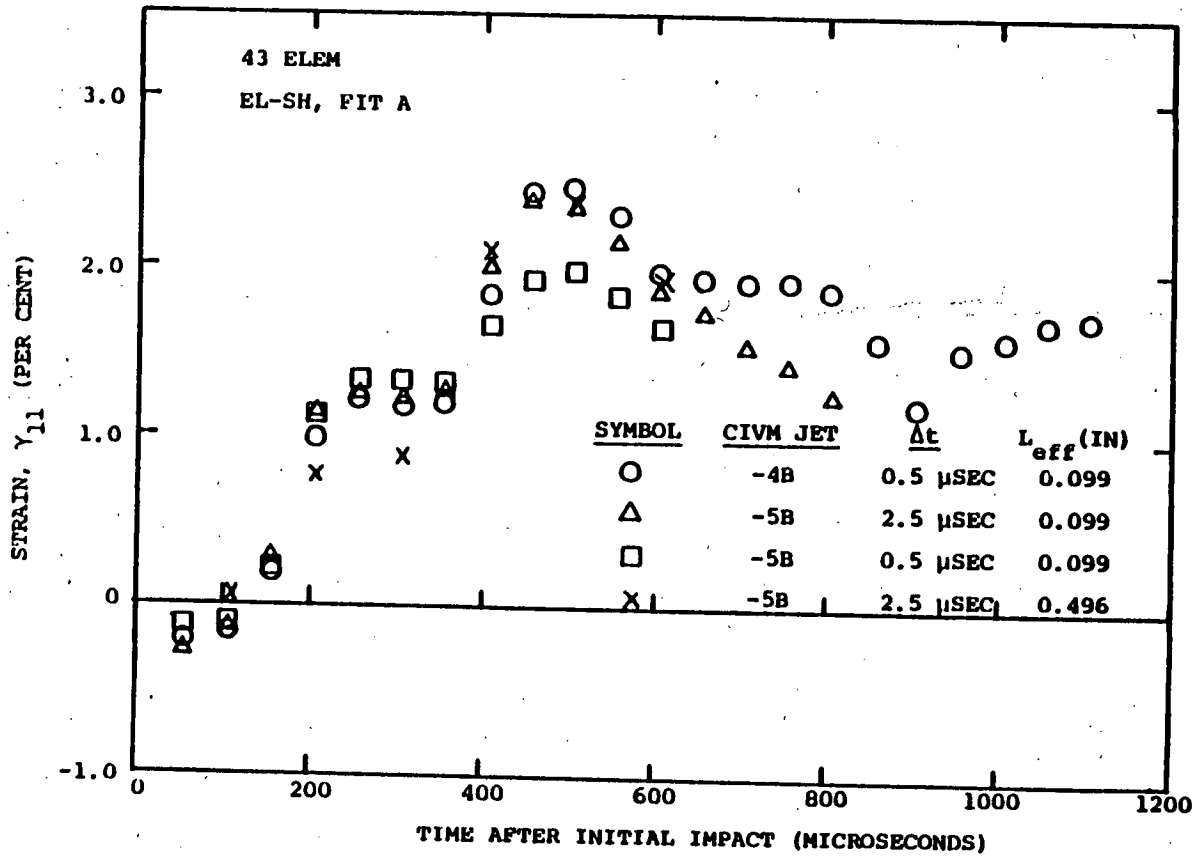

(c) Upper-Surface Strain at Station x=1.50 in

FIG. 21 CONTINUED (CB-18; CIVM-JET 4B VS. CIVM-JET 5B; 43 ELEM, EL-SH-FIT A)

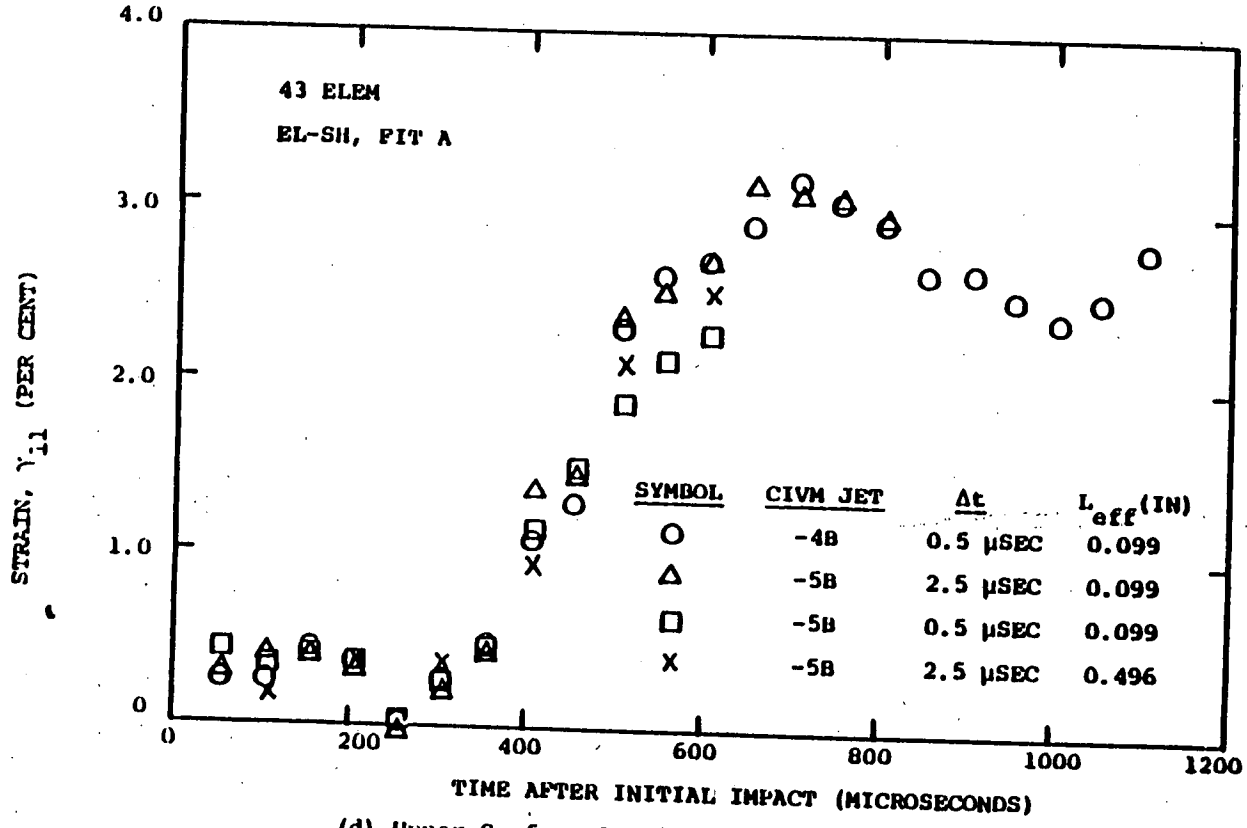

(d) Upper-Surface Strain at Station x=3.70 in

FIG. 21 CONCLUDED (CB-18; CIVM-JET 4B VS. CIVM-JET 5B; 43 ELEM, EL-SH-FIT A)

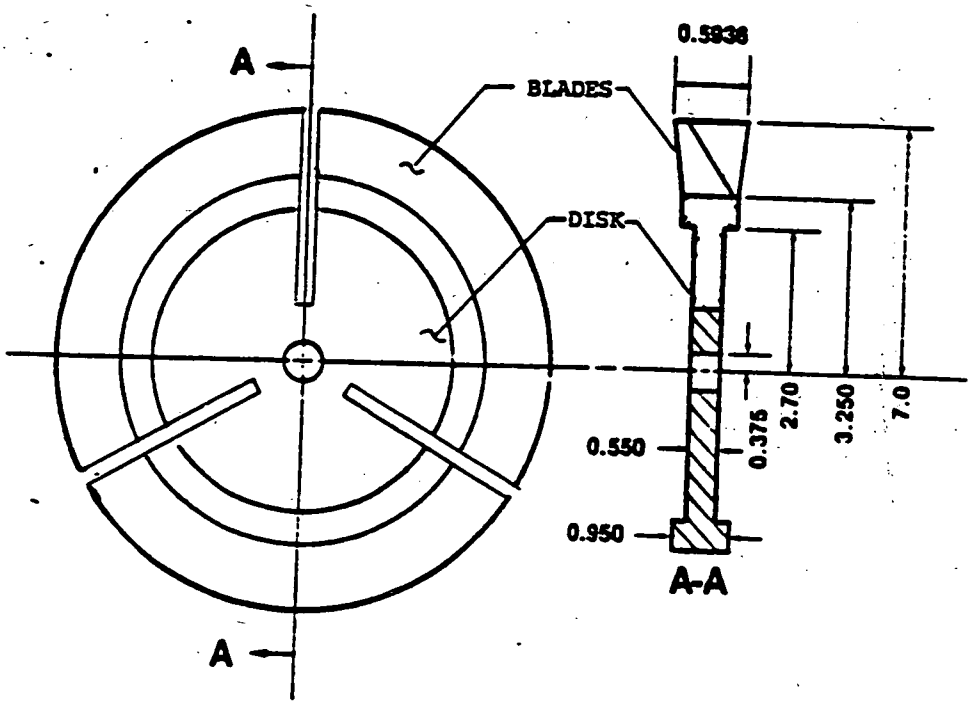

DISK MATERIAL : A-286

BLADE MATERIAL: SEL-15

(a) Schematic of Rotor Modified for a Three-Fragment Burst

FIG. 22 GEOMETRY AND VIEWS OF T58 TURBINE ROTOR TRI-HUB-BURST FRAGMENTS

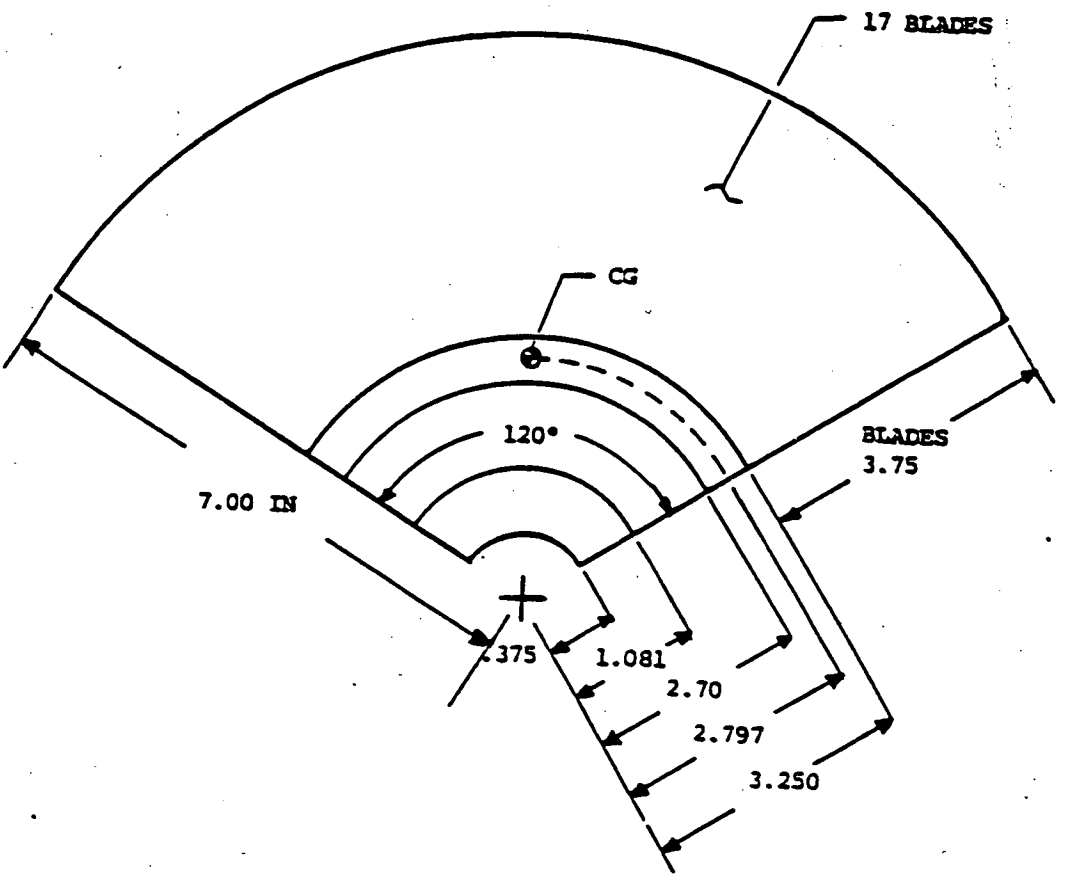

(b) Sketch of a T58 Turbine Rotor Tri-Hub Burst Fragment

FIG. 22 CONTINUED

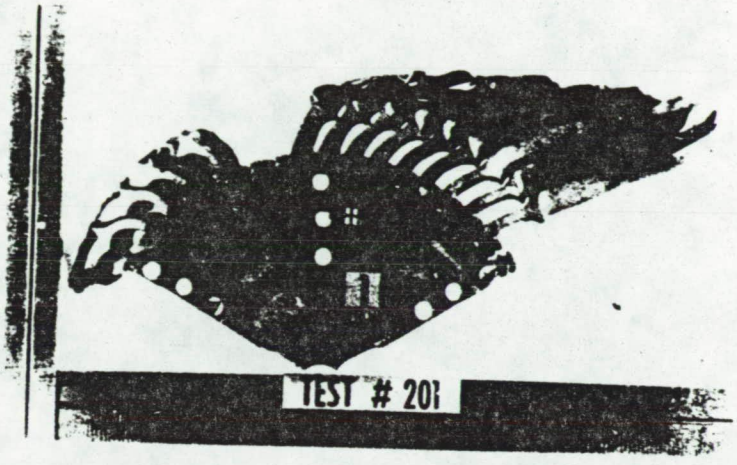

(c) Photograph of Post-Test T58 Turbine Rotor Tri-Hub Burst Fragment

FIG. 22 CONCLUDED

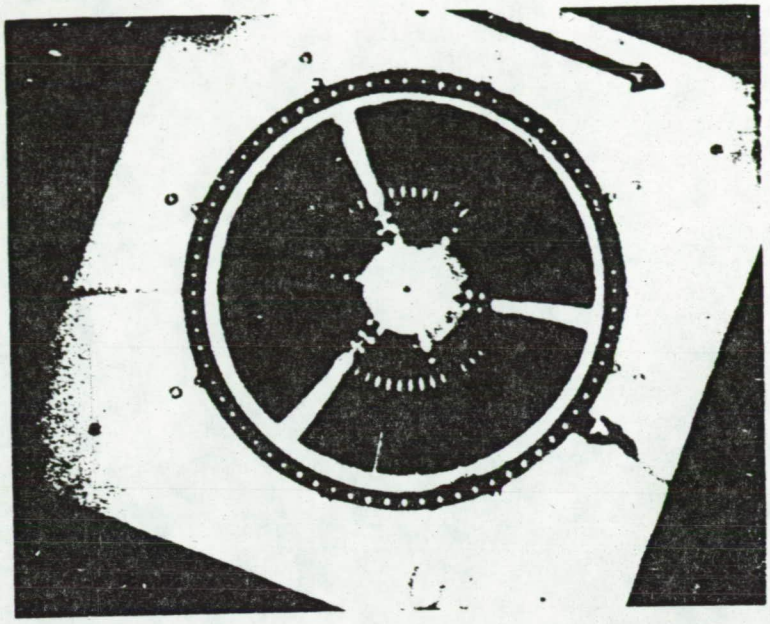

(a) Pre-Test

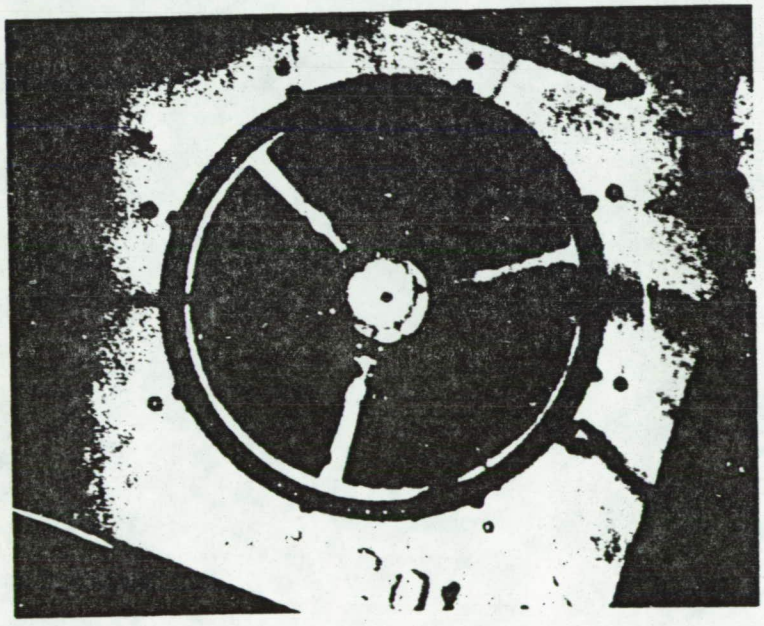

(b) After Rotor Burst but Before Impact

FIG. 23 DYNAFAX PHOTOGRAPHS OF T58 TRI-HUB ROTOR-BURST ATTACK AGAINST A STEEL CONTAINMENT RING IN NAPTC TEST 201

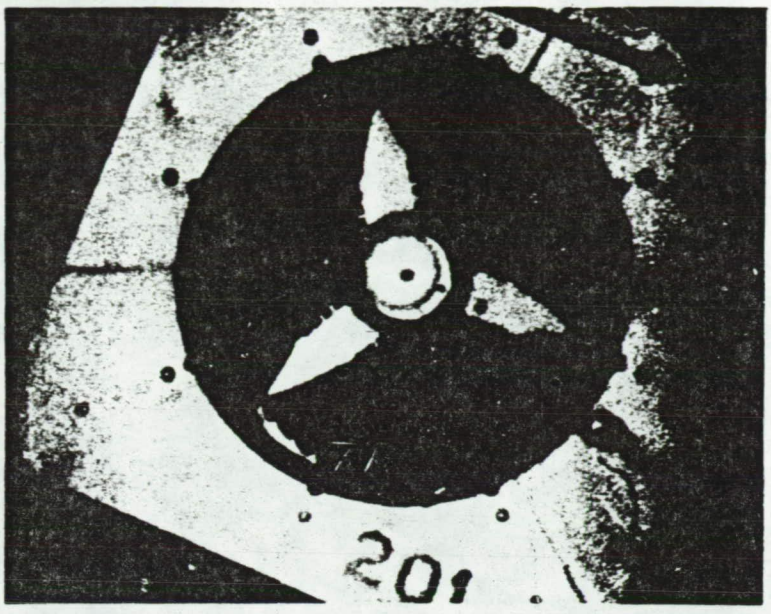

(c) Time After Initial Impact, TAII=200 μsec

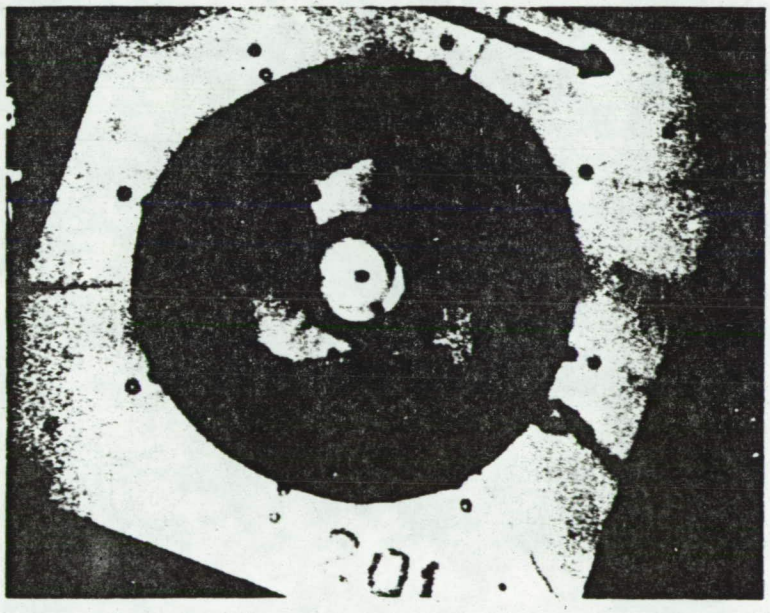

(d) TAII=514 μsec

FIG. 23 CONTINUED

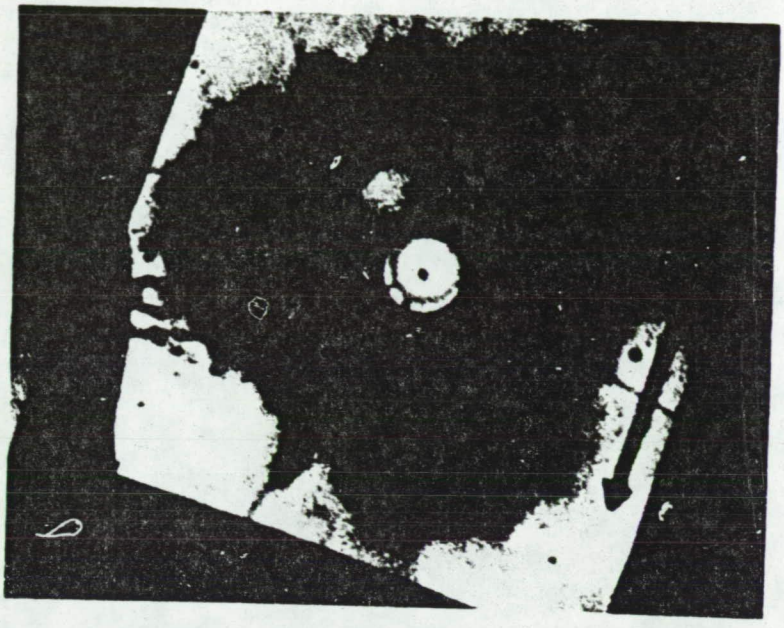

(e) TAII=1258 μsec

FIG. 23 CONCLUDED

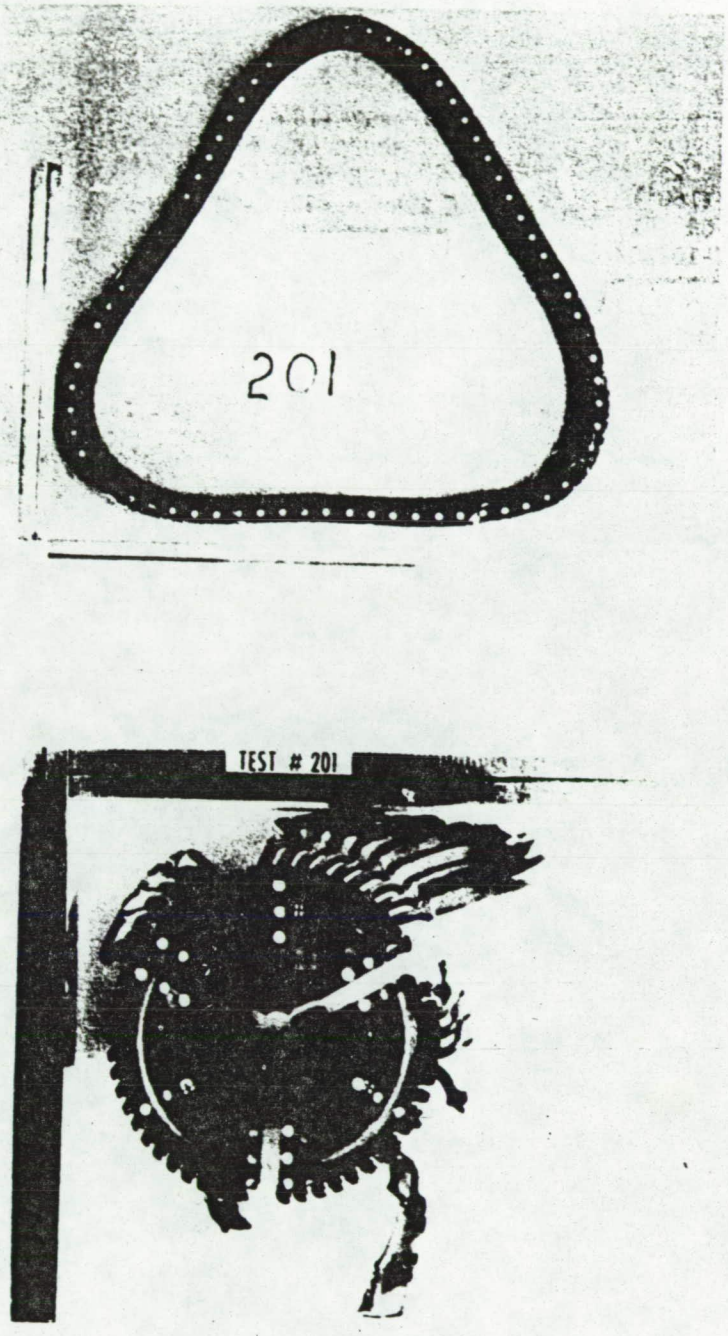

FIG. 24 POST-TEST VIEWS OF THE CONTAINMENT RING AND THE ROTOR-BURST FRAGMENTS IN NAPTC TEST 201

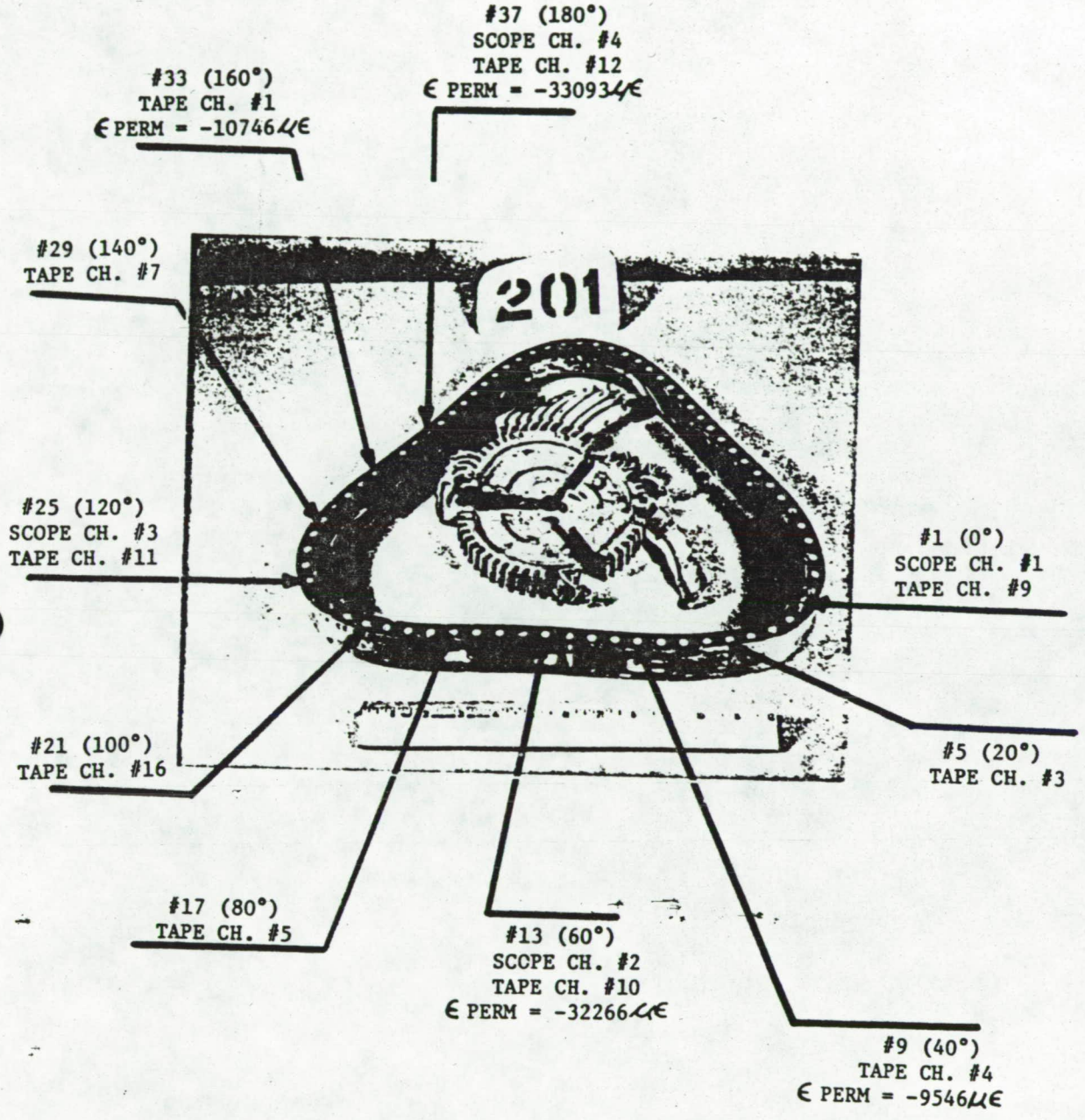

FIG. 25 POST-TEST 201 CONFIGURATION AND LOCATIONS OF STRAIN GAGES

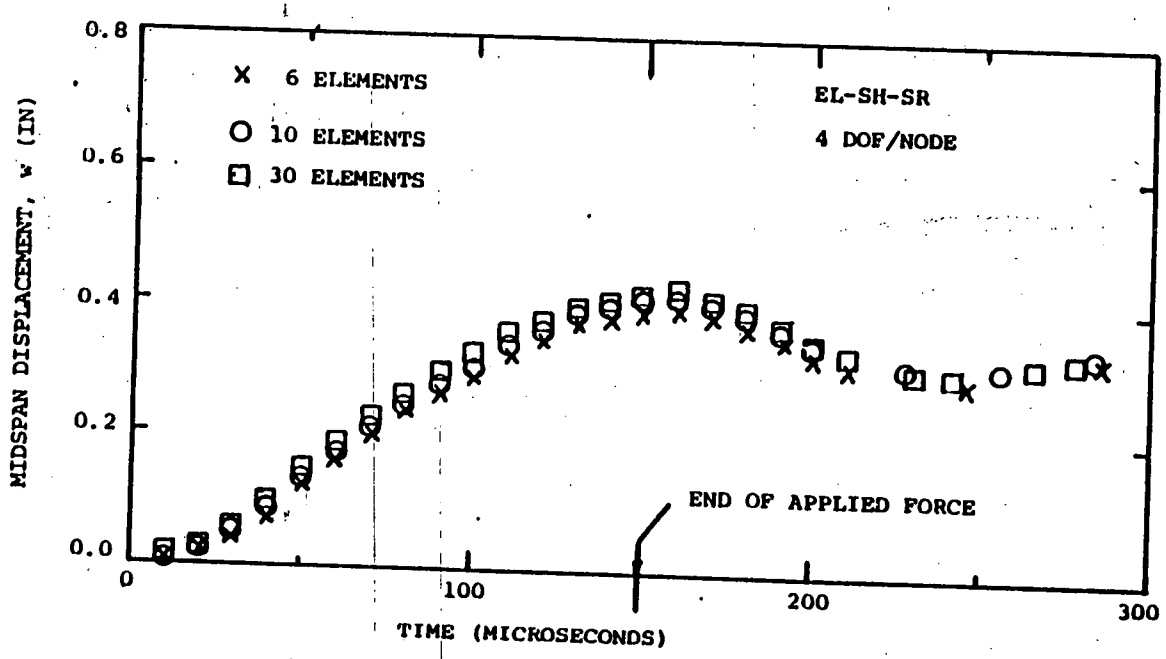

(a) Midspan Radial Displacement w

FIG. 26 EFFECT OF THE NUMBER OF EQUAL-LENGTH ELEMENTS ON THE PREDICTED TRANSIENT RESPONSE OF A 60-DEGREE-ARC CIRCULAR RING WITH BOTH ENDS PINNED-FIXED AND SUBJECTED AT MIDSPAN TO A CONCENTRATED RADIALLY-OUTWARD STEP-FUNCTION LOAD OF 7000 POUNDS WITH A 150 MICROSECOND DURATION

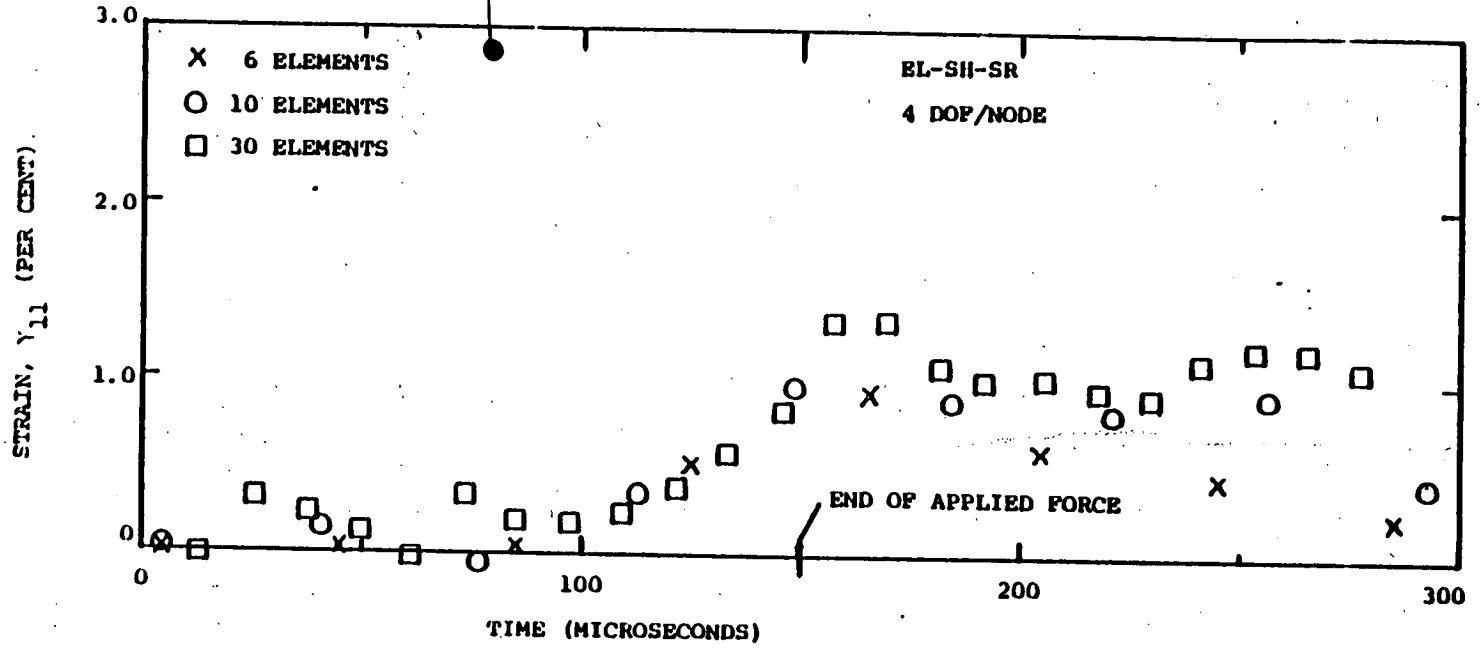

(b) Outer-Surface Strain at 15 Degrees from Midspan

FIG. 26 CONCLUDED (PINNED-FIXED 60-DEGREE CIRCULAR-ARC RING)

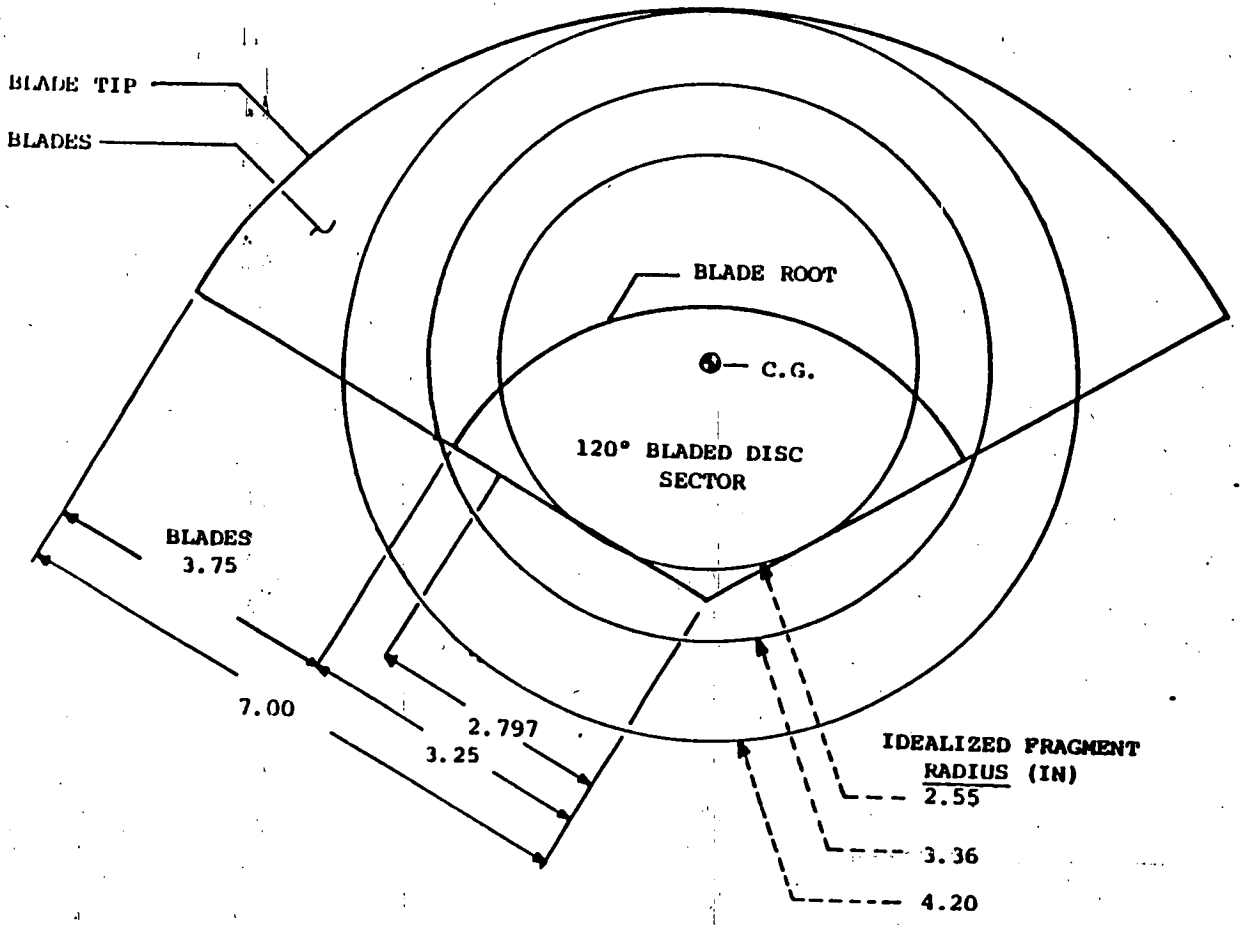

FIG. 27 SCHEMATIC OF UNDEFORMED TRI-HUB T58 ROTOR BURST FRAGMENT WITH IDEALIZED FRAGMENT-SIZE CHOICES

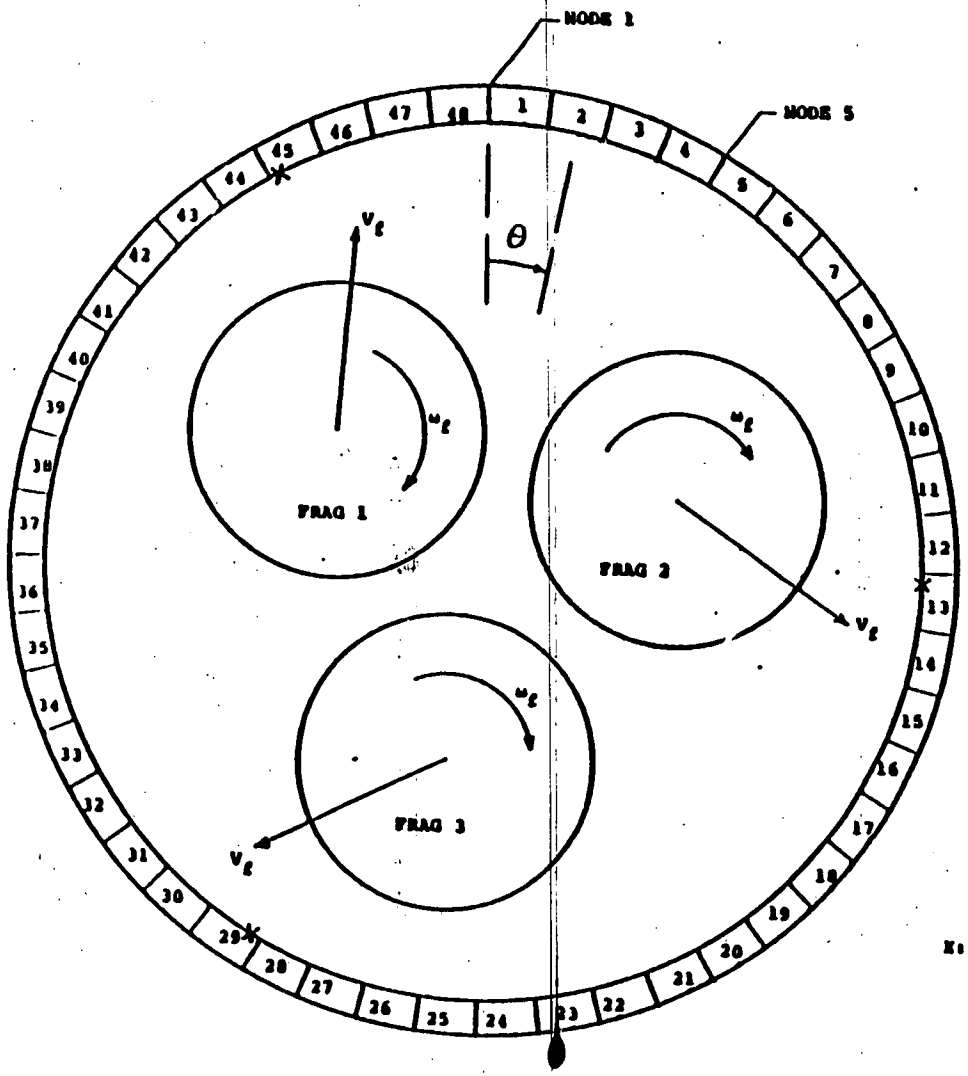

4130 STEEL RING

INNER RADIUS = 7.50 IN
THICKNESS = 0.625 IN
AXIAL LENGTH = 1.50 IN

FINITE-ELEMENT ANALYSIS

48 EQUAL ELEMS (FULL RING)
4 DOF/NODE
EL-SH-SH

FRAGMENTS: 3 EQUAL CIRCULAR AT 120-DEG. SPACING

FOR EACH FRAGMENT

RADIUS = 2.555 IN
MASS = 0.009395 $(LB\text{-}SEC^2)/IN$
MASS MOM. INER. = 0.0666 $IN\text{-}LB\text{-}SEC^2$
TRANSL. VEL., V_f = 5016.7 IN/SEC
ROT. VEL., ω_f = 2079.6 RAD/SEC
INITIAL KINETIC ENERGY
TRANSLATIONAL = 158,922 IN-LB
ROTATIONAL = 144,018 IN-LB
TOTAL = 302,940 IN-LB

X: POINT OF INITIAL IMPACT

FIG. 28 GEOMETRIC, TEST, AND MODELING DATA FOR THE 4130 STEEL CONTAINMENT RING SUBJECTED TO TRI-HUB T58 ROTOR BURST IN NAPTC TEST 201

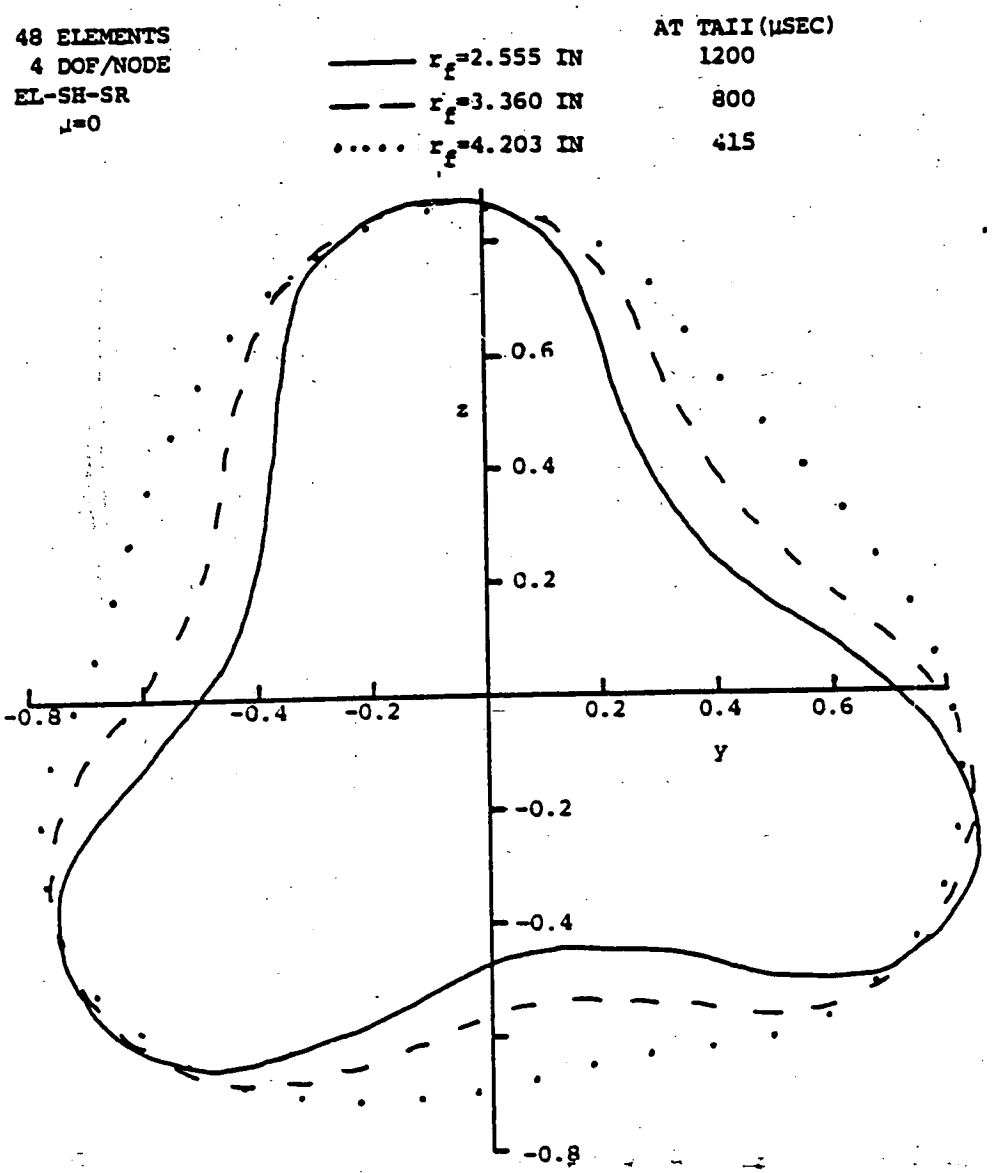

(a) Extreme Deformed Ring Configuration

FIG. 29 THE EFFECTS OF IDEALIZED FRAGMENT SIZE ON THE PREDICTED EXTREME RESPONSE OF THE STEEL CONTAINMENT RING IN NAPTC TEST 201

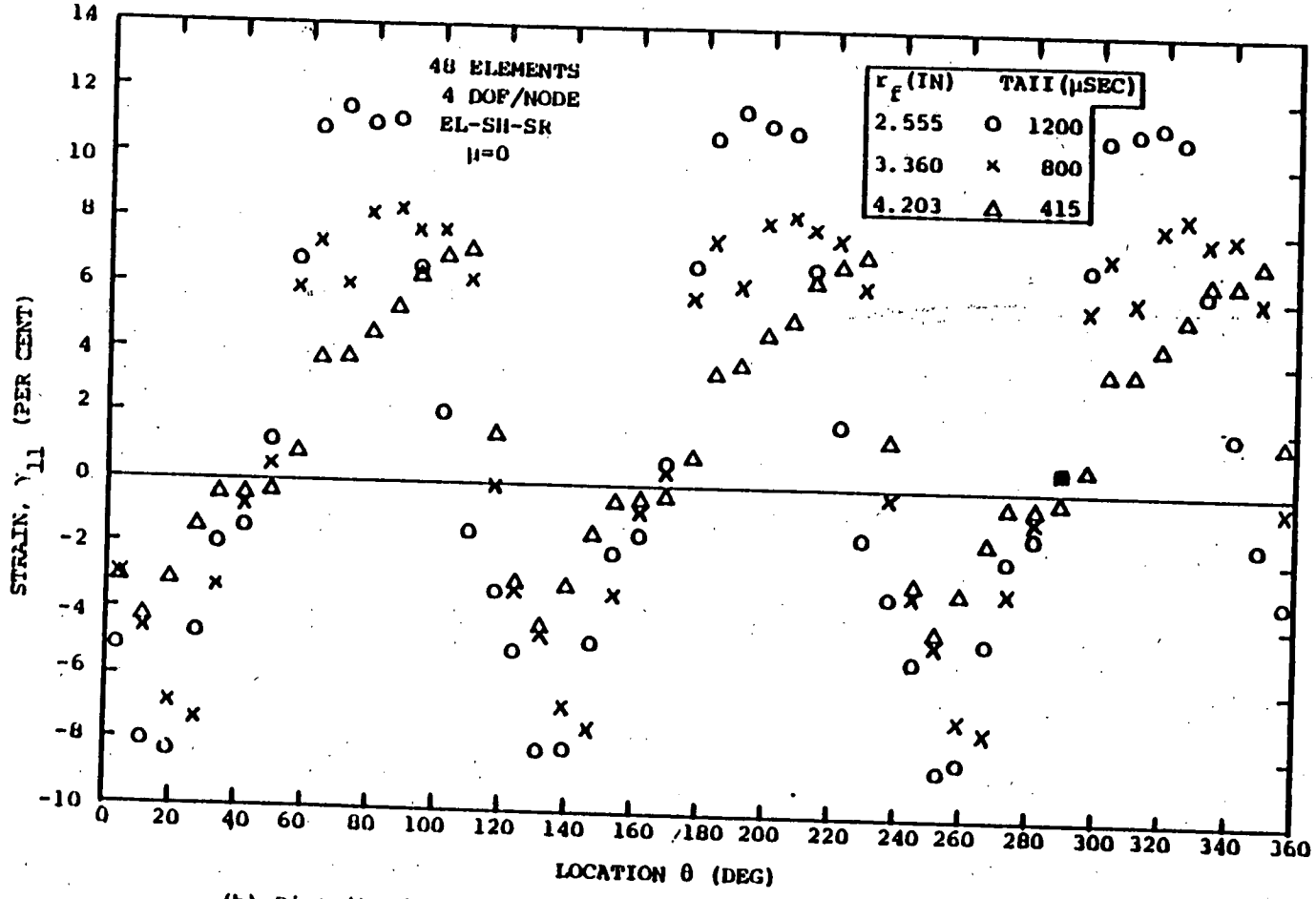

(b) Distribution of Extreme Outer-Surface Circumferential Strain

FIG. 29 CONCLUDED.

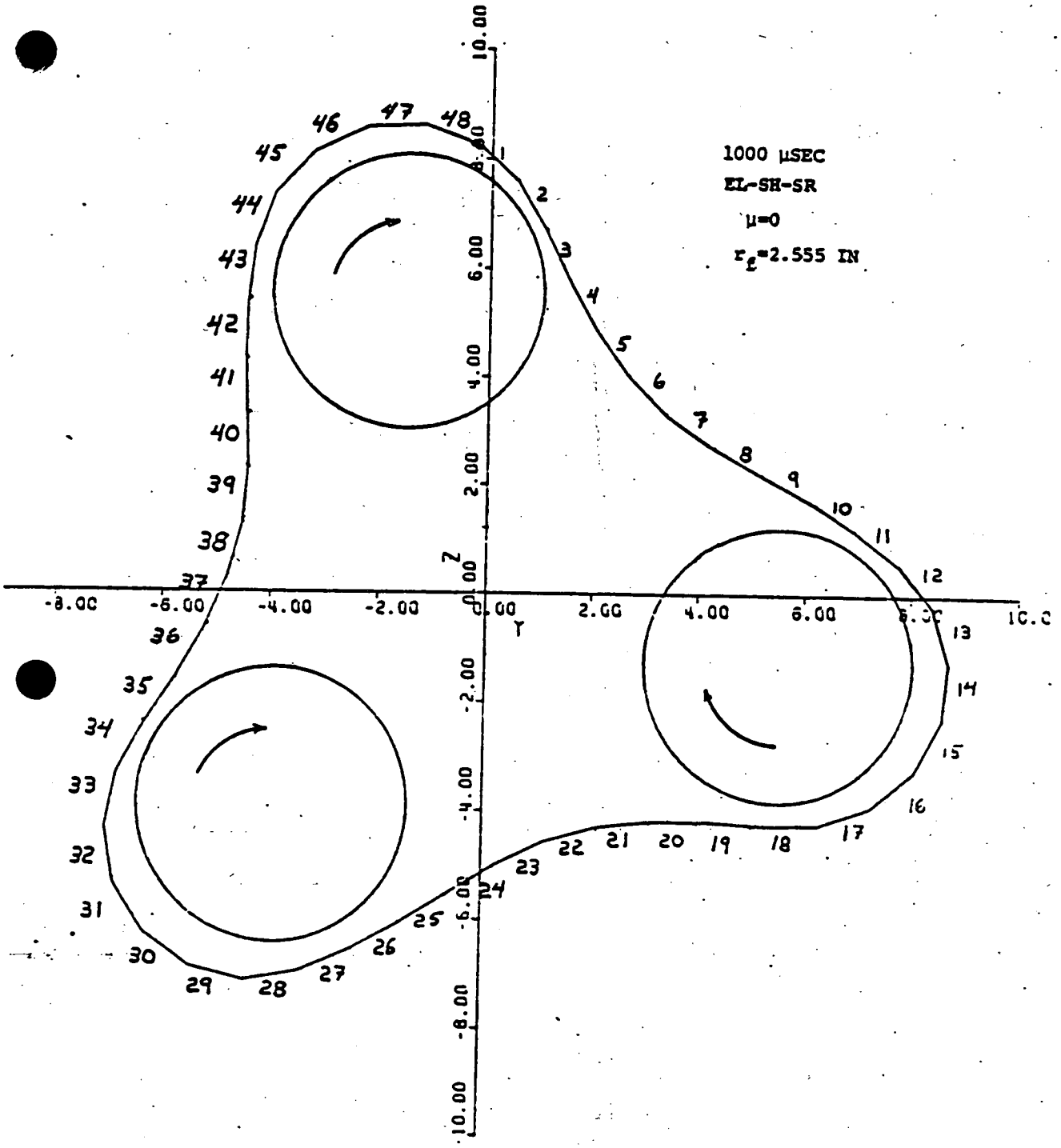

FIG. 30 PREDICTED DEFORMED RING CONFIGURATION AT 1000 MICROSECONDS AFTER INITIAL IMPACT FOR THE NAPTC TEST 201 CONTAINMENT RING

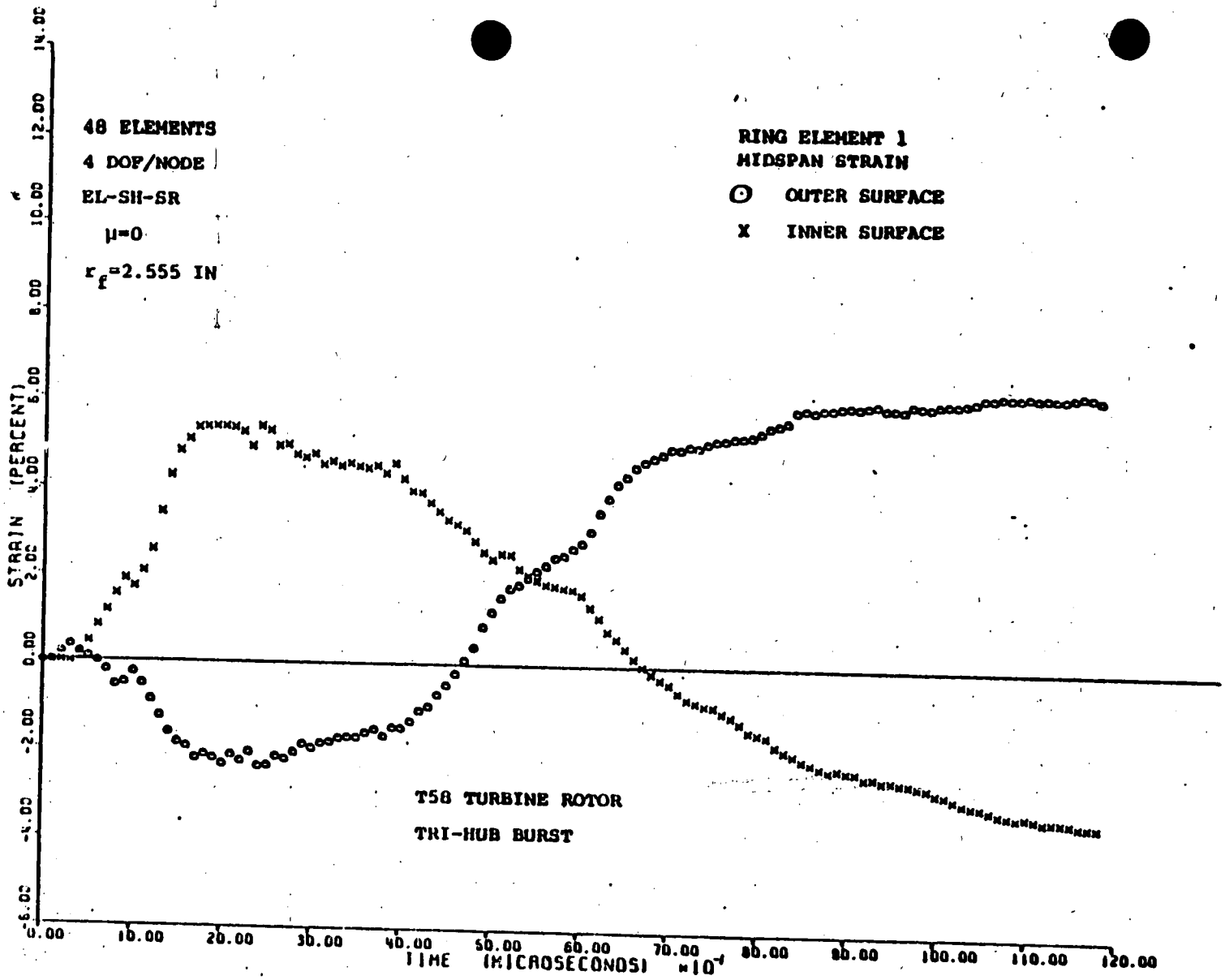

(a) Element 1 Midspan Strain

FIG. 31 PREDICTED TRANSIENT STRAIN ON THE NAPTC TEST 201 CONTAINMENT RING

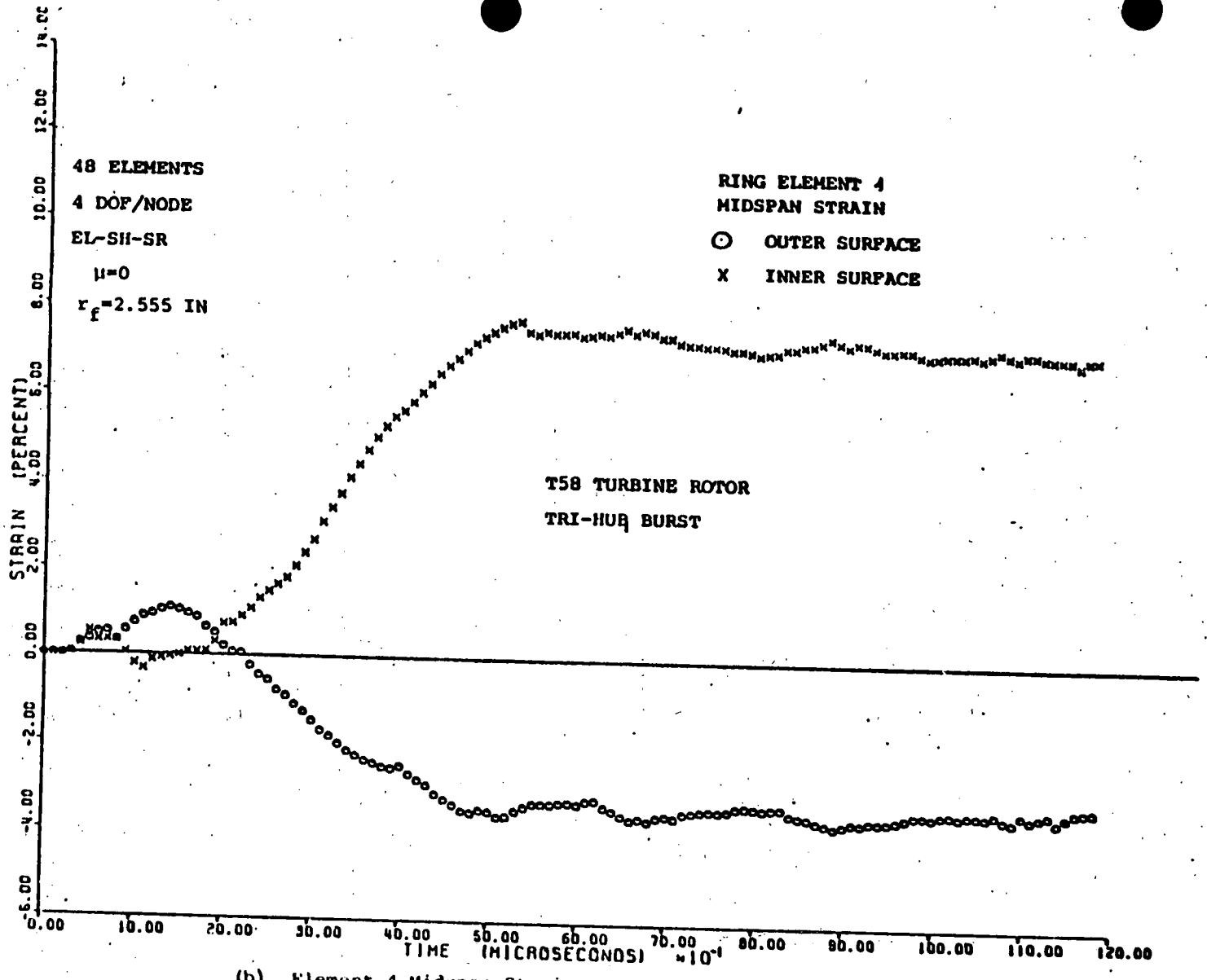

(b) Element 4 Midspan Strain

FIG. 31 CONTINUED (NAPTC TEST 201 RING)

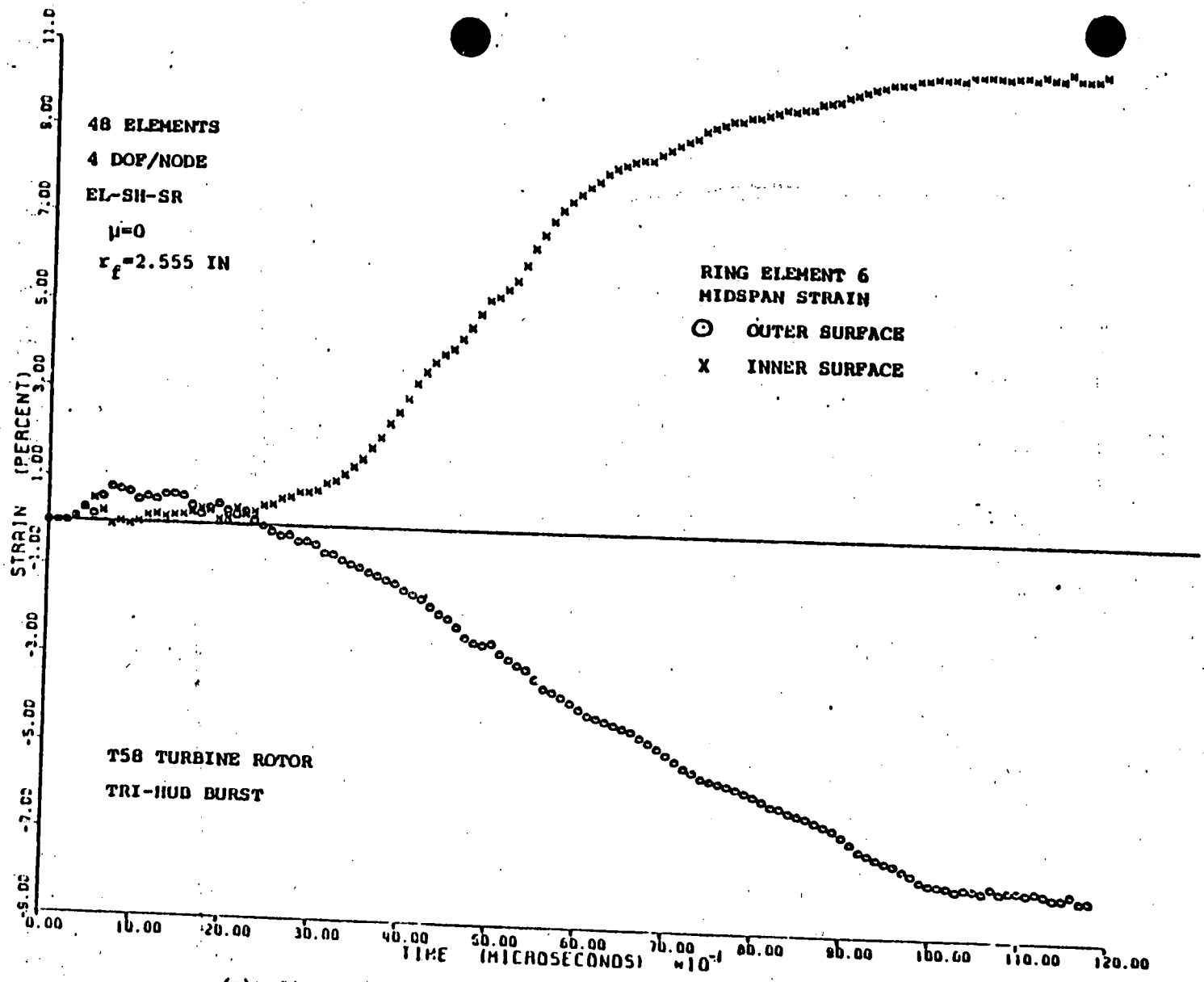

(c) Element 6 Midspan Strain

FIG. 31 CONTINUED (NAPTC TEST 201 RING)

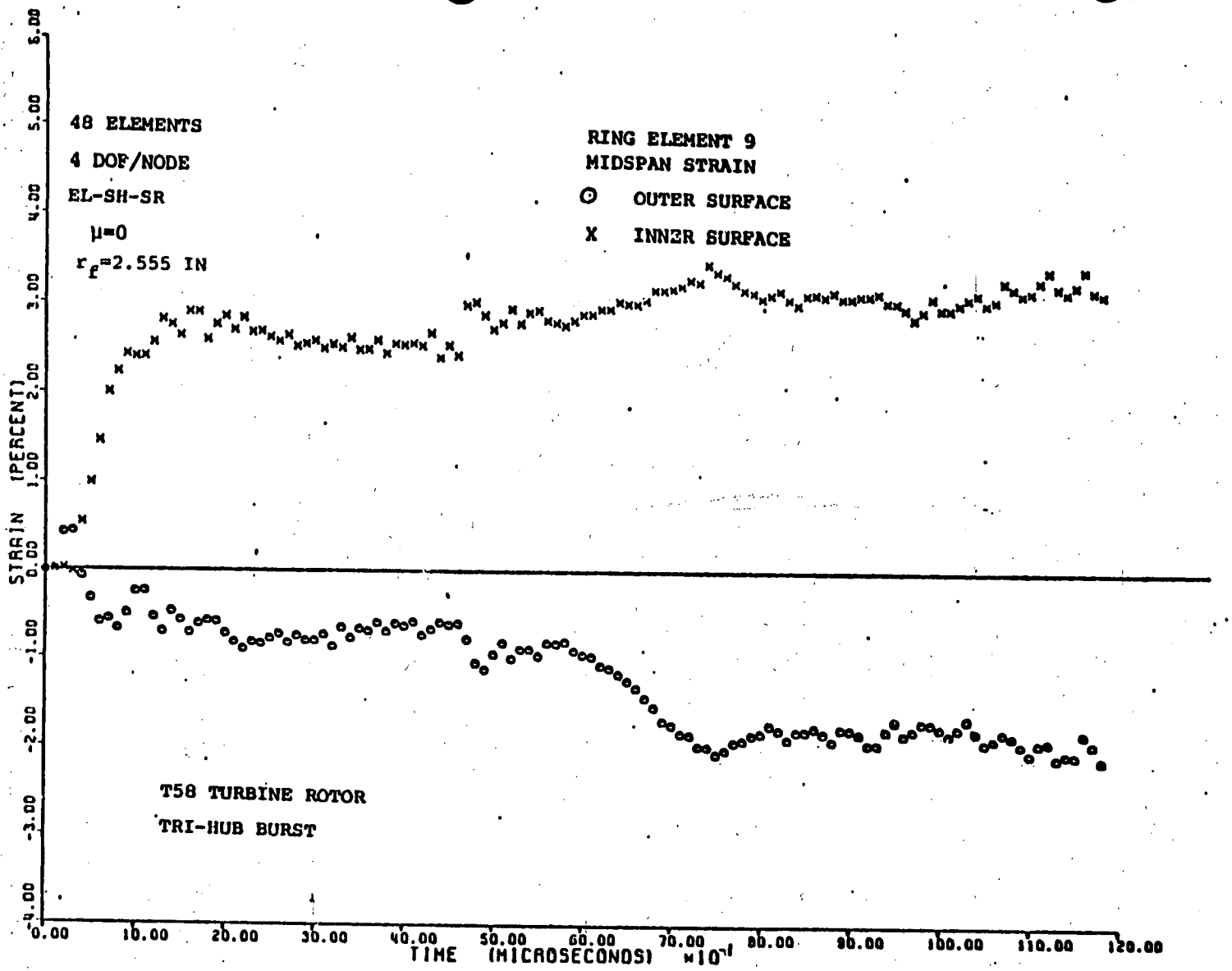

(d) Element 9 Midspan Strain

FIG. 31 CONTINUED (NAPTC TEST 201 RING)

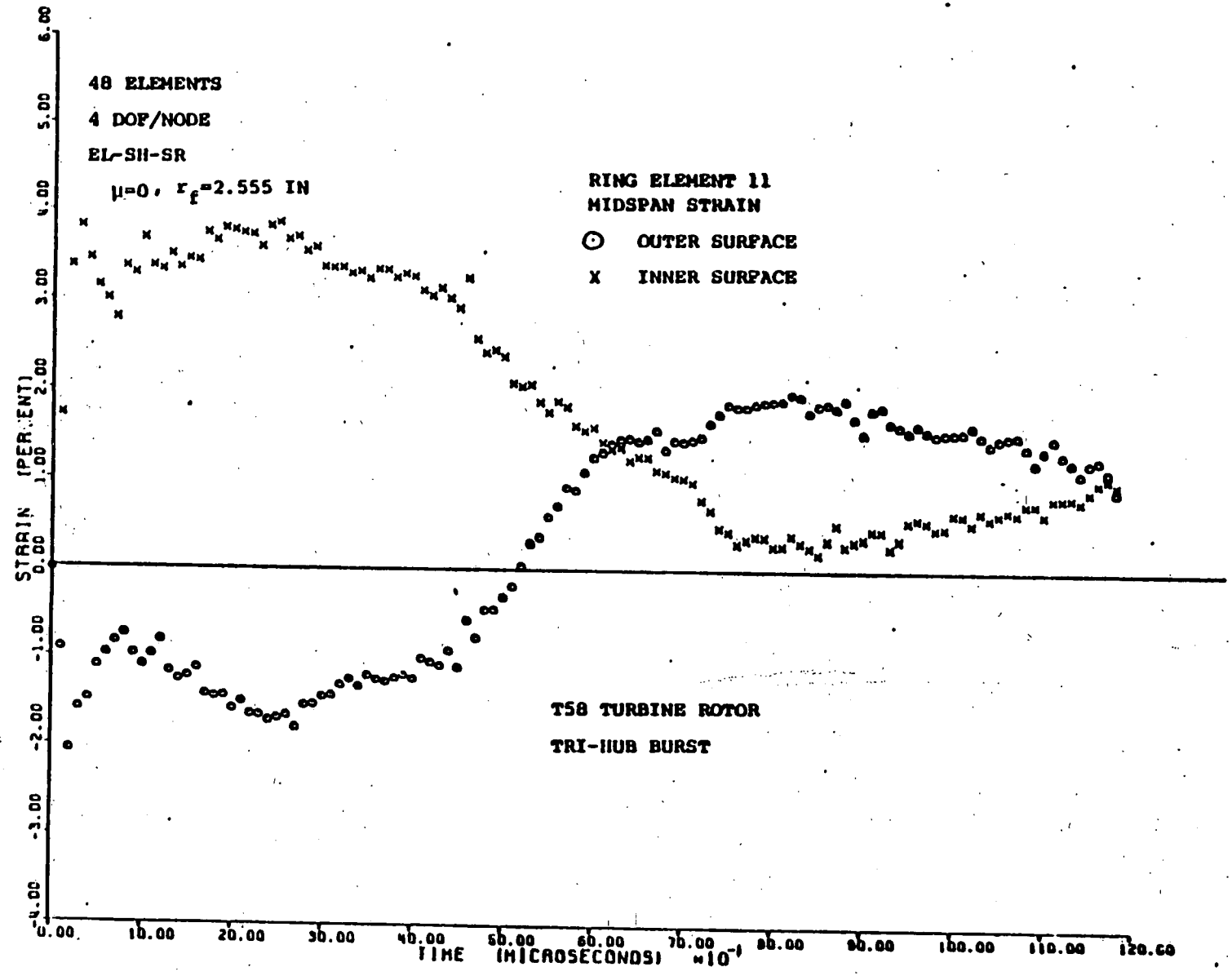

(e) Element 11 Midspan Strain

FIG. 31 CONTINUED (NAPTC TEST 201 RING)

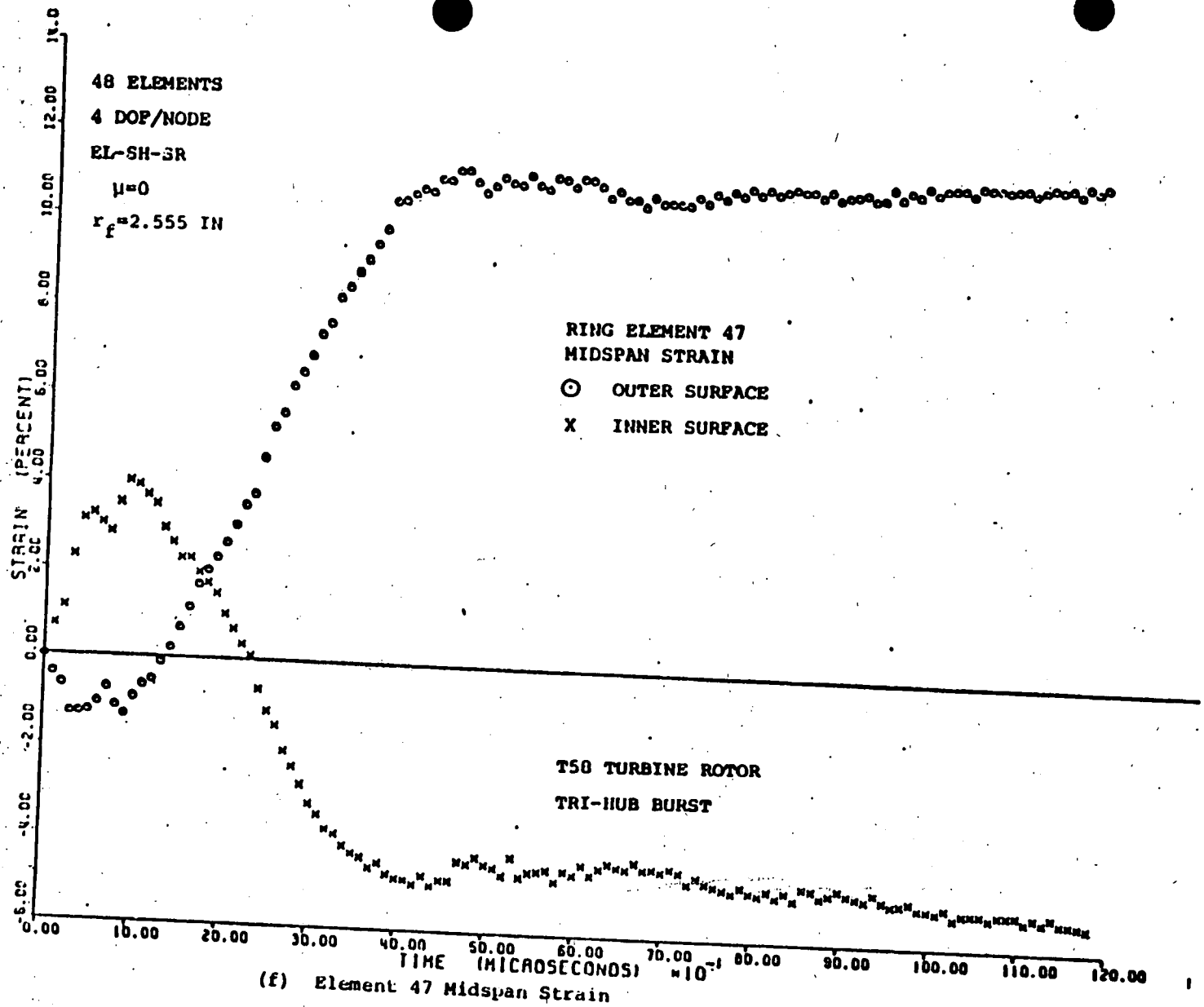

(f) Element 47 Midspan Strain

FIG. 31 CONCLUDED (NAPTC TEST 201 RING)

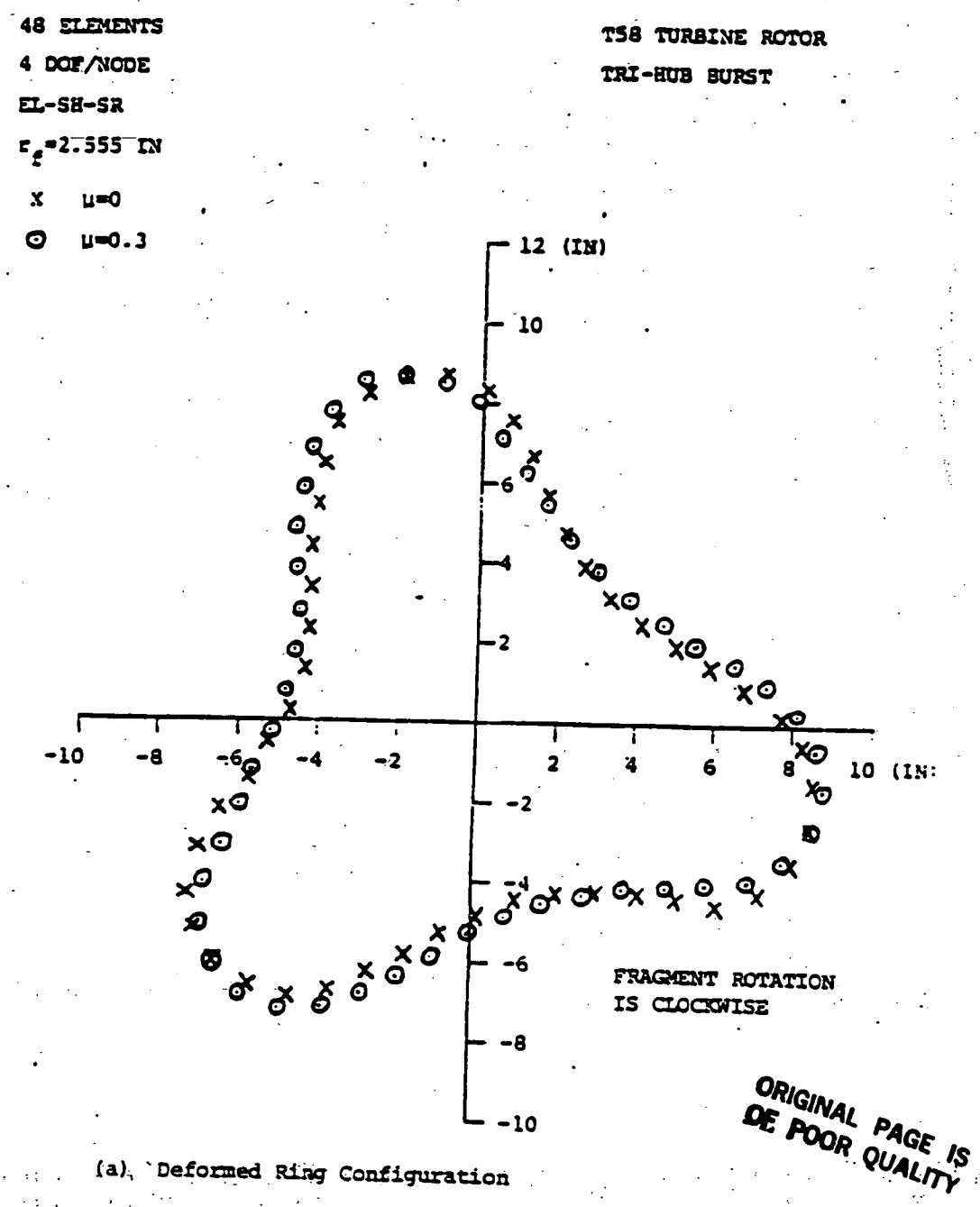

(a) Deformed Ring Configuration

FIG. 32 COMPARISON OF PREDICTED DEFORMED RING CONFIGURATIONS AND OUTER-SURFACE STRAINS AT 1200 MICROSECONDS AFTER INITIAL IMPACT FOR μ=0 AND μ=0.3 WITH r_f=2.555 IN FOR THE NAPTC TEST 201 CONTAINMENT RING

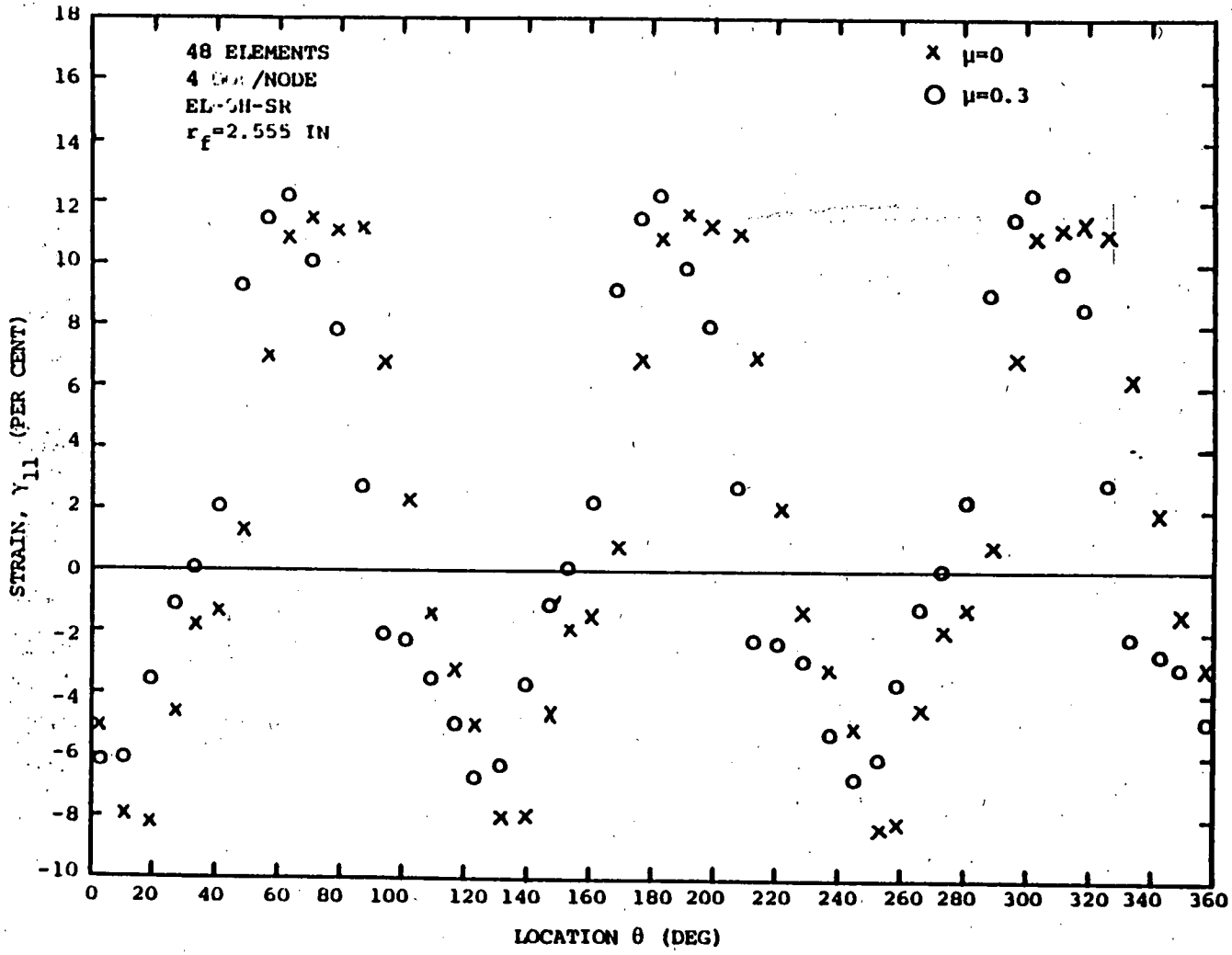

(b) Distribution of Outer-Surface Strains at TAII=1200 μSEC

FIG. 32 CONCLUDED

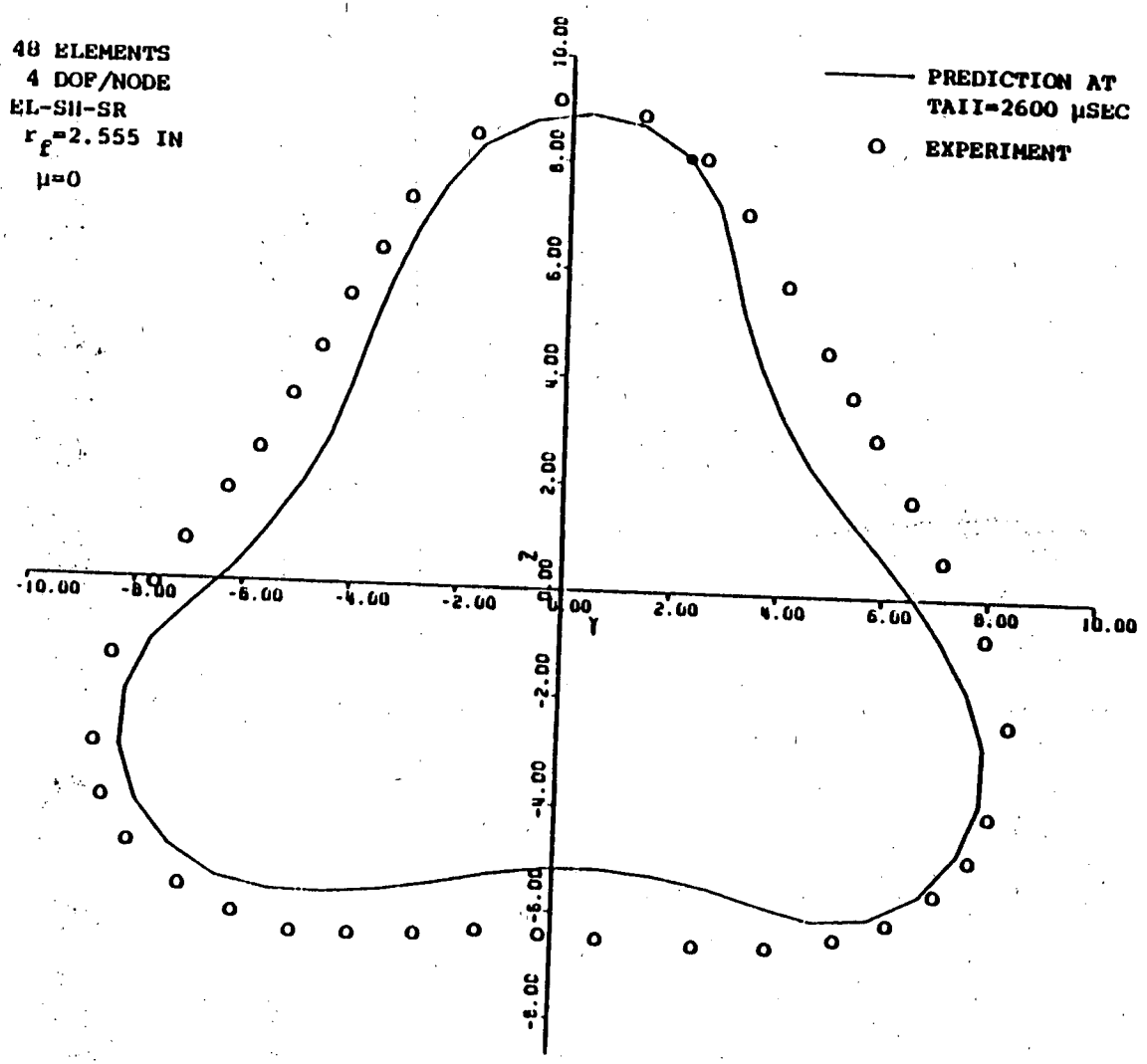

FIG. 33 COMPARISON OF PREDICTED WITH THE EXPERIMENTAL PERMANENTLY-DEFORMED RING CONFIGURATION FOR NAPTC TEST 201

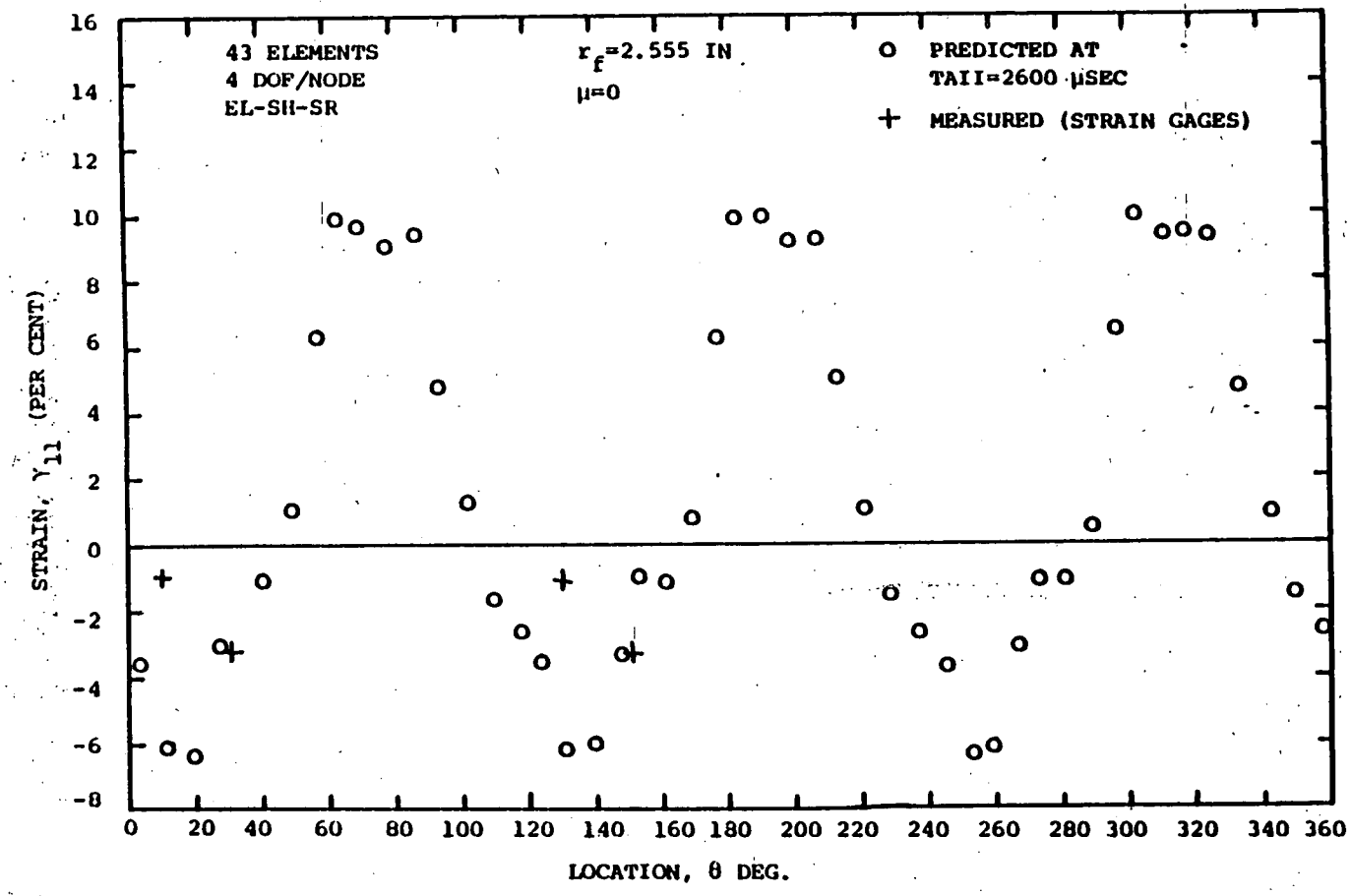

FIG. 34 PREDICTED AND MEASURED RING OUTER-SURFACE PERMANENT STRAINS ON THE NAPTC TEST 201 RING

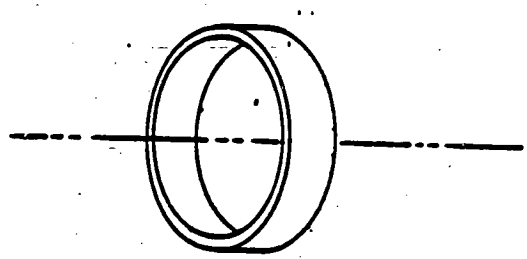

(a) Circular Ring

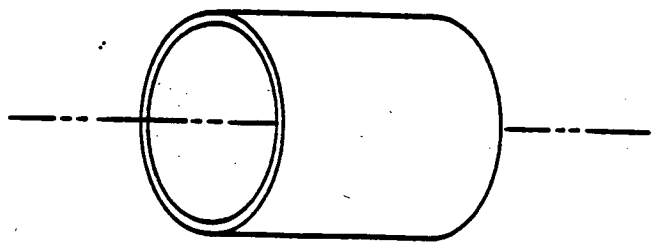

(b) Cylindrical Shell

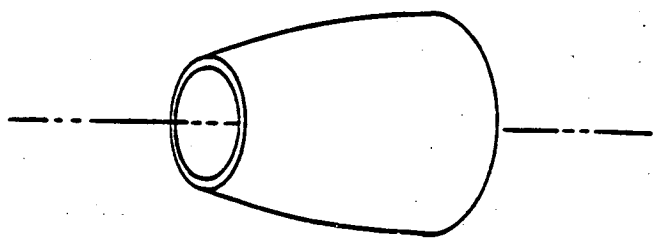

(c) Curved Shell

FIG. 35 SCHEMATICS OF SHELL-OF-REVOLUTION TYPE CONTAINMENT STRUCTURES

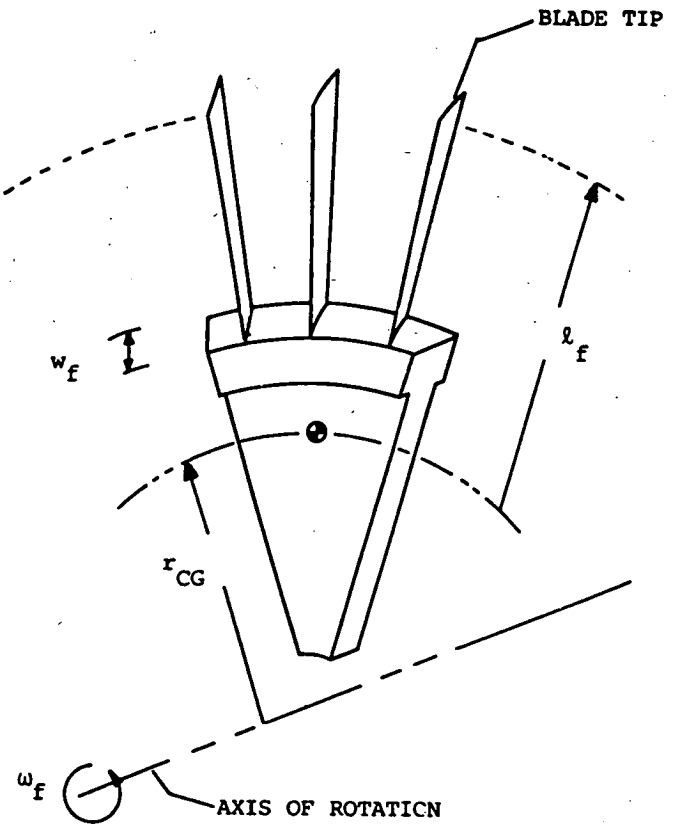

FIG. 36 SCHEMATIC AND GEOMETRY OF A BLADED-DISK FRAGMENT

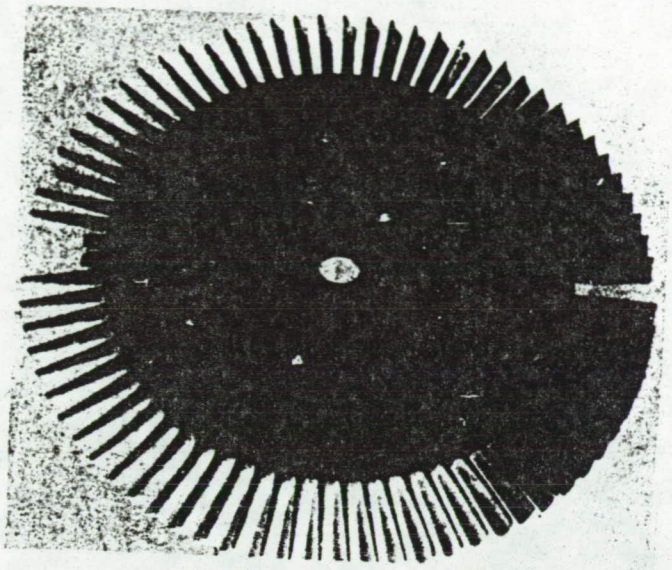

J65
30.64-IN O.D.

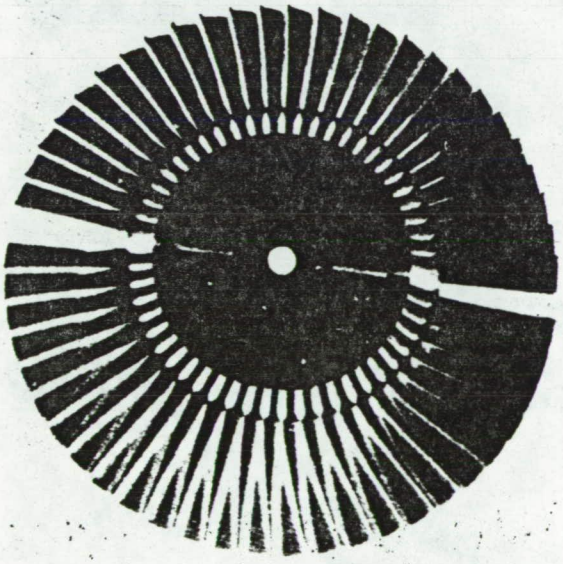

T58
14.0-IN O.D.

FIG. 37 T58 AND J65 ROTORS ILLUSTRATING MODIFICATIONS TO PRODUCE A TWO-FRAGMENT BURST (REF. 37)

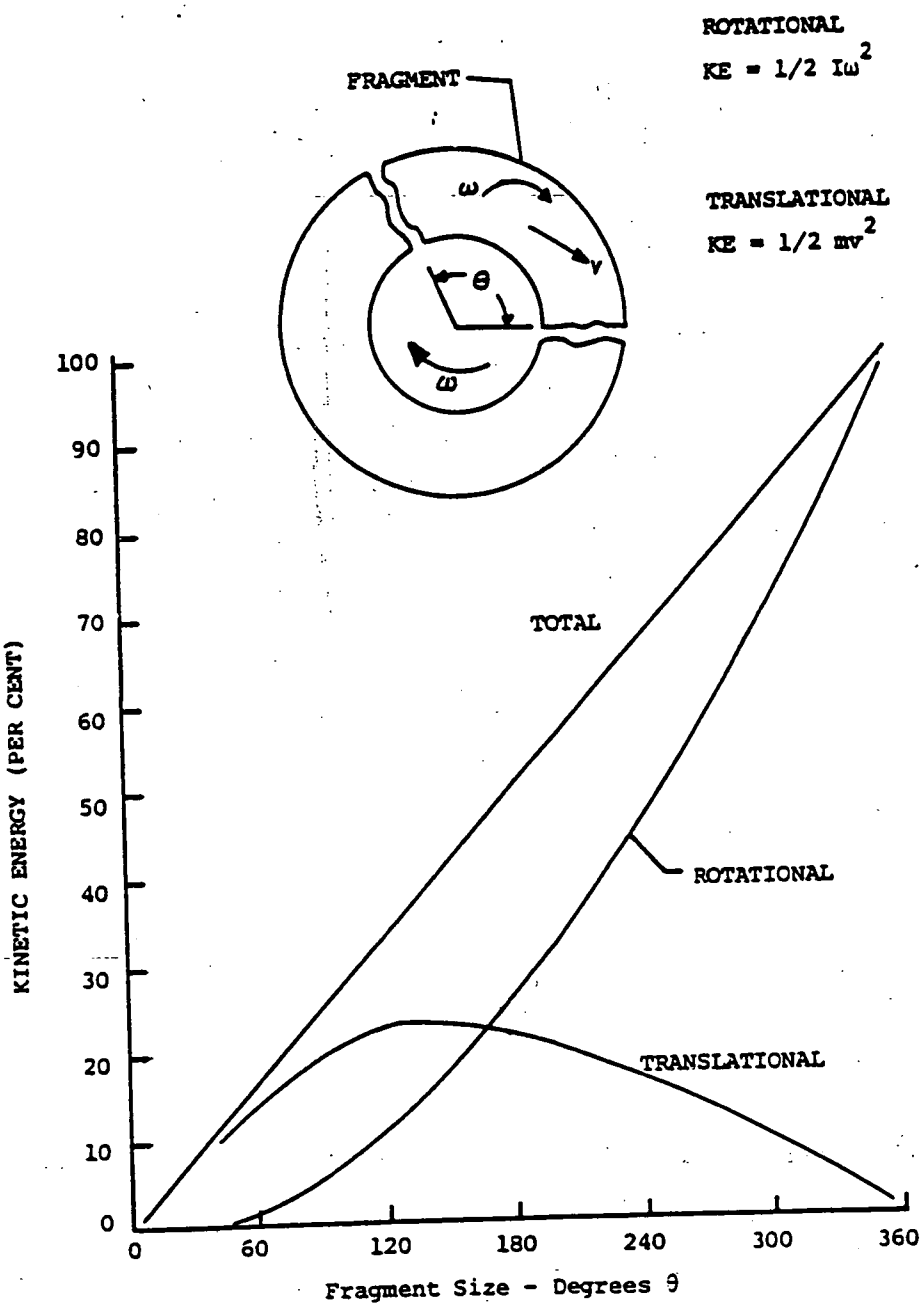

FIG. 38 DISTRIBUTION OF TRANSLATIONAL AND ROTATIONAL KINETIC ENERGY OF ROTOR-BURST FRAGMENTS AS A FUNCTION OF FRAGMENT SIZE ϑ

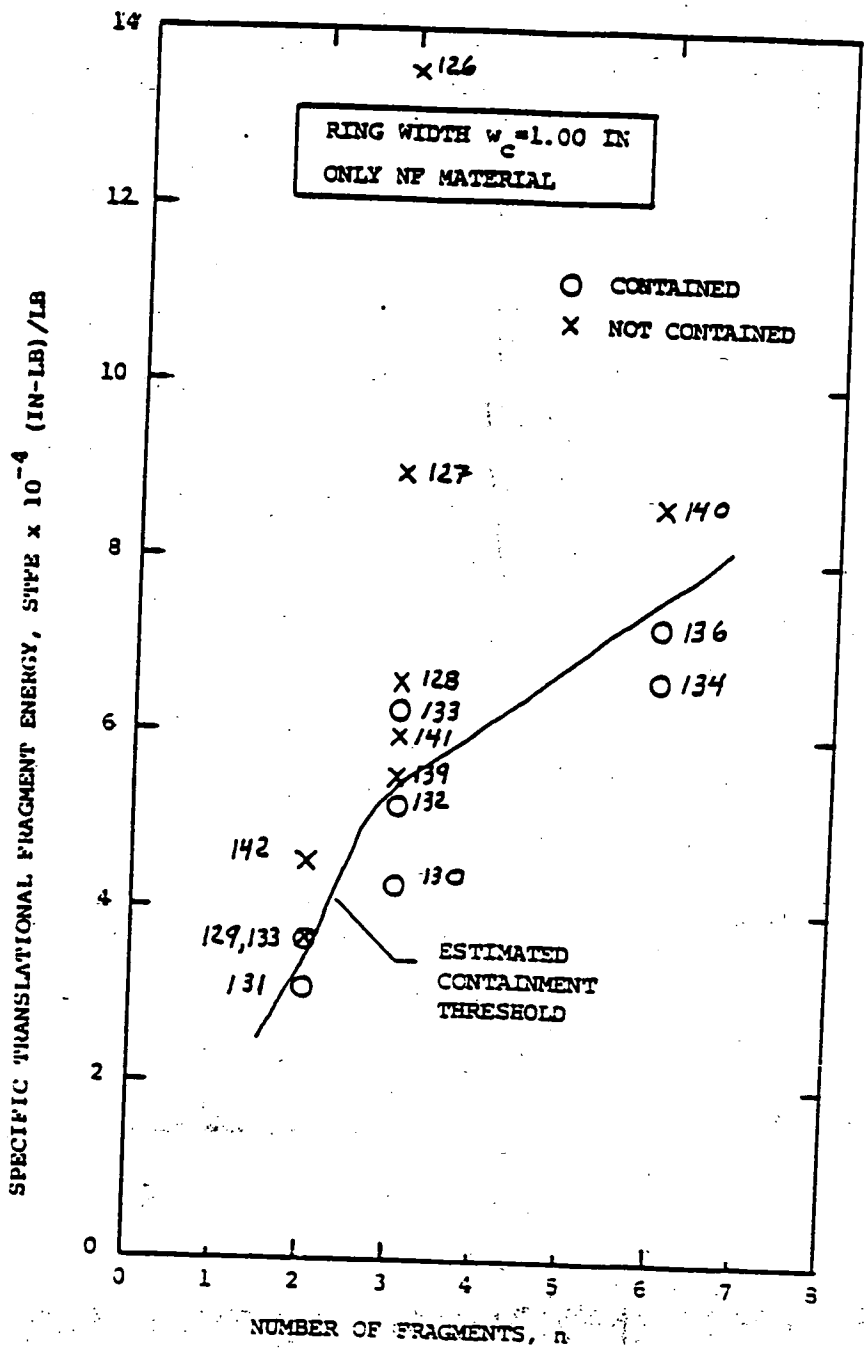

FIG. 39 NAPTC TESTS OF T58 TURBINE ROTOR BURST AGAINST 4130 CAST STEEL CONTAINMENT RINGS OF 1.0-IN AXIAL LENGTH (WIDTH) AS A FUNCTION OF THE NUMBER OF EQUAL-SIZE BLADED-DISK FRAGMENTS

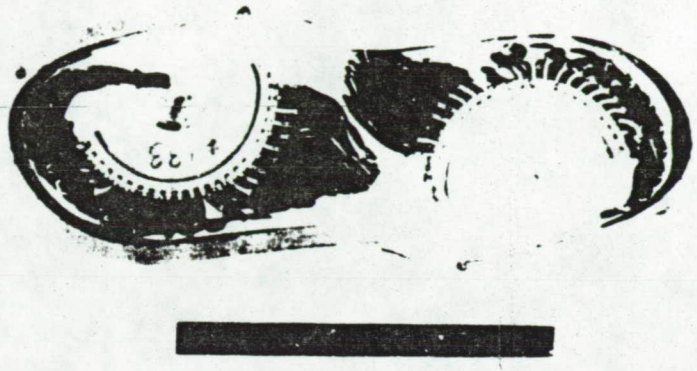

(a) Small Rotor 2-Fragment Containment Post Test Results

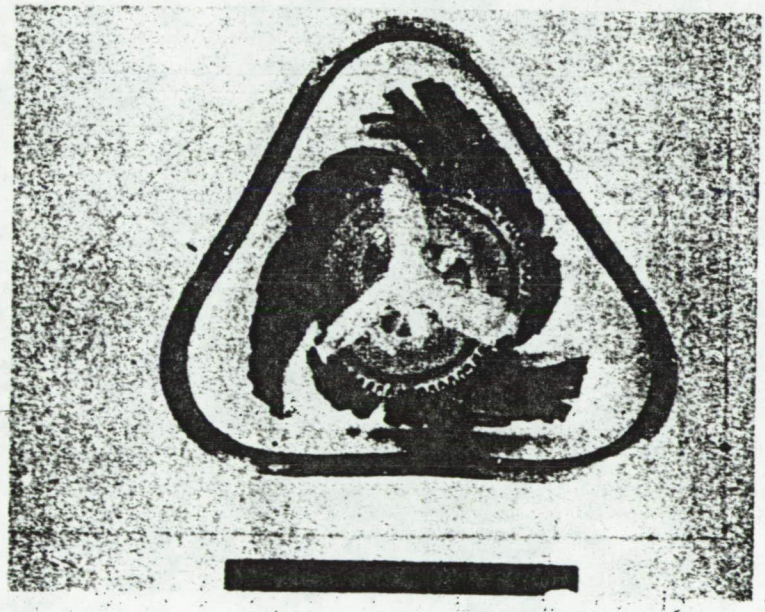

(b) Small Rotor 3-Fragment Containment Post Test Results

FIG. 40 ILLUSTRATION OF POST-TEST CONTAINMENT RING AND FRAGMENT CONFIGURATIONS FOR T58 2-FRAGMENT AND 3-FRAGMENT ROTOR BURSTS (REF. 37)

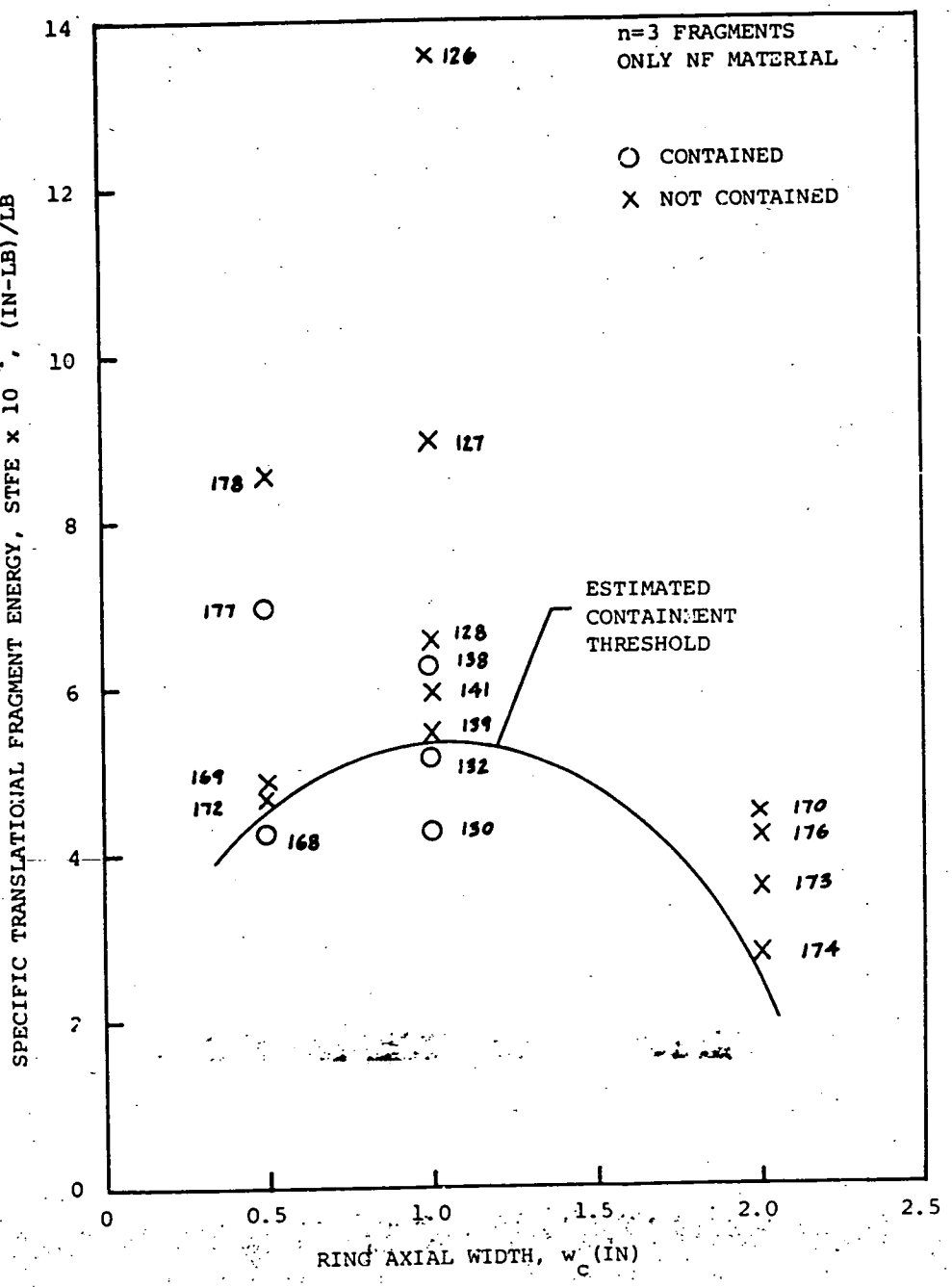

FIG. 41 NAPTC IMPACT TESTS OF THREE EQUAL-SIZE T58 TURBINE ROTOR BLADED-DISK FRAGMENTS AGAINST 4130 CAST STEEL CONTAINMENT RINGS AS A FUNCTION OF RING AXIAL LENGTH (WIDTH)

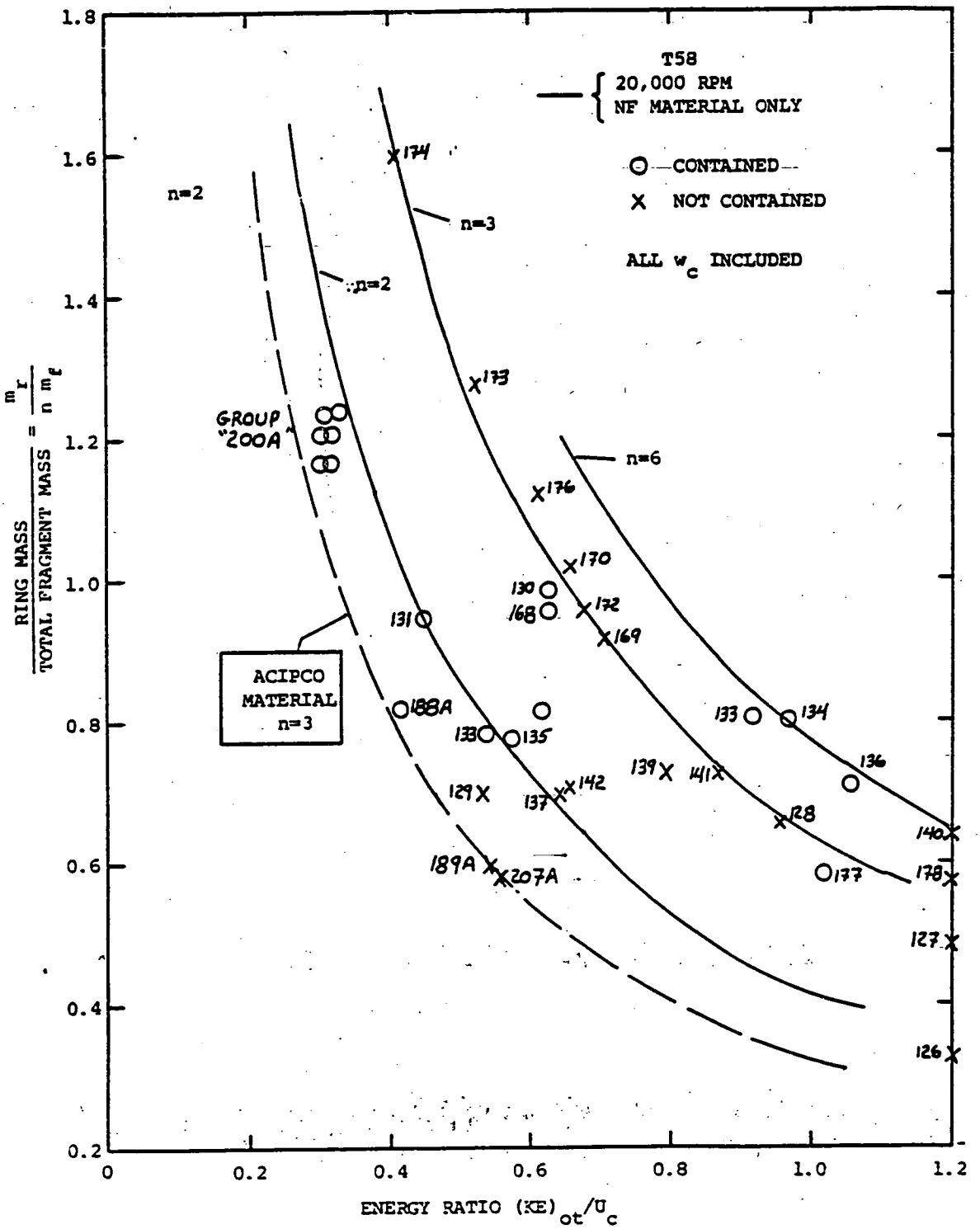

FIG. 42 NAPTC T58 TURBINE ROTOR BURST IMPACT DATA OF RING-TO-FRAGMENT MASS RATIO VS. $(KE)_{ot}/U_c$ FOR VARIOUS NUMBERS OF EQUAL-SIZE BLADED-DISK FRAGMENTS IMPACTING 4130 CAST STEEL CONTAINMENT RINGS

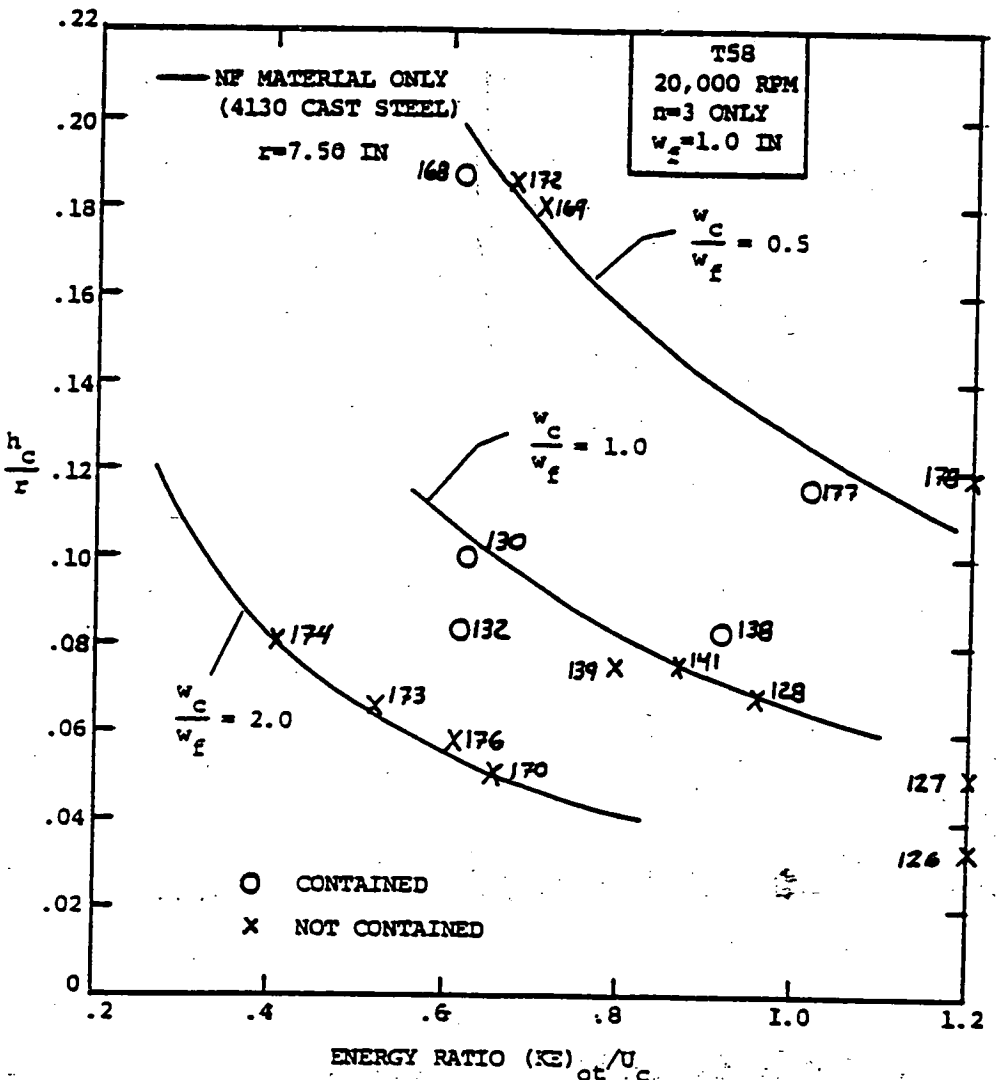

FIG. 43 NAPTC T58 TURBINE TRI-HUB ROTOR BURST DATA FOR CONTAINMENT RING THICKNESS-TO-RADIUS RATIO VS. $(KE)_{ot}/U_c$ FOR VARIOUS FIXED VALUES OF THE RING WIDTH TO FRAGMENT WIDTH RATIO w_c/w_f

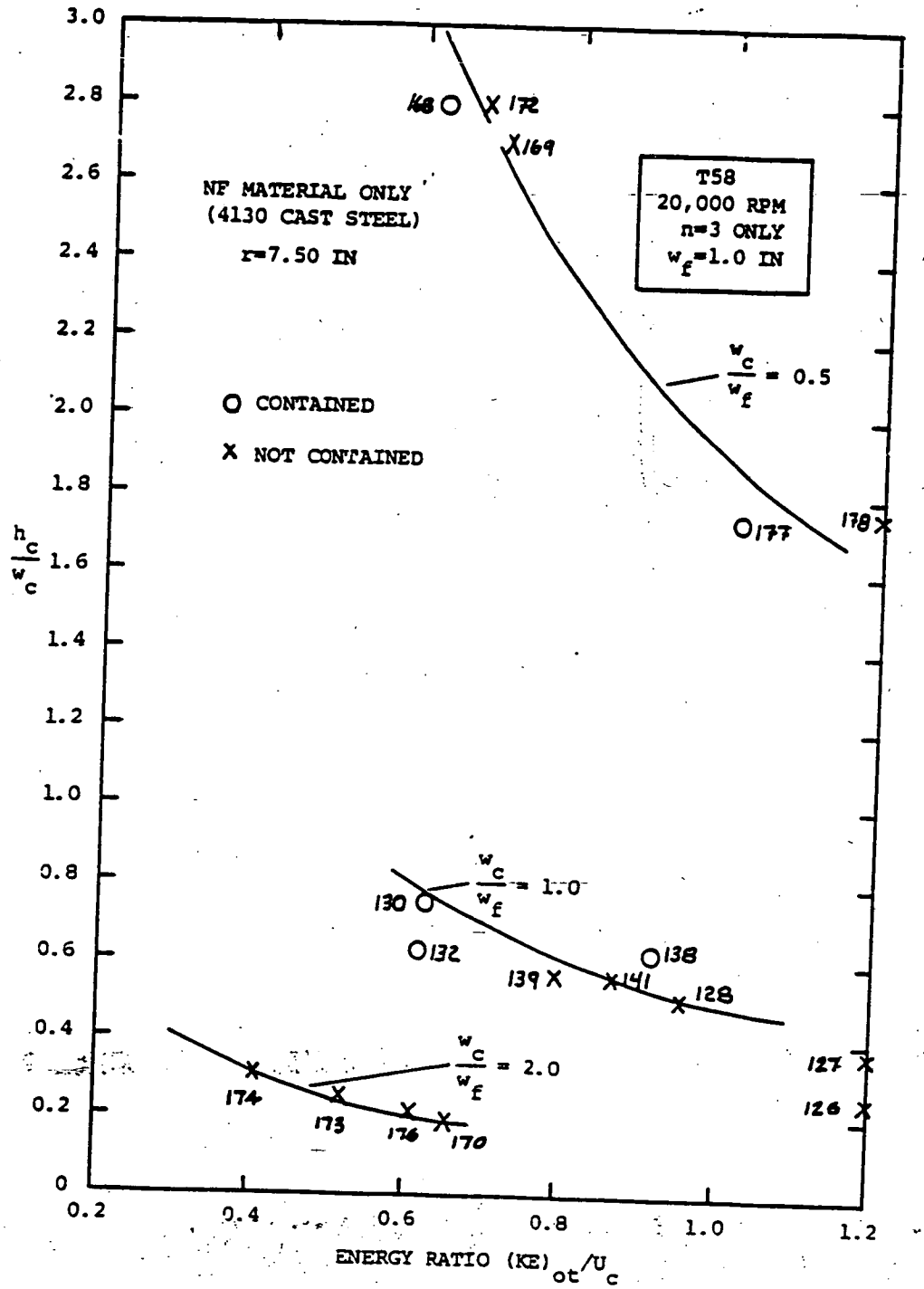

FIG. 44 NAPTC T58 TURBINE TRI-HUB ROTOR BURST DATA FOR CONTAINMENT RING THICKNESS-TO-WIDTH RATIO VS. $(KE)_{ot}/U_c$ FOR VARIOUS FIXED VALUES OF THE RING WIDTH TO FRAGMENT WIDTH RATIO w_c/w_f

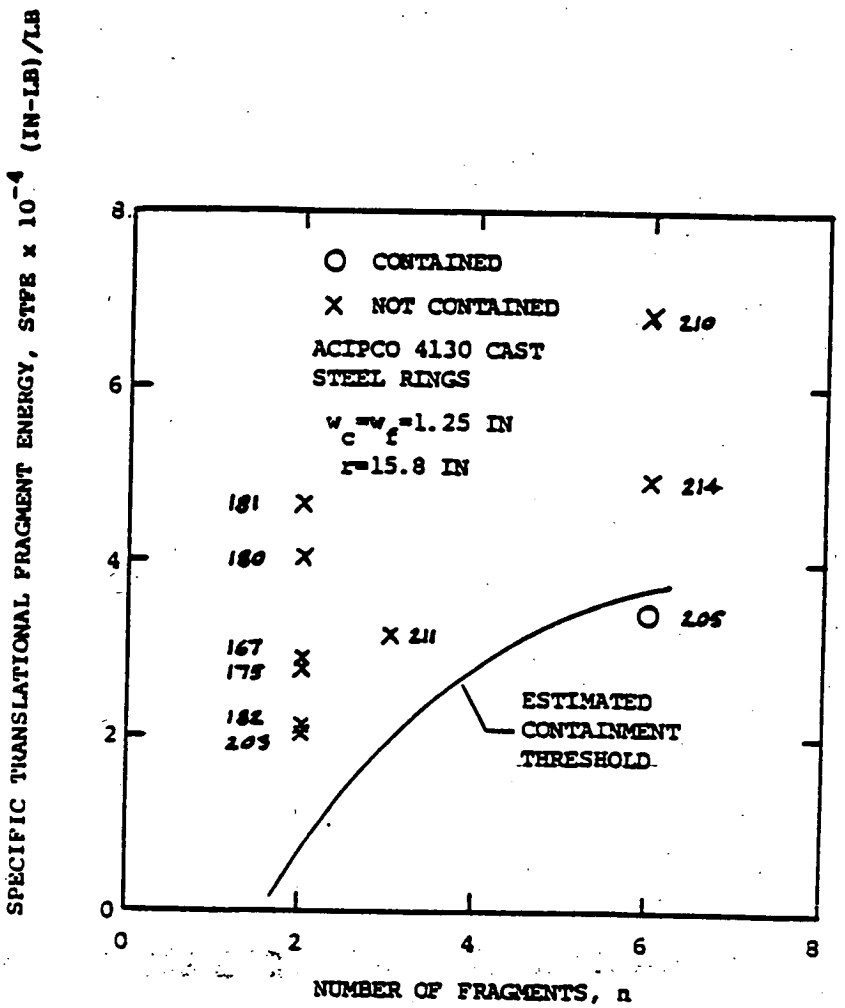

FIG. 45 NAPTC TESTS OF J65 TURBINE ROTOR BURSTS AGAINST 4130 CAST STEEL CONTAINMENT RINGS OF 1.25-IN AXIAL LENGTH (WIDTH) AS A FUNCTION OF THE NUMBER OF EQUAL-SIZE BLADED-DISK FRAGMENTS

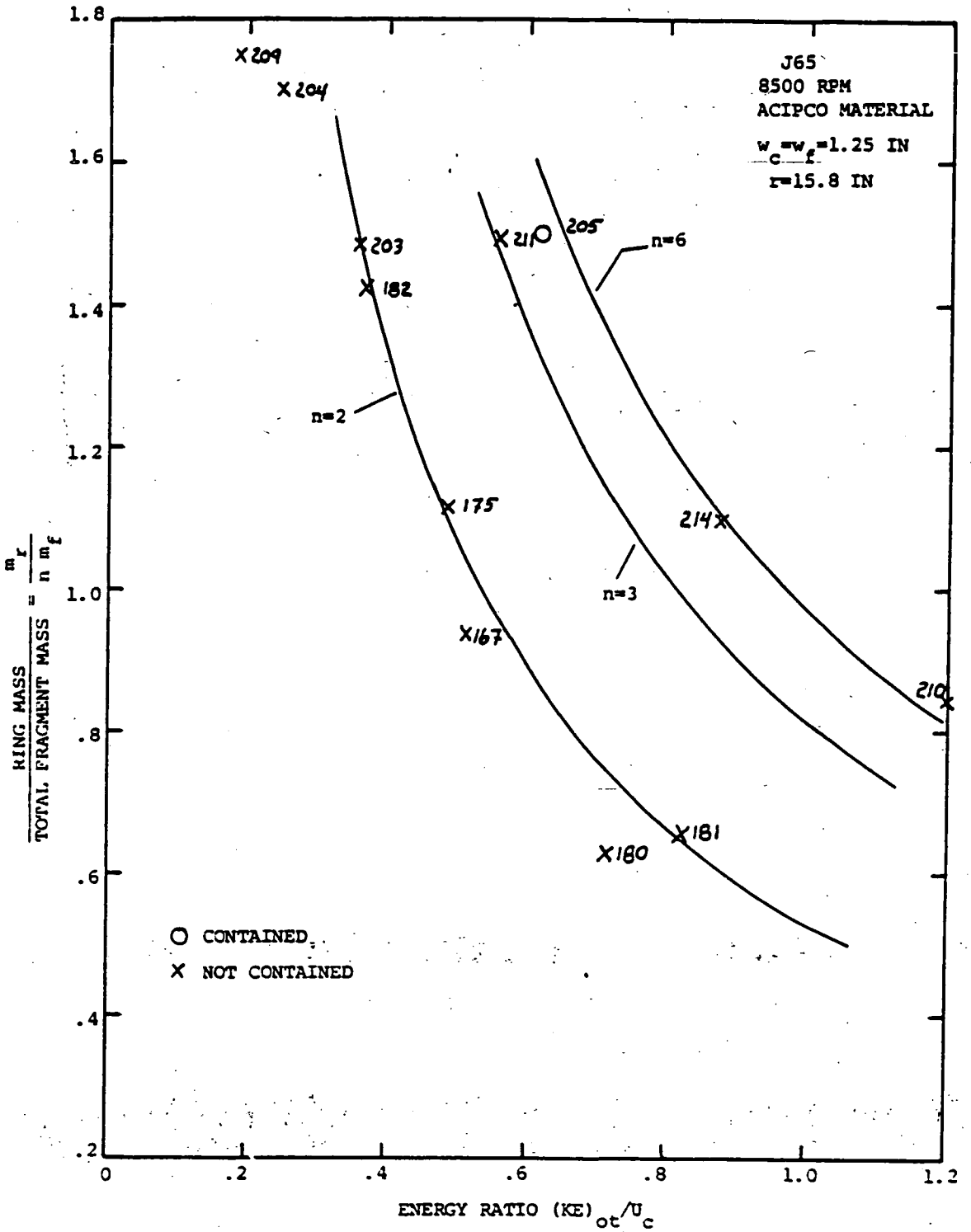

FIG. 46 NAPTC J65 TURBINE ROTOR BURST IMPACT DATA OF RING-TO-FRAGMENT MASS RATIO VS. $(KE)_{ot}/U_c$ FOR VARIOUS NUMBERS OF EQUAL-SIZE BLADED-DISK FRAGMENTS IMPACTING 4130 CAST STEEL CONTAINMENT RINGS

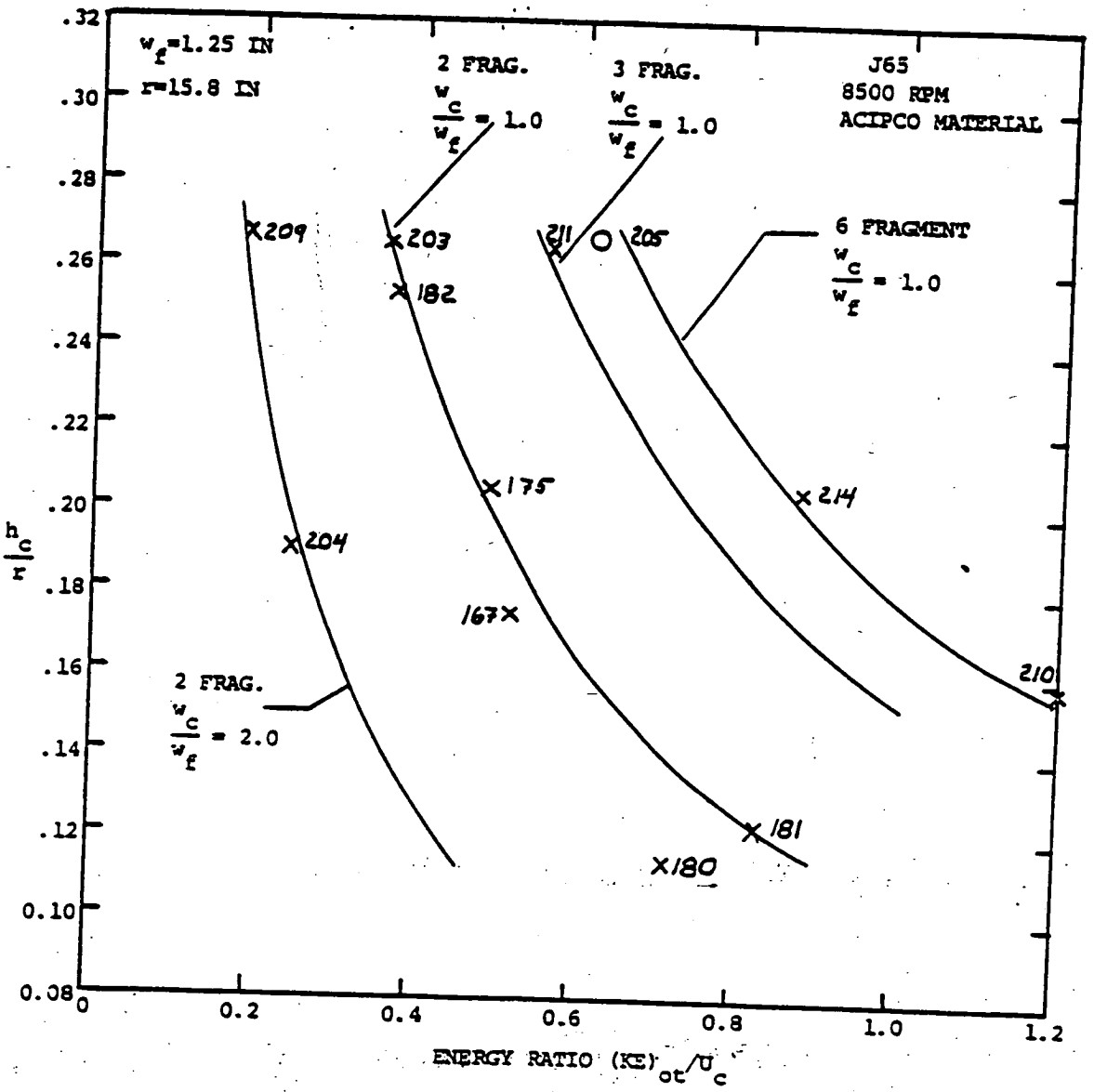

FIG. 47 NAPTC J65 TURBINE ROTOR BURST DATA FOR CONTAINMENT RING THICKNESS-TO-RADIUS RATIO VS. $(KE)_{ot}/U_c$ FOR VARIOUS NUMBERS OF EQUAL-SIZE BLADED-DISK FRAGMENTS.

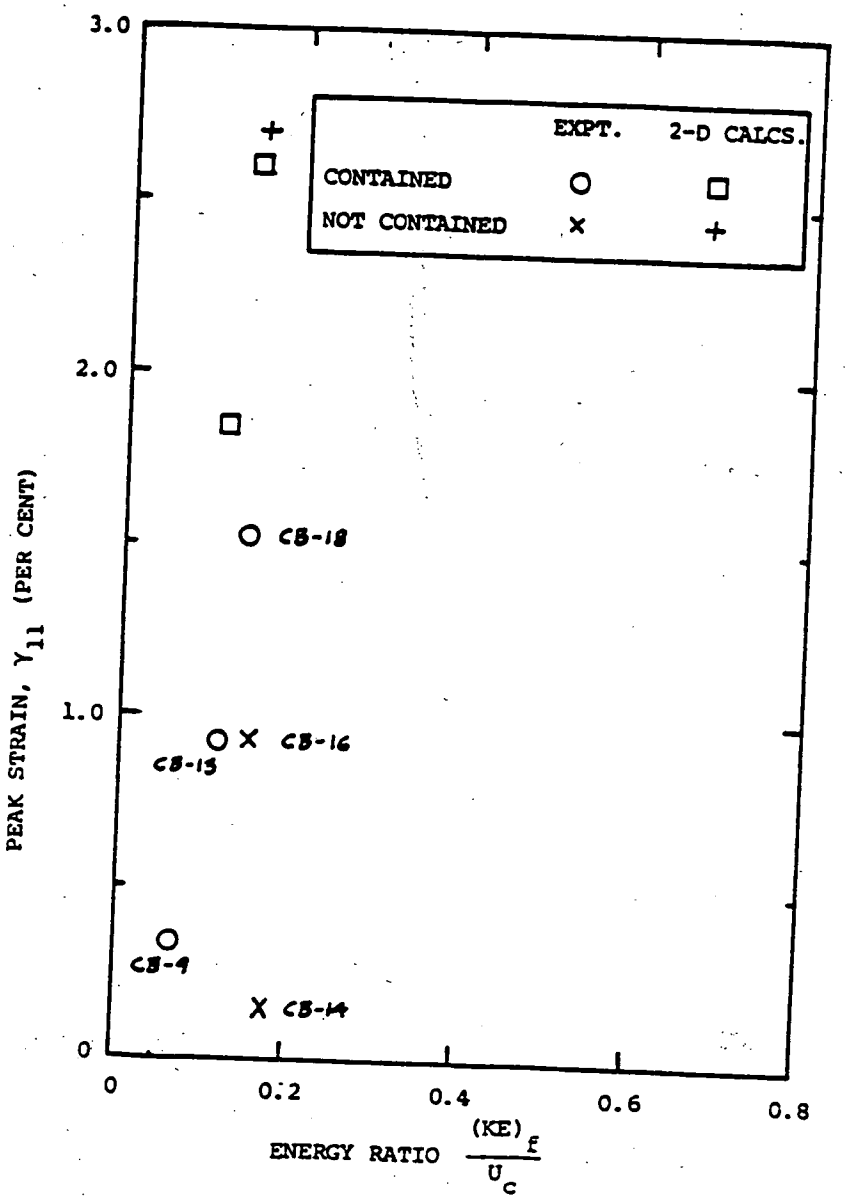

(a) Station $|x|=0.6$ in

FIG. 48 COMPARISON OF MEASURED AND 2-D PREDICTED PEAK UPPER-SURFACE STRAINS AT TWO SPANWISE STATIONS OF STEEL-SPHERE-IMPACTED 6061-T651 ALUMINUM BEAMS AS A FUNCTION OF THE ENERGY RATIO $(KE)_f/U_c$

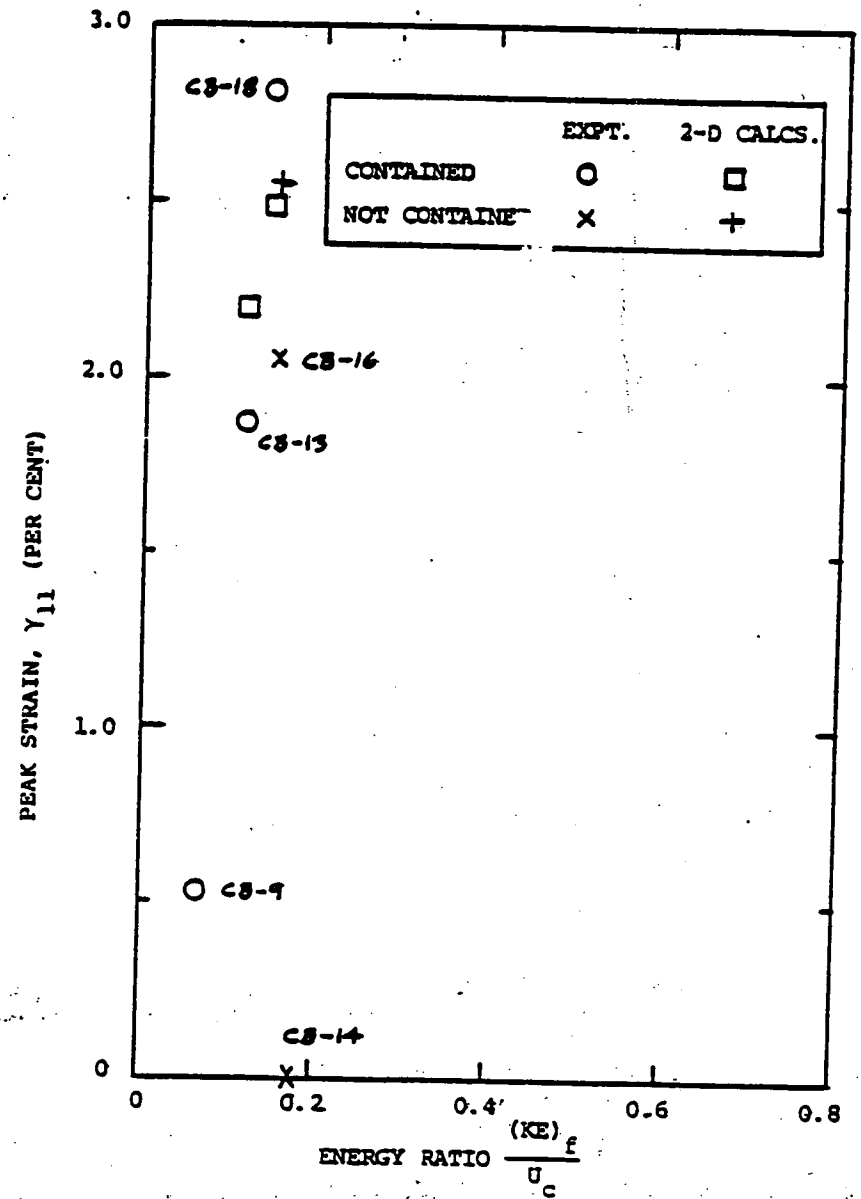

(b) Station $|x|=1.50$ IN

FIG. 48 CONCLUDED

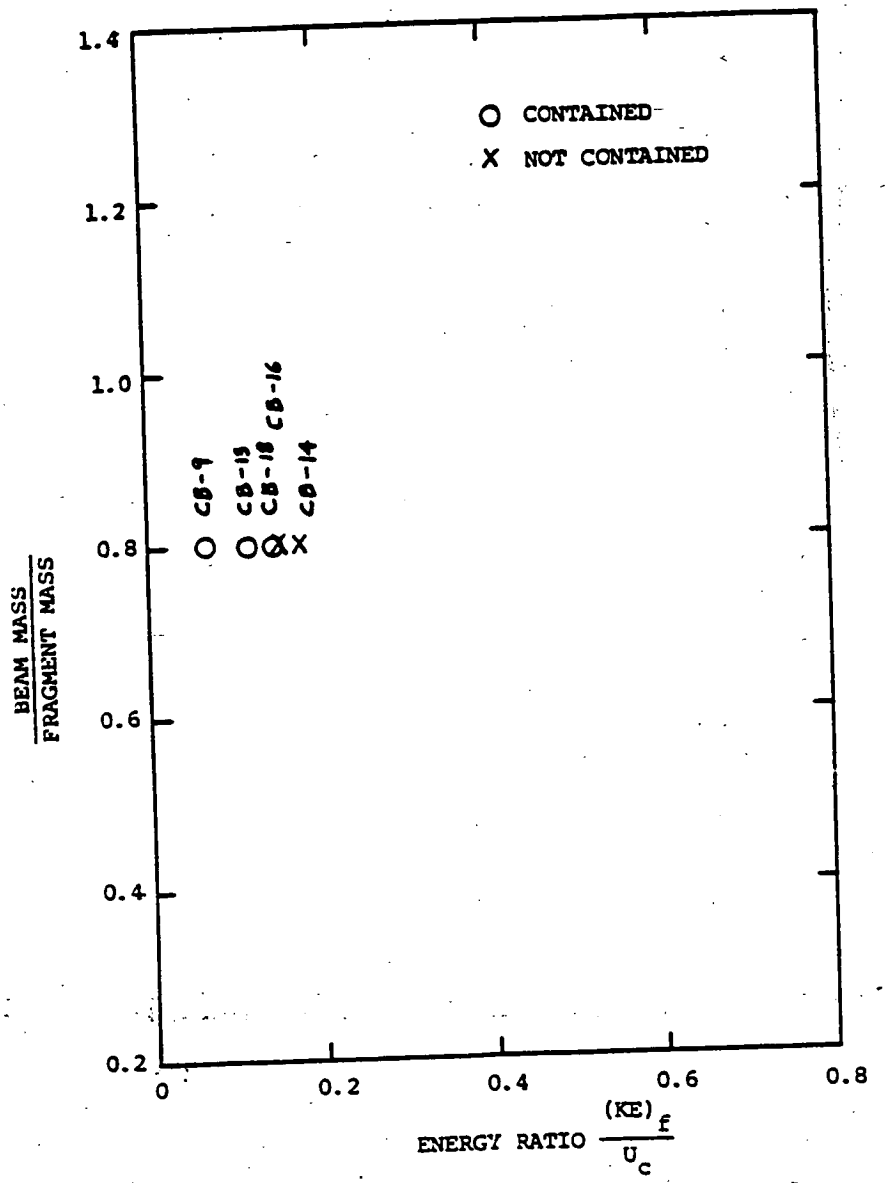

FIG. 49 SPHERE-BEAM IMPACT EXPERIMENTAL DATA [16] AS A FUNCTION OF THE RATIO OF BEAM MASS TO FRAGMENT MASS VERSUS THE ENERGY RATIO $(KE)_f/U_c$

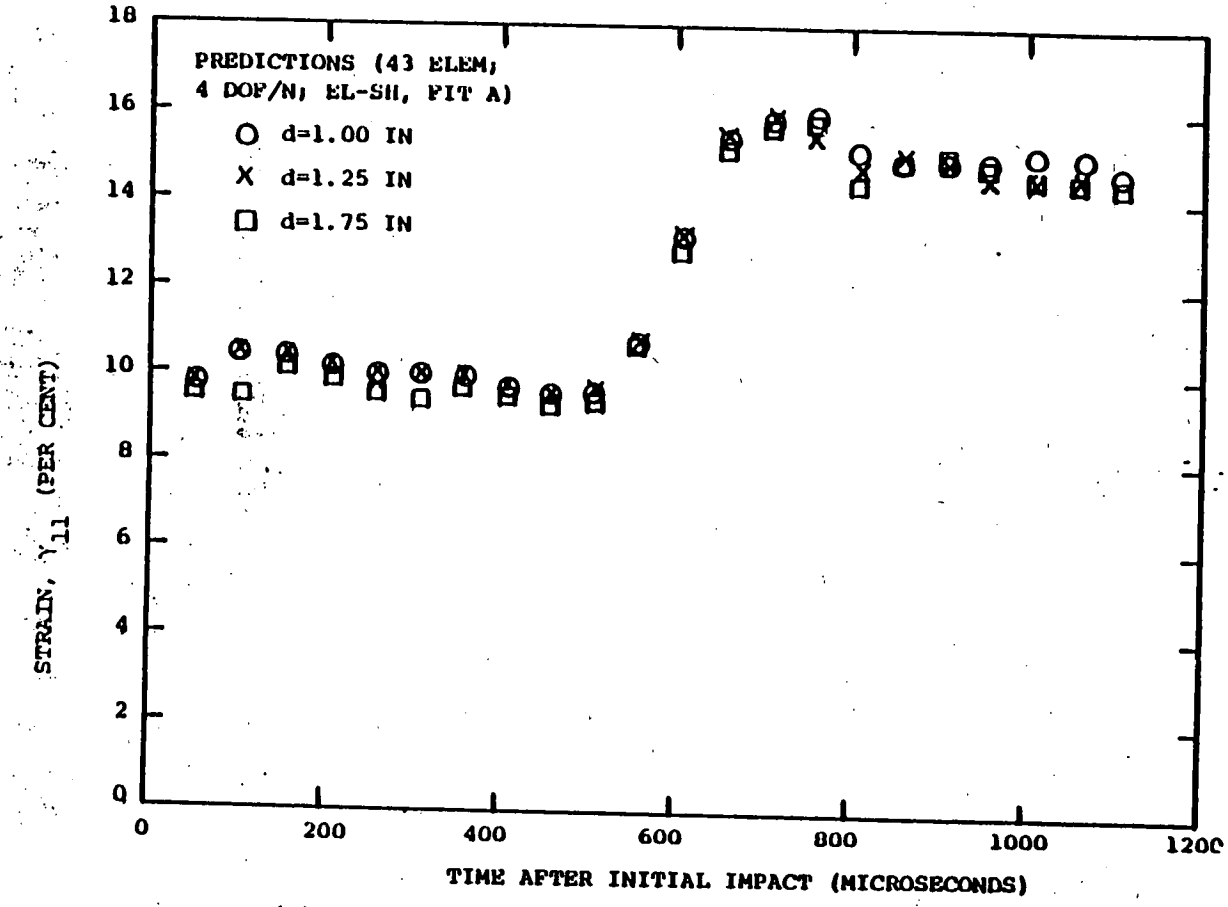

(a) Station x=0

FIG. 50 EFFECT OF VARIOUS POSTULATED FRAGMENT DIAMETERS ON THE 2-D PREDICTIONS OF UPPER-SURFACE BEAM STRAIN AT TWO SPANWISE STATIONS OF THE BEAM AS A FUNCTION OF TIME FOR THE CB-18 IMPACT CONDITIONS

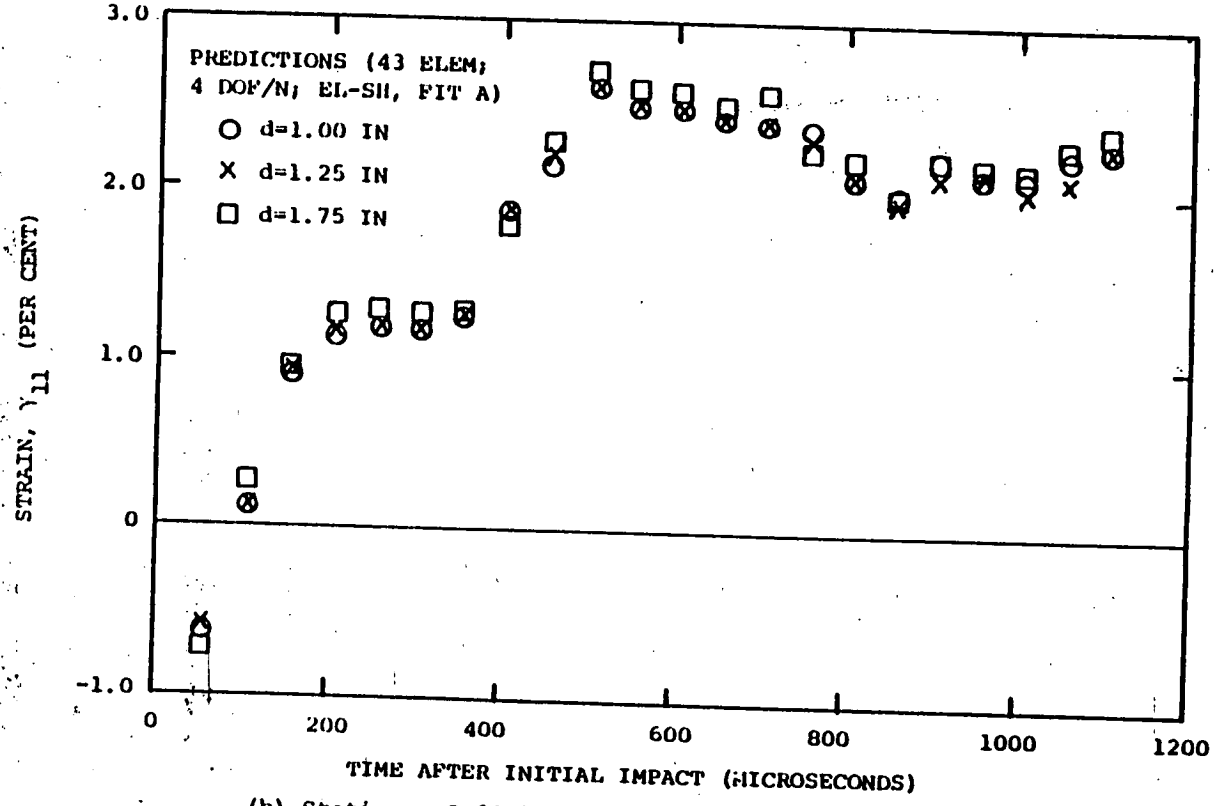

(b) Station x=0.60 in

FIG. 50 CONCLUDED (EFFECT OF d; CB-18)

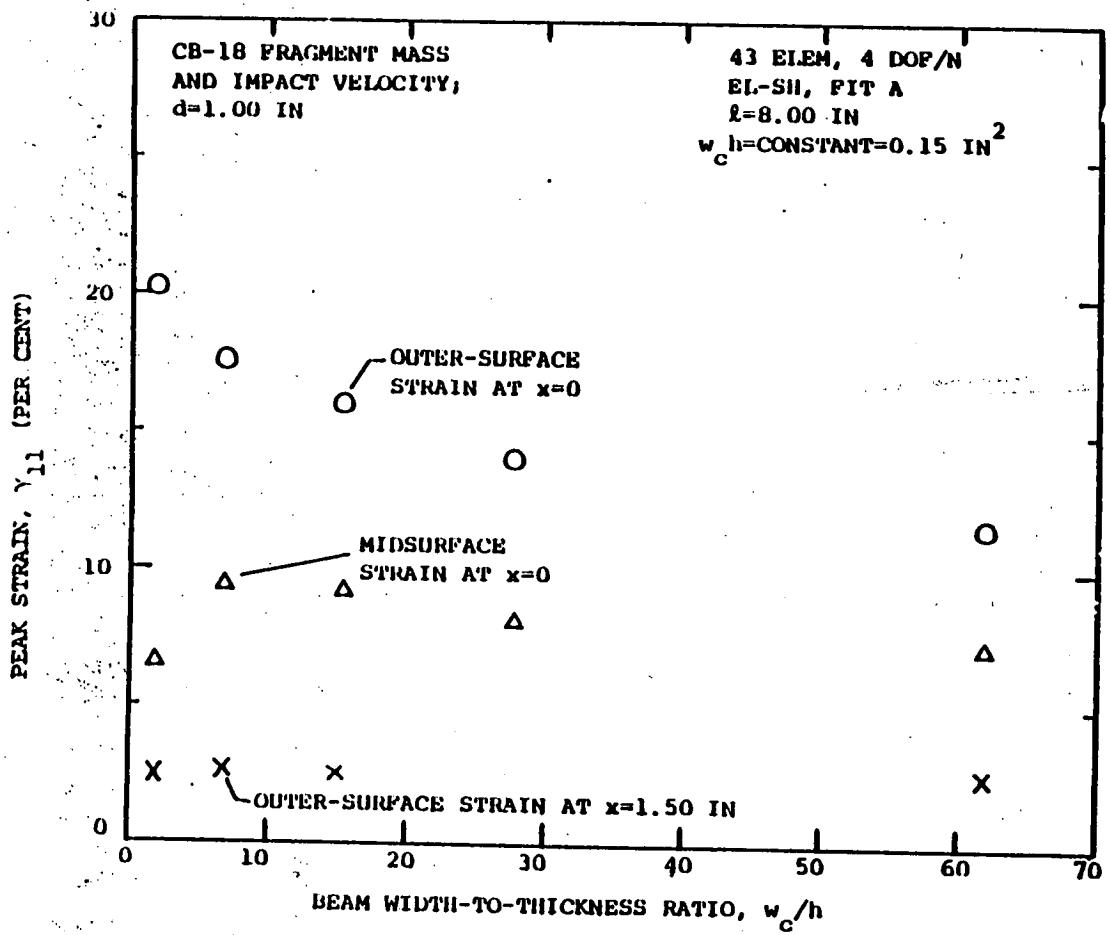

(a) Peak Predicted Strains

FIG. 51 CIVM-JET 4B 2-D PREDICTED PEAK STRAINS AND DEFLECTIONS AS A FUNCTION OF BEAM WIDTH-TO-THICKNESS RATIO FOR ALUMINUM BEAMS OF FIXED SPAN AND CROSS-SECTIONAL AREA FOR THE CB-18 FRAGMENT IMPACT CONDITIONS

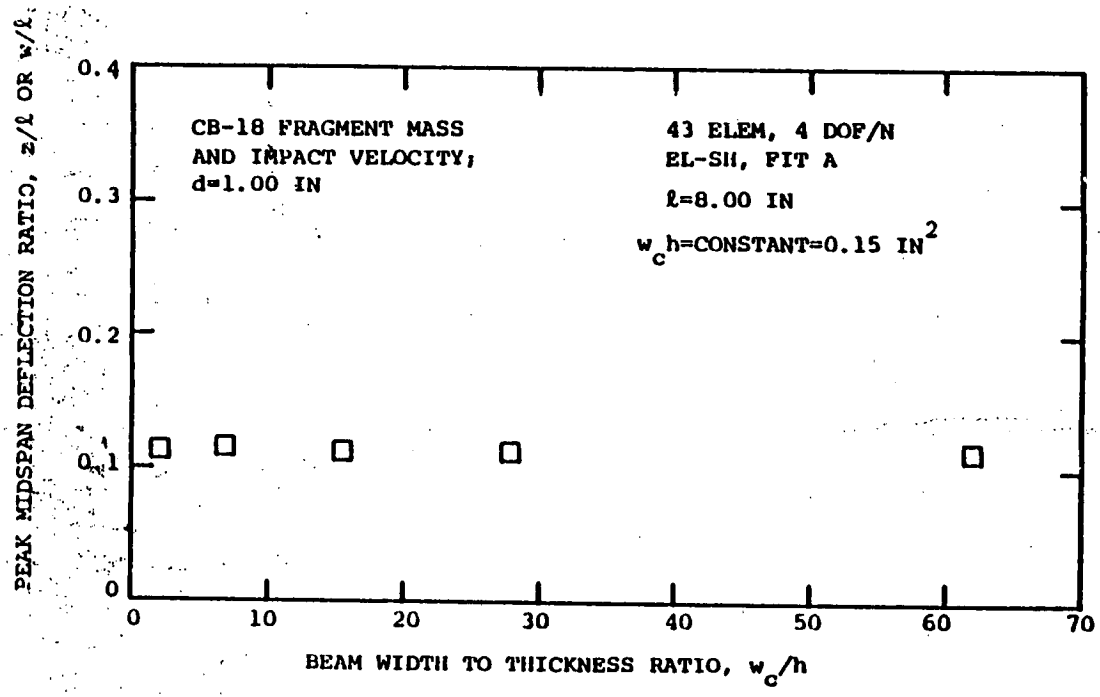

(b) Peak Predicted Deflections at Station x=0

FIG. 51 CONCLUDED (VARY w_c/h FOR $w_c h$=CONSTANT; CB-18 IMPACT CONDITIONS)

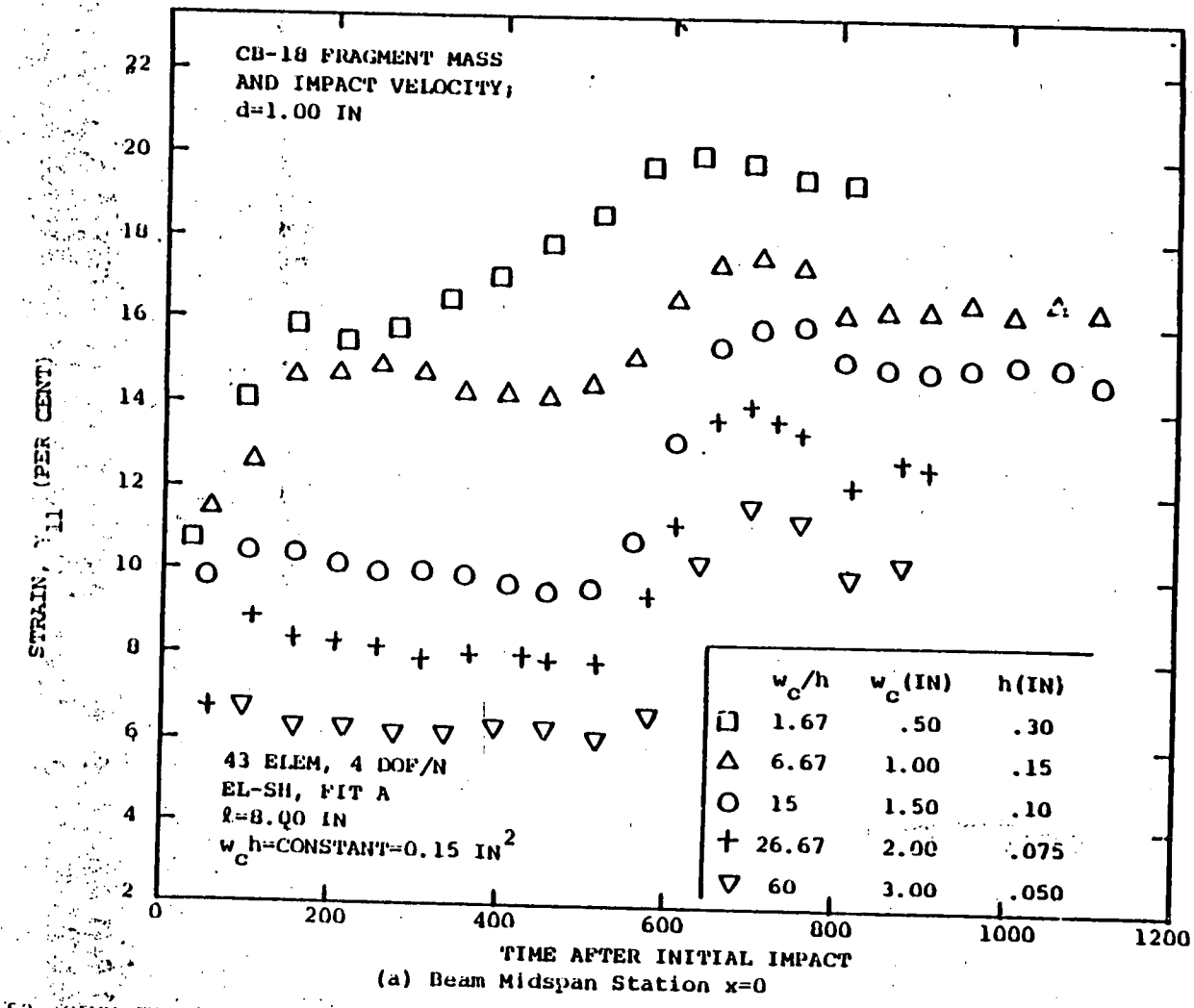

(a) Beam Midspan Station x=0

FIG. 52 CIVM-JET 4L 2-D PREDICTED TRANSIENT UPPER-SURFACE STRAINS AT TWO BEAM SPANWISE STATIONS FOR VARIOUS WIDTH-TO-THICKNESS RATIOS FOR ALUMINUM BEAMS OF FIXED SPAN AND CROSS-SECTIONAL AREA UNDER THE CB-18 FRAGMENT IMPACT CONDITIONS

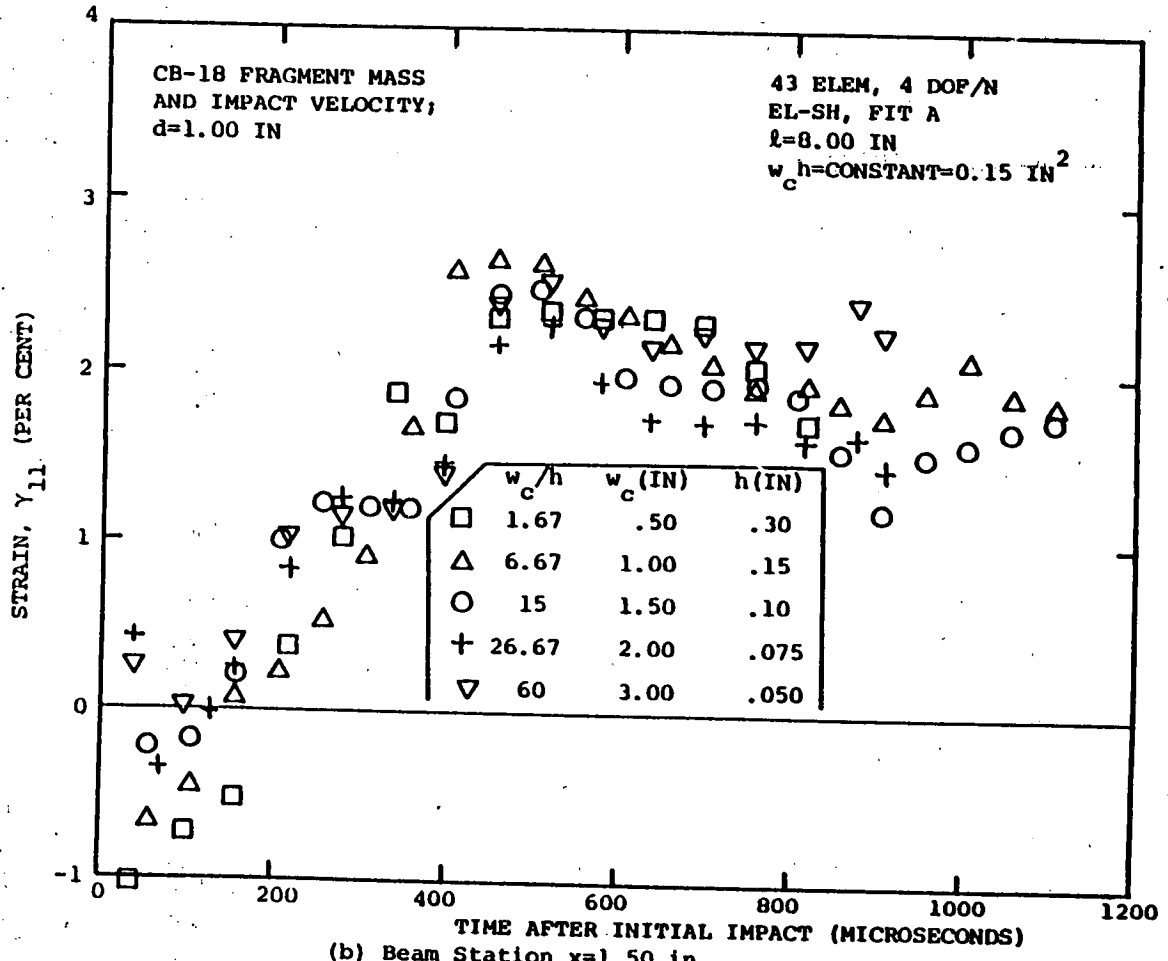

(b) Beam Station x=1.50 in

FIG. 52 CONCLUDED (VARY w_c/h FOR $w_c h$=CONSTANT; CB-18 IMPACT CONDITIONS)

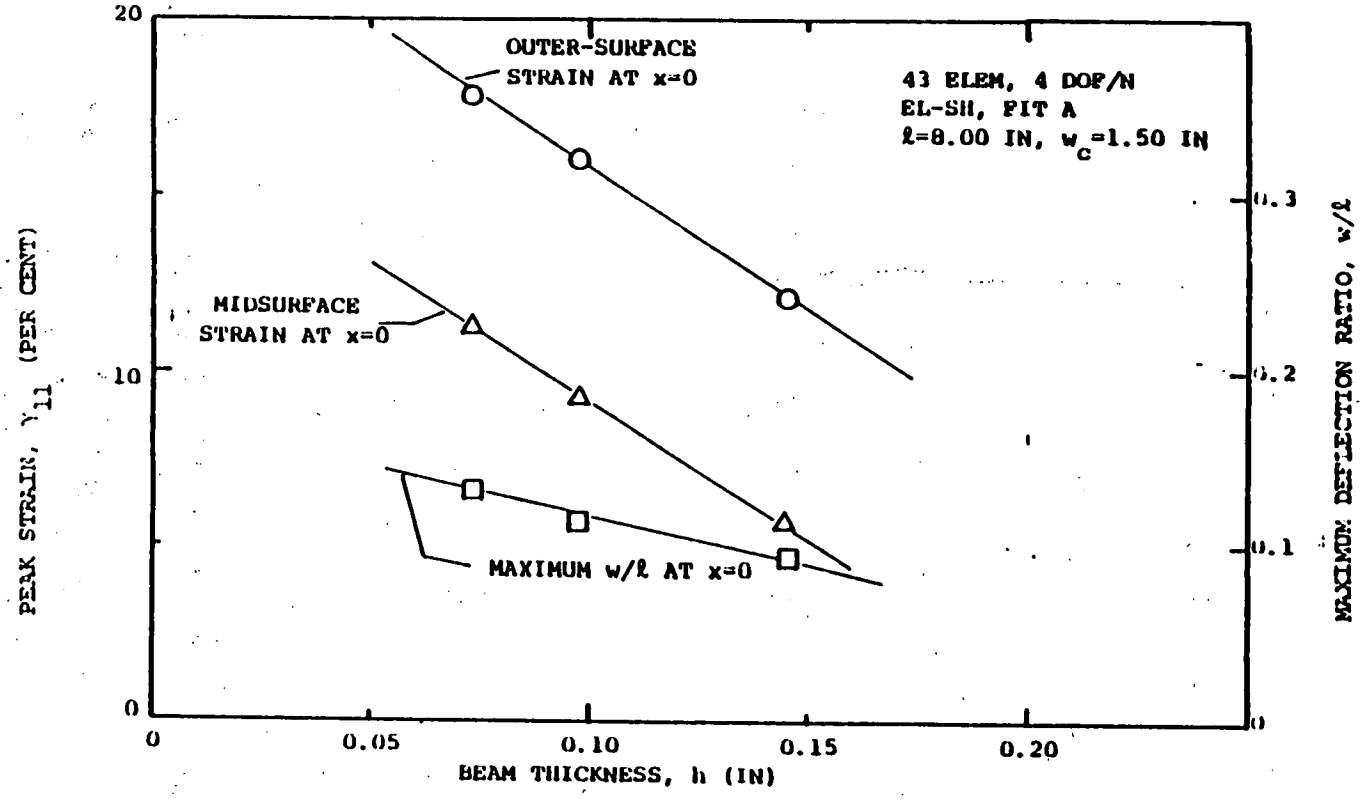

FIG. 53 EFFECT OF BEAM THICKNESS ON THE CIVM-JET 4B PREDICTED 2-D IMPACT-INDUCED PEAK MIDSPAN STRAIN AND DEFLECTION OF AN ALUMINUM BEAM OF FIXED WIDTH AND SPAN IMPACTED AT MIDSPAN BY A FRAGMENT WITH THE CB-18 IMPACT CONDITIONS

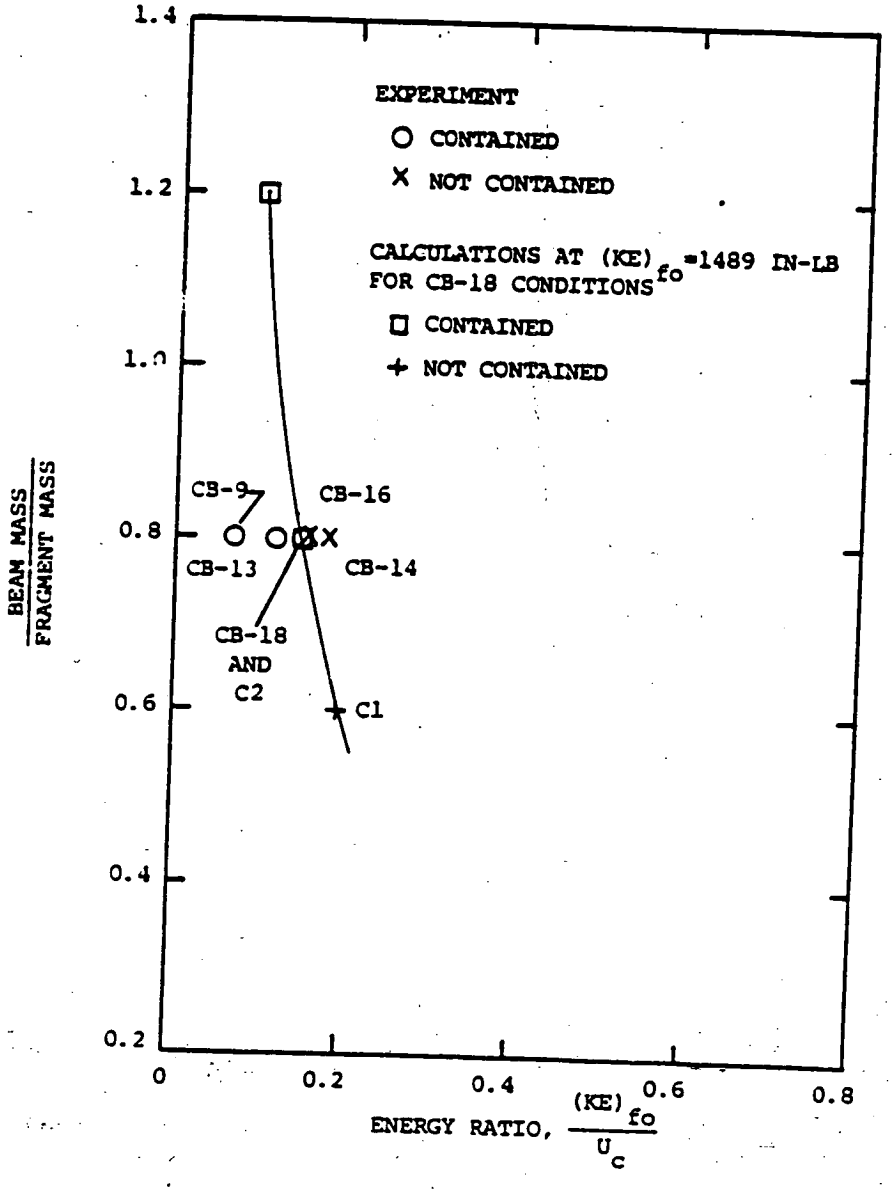

FIG. 54 FRAGMENT-BEAM IMPACT DATA AS A FUNCTION OF THE RATIO BEAM MASS TO FRAGMENT MASS VERSUS THE ENERGY RATIO $(KE)_f/U_c$

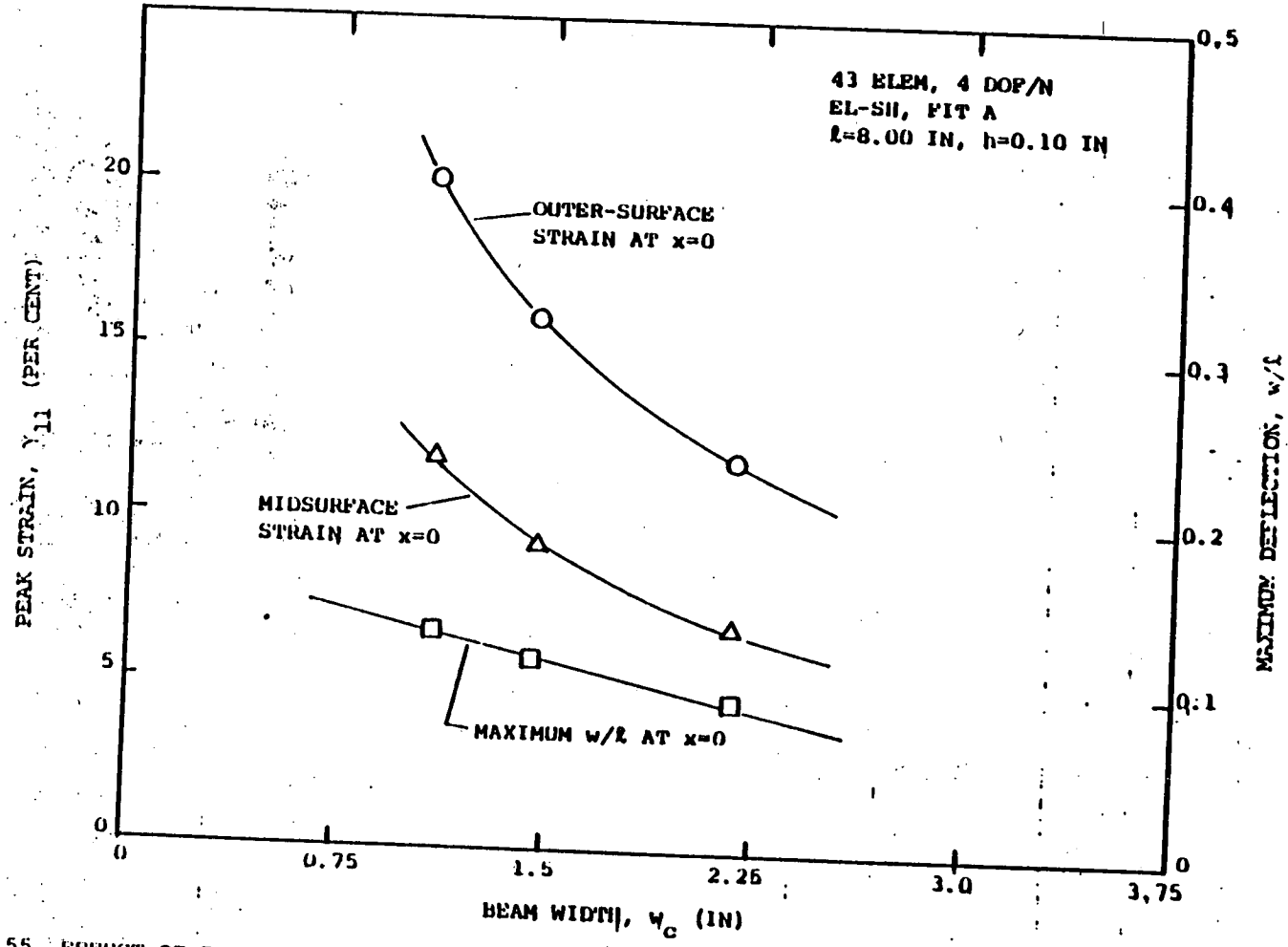

FIG. 55 EFFECT OF BEAM WIDTH ON THE CIVM-JET 4B PREDICTED 2-D IMPACT-INDUCED PEAK MIDSPAN STRAIN AND DEFLECTION OF AN ALUMINUM BEAM OF FIXED SPAN AND THICKNESS IMPACTED AT MIDSPAN BY A FRAGMENT WITH THE CB-18 IMPACT CONDITIONS

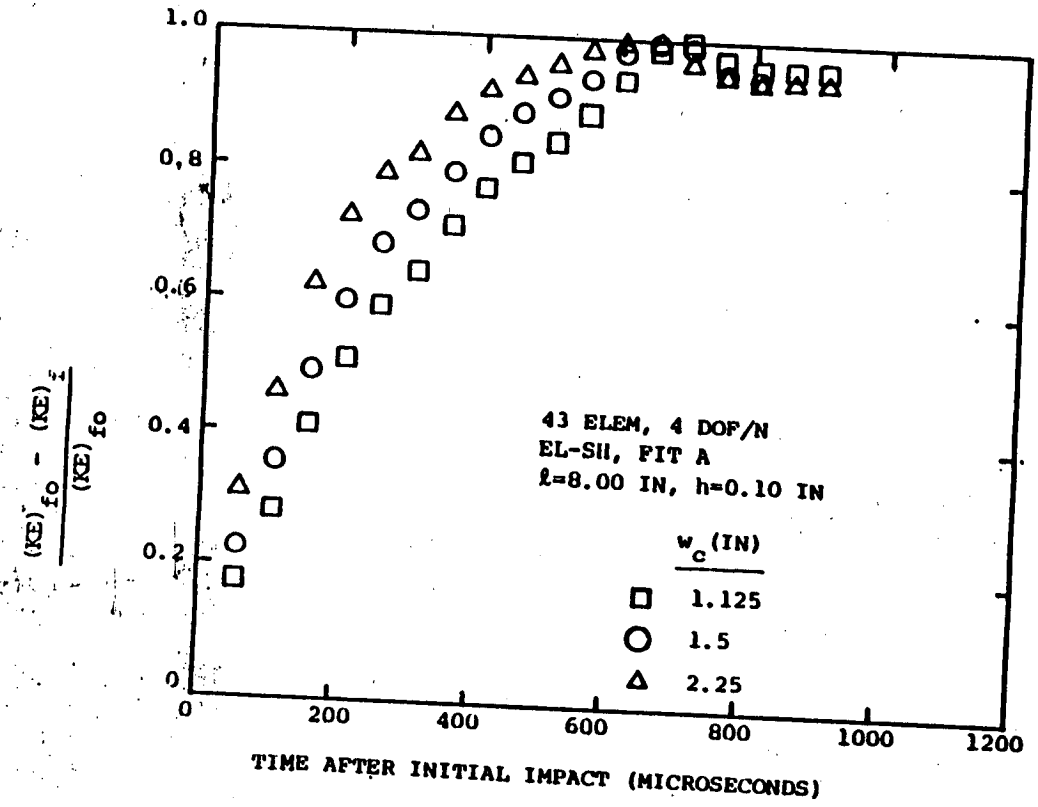

FIG. 56 EFFECT OF BEAM WIDTH ON THE PREDICTED HISTORY OF FRAGMENT KINETIC ENERGY LOSS FOR ALUMINUM BEAMS OF FIXED SPAN AND THICKNESS SUBJECTED TO MIDSPAN IMPACT BY A FRAGMENT WITH THE CB-18 IMPACT CONDITIONS

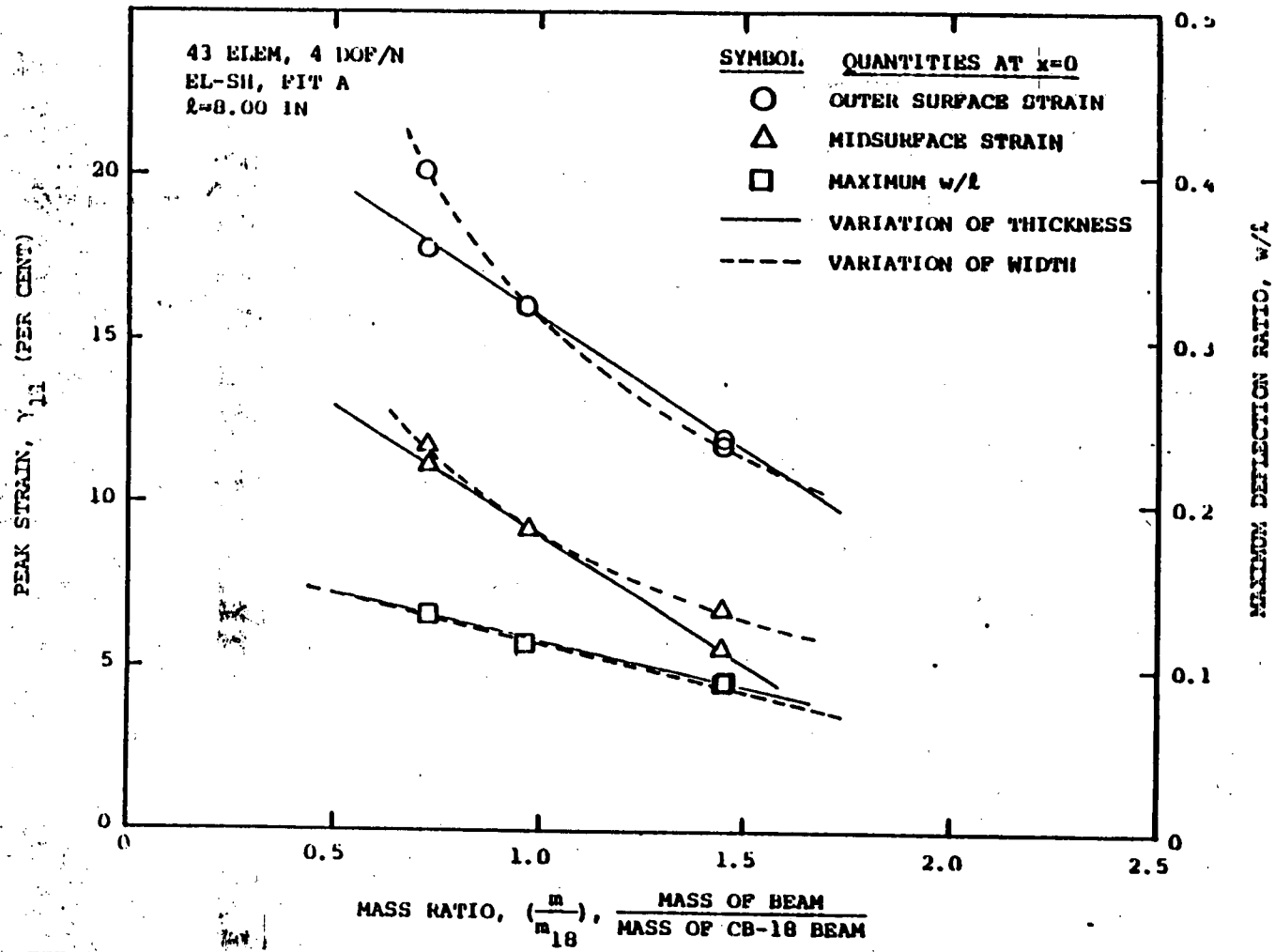

FIG. 57 EFFECT OF CROSS SECTIONAL ASPECT RATIO ON THE CIVM-JET 4B PREDICTED 2-D IMPACT INDUCED PEAK MIDSPAN UPPER SURFACE STRAIN AND DEFLECTION OF AN ALUMINUM BEAM OF FIXED SPAN AND VARIABLE MASS PER UNIT SPAN IMPACTED AT MIDSPAN BY A 2-D FRAGMENT WITH THE CB-18 IMPACT CONDITIONS

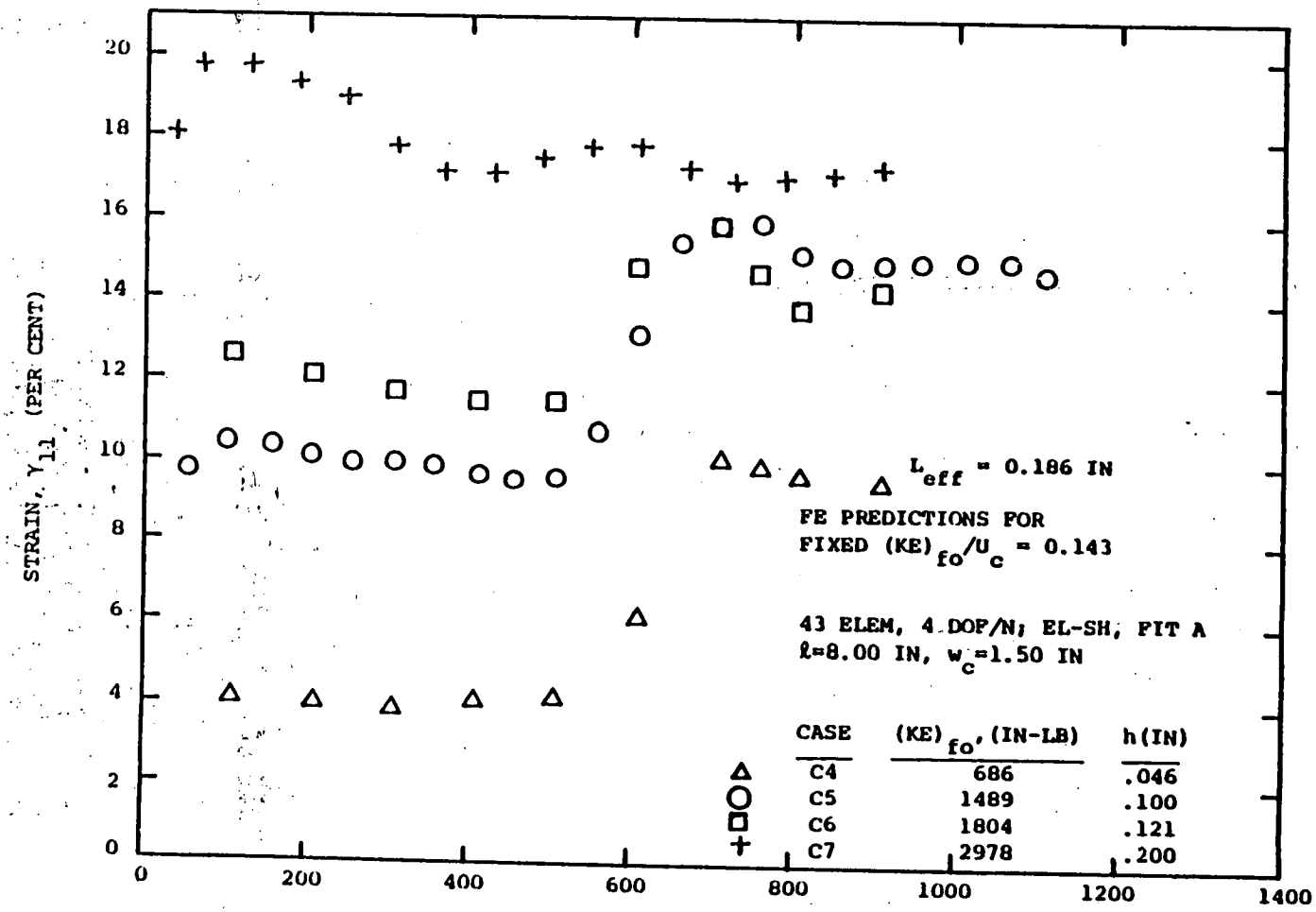

(a) Upper-Surface Strain at the Midspan Station x=0

FIG. 58 PREDICTED TRANSIENT RESPONSES OF ALUMINUM CONTAINMENT BEAMS OF FIXED SPAN AND WIDTH BUT WITH THICKNESS SELECTED FOR A GIVEN $(KE)_f/U_c$ RATIO AND SUBJECTED TO 2-D IDEALIZED MIDSPAN IMPACT FOR VARIOUS $(KE)_{fo}$ VALUES

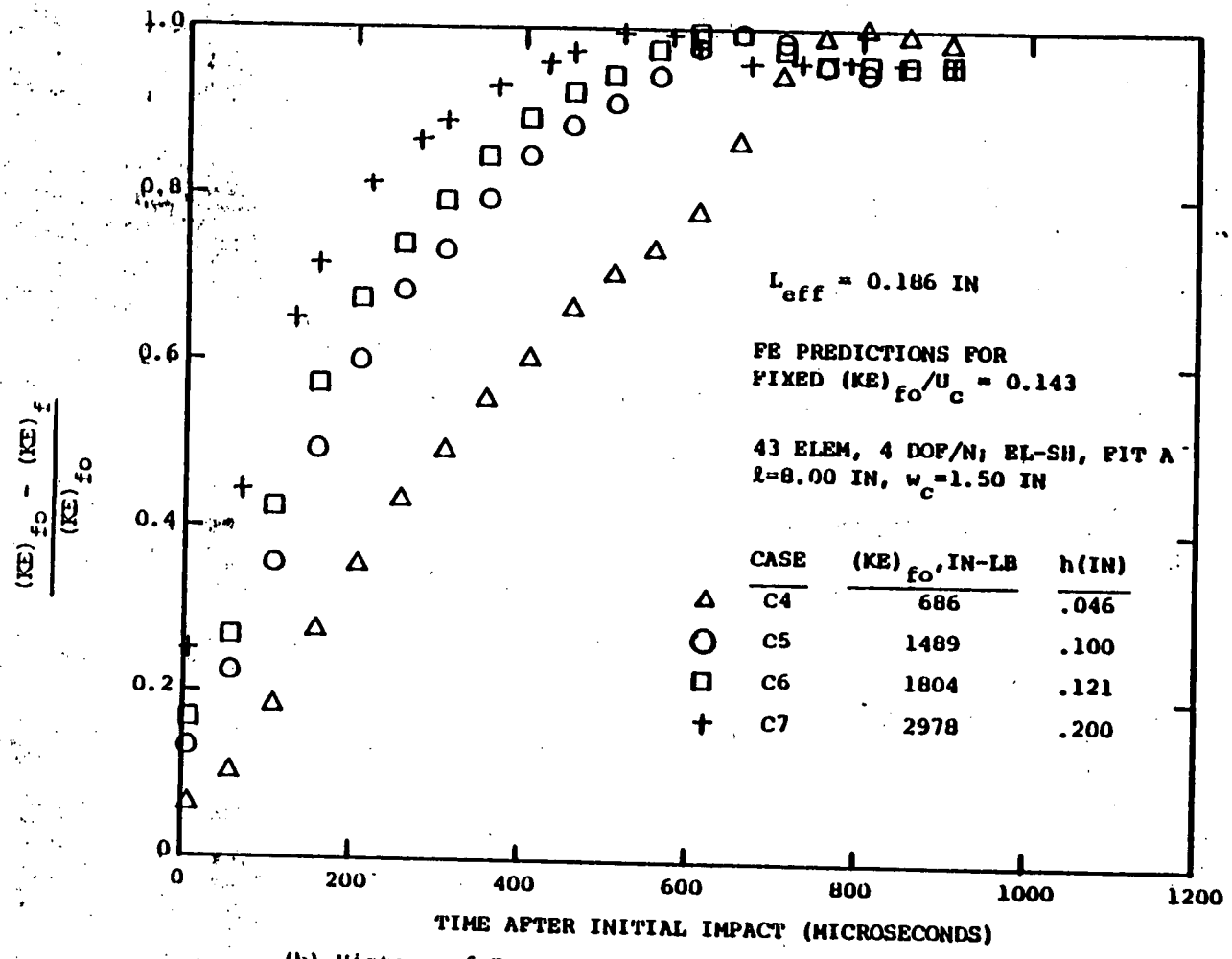

(b) History of Fragment Energy Loss Ratio

FIG. 58 CONCLUDED (VARY h AND $(KE)_{fo}$ WITH FIXED ℓ, w_c, AND $(KE)_{fo}/U_c$)

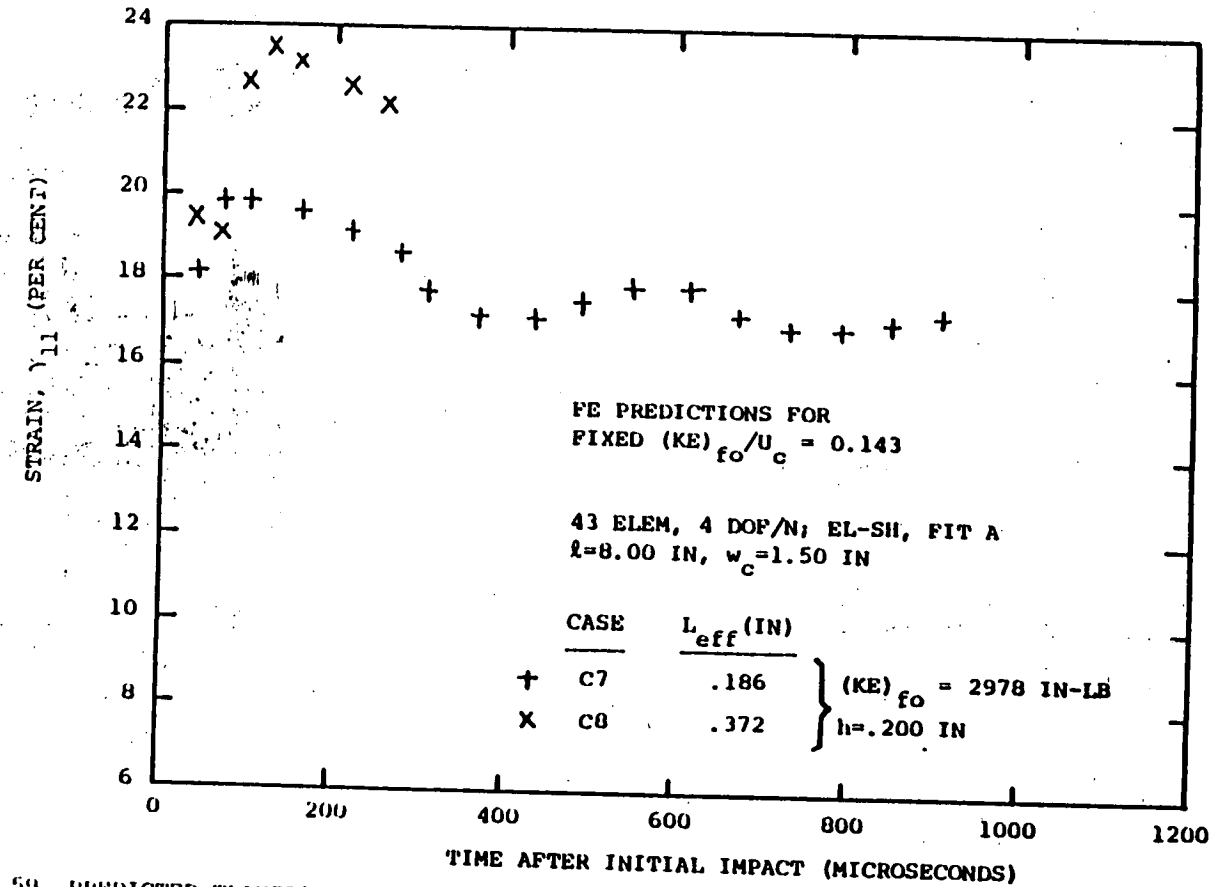

FIG. 59 PREDICTED TRANSIENT UPPER-SURFACE MIDSPAN STRAINS OF ALUMINUM CONTAINMENT BEAMS SUBJECTED TO FRAGMENT IMPACT OF FIXED $(KE)_{fo}$ AND FIXED ENERGY RATIO $(KE)_{fo}/U_c$ BUT WITH DIFFERENT IMPACT-AFFECTED LENGTHS

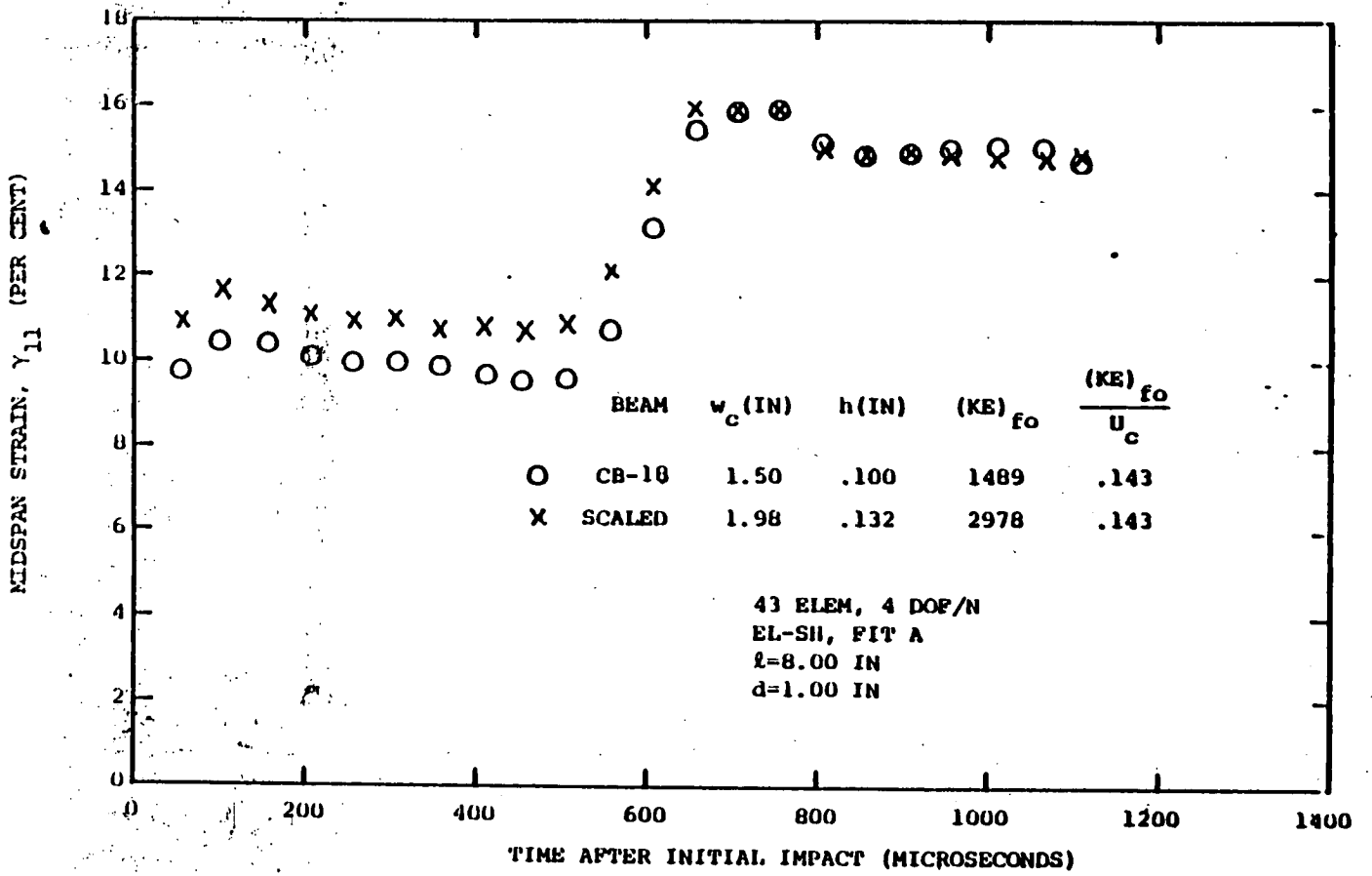

FIG. 60 COMPARISON OF CIVM-JET 4B PREDICTED UPPER-SURFACE MIDSPAN TRANSIENT STRAIN FOR THE CB-18 BEAM WITH THAT FOR A SCALED BEAM SUBJECTED TO MIDSPAN IMPACT AT THE CB-18 VELOCITY BY A 2-D FRAGMENT OF 75 PER CENT GREATER MASS

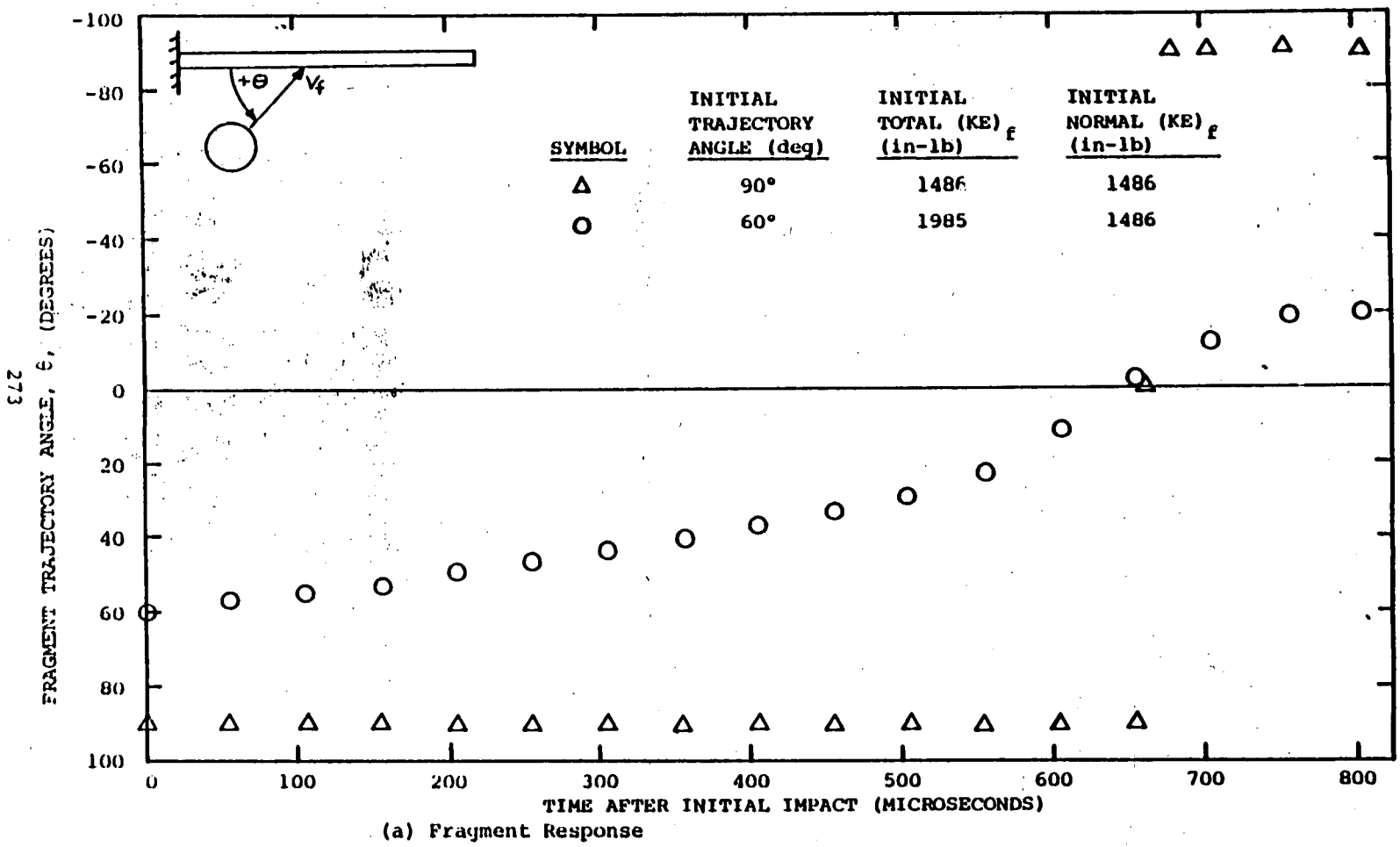

(a) Fragment Response

FIG. 61 EFFECTS OF POSTULATED INITIAL IMPACT ANGLES ON THE RESPONSES OF THE FRAGMENT AND THE IMPACTED DOUBLY-CLAMPED BEAM, FOR MIDSPAN INITIAL IMPACT AND CB-18 BEAM GEOMETRY

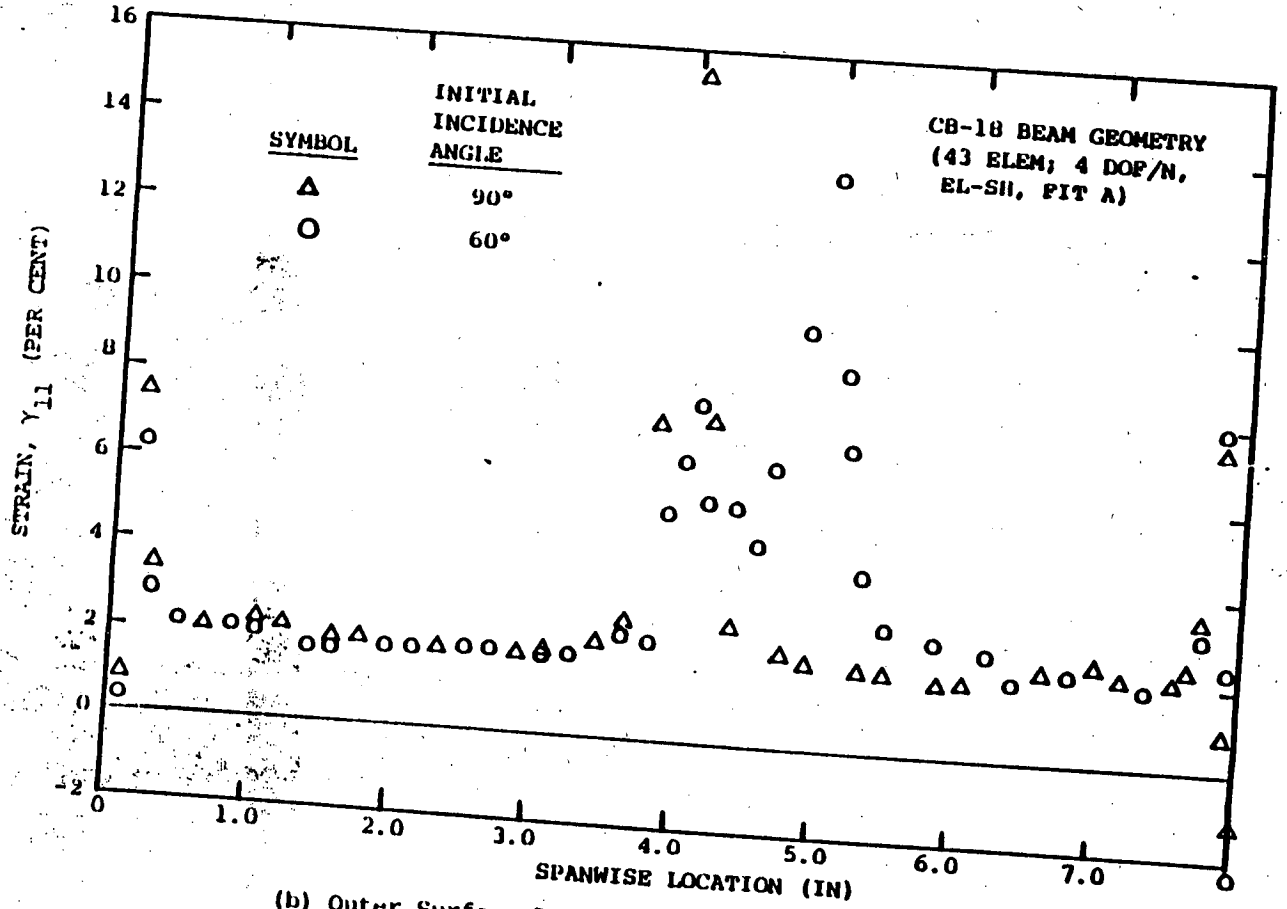

(b) Outer Surface Beam Response at Time of Peak Strain

FIG. 61 CONCLUDED (CB-18, IMPACT OBLIQUITY)

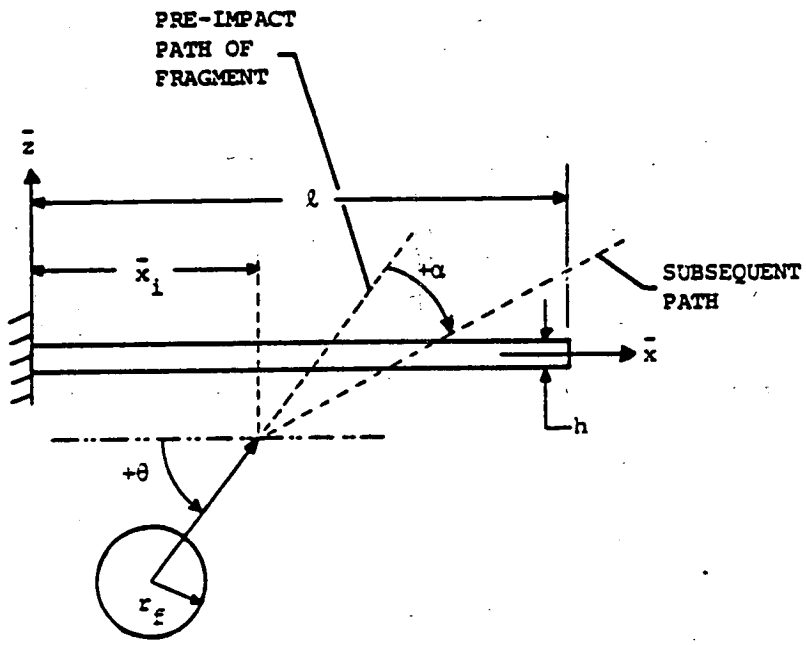

NOTE: α IS POSITIVE CLOCKWISE

θ IS POSITIVE COUNTERCLOCKWISE

$\xi = \bar{x}_i/\ell$

FIG. 62 SCHEMATIC OF A SIMPLIFIED CANTILEVER-BEAM DEFLECTOR WITH IMPACT BY AN IDEALIZED FRAGMENT

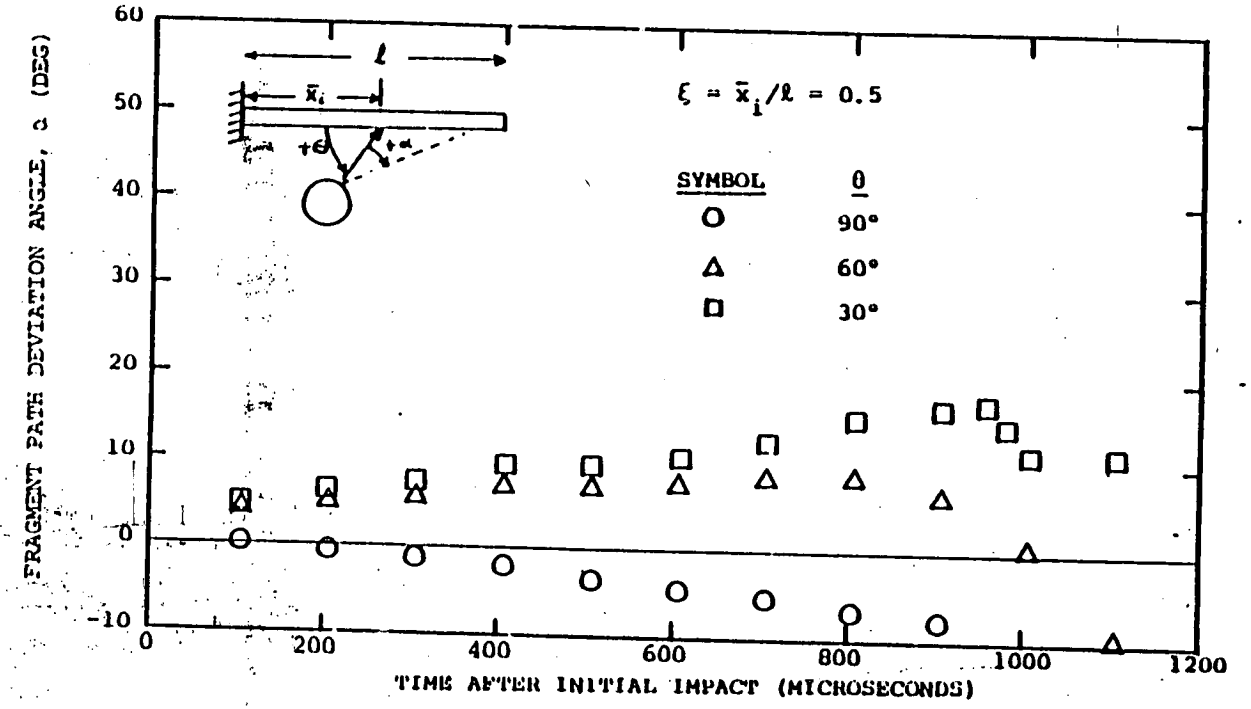

(a) Fragment Response

FIG. 63 RESPONSES OF A CANTILEVER-BEAM FRAGMENT DEFLECTOR, IMPACTED AT MIDLENGTH (ξ=0.5) BY AN IDEALIZED FRAGMENT AT THREE VALUES OF INITIAL INCIDENCE ANGLE: θ=90°, 60°, AND 30°.

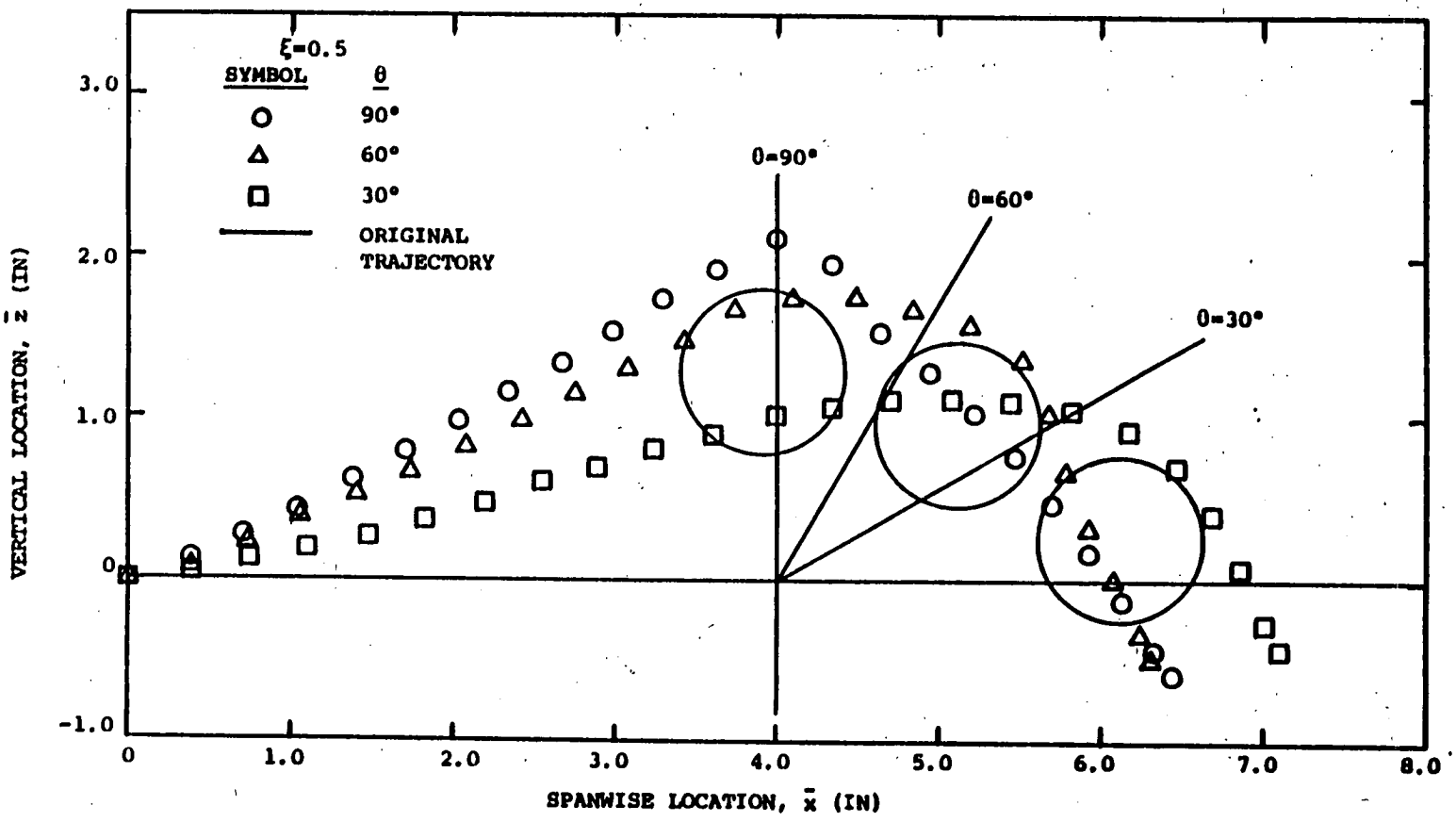

(b) Deflector Profile and Fragment Location at TAII = 905 Microseconds

FIG. 63 CONTINUED (ξ=0.5)

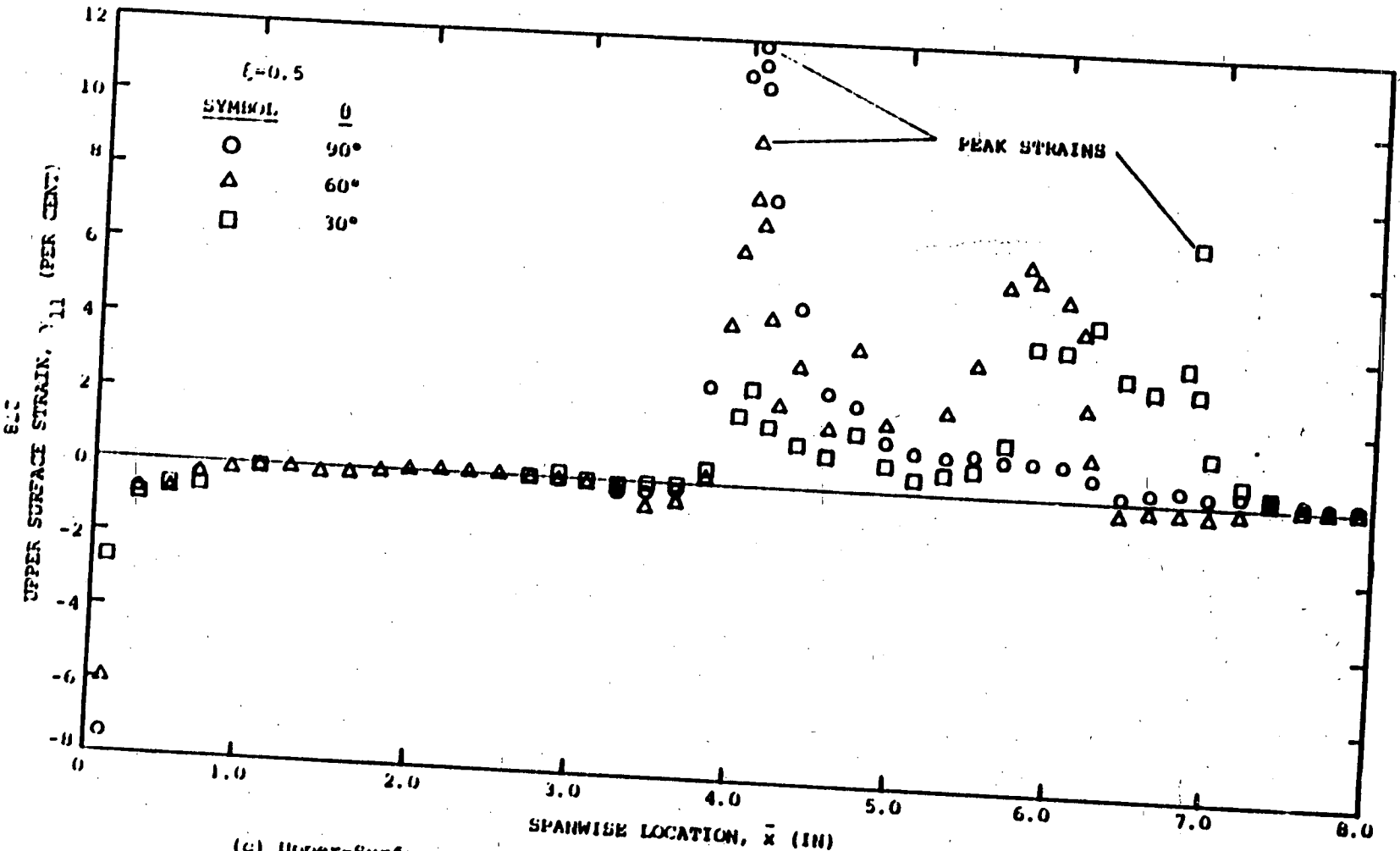

(c) Upper-Surface Strain Profile at TAII = 905 Microseconds and Peak Strains

FIG. 61 CONCLUDED (ξ=0.5)

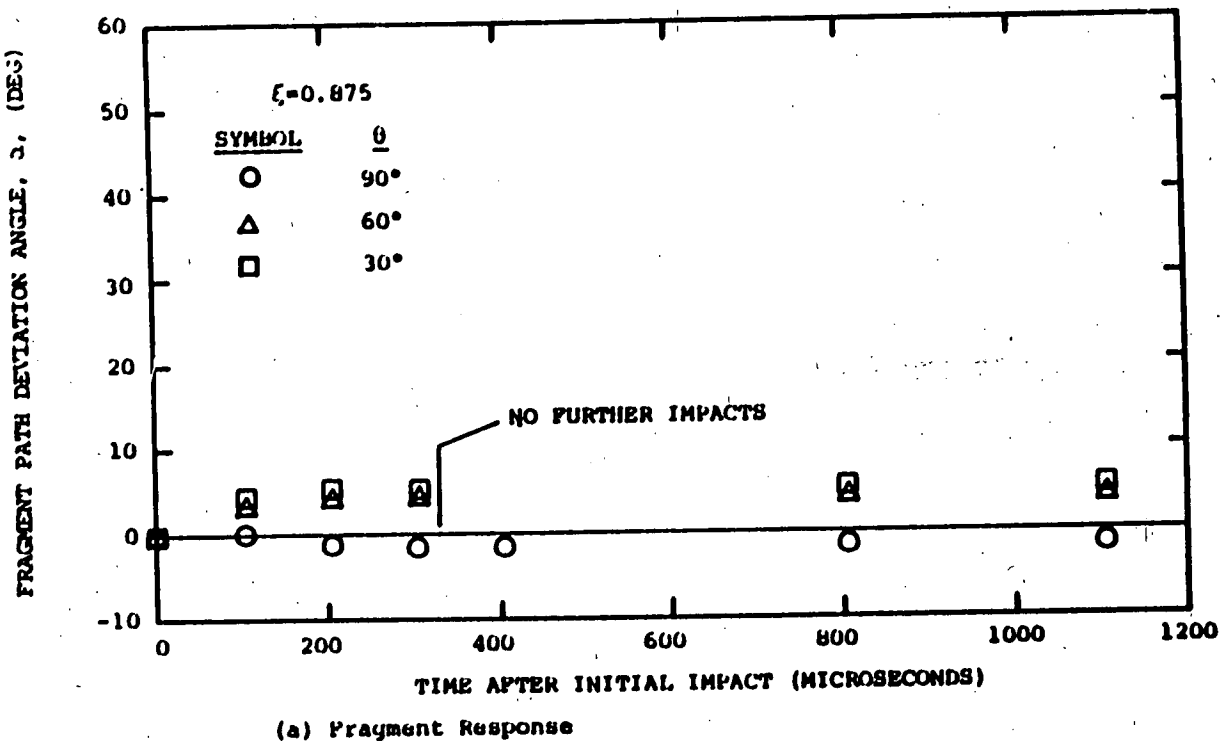

(a) Fragment Response

FIG. 64 RESPONSES OF A CANTILEVER-BEAM DEFLECTOR, IMPACTED AT ξ=0.875 BY AN IDEALIZED FRAGMENT AT THREE VALUES OF INITIAL INCIDENCE ANGLE: θ=90°, 60°, AND 30°

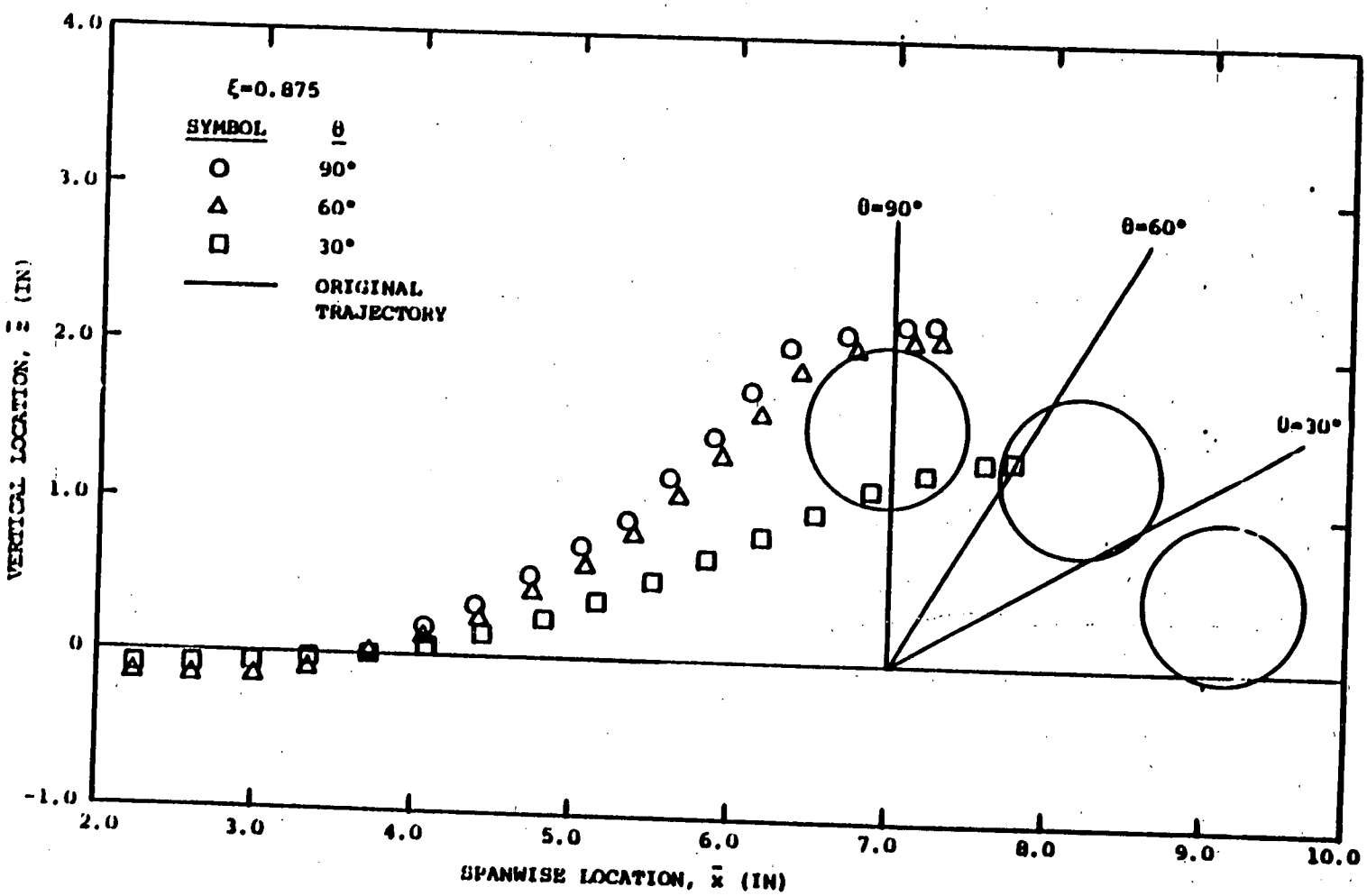

(b) Deflector Profile and Fragment Location at TAII = 905 Microseconds

FIG. 64 CONTINUED (ξ=0.875)

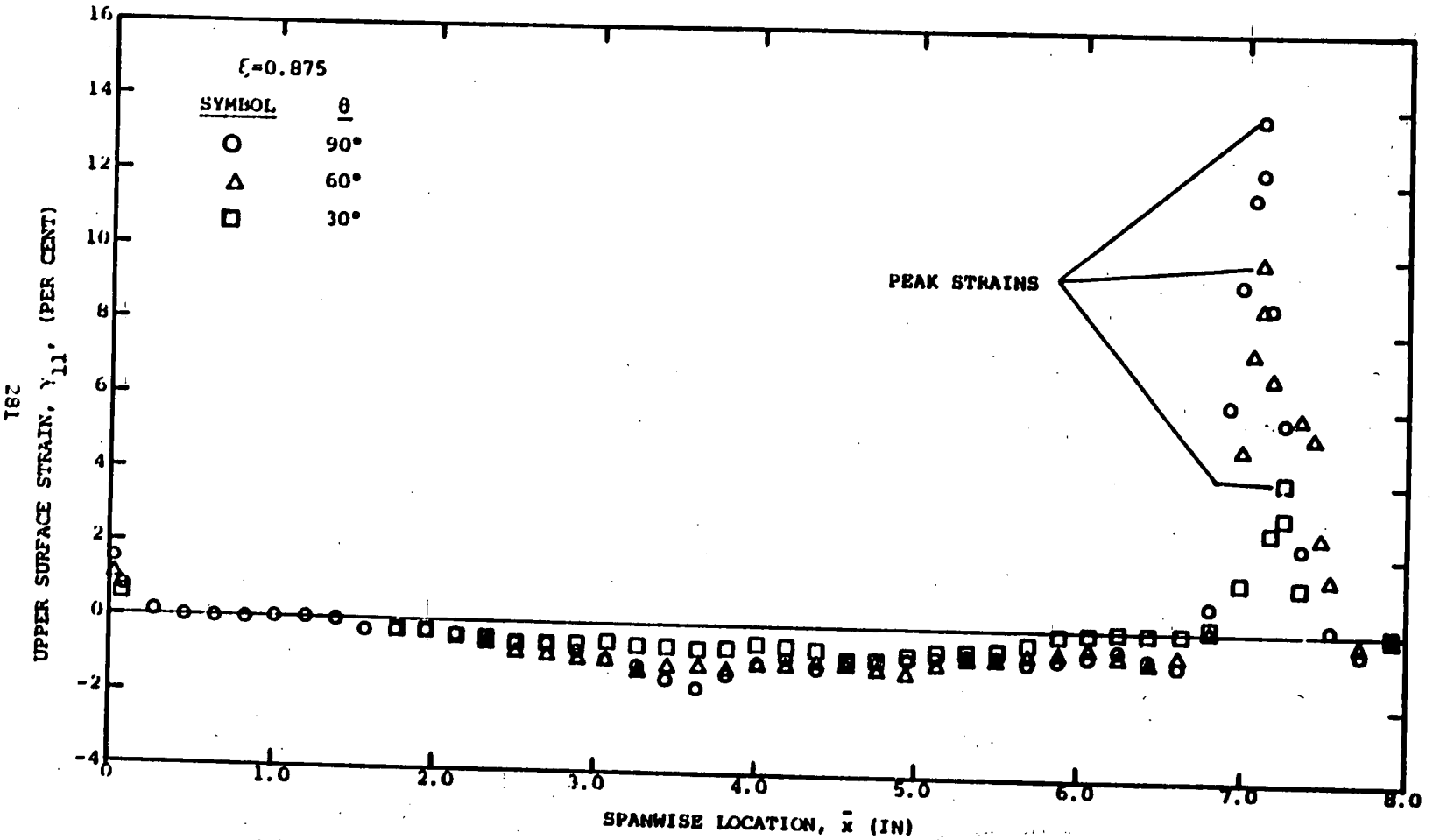

(c) Upper Surface Strain Profile at TAII = 905 Microseconds and Peak Strains

FIG. 64 CONCLUDED (ξ=0.875)

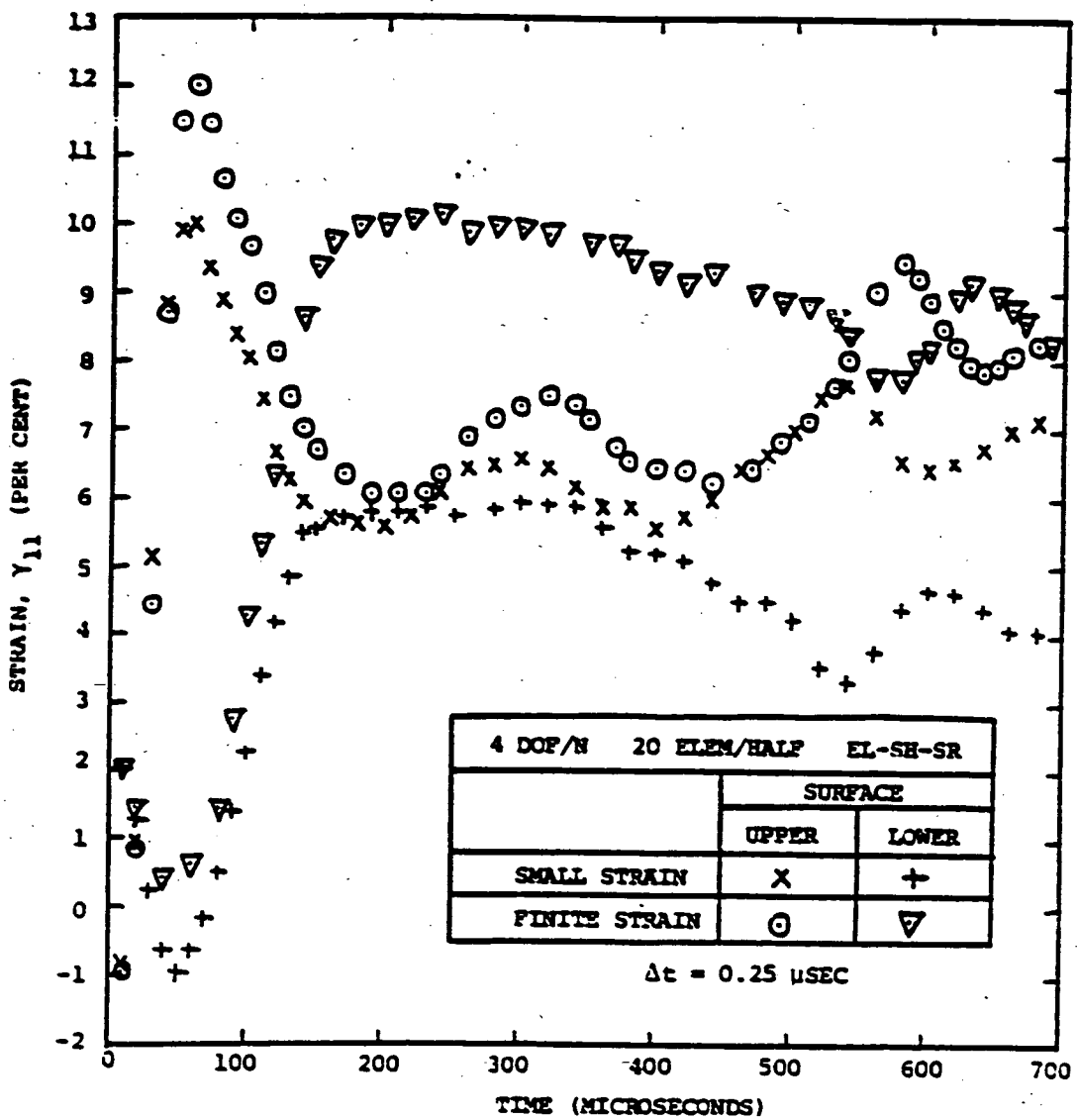

(a) Transient Strain at Station x=0

FIG. 65 MEASUREMENTS AND/OR PREDICTIONS OF TRANSIENT LONGITUDINAL LAGRANGIAN (GREEN) STRAIN ON THE SURFACE FOR VARIOUS SPANWISE STATIONS OF EXPLOSIVELY-IMPULSED 6061-T651 ALUMINUM BEAM CB-4

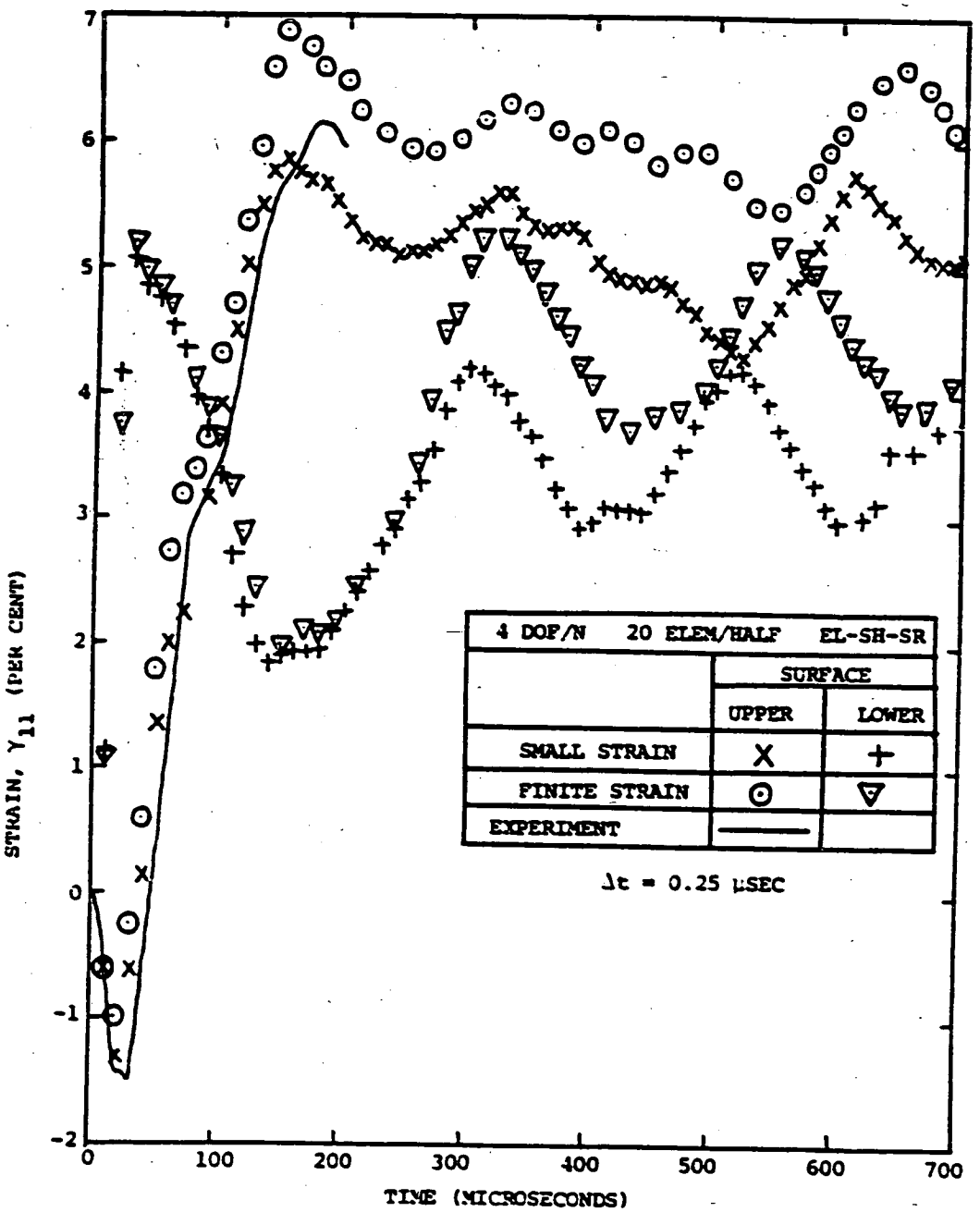

(b) Transient Strain at Station x=1.40 in

FIG. 65 CONTINUED (CB-4)

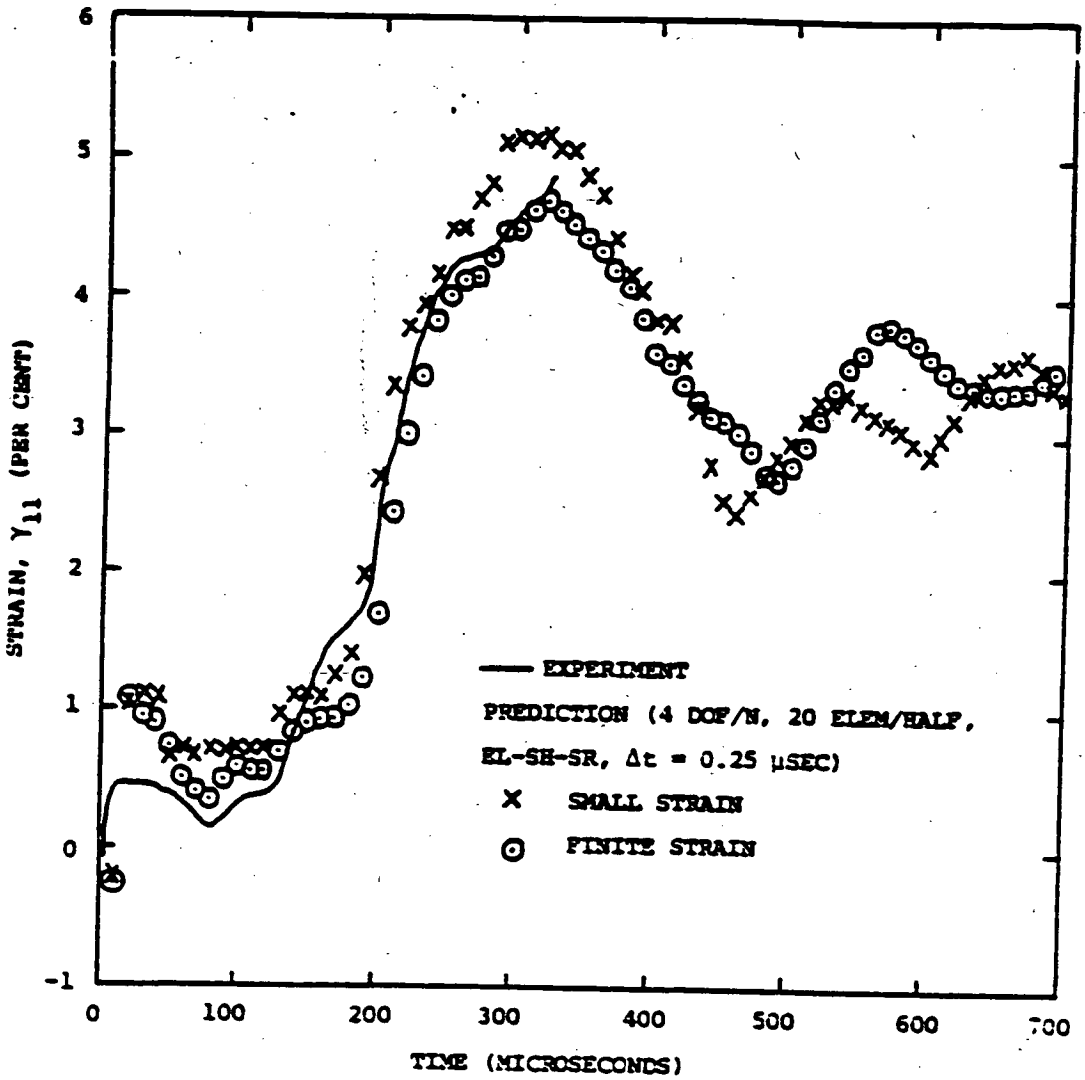

(c) Upper-Surface Transient Strain at x=2.20 in

FIG. 65 CONTINUED (CB-4)

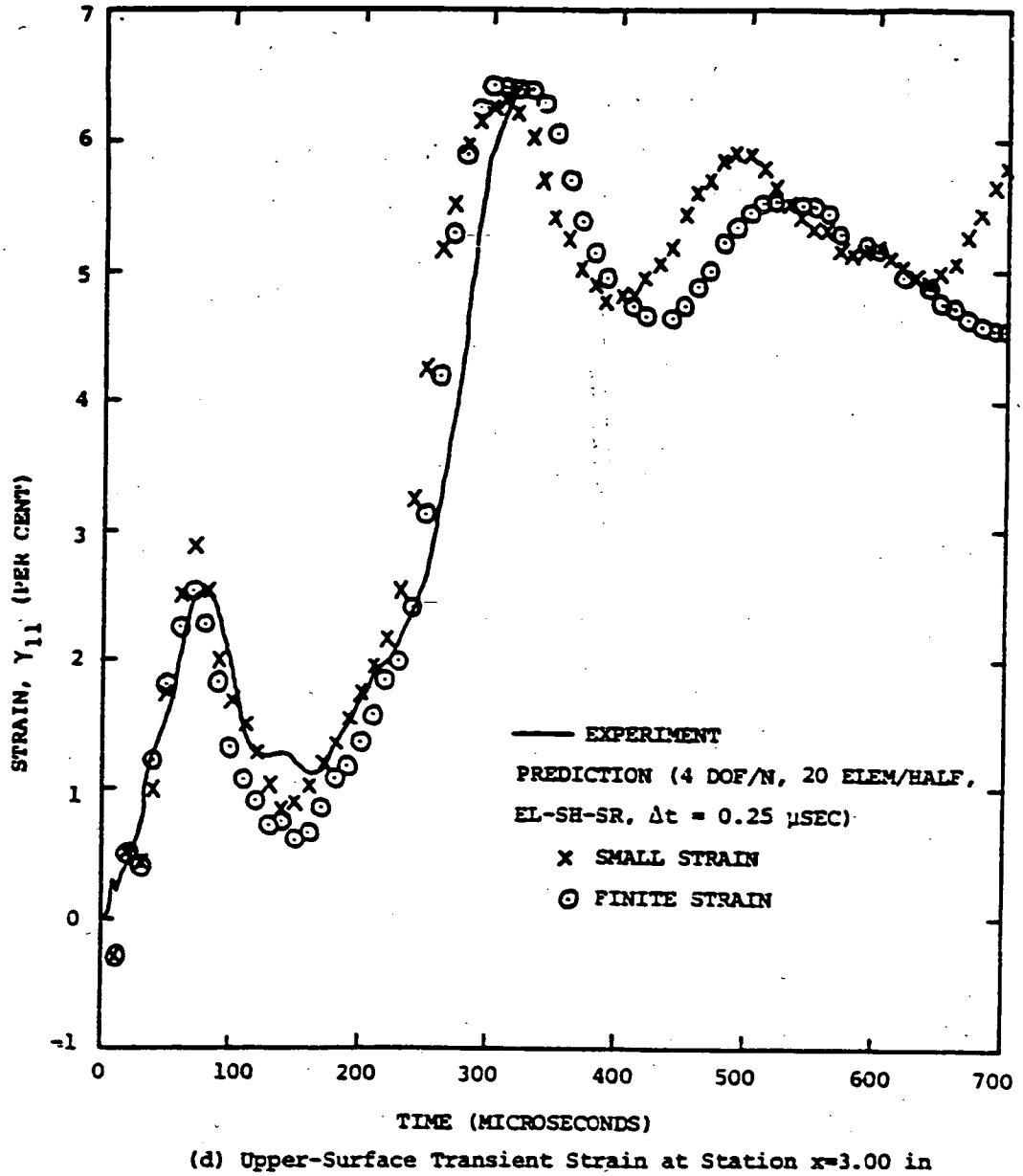

(d) Upper-Surface Transient Strain at Station x=3.00 in

FIG. 65 CONTINUED (CB-4)

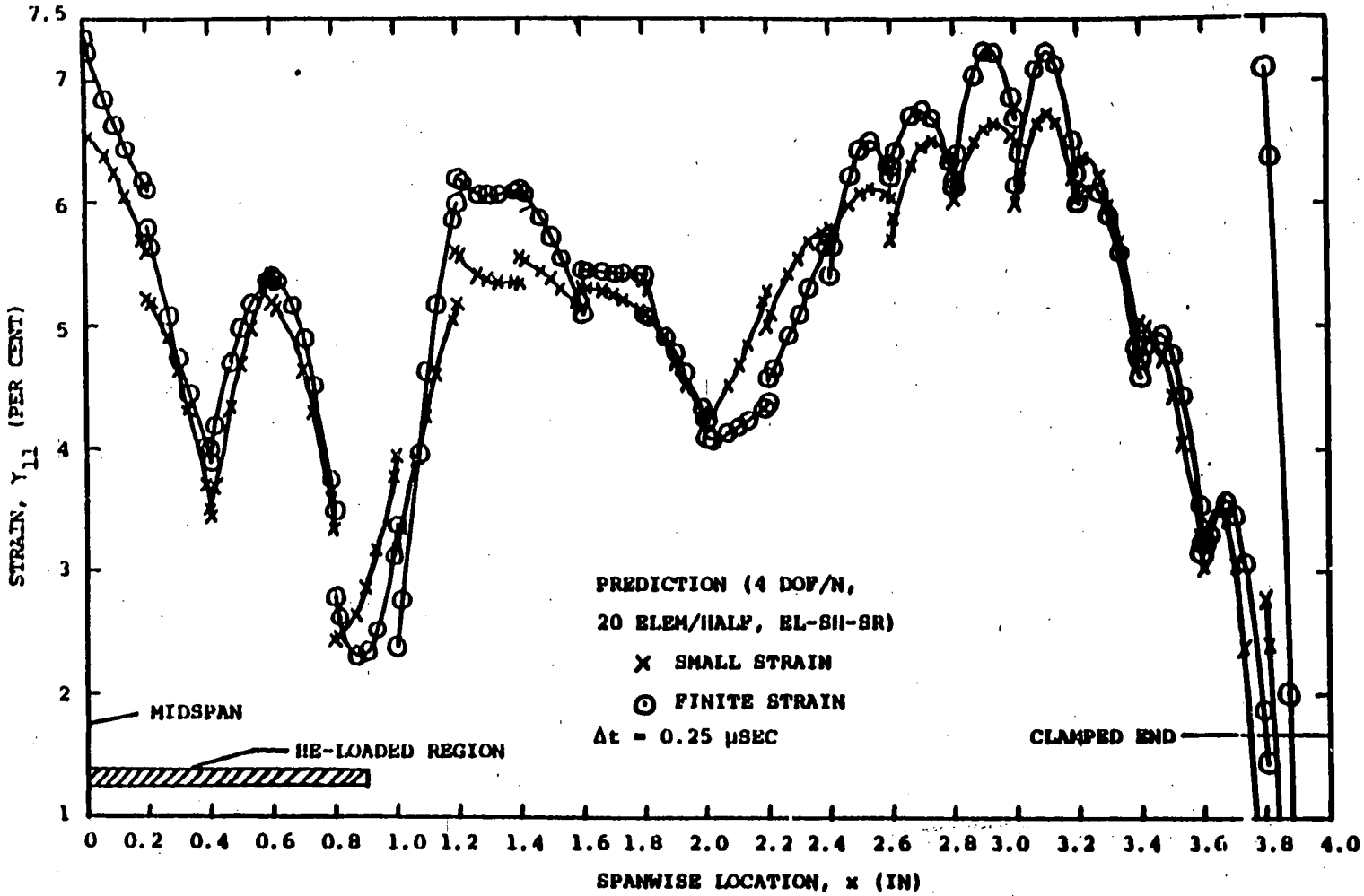

(e) Spanwise Distribution of Upper-Surface Strain at t=300 μsec

FIG. 65 CONCLUDED (CB-4)

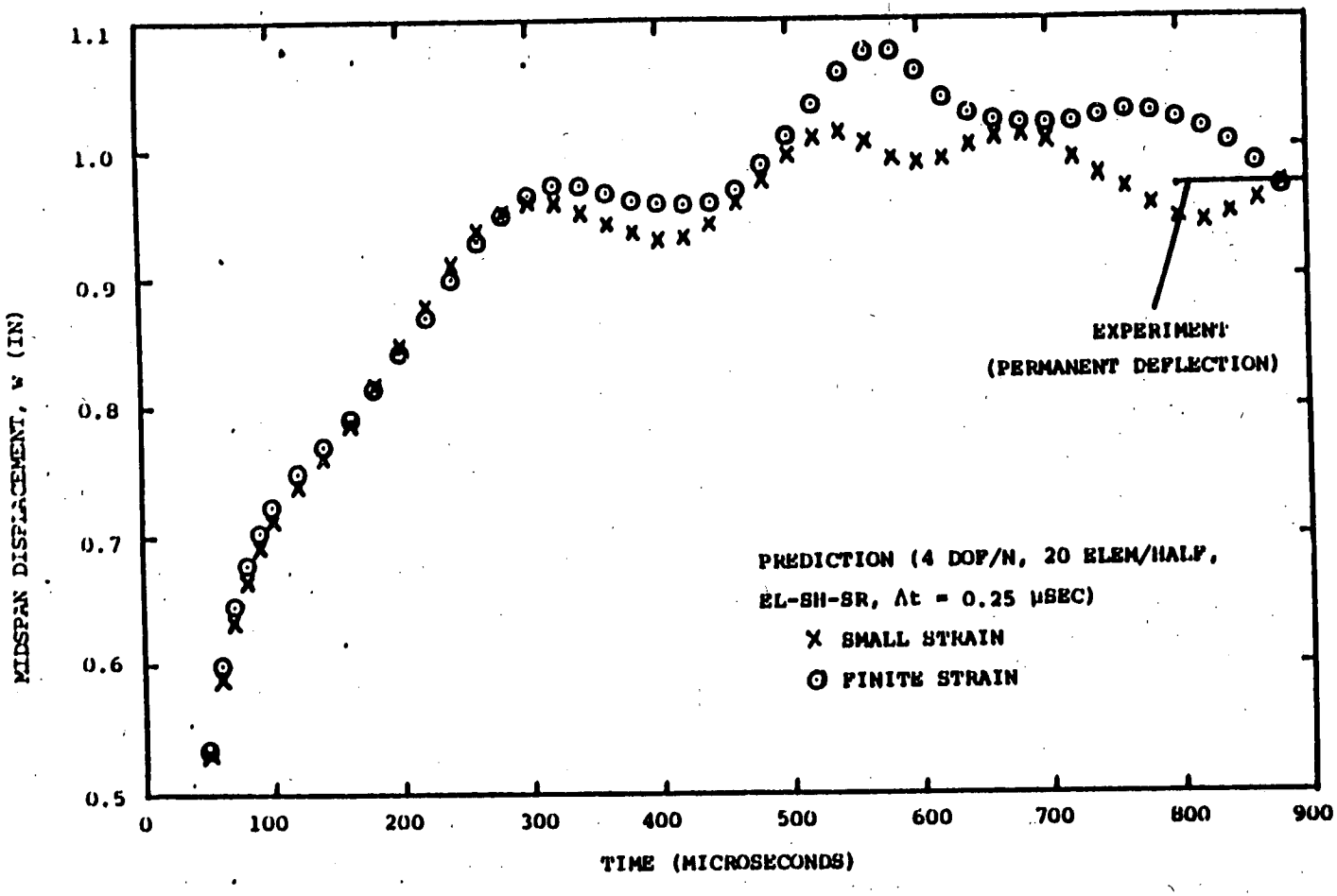

FIG. 66 COMPARISON OF TRANSIENT MIDSPAN DISPLACEMENT PREDICTED FROM THE SMALL-STRAIN AND THE FINITE-STRAIN FORMULATION FOR EXPLOSIVELY-IMPULSED 6061-T651 ALUMINUM BEAM CB-4

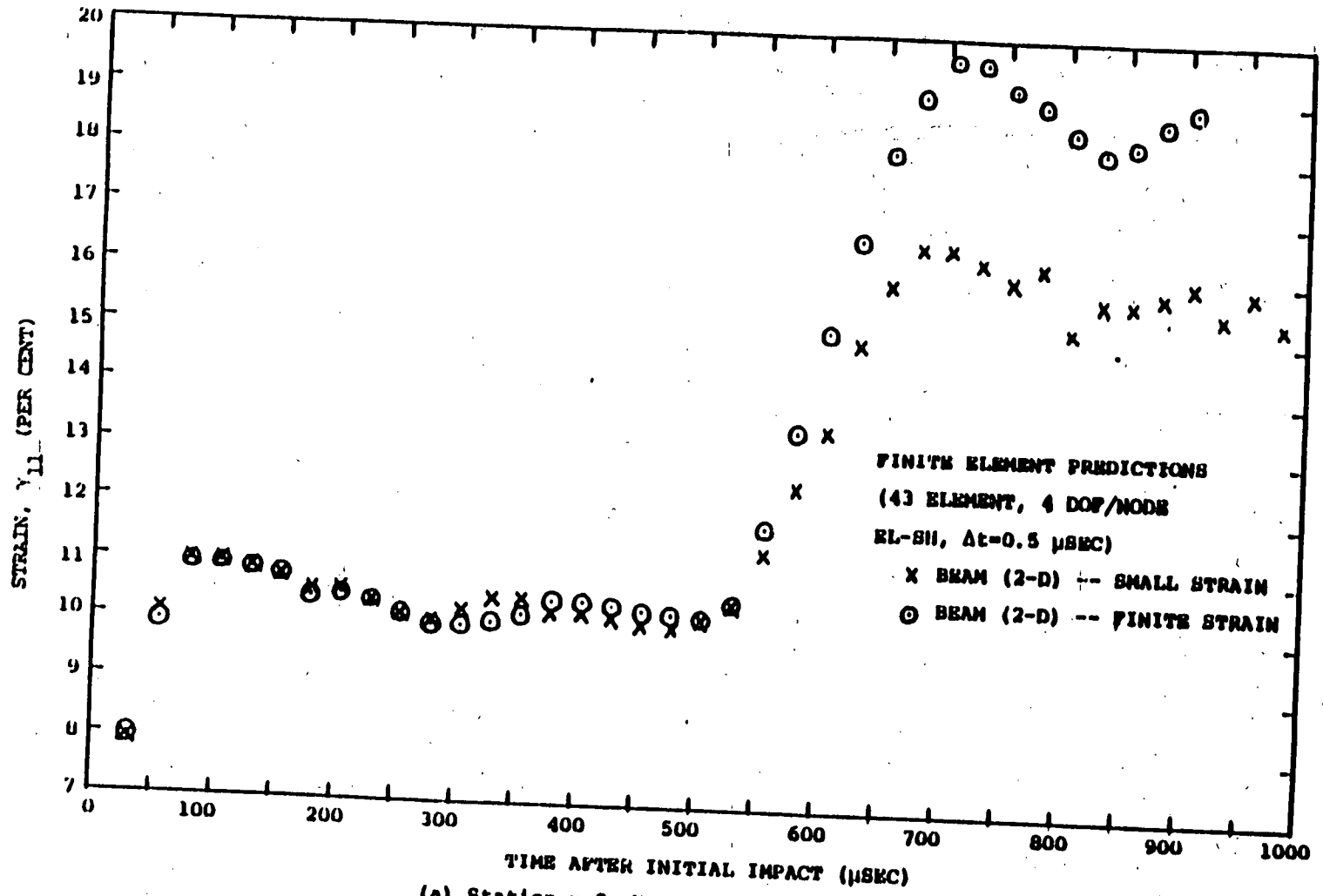

(a) Station x=0, Upper Surface

FIG. 67 MEASUREMENTS AND/OR PREDICTIONS OF TRANSIENT LONGITUDINAL LAGRANGIAN (GREEN) STRAIN ON THE SURFACE FOR VARIOUS SPANWISE STATIONS OF STEEL-SPHERE-IMPACTED 6061-T651 ALUMINUM BEAM SPECIMEN CB-18

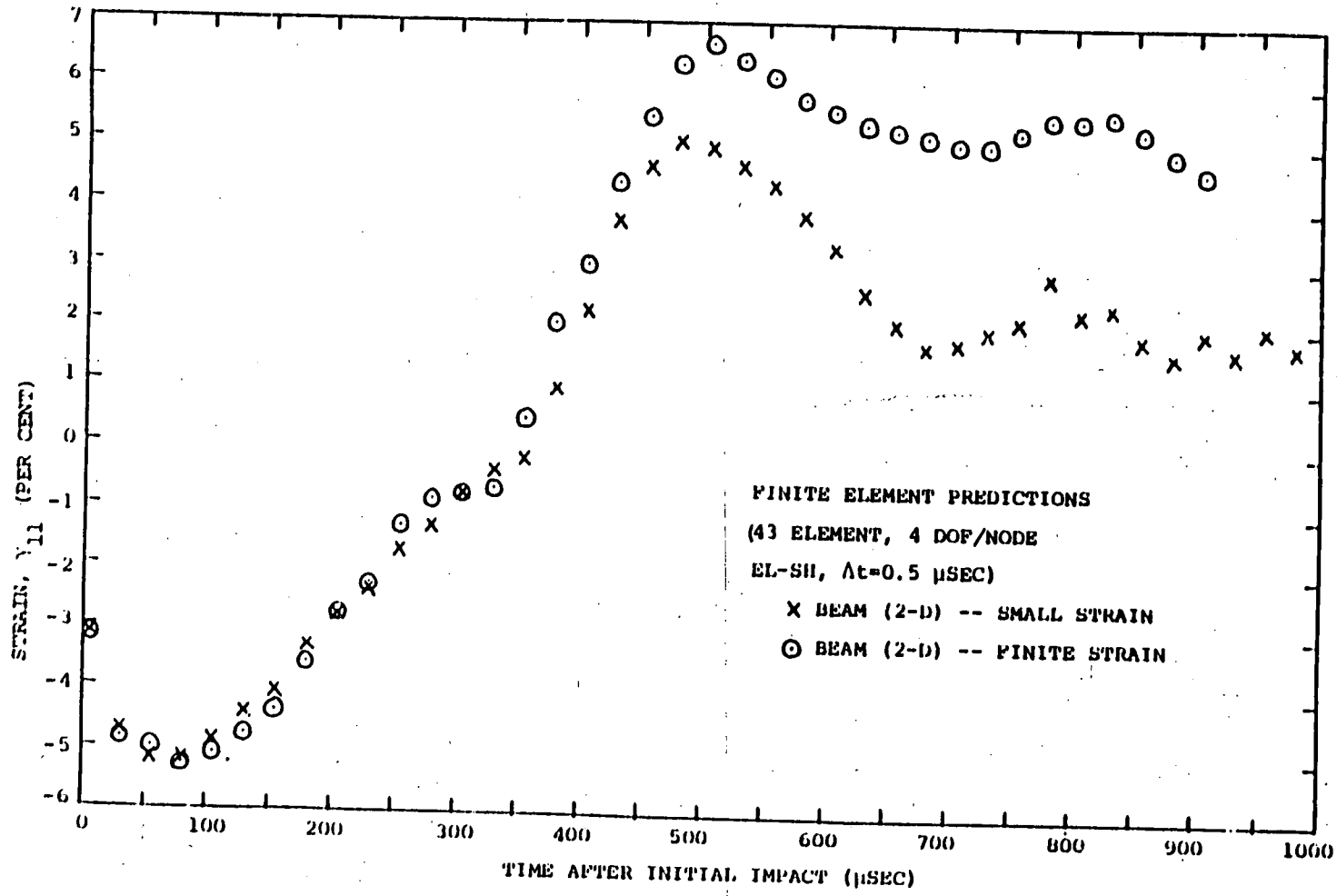

(b) Station x=0, Lower Surface

FIG. 67 CONTINUED (CB-18)

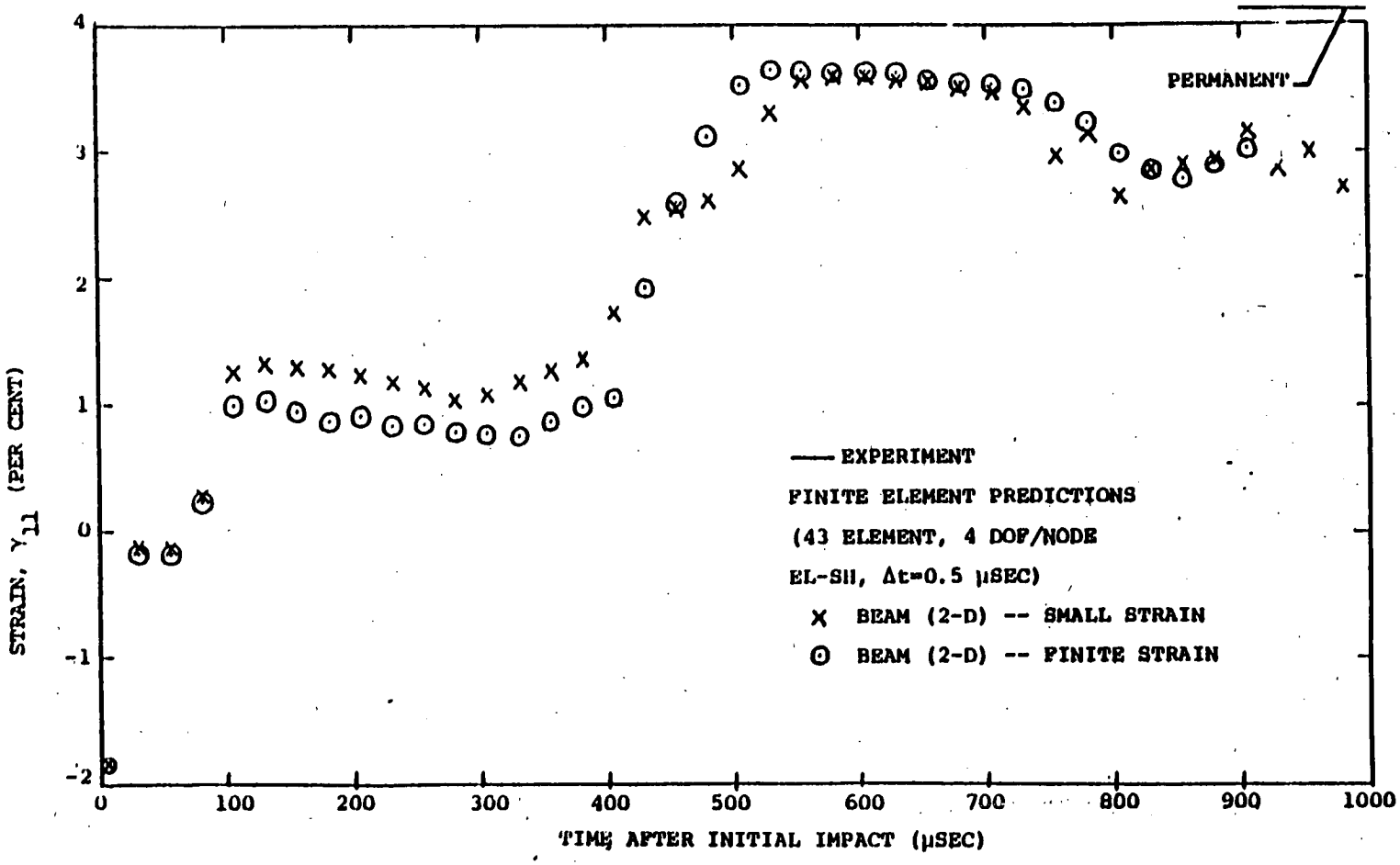

(c) Station x=0.3 in, Upper Surface

FIG. 67 CONTINUED (CB-18)

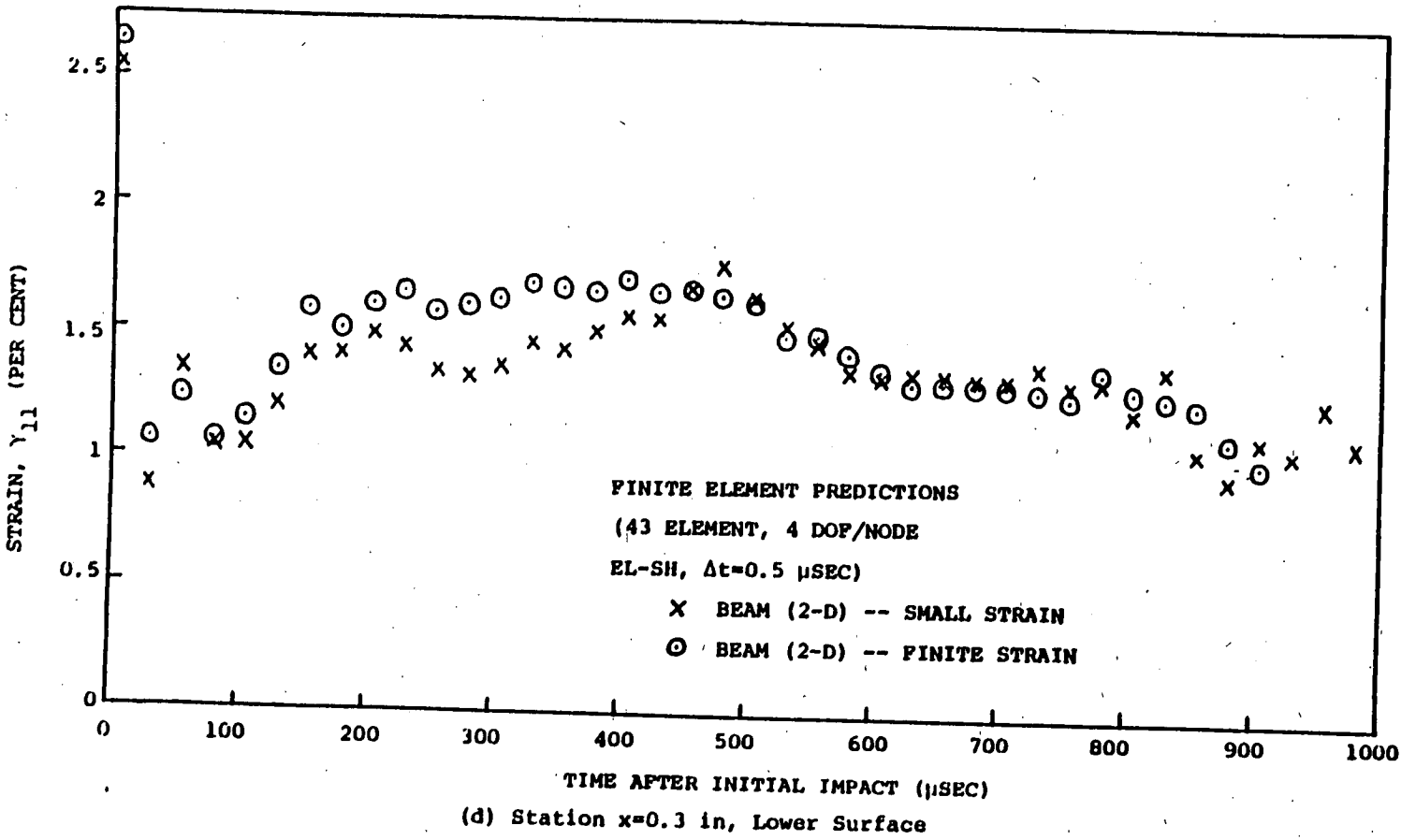

(d) Station x=0.3 in, Lower Surface

FIG. 67 CONTINUED (CB-18)

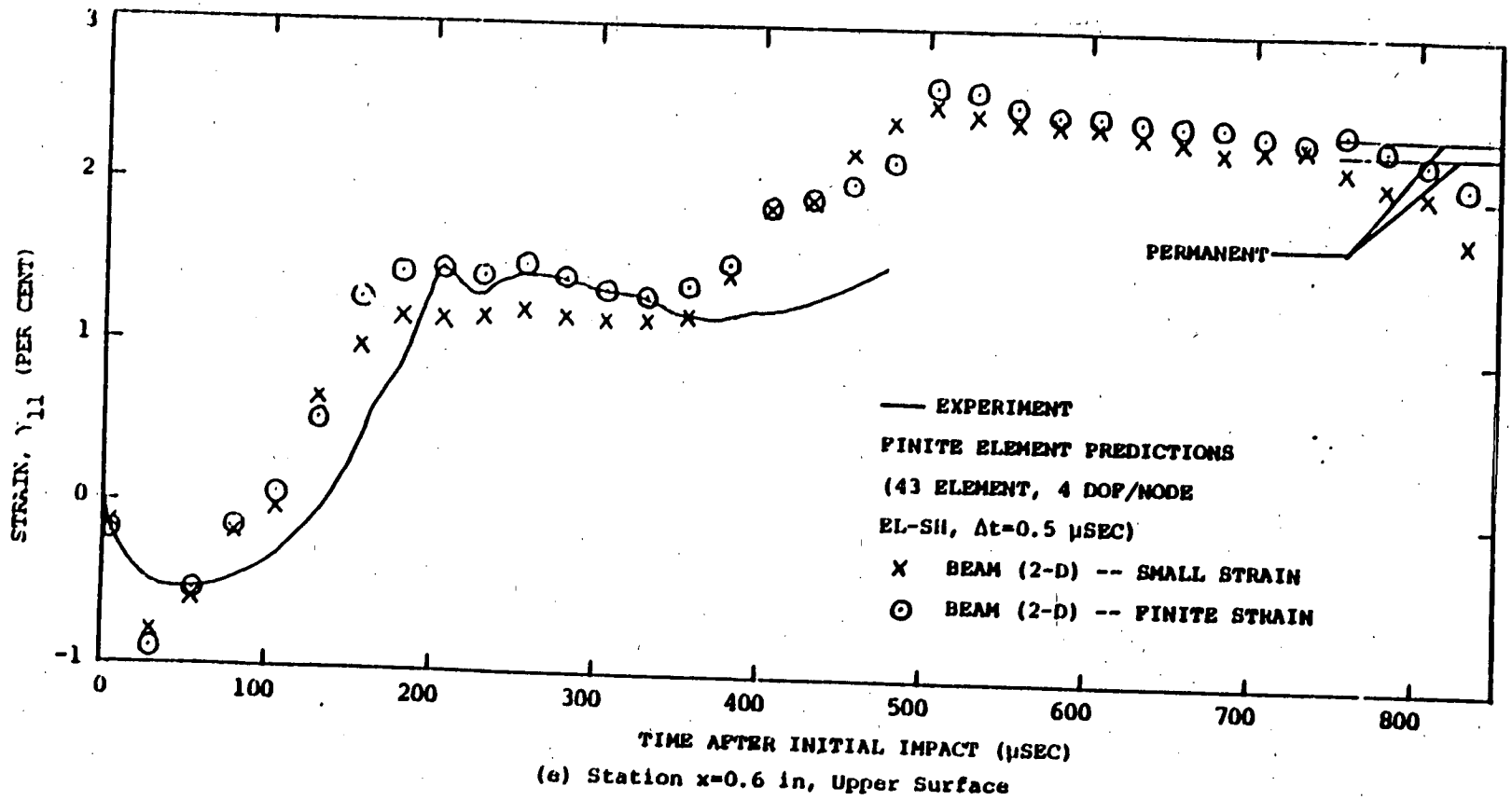

(e) Station x=0.6 in, Upper Surface

FIG. 67 CONTINUED (CB-18)

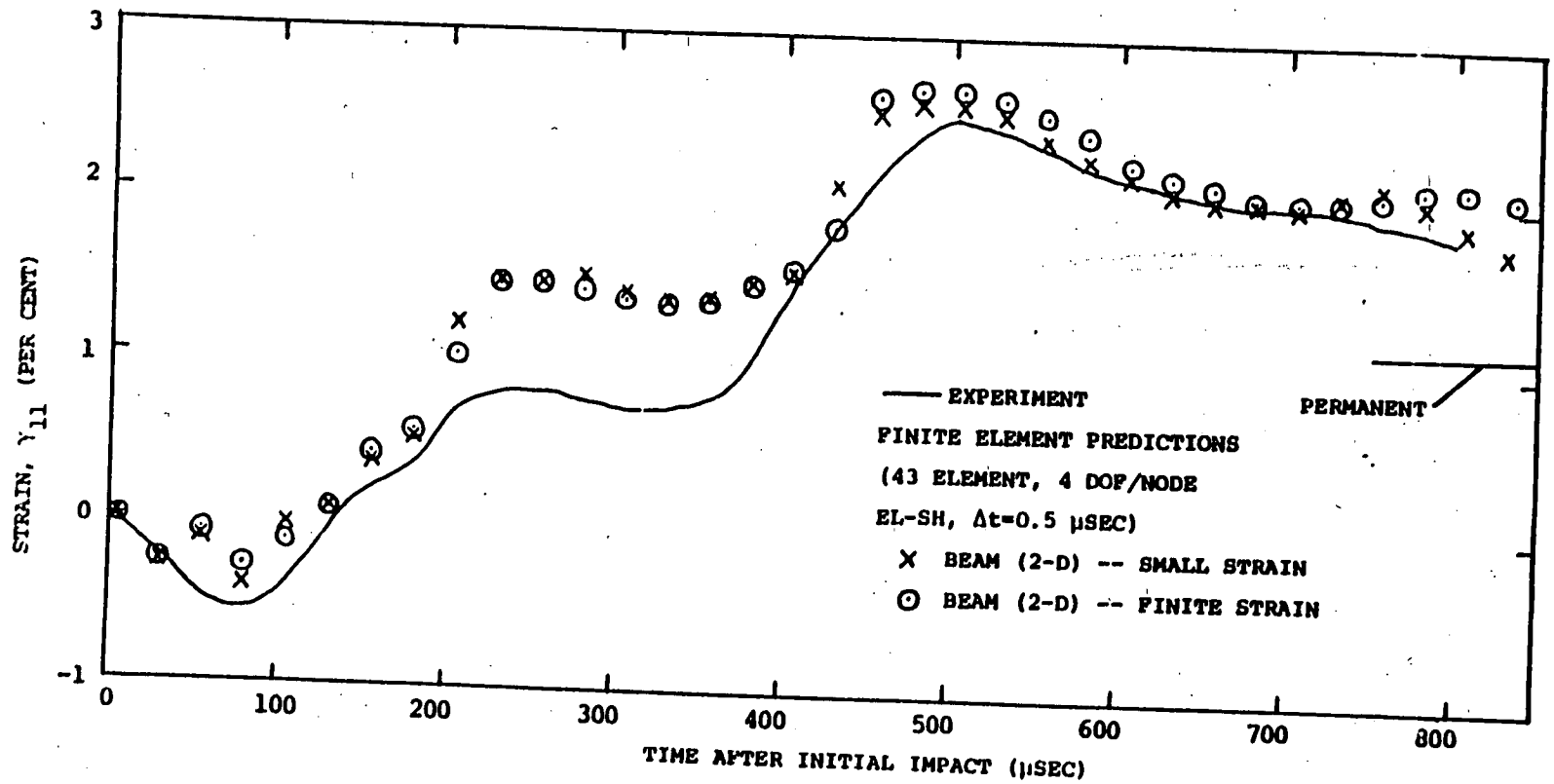

(f) Station x=1.20 in, Upper Surface)

FIG. 67 CONTINUED (CB-18)

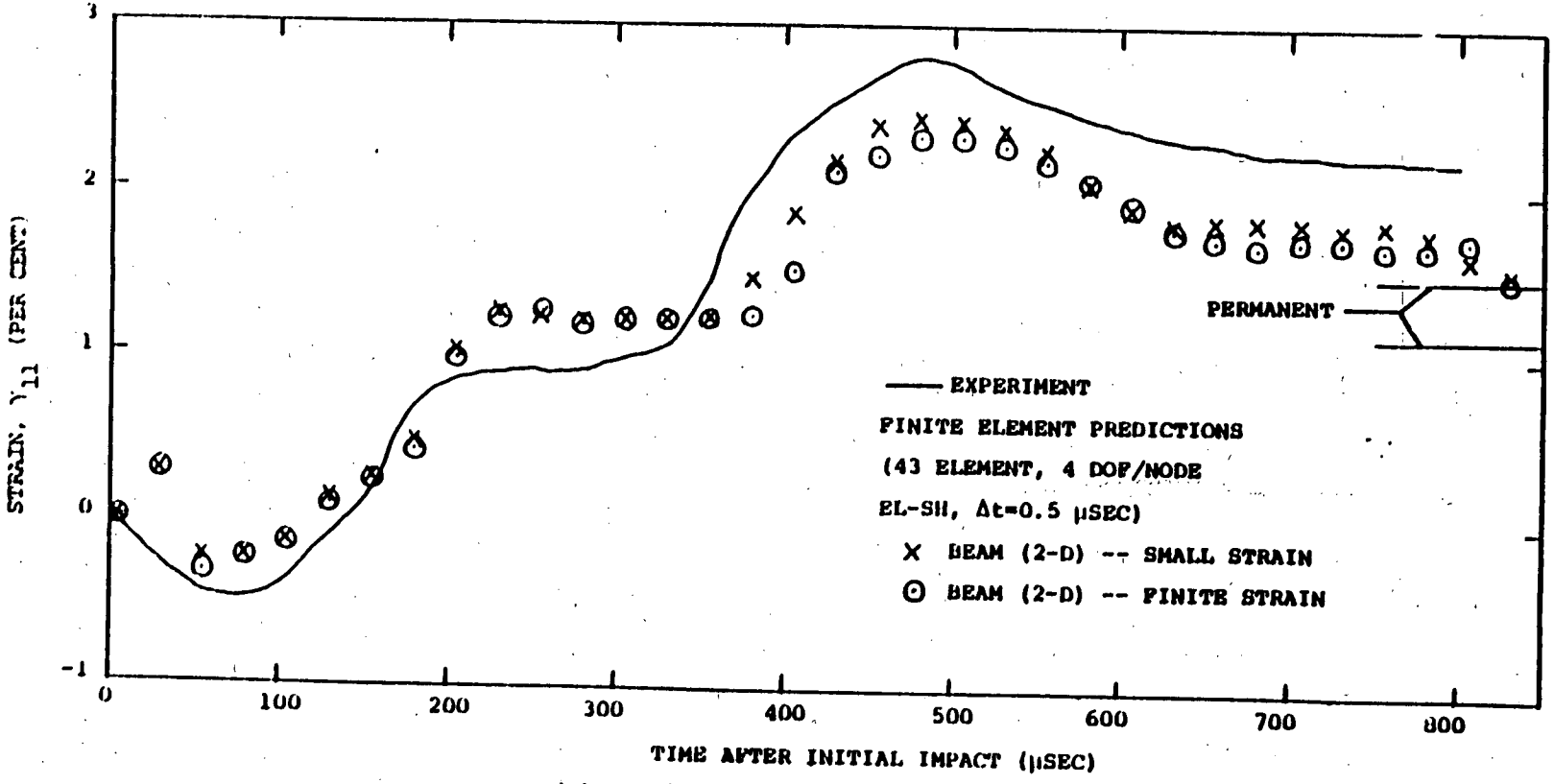

(g) Station x=1.50 in, Upper Surface

FIG. 67 CONTINUED (CB-18)

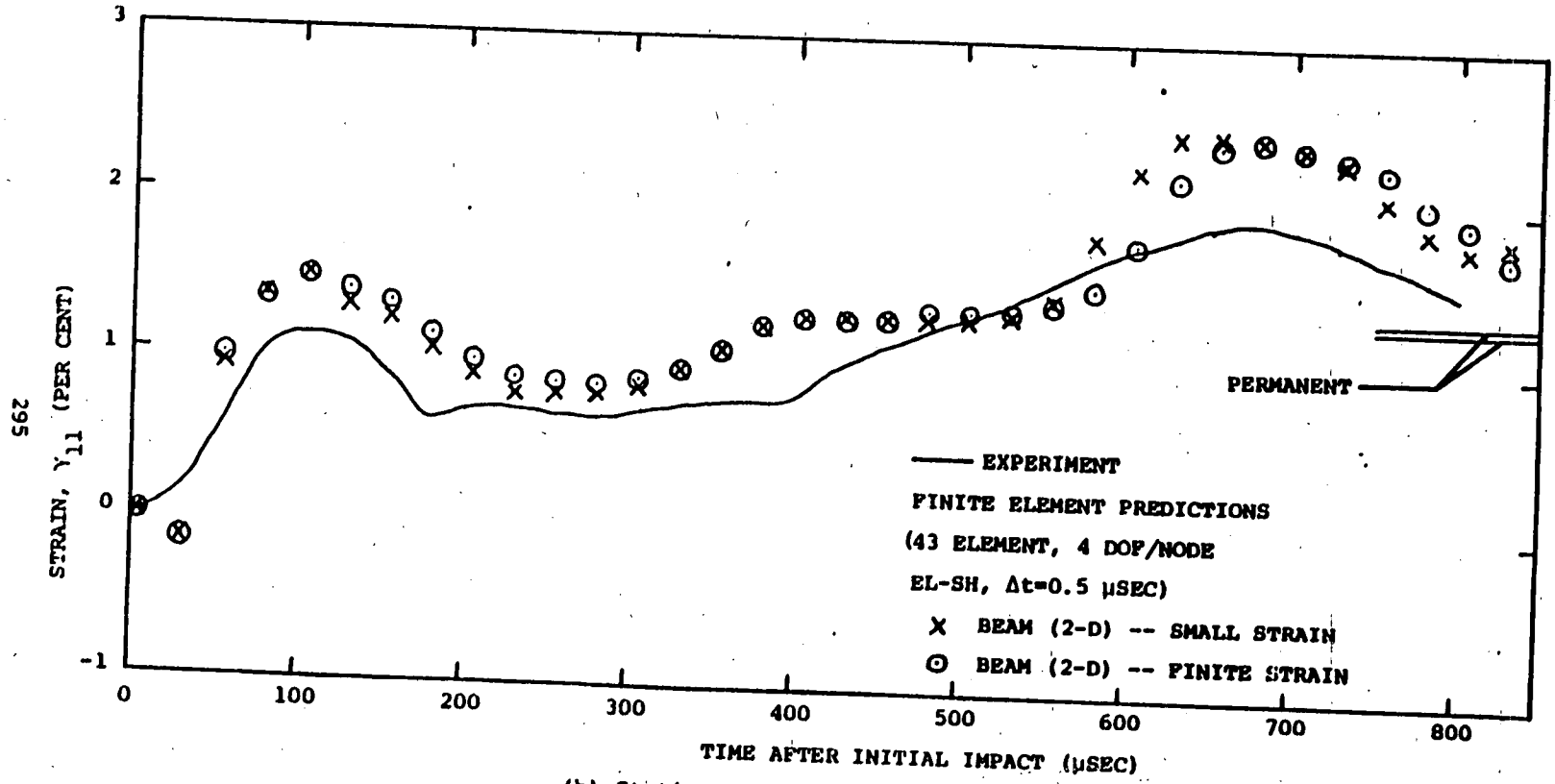

(h) Station x=1.50 in, Lower Surface

FIG. 67 CONTINUED (CB-18)

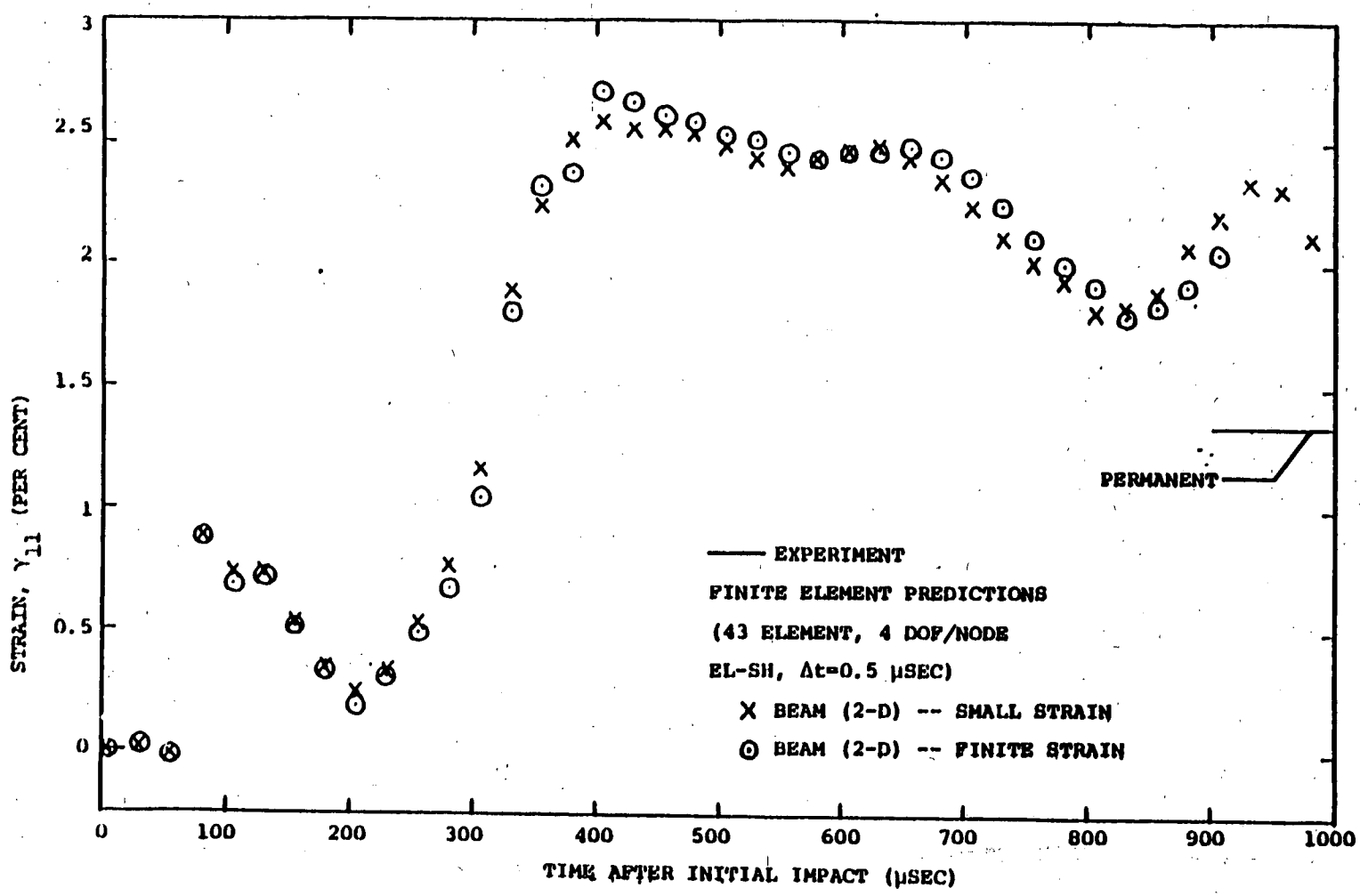

(i) Station x=3.00 in, Upper Surface

FIG. 67 CONTINUED (CB-18)

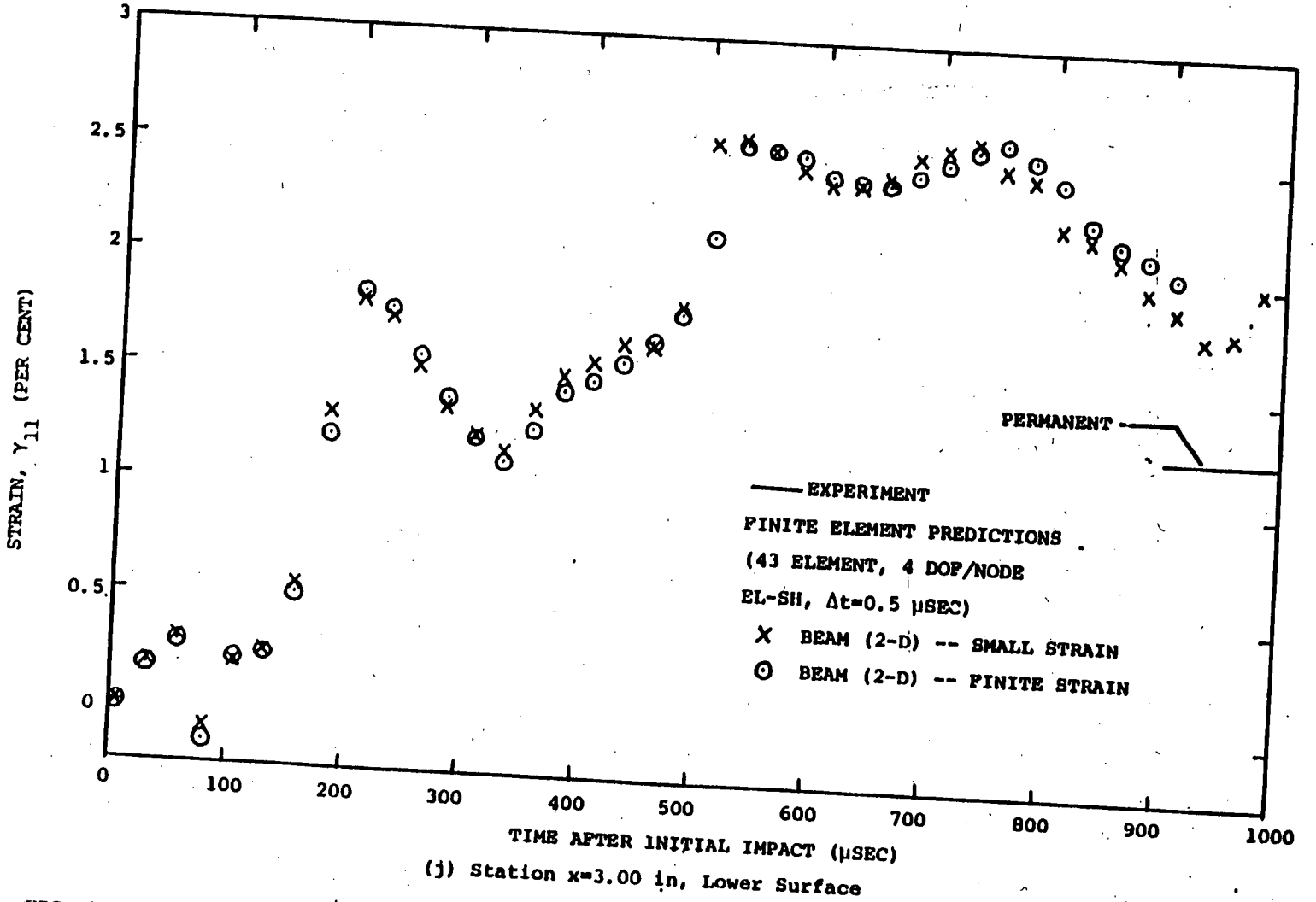

(j) Station x=3.00 in, Lower Surface

FIG. 67 CONTINUED (CB-18)

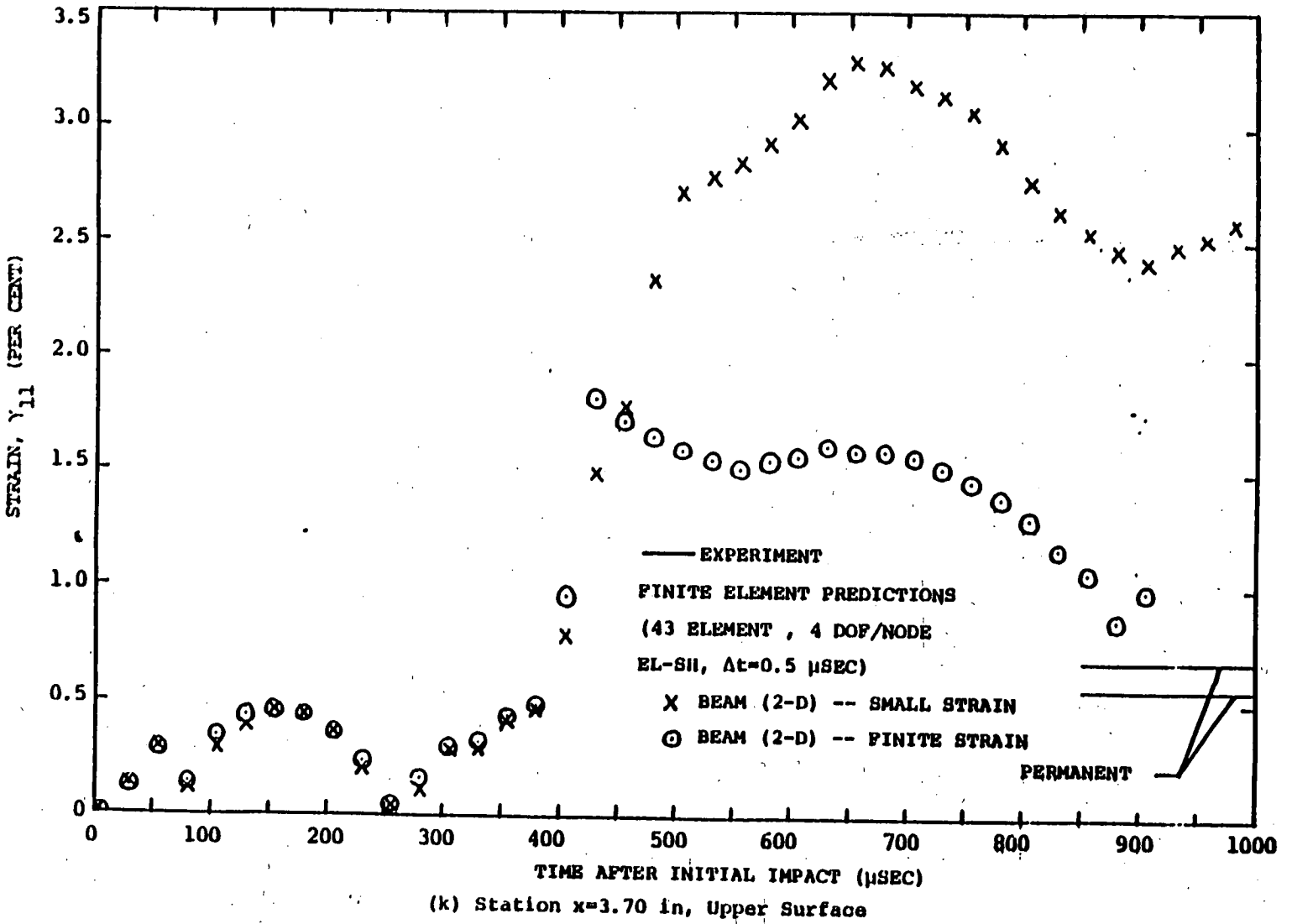

(k) Station x=3.70 in, Upper Surface

FIG. 67 CONTINUED (CB-18)

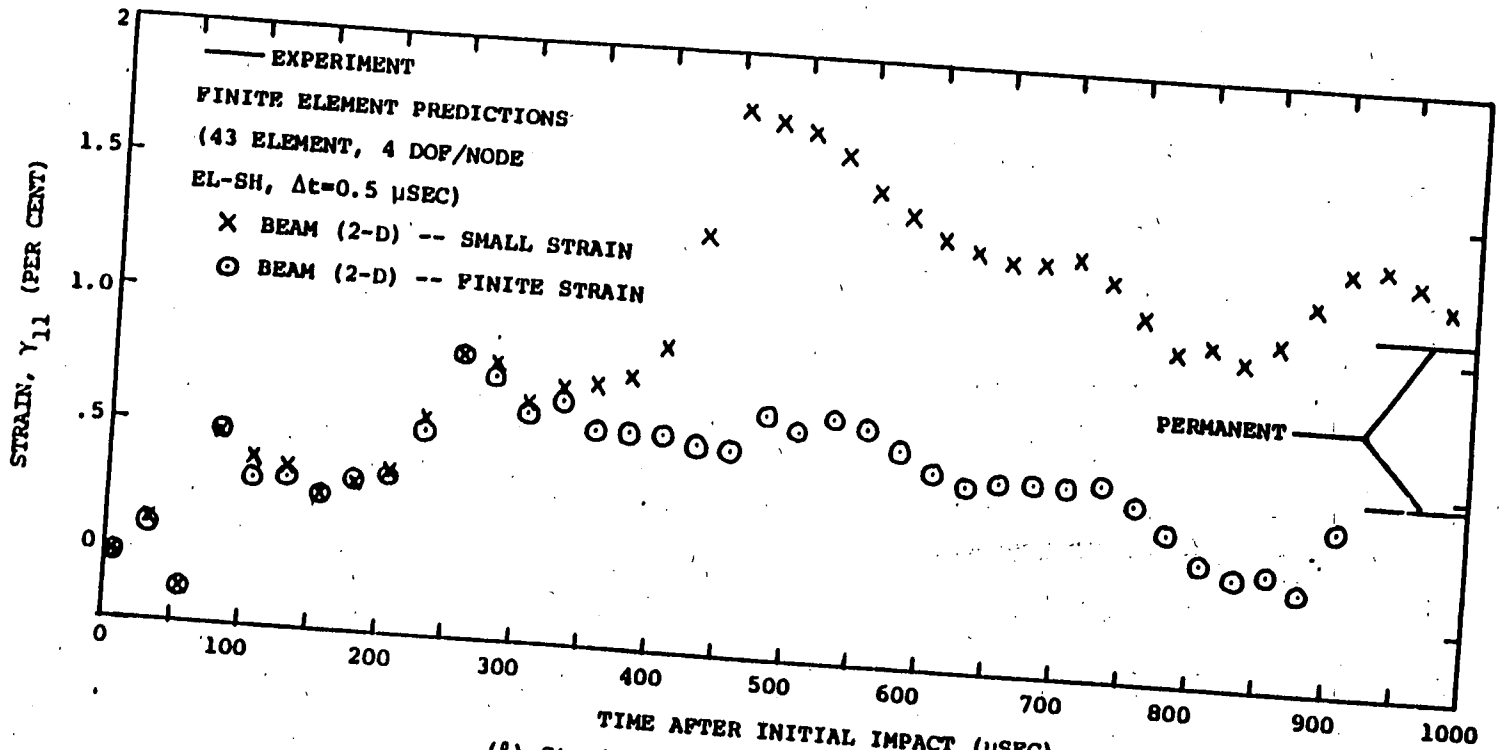

FIG. 67 CONTINUED (CB-18)

(ℓ) Station x=3.70 in, Lower Surface

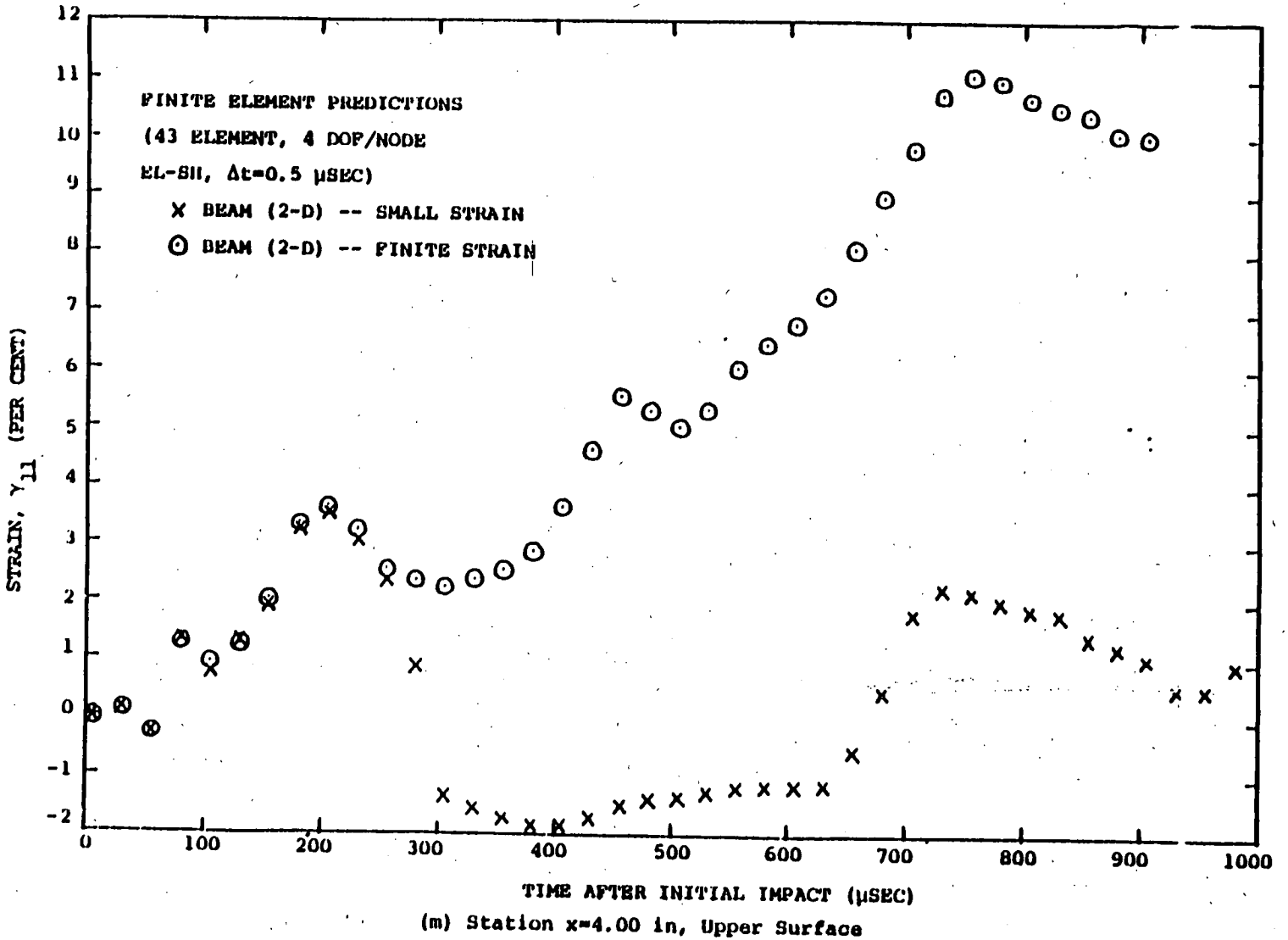

(m) Station x=4.00 in, Upper Surface

FIG. 67 CONTINUED (CB-18)

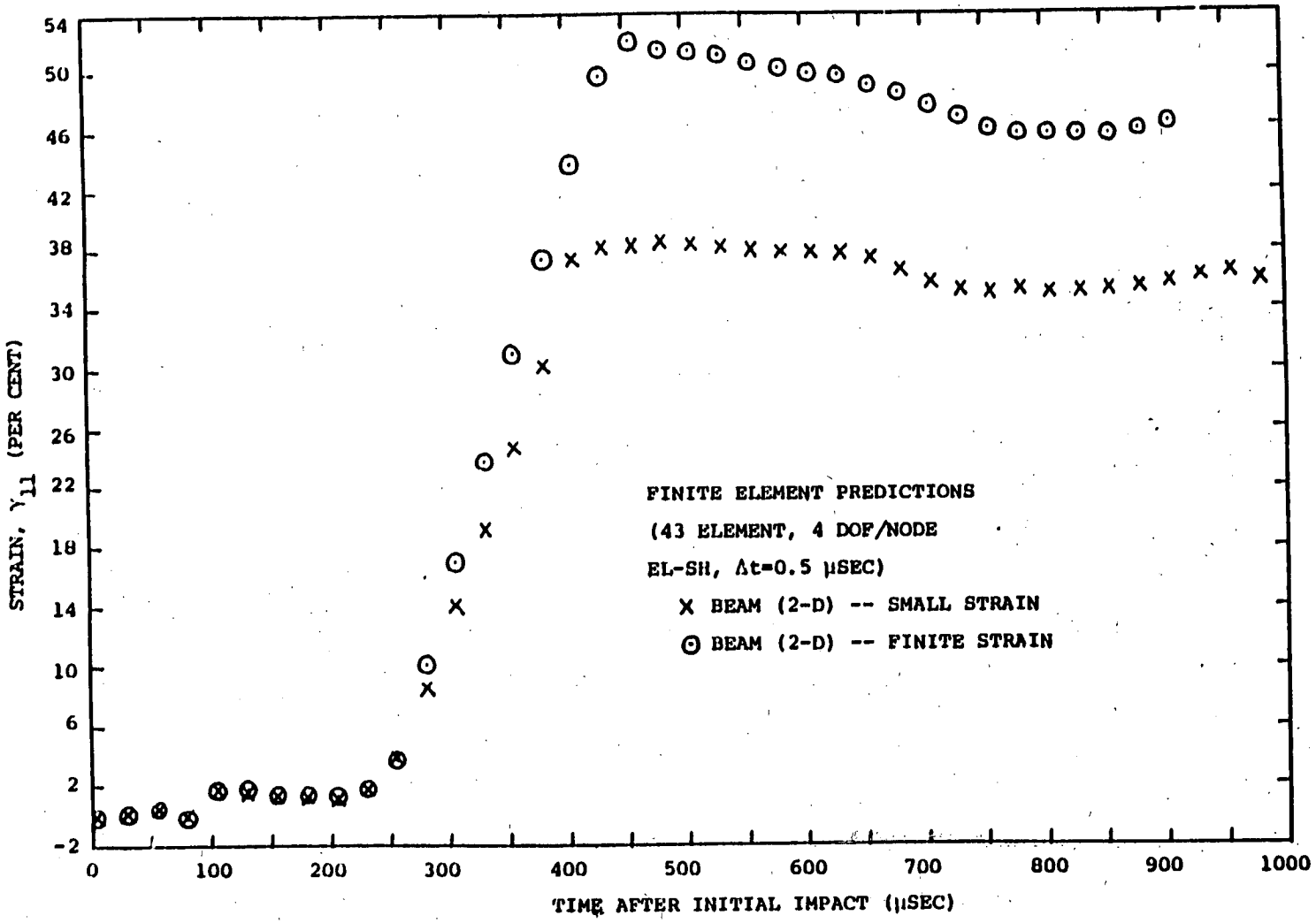

(n) Station x=4.00 in, Lower Surface

FIG. 67 CONCLUDED (CB-18)

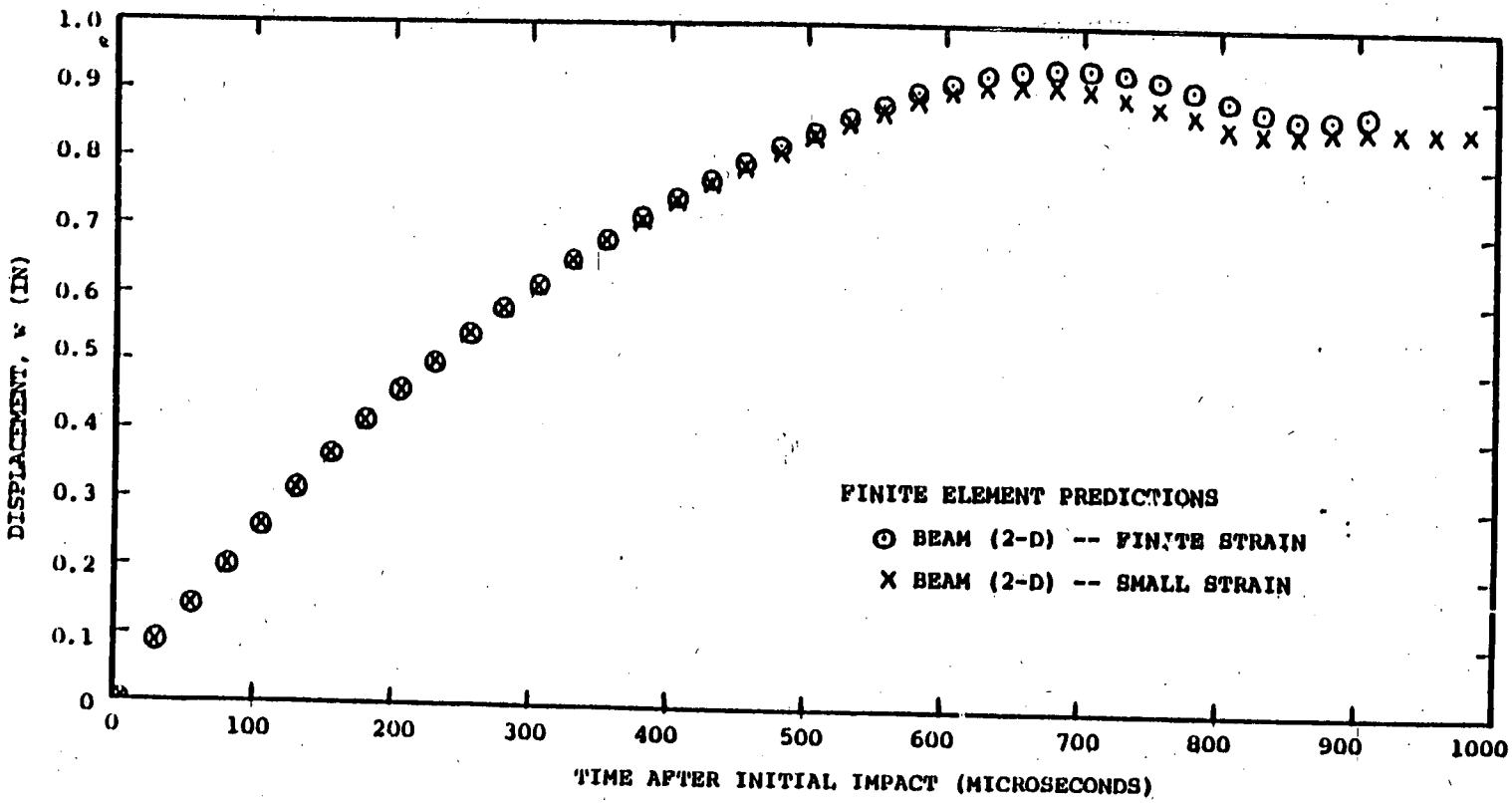

FIG. 68 PREDICTED TRANSIENT DEFLECTION AT THE MIDSPAN STATION (x=0) OF STEEL-SPHERE IMPACTED BEAM CB-18

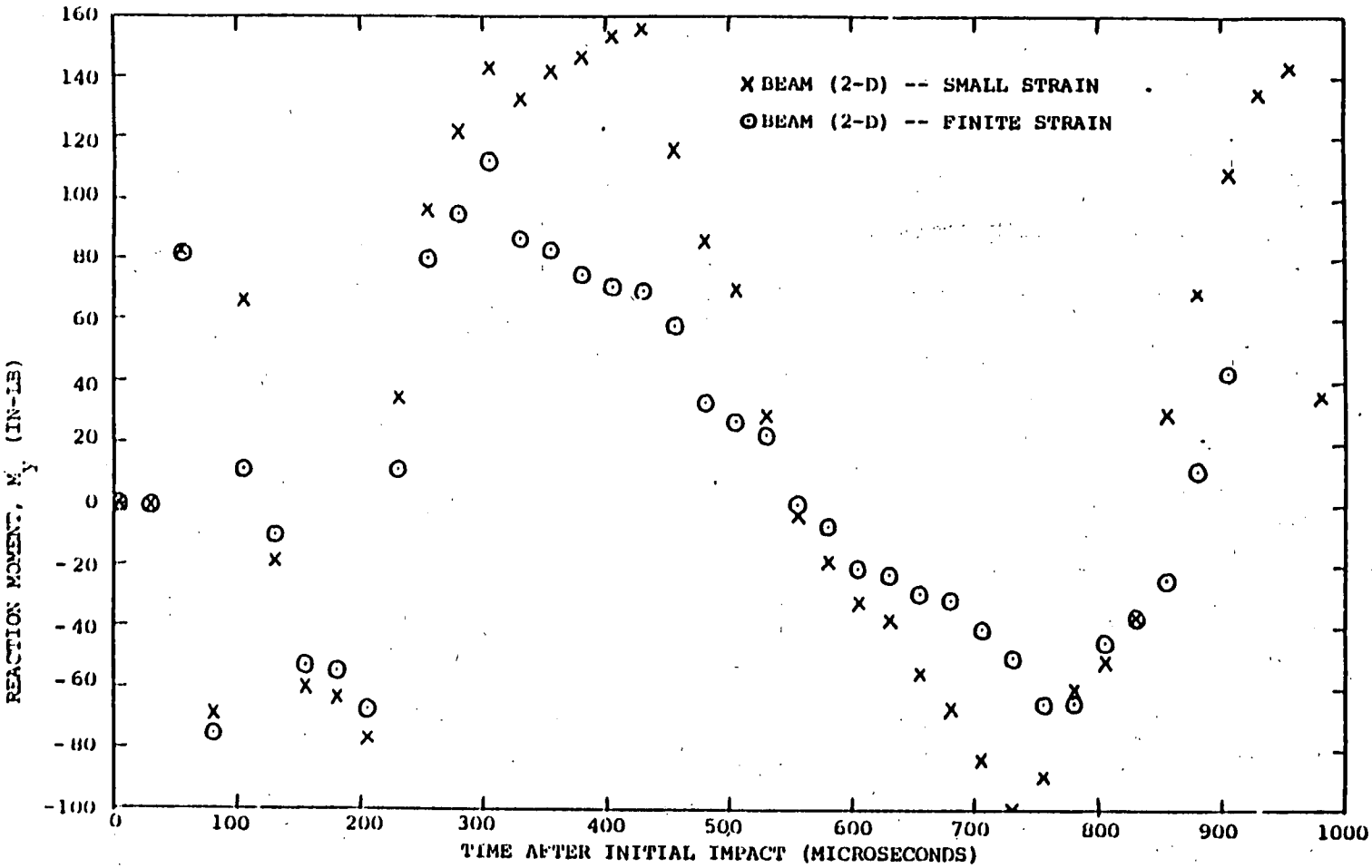

(a) Support Reaction M_y at Station x=4.00 in

FIG. 69 FINITE ELEMENT PREDICTIONS OF SUPPORT REACTIONS OF STEEL-SPHERE IMPACTED BEAM CB-18

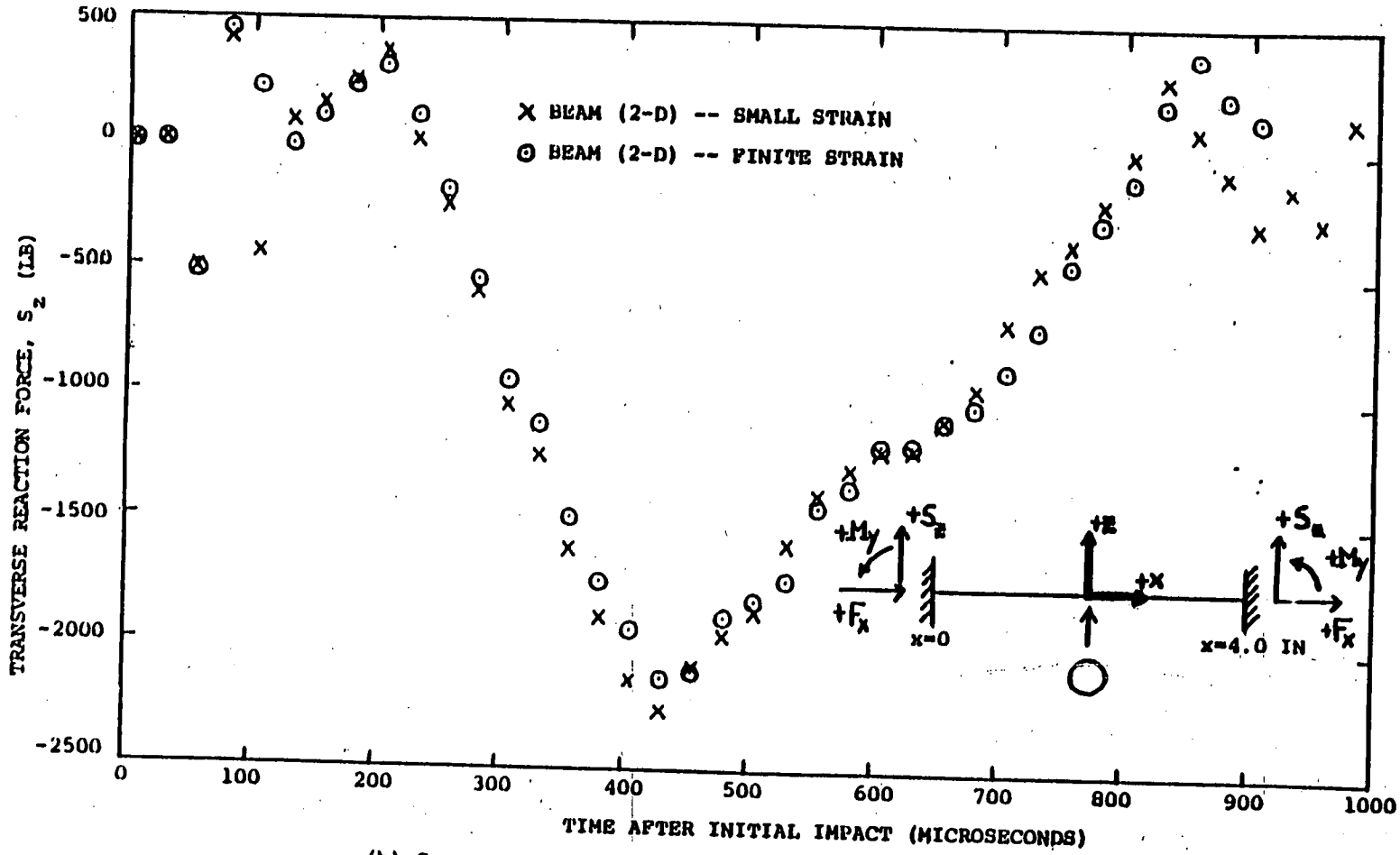

(b) Support Reaction S_z at Station x=4.00 in

FIG. 69 CONTINUED (CB-18)

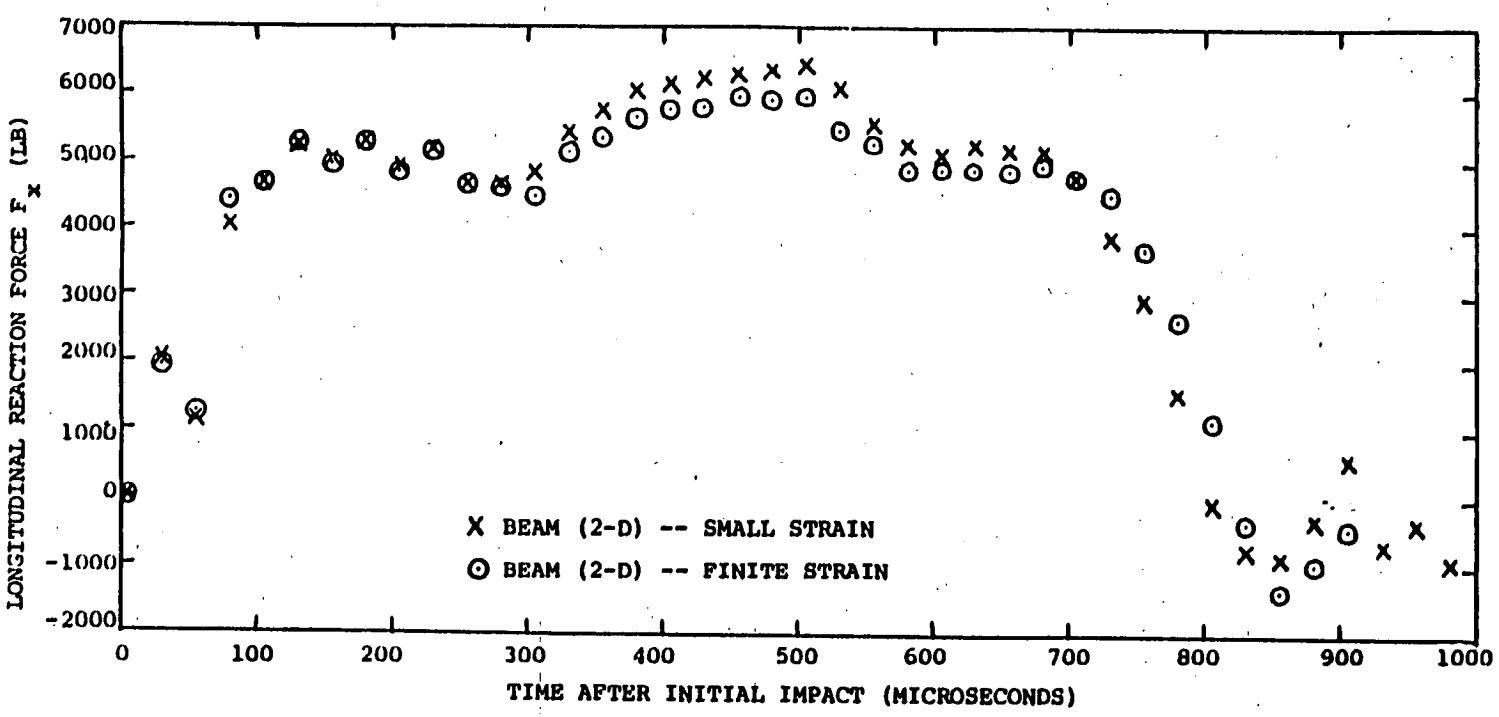

(c) Support Reaction F_x at Station x=4.00 in

FIG. 69 CONCLUDED (CB-18)

APPENDIX A

REVIEW OF GOVERNING EQUATIONS

A.1 Introduction

For the reader's convenience, a brief review is given here of the basic equations upon which the computer codes discussed in this report for predicting the large-deflection, elastic-plastic, transient structural 2-d responses (of beams and/or rings) to externally-applied loads are based. In particular, the equations of motion based upon the Principle of Virtual Work are described for a structure represented as a general solid continuum. These equations are then utilized to provide a finite-element analysis of 2-d beam/ring structures; included are the pertinent strain-displacement relations, the selections of appropriate generalized displacements and assumed displacement fields for the element, and the derivation of element properties. A convenient stress-strain representation for the mechanical behavior of the beam/ring structural material is described. Finally, an illustrative transient-response solution procedure, utilizing the timewise central-difference (explicit) operator for a 2-d structure subjected to prescribed externally-applied transient loading is given; Refs. 3 and/or 5 may be consulted for a description of the use of the (implicit) Houbolt timewise finite-difference operator for solving the nonlinear equations of motion.

To avoid unnecessary repetition, the procedures used to analyze the responses of 2-d beams and/or rings to fragment impact is not included. For that information, the reader is invited to consult (1) Ref. 4 concerning the CIVM-JET 4B (single-layer structure) program or (2) Ref. 5 for the CIVM-JET 5B (multilayer structure) program.

A.2 Formulation of the Equations of Motion

Consider a deformed continuum (or structure) to be in equilibrium under the action of body forces and prescribed externally-applied surface forces (or stresses) on the surface area A_{o_σ}; let prescribed geometric boundary conditions be given on the remainder of the surface area A_{o_u}. Let this body undergo arbitrary infinitesimal virtual displacement δu_i consistent with the prescribed geometric boundary conditions; for this situation, the Principle of Virtual Work requires that [17,20, and/or page 248 of Ref. 48]:

$$\int_{V_o} S^{ij}\,\delta\gamma_{ij}\,dV - \int_{V_o} \rho_o B_o^i\,\delta u_i\,dV - \int_{A_{o\sigma}} \underset{\sim}{T}_o^{\,i}\,\delta u_i\,dA = 0 \qquad \text{(A.1)}$$

where S^{ij} is the second Piola-Kirchhoff stress tensor (based on a unit area of the undeformed body), B_o^i is the body force (inertia, magnetic, etc.) per unit mass, $\underset{\sim}{T}_o^{\,i}$ is the externally-applied surface traction (measured per unit area of the undeformed state), γ_{ij} is the Lagrangian (or Green) strain tensor, the u_i are the displacement components, ρ_o is the mass per unit volume of the undeformed state, and only displacements variations are permitted. Note that Latin indices take on separately values 1, 2, and 3; repeated indices in a given term means automatic summation over these index values. These integrations are performed over the undeformed volume V_o and the undeformed surface area A_{o_σ}.

Note that the Lagrangian (or Green) strain tensor γ_{ij} may be expressed as

$$\gamma_{ij} = \frac{1}{2}\left(u_{i,j} + u_{j,i} + u_{a,i}\,u^{a}_{,j}\right) \qquad \text{(A.2)}$$

where $(\,)_{,j}$ denotes covariant differentiation with respect to the material coordinate ξ^j (j=1,2,3) using the metric tensor of the undeformed state.

By employing the concept of D'Alembert's Principle, the body forces $\rho_o B_o^i$ may be regarded as consisting of the D'Alembert inertia forces $(-\rho_o \ddot{u}^i)$ and other body forces $\rho_o f_o^i$ (magnetic, etc.). Hence, one may write:

$$\rho_o B_o^i = -\rho_o \ddot{u}^i + \rho_o f_o^i \qquad \text{(A.3)}$$

where $(\ddot{\ })$ denotes double differentiation with respect to time.

Applying Eq. A.3, Eq. A.1 becomes

$$\int_{V_o} S^{ij}\,\delta\gamma_{ij}\,dV - \int_{V_o}\left(-\rho_o \ddot{u}^i + \rho_o f_o^i\right)dV - \int_{A_{o\sigma}} \underset{\sim}{T}_o^{\,i}\,\delta u_i\,dA = 0 \qquad \text{(A.4)}$$

As usual in the assumed-displacement version of the finite element method, the actual continuous structure is modeled as a compatibly-joined assemblage of finite elements. Expressing Eq. A.4 in terms of the contributions from each of the N finite elements or regions, one obtains:

$$\sum_{n=1}^{N}\left(\int_{V_{n_o}} S^{ij}\,\delta\gamma_{ij}\,dV - \int_{V_{n_o}}(-\rho_o \ddot{u}^i + \rho_o f_o^i)\,\delta u_i\,dV - \int_{A_{\sigma_{n_o}}} \underset{\sim}{T}_o^{\,i}\,\delta u_i\,dA\right) = 0 \qquad \text{(A.5)}$$

Next, for each finite element one chooses a selected finite number of control stations or nodes at which "control generalized displacements" {q} are defined; these "control stations" may be on the boundaries and/or the interior of the element. Using these control-station q's, one assumes the spatial distribution of the displacements u_i in the element to be expressible in terms of appropriate interpolation functions such that one may write

$$u_i(\xi^j) = [U_i(\xi^j)]\{q\} \qquad \text{(A.6)}$$

where i (i=1, 2, and/or 3) represents a selected direction. Since the strains γ_{ij} are expressed in terms of displacement gradients and combinations thereof (see Eq. A.2), one may write

$$\gamma_{ij} = [D_{ij}]\{q\} + \tfrac{1}{2}[q]\{D_{ai}\}[D_j^a]\{q\} \qquad \text{(A.7)}$$

Hence,

$$\delta\gamma_{ij} = [D_{ij}]\{\delta q\} + [q]\{D_{ai}\}[D_j^a]\{\delta q\} \qquad \text{(A.8)}$$

Next, expressing Eq. A.5 in terms of the element's generalized displacements and using Eqs. A.6 and A.7, one has

$$\sum_{n=1}^{N}[\delta q]\left([m]\{\ddot{q}\} + \{p\} + [h]\{q\} - \{f\}\right) = 0 \qquad \text{(A.9)}$$

where the following are evaluated for each finite element (subscript "n"):

$$[m] = \int_{V_{n_o}} \{U_i\} \rho_o [U_i] \, dV \tag{A.9a}$$

$$\{p\} = \int_{V_{n_o}} \{D_{ij}\} S^{ij} \, dV \tag{A.9b}$$

$$[h] = \int_{V_{n_o}} \{D_{ai}\} [D_j^a] S^{ij} \, dV \tag{A.9c}$$

$$\{f\} = \int_{V_{n_o}} \rho_o \{U_i\} f_o^i \, dV + \int_{A_{\sigma_{n_o}}} \{U_i\}_b \underset{\sim}{T}_o^i \, dA \tag{A.9d}$$

Note that {p} and [h] involve stress information S^{ij} throughout the volume of each finite element.

Next, it is desired to express Eq. A.9 in terms of the independent global generalized displacements {q*} for the complete assembled discretized structure rather than in terms of the {q} for the individual finite elements. For every finite element one can take this into account and express the {q} of each element in terms of the {q*} by

$$\{q\} = [J]\{q^*\} \tag{A.10}$$

Applying Eq. A.10 to Eq. A.9 to describe the system in terms of <u>independent</u> global generalized displacements {q*}, one obtains:

$$\sum_{n=1}^{N} [\delta q^*] \left([m^*]\{\ddot{q}^*\} + \{p^*\} + [h^*]\{q^*\} - \{f^*\} \right) = 0 \tag{A.11}$$

where

$$[m^*] = [J]^T [m] [J] \tag{A.11a}$$

$$\{p^*\} = [J]^T\{p\} \tag{A.11b}$$

$$[h^*] = [J]^T[h][J] \tag{A.11c}$$

$$\{f^*\} = [J]^T\{f\} \tag{A.11d}$$

Performing the summation and since the δq^* are arbitrary and independent, one obtains:

$$[M]\{\ddot{q}^*\} + \{P\} + [H]\{q^*\} = \{F\} \tag{A.12}$$

where

$$[M] = \begin{bmatrix} m_1^* & & & \\ & m_2^* & & \\ & & \ddots & \\ & & & m_N^* \end{bmatrix} \tag{A.12a}$$

$$\{P\} = \{p_1^* \; p_2^* \; \ldots \; p_N^*\} \tag{A.12b}$$

$$[H] = \begin{bmatrix} h_1^* & & & \\ & h_2^* & & \\ & & \ddots & \\ & & & h_N^* \end{bmatrix} \tag{A.12c}$$

$$\{F\} = \{f_1^* \; f_2^* \; \ldots \; f_N^*\} \tag{A.12d}$$

Note that [M] is the global mass matrix, [H] {q*} represents "forces" associated with large deflections (nonlinear terms in the strain-displacement relations) and plastic effects[+], {P} represents internal elastic forces, plastic forces, and some plasticity effects associated with the linear terms of the strain-displacement relations[+], and {F} represents the generalized nodal load vector accounting for externally-applied distributed or concentrated loads.

The equations of motion represented by Eq. A.12 are usually termed the "unconventional form" but are very convenient for analysis and computer implementation. On the other hand, one can obtain the "conventional form" of the equations of motion by employing the stress-strain and strain-displacement relations to express the stress S^{ij} in terms of the element generalized displacements {q}, using the concept of initial strain:

$$S^{ij} = E^{ijkl}\left(\gamma_{kl} - \gamma^{p}_{kl}\right)$$

$$= E^{ijkl}\left([D_{kl}]\{q\} + \tfrac{1}{2}[q]\{D_{ckl}\}[D^{c}_{l}]\{q\} - \gamma^{p}_{kl}\right) \qquad \text{(A.13)}$$

where γ^{p}_{kl} is the plastic strain component of the total strain γ_{kl} and E^{ijkl} is the matrix of elastic constants. Applying Eqs. A.13 and A.10 to Eqs. A.9, A.9b, and A.9c, one obtains:

$$[M]\{\ddot{q}^{*}\} + [K]\{q^{*}\} = \{F\} + \{F^{NL}_{q}\} + \{F^{L}_{p}\} + \{F^{NL}_{p}\} \qquad \text{(A.14)}$$

where [M] is the global mass matrix, [K] is the usual global stiffness matrix (for linear-elastic small deflection behavior), {F} is the generalized nodal load vector representing externally-applied distributed or concentrated loads, $\{F^{NL}_{q}\}$ represents a "generalized loads" vector arising from large deflections and is a function of quadratic and cubic displacement terms, $\{F^{L}_{p}\}$ and $\{F^{NL}_{p}\}$

[+] See page 50 of Ref. 17.

are the generalized loac vectors due to the presence of plastic strains and are associated, respectively, with the linear and nonlinear terms of the strain-displacement relations.

Equation A.14 represents the so-called "conventional" formulation of the equations of motion for nonlinear responses, where the large deflection and plastic effects are taken into account through the use of generalized (or pseudo) loads which are function of plastic strains and displacements. The element stiffness matrix [k] may be readily shown to be

$$[k] = \int_{V_{n_e}} \{D_{ij}\} E^{ijkl} [D_{kl}] \, dV \qquad \text{(A.14a)}$$

Also,

$$[k^*] = [J]^T [k][J] \qquad \text{(A.14b)}$$

and

$$[K] = \begin{bmatrix} \underset{\sim}{k}_1^* & & & \\ & \underset{\sim}{k}_2^* & & \\ & & \ddots & \\ & & & \underset{\sim}{k}_N^* \end{bmatrix} \qquad \text{(A.14c)}$$

A more detailed discussion may be found in Refs. 17 and 20.

Note that the very compact and efficient "unconventional form", Eq. A.12, of the equations of motion is used together with the timewise central-difference operator to predict 2-D transient structural responses in the JET 3A and JET 3C codes of Ref. 3 and in the CIVM-JET 4B code of Ref. 4. On the other hand, in an endeavor to employ a larger allowable time-step-size increment Δt for the transient response solution, the Houbolt timewise finite-difference operator is used in the JET 3B and JET 3D codes of Ref. 3 and in the JET 5A and CIVM-JET 5B codes of Ref. 5; these codes utilize the "conventional form", Eq. A.14, of the equations of motion.

A.3 Finite Element Analysis of Curved Beams or Rings

Consider an initially-undeformed, arbitrarily-curved, variable-thickness, single-layer beam or ring subjected to prescribed transient externally-applied surface loads and to only D'Alembert body forces (inertia loads). Let it be assumed that the ring consists of ductile metal and that a large-deflection, elastic-plastic transient response will be produced. For analysis the structure will be represented by a compatibly-joined assemblage of N finite elements, one of which is depicted in Fig. A.1 where its geometry and nomenclature are shown and where the deformation plane is η, ζ ; the coordinates η along and ζ normal to the centroidal reference axis of the beam are employed as the reference coordinates for this curved beam element.

It is useful and convenient to use the following geometry to describe this typical curved beam element and to approximate the actual given complete beam or ring by a finite number of these "typical elements". Note first that a global Y,Z Cartesian reference axis system as well as a local y,z Cartesian reference axis system are defined; for the latter, the +y axis passes through the ends (that is, nodes i and i+1) of the element and makes an angle $+\alpha$ (for this ith element) with the +Y axis. The slope, ϕ, of the reference circumferential axis η, which is the angle between the tangent vector $\bar{a}$ to η and the y-axis of the local-reference Cartesian frame may be approximated by a second degree polynomial in η, as follows [17]:

$$\phi(\eta) = b_o + b_1 \eta + b_2 \eta^2 \tag{A.15}$$

where the constants b_o, b_1, and b_2 can be determined from the geometry of the curved beam element as described next. Assume that the change in element slope ϕ between nodes i and i+1 is small such that

$$\cos(\phi_{i+1} - \phi_i) \doteq 1 \tag{A.16a}$$

and

$$\sin(\phi_{i+1} - \phi_i) \doteq \phi_{i+1} - \phi_i \tag{A.16b}$$

This restricts the slope change within an element to ≤15 degrees. The arc length, η_i, of element i is approximated to be the same as the length of a circular arc passing through the nodal points at the slopes ϕ_i and ϕ_{i+1}; hence, η_i is given by

$$\eta_i = \frac{L_i(\phi_{i+1} - \phi_i)}{2 \sin\left(\frac{\phi_{i+1} - \phi_i}{2}\right)} \tag{A.17}$$

where L_i is the length of the chord joining nodes i and i+1, and is given by

$$L_i = \left[(Z_{i+1} - Z_i)^2 + (Y_{i+1} - Y_i)^2\right]^{\frac{1}{2}} \tag{A.17a}$$

The three constants in Eq. A.15 are then determined from the relations

$$\begin{aligned} \phi(0) &= \phi_i \\ \phi(\eta_i) &= \phi_{i+1} \\ \int_0^{\eta_i} \sin\phi(\eta)\, d\eta &\doteq \int_0^{\eta_i} \phi(\eta)\, d\eta = 0 \end{aligned} \tag{A.18}$$

From Eq. A.18, the constants in Eq. A.15 are found to be

$$\begin{aligned} b_0 &= \phi_i \\ b_1 &= -2(\phi_{i+1} - \phi_i)/\eta_i \\ b_2 &= 3(\phi_{i+1} + \phi_i)/(\eta_i)^2 \end{aligned} \tag{A.19}$$

Accordingly, the radius of curvature, R, of the centroidal axis may be expressed as $R = -(\partial\phi/\partial\eta)^{-1} = -(b_1 + 2b_2\eta)^{-1}$, and the coordinates $Y(\eta)$ and $Z(\eta)$ of the centroidal axis are given by

$$Y(\eta) = Y_i + \int_0^{\eta} \cos\left[\phi(\eta) + \alpha\right] d\eta \tag{A.20a}$$

and

$$Z(\eta) = Z_i + \int_0^{\eta} \sin\left[\phi(\eta) + \alpha\right] d\eta \qquad \text{(A.20b)}$$

where

$$\alpha = \tan^{-1}\left(\frac{Z_{i+1} - Z_i}{Y_{i+1} - Y_i}\right) \qquad \text{(A.20c)}$$

The thickness variation along the element is approximated as being linear in η between nodes; thus,

$$h(\eta) = h_i\left(1 - \frac{\eta}{\eta_i}\right) + h_{i+1}\frac{\eta}{\eta_i} \qquad \text{(A.21)}$$

This completes the needed description of the geometry of the curved beam element. To be reviewed next are the strain-displacement relations, the assumed-displacement field for the element, and the resulting "element property matrices" identified in Eqs. A.9a-A.9c and in Eq. A.14a.

A.3.1 Strain-Displacement Relations

Let it be assumed that the curved beam deforms according to the Bernoulli-Euler hypothesis; that is, (a) plane sections remain plane, (b) normals to the midsurface (or reference surface -- centroidal axis) before deformation remain normal to that reference surface after deformation, and (c) these normals do not stretch. Thus, the displacements $\tilde{v}(\eta,\zeta)$ and $\tilde{w}(\eta,\zeta)$ at any location (η,ζ) within the element can be expressed in terms of the displacements $v(\eta)$ and $w(\eta)$ at the reference axis (where $\zeta=0$) by

$$\tilde{v}(\eta,\zeta) = v(\eta) - \zeta\,\psi(\eta) \qquad \text{(A.22)}$$

$$\tilde{w}(\eta,\zeta) = w(\eta)$$

where

$$\psi(\eta) = \frac{\partial w}{\partial \eta} - \frac{v}{R} \qquad \text{(A.22a)}$$

By applying Eq. A.2 to Eq. A.22, one can show that the only Lagrangian (Green) strain component of importance in this problem $\gamma_{\eta\eta}$ (hereinafter denoted as γ_{11} for simplicity) is given by [20]:

$$\gamma_{11} = \underbrace{\underbrace{\chi}_{\text{Linear}} + \underbrace{\frac{1}{2}\chi^2 + \frac{1}{2}\psi^2}_{\text{Nonlinear}}}_{\text{Membrane}} + \underbrace{\zeta\left[-\frac{\partial \psi}{\partial \eta}\right]}_{\text{Linear}} \qquad \text{(A.23)}$$

Bending

or more compactly as

$$\gamma_{11} = \epsilon_o(\eta) + \zeta K(\eta) \qquad \text{(A.23a)}$$

where

$$\chi = \frac{\partial v}{\partial \eta} + \frac{w}{R} \qquad \text{(A.23b)}$$

$$\psi = \frac{\partial w}{\partial \eta} - \frac{v}{R} \qquad \text{(A.23c)}$$

$$\epsilon_o(\eta) = \chi + \frac{1}{2}\chi^2 + \frac{1}{2}\psi^2 \qquad \text{(A.23d)}$$

$$K(\eta) = -\frac{\partial \psi}{\partial \eta} \qquad \text{(A.23e)}$$

Note that the part of γ_{11} which does not depend upon ζ is often termed the membrane strain, and is complete in the sense that all of the linear and the nonlinear terms of this portion are present in Eq. A.23. On the other hand, only linear terms have been retained (in Refs. 3, 4, and 5 and for present purposes) in the bending part of this strain; the inclusion of nonlinear bending terms is discussed, for example, in Ref. 20.

Since (1) the displacements $\tilde{v}(\eta,\zeta)$ and $\tilde{w}(\eta,\zeta)$ can be expressed in terms of v and w and (2) the extensional strain γ_{11} is expressed conveniently in terms of the quantities χ and ψ, it is both convenient and natural to employ these four quantities as "generalized displacements" {q} at each end, i and i+1, of the ith finite element.

A.3.2 Assumed Displacement Field

To account for the strain-inducing displacements and small rigid-body displacements, the assumed displacement field takes the form [17,20]:

$$\begin{Bmatrix} v \\ w \end{Bmatrix} = \begin{bmatrix} \cos\phi & \sin\phi & -(Z-Z_i)\cos(\phi+\alpha)+(Y-Y_i)\sin(\phi+\alpha) \\ -\sin\phi & \cos\phi & (Z-Z_i)\sin(\phi+\alpha)+(Y-Y_i)\cos(\phi+\alpha) \end{bmatrix} \tag{A.24}$$

$$\begin{bmatrix} \eta & 0 & 0 & \eta^2 & \eta^3 \\ 0 & \eta^2 & \eta^3 & 0 & 0 \end{bmatrix} \begin{Bmatrix} \beta_1 \\ \vdots \\ \beta_8 \end{Bmatrix}$$

This can be written more compactly as

$$\{u\} \equiv \begin{Bmatrix} v \\ w \end{Bmatrix} = \begin{bmatrix} G_v(\eta) \\ G_w(\eta) \end{bmatrix} \{\beta\} \equiv [U(\eta)]\{\beta\} \tag{A.24a}$$

The eight undefined parameters $\beta_1 \cdots \beta_8$ may be expressed in terms of the eight generalized displacements {q} or degrees of freedom selected for this element -- four at each end (or node). These {q} are defined by

$$\begin{Bmatrix} q_1 \\ \vdots \\ q_8 \end{Bmatrix} = \begin{bmatrix} v_i & w_i & \psi_i & \chi_i & v_{i+1} & w_{i+1} & \psi_{i+1} & \chi_{i+1} \end{bmatrix}^T \tag{A.25}$$

Hence one may write

$$\begin{Bmatrix} q_1 \\ \vdots \\ q_8 \end{Bmatrix} \equiv \{q\} = [A]\{\beta\} \tag{A.26}$$

where

$$[A]=\begin{bmatrix}
\cos\phi_i & \sin\phi_i & 0 & 0 & 0 & 0 & 0 & 0\\
-\sin\phi_i & \cos\phi_i & 0 & 0 & 0 & 0 & 0 & 0\\
0 & 0 & 1 & 0 & 0 & 0 & 0 & 0\\
0 & 0 & 0 & 1 & 0 & 0 & 0 & 0\\
\cos\phi_{i+1} & \sin\phi_{i+1} & A_{53} & \eta_i & 0 & 0 & \eta_i^2 & \eta_i^3\\
-\sin\phi_{i+1} & \cos\phi_{i+1} & A_{63} & 0 & \eta_i^2 & \eta_i^3 & 0 & 0\\
0 & 0 & 1 & \eta_i(\phi')_{\eta_i} & 2\eta_i & 3\eta_i^2 & \eta_i^2(\phi')_{\eta_i} & \eta_i^3(\phi')_{\eta_i}\\
0 & 0 & 0 & 1 & -\eta_i^2(\phi')_{\eta_i} & -\eta_i^3(\phi')_{\eta_i} & 2\eta_i & 3\eta_i^2
\end{bmatrix} \tag{A.26a}$$

and

$$\begin{aligned}
A_{53} &= (Y_{i+1}-Y_i)\sin(\phi_{i+1}+\alpha)-(Z_{i+1}-Z_i)\cos(\phi_{i+1}+\alpha)\\
A_{63} &= (Y_{i+1}-Y_i)\cos(\phi_{i+1}+\alpha)+(Z_{i+1}-Z_i)\sin(\phi_{i+1}+\alpha)
\end{aligned} \tag{A.26b}$$

Corresponding to the assumed displacement field Eq. A.24, one finds

$$\psi=\left[\,0\;\;0\;\;1\;\;-\frac{\eta}{R}\;\;2\eta\;\;3\eta^2\;\;-\frac{\eta^2}{R}\;\;-\frac{\eta^3}{R}\,\right]\{\beta\}\equiv[G_\psi]\{\beta\} \tag{A.27a}$$

and

$$\chi=\left[\,0\;\;0\;\;0\;\;1\;\;\frac{\eta^2}{R}\;\;\frac{\eta^3}{R}\;\;2\eta\;\;3\eta^2\,\right]\{\beta\}\equiv[G_\chi]\{\beta\} \tag{A.27b}$$

Hence, the quantities $\epsilon_o(\eta)$ and $\kappa(\eta)$ appearing in the strain $\gamma_{11}(\eta,\zeta)$ which is denoted hereinafter simply as ϵ are given by Eq. A.23a and become.

$$\begin{aligned}
\epsilon_o(\eta) &= \left(\frac{\partial v}{\partial \eta}+\frac{w}{R}\right)+\frac{1}{2}\left(\frac{\partial v}{\partial \eta}+\frac{w}{R}\right)^2+\frac{1}{2}\left(\frac{\partial w}{\partial \eta}-\frac{v}{R}\right)^2\\
&\equiv [B_1]\{u\}+\frac{1}{2}[u]\{B_1\}[B_1]\{u\}+\frac{1}{2}[u]\{B_2\}[B_2]\{u\}
\end{aligned} \tag{A.28a}$$

$$\mathcal{K}(\eta) \equiv -\frac{\partial}{\partial \eta}\left(\frac{\partial w}{\partial \eta} - \frac{v}{R}\right) \equiv \lfloor B_3 \rfloor \{u\} \qquad \text{(A.28b)}$$

Combining Eqs. A.24 through A.28b, one obtains

$$\begin{Bmatrix} v \\ w \end{Bmatrix} \equiv \{u\} = [U(\eta)][A^{-1}]\{q\} \qquad \text{(A.29)}$$

and

$$\epsilon_o = \lfloor D_1 \rfloor \{q\} + \frac{1}{2} \lfloor q \rfloor \{D_1\} \lfloor D_1 \rfloor \{q\} + \frac{1}{2} \lfloor q \rfloor \{D_2\} \lfloor D_2 \rfloor \{q\}$$
$$\mathcal{K} = \lfloor D_3 \rfloor \{q\} \qquad \text{(A.30)}$$

where

$$\lfloor D_i \rfloor = \lfloor B_i \rfloor [U][A^{-1}] \qquad \text{for } i = 1, 2, 3 \qquad \text{(A.30a)}$$

and

$$\lfloor B_1 \rfloor [U] = \lfloor 0 \;\; 0 \;\; 0 \;\; 1 \;\; -\eta^2\phi' \;\; -\eta^3\phi' \;\; 2\eta \;\; 3\eta^2 \rfloor$$
$$\lfloor B_2 \rfloor [U] = \lfloor 0 \;\; 0 \;\; 1 \;\; \eta\phi' \;\; 2\eta \;\; 3\eta^2 \;\; \eta^2\phi' \;\; \eta^3\phi' \rfloor \qquad \text{(A.30b)}$$
$$\lfloor B_3 \rfloor [U] = \lfloor 0 \;\; 0 \;\; 0 \;\; -\phi' \;\; -\eta\phi'' \;\; -2 \;\; -2\eta\phi' - \eta^2\phi'' \;\; -3\eta^2\phi' - \eta^3\phi'' \rfloor$$

In the process of solution, it is necessary to evaluate the strain increment $\Delta\epsilon_m$ from time t_{m-1} to time t_m. Using Eqs. A.12 and A.14, one has

$$\Delta\epsilon_m = \Delta\epsilon_{o_m} + \zeta \Delta\mathcal{K}_m \qquad \text{(A.31)}$$

where

$$\Delta\epsilon_{o_m} = \lfloor D_1 \rfloor \{\Delta q_m\} + \lfloor q_m \rfloor \{D_1\} \lfloor D_1 \rfloor \{\Delta q_m\} + \lfloor q_m \rfloor \{D_2\} \lfloor D_2 \rfloor \{\Delta q_m\}$$
$$- \frac{1}{2} \lfloor \Delta q_m \rfloor \{D_1\} \lfloor D_1 \rfloor \{q_m\} - \frac{1}{2} \lfloor \Delta q_m \rfloor \{D_2\} \lfloor D_2 \rfloor \{q_m\} \qquad \text{(A.31a)}$$
$$\Delta\mathcal{K}_m = \lfloor D_3 \rfloor \{\Delta q_m\}$$

Also, from Eqs. A.24, A.23c, A.27a, and A.29, one may write

$$\begin{Bmatrix} v \\ w \\ \psi \end{Bmatrix} = \begin{bmatrix} U(\eta) \\ G_\psi(\eta) \end{bmatrix} \{\beta\} \equiv \begin{bmatrix} U(\eta) \\ G_\psi(\eta) \end{bmatrix} [A^{-1}] \{q\} \equiv [N(\eta)] \{q\} \tag{A.32}$$

Accordingly, consistent with the assumed displacement field, one may express the velocities $\dot{v}$, $\dot{w}$, and $\dot{\psi}$ (where $\dot{(\ )}$ denotes the time derivative) as

$$\begin{Bmatrix} \dot{v} \\ \dot{w} \\ \dot{\psi} \end{Bmatrix} = [N(\eta)] \{\dot{q}\} \tag{A.33}$$

A.3.3 Finite Element Properties

The finite element property matrices of interest are [m], {p}, [h], and {f} given, respectively, by Eqs. A.9a, A.9b, A.9c, and A.9d for use in the "unconventional formulation" -- to which the present review is being restricted. In addition, however, as explained later it is useful to evaluate the element stiffness matrix [k] for linear behavior as given by Eq. A.14a.

Element Mass Matrix [m]

Since

$$[m] = \int_{V_{n_e}} \{U_i\} \rho_o [U_i] \, dV \tag{A.9a}$$

one needs to form $U_i(\xi^j)$ as indicated by Eq. A.6. For this case, using Eqs. A.22 and A.32, one obtains

$$u_i(\xi^j) \equiv \begin{Bmatrix} \tilde{v} \\ \tilde{w} \end{Bmatrix} = \begin{bmatrix} 1 & 0 & -\zeta \\ 0 & 1 & 0 \end{bmatrix} \begin{Bmatrix} v \\ w \\ \psi \end{Bmatrix} = \underset{2\times 3}{\begin{bmatrix} 1 & 0 & -\zeta \\ 0 & 1 & 0 \end{bmatrix}} \underset{3\times 8}{[N(\eta)]} \underset{8\times 1}{\{q\}} \tag{A.34}$$

Comparing Eq. A.34 with Eq. A.6,

$$\underset{2\times 8}{[U_i]} = \underset{2\times 3}{\begin{bmatrix} 1 & 0 & -\zeta \\ 0 & 1 & 0 \end{bmatrix}} \underset{3\times 8}{[N(\eta)]} \tag{A.35}$$

Hence, from Eq. A.9a, [m] becomes

$$[m] = \int_{V_{n_o}} [N(\eta)]^T \rho_o \begin{bmatrix} 1 & 0 \\ 0 & 1 \\ -\zeta & 0 \end{bmatrix} \begin{bmatrix} 1 & 0 & -\zeta \\ 0 & 1 & 0 \end{bmatrix} [N(\eta)] \, d\xi \, d\eta \left(1 + \frac{\zeta}{R}\right) d\zeta \tag{A.36}$$

Performing the $d\xi \, d\zeta$ integration at any station η and neglecting the $\frac{\zeta}{R}$ terms for thin rings, one obtains

$$\underset{8\times 8}{[m]} = \int_0^{\eta_i} \underset{8\times 3}{[N(\eta)]^T} \underset{3\times 3}{[B(\eta)]} \underset{3\times 8}{[N(\eta)]} \, d\eta \tag{A.36a}$$

where for a beam of uniform width b,

$$B(\eta) = \iint \rho_o \begin{bmatrix} 1 & 0 \\ 0 & 1 \\ -\zeta & 0 \end{bmatrix} \begin{bmatrix} 1 & 0 & -\zeta \\ 0 & 1 & 0 \end{bmatrix} d\xi \, d\zeta = \rho_o b \begin{bmatrix} h(\eta) & 0 & 0 \\ 0 & h(\eta) & 0 \\ 0 & 0 & \frac{h^3(\eta)}{12} \end{bmatrix} \tag{A.36b}$$

Recall that ρ_o is the mass per unit volume of the undeformed body and the integration is performed over the undeformed volume. In practice, the integration indicated in Eq. A.36a to form [m] is performed numerically — by Gaussian quadrature. Note that [m] is formed by using the assumed displacement field which is used also to determine the strain γ_{11}; hence, this [m] is called the consistent mass matrix and is a heavily populated matrix. The use of both consistent-mass matrices and diagonalized-mass matrices is discussed in Subsection 2.5.3.

Element Matrices {p} and [h]

Note that these matrices are given by

$$\{P\} = \int_{V_{n_o}} \{D_{ij}\} S^{ij} \, dV \tag{A.9b}$$

$$[h] = \int_{V_{n_o}} \{D_{ai}\} [D_j^a] S^{ij} \, dV \tag{A.9c}$$

Since the only "mating non-zero strains and stresses" present in this problem are γ_{11} and S^{11}, the indicated summation becomes quite compact; for convenience, let $S^{11} \equiv \sigma$ and $\gamma_{11} \equiv \varepsilon$. Also, note from Eq. A.7 that D_{ij} pertains to the linear part of γ_{11}; hence, from Eqs. A.7, A.23a, and A.30, it is seen that

$$\lfloor D_{ij} \rfloor \equiv \lfloor D_{11} \rfloor \equiv \left(\lfloor D_1 \rfloor + \zeta \lfloor D_3 \rfloor \right) \tag{A.37a}$$

Also, the nonlinear-term contributions provide

$$\{D_{ai}\} \lfloor D_{ij}^{a} \rfloor \equiv \left(\{D_1\} \lfloor D_1 \rfloor + \{D_2\} \lfloor D_2 \rfloor \right) \tag{A.37b}$$

Hence, Eqs. A.9b and A.9c become

$$\{P\} = \int_{V_{n_o}} \left(\lfloor D_1 \rfloor + \zeta \lfloor D_3 \rfloor \right) \sigma \, dV \tag{A.38}$$

$$[h] = \int_{V_{n_o}} \left(\{D_1\} \lfloor D_1 \rfloor + \{D_2\} \lfloor D_2 \rfloor \right) \sigma \, dV \tag{A.39}$$

Since D_1, D_2, and D_3 are functions only of η, one can perform first the $d\xi \, d\zeta$ integration and then the $d\eta$ integration. Accordingly, let

$$L(\eta) = \iint \sigma \, d\xi \, d\zeta \quad \text{and} \quad \hat{M} = \iint \zeta \sigma \, d\xi \, d\zeta \tag{A.40}$$

Applying Eqs. A.40 to Eqs. A.38 and A.39, one obtains, respectively:

$$\{P\} = \int_0^{\eta_i} \left(\{D_1\} L(\eta) + \{D_3\} \hat{M}(\eta) \right) d\eta \tag{A.38a}$$

$$[h] = \int_0^{\eta_i} \left(\{D_1\} \lfloor D_1 \rfloor + \{D_2\} \lfloor D_2 \rfloor \right) L(\eta) \, d\eta \tag{A.38b}$$

Since the stress σ varies, in general, at each time step or instant at every location within the volume of the element, {p} and [h] are evaluated by

numerical Gaussian quadrature at each time instant of the timewise solution process.

Element Applied-Force Vector {f}

This element applied-force vector {f} involves only the surface traction term since, for this discussion, it has been assumed that no body forces f^i are present. Hence, Eq. A.9d simplifies to

$$\{f\} = \int_{A_{\sigma_{n_o}}} \{U_i\}_b \, \underset{\sim o}{T}^i \, dA \tag{A.41}$$

For convenience and simplicity, let it be assumed that the surface integrations of the prescribed applied surface tractions $\underset{\sim o}{T}^i$ have already been performed at each circumferential station η so as to provide force resultants $F_v(\eta)$ and $F_w(\eta)$, and the moment resultant $M_\psi(\eta)$ each per unit spanwise distance. In this case, Eq. A.41 reduces to

$$\{f\} = \int_o^{\eta_i} [N(\eta)]^T \begin{Bmatrix} F_v \\ F_w \\ M_\psi \end{Bmatrix} d\eta \tag{A.42}$$

Element Stiffness Matrix [k]

In the present discussion, the equations of motion for the complete discretized structure are based on an "unconventional" formulation in which the conventional elastic stiffness matrix, [K], for the "complete assembled structure" does not appear explicitly. However, in order to calculate an allowable time step size, Δt, for the conditionally-stable central-difference timewise operator, the largest natural frequency contained in the (linear) mathematical model of the structure must be determined. To perform this calculation, the elastic stiffness matrix for the assembled structure must be computed. The elastic stiffness matrix [k] for an element is given by Eq. A.14a:

$$[k] = \int_{V_{n_o}} \{D_{ij}\} E^{ijkl} [D_{kl}] \, dV \tag{A.14a}$$

For the present problem E^{ijkl} is simply the elastic modulus E and $[D_{kl}] \equiv ([D_1] + \zeta[D_3])$. Hence, one obtains, after performing the $d\xi\, d\zeta$ integration for thin rings:

$$[k] = \int_0^{\eta_i} \left(\{D_1\} E b h(\eta) [D_1] + \{D_3\} \frac{E b h^3(\eta)}{12} [D_3] \right) d\eta \qquad \text{(A.43)}$$

A.4 Stress-Strain Description

For convenience and simplicity, the mechanical sublayer model is employed to describe the mechanical behavior of the structural material which is assumed to be ductile. In the mechanical sublayer model, the uniaxial tension (or compression) stress-strain curve of the material is first approximated by (n+1) piecewise-linear segments which are defined at coordinates $[(\sigma_k, \varepsilon_k), k = 1, 2, \ldots n]$, as depicted in Fig. A.2a. Next, the material is envisioned as consisting, at any point in the material, of n equally-strained "sublayers" of elastic perfectly-plastic material, with each sublayer k having the same elastic modulus E, but an appropriately different yield stress σ_{ok} (see Fig. A.2b). For example, the yield stress of the kth sublayer is

$$\sigma_{ok} = E \epsilon_k \qquad k = 1, 2, \ldots, n \qquad \text{(A.44)}$$

Then, the stress value, σ_k, associated with the kth sublayer can be defined uniquely by the strain history and the value of strain and strain-rate present at that point. Taken collectively with an appropriate weighting factor C_k for each sublayer, the stress, σ, at that point corresponding to strain ε may be expressed as

$$\sigma = \sum_{k=1}^{n} C_k \, \sigma_k(\epsilon) \qquad \text{(A.45)}$$

where the weighting factor C_k for the kth sublayer may readily be confirmed to be

$$C_k = \frac{E_k - E_{k+1}}{E} \qquad \text{(A.46)}$$

where

$$E_1 \equiv E, \quad E_k = \frac{\sigma_k - \sigma_{k-1}}{\epsilon_k - \epsilon_{k-1}} \qquad (k = 2,3,\cdots n), \; E_{n+1} = 0 \tag{A.46a}$$

The elastic perfectly-plastic and linear strain-hardening constitutive relation may be treated as special cases. In the case of elastic perfectly-plastic behavior, there is only one sublayer, and in the case of linear strain-hardening material there are two sublayers and the yield limit of the second sublayer is taken sufficiently high so that the deformation in that sublayer remains elastic. Finally, it should be noted that the above rules for the mechanical-sublayer model require that the stress-strain curve being represented must be such that the stress either increases monotonically with increasing strain and/or reach a limit but it can not decrease; some of the implications of this restriction are discussed in Section 6.

From the computational point of view, the use of the mechanical-sublayer model is very convenient to analyze problems with general loading paths including loading, unloading, reloading, and cyclic loading. Its features include the "kinematic hardening rule" which takes the Bauschinger effect into account (see Fig. A.2c). Also, this mechanical sublayer model may readily accommodate the strain-rate effect. Figure A.3a illustrates schematically the uniaxial stress-strain behavior for a strain-rate dependent, elastic, perfectly-plastic material whose rate dependence is described by [24,25]:

$$\sigma_y = \sigma_o \left(1 + \left| \frac{\dot{\epsilon}}{D} \right|^{\frac{1}{p}} \right) \tag{A.47}$$

while Fig. A.3b depicts the corresponding behavior for a strain-hardening material which is represented by the mechanical sublayer model, each sublayer of which has the same values for the strain-rate constants D and p. For this special type of rate-dependent strain-hardening material, the stress-strain curve at a given strain rate $\dot{\epsilon}$ is simply a constant magnification of the static stress-strain curves along rays emanating from the origin.

Let it be assumed that at time instant t_m the stress and strains of all sublayers and, hence, of that material point are known. Between t_m and t_{m+1} let there be a strain increment $\Delta\varepsilon_{m+1}$ and an associated strain rate $(\Delta\varepsilon_{m+1})/(\Delta t)$. The individual sublayer stresses are found conveniently from the following:

$$\Delta\epsilon_{m+1} \begin{cases} > 0 \begin{cases} > \sigma_{yk} \longrightarrow \sigma_{k,m+1} = \sigma_{yk} \\ \leq \sigma_{yk} \longrightarrow \sigma_{k,m+1} = \sigma^{t}_{k,m+1} \end{cases} \\ = 0 \longrightarrow \sigma^{t}_{k,m+1} = \sigma_{k,m} \\ < 0 \begin{cases} \geq -\sigma_{yk} \longrightarrow \sigma_{k,m+1} = \sigma^{t}_{k,m+1} \\ < -\sigma_{yk} \longrightarrow \sigma_{k,m+1} = -\sigma_{yk} \end{cases} \end{cases} \tag{A.48}$$

where a "trial" value of stress at time t_{m+1} in the kth sublayer defined by:

$$\sigma^{t}_{k,m+1} = \sigma_{k,m} + E\,\Delta\epsilon_{m+1} \tag{A.49}$$

and

$$\sigma_{yk} = \sigma_{ok}\left(1 + \left|\frac{\dot{\epsilon}}{D}\right|^{\frac{1}{p}}\right) \tag{A.50}$$

is analogous to Eq. A.47 and applies to the kth sublayer. Once one has determined $\sigma_{k,m+1}$ for all sublayers at time t_{m+1}, Eq. A.45 is used to compute the actual uniaxial stress σ_{m+1} at that material location at t_{m+1}.

A.5 Transient Response Solution Procedure

For present illustrative purposes, let it be assumed that Eq. A.12, the "unconventional form" of the equations of motion, is to be used to carry out a timewise step-by-step solution in small increments Δt in time by using

the timewise central-difference operator. At time t=0, the structure is in a known unstressed unstrained state with $\{q^*\} = \{0\}$ and $\{\dot{q}^*\} = \{a\}$, for example. Also, the structure is subjected only to prescribed externally-applied transient loading.

Accordingly, Eq. A.12 is to be solved at a sequence of instants in time Δt apart by employing the following explicit, conditionally-stable, central difference, finite-difference time operator approximation for the acceleration $\ddot{q}_m$ at time t_m:

$$\ddot{q}_m = \frac{q_{m+1} - 2q_m + q_{m-1}}{(\Delta t)^2} + O(\Delta t)^2 \qquad \text{(A.51a)}$$

where $O(\Delta t)^2$ means that this finite-difference approximation has a truncation error of order $(\Delta t)^2$. Also, one may approximate the velocity $\dot{q}_m$ at time t_m by:

$$\dot{q}_m = \frac{q_{m+1} - q_{m-1}}{2(\Delta t)} + O(\Delta t)^2 \qquad \text{(A.51b)}$$

At time instant t_m the equations of motion (Eq. A.12) become:

$$[M]\{\ddot{q}^*\}_m + \{P\}_m + [H]_m\{q^*\}_m = \{F\}_m \qquad \text{(A.52)}$$

In Eq. A.52 all quantities, in general, except [M] change with time. If the solution of Eq. A.52 has been obtained for earlier times, one can compute $\{\ddot{q}^*\}_m$ from Eq. A.52 and then obtain $\{q^*\}_{m+1}$ from Eq. A.51a.

Assuming that at t=0 the structure is in a known condition $\{q^*\}_o = 0$ and $\{\dot{q}^*\}_o = \{a\}$, for example, one can readily obtain $\{q^*\}_1$ at $t = m\Delta t$ for m=1 from the following Taylor series expansion:

$$\{q^*\}_1 = \{q^*\}_o + \{\dot{q}^*\}_o \Delta t + \frac{1}{2}\{\ddot{q}^*\}_o (\Delta t)^2 + O(\Delta t)^3 \qquad \text{(A.53)}$$

since $\{F\}_o$ is prescribed and all other quantities are known.

In the timewise step-by-step solution process involving large-deflection elastic-plastic transient responses, $\{P\}_m$ and $[H]_m$ change with time and hence must be reevaluated, in general, at each instant in time. These quantities in turn are composed by assembling the contributions $\{p^*\}_m$ and $[h^*]_m$ from each finite element. It is seen that these quantities involve <u>volume</u> integrals of information involving, in general, the stress state S^{ij}. In practice, these evaluations are carried out by appropriate numerical integration; namely, Gaussian quadrature.

At any instant in time t_m (m=0,1,2,...), one needs to solve Eq. A.52 for $\{\ddot{q}^*\}_m$, which is of the form:

$$[M]\{x(t)\}_m = \{b(t)\}_m \qquad \text{for} \quad m = 0, 1, 2, \cdots \qquad \text{(A.54)}$$

where

- $[M]$ is a <u>known</u> banded positive definite symmetric matrix (the mass matrix for the restrained or unrestrained structure, whichever case is being treated).
- $\{x(t)\}_m$ is a vector of unknowns which must be determined by solving Eq. A.54.
- $\{b(t)\}_m$ is a known vector (representing all terms except $[M]\{\ddot{q}^*\}_m$ in Eq. A.52).

In principle, one can always form the inverse matrix $[M]^{-1}$ and pre-multiply Eq. A.54 by $[M]^{-1}$ to obtain

$$[M]^{-1}[M]\{x(t)\}_m = [M]^{-1}\{b(t)\}_m$$

which results in the solution:

$$\{x(t)\}_m = [M]^{-1}\{b(t)\}_m \qquad \text{(A.55)}$$

since $[M]^{-1}[M] = [I]$ where $[I]$ is the unit diagonal matrix. However, it has been found that independent of the number of time instants at which one

wishes to solve Eq. A.54, such a procedure is not as efficient as is the Choleski method [49].

Briefly, the Choleski method involves factoring the matrix [M] to form a lower triangular matrix [L] and an upper triangular matrix (which is the transpose of the former) such that $[M] = [L]\,[L]^T$ where $[L]^T$ is the transpose of [L]. Thus, Eq. A.54 may be rewritten as

$$[L][L]^T\{x(t)\}_m = \{b(t)\}_m \tag{A.56}$$

Next, form an intermediate matrix $\{y\}_m$ which is defined as

$$\{y\}_m = [L]^T\{x(t)\}_m \tag{A.57}$$

From Eqs. A.56 and A.57, it follows that

$$[L]\{y\}_m = \{b(t)\}_m \tag{A.58}$$

At each time instant, one solves Eq. A.58 for $\{y\}_m$ very readily because [L] is a lower triangular matrix. One then solves Eq. A.57 for $\{x\}_m$ very rapidly also by algebraic back-substitution.

The following gives a concise step-by-step description of the typical problem formulation and solution process.

Starting from a set of given initial conditions at time $t = t_o = 0$ on the generalized displacements ($\{q^*\} = \{0\}$, for example) and the generalized velocities $\{\dot{q}\}_o$, one can solve Eq. A.52 for $\{\ddot{q}^*\}_o$ at time t_o and then employ Eq. A.53 to compute $\{q^*\}_1$. A slightly different but similar procedure is then used to advance the solution in successive time increments Δt. The process involved in using the finite-element method and the present timewise solution procedure follows [20]:

Step 1: Construct the mass matrix [m] for each finite element and then assemble these contributions according to Eq. A.12a to form the mass matrix [M] for the complete assembled discretized structure. This [M]

represents the "final" mass matrix if the structure has none of its generalized displacements constrained (that is, held equal to zero, for example); however, if such constraints exist, one forms a reduced or constrained mass matrix (and, in fact, a reduced set of the equations of motion) by deleting the rows and columns of [M] associated with those generalized displacements which are prescribed to be zero. Next, this constrained mass matrix is factored to consist of a lower triangular matrix [L] and an upper triangular matrix $[L]^T$ according to the Choleski scheme:

$$[M] = [L][L]^T \tag{A.59}$$

Since [M] does not change in value with time as the transient structural response proceeds, one needs to determine [L] and $[L]^T$ only once — these quantities need not be re-evaluated at each time step of the calculation.

Step 2: The prescribed externally-applied transient forces can be employed to calculate the generalized applied forces {f*} acting on each discrete element at each time instant t_m of interest. These, in turn, can be assembled according to Eq. A.12d to form the assembled applied-loads vector {F} for the complete assembled discretized structure.

Step 3: Assuming that at zero time (t = 0), the generalized displacements $\{q^*\}_o = 0$, the generalized velocities are nonzero $\{\dot{q}^*\}_o = \{a\}$, and that nonzero external forces $\{F\}_o$ are present, Eq. A.52 becomes

$$[M]\{\ddot{q}^*\}_o = \{F\}_o \tag{A.60}$$

or

$$[L][L]^T\{\ddot{q}^*\}_o = \{F\}_o \tag{A.60a}$$

from which one can calculate $\{\ddot{q}^*\}_o$ by using the earlier-described Choleski scheme. Then from Eq. A.53 one obtains

$$\{\Delta q^*\}_1 = \Delta t \{\dot{q}^*\}_o + \frac{1}{2}(\Delta t)^2 \{\ddot{q}^*\}_o \tag{A.61}$$

where

$$\{\Delta q^*\}_1 = \{q^*\}_1 - \{q^*\}_o \tag{A.62}$$

$$\{\dot{q}^*\}_o = \{a\} = \text{prescribed initial generalized velocities} \tag{A.62a}$$

Also,

$$\{q^*\}_1 = \{q^*\}_o + \{\Delta q^*\}_1 \tag{A.63}$$

For this case, however, it has been assumed that $\{q^*\}_o = \{0\}$. Thus, the displacement configuration $\{q^*\}_1$ at time $t_1 = t_o + \Delta t$ is known.

Step 4: Knowing the generalized nodal displacement increments $\{\Delta q^*\} \equiv \{q^*\}_1 - \{q^*\}_o$ and the generalized nodal displacements $\{q^*\}_1$ at time t_1, one knows also the unstarred individual element quantities $\{\Delta q\}_1$ and $\{q\}_1$ via Eq. A.10. Hence, one can calculate, in general, the strain increment $(\Delta\gamma_{ij})_1$ developed from t_o to t_1 at every Gaussian station (or point) required over and depthwise through each finite element from Eqs. A.23a and A.30:

$$(\Delta\gamma_{ij})_1 = (\gamma_{ij})_1 - (\gamma_{ij})_o \tag{A.64}$$

$$= [D_{ij}]\{\Delta q\}_1 + [q]_1\{D_{ai}\}[D_j^a]\{\Delta q\}_1 - \frac{1}{2}[\Delta q]_1\{D_{ai}\}[D_j^a]\{\Delta q\}_1$$

With a knowledge of (a) the stresses at $t_o = t_1 - \Delta t$, and (b) the strain increment $(\Delta\gamma_{ij})_1$, one can determine the stress increments $(\Delta S^{ij})_1$ and the stresses $(S^{ij})_1$ at time t_1 at each Gaussian station by using the pertinent elastic-plastic stress-strain relations,

including the yield condition and flow rule, in general. However, a simpler procedure will suffice for the present problems[+].

Step 5: Next, one can calculate $\{p\}_1$ and $[h]_1$ for each individual finite element by using Eqs. A.38a and A.38b, respectively. Assembly of this information according to Eqs. A.12b and A.12c, respectively, provides $\{P\}_1$ and $[H]_1$. Since the prescribed generalized force vector $\{F\}_1$ is available from known $\{f\}_1$ information, the equation of motion, Eq. A.52, at time instant t_1 becomes:

$$[M]\{\ddot{q}^*\}_1 = \{F\}_1 - \{P\}_1 - [H]_1\{q^*\}_1 \tag{A.65}$$

In the interest of minimizing computer storage and the number of manipulations, one first forms for each individual element $\{b_n\}_1 \equiv (\{f\} - \{p\} - [h]\{q\})_1$. Then one forms the right-hand side vector of Eq. A.65 by

$$[J]^T\{\underset{\sim}{b}_1 \quad \underset{\sim}{b}_2 \quad \cdots \quad \underset{\sim}{b}_N\} \tag{A.66}$$

For clarity of discussion, however, the form of the equation represented by Eq. A.65 is used here.

Step 6: Since the right-hand side of Eq. A.65 is now known, one can use the Choleski scheme to solve the following equation for the acceleration $\{\ddot{q}^*\}_1$:

$$[L][L]^T\{\ddot{q}^*\}_1 = \left(\{F\} - \{P\} - [H]\{q^*\}\right)_1 \tag{A.66a}$$

Step 7: With $\{\ddot{q}^*\}$ now known, one can calculate the generalized displacement increment $\{\Delta q^*\}_2$ from Eq. A.51a as

$$\{\Delta q^*\}_2 = \{\Delta q^*\}_1 + (\Delta t)^2\{\ddot{q}^*\}_1 \tag{A.66b}$$

where

$$\{\Delta q^*\}_2 = \{q^*\}_2 - \{q^*\}_1 \tag{A.67a}$$

[+]See Eqs. A.48 - A.50.

$$\{\Delta q^*\}_1 = \{q^*\}_1 - \{q^*\}_0 \qquad \text{(A.67b)}$$

Thus, from Eq. A.67a one has

$$\{q^*\}_2 = \{q^*\}_1 + \{\Delta q^*\}_2 \qquad \text{(4.37)}$$

The process then proceeds cyclically from Step 4 onwards for as many time steps as desired.

For the central-difference time operator applied to a system of equations such as Eq. A.12 or Eq. A.14, it has been shown [50,51] that Δt must be less than or equal to $2/\omega_{max}$ to avoid exponential growth of error (roundoff, truncation, gross) where ω_{max} is the largest frequency embedded in the mathematical model of the system. The criterion $\Delta t < 2/\omega_{max}$ must be satisfied for a linear dynamic system such as that involving small-displacement linear-elastic behavior. However, for nonlinear large-displacement elastic or elastic-plastic behavior, numerical experimentation [17, for example] has confirmed that a smaller Δt is usually required to avoid this instability. As a rough guide one may try $\Delta t \lesssim 0.8(2/\omega_{max})$ as an initial selection; if this value is not small enough, the calculation will blow up (overflow) before many time steps have elapsed -- this behavior will be readily apparent. In such a case one must choose a smaller time increment Δt.

Alternately, one could employ an implicit finite-difference time operator such as that of Houbolt [3,17,52] or Park [53], for example. The solution procedure is similar except that nonlinear large-deflection and plasticity effects are handled either by iteration or extrapolation. Further discussion of these alternate procedures is beyond the intended scope of this review.

Finally, this review of the solution procedure for the governing equations for large-deflection, elastic-plastic, 2-D structural response has has dealt with the case in which the structure has been subjected to prescribed transient externally-applied loading. For cases involving 2-D structural response produced by fragment impact, the reader is invited to read the (more lengthy) descriptions given in (1) Ref. 4 concerning single-layer structures and the CIVM-JET 4B program and (2) Ref. 5 concerning multilayer hard-bonded Bernoulli-Euler 2-D structures.

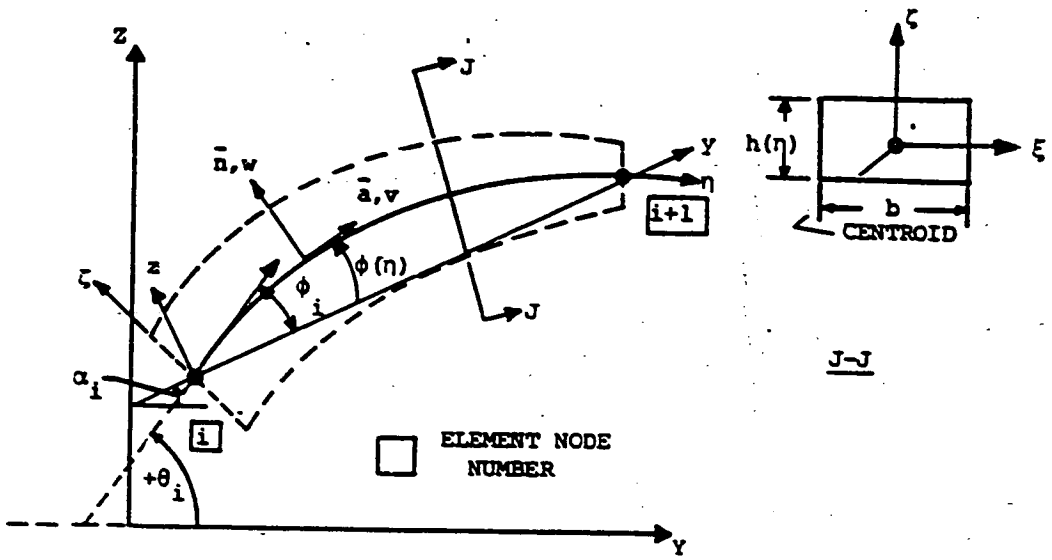

$$-15° \leq \phi_{i+1} - \phi_i \leq 0$$

$$-180° < \phi_i \leq 180°$$

$$\phi(\eta) = b_o + b_1 \eta + b_2 \eta^2$$

$$R(\eta) = -(\partial\phi/\partial\eta)^{-1}$$

$$h(\eta) = h_i \left(1 - \frac{\eta}{\eta_i}\right) + h_{i+1} \frac{\eta}{\eta_i}$$

LOCAL SYSTEM

ξ, η, ζ - COORDINATES

v, w, ψ, χ - DISPLACEMENTS

$q_1, q_2, \ldots q_8$ - ELEMENT GENERALIZED DISPLACEMENTS

$q_1\ q_2\ q_3\ q_4 = v_i\ w_i\ \psi_i\ \chi_i$

$$\psi = \frac{\partial w}{\partial \eta} - \frac{v}{R} \qquad \chi = \frac{\partial v}{\partial \eta} + \frac{w}{R}$$

CARTESIAN REFERENCE

Y,Z - GLOBAL COORDINATES

y,z - LOCAL COORDINATES

FIG. A.1 NOMENCLATURE FOR GEOMETRY, COORDINATES, AND DISPLACEMENTS OF A CURVED-BEAM FINITE ELEMENT

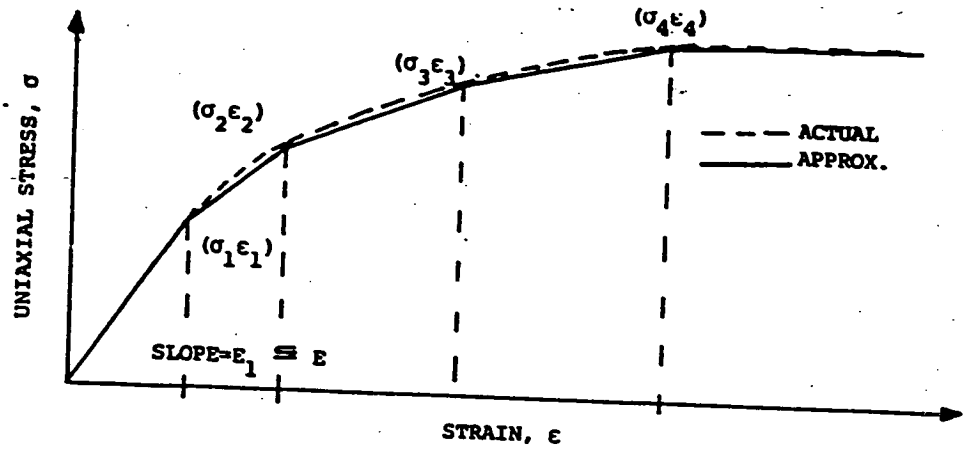

(a) Actual and Approximated Curves

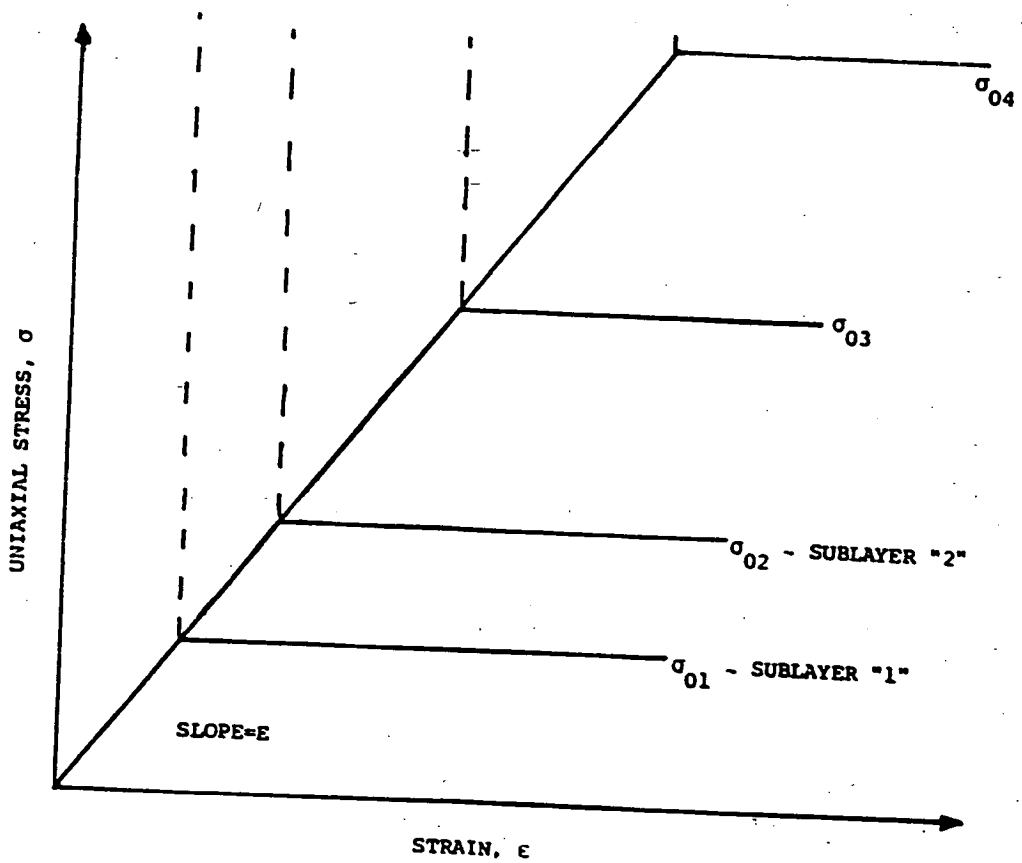

(b) Properties of the Elastic, Perfectly-Plastic Sublayers

FIG. A.2 APPROXIMATION OF A UNIAXIAL-STRESS-STRAIN CURVE BY THE MECHANICAL SUBLAYER MODEL

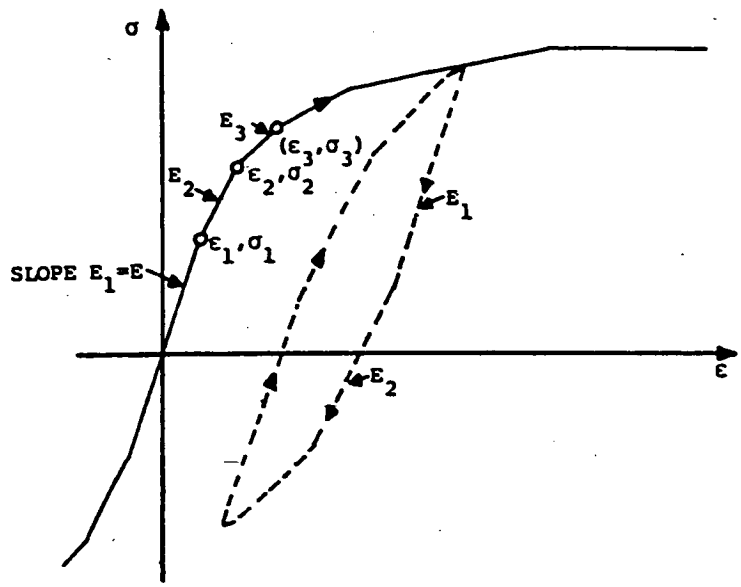

(c) Schematic of Loading, Unloading, and Reloading Paths

FIG. A.2 CONCLUDED

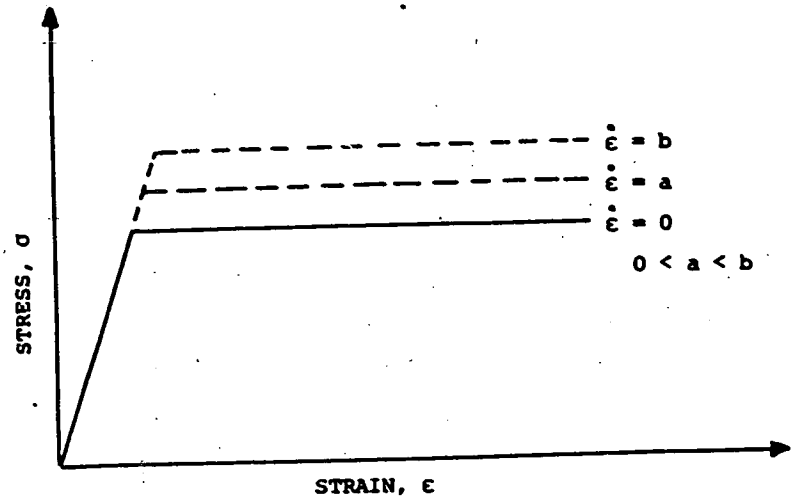

(a) Elastic, Perfectly-Plastic Material

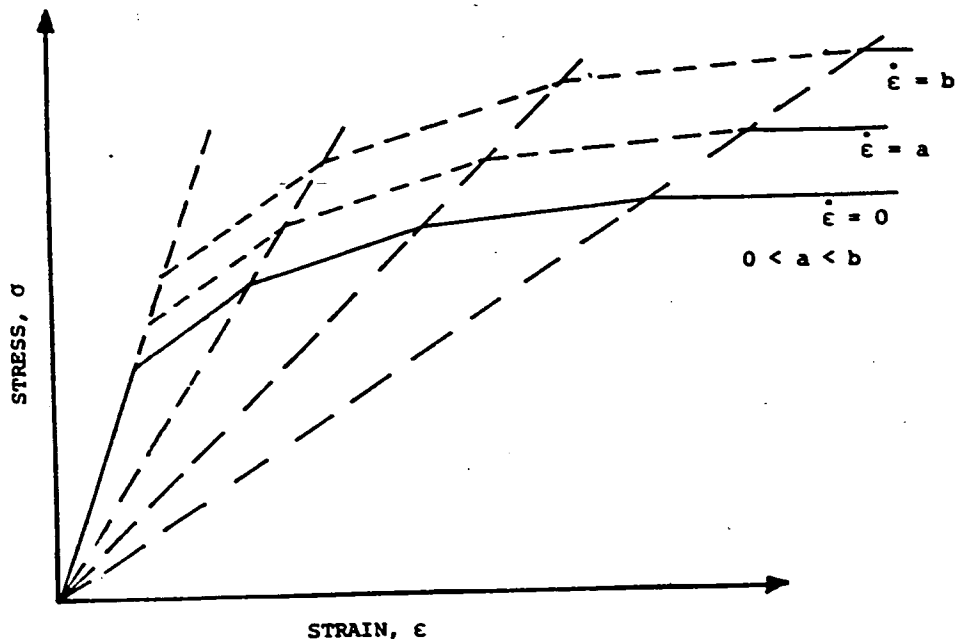

(b) Special Strain Hardening Material

FIG. A.3 SCHEMATIC OF STRAIN-RATE DEPENDENT UNIAXIAL STRESS-STRAIN CURVES

APPENDIX B

SUMMARY OF RELATIONS FOR FINITE STRAIN CONDITIONS

B.1 Objectives

The intention in this appendix is to summarize the pertinent strain-displacement and stress-strain relations needed for the finite element transient elastic-plastic response analysis of 2-D beams and/or rings when finite strains must be taken into account. These relations are developed in detail in Ref. 54.

B.2 Strain-Displacement Relations

Let it be assumed that a curved beam element (such as depicted in Fig. A.1 with curvilinear coordinates ξ, η, ζ in directions 1, 2, and 3, respectively) deforms according to the Bernoulli-Euler hypothesis but modified to account for deformation-induced thickening or thinning of the structure. That is, it is assumed that:

(a) plane sections remain plane,

(b) normals to the midsurface (or reference surface -- centroidal axis) before deformation remain normal to that reference surface after deformation, but

(c) these normals may stretch or contract -- according to the imposed approximation that in the plastic range the material behaves as being incompressible (this is also assumed to be true in the elastic range since the elastic strains are assumed to be small).

Further, concerning item (c) let it be assumed that when a finite circumferential extensional strain γ_2^2 is present, structural thickening or thinning occurs ($\gamma_3^3 \neq 0$) but the structure undergoes no strain in the across-the-width (or ξ) direction (that is, $\gamma_1^1 = 0$). In this case, one can show [54] that the extensional strains γ_1^1, γ_2^2, and γ_3^3 at any Lagrangian ξ, η, ζ^o location in the structure are given by:

$$\gamma_1' = 0 \tag{B.1}$$

$$\gamma_2^2 = \overset{\circ}{\gamma}_2^2 + \zeta^\circ \frac{\mathcal{K}}{(1+2\overset{\circ}{\gamma}_2^2)} \tag{B.2}$$

$$\gamma_3^3 = \frac{1}{2}\left[\frac{1}{(1+2\overset{\circ}{\gamma}_2^2)} - 1\right] \tag{B.3}$$

where

ζ° is the ζ-location of the "material" before deformation (identified by superscript "o")

$$\overset{\circ}{\gamma}_2^2 = \chi + \frac{1}{2}\psi^2 + \frac{1}{2}\chi^2 \tag{B.2a}$$

= the membrane strain at $\zeta^\circ = 0$

$$\mathcal{K} = \left(-\frac{\partial\psi}{\partial\eta}\right)(1+\chi) + \psi\frac{\partial\chi}{\partial\eta} \tag{B.2b}$$

= "change of curvature"

The quantities χ and ψ are as defined by Eqs. A.23b and A.23c, respectively. Also, it can be shown [54] that the true change of curvature referred to the deformed midsurface is given by

$$\frac{d\theta}{ds} = -\frac{\mathcal{K}}{(1+2\overset{\circ}{\gamma}_2^2)^{3/2}} \tag{B.4}$$

where θ is the angle of rotation, and s is the coordinate along the deformed reference surface. Thinning effects are also included in Eqs. B.1-B.3.

It should be noted that Eqs. B.1 through B.3 apply for finite strains and are denoted hereinafter, for convenience, as the Type F strain-displacement relations; however, the structure must be thin such that $1 + \frac{\zeta^\circ}{R} \simeq 1$, where R is the original undeformed radius of curvature. On the other hand, it should be emphasized that the "small strain" expression for γ_2^2 given by

Eq. A.23 applies to both small strains and small rotations such that $1 + \frac{1}{2}\gamma_2^2 \simeq 1$, $\sin\theta \simeq \theta$, and $\cos\theta \simeq 1$ where θ is the angle of rotation.

B.3 Assumed-Displacement Field

For the Bernoulli-Euler displacement behavior cited in Subsection B.2, the assumed-displacement field for a curved beam or ring remains the same as that defined in Subsection A.3.2.

For convenient reference, the strain-displacement relations termed Types A, B, C, D, and E in Ref. 20 are (in the present notation) given by:*

$$\gamma_2^2 = \chi + \frac{1}{2}\psi^2 + \frac{1}{2}\chi^2 + \zeta^o\left[\left(-\frac{\partial\psi}{\partial\eta}\right)(1+\chi) + \psi\frac{\partial\chi}{\partial\eta}\right] + \frac{(\zeta^o)^2}{2}\left[\left(\frac{\partial\psi}{\partial\eta}\right)^2 + \left(\frac{\partial\chi}{\partial\eta}\right)^2\right] \qquad \text{(B.5)}$$

Type A

Type B

Type D

Type E

Type C

B.4 Finite-Element Properties

The finite element property matrices of interest are [m], {p}, [h], and {f} as given by Eqs. A.9a, A.9b, A.9c, and A.9d, respectively, and/or by Eqs. A.36a, A.38, A.39, and A.41, respectively. Note that each of these matrices is evaluated by volume or surface integrals over the original undeformed volume or surface. These evaluations are straightforward except for {p} and [h] given by Eqs. A.9b and A.9c, respectively, which involves the use of the second Piola-Kirchhoff stress S^{ij} -- however, in finite-strain plasticity one works with the Kirchhoff stress τ versus logarithmic strain ε^*. Thus, one can represent the mechanical stress-strain property data from uniaxial (direction η or "2") static (superscript "s") tensile and/or compression data in terms of τ_u vs. ε_u^* since this stress-strain information is essentially perfectly antisymmetric with τ monotonically increasing (decreasing) as ε^* increases (decreases), where

* Note that Eq. B.2 may be viewed as a "modification" of the Type E relation given in Eq. B.5.

$$\overset{s}{\tau}_u = \sigma_E \left(1 + \tilde{E}_u\right) \tag{B.6}$$

$$\epsilon_u^* \doteq \ln \frac{l}{l_o} \equiv \ln \left(1 + \tilde{E}_u\right) \tag{B.7}$$

and

$\sigma_E = \frac{P}{A_o}$ = engineering stress of a uniaxial static test specimen; P is the applied load and A_o is the pre-test cross-sectional area of the specimen

$\tilde{E}_u$ = the measured axial (η-direction) relative elongation (also known as the engineering strain) of the uniaxial test specimen

= $\frac{\text{change in gage length}}{\text{original gage length}}$

= output which strain gages or extensometers can provide

Necking effects, if any, should be deleted from the data. Next, one makes a piecewise-linear fit of the τ_u vs. ϵ_u^* data in terms of n + 1 segments defined by the coordinate $(\tau_u)_k$, $(\epsilon_u^*)_k$, k = 1,2,...,n; the coordinates of these segments are used in the mechanical sublayer material model to represent this behavior. According to the mechanical sublayer model, the material is envisioned as consisting, at any point in the material, of n equally-strained sublayers of elastic, perfectly-plastic material with each sublayer having the same elastic modulus E but an appropriately different yield stress. For example, the static yield stress of the kth sublayer is given by

$$\left(\overset{s}{\tau}_u\right)_k = E \left(\epsilon_u^*\right)_k \tag{B.8}$$

Hence, at any given state of strain ϵ_u^*, the associated stress τ_u is given by

$$\overset{s}{\tau}_u = \sum_{k=1}^{n} A_k \left(\tau_u\right)_k \tag{B.9}$$

where the weighting factor A_k for the kth mechanical sublayer may be readily confirmed to be:

$$A_k = \frac{E_k - E_{k-1}}{E} \tag{B.10}$$

where $E_1 \equiv E$ for k = 1

$$E_k = \frac{(\tau_u)_k - (\tau_u)_{k-1}}{(\epsilon_u^*)_k - (\epsilon_u^*)_{k-1}} \quad \text{for } k = 2,3,\ldots n \tag{B.11}$$

$$E_{n+1} = 0$$

The mechanical sublayer model is very convenient to analyze problems with general loading paths -- including loadin. unloading, reloading, and cyclic loading; also, it approximates the Bauschinger effect reasonably well. Further, strain-rate effects can be accommodated by treating the sublayer yield stress as being strain-rate dependent according to:

$$\left(\tau_u\right)_k = \left(\overset{s}{\tau}_u\right)_k \left[1 + \left|\frac{D_u}{d}\right|^{\frac{1}{p}}\right] \tag{B.12}$$

where $(\tau_u)_k$ is the rate-dependent yield stress, $D_u \equiv \frac{\dot{\ell}}{\ell}$ = rate-of-deformation axial component in a uniaxial test, and d and p are material constants which could be evaluated from experiments for each mechanical sublayer. Hence, the stress at any given condition of strain ε^* and strain rate D_u may be written as

$$\tau_u = \sum_{k=1}^{n} A_k \left(\tau_u\right)_k \tag{B.13}$$

For a curved beam which experiences: (1) significant circumferential (η or "2" direction) strain and through-the-thickness (ζ or "3" direction)

strain but negligible lateral (ξ or "1" direction) strain and (2) non-negligible stresses τ_2^2 only in the η-direction, one may express the stress rate $(\dot{\tau}_2^2)_k$ for the kth sublayer in terms of the circumferential component D_2^2 of the rate of deformation tensor by

$$(\dot{\tau}_2^2)_k = E\, D_2^2 \tag{B.14}$$

if D_2^2 is entirely elastic (i.e., if $D_2^2 = (D_2^2)^e$) and hence $[(\tau_2^2)_k]^2 \leq [(\tau_u)_k]^2$. However,

if $$(\tau_2^2)_k > (\tau_u)_k \;,\; (\tau_2^2)_k = (\tau_u)_k \tag{B.15}$$

and if $$(\tau_2^2)_k < -(\tau_u)_k \;,\; (\tau_2^2)_k = -(\tau_u)_k \tag{B.16}$$

Accordingly, the total stress τ_2^2 at a given deformation and rate of deformation is given by

$$\tau_2^2 = \sum_{k=1}^{n} A_k (\tau_2^2)_k \tag{B.17}$$

However, for the evaluation of the element property matrices {p} and [h], one needs to evaluate and use the second Piola-Kirchhoff stress S^{ij} or S^i_j and the associated Lagrangian or Green strain γ_{ij} or γ^j_i. Thus, one makes use of the following relations [54]:

$$\tau_2^2 = S_2^2 (1 + 2\gamma_2^2) \tag{B.18a}$$

$$\dot{\tau}_2^2 = \dot{S}_2^2 (1 + 2\gamma_2^2) + 2 S_2^2 \dot{\gamma}_2^2 \tag{B.18b}$$

$$D_2^2 = \frac{\dot{\gamma}_2^2}{(1 + 2\gamma_2^2)} \tag{B.18c}$$

In the timewise step-by-step solution process and associated computer program, one has available γ_2^2 and $\dot{\gamma}_2^2$. Thus, since

$$\tau_2^2 = \sum_{k=1}^{n} A_k \left(\tau_2^2\right)_k \tag{B.19a}$$

and

$$\left(\tau_2^2\right)_k = \left(S_2^2\right)_k \left(1 + 2\gamma_2^2\right) \tag{B.19b}$$

it follows that

$$S_2^2\left(1+2\gamma_2^2\right) = \sum_{k=1}^{n} \left[A_k \left(S_2^2\right)_k \left(1+2\gamma_2^2\right)\right] \tag{B.19c}$$

$$= \left(1+2\gamma_2^2\right) \sum_{k=1}^{n} A_k \left(S_2^2\right)_k$$

Hence,

$$S_2^2 = \sum_{k=1}^{n} A_k \left(S_2^2\right)_k \tag{B.20}$$

Next, one can rewrite Eq. B.14 in terms of second Piola-Kirchhoff stress and Lagrangian (Green) strain information from Eqs. B.18b and B.18c to obtain for the kth sublayer:

$$\left(\dot{S}_2^2\right)_k \left(1+2\gamma_2^2\right) + 2\left(S_2^2\right)_k \dot{\gamma}_2^2 = E \frac{\dot{\gamma}_2^2}{\left(1+2\gamma_2^2\right)}$$

or

$$\left(\dot{S}_2^2\right)_k = \frac{\left[E - 2\left(1+2\gamma_2^2\right)\left(S_2^2\right)_k\right]}{\left(1+2\gamma_2^2\right)^2} \dot{\gamma}_2^2 \tag{B.21}$$

One may integrate this differential expression by means of the trapezoidal rule, for example, from time instant i-1 to an incrementally close instant i to obtain:

$$\Delta S_k = \frac{\left\{E - 2\,S_k^{i-1}\left[(1+2\gamma^i) - \Delta\gamma\right]\right\}}{\left[(1+2\gamma^i)^2 - (1+2\gamma^i)\Delta\gamma + 2(\Delta\gamma)^2\right]}\,\Delta\gamma \qquad \text{(B.22)}$$

where

$$S_k \equiv \left(S_2^2\right)_k \qquad \text{(B.22a)}$$

$$\gamma \equiv \gamma_2^2 \qquad \text{(B.22b)}$$

$$\Delta S_k \equiv S_k^i - S_k^{i-1} \qquad \text{(B.22c)}$$

$$\Delta\gamma \equiv \gamma^i - \gamma^{i-1} \qquad \text{(B.22d)}$$

An illustration of the method used for computing the circumferential stress $(S_2^2)_i \equiv S^i$ at time t_i at any given circumferential station and any given depthwise station in a curved-beam element follows; such information is needed since the volume integrals defining {p} and [h] are evaluated by spanwise/depthwise numerical integration (in particular, Gaussian quadrature). Typically, one begins at the station in question by knowing the stress (S_k^{i-1}) and the strain (γ_k^{i-1}) of the kth sublayer at time t_{i-1} and the strain increment $\Delta\gamma$ at that station from time t_{i-1} to time t_i. To begin, one assumes as a trial (superscript T) that the trial stress at time t_i: S_k^{Ti} may be evaluated by following an incrementally-elastic path:

$$S_k^{Ti} = S_k^{i-1} + \frac{\left[E - 2\,S_k^{i-1}\left\{(1+2\gamma^i) - \Delta\gamma\right\}\right]}{\left[(1+2\gamma^i)^2 - (1+2\gamma^i)\Delta\gamma + 2(\Delta\gamma)^2\right]}\,\Delta\gamma \qquad \text{(B.23)}$$

A check is then performed as follows to see what the correct value of S_k^i must be:

(1) If $$-(\tau_u)_k \le \overset{T}{S}{}^i_k (1+2\gamma^i) \le (\tau_u)_k \ ,$$

$$S^i_k = \overset{T}{S}{}^i_k \tag{B.24}$$

(2) If $$\overset{T}{S}{}^i_k (1+2\gamma^i) > (\tau_u)_k \ ,$$

$$S^i_k = \frac{(\tau_u)_k}{(1+2\gamma^i)} \tag{B.25}$$

(3) If $$\overset{T}{S}{}^i_k (1+2\gamma^i) < -(\tau_u)_k \ ,$$

$$S^i_k = -\frac{(\tau_u)_k}{(1+2\gamma^i)} \tag{B.26}$$

This procedure is applied to all sublayers at the station in question. Hence, the stress $S_2^2 \equiv S^i$ at time t_i is given by

$$S^i \equiv (S_2^2)^i = \sum_{k=1}^{n} A_k \, S^i_k \tag{B.27}$$

In the above process, strain-rate effects have been taken into account by using:

$$(\tau_u)_k = (\overset{s}{\tau_u})_k \left[1 + \left| \frac{D_2^2}{d} \right|^{\frac{1}{p}} \right] \tag{B.28}$$

where D_2^2 is given by Eq. B.18c. Thus,

$$(\tau_u)_k = (\overset{s}{\tau_u})_k \left[1 + \left| \frac{\dot{\gamma}_2^2}{d(1+2\gamma_2^2)} \right|^{\frac{1}{p}} \right] \tag{B.29}$$

NASA-CR 159645 Two-dimensional finite-element analyses of simulated rotor-fragment impacts...

END

DATE

FILMED

JUN 24 1980